

**Some pages of this thesis may have been removed for copyright restrictions.**

If you have discovered material in AURA which is unlawful e.g. breaches copyright, (either yours or that of a third party) or any other law, including but not limited to those relating to patent, trademark, confidentiality, data protection, obscenity, defamation, libel, then please read our [Takedown Policy](#) and [contact the service](#) immediately

CATHODIC PROTECTION OF REINFORCED CONCRETE:

Anodic processes in cements and related electrolytes

CHRISTOPHER JOHN WEALE

Doctor of Philosophy

THE UNIVERSITY OF ASTON IN BIRMINGHAM

October 1992

This copy of the thesis has been supplied on condition that anyone who consults it is understood to recognise that its copyright rests with its author and that no quotation from the thesis and no information derived from it may be published without proper acknowledgement.



## SUMMARY

THE UNIVERSITY OF ASTON IN BIRMINGHAM

### CATHODIC PROTECTION OF REINFORCED CONCRETE:

Anodic processes in cements and related electrolytes

Christopher John WEALE

Doctor of Philosophy 1992

The nature and kinetics of electrode reactions and processes occurring for four lightweight anode systems which have been utilised in reinforced concrete cathodic protection systems have been studied. The anodes investigated were flame sprayed zinc, conductive paint and two activated titanium meshes. The electrochemical properties of each material were investigated in rapidly stirred de-oxygenated electrolytes using anodic potentiodynamic polarisation. Conductive coating electrodes were formed on glass microscope slides, whilst mesh strands were immersed directly. Oxygen evolution occurred preferentially for both mesh anodes in saturated  $\text{Ca(OH)}_2/\text{CaCl}_2$  solutions but was severely inhibited in less alkaline solutions and significant current only passed in chloride solutions. The main reactions for conductive paint was based on oxygen evolution in all electrolytes, although chlorides increased the electrical activity. Self corrosion of zinc was controlled by electrolyte composition and the experimental set-up, chlorides increasing the electrical activity.

Impressed current cathodic protection was applied to 25 externally exposed concrete slabs over a period of 18 months to investigate anode degradation mechanisms at normal and high current densities. Specimen chloride content, curing and reinforcement depth were also variables. Several destructive and non-destructive methods for assessing the performance of anodes were evaluated including a site instrument for quantitative "instant-off" potential measurements. The impact of cathodic protection on the concrete substrate was determined for a number of specimens using appropriate methods. Anodic degradation rates were primarily influenced by current density, followed by cementitious alkalinity, chloride levels and by current distribution. Degradation of cementitious overlays and conductive paint substrates proceeded by sequential neutralisation of cement phases, with some evidence of paint binder oxidation. Sprayed zinc progressively formed an insulating layer of hydroxide complexes, which underwent pitting attack in the presence of sufficient chlorides, whilst substrate degradation was minimal. Adhesion of all anode systems decreased with increasing current density.

The influence of anode material on the ionic gradients which can develop during cathodic protection was investigated. A constant current was passed through saturated cement paste prisms containing calcium chloride to central cathodes via anodes applied or embedded at each end. Pore solution was obtained from successive cut paste slices for anion and cation analyses. Various experimental errors reduced the value of the results. Characteristic S-shaped profiles were not observed and chloride ion profiles were ambiguous. Mesh anode specimens were significantly more durable than the conductive coatings in the high humidity environment. Limited results suggested zinc ion migration to the cathode region.

Electrical data from each investigation clearly indicated a decreasing order of anode efficiency by specific anode material.

Key words: cathodic protection, anode reaction, reinforced concrete, potentiodynamic polarisation, ionic migration



## Acknowledgements

The research described in this thesis was jointly funded as a Cooperative Award in Science and Engineering by the Science and Engineering Research Council and Taywood Engineering Ltd and I acknowledge this support. In addition I am grateful for further financial support provided by the Department of Civil Engineering at Aston University.

I am indebted to my academic supervisor Professor C. L. Page for his sustained guidance, advice and patience. Many thanks are extended for valuable technical assistance and advice at Aston University by Dr. G. Sergi, Dr. G. K. Glass and Mr. C. J. Thompson and in addition, Mr. R. Howell (SEM and XRD), Mr. R. G. Sibbick (Petrography), Dr. P. Corkhill (FT-IR), Dr. G. L. Hendry (ICP), Mr. R. Brueton (Thin sections) and the Civil Engineering department technicians.

I am grateful for the wide support provided by the Directors and staff of Taylor Woodrow Engineering Ltd., in particular the encouragement of my industrial supervisor Mr. K. W. J. Treadaway, the support of Dr. R. D. Browne, Mr. A. F. Winfield and Mr. R. Blundell, the helpful discussions with Dr. P. B. Bamforth, Mr. D. C. Pocock, Mr. R. A. Palmer, Mr. R. P. McAnoy and Mr. M. P. Geoghegan and the technical assistance of Mr. J. Barrass, Mr. W. Price, Mr. A. Blake, Mr C. Savvides and Mr. A. J. Ewins, who designed and built the freeze-hold voltmeter used in the project.

In addition, the help of Mr. M. J. Round of Metallisation Service Ltd. for flame spraying of microscope slides, ICI Chemicals and Polymers Ltd. and Thoro System Products Ltd.. for the supply of materials, and British Rail Research (Derby) for XRD analysis of corrosion products is acknowledged.

Finally, I wish to thank Victoria for her constant support and encouragement and our parents, family and friends who have helped me throughout this project.

## List of contents

<b>Summary .....</b>	<b>2</b>
<b>Acknowledgements.....</b>	<b>3</b>
<b>List of contents.....</b>	<b>4</b>
<b>1. Chapter One. Introduction.....</b>	<b>25</b>
1.1. Introduction .....	25
1.1.1. Corrosion of concrete .....	25
1.1.2. Corrosion of steel .....	25
1.1.3. Passivation and corrosion of steel in concrete .....	26
1.1.4. Carbonation induced corrosion .....	27
1.1.5. Chloride induced corrosion .....	28
1.1.6. Repair options for chloride induced corrosion.....	31
1.2. Scope of the investigation .....	34
1.3. Plan of presentation.....	35
<b>2. Chapter Two. Literature review: Cathodic protection.....</b>	<b>37</b>
2.1. Introduction .....	37
2.2. Cathodic protection of concrete .....	38
2.3. Theoretical basis for cathodic protection .....	39
2.4. Chemical processes of cathodic protection .....	40
2.5. Galvanic cathodic protection.....	42
2.6. Impressed current cathodic protection systems.....	42
2.7. Conductive paint .....	44
2.8. Sprayed zinc .....	46
2.8.1. Zinc as an impressed current anode .....	47
2.9. Mesh anodes.....	49
2.9.1. Conductive polymer anode.....	49
2.9.2. Activated titanium mesh.....	49
2.9.3. Cementitious overlays .....	51
<b>3. Chapter Three. Materials and analytical techniques.....</b>	<b>53</b>
3.1. Introduction .....	53
3.2. Materials.....	53
3.2.1. Cement .....	53
3.2.2. Aggregate .....	53
3.2.3. Water.....	53
3.2.4. Steel.....	53
3.2.5. Admixtures and chemicals .....	54



3.2.6. Anode Materials .....	54
3.2.6.1. Mixed metal oxide titanium mesh/cementitious overlay .....	54
3.2.6.2. Flame sprayed zinc.....	54
3.2.6.3. Conductive paint .....	55
3.3. Compressive strength .....	55
3.4. Resistivity.....	55
3.5. Water permeability .....	56
3.6. Pore solution expression.....	57
3.7. Profile grinding .....	58
3.8. Chemical analysis.....	58
3.8.1. Hydroxyl ion analysis.....	58
3.8.2. pH of hardened concrete .....	59
3.8.3. Evaporable and non-evaporable water .....	59
3.8.4. Chloride ion analysis.....	59
3.8.5. Metal ion analysis.....	60
3.8.5.1. Calcium and zinc ion analysis.....	61
3.8.5.2. Sodium and potassium ion analysis .....	61
3.9. Differential thermal analysis .....	61
3.10. X-Ray diffraction .....	62
3.11. Mercury intrusion porosimetry.....	63
3.12. Visual examination.....	64
3.13. Scanning electron microscopy .....	64
3.14. Thin section petrography.....	64
3.15. Adhesion pull-off test.....	65
3.16. Down-coat resistance .....	66
3.17. Electrode potentials .....	66
3.18. Instant-off potentials .....	66
3.19. Linear polarisation resistance.....	67
3.20. Potentiodynamic polarisation.....	68
3.21. Infra-red spectroscopy .....	68
3.21.1. FT-IR spectroscopy .....	69
3.21.2. Photo-acoustic spectroscopy .....	69
3.21.3. Horizontal attenuated total reflectance (ATR) .....	69
<b>4. Chapter Four. An electrochemical study of anode materials in idealised solutions.....</b>	<b>71</b>
4.1. Introduction .....	71
4.1.1. Theory of polarisation .....	72
4.1.2. Potentiodynamic polarisation.....	73

4.2.	Previous work.....	75
4.2.1.	Activated titanium mesh electrodes .....	75
4.2.2.	Carbon pigmented paint electrodes .....	77
4.2.3.	Sprayed zinc electrodes.....	78
4.3.	Experimental .....	79
4.3.1.	Specimen preparation.....	80
4.3.1.1.	Titanium mesh.....	80
4.3.1.2.	Conductive coatings .....	80
4.3.1.2.1.	Anode Z.....	80
4.3.1.2.2.	Anode P .....	81
4.3.2.	Electrode areas .....	82
4.3.3.	Electrolytes.....	82
4.3.4.	Experimental procedure .....	83
4.4.	Results .....	84
4.4.1.	Anode Z.....	85
4.4.1.1.	Chloride-free electrolytes.....	86
4.4.1.2.	Chloride electrolytes .....	86
4.4.1.3.	Discussion: Anode Z .....	87
4.4.2.	Anode T.....	89
4.4.2.1.	Specimens C12T and N12T .....	90
4.4.2.2.	Specimens C9T and N9T .....	90
4.4.2.3.	Specimen C7T and N7T.....	91
4.4.2.4.	Specimens C2T and N2T .....	91
4.4.2.5.	Discussion: Anode T .....	91
4.4.3.	Anode E.....	92
4.4.3.1.	Specimens C12E and N12E .....	92
4.4.3.2.	Specimens C9E and N9E .....	92
4.4.3.3.	Specimens C7E and N7E .....	93
4.4.3.4.	Specimens C2E and N2E .....	93
4.4.3.5.	Discussion: Anode E .....	93
4.4.4.	Anode P .....	94
4.4.4.1.	Specimens N12P and C12P.....	95
4.4.4.2.	Specimens N9P and C9P.....	95
4.4.4.3.	Specimens N7P and C7P.....	96
4.4.4.4.	Specimens C2P and N2P.....	97
4.4.4.5.	Discussion: Anode P .....	97
4.5.	Conclusions .....	99



<b>5. Chapter Five. Ionic migration in cement paste prisms during cathodic protection.</b>	<b>101</b>
5.1. Introduction	101
5.2. Previous work	102
5.2.1. Ionic profiles from HCP dissolved in acid	102
5.2.1.1. Chlorides	102
5.2.1.2. Chloride and metal ions	103
5.2.2. Charge balance in cement pastes	104
5.2.3. Hydroxyl ion migration	104
5.2.4. Ionic profiles from expressed pore solution	105
5.3. Experimental	108
5.3.1. Introduction	108
5.3.2. Experiment design	108
5.3.3. Specimen preparation	110
5.3.3.1. Cathode plates	110
5.3.3.2. Mesh anodes	110
5.3.3.3. Casting	110
5.3.3.4. Anode coatings application	111
5.3.3.5. Connections	111
5.3.3.6. Moisture conditioning	112
5.3.4. Testing	112
5.3.4.1. Electrical measurements	112
5.3.4.2. Analysis of specimens	112
5.4. Results	113
5.4.1. Introduction	113
5.4.2. Durability of powered specimens	114
5.4.3. Electrical data	115
5.4.4. Ionic concentration profiles	117
5.4.4.1. Anode T	118
5.4.4.2. Anode E	119
5.4.4.3. Anode P	120
5.4.4.4. Anode Z	121
5.4.5. Discussion	122
5.5. Conclusions	126
<b>6. Chapter Six. CP trial: The physical performance of lightweight anodes.</b>	<b>127</b>
6.1. Introduction	127
6.2. Experimental design	128
6.2.1. Current density	128

6.2.2.	Accelerated testing .....	129
6.2.3.	Chloride content .....	130
6.2.4.	Specimen geometry .....	130
6.2.5.	Mix design.....	130
6.2.6.	Curing.....	131
6.3.	Specimen fabrication.....	131
6.3.1.	Concrete slabs production .....	131
6.3.1.1.	Formwork .....	131
6.3.1.2.	Reinforcement preparation .....	131
6.3.1.3.	Casting procedure.....	132
6.3.2.	Anode application .....	132
6.3.2.1.	Surface preparation .....	133
6.3.2.2.	Flame sprayed zinc application .....	133
6.3.2.3.	Paint coating application .....	133
6.3.2.4.	Titanium mesh fixing .....	134
6.3.2.5.	Overlay application .....	134
6.3.2.6.	Pitch tar application.....	135
6.3.3.	Specimen arrangement and numbering .....	135
6.3.4.	Potential measurements.....	135
6.3.5.	Power supply and electrical connections .....	135
6.4.	Pre-polarisation tests .....	136
6.4.1.	Linear polarisation.....	136
6.4.2.	Casting data.....	137
6.4.3.	Permeability .....	137
6.4.4.	Resistivity.....	138
6.5.	Experimental procedures for the determination of anode durability.....	138
6.5.1.	Conductive coatings .....	138
6.5.1.1.	Adhesive strength/ visual inspection.....	138
6.5.2.	Mesh anodes/cementitious overlay .....	139
6.5.2.1.	Ultra-sonic pulse velocity.....	139
6.5.2.2.	Wet coring/ visual inspection .....	140
6.5.2.3.	Adhesive strength.....	140
6.6.	Results .....	140
6.6.1.	Anode P .....	141
6.6.1.1.	Visual inspection.....	141
6.6.1.2.	Pull-offs.....	142
6.6.1.2.1.	Visual inspection of fracture surfaces .....	142
6.6.1.2.2.	Adhesive strength.....	143



6.6.1.3. Examinations of degraded coating sites .....	143
6.6.1.3.1. Bubble site.....	143
6.6.1.3.2. Debonded area.....	144
6.6.1.4. Analysis of rust spot and white top coat .....	145
6.6.1.5. FTIR analyses of paint coating.....	145
6.6.1.5.1. Experimental .....	145
6.6.1.5.2. Results .....	145
6.6.1.5.3. Summary: FT-IR spectroscopy .....	146
6.6.1.6. Down coating voltage drop measurements .....	147
6.6.1.6.1. Introduction .....	147
6.6.1.6.2. Results .....	147
6.6.1.6.3. Discussion of down coating voltage drop results.....	148
6.6.1.7. Discussion: Anode P .....	149
6.6.2. Anode Z.....	150
6.6.2.1. Visual inspection.....	150
6.6.2.2. Pull-offs.....	151
6.6.2.2.1. Visual inspection of fracture surfaces .....	151
6.6.2.2.2. Adhesive strength.....	152
6.6.2.3. Analysis of corrosion products.....	153
6.6.2.3.1. Alkalinity of zinc/substrate interface .....	153
6.6.2.3.2. White rust .....	153
6.6.2.3.3. Warts .....	154
6.6.2.3.4. Examination of section through zinc films .....	154
6.6.2.4. Discussion: Anode Z.....	155
6.6.3. Anodes E and T.....	159
6.6.3.1. Visual inspection.....	159
6.6.3.1.1. 25 mm cores .....	160
6.6.3.1.2. Rust spotting.....	161
6.6.3.2. Examination of anodic products.....	161
6.6.3.3. Adhesion Test.....	162
6.6.3.3.1. Introduction .....	162
6.6.3.3.2. Results .....	163
6.6.3.3.3. Discussion .....	163
6.6.3.4. Discussion: Anodes E and T .....	163
6.7. Conclusions .....	167
<b>7. Chapter Seven. Electrical operating performance of the CP trial. ....</b>	<b>169</b>
7.1. Introduction .....	169
7.2. Literature Review .....	169



7.2.1. CP system control.....	169
7.2.1.1. Criteria.....	170
7.2.1.1.1. Absolute potential values .....	170
7.2.1.1.2. Potential shift.....	172
7.2.1.1.3. Potential decay .....	172
7.2.1.2. System voltage .....	174
7.3. Experimental .....	175
7.4. Results .....	176
7.4.1. Air and specimen temperature.....	176
7.4.2. $E_{\text{corr}}$ of control specimens.....	177
7.4.3. Circuit voltages .....	177
7.4.3.1. Anode T.....	178
7.4.3.2. Anode E.....	178
7.4.3.3. Anode P.....	178
7.4.3.4. Anode Z.....	179
7.4.4. Cathodic potentials.....	180
7.4.5. Instant-off potentials .....	181
7.4.5.1. Depolarisation decays .....	181
7.4.5.1.1. 1 month.....	181
7.4.5.1.2. 6 months.....	182
7.4.5.1.3. 18 months.....	182
7.4.5.2. Current “off” potentials: Months 1 to 18 .....	183
7.4.5.3. Variation of IR drop (dE) over months 10 to 18.....	183
7.4.6. Discussion .....	184
7.5. Conclusions .....	188
<b>8. Chapter Eight. The influence of CP on the concrete substrate.....</b>	<b>190</b>
8.1. Introduction .....	190
8.2. Sampling methods.....	190
8.3. Thin sections .....	191
8.3.1. Introduction.....	191
8.3.1.1. General observations.....	191
8.3.1.2. Anode P.....	191
8.3.1.3. Anode Z.....	192
8.3.1.4. Anodes E and T.....	192
8.3.2. Discussion .....	193
8.4. Variation of pore structure .....	194
8.4.1. Introduction .....	194
8.4.2. Results .....	194

8.4.2.1. Cementitious overlay.....	194
8.4.2.2. Anodes E and T.....	195
8.4.2.3. Anode Z.....	195
8.4.2.4. Anode P.....	195
8.4.3. Conclusions.....	196
8.5. Ionic concentration profiles.....	196
8.5.1. Introduction.....	196
8.5.2. Results.....	197
8.5.2.1. Calcium and magnesium ions.....	197
8.5.2.2. Chloride ions.....	198
8.5.2.3. Sodium and potassium ions.....	199
8.5.2.4. Hydroxide ions.....	200
8.5.2.5. Zinc ions.....	201
8.5.3. Discussion.....	201
8.6. Influence of CP on cement phases - DTA.....	203
8.6.1. Introduction.....	203
8.6.2. Results and discussions.....	204
8.6.2.1. Anode Z.....	205
8.6.2.2. Anode P.....	205
8.6.2.3. Anodes E and T.....	206
8.6.2.4. Weight loss during DTA.....	206
8.6.3. Conclusions.....	207
8.7. General conclusions.....	208
<b>9. Chapter Nine. General conclusions and recommendations for further work.....</b>	<b>209</b>
9.1. General Conclusions.....	209
9.1.1. A critique of anode inspection methods.....	214
9.2. Recommendations for further work.....	215
<b>References.....</b>	<b>219</b>
<b>Appendix A.....</b>	<b>232</b>
Appendix 3.1 The adjustment of mix water due to aggregate and admixture moisture content.....	232
Appendix 3.2 The calculation of hydroxyl ion concentration [OH <sup>-</sup> ] / pH.....	233
Appendix 3.3 The calculation of evaporable and non-evaporable water content.....	233
Appendix 3.4 The calculation of chloride ion concentration.....	235
Calculation of total chloride (acid soluble).....	235
Calculation of bound chloride.....	236
Calculation of expected chloride concentration.....	236



Accuracy of test method.....	237
Appendix 3.5 The calculation of metal ion concentrations.....	239
Appendix 3.6 Characteristic peak temperatures for DTA thermograms.....	242
Appendix 3.7 Calculation of conductive coating resistance .....	242
Appendix 3.8. The development and testing of a freeze-hold voltmeter .....	243
Introduction .....	243
Previous Work.....	243
Experimental .....	243
Preliminary work.....	243
Investigation of freeze-hold (Instant-off) instrument.....	244
General discussion.....	247
Conclusions .....	247
Appendix 3.9 Copy of a technical note describing the operation of the freeze-hold (instant-off) voltmeter. ....	252
Appendix 4.1 Potentiodynamic polarisation program variables .....	261
Appendix 4.2 Thermodynamic equations used in Chapter 4 .....	262
Appendix 5.1 The calculation of cement total alkali content.....	263
Appendix 5.2 Calculation of the minimum solubility of bizincate ions .....	263
Appendix 6.1 Schedule of experimental tests/chapter for the external CP trial .....	264
Appendix 6.2 Calculation of mesh anode surface areas.....	265
Appendix 6.3 DTA analysis of acidified paste, specimen P:2:50:1, 9 months .....	266
Appendix 6.4 Examination of Taywood Engineering Ltd. Zinc CP Trial .....	266
Appendix 8.1 Summary of MIP results.....	267
<b>Appendix B. Plates .....</b>	<b>268</b>
Plate 3.1 Elecometer pull-off instrument. ....	268
Plate 4.1 Pyrex corrosion cell.....	269
Plate 4.2 Potentiostat and Nylox deoxygenator. ....	269
Plate 5.1 Compressed mesh anode and plate cathodes of paste block specimens. ....	270
Plate 5.2 Experimental arrangement of specimens in humidity boxes.....	270
Plate 5.3 Specimen T:50a paste prism, broken in half at the cathode plates. ....	271
Plate 5.4 Micrograph of specimen E:50b, interface between mesh and cement.....	271
Plate 5.5 Specimen P:50a, showing the removed primary and secondary anodes.....	272
Plate 5.6 Specimen Z:50a, showing the alkaline zinc corrosion products. ....	272
Plate 6.1 Typical fixing of a mesh anode fixed to a concrete slab .....	273
Plate 6.2 Specimen E:2:50:2: location of USPV (Pundit) measurements using flat transducer heads. ....	273
Plate 6.3 Specimen P:2:50:2, 8 months: Surface degradation.....	274
Plate 6.4 Specimen P:0.4:50:1, 18 months: Primary anode repair .....	274



Plate 6.5 Specimen P:2:50:1, 8 months: Surface degradation.....	275
Plate 6.6 Specimen P:2:50:1, 18 months: Severe localised degradation.....	275
Plate 6.7 Specimen P:0.4:20:1, 18 months: Anode P, type 4 failure. ....	276
Plate 6.8 Specimen P:2:20:1, 18 months: Anode P, type 3 failure. ....	276
Plate 6.9 Specimen P:0.4:0:1, 18 months: Anode P, type 2 failure. ....	277
Plate 6.10 Specimen P:0.4:0:1, 2 months: Orange staining of substrate paste. ....	277
Plate 6.11 Specimen P:2:50:2, 2 months: White crystalline deposit at coating/substrate interface.....	278
Plate 6.12 Specimen P:2:50:1, 9 months: View of a cored bubble site.....	278
Plate 6.13 Specimen P:2:50:1, 9 months: View of acidified, disbonded coating. ....	279
Plate 6.14 Specimen P:2:50:1, 9 months: SEM micrograph of acidified coating.....	279
Plate 6.15 Specimen P:2:50:1, 9 months: SEM micrograph showing open morphology of acidified coating, with adhering substrate surface particles.....	280
Plate 6.16 Specimen Z:2:50:1, 8 months: Surface “warts” and “white rust” formation over zinc pull-off sites.....	280
Plate 6.17 Specimen Z:2:50:1, 12 months: Variation of zinc surface degradation.....	281
Plate 6.18 Specimen Z:0.4:20:1, 12 months: Low zinc surface corrosion.....	281
Plate 6.19 Specimen Z:2:50:1, 18 months: Debonding of central area.....	282
Plate 6.20 Specimen Z:2:0:1, 4 months: Type 2 failure: zero degradation case.....	282
Plate 6.21 Specimen Z:0.4:20:2, 8 months: Type 3 failure (upper dolly) and type 4 failure (lower dolly). ....	283
Plate 6.22 Specimen Z:2:50:1, 4 months: Type 5 failure.....	283
Plate 6.23 Specimen Z:2:50:2, 4 months: Type 5 failure, amorphous ‘white rust’ /dull zinc surface. ....	284
Plate 6.24 SEM Micrograph of white zinc corrosion product.....	284
Plate 6.25 SEM micrograph of zinc wart corrosion product, outer surface. ....	285
Plate 6.26 SEM micrograph of zinc wart corrosion product, inner surface. ....	285
Plate 6.27 SEM micrograph of zinc wart corrosion product, inner surface. ....	286
Plate 6.28 SEM micrograph of zinc fracture surface, sample from paste block.....	286
Plate 6.29 SEM micrograph , detail of lateral crack observed in plate 6.28.....	287
Plate 6.30 SEM micrograph of zinc fracture surface, sample from zinc sprayed onto a microscope slide. ....	287
Plate 6.31 SEM micrograph of zinc fracture surface, specimen Z:2:50:1. ....	288
Plate 6.32 SEM micrograph, detail of plate 6.31, interface of zinc corrosion site and zinc film.....	288
Plate 6.33 Specimen E:2:50:1, 8 months. Drying shrinkage cracking of cementitious overlay and light rust spotting. ....	289
Plate 6.34 Specimen E:0.4:20:2. 8 months. Anode strand corrosion products. ....	289



Plate 6.35 Specimen E:2:50:2, 22 months. Carbonate precipitation in cored hole. ....	290
Plate 6.36 Specimen E:4:20:1, 9 months. Type 2/3 degradation. ....	290
Plate 6.37 Specimen T:2:50:1, 9 months. Type 4/5 degradation. ....	291
Plate 6.38 Specimen E:2:50:1, 9 months. Type 5 degradation . ....	291
Plate 6.39 Specimen E:2:50:1, 12 months. Type 6 degradation. ....	292
Plate 6.40 Specimen T:2:50:1, 12 months. Carbonate precipitation along line of anode strand and within macro void. ....	292
Plate 6.41 SEM micrograph of crystalline precipitate shown in plate 6.40. ....	293
Plate 6.42 Specimen E:2:50:1, 18 months. Overlay adhesion test (Limpit). ....	293
Plate 7.1 Arrangement of slabs during cathode potential measurements. ....	294
Plate 8.1 Specimen P:2:0:1, 6 months, general view. ....	295
Plate 8.2 Specimen P:2:0:1, 6 months, detail of cracked area. ....	295
Plate 8.3 Specimen P:2:50:1, 12 months, general view, high surface porosity. ....	296
Plate 8.4 Specimen P:2:50:1, 12 months, same area as plate 8.3. ....	296
Plate 8.5 Specimen P:2:50:1, 12 months, general view area adjacent to plate 8.3. ....	297
Plate 8.6 Specimen P:2:50:1, 9 months, acidified bubble site. ....	297
Plate 8.7 Specimen Z:2:50:1, 3 months, shattered surface aggregate. ....	298
Plate 8.8 Specimen Z:2:0:1, 3 months, shattered aggregate/surface cracking. ....	298
Plate 8.9 Specimen Z:2:0:1, 6 months, general view. ....	299
Plate 8.10 Specimen Z:2:50:1, 9 months, glassy phase/ zinc with crack. ....	299
Plate 8.11 Specimen Z:2:50:1, 9 months, detail of glassy phase at lift-off site. ....	300
Plate 8.12 Specimen Z:2:50:1, 3 months, detail of glassy phase/zincboundary. ....	300
Plate 8.13 Specimen E:2:50:1, 6 months, porosity banding in cementitious overlay ....	301
Plate 8.14 Specimen T:2:0:1, 6 months, overlay/substrate boundary. ....	301
Plate 8.15 Specimen T:2:50:1, 12 months, crack at overlay/substrate boundary. ....	302
Plate 8.16 Specimen T:2:50:1, 9 months, needle portlandite crystals in overlay macro voids. ....	302
Plate 8.17 Specimen T:2:50:1, 9 months, detail of needle portlandite crystals. ....	303
Plate 8.18 Specimen T:4:20:1, 3 months, zero paste degradation at anode ....	303
Plate 8.19 Specimen T:4:20:1, 12 months, early neutralisation of paste area. ....	304
Plate 8.20 Specimen T:2:50:1, 3 months, increased paste neutralisation. ....	304
Plate 8.21 Specimen T:2:50:1, 12 months, severe mesh anode degradation ....	305
Plate 8.22 Specimen T:2:50:1, 12 months, upper area of plate 8.21. ....	306
<b>Appendix C. Tables</b> .....	<b>307</b>
Table 3.1 Chemical analysis of OPC cement. ....	307
Table 3.2 Standard half cell potentials at 25°C. ....	307
Table 4.1 Anode electrode areas ....	307
Table 4.2 Potentiodynamic scan rates and Media ....	307



Table 4.3	pH values of test electrolytes .....	307
Table 4.4	Schedule of polarisation curves .....	308
Table 4.5	Potentiodynamic anodic polarisation results for anode Z.....	308
Table 4.6	Potentiodynamic anodic polarisation results for anode T .....	309
Table 4.7	Potentiodynamic anodic polarisation results for anode E.....	309
Table 4.8	Potentiodynamic anodic polarisation results for anode P .....	310
Table 4.9	Potentiodynamic anodic polarisation results for graphite in sat. $\text{Ca(OH)}_2$ + 1 M NaCl (after Slater et al, 1976) .....	310
Table 5.1	Paste block specimen schedule .....	311
Table 5.2	Electrode Areas .....	311
Table 5.3	Ecorr and icorr values for paste specimens before polarisation.....	311
Table 6.1	CP trial specimen schedule. ....	312
Table 6.2	Concrete batch quantities. ....	313
Table 6.3	Casting and concrete characterisation data. ....	313
Table 6.4	Relative humidity and temperature during anode application. ....	313
Table 6.5	Initial corrosion rates of CP trial specimens. ....	313
Table 6.6	Summary of visual inspections anode P surfaces at 20 mA/m <sup>2</sup> .....	314
Table 6.7	Summary of visual inspections anode P surfaces at 50 mA/m <sup>2</sup> .....	314
Table 6.8	Summary of visual inspections of anode P pull-off dolly surfaces.....	315
Table 6.9	Adhesion failure loads: Anode P.....	315
Table 6.10	Summary of pull-off failure modes for anode P .....	316
Table 6.11	Summary of EDXA data for anode P.....	316
Table 6.12	Specimen P:2:20:1 voltage drops from primary anode.....	317
Table 6.13	Specimen P:0.4:20:1 voltage drops from primary anode. ....	317
Table 6.14	Specimen P:0.4:20:2 voltage drops from primary anode.....	318
Table 6.15	Specimen P:2:50:1 voltage drops from primary anode.....	318
Table 6.16	Specimen P:2:50:2 voltage drops from primary anode.....	319
Table 6.17	Specimen P:0.4:50:1 voltage drops from primary anode.....	319
Table 6.18	Average values of voltage drops from primary anode.....	320
Table 6.19	Summary of visual inspections anode Z surfaces at 20 mA/m <sup>2</sup> . ....	321
Table 6.20	Summary of visual inspections anode Z surfaces at 50 mA/m <sup>2</sup> . ....	321
Table 6.21	Summary of visual inspections of anode Z pull-off dolly surfaces. ....	322
Table 6.22	Adhesion failure loads (Kg/cm <sup>2</sup> ): Anode Z. ....	322
Table 6.23	Summary of pull-off modes for anode Z.....	322
Table 6.24	Summary of EDXA data for anode Z. ....	323
Table 6.25	Anode Z: XRD analysis for white zinc corrosion product.....	323
Table 6.26	Anode Z: XRD analysis for zinc "wart"corrosion product.....	324
Table 6.27	Summary of visual inspections of anode E surfaces at 20 mA/m <sup>2</sup> .....	325



Table 6.28	Summary of visual inspections of anode E surfaces at 50 mA/m <sup>2</sup> .....	325
Table 6.29	Summary of visual inspections of anode T surfaces at 20 mA/m <sup>2</sup> .....	326
Table 6.30	Summary of visual inspections of anode T surfaces at 50 mA/m <sup>2</sup> .....	326
Table 6.31	Summary of visual inspections of anodes E and T core surfaces. ....	327
Table 6.32	Summary of mesh anodic current densities. ....	327
Table 6.33	Summary of EDXA data for anodes E and T.....	328
Table 6.34	“Limpit” adhesive strength measurements for anodes E and T. ....	329
Table 6.35	Summary of overlay adhesive strengths for anodes E and T.....	330
Table 6.36	Average overlay adhesive strengths by failure mode. ....	330
Table 7.1	Dates/times of the electrical potential measurements. ....	331
Table 7.2	Air/specimen surface temperatures .....	331
Table 7.3	Various cathode potentials for selected anode T specimens.....	332
Table 7.4	Instant-off cathode potentials for selected anode T specimens.....	333
Table 8.1	Summary:thin section examination: Specimens P:2:0:1 & P:2:50:1.....	334
Table 8.2	Summary: thin section examination: Specimens Z:2:0:1& Z:2:50:1.....	334
Table 8.3	Summary: thin section examination: Specimens T:2:0:1& T:2:50:1.....	335
Table 8.4	Summary: thin section examination: Specimens E:2:0:1& E:2:50:1.....	335
Table 8.5	Summary: thin section examination: Specimens T:0:0:1& E:4:20:1.....	336
Table 8.6	Ionic concentrations of non-standard specimens. ....	336
<b>Appendix D. Figures</b>	.....	<b>337</b>
Figure 2.1	Simplified Evans diagram demonstrating the principle of CP .....	337
Figure 3.1	Schematic illustration of flame spraying operation. ....	337
Figure 3.2	Water permeability test rig. ....	338
Figure 3.3	The pore solution expression pressure vessel.....	338
Figure 3.4	Schematic illustration of profile grinding of concrete samples. ....	339
Figure 3.5	Schematic illustration of sampling for MIP.....	339
Figure 3.6	Applied-current linear polarisation curve. ....	339
Figure 3.7	Schematic illustration of Horizontal ATR. ....	340
Figure 4.1	Idealised anodic polarisation curve.....	340
Figure 4.2	Polarisation curve for zinc in 0.01M KOH (after Sergi et al, 1985).....	340
Figure 4.3	Corrosion cell arrangement.....	341
Figure 4.4	Polarisation curves for 12Z specimens. ....	342
Figure 4.5	Polarisation curves for 9Z specimens. ....	342
Figure 4.6	Polarisation curves for 7Z specimens. ....	343
Figure 4.7	Polarisation curves for 12T specimens. ....	343
Figure 4.8	Polarisation curves for 9T specimens. ....	344
Figure 4.9	Polarisation curves for 7T specimens. ....	344
Figure 4.10	Polarisation curves for 2T specimens. ....	345



Figure 4.11	Polarisation curves for 12E specimens. ....	345
Figure 4.12	Polarisation curves for 9E specimens. ....	346
Figure 4.13	Polarisation curves for 7E specimens. ....	346
Figure 4.14	Polarisation curves for 2E specimens. ....	347
Figure 4.15	Polarisation curves for 12P specimens. ....	347
Figure 4.16	Polarisation curves for 9P specimens. ....	348
Figure 4.17	Polarisation curves for 7P specimens. ....	348
Figure 4.18	Polarisation curves for 2P specimens. ....	349
Figure 5.1	Coated anode HCP prism connected to the galvanostat.....	350
Figure 5.2	Mesh anode HCP prism connected to the galvanostat.....	350
Figure 5.3	Re-saturation weight gains for control cement paste prisms. ....	351
Figure 5.4	Cement paste prism sectioning detail. ....	351
Figure 5.5	Variation of potential / time for specimen T:50a.....	351
Figure 5.6	Variation of potential / time for specimen T:50b. ....	352
Figure 5.7	Variation of potential / time for specimen T:20. ....	352
Figure 5.8	Variation of potential / time for specimen E:50a.....	352
Figure 5.9	Variation of potential / time for specimen E:50b. ....	352
Figure 5.10	Variation of potential / time for specimen T:20.. ....	353
Figure 5.11	Variation of potential / time for specimen P:50a.....	353
Figure 5.12	Variation of potential / time for specimen P:50b.....	353
Figure 5.13	Variation of anodic potential / time graph for specimen Z:50a.....	353
Figure 5.14	Variation of cathodic potential / time graph for specimen Z:50a. ....	354
Figure 5.15	Variation of anodic potential / time graph for specimen Z:50b.....	354
Figure 5.16	Variation of cathodic potential / time graph for specimen Z:50b.....	354
Figure 5.17	Variation of laboratory temperature /time during paste block trial. ....	354
Figure 5.18	Na, K, Cl and OH concentration profiles for specimen T:20.. ....	355
Figure 5.19	Chloride ion concentration profiles for specimen T:20.....	355
Figure 5.20	Summation of positive/negative ion profiles for specimen T:20.....	355
Figure 5.21	Na, K, Cl and OH concentration profiles for specimen T:50b. ....	355
Figure 5.22	Chloride ion concentration profiles for specimen T:50b.....	355
Figure 5.23	Summation of positive/negative ion profiles for specimen T:50b.....	355
Figure 5.24	Na, K, Cl and OH concentration profiles for specimen T:50a. ....	356
Figure 5.25	Chloride ion concentration profiles for specimen T:50a. ....	356
Figure 5.25	Summation of positive/negative ion profiles for specimen T:50a.....	356
Figure 5.27	Na, K, Cl and OH concentration profiles for specimen T:0. ....	356
Figure 5.28	Chloride ion concentration profiles for specimen T:0. ....	356
Figure 5.29	Summation of positive/negative ion profiles for specimen T:0.....	356
Figure 5.30	Na, K, Cl and OH concentration profiles for specimen E:20. ....	357



Figure 5.31 Chloride ion concentration profiles for specimen E:20.....	357
Figure 5.32 Summation of positive/negative ion profiles for specimen E:20.....	357
Figure 5.33 Na, K, Cl and OH concentration profiles for specimen E:50b. ....	357
Figure 5.34 Chloride ion concentration profiles for specimen E:50b.....	357
Figure 5.35 Summation of positive/negative ion profiles for specimen E:50b.....	357
Figure 5.36 Na, K, Cl and OH concentration profiles for specimen E:50a. ....	358
Figure 5.37 Chloride ion concentration profiles for specimen E:50a. ....	358
Figure 5.38 Summation of positive/negative ion profiles for specimen E:50a. ....	358
Figure 5.39 Na, K, Cl and OH concentration profiles for specimen E:0. ....	358
Figure 5.40 Chloride ion concentration profiles for specimen E:0. ....	358
Figure 5.41 Summation of positive/negative ion profiles for specimen E:0.....	358
Figure 5.42 Na, K, Cl and OH concentration profiles for specimen P:50b. ....	359
Figure 5.43 Chloride ion concentration profiles for specimen P:50b. ....	359
Figure 5.44 Summation of positive/negative ion profiles for specimen P:50b.....	359
Figure 5.45 Na, K, Cl and OH concentration profiles for specimen P:50a.....	359
Figure 5.46 Chloride ion concentration profiles for specimen P:50a. ....	359
Figure 5.47 Summation of positive/negative ion profiles for specimen P:50a. ....	359
Figure 5.48 Na, K, Cl and OH concentration profiles for specimen P:0. ....	360
Figure 5.49 Chloride ion concentration profiles for specimen P:0. ....	360
Figure 5.50 Summation of positive/negative ion profiles for specimen P:0.....	360
Figure 5.51 Na, K, Cl and OH concentration profiles for specimen Z:50b. ....	360
Figure 5.52 Chloride ion concentration profiles for specimen Z:50b.....	360
Figure 5.53 Summation of positive/negative ion profiles for specimen Z:50b.....	360
Figure 5.54 Na, K, Cl and OH concentration profiles for specimen Z:50a. ....	361
Figure 5.55 Chloride ion concentration profiles for specimen Z:50a. ....	361
Figure 5.56 Summation of positive/negative ion profiles for specimen Z:50a.....	361
Figure 5.57 Na, K, Cl and OH concentration profiles for specimen Z:0. ....	361
Figure 5.58 Chloride ion concentration profiles for specimen Z:0.....	361
Figure 5.59 Summation of positive/negative ion profiles for specimen Z:0.....	361
Figure 5.60 Zinc ion profiles for anode Z anode specimens.....	361
Figure 6.1 Sketch of CP trial concrete slab.....	362
Figure 6.2 Steel reinforcement bar preparation.....	362
Figure 6.3 Location of half cell measurement positions.....	363
Figure 6.4 Circuit diagram of 3 terminal, variable constant current source.....	364
Figure 6.5 Sketches of primary anodes and external electrical connections.....	365
Figure 6.6 Linear decay polarisation curves for anode T specimens. ....	365
Figure 6.7 Linear decay polarisation curves for anode E specimens. ....	365
Figure 6.8 Linear decay polarisation curves for anode P specimens. ....	365



Figure 6.9 Linear decay polarisation curves for anode Z specimens. ....	365
Figure 6.10 Permeability coefficients vs. % chloride content:specimen curing. ....	367
Figure 6.11 Location of on-going cores/ coating pull-offs .....	367
Figure 6.12 Plot of time for ultra-sound pulse to travel through specimen E:2:50:1 against increasing distance from a corner location .....	368
Figure 6.13 Surface visual inspection 6 monthly summary: Specimen P:2:20:1.....	369
Figure 6.14 Surface visual inspection 6 monthly summary: Specimen P:0.4:20:1.....	369
Figure 6.15 Surface visual inspection 6 monthly summary: Specimen P:0.4:20:2.....	370
Figure 6.16 Surface visual inspection 6 monthly summary: Specimen P:2:50:1.....	370
Figure 6.17 Surface visual inspection 6 monthly summary: Specimen P:2:50:2.....	371
Figure 6.18 Surface visual inspection 6 monthly summary: Specimen P:0.4:50:1.....	371
Figure 6.19 Plot of pull-off loads/time for Anode P (20 mA/m <sup>2</sup> ) specimens.....	372
Figure 6.20 Plot of pull-off loads/time for Anode P (50 mA/m <sup>2</sup> ) specimens.....	372
Figure 6.21 EDXA elemental plot: Specimen P:2:50:1, 9 months, acidified paste adhering to debonded coating. ....	373
Figure 6.22 EDXA elemental plot: Specimen P:2:50:1, 9 months, acidified paint surface. ....	373
Figure 6.23 EDXA elemental plot: Rust spot on top-coat surface, anode P.....	374
Figure 6.24 EDXA elemental plot: White top-coat surface, anode P. ....	374
Figure 6.25 FT-IR spectra (reflectance mode): Anode P control sample. ....	375
Figure 6.26 FT-IR spectra (identification): Anode P control sample/Poly vinyl chloride:ethylene. ....	376
Figure 6.27 FT-IR spectra (idenufication): Specimen P:2:50:1(9 months) highly degraded blister area/Poly vinyl acetate:ethylene. ....	376
Figure 6.28 FT-IR spectra: Comparison of specimen P:2:50:1(9 months) blister area to control sample. ....	377
Figure 6.29 FT-IR spectra: Comparison of specimen P:0.4:0:1(3 months) blister area to control sample. ....	377
Figure 6.30 FT-IR spectra: Comparison of specimen P:0.4:20:1(12 months) blister area to control sample. ....	378
Figure 6.31 FT-IR spectra: Comparison of specimen P:0.4:50:1(3 months) blister area to control sample. ....	378
Figure 6.32 Location of drop voltage measurements for anode P specimens.....	379
Figure 6.33 Plot of average resistance values vs. time for anode P specimens .....	379
Figure 6.34 Surface visual inspection 6 monthly summary: Specimen Z:2:20:1 .....	380
Figure 6.35 Surface visual inspection 6 monthly summary: Specimen Z:0.4:20:1 .....	380
Figure 6.36 Surface visual inspection 6 monthly summary: Specimen Z:0.4:20:2 .....	381
Figure 6.37 Surface visual inspection 6 monthly summary: Specimen Z:2:50:1 .....	381



Figure 6.38 Surface visual inspection 6 monthly summary: Specimen Z:2:50:2 .....	382
Figure 6.39 Surface visual inspection 6 monthly summary: Specimen Z:0.4:50:1 .....	382
Figure 6.40 Plot of pull-off loads/time for Anode Z (20 mA/m <sup>2</sup> ) specimens.....	383
Figure 6.41 Plot of pull-off loads/time for Anode Z (50 mA/m <sup>2</sup> ) specimens.....	383
Figure 6.42 EDXA elemental plot: White zinc corrosion product.....	384
Figure 6.43 EDXA elemental plot: Zinc “wart” corrosion product, inner surface. ....	384
Figure 6.44 EDXA elemental plot: Zinc “wart” corrosion product, outer surface. ....	385
Figure 6.45 EDXA elemental plot: White zinc corrosion product at fracture surface. ....	385
Figure 6.47 Anode E, 22 months: Summary of anodic degradation in cored holes.....	387
Figure 6.48 Anode T, 22 months: Summary of anodic degradation in cored holes.....	388
Figure 6.49 EDXA elemental plot: Carbonate precipitate in cementitious overlay.....	389
Figure 6.50 EDXA elemental plot: Cementitious overlay .....	389
Figure 6.51 EDXA elemental plot: Coloured precipitate forming in cored hole.....	390
Figure 6.52 Location of 50 mm diameter “Limpit” probes.....	391
Figure 6.53 Failure modes of “Limpit” probes. ....	391
Figure 7.1 Air temperature/time plot at time of potential measurements/ comparative average data for London (adapted from Hankin et al, 1985). ....	392
Figure 7.2 Plot of E <sub>corr</sub> /time for 0.4% & 0% chloride control specimens.....	392
Figure 7.3 Plot of E <sub>corr</sub> /time for 2% chloride control specimens. ....	392
Figure 7.4 Plot of system voltage/time for T:20 specimens.....	393
Figure 7.5 Plot of system voltage/time for T:50 specimens.....	393
Figure 7.6 Plot of system voltage/time for E:20 specimens.....	393
Figure 7.7 Plot of system voltage/time for specimen E:0.4:20:2 .....	394
Figure 7.8 Plot of system voltage/time for E:50 specimens.....	394
Figure 7.9 Plot of system voltage/time for P:20 specimens.....	394
Figure 7.10 Plot of system voltage/time for P:50 specimens.....	395
Figure 7.11 Plot of system voltage/time for specimens Z:2:20:1 and Z:0.4:20:1 .....	395
Figure 7.12 Plot of system voltage/time for specimen Z:0.4:20:2.....	395
Figure 7.13 Plot of system voltage/time for specimen Z:2:50:1.....	396
Figure 7.14 Plot of system voltage/time for specimen Z:2:50:2.....	396
Figure 7.15 Plot of system voltage/time for specimen Z:0.4:50:1.....	396
Figure 7.16 Plot of current/time for Z:20 specimens. ....	397
Figure 7.17 Plot of current/time for Z:50 specimens. ....	397
Figure 7.18 Plot of ‘on’ cathodic potential /time: T:20 specimens.....	398
Figure 7.19 Plot of ‘on’ cathodic potential /time: T:50 specimens.....	398
Figure 7.20 Plot of ‘on’ cathodic potential /time: E:20 specimens.....	398
Figure 7.21 Plot of ‘on’ cathodic potential /time: E:50 specimens.....	398



Figure 7.22 Plot of 'on' cathodic potential /time: P:20 specimens. ....	398
Figure 7.23 Plot of 'on' cathodic potential /time: P:50 specimens. ....	398
Figure 7.24 Plot of 'on' cathodic potential /time: Z:20 specimens. ....	398
Figure 7.25 Plot of 'on' cathodic potential /time: Z:50 specimens. ....	398
Figure 7.26 Plot of potential decay/time: T:20 specimens (1 month). ....	399
Figure 7.27 Plot of potential decay/time: T:50 specimens (1 month). ....	399
Figure 7.28 Plot of potential decay/time: E:20 specimens (1 month). ....	399
Figure 7.29 Plot of potential decay/time: E:50 specimens (1 month). ....	399
Figure 7.30 Plot of potential decay/time: P:20 specimens (1 month). ....	399
Figure 7.31 Plot of potential decay/time: P:50 specimens (1 month). ....	399
Figure 7.32 Plot of potential decay/time: Z:20 specimens (1 month). ....	399
Figure 7.33 Plot of potential decay/time: Z:50 specimens (1 month). ....	399
Figure 7.34 Plot of potential decay/time: T:20 specimens (18 month). ....	400
Figure 7.35 Plot of potential decay/time: T:50 specimens (18 month). ....	400
Figure 7.36 Plot of potential decay/time: E:20 specimens (18 month). ....	400
Figure 7.37 Plot of potential decay/time: E:50 specimens (18 month). ....	400
Figure 7.38 Plot of potential decay/time: P:20 specimens (18 month). ....	400
Figure 7.39 Plot of potential decay/time: P:50 specimens (18 month). ....	400
Figure 7.40 Plot of potential decay/time: Z:20 specimens (18 month). ....	400
Figure 7.41 Plot of potential decay/time: Z:50 specimens (18 month). ....	400
Figure 7.42 Plot of 'off' cathodic potential /time: T:20 specimens. ....	401
Figure 7.43 Plot of 'off' cathodic potential /time: T:50 specimens. ....	401
Figure 7.44 Plot of 'off' cathodic potential /time: E:20 specimens. ....	401
Figure 7.45 Plot of 'off' cathodic potential /time: E:50 specimens. ....	401
Figure 7.46 Plot of 'off' cathodic potential /time: P:20 specimens. ....	401
Figure 7.47 Plot of 'off' cathodic potential /time: P:50 specimens. ....	401
Figure 7.48 Plot of 'off' cathodic potential /time: Z:20 specimens. ....	401
Figure 7.49 Plot of 'off' cathodic potential /time: Z:50 specimens. ....	401
Figure 7.50 Plot of dE/time for T:20 specimens (10-18 months). ....	402
Figure 7.51 Plot of dE/time for T:50 specimens (10-18 months). ....	402
Figure 7.52 Plot of dE/time for E:20 specimens (10-18 months). ....	402
Figure 7.53 Plot of dE/time for E:50 specimens (10-18 months). ....	402
Figure 7.54 Plot of dE/time for P:20 specimens (10-18 months). ....	402
Figure 7.55 Plot of dE/time for P:50 specimens (10-18 months). ....	402
Figure 7.56 Plot of dE/time for Z:20 specimens (10-18 months). ....	402
Figure 7.57 Plot of dE/time for Z:50 specimens (10-18 months). ....	402
Figure 8.1 Cumulative PSD: Overlay specimens E:2:0:1 & E:2:50:1. ....	403
Figure 8.2 Cumulative PSD: Overlay specimens T:2:0:1 & T:2:50:1. ....	403



Figure 8.3 Cumulative PSD: Specimens E:2:0:1 & E:2:50:1 .....	404
Figure 8.4 Cumulative PSD: Specimens T:2:0:1 & T:2:50:1 .....	404
Figure 8.5 Cumulative PSD: Specimens Z:2:0:1 & Z:2:50:1 .....	405
Figure 8.6 Cumulative PSD: Specimens P:2:0:1 & T:2:0:1 .....	405
Figure 8.7 Cumulative PSD: Specimens P:2:0:1 & P:2:20:1 & P:2:50:1 .....	406
Figure 8.8 Cumulative PSD: Specimens P:2:50:1 & T:2:0:1 .....	406
Figure 8.9 Calcium ion concentration profile for anode T .....	407
Figure 8.10 Calcium ion concentration profile for anode E .....	407
Figure 8.11 Calcium ion concentration profile for anode P .....	407
Figure 8.12 Calcium ion concentration profile for anode Z .....	407
Figure 8.13 Magnesium ion concentration profile for anode T .....	407
Figure 8.14 Magnesium ion concentration profile for anode E .....	407
Figure 8.15 Magnesium ion concentration profile for anode P .....	407
Figure 8.16 Magnesium ion concentration profile for anode Z .....	407
Figure 8.17 Chloride ion concentration profile for anode T .....	408
Figure 8.18 Chloride ion concentration profile for anode E .....	408
Figure 8.19 Chloride ion concentration profile for anode P .....	408
Figure 8.20 Chloride ion concentration profile for anode Z .....	408
Figure 8.21 Ratio of chloride/calcium ion concentrations for anode Z .....	408
Figure 8.22 Sodium ion concentration profile for anode T .....	408
Figure 8.23 Sodium ion concentration profile for anode E .....	408
Figure 8.24 Sodium ion concentration profile for anode P .....	408
Figure 8.25 Sodium ion concentration profile for anode Z .....	408
Figure 8.26 Potassium ion concentration profile for anode T .....	409
Figure 8.27 Potassium ion concentration profile for anode E .....	409
Figure 8.28 Potassium ion concentration profile for anode P .....	409
Figure 8.29 Potassium ion concentration profile for anode Z .....	409
Figure 8.30 Hydroxyl ion concentration profile for anode T .....	409
Figure 8.31 Hydroxyl ion concentration profile for anode E .....	409
Figure 8.32 Hydroxyl ion concentration profile for anode P .....	409
Figure 8.33 Hydroxyl ion concentration profile for anode Z .....	409
Figure 8.34 Ratio of hydroxyl/calcium ion concentrations for anode P .....	410
Figure 8.35 Ratio of hydroxyl/calcium ion concentrations for anode Z .....	410
Figure 8.36 Zinc ion concentration profile for anode Z .....	410
Figure 8.37 Summary of DTA peaks: Specimen Z:2:0:1 .....	410
Figure 8.38 Summary of DTA peaks: Specimen Z:2:20:1 .....	410
Figure 8.39 Summary of DTA peaks: Specimen Z:2:50:1 .....	410
Figure 8.40 Summary of DTA peaks: Specimen P:2:0:1 .....	410



Figure 8.41 Summary of DTA peaks: Specimen P:2:20:1.....	410
Figure 8.42 Summary of DTA peaks: Specimens P:2:50:1. ....	410
Figure 8.43 Summary of DTA peaks: Specimen T:2:0:1.....	411
Figure 8.44 Summary of DTA peaks: Specimen T:2:20:1.....	411
Figure 8.45 Summary of DTA peaks: Specimen T:2:50:1.....	411
Figure 8.46 Summary of DTA peaks: Specimen E:2:0:1.....	411
Figure 8.47 Summary of DTA peaks: Specimen E:2:20:1.....	412
Figure 8.48 Summary of DTA peaks: Specimen E:2:50:1.....	412
Figure 8.49 Sample weight loss during DTA: Z anode specimens.....	412
Figure 8.50 Sample weight loss during DTA: P anode specimens. ....	412
Figure 8.51 Sample weight loss during DTA: T anode specimens.....	412
Figure 8.52 Sample weight loss during DTA: E anode specimens.....	412
<b>Appendix E. List of abbreviations .....</b>	<b>413</b>

#### **Tables in Appendix A**

Table A3.3.1 Water contents of saturated HCP specimens (Chapter 5) .....	234
Table A3.4.1 Computation of total chloride from dust samples .....	236
Table A3.4.2 Chloride concentration of parallel control determinations.....	238
Table A3.8.1 Test 1: 0.1 to 1.0 second instant-off potentials/ potential decay for specimen Z:0.4:20:1 .....	248
Table A3.8.2 Test 2: Instant-off results at 0.2 and 1.0 seconds for specimen E:0.4:20:1 .....	248
Table A3.8.3 Test 2: Instant-off results at 0.2 and 1.0 seconds for specimen E:0.4:50:1 .....	249
Table A3.8.4 Test 3: 'On' potentials and repeat instant-off potentials at 9 half-cell locations for specimen T:2:20:1 .....	249
Table A4.1.1 Theoretical equilibrium electrode potential (Eo) values .....	262
Table A6.1.1 Schedule of experimental tests/chapter for the external CP trial .....	264
Table A6.3.1 DTA: relative intensities of peak temperatures for acidified paste from specimen P:2:50:1 at 9 months.....	266
Table A6.4.1 Summary of pull-off tests of Taywood Engineering Ltd. Zinc CP trial .....	266
Table A8.1.1 Summary of MIP data .....	267

#### **Figures in appendix A**

Figure A3.4.1 Chloride calibration curve.....	235
Figure A3.4.2 Histogram of control specimen chloride determinations.....	238
Figure A3.5.1 Calibration curve for sodium ions.....	241

Figure A3.5.2 Calibration curve for potassium ions.....	241
Figure A3.5.3 Calibration curve for zinc ions.....	241
Figure A3.6.1 Schematic representation of characteristic DTA peak temperatures. ....	242
Figure A3.8.1 Potential decay/recovery on current interruption/restoration at increasing time intervals for specimen Z:0.4:20:1.....	250
Figure A3.8.2 Variation of potential decay with increasing delay period at a single point for specimen Z:0.4:20:1.....	251
Figure A3.8.3 Potential decay plot over 60 seconds at a single point for specimen Z:0.4:20:1 .....	251
Figure A3.8.4 Variation of potential with increasing delay period at nine half-cell locations for specimen T:2:20:1.....	251



## **1. Chapter One. Introduction**

### **1.1. Introduction**

Concrete is the most successful and widely used construction material. It can form any architectural shape and exhibits excellent compressive strength, but has low tensile strength. Steel reinforcement is incorporated into concrete members to improve structural performance by accommodating induced tensile forces. Awareness of the importance of the durability of reinforced concrete in the UK has increased greatly during the last 10 years, mainly due to the deleterious effects of chloride ion induced corrosion of steel reinforcement. The problem of chloride attack exists world-wide and the maintenance and repair of afflicted structures has developed into a multi-billion pound industry (Broomfield, 1991). Primarily in North America and more recently in the UK, cathodic protection (CP) has been identified as an economical technique for the rehabilitation of chloride damaged structures (McKenzie, 1990).

#### **1.1.1. Corrosion of concrete**

Concrete may be subject to a number of chemical or external physical processes which modify and degrade its structure. Durable concrete accommodates these modifications during a design life period such that the intended structural function is achieved. In this respect, the performance of concrete depends on its inherent quality, which is influenced by its composition and the workmanship during manufacture, and the environment in which it is placed. The reader is referred to Biczok (1964) or Lea (1970) for full accounts of the many processes of degradation which may occur.

#### **1.1.2. Corrosion of steel**

The corrosion of steel involves oxidation of the metal to form a more stable substance. Aqueous corrosion occurs when a steel surface comes into contact with both water and dissolved oxygen and proceeds by the coupled processes of anodic dissolution of the metal and cathodic reduction of water and oxygen to hydroxyl ions. Anodic areas are electrically positive in relation to cathodic areas, hence electronic conduction occurs from one site to another on the metal surface and ions are transported through the solution (electrolytic



conduction). Iron hydroxide forms which may be subsequently oxidised to give hydrated iron oxide, or rust (Shreir, 1982).

The corrosion product is important in controlling the rate of corrosion; rust forms as a porous, non-protective layer and allows the corrosion to continue. The phenomenon of passivation occurs when corrosion products form uniformly on a metal surface which are highly insoluble and have a permeability so low that the rate of corrosion becomes practically zero.

#### **1.1.3. Passivation and corrosion of steel in concrete**

Concrete is composed of dense aggregates of various particle sizes from rock to gravels and sands, bound with hardened cement paste. Ordinary portland cement (OPC) mainly consists of the cement minerals tricalcium silicate ( $C_3S$ ), dicalcium silicate ( $C_2S$ ), tricalcium aluminate ( $C_3A$ ) and tetracalcium aluminoferrite ( $C_4AF$ ) with traces of gypsum and the alkali impurities sodium oxide ( $Na_2O$ ) and potassium oxide ( $K_2O$ ). On mixing with water, the cement grains hydrate to form a complex, rigid structure of calcium silicate and aluminate hydrates (CSH gel), calcium hydroxide, calcium sulfo-aluminate hydrate and hydrated ferric oxide (Lea, 1970). A liquid phase remains within the pores which is composed of an aqueous solution of sodium hydroxide, potassium hydroxide and trace amounts of calcium hydroxide, and is commonly termed pore water. Pore water in cement pastes has been reported to have a pH in the range 12.5 to 14, dependent on the cement composition (Page, 1975).

The formation of a passive layer on iron in a calcium hydroxide solution has long been known (Rosa *et al*, 1913) and many studies have established that steel passivates in fresh concrete with no contaminants, characterised by a positive change in metal potential. Steel in alkaline concrete can exhibit passivity over a range of potentials, typically between +175 and -590 mV (SCE) for concrete of pH 13.5 (Hansson, 1984), dependent on oxygen availability, moisture content and the chloride content. Increasing the chloride contamination has been shown to reduce the passive potential range and results in

increasingly negative potentials (Treadaway, 1988). Passivity of steel in concrete is widely attributed to the formation of a film of  $\gamma\text{-Fe}_2\text{O}_3$  (Page, 1975, Weyers and Cady, 1984), which is buffered by adjacent CSH gel and calcium hydroxide layers (Page, 1975, Leek and Poole, 1990) and generally becomes unstable at pH values below about 11.5. A small supply of oxygen is required to maintain the passive film. Where oxygen availability becomes very low, such as in a buried or submerged structure, the metal surface becomes bare and undergoes uniform anodic dissolution at a generally insignificant rate. Corrosion controlled by a low oxygen flux to cathodic sites is characterised by low rest potentials, more negative than -850 mV (SCE) (Page and Lambert, 1986).

In above ground construction, reinforcement steel relies on the high alkalinity and physical barrier provided by the surrounding concrete for corrosion protection. The two main mechanisms responsible for disruption of the protective passive layer and initiation of reinforcement corrosion are neutralisation of the hardened cement paste by dissolved carbon dioxide and the presence of chloride ions, which can destabilise the passive film in conditions of high alkalinity. The volume of steel corrosion products can be up to 2.5 times greater than the original steel and hence generate high bursting pressures (Rosa *et al*, 1913), resulting in cracking and spalling of the concrete. Indirect methods for detecting the occurrence and rate of corrosion in reinforced concrete have been conveniently summarised by Dhir *et al* (1991), whilst comprehensive accounts of diagnostic procedures is given in technical reports and papers (Concrete Society, 1984, Browne *et al*, 1983, Naish *et al*, 1991).

#### **1.1.4. Carbonation induced corrosion**

Carbonation of concrete proceeds by the slow ingress of carbon dioxide into surface layers through micro-pores. The acidic gas dissolves in pore water and reacts primarily with calcium hydroxide to form calcium carbonate in voids (Concrete Society, 1984). Water is released and the concrete permeability tends to decrease whilst the alkalinity is reduced. Decomposition of the CSH gel and other hydration products is possible at a later stage (Roberts, 1981). Carbonation is progressive and the rate largely dependent on permeability



of the cover concrete and on the cement content. After a time the carbonated zone may reach the level of the reinforcement and depassivation then occurs due to the rapid reduction from pH 12.5 to around pH 8 (Gray, 1985). In dense, well compacted concrete the carbonation front may extend only a few millimetres from the surface after many years of exposure. Although concern over the effects of carbonation has increased, particularly for pre-cast concrete cladding panels (Browne *et al*, 1983), an extensive survey of UK highway structures indicated that carbonation was not a significant cause of corrosion (Wallbank, 1989). It is generally accepted that the greatest threat to the integrity of many types of structure is chloride induced corrosion.

Methods to economically repair structures afflicted by carbonation have been developed and are described in some detail in authoritative guides and books (Concrete Society, 1984, Pullar-Strecker, 1987, Bijen, 1989). Repair strategies generally involve cutting out affected concrete, application of a protective coating to the cleaned reinforcement, replacement of the carbonated concrete with a proprietary mortar and application of a surface sealer to prevent further carbon dioxide ingress.

#### **1.1.5. Chloride induced corrosion**

Chlorides added during concrete manufacture will usually be distributed uniformly within the cement matrix. Calcium chloride was widely used as an accelerating admixture during the 1960's and chlorides may be present as contaminants in mixing water or locally available aggregates in areas such as the Arabian Gulf, or from sea-dredged aggregates (Bijen, 1987). During service, chlorides may penetrate into concrete from external sources such as road de-icing salts, airborne salts or sea splash in marine environments. Alternatively, chlorides may be applied to immature concrete surfaces in the form of a hydrochloric acid wash to reveal aggregates particles, or sea water for curing (Gray, 1985). Such chloride contamination can be extremely rapid; in a Middle Eastern marine environment, the threshold level of chloride deemed to initiate corrosion at a cover depth of 50 mm in good quality concrete was exceeded within six months of exposure (Anderson and Sweeney, 1989).

Chloride ions are removed from the pore water of fresh concrete by the cement minerals  $C_3A$  and to a lesser extent  $C_4AF$  as solid calcium chloroaluminate hydrates and calcium chloro-ferrite hydrates. In addition, chlorides may be physically adsorbed on to cement gel surfaces (Gray, 1985) and the combined and adsorbed chlorides are often referred to as "bound chlorides". These solid phases are in equilibrium with the remaining chloride ions in solution, termed "free chlorides", which are responsible for depassivation of the steel reinforcement. The chloroaluminates may decompose due to leaching of free chlorides, dilution of the pore water, sustained temperatures above 40°C (Benjamin and Sykes, 1990), and carbonation (Tuutti, 1982), hence these conditions increase the risk of depassivation.

The absence of chloride in the corrosion products of steel in an alkaline solution containing calcium chloride (Treadaway and Russell, 1968) indicated that the chloride ion behaves as a catalyst in the depassivation of the metal. The mechanism, however, is complex and despite much subsequent research is not fully understood, although several theories have been proposed (Leek and Poole, 1990, Sagoe-Crentsil and Glasser, 1990) and research into associated factors is ongoing (Benjamin and Sykes, 1990, Lambert *et al*, 1991).

The ratio of chloride/hydroxide ions at a steel surface has been shown to be influential in controlling the initiation of depassivation (Hausmann, 1967), which appears to proceed once a certain threshold chloride concentration develops in the pore solution at the surface of the reinforcement. Chlorides from an external source are complexed less by hydrated cement, probably owing to lower availability of unhydrated  $C_3A$  (Midgley and Illston, 1984), and the ratio of free:bound chloride will be higher. Consequently, chlorides which diffuse or are imbibed into concrete constitute a greater risk to the reinforcement and can be tolerated in lower concentrations than admixed chlorides. Further information regarding concrete chloride contents likely to initiate corrosion is given elsewhere (Concrete Society, 1984, American Concrete Institute, 1985).



It is generally accepted that the chloride induced corrosion of steel is initiated in the form of highly localised attack, or pitting (Tuutti, 1982). Local variations in environment and structural detail will often result in uneven chloride concentrations within the cover concrete and corrosion initiation usually occurs in regions of greatest chloride content. Steel becomes activated locally to form anodic sites, or pits, with the remaining passive surface forming cathodic areas. An acidic environment develops within a pit, which therefore remains active and increases in depth. The type of pitting corrosion product is dependent on the rate of oxygen diffusion and if this is limited, a low volume, partially soluble, product of low oxidation state is said to form. This may be black, green or grey in colour and may be complexed with chloride (Treadaway, 1988). The product may migrate away from the anode pit and be further oxidised to precipitate with volumetric expansion. The large scale spread of corrosion is possible if there are high levels of chloride (Neville, 1977). Considerable loss of cross-sectional area can occur and the corrosion is characterised by extensive surface cracking and rust coloured staining.

The electrical resistivity of concrete influences corrosion activity. For a given pore structure<sup>1</sup>, concrete resistivity is dependent on moisture content and temperature (Figg and Marsden, 1985), which vary with ambient conditions, and with the concrete chloride content, chlorides tending to reduce resistivity (Harrop, 1977). Under conditions where the resistivity of the concrete separating anode and cathode regions is low, the ratio of cathode to anode areas can be large with high associated corrosion rates (American Concrete Institute, 1985).

---

<sup>1</sup>For full hydration of cement, the necessary quantity of added water is equivalent to a water/cement ratio of only about 0.2 (Neville, 1977). However, when combined with aggregate, such a mix would be unworkable and water/cement ratios of 0.35 to 0.75 are generally used in concrete (Browne, 1986). As the ratio exceeds approximately 0.4, interconnected capillaries form within the hydrating cement gel of the order of 1  $\mu\text{m}$  in size, which permit easy movement of water or gases (Neville, 1977). Much smaller interstitial gel pores also form so that a wide distribution of pore sizes exists within cement paste.

The potential of anodic sites becomes more negative on pit formation and propagation, which can inhibit new pit formation as the corroding areas provide a form of cathodic protection to less active sites (Arup, 1983).

#### **1.1.6. Repair options for chloride induced corrosion**

Partial repairs of highway bridges suffering chloride induced corrosion which used the techniques described for carbonation induced corrosion were shown to be largely ineffective (Thompson, 1991), since chlorides remained in unrepaired sections. A repair which reinstates high alkalinity at the original anode site eliminates the effective cathodic protection action to adjacent areas as the repair site becomes cathodic relative to unrepaired bar. Previously protected sites immediately adjacent to the repair activate and new pitting corrosion occurs in a phenomenon known as incipient anode activation (Bijen, 1987). In practice, large areas of concrete may need to be replaced to limit this effect and the cost implications may be greater than total replacement of structural members (Lewis and Boam, 1987, DOT, 1990, Thompson, 1991). Other problems with this repair method include difficulty in removing pitting sites insitu and shrinkage of certain repair materials owing to incompatibilities with the original concrete leading to further chloride penetration (Keer *et al*, 1990).

In order to protect steel in chloride contaminated concrete from continuing corrosion, the electrochemical reactions occurring at the steel-concrete interface must be artificially modified. Possible methods to accomplish this are insulating the concrete surfaces from the corrosive environment, making the concrete environment less aggressive and controlling the electron flow within the concrete.

Several surface treatments have been shown to limit the further ingress of chloride ions, although only one significantly reduced the rate of corrosion due to chloride induced corrosion and no treatment appeared to reduce the oxygen content of concrete (Vassie, 1990). An insulating barrier will seal in any aggressive contaminants and corrosion may continue.



The principle of desalination is to reduce the concentration of free and bound chlorides in the surface concrete, which lowers the ratio of chloride/hydroxyl ions at the reinforcement, allowing corroding areas to repassivate. The removal of chloride ions from concrete surrounding steel reinforcement was shown to be technically feasible using a technique identical in principle to cathodic protection; a conductive material, placed on the concrete surface, was connected into a circuit as the positive pole with the embedded reinforcement as negative pole and a direct current applied. The negatively charged chloride ions were attracted from the reinforcement region to the surface mounted anode. High current densities of up to  $1000 \text{ A/m}^2$  were found to remove 90% of chloride above the reinforcement of laboratory specimens and a bridge deck over a period of 24 to 48 hours, halting corrosion (Slater *et al*, 1976). The anode used was a platinised titanium expanded mesh within an ion exchange resin soaked in calcium hydroxide as the electrolyte. The process was later applied in the US but not continued due to high heat generation and poor efficiency of extraction.

The procedure is presently attracting much interest due to new developments and trials (TEL, 1991), although little published work is available. The anode system has been modified by substituting an electrolyte soaked papier-mache for the ion exchange resin, with either a steel, aluminium or mixed oxide/coated titanium mesh as the anode. The system has been applied to soffits and vertical surfaces and a waterproofing sealant, applied after removal of the temporary anode system, is said to prevent further ingress of chlorides. One research project has recommended adoption of a maximum current density of  $2 \text{ A/m}^2$  (Bennett and Shue, 1990), the treatment time being longer owing to the lower current density.

Two processes can occur during the electrolysis, the restoration of alkalinity in carbonated concrete due to cathodic oxygen reduction and the removal of chloride ions if present. Considerable electro-osmosis towards the cathode may be expected to occur due to the high

current density, which may have a leaching effect if a neutral electrolyte is used. Several other possible problems will require careful evaluation. These include: hydrogen embrittlement of pre-stressed steel due to hydrogen evolution from 'over protection' of the steel; re-migration or diffusion of chlorides from other areas or from the environment after treatment; generation of high alkali levels at the cathode may initiate alkali-silica reaction (Sergi *et al*, 1991); cracking of the concrete as a result of heat generation; and the contention that loss of bond strength between reinforcement and concrete may occur due to cathodic accumulation of potassium and sodium ions (Rosa *et al*, 1913, Locke *et al*, 1983).

The technique is still considered to be in the development stage, with full scale trials in progress in Europe and Scandinavia. Re-alkalisation/desalination remains an interesting option for the repair of chloride induced corrosion of reinforced concrete since it offers a one treatment solution, although long term performance is not proven. It may be only the second technique, with cathodic protection, which can halt the corrosion process, although neither may be appropriate for concrete which requires significant repairs due to spalling damage.

Cathodic protection drives the electrical potential of corroding steel more negative so that its rate of corrosion is reduced or halted by the formation of a passive film, or alternatively the metal surface becomes thermodynamically stable, that is, immune from corrosion. CP is effected either by making the steel the negative electrode of a cell powered by a source of direct current or by connecting it to a 'reactive' anode such as zinc or magnesium, which corrodes sacrificially. Cathodic protection has been defined more generally as "the establishment of a state of immunity or of perfect passivity by cathodic polarization" (Pourbaix, 1966).

Cathodic protection of above ground reinforced concrete has progressed from an original experimental trial (Stratfull, 1959) to an accepted technology as described by technical reports, standards and specifications (Concrete Society, 1989, NACE, 1990). A



conductive material is secured to the concrete surface to act as the anode in the CP process. Innovation in anode materials during the 1980's extended the application of CP from horizontal surfaces to soffits and vertical surfaces. Continuing areas of uncertainty with regard to the cathodic protection of reinforced concrete include the long term effects of low voltage electrolysis of concrete, the monitoring protection criteria and durability of the anode systems (Concrete Society TR36, 1989). This thesis is concerned with aspects of each of these areas and also seeks to provide fundamental information on the operating characteristics of specific anode materials.

## **1.2. Scope of the investigation**

The aims of the investigation were as follows:

1. To characterise the nature and kinetics of electrode reactions and processes occurring for several anode systems which have been utilised in reinforced concrete CP systems.
2. To assess the influence of current density on the durability of anode systems.
3. To assess the influence of concrete chloride ion content on CP system performance.
4. To determine the influence of anode material on ionic migration during CP
5. To identify criteria which will allow further development of novel anode materials.

The work was of interest since the durability of some cathodic protection anodes had been unsatisfactory (Schell, 1987, King, 1988). It was intended to be relevant to the full scale, where variations in the ground-bed conditions may give rise to high local current drains whose effect on anode performance requires monitoring and understanding. With increased knowledge of the interactions between anodic reaction products and the cement matrix adjacent to the anode it may be possible to design anode systems of enhanced durability and efficiency.

Three generic types of anode were selected for investigation:

- Flame sprayed zinc
- Conductive paint
- Titanium mesh with catalytic oxide coating/cementitious overlay system

The work was conceived as three complementary investigations, which were performed concurrently:

1. A laboratory study of the electrochemical behaviour of each material in de-oxygenated, idealised solutions by means of potentiodynamic anodic polarisation measurements.
2. Measurement of the ionic concentration gradients which develop during cathodic protection by analysis of expressed pore solution from cement paste prisms.
3. An exposure trial lasting 18 months at Taywood Engineering, involving application of cathodic protection to concrete slabs of area  $0.25 \text{ m}^2$  with varied levels of chloride contamination, at current densities of  $20 \text{ mA/m}^2$  and  $50 \text{ mA/m}^2$ .

### **1.3. Plan of presentation**

This thesis is divided into nine chapters, followed by references and appendices. Supplementary text is given in Appendices 'A', which are numbered primarily with reference to the chapter to which an appendix relates, hence Appendix 3.1 is the first appendix of chapter 3. Tables and figures referred to in an appendix are located within that appendix and prefixed by 'A', hence table A3.2.2 is the second table of Appendix 3.2.

Plates, tables and figures relating to the main text of Chapters 1 to 9 are arranged in separate appendices, titled B, C and D respectively, owing to the large number of illustrations, which it is felt would otherwise adversely break the flow of the text. These illustrations are numbered by chapter and sequential order of appearance, hence plate 3.1 is the first plate of Chapter 3 and would be located in appendix B.

Following the introduction in chapter 1, chapter 2 consists of a review of cathodic protection of reinforced concrete. Chapter 3 describes the materials and analytical methods used in the work.

The experimental work is described in five chapters, of which chapters 4 and 5 describe laboratory studies and chapters 6, 7 and 8 describe different aspects of the cathodic



protection exposure trial. Each chapter starts with a general introduction and review of relevant literature, followed by a description of experimental procedure, results and discussion. Each chapter ends with a summary of results and conclusions. Chapter 4 describes the electrochemical studies of the anode materials in idealised solutions whilst Chapter 5 describes ionic migration in cement pastes during cathodic protection. Chapter 6 examines the physical performance and durability of each anode material using a variety of destructive and non-destructive techniques, Chapter 7 analyses the electrical performance and Chapter 8 investigates the effect of ionic migration within concrete during cathodic protection and examines the influence of CP on the concrete substrate.

Chapter 9 relates aspects of each investigation to one another in order improve the theoretical basis for cathodic protection and to provide insights into the behaviour of each anode material under investigation. Finally, further areas of research are outlined.

## **2. Chapter Two. Literature review: Cathodic protection**

### **2.1. Introduction**

Cathodic protection was first used to reduce the corrosion of the copper sheathed hulls of British Navy sailing ships, as reported by Sir Humphrey Davy in 1824 (Uhlig, 1977). Blocks of iron and zinc, attached to the hulls, corroded preferentially to the copper and thereby supplied a source of protective current. Davy had originally conceived supplying the protective current using the recently developed Voltaic battery but this was impractical at the time (Shreir and Hayfield, 1986). Impressed current CP was developed as a practical way of reducing corrosion with the invention of d.c. generators and efficient storage batteries and initial applications were to underground structures from around 1910 (Lynes, 1951). By the 1930's it was a measure widely adopted to mitigate corrosion of buried steel structures. The anodes were placed in groups of holes, known as groundbeds, either adjacent to or at a distance from the structure, depending on the anode material and structural dimensions (Wilkins, 1986). Soil and water generally offer a low resistance and low resistance circuits were easily established, enabling the efficient use of sacrificial anodes or of low impressed current densities. The anode materials initially used in these systems were scrap iron and steel, aluminium and graphite, adapted from the chemical processing industry. Anodic products were found to polarise steel electrodes and this was overcome by placing the steel in a carbonaceous backfill. The material used as backfill was coke breeze, an industrial by-product, which had the added advantage of increasing the anode dimensions. Graphite was impregnated in inert resins and waxes to reduce its permeability and often placed in a coke breeze filled steel canister to improve its mechanical properties and the anode dimensions. High silicon cast iron was similarly placed in carbonaceous backfill (Moreland and Howell, 1989). The application and characteristics of these materials are given in some detail in national codes of practice (Francis, 1989).



Cathodic protection has been successfully applied to offshore and buried structures by sacrificial anodes and impressed current systems and this technology is well documented elsewhere (Wyatt, 1986, Crundwell, 1989, Willis, 1989).

## **2.2. Cathodic protection of concrete**

The design principles and anode materials developed for cathodic protection of underground structures were applied to protect prestressed reinforced concrete pipes in North Africa and in France in 1946 (Franquin, 1964, Heuzé, 1965). Cathodic protection was first applied to above ground reinforced concrete in 1957 as part of an experimental programme investigating ways to repair highway bridge decks which were suffering severe corrosion due to winter de-icing salts. The major difference between this and CP of underground/submerged structures was that the anode had to be in direct contact with the bridge deck surface, and a carbon anode with a conductive grout overlay was applied to the side of a beam to inhibit the galvanic corrosion of anodic areas as identified by a structural survey (Stratfull, 1959). Experimental work during the 1960's concentrated on evaluating the cathodic behaviour of steel in simulated concrete pore water solutions and in concrete (Hausmann, 1967, Robinson, 1968). Cast iron primary anodes embedded in a coke-breeze conductive overlay were placed on a bridge deck for a full scale cathodic protection trial, undertaken in 1973, which established the practical application and procedures of cathodic protection to above ground concrete structures (Stratfull, 1974). This system has been refined and is now a standardised method generally adopted for much of the bridge deck repair work in the US and Canada (Boam, 1989).

Subsequent research effort has largely been associated with establishing operating criteria and developing novel anode systems. Slotted anode systems were designed to limit increases in road base depth and additional dead load associated with the conductive overlay system. These systems generally consisted of platinised wire strands or carbon fibres which were placed in grooves cut into bridge decks and embedded in various conductive cementitious and polymer grouts (Wyatt, 1989). Poor performance was related to the

relatively small anode:concrete surface area and consequent high current densities generating high acidity. Several other anode systems have been applied to horizontal wearing surfaces utilising conductive rods, mounds and polymer wires embedded in conductive overlays or in slotted systems (Manning, 1990).

The systems developed for wearing surfaces were unsuitable for vertical faces or soffits and an increasing awareness of corrosion of columns, piers and bridge sub-structures led to the development of more lightweight anodes during the 1980's. These may be generally classified into two groups; conductive coatings and mesh anodes encapsulated in an overlay. Trials of a variety of conductive coatings identified conductive paints and sprayed zinc as the most suitable for cathodic protection (Apostolos, 1984, Das and Geoghegan, 1984). Conductive coatings have the advantage that they can be applied to geometrically complex structures with little additional dead load. Three types of mesh anodes have been developed; carbon fibre, conductive polymer and metal oxide coated titanium. These are designed to be encapsulated in an overlay, although mesh manufacturer's have tended to expect cathodic protection system designers to select an appropriate overlay, that is the mesh anodes have not always been designed as a complete system (Wyatt, 1989). An overlay would increase structural loading to a greater extent than a coating.

### **2.3. Theoretical basis for cathodic protection**

The anodic dissolution of iron and the cathodic oxygen reduction reaction involve electron evolution and consumption and occur simultaneously to maintain charge neutrality. It is possible to express the rates of these part reactions in terms of the charge passed, that is, as current densities. The part reaction rates may be represented graphically as straight lines in an idealised Evans diagram, which plots the logarithm of the current density of individual part reactions against potential, as shown in figure 2.1. Where the lines intersect, the rates of reduction and oxidation are equal and the current density is equal to the corrosion rate, termed  $i_{\text{corr}}$ . The potential at which this occurs is termed the corrosion potential, or  $E_{\text{corr}}$ .

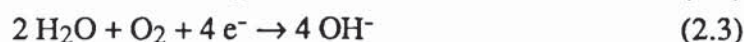


Further theoretical considerations regarding Evans diagrams, also known as polarisation curves, is given in Chapter 4.

When a negative overvoltage is applied to the steel (cathodic protection), the excess electrons accelerate the cathode reaction and retard the iron dissolution reaction. The corroding metal, represented by the anodic line, is reduced to a potential value below the reversible potential of the anode  $E_a$  and the corrosion current from  $I_{corr}$  at the corrosion potential to zero at  $E_a$ . The cell current, or cathodic protection current, is now equal to the applied current,  $I_{applied}$ . Hence the metal surface becomes equipotential and no corrosion current can flow as long as  $I_{applied}$  is maintained.

## 2.4. Chemical processes of cathodic protection

The cathodic reactions associated with steel are universally accepted to be the reduction of oxygen and water with the products hydroxyl ions and hydrogen:

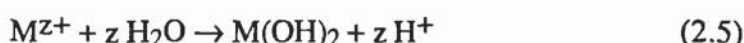


The rate of oxygen reduction is determined by the rate of diffusion of oxygen in concrete whereas the water reduction reaction is controlled by the kinetics of the charge transfer process (Evans, 1989). The reactions lead to an increase in alkalinity at the cathode, restoring and maintaining steel passivation.

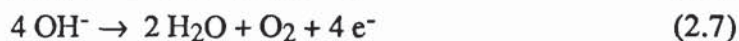
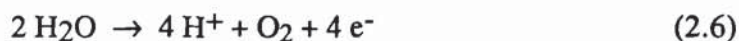
The primary anodic reaction for sacrificial anodes is spontaneous and involves ionisation of the metal:



In neutral or alkaline solutions the metal cation will be unstable and become hydrolysed:



Anodic reactions for impressed current systems are widely held to be the generation of oxygen, water and chlorine gas with the overall effect of lowering the local pH. In neutral solutions oxygen is evolved and in alkaline solutions, water also evolved as follows:



Chlorine evolution is possible at inert electrodes at relatively small concentrations of chloride ions (Shreir and Hayfield, 1986):

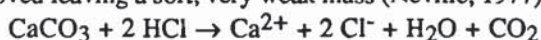


The anode material directly influences the reactions occurring and these are likely to change with time as the environment adjacent to the anode varies. This may be due to reaction products inculcating secondary reactions or due to external factors such as variation in temperature and moisture. Concrete in contact with the anode may become dehydrated as water is consumed and calcium silicates and aluminates may become unstable in the less alkaline conditions and dissolve<sup>2</sup>, resulting in a deterioration of the anode/concrete interface. In addition, corrosion of the anode material may occur due to the development of an aggressive operating environment. These factors have often been ignored by other workers when considering the long term durability of CP systems.

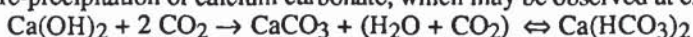
Accelerated and long-term testing of CP systems has confirmed that production of some anodic products leads to acidification at anode/concrete interfaces with subsequent local modifications to cement paste (Schell *et al*, 1984, Mussinelli *et al*, 1987). These results will be discussed presently.

---

<sup>2</sup>Acids attack all OPC concretes by converting hydrated cement paste into soluble salts, which dissolve and are removed leaving a soft, very weak mass (Neville, 1977):



Attack of cement gel occurs at pH values below about 11.5, increasing as the pH decreases and is severe at values less than pH 4.5. During a mild attack, calcium hydroxide tends to be precipitated as calcium carbonate which may react with carbonic acid to form soluble bicarbonate. Dehydration of the bicarbonate leads to re-precipitation of calcium carbonate, which may be observed at external surfaces:





## **2.5. Galvanic cathodic protection**

Several workers investigated sacrificial cathodic protection systems for reinforced concrete piers. Zinc in the form of perforated sheets with an asphaltic overlay was shown to polarise reinforcement in the range -600 to -800 mV (SCE) (Whiting and Stark, 1981) and this stimulated further work. Steel cored zinc ribbon, placed at 150 mm centres with a 0.5% chloride (by weight cement) contaminated sprayed concrete overlay, was applied to a bridge substructure and generated a current density in the range 1 to 4 mA/m<sup>2</sup>, which was considered insufficient to protect the reinforcement. The driving voltage during system operation was in the range 70 to 140 mV, lower than the maximum theoretical potential difference of 323 mV between steel and zinc in solutions due to the voltage losses from passing current through highly resistive concrete (Manning *et al*, 1984). In general, zinc sacrificial anodes have been shown to provide inadequate voltage in high resistivity media such as above ground concrete and the galvanic current cannot be adjusted. To increase the current density it would be necessary to increase the zinc area by applying a continuous zinc coating, however there are no reports of such systems.

The alternative to galvanic current is to impress rectified d.c. voltage into the concrete using surface mounted anode materials.

## **2.6. Impressed current cathodic protection systems**

Impressed current systems are made up from several components:

- a surface anode
- a power supply
- control instrumentation
- electrical connections to complete the system

It is essential for the reinforcement to be electrically continuous to prevent induced corrosion in unconnected steel and for the concrete to have a sufficiently low resistivity (Broomfield *et al*, 1987). Descriptions of the system components are given elsewhere (Concrete Society TR36 & TR37, 1989, Schell *et al*, 1984) and the importance of components' compatibility and competent, integrated design has been emphasised (Wyatt, 1989, Boam, 1989, John

and Messham, 1989). In addition, questions relating to the efficacy and appropriateness of CP have been addressed by others (Ashworth, 1987, Boam, 1989) and will not be considered in this work as they relate to engineering judgements which must be applied to individual cases: the decision to apply CP is dependent on an economic appraisal of all possible repair or replacement options with consideration for the remaining design life of the structure.

The ultimate success of CP systems has generally been measured by evidence of any further structural deterioration and by the continued operation of the CP system (Boam, 1989). The anode material has been identified as the most important system component (Wyatt, 1989). This is perhaps not surprising considering the need for continuous, intimate contact between anode and concrete electrolyte and the thermodynamic tendency for acid generation at this interface.

The most important property of an impressed current anode is to provide protection to the structure over the required design life. This is best achieved by maintaining the reinforcement at an even potential using a minimum applied current (Manning, 1990). Desirable properties for an anode to facilitate this would be a low circuit resistance and a high anode:concrete surface area ratio to minimise the current density and to effect an efficient distribution of current to all areas of reinforcement (McKenzie, 1990).

Concrete structures often have uneven cover to reinforcement, which approaches zero in some cases and this is often a contributory reason for corrosion. Current will preferentially take the path of least electrical resistance through concrete, often the shortest distance, hence current density distribution may be influenced by the depth of reinforcement and by areas of low resistivity due to high moisture or chloride concentrations. In one investigation, the distribution of CP current through a concrete slab was determined and significant proportions of current were measured at depths of 150 mm, demonstrating that the surface anode had the ability to "throw" current to reinforcement at great cover depths (Schell *et al*,



1984). Additionally, current levels were shown to be a maximum directly beneath a strand primary anode, decreasing significantly with horizontal distance (Stratfull, 1983). Single strand and mesh anodes effectively behave as a point source electrically and the majority of current passes through a narrow arc towards the cathode. As the spacing between strands decreases, the current distribution may approximate to the uniform field associated with a continuous coating and the anode surface current density decreases, reducing the likelihood of overlay acid attack.

Some anode systems utilise two materials to make the most efficient use of materials. The material connected to the power supply is termed the primary anode and this conducts electronically to a secondary anode, which is in contact with the concrete surface.

## **2.7. Conductive paint**

A conductive paint consists of a binder, which may be based on a variety of materials, and graphite pigmentation. Conductivity relies on the electrical transfer between the pigmented particles which are maintained in electrical contact with a binder having low insulating properties (Das and Geoghegan, 1984). The binder must exhibit good adhesion to the substrate under all operating conditions and be resistant to degradation processes. Conductive paints with solvent based acrylic and chlorinated rubber binders have both performed well in laboratory trials and subsequently been applied to full scale structures (Lewis, 1989, McAnoy *et al*, 1987, Wyatt, 1989). These materials were used originally as anti-fouling paints and subsequently as marine anodes (Bingham, 1991).

Conductive paints are applied by brush or airless spray direct to the concrete surface using platinised titanium wire as the primary anode and carbon fibre as current distributors. A CP coatings selection trial indicated that a dry film thickness of 800  $\mu\text{m}$ , obtained by six coatings, provided an optimal film conductivity (Broomfield *et al*, 1985). However, this was modified for site applications to a specification for a wet film thickness of 800-1200  $\mu\text{m}$ , obtained by two coatings (Palmer, 1986) and a typical dry film thickness for

conductive coatings is 400  $\mu\text{m}$  (Concrete Society TR36, 1989). Conductive paint is said to be relatively easy to apply and repair (NCHRP, 1985, Lewis, 1987). Some preparation may be required to facilitate paint adhesion to the concrete; grit blasting or water jetting can provide a key for mechanical bonding and some paints require prior application of an adhesion promoter (McAnoy *et al*, 1985). It is considered essential however that the concrete substrate is dry to ensure long term adhesion (Concrete Society TR36, 1989). Cosmetic overcoats, used to mask the black colour of the conductive paint, have been shown to improve system performance by reducing thermal cycling effects (Broomfield *et al*, 1985). Operating systems have achieved successful cathodic polarisation at current densities in the range 10 to 50  $\text{mA/m}^2$  (reinforcement area) (Wyatt and Irvine, 1987, Broomfield *et al*, 1987).

The carbon element of conductive paints is consumable as carbon dioxide formation is thermodynamically possible during cathodic protection. The carbon loading in the available coatings is said to be sufficient to give a life expectancy exceeding 25 years at 20  $\text{mA/m}^2$  (Concrete Society TR36). Adhesion is generally reported to increase with time due to continued solvent evaporation leading to consolidation of the carbon particles (Palmer and Bradley, 1989). However, in practice, both acrylic and chlorinated rubber based coatings have been reported to deteriorate and blister badly at isolated locations or debond under applied current (Schell, 1984, Palmer, 1986, Lewis and Boam, 1987, McKenzie, 1990). Blistering has been attributed to areas of high chloride concentration and high moisture content leading to high current drains, in combination with poor weather during coating application (Wyatt, 1987, Palmer and Bradley, 1989). A trial undertaken to determine the influence of surface preparation and environment on conductive paint deterioration indicated that adhesion was impaired by high humidity, the application of thicknesses greater than recommended by the manufacturer, surface preparation and a high concrete substrate chloride content (Burns, 1988). Unpolarised specimens were generally unaffected by a wide range of environmental conditions, including static brine ponding, freeze/thaw and high ultraviolet light levels, other than when the substrate chloride content was high.



Applied current led to deterioration under a range of exposure conditions and was accelerated by higher currents, high substrate chloride content and by moist conditions. Others workers have indicated the need to determine the adhesive failure mechanism, since an apparently low value of adhesive strength may not relate to deterioration of the adhesion between coating and substrate (Palmer and Bradley, 1989).

Clearly the application of any concrete coating will be sensitive to poor workmanship and this may be exacerbated by the acid forming reactions at the coating/concrete interface. However, there have been no descriptions of a progressive failure due to a coating operating close to the maximum specified current density thresholds, and the exact mechanisms involved in blistering are uncertain. It was of interest therefore to include a conductive paint in this investigation.

## **2.8. Sprayed zinc**

The technique of flame spraying zinc on to concrete was initially used to electrically screen reinforced concrete elements (Palmer, 1987). Concrete surface preparation is similar to that required for application of conductive paints, although no primer is required. The flame spraying process is generally carried out by a specialised contractor and involves melting a continuously fed metal wire by an oxygen-acetylene or propane-oxygen flame and spraying the molten metal by compressed air on to the concrete surface (Apostolos, 1984). Alternative metallizing techniques are electric arc spraying and plasma spraying, whereby zinc in powder form is melted in an argon-hydrogen flame. The heat from zinc plasma is dissipated into the bulk concrete and the surface temperature can become very high, causing micro-cracking of the concrete surface and reducing the mechanical bonding strength (Palmer, 1987). It has been suggested that the surface heating effect of the technique may reduce the moisture limits placed on the concrete surface for successful application of other coatings (Wyatt, 1989). With regard to this, the depth and size of the concrete element would be influential in dissipating the heat from molten zinc. Successive multiple passes would be likely to generate high surface temperatures which may weaken the mechanical

zinc-concrete bond, although there have been no reports of this effect and it would be avoidable by a careful operator. The zinc coating composition would be influenced by the method of metallizing adopted, the flame spraying technique possibly partially oxidising zinc particles (Short, 1990). A zinc coating may therefore contain impurities and exhibit a heterogeneous crystalline structure.

#### **2.8.1. Zinc as an impressed current anode**

Zinc may be considered as a fully consumable anode and the primary anodic reaction is given in equation (2.4). Since a continuous zinc anode consists of a certain thickness of zinc over the total concrete surface, little room for manoeuvre exists in design of the basic system. The coating thickness of 200  $\mu\text{m}$ , used in early work, has been specified as a minimum average value (Concrete Society TR36, 1989). This appears to be an empirically derived value and may not be as appropriate for a concrete cathodic protection anode. The Concrete Society report above indicates a zinc coating life expectancy of 10 years at common current densities, assuming no lowering of electrical efficiency or loss of bond due to corrosion products. This value would appear to be based on the work of Apostolos (1984), with an assumed current density of approximately 7  $\text{mA/m}^2$  (concrete area), a zinc consumption rate in salt water of 808 ampere hour/kg and an efficiency factor of two. The validity of this has been questioned by some, since current density requirements may approach 20  $\text{mA/m}^2$  and the utilisation factor may be greater than 50 % (Wyatt, 1989). Further, the calculation assumes total coating consumption without allowing for early total bond failure.

Flame sprayed zinc coatings were first used as an impressed coating anode as part of a trial of several metallized coatings and carbon paints. The current density applied was 300  $\text{mA/m}^2$  (anode area), which may be considered an accelerated test (Apostolos, 1984). Surprisingly, no degradation of the zinc coatings used in the trial was reported, although the specimens were shown to be affected by drying out of the concrete surface, when the circuit resistivity increased and cathodic current density decreased.



The first application of sprayed zinc to a structure was again part of a trial of several anode systems in 1983. A potential problem highlighted by the work was short circuiting between the zinc and the steel reinforcement at areas of minimal concrete cover (Schell, 1987). The system was reported to protect the reinforcement with again, no deterioration of the zinc coating (Manning, 1990). However, no operating data has been made available to date. Considering the natural aggressiveness of concrete to zinc and the theoretical reactions for cathodic protection already outlined, the apparent lack of zinc deterioration is notable.

Sprayed zinc is currently under trial at the Midland Links CP trials and has been used in a CP effectiveness assessment at the Transport and Road Research Laboratory (McKenzie, 1990), although with no published data to date of zinc durability.

Recommendations, largely based on the pre-mentioned research, indicate that zinc coatings for cathodic protection may not be appropriate for several situations (Concrete Society TR36, 1989): wearing surfaces due to potential mechanical damage; porous concrete due to short circuits to the reinforcement; structures with large variation of chloride, presumably to prevent uneven high current flow through the least resistive chloride areas; and frequently wetted structures due to the possibility of zinc self corrosion. It may be inferred from the high sensitivity of the zinc coatings to the environment, and the increases in system voltage, that degradation of the CP zinc coatings does occur by some corrosion mechanism. Experience of galvanised zinc coatings in alkaline solutions and concretes suggests that a zinc hydroxide complex may form at the interface between the zinc and concrete which influences the anodic processes (Sergi *et al*, 1985).

At present the factors affecting zinc consumption have not been fully elucidated. Owing to the lack of information on the behaviour of zinc as a CP anode, it was included in the research programme.

## **2.9. Mesh anodes**

Mesh anodes are said to provide an even distribution of current to a structure. Titanium mesh based anode dimensions vary from of 200 x 75 mm to 50 x 23 mm (ICI, 1989, Kotowski *et al*, 1989, Eltech Systems Corporation, 1990, Oronzio de Nora S.A., 1987). The mesh is generally pinned to the concrete surface using plastic anchors and a cementitious mortar or concrete, often polymer modified, is applied by hand or spray gun to encapsulate the mesh.

### **2.9.1. Conductive polymer anode**

The polymer anode is supplied either as a continuous strand or is woven into a grid. It consists of a copper cored cable with an outer sheath, based on a polyolefin insulation polymer modified with carbon to be conductive (Wyatt, 1987). The anode was initially designed to limit the anodic current density to a maximum in the range 80-108 mA/m<sup>2</sup>, with a normal operating cathodic current density in the range 6-20 mA/m<sup>2</sup> (Lewis, 1987). If these values were adopted it was indicated that no anode degradation due to acid production should occur and apparently successful applications have been reported (Kendell and Pithouse, 1987, Nuiten, 1990). However, the anode material was shown to crack locally due to current overload and also to promote the dissolution of surrounding overlay at a mean current density of 10 mA/m<sup>2</sup> in a tunnel road deck, of uneven chloride contamination (Hunkeler, 1989). An expanded titanium mesh in the same trial was reported not to suffer from similar degradation. The polymer anode tended to fail due to the large spacing of the anode wire with the resultant high current density to allow adequate reinforcement polarisation. Although it was intended to include a polymer anode in this work, the material was withdrawn from the reinforced concrete CP market by the manufacturer in 1988.

### **2.9.2. Activated titanium mesh**

Titanium itself will not function efficiently as an anode as passivation occurs up to very high anodic potentials without the evolution of oxygen (Epelboin *et al*, 1981), but the metal is often used as a base for a sintered mixed metal oxide electrode system (Martin and Bennett, 1987). This composite material, consisting mainly of ruthenium oxide coated onto a titanium substrate, was developed to replace graphite anodes in the chlor-alkali industry and



enabled higher current densities, lower over-potentials and a longer life to be achieved (Randin, 1981). Titanium has a high corrosion resistance, the dissolution potential depending on the electrolyte. At ambient temperatures, anode grade titanium in chloride-containing electrolytes is reported to withstand potentials of 8 to 10 volts, although this decreases with impurities and at temperatures greater than 40 °C (Harco Corporation, 1984, Martin and Bennett, 1987). As a result, there is no need to make good small abrasions to the catalytic coating or to mask-off cut ends.

Several proprietary catalytic coatings have been developed for titanium mesh substrates. The manufacturers of certain proprietary mesh anodes indicate that their catalytic coatings have been designed to allow only oxygen evolution at normal operating current densities of between 5 to 20 mA/m<sup>2</sup> (steel reinforcement area) and that less acidity is generated as a result. However, the technical information provided by the anode mesh manufacturers has not been backed up by detailed published research hence cathodic protection engineers have been unable to specify anode materials with confidence (Lewis, 1989, Wyatt, 1989). The various meshes have been utilised extensively in CP systems, particularly in the USA, and of the many technical papers describing installations, few have indicated the occurrence of anodic degradation.

The most comprehensive published study of the performance of an embedded activated titanium mesh concerned a mesh cast into small reinforced concrete slabs which were held at 0.1, 0.2, 1 and 2 A/m<sup>2</sup> (anode area) (Mussinelli *et al*, 1987, Pedferri *et al*, 1989). The pH was measured in drilled holes adjacent to the anode mesh using a pH electrode and liquid indicators. The concrete pH fell to pH 10 within 40 days at 100 mA/m<sup>2</sup> and pH 8.7 and pH 6 at 1 and 2 mA/m<sup>2</sup> respectively. Subsequently over a period of 26 months, the specimen held at 100 mA/m<sup>2</sup> showed variation in the range pH 8 to pH 10, tending to decrease towards pH 9. It is likely that a concrete depth of only 1-2 mm from the anode would carbonate due to atmospheric gases and a proportion of the decrease may be attributed to this. The pH of the specimen held at 1 A/m<sup>2</sup> tended to decrease to around pH 5, whilst the

specimen held at  $2 \text{ A/m}^2$  quickly decreased to a plateau of pH 5 for a period of approximately 240 days followed by a decrease to around pH 2. The latter specimen was cored at around 470 days and the interface between mesh and concrete inspected. A well defined, 3 mm wide zone of damaged concrete was noted adjacent to the mesh with a pH value of 1.5 to 2. The pH was unaltered elsewhere. A specimen containing 6% chloride (by weight cement) and held at  $200 \text{ mA/m}^2$  for about 12 months was similarly examined and displayed a local pH of 3.5 to 4. These results suggest that the acidification process was progressive and was related to both the magnitude of the applied current density and to the chloride content of the surrounding concrete. No modifications were observed to the anode mesh in any of the specimens.

The influence of the chloride content of the concrete substrate or overlay on mesh anode performance appears to be of interest, but has not been addressed directly in the literature.

Two titanium based mesh anodes were included in the present research programme to determine whether any practical difference in performance between them could be observed and for comparisons to be made with the performance of the conductive coatings.

### **2.9.3. Cementitious overlays**

The potential for disbondment of cementitious overlays for CP meshes was demonstrated during a trial of a polymer concrete anode with a sprayed concrete coating, with an applied current density of around  $120 \text{ mA/m}^2$  (anode area) for eight months (Schell *et al*, 1984). A strong chlorine smell was noted on removal of cores. The concrete adjacent to the anode was discoloured and degraded with a pH of 6, whilst the anode was undamaged with a surface pH of 2. However, the location of disbondments did not relate to anode positions or other structural features. Disbondments on commercial projects have also occurred but are not generally reported (Humphrey and Lambe, 1989). The movement of water within concrete towards a cathode during electrolysis at very high current densities was deduced from weight loss and resistivity measurements (Rosa *et al*, 1913). It has been suggested that such electro-osmotic flow may have contributed to concrete/cementitious overlay



failures during CP by inducing interfacial bond stresses (Page, 1988). However, investigation of such factors was outside the scope of this work.

Mesh manufacturers have indicated that some local degradation at the anode/cover interface may be expected due to acidic anode reactions and emphasise the importance of cementitious overlay specification and the total encapsulation of the anode by the overlay in order to contain anodic products (ICI, 1989). A number of different formulations of cementitious overlays have been developed which are often a complex mixture of cement replacement additions, additives and polymers to promote adhesion and reduce shrinkage. The materials are generally applied by spray, trowelling, flowing and pumping (Concrete Society TR36, 1989) and thicknesses vary from 10 to 50 mm. However, little guidance exists regarding the performance or selection of the most appropriate material for CP systems. A range of overlay materials appeared to offer satisfactory performance during a CP trial, as determined by tensile bond tests and electrical performance data (Humphrey and Lambe, 1989). Concrete specimens of area  $0.25 \text{ m}^2$  containing 2% chloride (weight cement) were energised at  $67 \text{ mA/m}^2$  (mesh anode area) over a period of about 11 months and no deterioration of the overlays was reported to occur. The study also demonstrated that resistivity of the overlays depended on the precise formulation, increased polymer content tending to increase resistivity, and the degree of curing. The results indicated that the resistivity of an overlay stored in dry conditions could progressively exceed a maximum recommended value of  $50 \text{ k}\Omega\text{cm}$ , as proposed in the Concrete Society TR36 (1989).

An investigation of the debonding of sprayed concrete was planned as a part of the CP trial. However, on the withdrawal of the polymer cable anode, which required a thick overlay, this was no longer appropriate. The direction of the investigation was altered and a proprietary acrylic modified cementitious mortar was used to allow direct comparisons between the mesh anodes and for practical application convenience.

### **3. Chapter Three. Materials and analytical techniques**

#### **3.1. Introduction**

This chapter describes the majority of analytical techniques and the materials used for the study.

#### **3.2. Materials**

##### **3.2.1. Cement**

The cement used to manufacture all cementitious specimens was from a single batch of Ordinary Portland Cement supplied by Blue Circle cement company from the Northfleet, England works. A chemical analysis is given in table 3.1, as determined by BS 4550 Part 2: 1970 "Methods of Testing Cement".

##### **3.2.2. Aggregate**

The fine aggregate was a medium grade Thames Valley sand and coarse aggregate was a 10 mm maximum particle size Thames Valley chert aggregate. Both were stored externally hence a value for the moisture content was determined to allow surface moisture to be compensated for in each mix batched. This was determined by the "speedy" method following the instructions supplied with the apparatus. A sample of the aggregate was mixed with an excess of calcium carbide in a sealed metal flask. The pressure produced by the acetylene liberated by the reaction between water and carbide was related to the moisture content, which was read directly off a dial. Three samples were tested to obtain a representative value and the mix quantities adjusted accordingly. A typical calculation is provided in Appendix 3.1.

##### **3.2.3. Water**

Ordinary tap water was used in concrete mixes and de-ionised water was used in cement paste mixes.

##### **3.2.4. Steel**

Mild steel was used for cathodes embedded in cements and was prepared as described within the appropriate experimental chapters. Descaling was achieved by placing the steel in



a bath of 6 M hydrochloric acid with 1 gramme of dissolved hexamine, to inhibit further corrosion, for 120 minutes and subsequently placed in a bath of deionised water for 5 minutes to wash off the dissolved corrosion products. A second bath of 1 M sodium carbonate for 5 minutes neutralised any remaining hydrochloric acid and was followed by a final wash in deionised water. The steel was dried by paper towel and stored in a desiccator before use.

### **3.2.5. Admixtures and chemicals**

Chemical solutions were prepared from Analytical grade reagents and de-ionised water. The amount of water required for a mix was adjusted to accommodate any water of crystallisation. Calcium chloride as required by a mix design was dissolved in the mix water before addition to the pre-mixed dry constituents.

### **3.2.6. Anode Materials**

Three generic types of anode material were selected for investigation. Specific application details are given in the relevant chapters.

#### **3.2.6.1. Mixed metal oxide titanium mesh/cementitious overlay**

Two proprietary activated titanium mesh anodes were used, each composed of precious mixed metal oxide catalysts sintered on to an expanded titanium mesh substrate. These will be referred to as anode E and anode T throughout this thesis. The overlay material was a proprietary two-component, acrylic polymer-modified cement-based mortar coating, specifically designed to be part of a cathodic protection system. The material is usually specified by both mesh manufacturers as suitable for use with their products and is believed to contain added chloride to improve conductivity.

#### **3.2.6.2. Flame sprayed zinc**

High purity zinc wire, a non-proprietary material, was applied by the flame spraying technique. No further coating was applied to the zinc surface. The flame spraying operation was conducted in a dry, air conditioned room. Figure 3.1 shows the flame spraying technique schematically. Pure zinc wire was fed by pinch rollers, driven by compressed air, into the centre of the spray gun head and was vaporised by a propane gas flame. A concentrated jet of compressed air, directed over the zinc wire, formed a molten

zinc arc which was directed onto the dry concrete surface. To ensure an even build up of zinc on the surface the distance between the spray gun and surface was in the range 100 to 150 mm. Two perpendicular passes built up a coating thickness of 200  $\mu\text{m}$ .

#### 3.2.6.3. Conductive paint

The proprietary conductive paint comprised a chlorinated rubber paint base with conductive graphite/carbon filler. A white proprietary cosmetic masonry top coat was applied to some specimens, variations in application detail being given in the relevant chapters. The paint application methods were based on the standard Taylor Woodrow Engineering method statement for this material (Palmer, 1986). A single source of paint was used throughout the work, manufactured in March 1986. Advice was sought from the paint manufacturer as to an appropriate technique to prepare the paint for application due to its age, as it was felt that the carbon filler may have sedimented out. The paint container was therefore turned upside down for two days and remixed using an electric drill with paddle stirrer for 10 minutes. It was then assessed for even consistency, colour and viscosity, ensuring that no particles remained at the sides or base. A coating adhesion promoter was manually applied to specimens by brush and allowed to dry for 24 hours prior to application of the conductive coating.

### **3.3. Compressive strength**

Compressive strength tests to BS 1881 Part 4: section 2: 1970 "Tests for compressive strength of test cubes" were carried out to ensure that concrete specimens complied with the mix design parameters. Three 100 mm standard test cubes were cast for each concrete batch, demoulded at 24 hours and stored underwater before testing at 28 days. Each cube was surface dried, weighed and then tested to failure.

### **3.4. Resistivity**

Concrete resistivity measurement has become an established technique for determining the degree of corrosion risk (Wilkins, 1982; Figg and Marsden, 1985). The method was originally based on the Wenner probe soil resistivity method but has been modified to overcome polarizing effects which occur at the probe/concrete interface (Ewins, 1990).



The proprietary instrument used in this work utilised probes with softwood tips which, when saturated with water, reduced the high-resistance surface skin effect. Four equidistant probes were placed on the concrete surface with 50 Hz alternating current passing between the two outer probes and the potential difference between the two middle probes was recorded. The instrument displayed the resistivity value directly in units of ohm cm. Three readings were taken for each slab and an average resistivity value calculated for each batch of specimens.

### **3.5. Water permeability**

The water permeability of concrete is a function of its porosity and the connections between pores and so this property was measured as part of mix characterisation, as described in chapter 6. The permeability coefficient is not constant, but tends to reduce with time, hence a standard methodology is essential (Concrete Society, 1985). The water permeability coefficients were measured using a standard test procedure developed at Taywood Engineering (Taywood Engineering Limited, 1988). Values obtained by measuring the time to penetrate the specimen are generally higher than subsequent flow values due to silting of pores by loose particles, swelling of cement gel and continued hydration of cement, accelerated by pressure (Taywood Engineering Limited, 1988). Although the recommended method involves a test duration of 7 days, this was limited to approximately 24 hours in the present work owing to constraints on apparatus availability. Since the coefficient value is dependent on the test procedure and changes during the test, this was considered sufficient to allow comparisons between mixes.

The concrete specimen of thickness between 40 and 50 mm and maximum diameter 100 mm was dried to constant weight in a desiccator. The top and bottom faces were sealed with plasticine and tape and the specimen placed in a tapered brass sleeve, dimensionally identical to the test rig, which was then filled with a sand/epoxy resin mixture. The epoxy resin was allowed to cure for 24 hours and then the specimen was demoulded and its tape was removed before re-weighing. The specimen was then placed in a specialised water

permeability test rig and a constant water pressure of 10 bar was applied to the as-cast face, as shown in figure 3.2. The time for water to appear at the top surface was noted and the subsequent flow rate was measured through a calibrated glass tube, taking an average over five rates. The permeability coefficient was calculated from the flow measurement using Darcy's equation in the following form:

$$k = \frac{Q \cdot L}{A \cdot H} \quad (3.1)$$

where  $k$  = permeability coefficient (m/s)  
 $Q$  = flow rate (m<sup>3</sup>/s)  
 $A$  = area (m<sup>2</sup>)  
 $L$  = depth of specimen (m)  
 $H$  = head of water (m)

If full penetration was not achieved during the test period, the specimen was surface dried, re-weighed, split in half and the average depth of penetration measured. The flow rate was then calculated using a modification of the Valenta formula (Taywood Engineering, 1988):

$$k = \frac{X \cdot \Delta M}{2000 \cdot T \cdot H} \quad (3.2)$$

where  $k$  = permeability coefficient (m/s)  
 $\Delta M$  = wet weight - dry weight (Kg)  
 $T$  = time of test (s)  
 $X$  = depth of penetration (m)  
 $H$  = head of water (m)

The adverse influence of the initial moisture condition and the rate of absorption on the calculated coefficient by the latter method has led to its' criticism by some (Wood *et al*, 1989), although its main value in the present work was as a comparative measure.

### 3.6. Pore solution expression

The pore solution expression device, commonly termed a pore press, was originally developed by Longuet and removes capillary pore solution from hardened cement paste by pressure. Studies have demonstrated that the liquid extracted is representative of the solution in the pores (Sergi, 1986). The device consists of a cylindrical pressure vessel with a central piston which compresses the cement sample as shown in figure 3.3. A PTFE disc prevents pore water from escaping up the sides of the piston. The sample was placed



within the device and load was applied at the rate of 3 kN/s to a maximum of 600 kN. Between 1 to 2 ml of fluid was collected by sterile plastic syringe from the fluid drain and stored before analysis in an airtight plastic vial to minimise vapour loss and neutralisation. The individual elements of the apparatus were cleaned with deionised water and acetone and then coated with a PTFE based mould release spray before re-assembly.

### **3.7. Profile grinding**

Profile grinding was developed by Taywood Engineering as a sampling method capable of removing material from a concrete core at incremental depths of 2 mm with an accuracy of  $\pm 0.1$  mm, without using an aqueous medium (Pratt, 1988). The advantages of this technique over the more widely adopted one of sampling by drilling using a masonry bit are greater accuracy and less cross-contamination of material.

Cored samples were wet cut in half by Clipper saw and allowed to dry out. A flat diamond impregnated grinding tool was inserted into a vertical mill which utilised precision depth control. The sample was secured in the mill with a wooden template and raised towards the grinding tool until it just skimmed the surface and the depth control was set. Grinding was then undertaken in 2.03 mm increments, as shown in figure 3.4, and the powdered sample collected on sheets of paper and placed in an air free sample bag. The sample bags were stored in a closed vessel containing “carbosorb” chemical and silica gel to provide a dry, carbon-dioxide free environment until analysis could be undertaken.

### **3.8. Chemical analysis**

Chemical analysis of concretes was performed on powdered samples obtained from the profile grinding technique as described above. Analysis of cement pastes was performed on pore solution squeezed from dry-sawn slices of the paste blocks and on dust collected during sawing.

#### **3.8.1. Hydroxyl ion analysis**

Hydroxyl ion concentration within the pore solution was determined by acid/base titration with 0.01 molar nitric acid and phenolphthalein as the indicator. 100  $\mu$ l aliquots of pore

solution were made up to 1 ml with deionised water and acid dispensed from a 10  $\mu$ l graduated microburette. The pH was calculated from the hydroxyl ion concentration, as set out in Appendix 3.2.

#### **3.8.2. pH of hardened concrete**

A qualitative measure of the alkalinity of concrete powder obtained from profile grinding was determined by shaking 0.5 gramme of the powder in 25 ml of distilled water for two hours at 25°C and measuring the pH with a Phillips digital pH meter. The pH meter was calibrated with buffers at pH 4, 7 and 9 and provided results accurate to within 0.01 of a pH unit. A sample calculation is given in Appendix 3.2.

#### **3.8.3. Evaporable and non-evaporable water**

It is convenient to express chloride concentrations from pore water as total present as a fraction of the unhydrated cement in order, together with values for acid soluble chloride, to determine total chloride present by weight of sample. To convert the chloride concentration in solution to that by cement weight it is necessary to determine the evaporable (free) and non-evaporable (bound) water contents in the cement. The method used in this work was found that to produce results of reasonable accuracy (Sergi, 1986), and is based on the assumption that water evaporating at 105°C represents free water and that bound water will be completely removed by heating to 950°C.

Approximately 2 g of sample was broken into small fragments, placed in a platinum crucible and immediately weighed. The sample was heated in an oven, held at 105°C and cooled by desiccator until it achieved a constant weight. The sample was then heated in a furnace to 950°C for 30 minutes, cooled in a desiccator and re-weighed. Losses due to cement ignition were determined by performing the preceding procedure with approximately 1 g of unhydrated cement (BS 4550, 1970). Calculations for determination of the evaporable and non-evaporable water contents are given in Appendix 3.3.

#### **3.8.4. Chloride ion analysis**

Concrete powder obtained by profile grinding was passed through a 150  $\mu$ m sieve and dried in an oven at 105 °C for one hour and then cooled in a desiccator for 30 minutes.



Approximately one gramme was dissolved in 10 ml of 4.8 molar nitric acid at 80°C for 40 minutes. After cooling, the flask and contents were re-weighed to allow determination of the acid added. For cement powder, 300 mg were dissolved. A 100 µl aliquot of solution was made up to 10 ml with deionised water and used for analysis. A 100 µl aliquot of pore solution was made up to 50 ml with deionised water prior to analysis.

A Beckman model 24 spectrophotometer was used to determine chloride concentrations of the solutions. To 10 ml of prepared solution was added 2 ml of 0.25 molar ferric ammonium sulphate in 9 molar nitric acid and 2 ml of saturated mercuric thiocyanate in ethanol. The thiocyanate ion was complexed with the ferric ion in the presence of the chloride ions to form a highly coloured solution. The intensity of the colour was proportional to the chloride ion concentration and was determined by the spectrophotometer, which measures the absorption of light at specific wavelengths. A beam of monochromatic light, of characteristic wavelength 460 nm, was passed through glass cells containing the coloured solution and a water blank reference and detected by a photoelectric cell. The difference in absorption was displayed digitally. The chloride concentration was then calculated from the equation of a calibration curve constructed from chloride standards, as shown in Appendix 3.4.

#### **3.8.5. Metal ion analysis**

Ionic metals in solutions display a characteristic colour when placed in a flame, due to the emission of light energy at specific wavelengths. Analytical techniques which incorporate this phenomenon include atomic absorption and flame photometry. Both techniques involve the solution being drawn through a thin tube into the instrument which atomises and sprays the solution into a flame. A filter, specific for the element, is placed in front of a photoelectric cell which measures the intensity of emitted light. This is related to the ionic concentration by using a calibration curve constructed from standard solutions.

Inductively coupled plasma atomic emission spectrometry (ICPS) is a spectroscopic technique which can be used for the simultaneous determination of many elements over an

analyte concentration range typically of five orders of magnitude (Thompson and Walsh, 1983). The sample solution is drawn into a fine tube and converted into a fine spray by a nebuliser and passed with argon injector gas into an inductively heated argon plasma, where it is atomised at temperatures around 8000°C. The atoms become partly ionised and highly excited, emitting characteristic spectra which are measured using a conventional spectrometer.

For cement paste analysis, a 100µl aliquot of the expressed pore solution was diluted by 500 or 1000 times with deionised water depending on the expected concentration. Concrete powder was prepared for ICPS by dissolving 50 mg of powder into 50 ml of 0.4 molar aristar grade hydrochloric acid for 24 hours at room temperature. The solute was decanted off and passed through the ICPS apparatus. Concrete and cement paste powder were prepared for flame photometry by dissolving in acid as described for chloride analysis. A 100µl aliquot was made up to 50 ml using deionised water for analysis. Example calculations are given in appendix 3.5.

#### 3.8.5.1. Calcium and zinc ion analysis

Calcium and Zinc ion concentrations were determined with a Perkin-Elmer atomic absorption spectrophotometer and by ICPS.

#### 3.8.5.2. Sodium and potassium ion analysis

ICPS apparatus which is optimised for calcium is reported to have a low sensitivity for sodium and potassium (Thompson and Walsh, 1983) hence sodium and potassium ion concentrations were determined with a flame photometer.

### **3.9. Differential thermal analysis**

A Stanton Redcroft model 273-4 differential thermal analyser was used to determine compositional variations in concrete, with calcined alumina as the inert reference. Approximately 0.14 g of powdered concrete, dried in a desiccator, was placed in the instrument and heated at the rate of 20 °C/min up to 950 °C. Thermal changes occurred in the sample, due to endothermic or exothermic events, at specific temperatures and the



difference in temperature between the sample and inert reference was recorded by chart recorder as troughs and peaks of varying magnitude. The recorder trace allowed identification and to some extent the quantification of the phase changes using the peak heights, which were characteristic of the hydrated cement and minerals present. The technique is only semi-quantitative, since the resulting trace is influenced by the characteristics of the instrument and the specific heat and conductivity of the specimen. The references from which peaks were identified are given in Appendix 3.6.

### 3.10. X-Ray diffraction

X-Rays of specific wavelength incident on a crystalline specimen are reflected at a number of angles related to the crystal lattice structure by Bragg's law:

$$n\lambda = 2d \sin \vartheta \quad (3.3)$$

where  
 $n$  = the order of reflection ( 1, 2 etc)  
 $\lambda$  = the wavelength of the X-Rays  
 $d$  = the spacing of the crystal planes  
 $\vartheta$  = the angle of incidence or reflection

A Phillips X-Ray spectrometer incorporating Cu K $\alpha$  radiation was used to analyse anodic products, as described in chapter 6. An electronic counter tube, rotating at twice the speed of the specimen, measured the intensity of X-Ray reflections. A chart recorder produced a trace of intensity against angle of incidence, allowing the calculation of the "d", or atomic spacing. The values of  $2\vartheta$  were taken as the centre of a peak and magnitudes were determined from the height of the peak. The d spacing was calculated using the Bragg formula and intensities determined relative to the highest peak. The d spacings were thus ranked according to the relative intensities and the Hanawalt Search Method, which takes the three strongest peaks, was adopted for primary compound identification. Compound identification was confirmed by reference to the full citation in the powder diffraction file. The relative intensity (RI) is indicated by the secondary lowercase number where 'x' represents 10. The values are accurate to  $\pm 0.01$ . The relative intensities of the standard compound may vary from those of the compound under investigation due to the orientation of the crystals during their formation (Hanawalt , 1978).

### 3.11. Mercury Intrusion porosimetry

Measurements of pore size distribution in hardened concrete were made by mercury intrusion porosimetry (MIP). The method relies on forcing mercury, a non-wetting liquid, into the sample under pressures increasing from 1.2 psi to approximately 30,000 psi in various increments. Equilibrium is allowed to develop at each pressure level and the extra mercury required to maintain the increased pressure is taken as that which has penetrated a certain size of pores, termed the penetration volume. As pressure is increased the smaller pores are progressively penetrated. The pressure at which mercury penetrates a pore of a given size may be calculated by the Washburn equation (Washburn, 1921):

$$P = \frac{-4\gamma \cos\theta}{d} \quad (3.4)$$

where

- P = the applied pressure (psi)
- $\gamma$  = the surface tension of mercury (N/m)
- $\theta$  = the contact angle between mercury and the material (°)
- d = the pore diameter ( $\mu\text{m}$ )

A contact angle of 115° for hardened cement paste was adopted for this study, as recommended by the apparatus manufacturer, although other workers have adopted a value of 117° (Sergi, 1986, Hardon, 1989). The Washburn equation is used to convert the pressure into values of pore diameter, which can then be plotted against the cumulative penetration volume.

It is likely that the test procedure affects the cement pores such that the results do not exactly represent the pore size distribution. Simply forcing mercury into an essentially brittle material may be expected to alter pore structure (Feldman, 1984). In addition, the sample drying technique has been shown to influence pore sizes. However, MIP still has value when used as a comparative technique.

A Micrometrics Poresizer 9310 was used in this work with dedicated computer control. Samples of substrate concrete and overlay were cut from 100 mm concrete cores by wet



diamond Clipper saw as shown in figure 3.5 and coarse aggregate and anodes removed. The overlay/concrete specimens were cut at the interface to prevent cross contamination of material. Pieces of cement paste were oven dried at 105°C for 2 days, weighed and placed in a glass cell which was fixed into the instrument. The system was evacuated to remove adsorbed moisture and gases and then mercury was introduced into the cell. Low pressure measurements were undertaken by controlling pressure increases manually and capturing data on the computer, whilst the high pressure measurements were performed under full computer control. All data was collected by computer and results calculated and plotted by the dedicated software.

### **3.12. Visual examination**

Information regarding physical changes or signs of deterioration was obtained from visual examinations. Optical binocular microscopy was used to enhance observations and images were recorded using an attached camera. Greater depth of field and magnification were achieved by scanning electron microscopy.

### **3.13. Scanning electron microscopy**

A Cambridge stereoscan 90B scanning electron microscope was used for microscopy studies. A "Link" microcomputer controlled energy dispersive x-ray analysis spectrometer (EDXA) was used to perform semi-quantitative elemental analysis of specific surfaces under observation. On bombardment with an electron beam, excited atoms emit x-rays at characteristic energies which are measured by a silicon detector, held at liquid nitrogen temperature. The microcomputer captures the emitted energies over a fixed time period and produces an energy/frequency plot from which an elemental analysis is obtained. This was used to assess the composition of cement minerals and corrosion products.

### **3.14. Thin section petrography**

Thin sections are prepared by grinding a cross section of interest to a thickness of around 20µm, which allows light to pass through translucent cement minerals and aggregates. This allows an examination of porosity and petrography of cross-sections of interest with the potential for sophisticated image analysis techniques (Pitts, 1987). Specimens were

impregnated with a blue resin to facilitate porosity examination and fixed to a glass slide with an optically clear epoxy resin prior to preparation of the thin section by a standard technique.

### **3.15. Adhesion pull-off test**

The adhesive strength of surface coatings is routinely measured using bond tests which involve fixing a metal dolly to the coating surface and pulling it with a calibrated device until bond failure occurs. This quantitative “pull-off” test is simple and has been widely used to assess conductive coating durability (Apostolos, 1984, Palmer and Bradley, 1989). Minimum recommended failure loads range from 4.5 to 7 Kg/m<sup>2</sup> for conductive paints (McAnoy *et al*, 1987, NRCCPA, 1990), whilst failure loads in the range 7.5 to 22.3 Kg/cm<sup>2</sup> (Palmer, 1987) and 13.8 Kg/cm<sup>2</sup> (Apostolos, 1984) have been reported for sprayed zinc coatings.

An Elecometer pull-off instrument was used to measure the uniaxial adhesive strength of the conductive coating to concrete bond, and a value was directly read from the instrument in units of Kg/cm<sup>2</sup>. The test was performed by fixing a circular aluminium dolly on to the coating surface using a quick setting epoxy resin, which was allowed adequate time to harden. The Elecometer instrument was then placed over the dolly and a uniform axial load manually applied at a constant rate until failure occurred (plate 3.1). The failure mechanism was recorded and the rupture surface was examined to aid interpretation of the test data.

The adhesive strength of mesh/overlay anodes was measured using the “Limpet” test instrument. Specimens were partially cored to a substrate depth of approximately 30 mm using a 50 mm diameter water cooled diamond tipped coring bit. Circular steel probes of 50 mm diameter were fixed to the overlay surface using epoxy resin adhesive which was allowed to cure. The instrument was connected to the probe and load was applied at a controlled rate in accordance with the operating instructions. The load was measured



electronically by transducer and the maximum load displayed on a liquid crystal display. The location of the failure plane was noted.

### **3.16. Down-coat resistance**

Down-coat voltage measurements have been made in earlier and on-going CP trials of a conductive paint anode to provide an indication of current distribution (Palmer and Bradley, 1989). This involved measuring the voltage drop between the primary anode and locations on the coating surface at varying distances. Significant voltage variations were attributed to a high CP current sink which caused significant acid attack of the concrete substrate and coating adhesion failure.

The voltage drop between the primary anode and locations on the conductive paint coating surface at varying distances was measured using a hand-held, high impedance voltmeter, with one lead connected to the positive primary anode and a negative electrical probe which pierced the cosmetic masonry paint. Voltage drops were converted into coating resistance values. A sample calculation is given in Appendix 3.7.

### **3.17. Electrode potentials**

Phillips saturated calomel reference electrodes were used to determine electrode potentials in the laboratory anodic polarisation studies and in the paste block study. Steel in concrete potentials were measured with a hand held silver/silver chloride half cell, contact being achieved through a moist sponge tip and a digital volt meter with an impedance greater than 10 Mohm. The half cell potentials may be related to the standard hydrogen electrode (SHE) and copper/saturated copper sulphate electrodes as shown in table 3.2 (Figg and Marsden, 1985, Ewins, 1988).

### **3.18. Instant-off potentials**

A portable instrument for measuring "instant-off" potentials for cathodic protection installations was developed during this work, as reported in Appendix 3.8. Operational details are given in Appendix 3.9. The instrument was incorporated into the CP circuit and momentarily interrupted the CP current. The cathodic potential increased positively as the

IR-error was removed and was 'frozen' and displayed after a time interval of 0.2 seconds on the integral Digital Volt Meter. Data was also stored via the Taywood Data Bucket. Since CP current was restored within a further 0.1 seconds, cathodic depolarisation was minimised and multiple readings for a specimen were possible.

### 3.19. Linear polarisation resistance

Instantaneous corrosion rates of steel in concrete were determined by linear polarisation resistance. This method relies on the assumption that within a few millivolts of the corrosion potential,  $E_{\text{corr}}$ , the applied current density is a linear function of the electrode potential, as illustrated in figure 3.6. This figure shows a plot of overvoltage versus applied cathodic and anodic current, the corrosion potential being the overvoltage reference point. The slope of the linear polarisation part of the curve is termed the polarisation resistance ( $R_p$ ) and may be calculated using the equation:

$$R_p = \frac{\Delta E}{\Delta I} \quad (3.5)$$

and can be related to the corrosion rate by the Stern Geary equation,

$$R_p = \frac{B}{(i_{\text{corr}})} \quad (3.6)$$

where  $B = \frac{\beta_a \beta_c}{2.3(\beta_a + \beta_c)} \quad (3.7)$

and  $\beta_a$  and  $\beta_c$  are the anodic and cathodic Tafel constants for the system. The value for the constant B is generally assumed to approximate to 26 mV for active steel in concrete and 52 mV for passive steel, these values giving good agreement with gravimetric data (Andrade and González, 1978). Extensive studies of linear polarisation results in cementitious systems have elucidated possible errors and the experimental methods required to ensure accurate data (González *et al*, 1985). If the ohmic drop (IR-drop) between reference and working electrode is not eliminated, the  $R_p$  measured will incorporate the error and be overestimated, resulting in the  $i_{\text{corr}}$  being smaller than the true value (Andrade *et al*, 1978).  $I_{\text{corr}}$  values greater than  $0.1 \mu\text{A}/\text{cm}^2$  are said to indicate a significant corrosion rate (Andrade *et al*, 1986).



Potentiostatic methods were used in the present study, rather than potentiodynamic for reasons of apparatus availability. The first method was applied to the external CP slab specimens. Two isolated reinforcement bars were used as electrodes and a hand held silver/silver chloride half cell measured potentials. A Thompson mini-potentiostat with IR compensation was used to control the electrode potentials. The test involved positively polarising an electrode by 20 mV ( $\Delta E$ ) from the rest potential ( $E_{\text{corr}}$ ) and measuring the current passed per unit area ( $\Delta I$ ) at the time periods of 10, 30, 60 and 120 seconds from disturbing the corrosion equilibrium. The current was observed to decay as the corrosion equilibrium shifted. Andrade has demonstrated that ( $i_{\text{corr}}$ ) values calculated using the current measured at 30 seconds agree well with gravimetric weight loss (Andrade *et al*, 1986).

The second method was applied to the laboratory paste block samples, with the anode utilised as the counter electrode. An Amel model 551 potentiostat was coupled to a Solartron voltmeter, with data capture and  $R_p$  calculation by a micro-computer. The ohmic potential drop between the working electrode and calomel reference electrode was compensated for using the positive feedback feature of the potentiostat. The value of  $E_{\text{corr}}$  was measured and the electrode positively polarised by 15 mV. The current was recorded after 60 seconds to allow for long time constants associated with the measurement. The electrode area was entered and  $i_{\text{corr}}$  determined by the software.

### **3.20. Potentiodynamic polarisation**

Potentiodynamic polarisation scans were performed on the selected anode materials in various solutions. Full details of this work are described in chapter 4.

### **3.21. Infra-red spectroscopy**

The following analytical techniques are based on the absorbance of infra-red radiation by molecular bonds in a compound and are generally used to identify organic compounds. The bonds of chemical functional groups absorb radiation at unique, characteristic frequencies

and the proportion of radiation absorbed is related to the number of bonds. A plot of radiation intensity against frequency produces a characteristic spectra which is a finger print of the chemical groups present and can be compared with standard spectra for the identification of the compound. In fourier transform infra-red (FT-IR) spectroscopy, the detector observes all frequencies simultaneously, allowing rapid analysis, whereas earlier systems required multiple measurements which had lower sensitivity and high noise levels (Nicolet, 1986).

#### **3.21.1. FT-IR spectroscopy**

A Nicolet 510 FT-IR spectrometer, together with a Spectratech IR-plan analytical microscope and dedicated computer control was used in the work. Infra-red radiation was produced by a source and a condensed beam generated by optical means and directed at the sample. The instrument operated in transmission or in reflectance modes. In the former, the sample was obtained on a glass slide, which the beam passed through to a collector. In the latter, the sample was rolled into a thin film on a metal cylinder and the beam passed into the film and reflected back by the cylinder, through the film, to a collector.

#### **3.21.2. Photo-acoustic spectroscopy**

The sample was dissolved in xylene and the resulting solution passed through a paper filter and put into a glass cell which was placed in the spectrometer. Vibrations induced by the infra-red source were measured and analysed by the instrument. A blank run of the solvent allowed interference to be removed from the resulting spectra.

#### **3.21.3. Horizontal attenuated total reflectance (ATR)**

Horizontal ATR is a similar technique to photo-acoustic spectroscopy, which uses a specialised accessory, as shown in figure 3.7. Samples were dissolved in 1 ml of xylene for 4 hours, aided by a mechanical shaker. The solid carbon was separated out by placing the solution in a centrifuge at 17000 rpm for a period of 5 minutes, and the solute removed by pipette and placed in the horizontal ATR sample holder. The xylene was driven off by hot air to leave a thin film on the underlying crystal. The infra-red beam was reflected on carefully adjusted mirrors and entered the crystal. At each reflection point, an evanescent wave formed which typically penetrated the sample above the crystal to a depth of 0.2 to 0.4



$\mu\text{m}$ . The amplitude of the beam decayed within the sample phase due to vibrations induced in the sample molecules. The beam emerged from the crystal and passed to the collector for analysis by the instrument.

## **4. Chapter Four. An electrochemical study of anode materials in idealised solutions.**

### **4.1. Introduction**

Theoretical chemical reactions which are widely held to occur during cathodic protection were described in Chapter 2. An inevitable result of cathodic protection in cement systems is acidification, or reduction in alkalinity, of the cement phases adjacent to the anode. The anode materials will therefore tend to operate in an environment of variable pH. Most cathodic protection trials have been aimed at establishing how operational factors, such as current density and applied voltage, influence corrosion prevention, or, in effect, to prove that cathodic protection works (Lewis and Boam, 1987, Palmer, 1987, Schell, 1987, McKenzie, 1990). However, very little systematic investigation of the electrochemical behaviour of anodes has been reported.

Accelerated testing of various anodes at high current densities has been performed by anode manufacturers and researchers in aqueous solutions which simulate concrete pore solution (reported by Mussinelli *et al*, 1987, Kotowski *et al*, 1989) and in neutral brines (Apostolos, 1984, Martin and Bennett, 1987). Although it is possible to extrapolate these short term test results to give an indication of an anode's long term life expectancy (Bennett and Martin, 1987), or of its consumption rate in particular solutions (Apostolos, 1984), this is of limited value for cathodic protection systems where a particular anode must work within a cementitious environment at low current densities. Accelerated testing of mesh anodes in concrete resulted in rapid failure of the concrete due to acidification (Bennett and Martin, 1987), whilst application of excessive current density to a conductive paint anode resulted in rapid coating failure (Pollard and Page, 1988). Such testing does not elucidate probable anodic reactions, nor allow subtle interactions between anode and concrete to be observed. Rather it underlines the importance of considering the anode as part of a system.



Several workers have used anodic potentiodynamic polarisation in attempts to determine which anodic reactions occur as current density increases for a number of anode materials (Slater *et al*, 1976, Bennett and Martin, 1987, Mussinelli *et al*, 1987). The theoretical basis for this technique will be outlined and the previous work reviewed.

#### 4.1.1. Theory of polarisation

Electrode polarisation occurs when current flows in an electrochemical cell. The resulting shift of the measured potential away from the reversible equilibrium potential is called overpotential and exhibits three forms which can be present simultaneously: Activation polarization occurs if a thermally activated charge transfer process is the slowest step of the electrode reaction sequence controlling the overall reaction rate; concentration polarization occurs when the electrolyte composition adjacent to an electrode changes due to transport restraint; ohmic polarization is due to the passage of current through a resistive electrolyte which results in a potential drop according to Ohm's Law (Shreir, 1982).

When activation overpotential predominates, the relationship between overvoltage and the log of cell current density is linear and termed Tafel behaviour, as described by the equation:

$$\eta_a = a \pm \beta_a \log i \quad (4.1)$$

where  $\eta_a$  is the activation overpotential,  $a$  is the Tafel intercept parameter, a measure of the reversibility of the reaction and related to the equilibrium exchange current density,  $i_0$ , and  $\beta_a$  is the Tafel slope parameter, which takes a negative sign for cathodic reactions and a positive sign for anodic reactions (Shreir, 1982). The straight lines in figure 2.1 represent Tafel behaviour. Tafel slopes are held to lie in the range 50 to 150 mV/decade (Fontana, 1986), and slopes exceeding this range relate to concentration polarisation controlled reactions. At high reaction rates, that is at high current densities, the concentration of reactants may become depleted at an electrode surface, and the current density approaches a limiting value; hence the increase in slope. The total polarisation of an electrode is the sum of the various overpotentials. It is related to the kinetics of the electrochemical processes occurring at the electrode surface and is influenced by modifications to the diffusion

parameters of the electrolyte. The influence of overvoltage on reaction rates for specific electrodes under specific conditions can be determined experimentally by potentiodynamic polarisation, where the anodic and cathodic sites are separated.

#### **4.1.2. Potentiodynamic polarisation**

Potentiodynamic polarisation involves varying the overpotential of an electrode at a constant rate and measuring the consequent current flow. The measured potential is usually plotted to a linear scale and current as current density to a logarithmic scale, hence the curves are commonly termed polarisation curves or  $E \log I$  plots. An idealised polarisation curve is given in figure 4.1. The test is usually conducted in a corrosion cell consisting of the electrode of interest, a second counter electrode, used to polarise the first, and a reference half-cell electrode to measure the overpotential of the electrode of interest. The electrode is polarised by a potentiostat, often under computer control.

The electrode is observed to switch from cathodic to anodic behaviour at the potential  $E_{\text{corr}}$ . The minimum current density corresponding to  $E_{\text{corr}}$  is called the corrosion current density,  $i_{\text{corr}}$ , and indicates the rate of oxidation and reduction reactions occurring at the electrode at equilibrium. The magnitude of  $i_{\text{corr}}$  is influenced by the specific redox reactions, the ratio of oxidised:reduced species, the electrode composition and surface roughness and temperature (Fontana, 1986).

The shape of a polarisation curve gives an indication of the type of processes occurring at an electrode surface. Generally, the current density is observed to increase with increased applied potential in an active curve. Tafel behaviour, where the slope of the active curve is reasonably linear, can be seen in some polarisation curves. In figure 4.1, the current density and corresponding potential at which Tafel behaviour starts is denoted  $i_n$  and  $E_n$  and those at which mass transport, that is concentration polarisation, appears to predominate are denoted  $i_t$  and  $E_t$ .



Passivation is indicated by a “passive loop”, where the current density reaches a maximum critical value,  $i_{crit}$ , at a passivation potential,  $E_{pp}$ . On increasing the potential, the transition from an active to passive state results in a decrease in the current density from the value  $i_{crit}$  to a limiting value  $i_l$ , termed the passive film leakage current density. The passive state may be disrupted at a higher potential,  $E_{tp}$ , and the current increases with further increases in potential. The value of  $E_{tp}$  is influenced by the scan rate and related to the time to the initiation of pitting or passive film breakdown under the specific experimental conditions (Berke, 1986). Where passivation occurs, the maximum current density,  $i_m$ , may not always relate to the final potential,  $E_m$ .

Potentiodynamic polarisation was previously used for investigations into the depassivation of steel in aqueous solutions and in cement pastes (Harrop, 1977, Page and Treadaway, 1982, Berke, 1986, Treadaway, 1988). The use of aqueous solutions allows the establishment of trends related to experimental variables, such as electrolyte composition or electrode material, in relatively short experiments. It has been noted that the results of such studies cannot fully model the electrochemistry of similar electrodes in concrete, due to significant differences between the kinetics of diffusion of ions within the two media (Page and Treadaway, 1982). However, a polarisation study in cementitious materials indicated that ionic diffusion in cements was too slow to determine accurate potentiodynamic polarisation curves, (Harrop, 1977), which suggested that the technique was most appropriate when using solutions. Polarisation studies are usually performed in de-aerated solutions to eliminate the cathodic reduction of oxygen, which may mask the anodic reactions. Similar de-aeration of concrete has been shown to be difficult and likely to change the concrete's properties (Arup, 1983). For aerated concrete, the cathodic oxygen reduction reaction may be expected to mask the true anodic potentials.

The required current density for a CP system is sometimes determined from a cathodic  $E \log I$  plot (Stratfull, 1983). In this case, the polarisation curve is generated by applying increments of direct current via a CP anode to the reinforcement and measuring the

reinforcement potential using a surface mounted half-cell with correction for the IR drop. As such, the polarisation curve relates to the steel rather than the anode material.

## 4.2. Previous work

### 4.2.1. Activated titanium mesh electrodes

Polarisation curves for two activated titanium meshes have been reported. Potentiodynamic polarisation was used to obtain a curve which exhibited anode potentials in the range 250 to 750 mV (SCE) over the current density range of 20 to 1000 mA/m<sup>2</sup> (anode area), for a mesh embedded in concrete with 2% chloride (wt. cement) (Mussinelli *et al*, 1987). The upper potential value was less than the standard reduction potential for chlorine evolution<sup>3</sup>, thus apparently indicating preferential oxygen generation over the operating range.

Two polarisation curves were reported for the second mesh which was embedded in concrete (Martin and Bennett, 1987, Tvarusko and Bennett, 1987). The curves show different starting potentials and slopes, but considered together, the polarised potential varied from approximately 40 mV to 740 mV (SCE) over the current density range 50 to 510 mA/m<sup>2</sup> (anode area). Again, the authors indicated that only oxygen evolution was possible at the anode potentials measured. Detailed interpretation of these polarisation curves is difficult as the full experimental conditions and procedure used to obtain the curves have not been reported. However, the electrical activities of the meshes appear to be different.

Other activated titanium mesh manufacturers have not published specific data on anode performance but indicate that their catalytic coatings are acid and chlorine resistant with oxygen specificity (ICI, 1989) or simply state that the anodic reaction will generate oxygen (Kotowski, 1989).

---

<sup>3</sup>  $2\text{Cl}^- \rightarrow \text{Cl}_2 + 2\text{e}^-$        $E^\theta = +1119 \text{ mV (SCE) at } 25^\circ\text{C and unit activity (Vogel, 1978)}$



The exact nature of the various mixed metal oxides used as electro-catalysts on titanium have not been published due to their proprietary nature. Formulations are reported to include oxides of ruthenium, iridium, tantalum, palladium and platinum (Wyatt, 1989). In order to consider the claim of oxygen specificity for these anodes from a theoretical point of view, the well-documented properties of platinum anodes in the electrolysis of chloride solutions will be considered, as some of the metal oxides are reported to have similar electrochemical properties to platinum (Shreir and Hayfield, 1986).

Platinum is an efficient electrochemical catalyst with a high corrosion resistance and low consumption rate. Although oxygen evolution is thermodynamically favoured, if an electrolyte contains chlorides, chlorine evolution can occur at a platinum anode in preference to oxygen evolution due to platinum's low chlorine overpotential. In solutions where concentration polarisation is low, current densities of  $1000 \text{ A/m}^2$  (anode area) can be generated at voltages of only 2.5 V (Shreir and Hayfield, 1986). Where chloride transport is sufficiently restricted, oxygen evolution predominates with a very large overpotential leading to higher operating voltages at significant evolution rates and with greater acid generation than that observed where chlorine generation predominates. Chlorine is evolved as gas in acidic electrolytes during the oxidation of chlorides but in neutral and alkaline solutions the chlorine reacts with the alkali to form chloride and oxygen compounds of chlorine. At  $25^\circ\text{C}$ , the predominant species are hypochlorous acid and hypochlorite ions, although the formation of chlorates and perchlorates is also possible at high current densities (Pourbaix, 1966).

From the foregoing, predictions from polarisation curves of long term oxygen generation for an activated titanium mesh embedded in concrete should be questioned. The respective investigators do not appear to have taken the influence of anodic overvoltage into consideration when implying which reaction would occur at a specific potential and further have neglected the influence of the pore solution pH. At the low current densities adopted in cementitious systems, chlorine evolution may be favoured as the chloride concentration

increases adjacent to the anode due to electro-migration or continued contamination from external sources.

#### **4.2.2. Carbon pigmented paint electrodes**

The active element in conductive paints is the carbon filler. Characteristic polarisation curves for conductive paints have not been published, although the electrochemical behaviour of carbon is well documented. A short review will therefore be made of the electrochemical properties of carbon.

Carbon exists in the crystalline forms of diamond and graphite and in the amorphous forms of charcoal, carbon black and soot. On heating, the latter forms of carbon tend to evolve towards the ordered graphite type of structure (graphitization). Graphite anodes, coupled to mild steel cathodes, have long been used to electrolyse aqueous acidic brines to produce chlorine. The graphite is in a passive state, inhibiting thermodynamically possible corrosion reactions, and it exhibits a low chlorine overpotential.

The nature of the reactions occurring on a carbon electrode depend on the kind of carbon, the electrolysis conditions, and chemical nature of the electrolyte. Carbon corrodes to a greater extent in acidic electrolytes than in alkaline electrolytes. In chloride-free solutions of up to around pH 10, carbon dioxide evolution occurs and as the pH increases further, oxygen evolution predominates with a lower level of anode deterioration (Randin, 1981). However, oxygen evolution is also reported to occur in acidic solutions at glassy carbon surfaces (Laser and Ariel, 1974). Where chlorides are present, chlorine evolution is also likely and the rate of anode consumption decreases with increasing chloride concentration due to suppression of the oxygen reaction (Shreir and Hayfield, 1986). Carbon may be oxidised to carbon dioxide by hypochlorous acid and hypochlorite ions. Graphite is said to be more resistant to chemical attack than amorphous carbon, although both are highly porous and liable to surface softening (Randin, 1981).



Polarisation curves were obtained for carbon-based anodes, embedded in concrete blocks, which were held to generate carbon dioxide, chlorine and oxygen. Some confusion is apparent over the current density scale of the two curves published, both showing the potential range -320 to 1600 mV over a log current density of 0.1 to 10 (concrete area<sup>4</sup>), but with different units of mA/ft<sup>2</sup> (Bennett and Martin 1987) and mA/m<sup>2</sup> (Tvarusko and Bennett, 1987). By contrast, a carbon anode embedded in concrete with 2% chloride (wt. cement) exhibited potentials in the range +100 to +270 mV (SCE) at current densities between 20 to 80 mA/m<sup>2</sup> (anode area) (Mussinelli *et al*, 1987). On increasing the current density slightly from 80 mA/m<sup>2</sup> to 130 mA/m<sup>2</sup>, the slope of the curve increased significantly in the potential range +270 mV to over +900 mV, reportedly due to chlorine evolution, but more likely due to limiting concentration polarisation.

The behaviour of the carbon anodes in the two investigations appears different, although comparisons between the two sets of data and interpretation are difficult, as neither investigator characterised their specimens adequately. Both sets of investigators plotted data for activated titanium and carbon anodes together to demonstrate the differences in anodic performance. However, graphite and platinized titanium anodes were shown to exhibit similar electro-catalytic activity in saturated calcium hydroxide/sodium chloride solution, as determined by anodic potentiodynamic polarisation, during an investigation into the desalination of concrete (Slater *et al*, 1976).

It is clear from the foregoing that the reactions of carbon based CP anodes are likely to be complex and influenced, in addition to applied current density, by carbon morphology, the local pH and diffusion processes within the concrete.

#### 4.2.3. Sprayed zinc electrodes

No studies of the anodic behaviour of flame sprayed zinc anodes, as applied in cathodic protection systems, have been reported. However, a substantial electrochemical study of

---

<sup>4</sup> Anode surface area not reported.

galvanised and galvannealed coatings for steel has been performed which provides strong indications of the anodic behaviour of zinc in alkaline solutions. Zinc coatings were isolated from the steel substrate and immersed in various stagnant, de-aerated solutions and anodic potentiodynamic polarisation tests performed (Sergi *et al*, 1985). A typical polarisation curve is shown in figure 4.2.

A transition from active to passive behaviour was observed for all combinations of pH and chloride concentration, at a passivation potential ( $E_{pp}$ ) of approximately -1300 mV (SCE). The passive region ceased at approximately +1000 mV (SCE) for solutions with no chlorides, but was terminated at lower potentials on addition of small chloride concentrations, as shown in figure 4.2, for solutions of pH 12.6 and below. The chloride concentration similarly influenced the current density passed at the onset of passivation in solutions of low alkalinity, with higher currents recorded at increasing chloride concentrations. However the magnitude of current density was influenced to a greater degree by the solution alkalinity, with higher current densities at higher pH values. The results demonstrated that the electrochemical activity of zinc was dependent on pH and the presence of chlorides, since these factors control the passivation of the zinc surface. Oxygen evolution was indicated at potentials exceeding approximately 1.7 V (SCE) during cyclic voltammetry of zinc in 0.1 M sodium hydroxide (Bohe *et al*, 1991).

#### **4.3. Experimental**

This experimental chapter aims to elucidate the electrochemical behaviour of conductive coatings and activated mesh anode materials in solutions of range pH 2 to 12.6 and varied chloride ion concentration using potentiodynamic anodic polarisation curves. The polarization curves are used to assess the relationship between environment and electrocatalytic performance and elucidate the probable chemical reactions. Further, the anode material corrosion resistance is observed. De-aerated solutions of variable pH simulate concrete pore liquid and allow straightforward specimen preparation and a reproducible test procedure.



#### **4.3.1. Specimen preparation**

Electrochemical investigations of metals generally use standardised specimens which are placed in proprietary corrosion cells (PARC, 1986). Electrode specimens were designed for use in a readily available “pyrex” glass corrosion cell, as shown in figure 4.3. This consisted of two compartments connected by a sintered glass plug which allowed conductance between working and counter electrodes, whilst minimising ionic diffusion. The assembled cell was air-tight and allowed for flushing with an inert gas.

##### 4.3.1.1. Titanium mesh

Mesh samples were prepared by cutting a suitable area of strand to be immersed in solution and leaving a continuous strand with which to suspend the whole. Stopping off lacquer was used to isolate the required electrode area and mask the hanging strand within the corrosion cell. The strand was then sealed in place.

##### 4.3.1.2. Conductive coatings

In order to perform anodic polarisation of the conductive coatings it was necessary to apply them to an inert substrate which could then be suspended in the solution within the corrosion cell. It was convenient to use a 24 x 75 mm glass microscope slide fixed with epoxy resin to a 2 mm diameter mild steel rod, which served a secondary role as conductor between the coating and potentiostat. The design of the zinc and paint electrodes differed slightly although the basic substrate was prepared in a similar way. A suitable length of mild steel rod was cleaned using 600 grade silicon carbide paper and deionised water. One side of the microscope slide was roughened with silicon carbide and then degreased with acetone.

##### **4.3.1.2.1. Anode Z**

The zinc was flame sprayed to completely cover one side of suitably prepared glass slides, to a thickness of approximately 50  $\mu\text{m}$ . The uncoated side of each slide was fixed to a steel bar as described above. Electrical contact between zinc and steel was made using 2 applications of Electrodag 915 and the continuity of each specimen was checked using a multimeter, with no value of resistance exceeding 5 ohms. The electrical connection was then covered with epoxy resin which was allowed to cure. The required surface area was

isolated using two coatings of stopping off lacquer and any exposed steel rod similarly masked.

Zinc forms surface oxides when in contact with air and it is necessary to remove these prior to electrochemical experiments. To achieve this, some workers have polarised polished, degreased, acid etched zinc electrodes in the hydrogen evolution region for a period of 5 minutes (Bohe *et al*, 1992) prior to electrochemical measurements whilst others polished and degreased specimens and started the polarisation scan from -1600 mV (SCE), again hydrogen evolution territory (Sergi *et al*, 1985). Both of these techniques resulted in  $E_{\text{corr}}$  values of the order -1300 mV(SCE) in alkaline solutions. In this study, the “as sprayed” zinc surface was exposed to the electrolytes since this was considered to more realistically reflect the anode interfacial region. Consequently, specimens were placed as manufactured into the corrosion cell and the de-oxygenated electrolyte introduced. The corrosion potential ( $E_{\text{corr}}$ ) was monitored and the sample allowed to equilibrate. This was achieved by delaying polarisation until the rate of change of potential became less than 1.5 mV/s. The specimen was then polarised to -250 mV (SCE) from  $E_{\text{corr}}$  to reduce surface oxide films and the scan started. Since the potential increased at the rate of 0.5 mV/s, any surface layer was reduced during a period of around 8 minutes, which was in line with the previously described techniques, and the results in table 4.5 indicate that comparable  $E_{\text{corr}}$  values were recorded.

#### 4.3.1.2.2. Anode P

The conductive paint was applied after the connection of the microscope slide to steel bar. Adhesion promoter was applied to the free side and allowed to dry. One coating of paint was applied to cover the entire slide and part of the steel rod. Carbon fibre strands were then placed between steel rod and glass slide and a further layer of paint applied to fix the strands in place. Upon drying, a second coating was applied and allowed to dry. Again, conductance checks were performed. An area was isolated as for the zinc specimens and the exposed steel bar was masked. The dry coating thickness was approximately 100  $\mu\text{m}$ . Again, prepared electrodes were placed into the corrosion cell without further preparation.



#### 4.3.2. Electrode areas

The electrode areas exposed within the corrosion cell are given in table 4.1.

#### 4.3.3. Electrolytes

A range of electrolytes were selected to simulate the various solutions in which the anodes could be anticipated to operate. Saturated calcium hydroxide (pH 12.6) has been used to simulate concrete pore solutions in many studies, as shown in table 4.2, although concrete pore solution has generally been shown to exhibit a pH in the range 13 to 14 due to sodium and potassium hydroxides (Page and Treadaway, 1982). Saturated calcium carbonate (pH 9.2) was used to simulate carbonated concrete in a durability test of half cells (Broomfield *et al*, 1985) and was used in this study as a convenient mildly alkaline solution. It was anticipated that the pH of saturated solutions would be less sensitive to acidification due to electrolysis products. Acidity in the range pH 1.5-9 has been reported adjacent to a mesh anode embedded in concrete, varying with net applied current (Pedefferri *et al*, 1989, Schell *et al*, 1984), hence a highly acidic electrolyte was simulated by hydrochloric acid. Acidic conditions have also been reported for paint coatings (Palmer and Bradley, 1989), but are unlikely to occur at a zinc anode hence zinc specimens were not tested in acidic electrolytes. Neutral salt solutions and deionised water were also used as an intermediate between acidic and alkaline conditions, although it was anticipated that the pH of such non-buffered solutions could vary significantly during electrolysis.

The pH value for each electrolyte was determined using a electronic pH meter and an average over 5 readings is given in table 4.3. It can be seen that the pH values of calcium chloride solutions were lower due to hydrolysis. The solution pH was measured at the end of each test using universal indicator paper. This provided an indication of variation in pH during the test but the accuracy of universal indicator in complex solutions was questionable, as indicated by later checks made with a pH electrode.

For simplicity, each electrolyte is referred to throughout the thesis by the absolute value of the theoretical pH. Similarly, each anode material is referred to by its first letter. A schedule of the polarisation curves is given in table 4.4.

#### 4.3.4. Experimental procedure

Several experimental factors influence the polarisation curve obtained. The rate of potential change must be slow enough for representative reactions to occur at the electrode surface, although there is little guidance in the literature regarding appropriate values. A number of different rates have been used in solution and paste work as shown in table 4.2. It was decided to adopt the rate 0.5 mV/s as a compromise between accuracy and practical speed.

Some workers have adopted stagnant solutions and constant temperatures (Sergi *et al*, 1985) whilst others do not report these aspects of experiments. The composition of an electrolyte, and hence the pH, adjacent to an electrode can differ greatly from the mean composition of the bulk electrolyte (Pourbaix, 1966). Concentration polarisation may therefore be expected for an electrode immersed in a still solution due to electrolyte variations at the specimen surface and gas and corrosion product formation. Rapid stirring may limit this and provide a more reproducible test. A magnetic stirrer was placed within the corrosion cell and operated at the highest practical constant speed to give a rapidly stirred solution.

Temperature is influential in all chemical reactions and would be expected to vary in some cases due to exothermal or endothermal reactions. Electrolyte temperature is generally controlled by placing the corrosion cell in a thermostatically controlled water bath, however this was not possible in these tests due to the requirement for magnetic stirring. The laboratory temperature was reasonably constant at  $20.5\text{ }^{\circ}\text{C} \pm 3\text{ }^{\circ}\text{C}$  throughout the experimental period and prepared electrolytes were stored at laboratory temperature. The electrolyte temperature was measured at the start and completion of each test.



An EG & G Princeton Applied Research model 273 potentiostat, with Model 342 Softcorr corrosion measurement software, was used to perform the potentiodynamic anodic polarisation measurements. To facilitate comparisons between anode materials, the same instructions were used for tests on each specimen. The programme variables are given in Appendix 4.1.

In order to eliminate the masking effect of oxygen reduction, electrolytes were de-oxygenated for one hour in a nylox gas scrubber utilising nitrogen gas and nitrogen was bubbled through during the test. Electrode specimens were placed in the custom designed glass corrosion cell, as shown in figure 4.3 and the apparatus flushed with nitrogen. On passing the de-oxygenated electrolyte into the corrosion cell, the potentiostat was activated and the measurements conducted according to the pre-programmed instructions. After specimen equilibration, the potential was increased positively at a constant rate of 0.5 mV/s to a maximum of +1500 mV (SCE) from  $E_{\text{corr}}$  and the cell current measured and related to specimen area as current density. A plot of potential against the logarithm of current density was recorded and the data stored on computer disc for analysis and plotting. The final experimental set up is shown in plates 4.1 and 4.2.

#### **4.4. Results**

It is convenient to consider the results for each material separately, followed by a general discussion to make comparisons between materials.

All potential values are given in mV (SCE) scale. A number of values have been taken from the polarisation curves and tabulated to facilitate data analysis, as shown in the idealised polarisation curve of figure 4.1. The potential at which the material switched from cathodic to anodic behaviour,  $E_{\text{corr}}$ , did not always relate to the corrosion potential measured before the polarisation scan. The final potential is related to  $E_{\text{corr}}$  in that the scan was programmed to terminate 1500 mV more positive than  $E_{\text{corr}}$ . The maximum current density,  $i_m$ , did not always occur at the final potential, hence the tables give the maximum current density

passed and the corresponding potential,  $E_m$ . The Tafel slope,  $\beta_a$ , was calculated from each curve directly. Although a certain degree of error will result from manually taking off values, it is thought that this error will be within an order of magnitude. The data values used to determine the Tafel constants are given in the tables.

Standard thermodynamic equilibrium data, calculated from the thermodynamic equations outlined by Pourbaix, has been tabulated to aid curve interpretation, as shown in Table A4.1.1 in Appendix 4.2.

Although no apparent change in anode pH was recorded for any specimen, this is unrealistic and reflects inadequacies in the measurement by indicator paper. Some of the results indicate that the pH immediately adjacent to the anodes, if not in the bulk, varied during the electrolysis. Similarly, the temperature data was only approximate and heat losses to the environment would have been expected during each test.

#### 4.4.1. Anode Z

The polarisation curves are shown in figures 4.4 to 4.6 and experimental data summarised in table 4.5. In contrast to the other anode results, which are considered by electrolyte pH, the zinc results will be considered by chloride/chloride-free electrolyte.

Table 4.5 shows that the value of  $E_{\text{corr}}$  became more negative as the pH increased for all solutions.  $E_{\text{corr}}$  decreased further on addition of chloride, the influence of the chlorides overcoming the influence of a slightly lower pH.

It can be seen from figures 4.4 to 4.6 that the corrosion current densities ( $i_{\text{corr}}$ ), corresponding to  $E_{\text{corr}}$ , for specimens in saturated calcium hydroxide were one to two orders of magnitude higher than for specimens in solutions of lower pH. A similar relationship between  $i_{\text{corr}}$  and pH was also apparent in the work of Sergi *et al* (1985). For chloride electrolytes of pH 9 to 7,  $i_{\text{corr}}$  values of magnitude  $0.1 \mu\text{A}/\text{cm}^2$  were observed and for the corresponding chloride free electrolytes, the  $i_{\text{corr}}$  values were three orders of



magnitude less, at  $1 \times 10^{-4} \mu\text{A}/\text{cm}^2$ . These results are in agreement with the established view that the corrosion rate of zinc is a minimum in aggressive ion free solutions of pH 8.5 to 10.5 (Chatalov, 1952).

#### 4.4.1.1. Chloride-free electrolytes

The shiny zinc electrodes were observed to form a dull grey film during polarisation in chloride free electrolytes, with minimal material loss. Anode performance was low, as can be seen from the maximum current densities passed over the potential ranges. As the pH decreased, the maximum current passed, determined as either  $i_{\text{crit}}$  or  $i_m$ , decreased and the passivation potential  $E_{\text{pp}}$  became more positive. This was in broad agreement with the findings of Sergi *et al* (1985) and Bohe *et al* (1991). Figure 4.4 indicates that specimen N12Z underwent active corrosion before forming a passive film at a passivation potential ( $E_{\text{pp}}$ ) of approximately -1200 mV, which was stable at higher potentials. Figures 4.5 and 4.6 indicate that specimens N9Z and N7Z quickly formed passive films, which limited the current densities.

From table 4.5, the Tafel slope of  $\beta_a=100 \text{ mV/decade}$  for specimen N12Z was slightly higher than the Tafel slope for specimen C12Z in chloride solution, indicating that active zinc dissolution was enhanced by chlorides. Owing to the low activity of specimens N9Z and N7Z, Tafel behaviour was not observed.

#### 4.4.1.2. Chloride electrolytes

The zinc electrodes suffered significant corrosion in chloride electrolytes, with the production of white precipitates and the polarisation curves in figures 4.4 to 4.6 show increased electrical activity for zinc in chloride solutions. Figure 4.4 indicates that the  $i_{\text{crit}}$  value increased on addition of chloride to saturated calcium hydroxide. Two passive loops can be seen for sample C12Z, passive film disruption occurring at  $E_{\text{tp}} = -840 \text{ mV}$  and at  $E_{\text{tp}} = -260 \text{ mV}$ . The  $i_{\text{crit}}$  and  $i_l$  values increased at the second passive loop, probably due to a more porous passive film.

Chlorides had a significant effect on the current density passed in the less alkaline solutions. Figures 4.5 and 4.6, and the results in table 4.5, show that the behaviour of specimens C9Z and C7Z was similar. The Tafel slope for specimen C7Z was lower than for C9Z and the  $i_m$  value greater, indicating greater activity for the former. The electro-catalytic activity appeared to increase with decreasing pH, for the chloride concentration and for the electrolytes used, in contrast to the opposite trend observed in electrolytes of pH 12 to pH14 (Sergi *et al*, 1985).

A secondary indicator of activity was the change in solution pH. No changes to the anode electrolyte was noted for any specimen, indicating that the sole anodic reaction was zinc consumption. As expected, the pH of the non-buffered electrolytes increased at the cathode due to hydrogen ion removal as hydrogen gas. The pH of the cathode electrolyte increased for specimen C9Z due to the high current density passed.

The current density decreased significantly for each chloride electrolyte at potentials exceeding approximately -125 mV. This may have been due to a reduced anode surface area as a result of zinc consumption. It was noted that the platinum cathode became encased in a white deposit during the electrolysis, which may have resulted in a degree of cathodic polarisation. These deposits were not observed in chloride free solutions. The deposits were not analysed for composition, but were probably calcium hydroxide which precipitated out of solution as the cathode electrolyte pH increased to around 12.5. Figure 4.6 exhibits a sudden increase in current at 60 mV, with subsequent current decay. This was caused by the author remedying a differential of electrolyte levels which had developed during the test, due to excessive gas pressure within the cathodic side of the corrosion cell. This experimental feature confirms the supposition that cathodic polarisation was influential in limiting the current density.

#### 4.4.1.3. Discussion: Anode Z

Zinc is thermodynamically unstable in aqueous solutions and tends to form a variety of amphoteric hydroxide species which dissolve in acidic solutions to give  $Zn^{2+}$  ions and in



alkaline solutions to give soluble bi-zincate  $\text{HZnO}_2^-$  (pH 9.3 to pH 13.4) or zincate  $\text{ZnO}_2^{2-}$  ions (pH  $\geq$  13.4) (Pourbaix, 1966).

The Pourbaix diagram for the system zinc-water at 25°C indicates that zinc corrodes to form soluble bi-zincate in saturated calcium hydroxide (pH 12.6), at potentials more noble than -1484 mV (SCE) (Pourbaix, 1966). Specimens N12Z and C12Z show classic passive loop behaviour, which may be explained as follows: At high current densities the supply of aqueous hydroxyl ions to the zinc surface becomes the limiting factor in the production of bi-zincate ions and insoluble oxides or hydroxides may be formed (Pourbaix, 1966), causing a reduction in the current density. The partly protective surface layer is disrupted in the presence of chlorides and the zinc corrosion rate increases with an associated increase in current density.

Bicarbonate has the effect of broadening the domain of zinc passivation at lower pH values owing to the stability of passivating zinc carbonate (Pourbaix, 1966) and zinc immersed in a calcium carbonate electrolyte may be expected therefore to form a mixed passive film of zinc carbonate and zinc oxide. This would explain the reduced catalytic activity of specimen N9Z. Chloride may be expected to have a disruptive effect on any such passive film. However the polarisation curve for specimen C9Z does not appear to undergo a passive to active transition. Addition of chloride to the calcium carbonate lowered the pH to around 6.68, which is close to the border between active and passive behaviour. It seems likely that the zinc did not form a passive film in this case and  $\text{Zn}^{2+}$  formation occurred.

Table 4.3 indicates a pH of 8.34 for the deionised water used. The Pourbaix diagram for the system zinc-water indicates that zinc forms passivating zinc hydroxide under these conditions, which may explain the very low catalytic activity of specimen N7Z. The electrolyte pH for specimen C7Z would place the zinc in the zone of corrosion as for specimen C9Z, with similar results. As the zinc ion concentration in the electrolyte increased, zinc hydroxide would be precipitated.

The results clearly show the significant influence of chloride ions on the corrosion of zinc in solutions of low alkalinity. In the presence of chlorides, the anodic overvoltage would be reduced. This would be beneficial for cathodic protection power requirements, although the rate of zinc consumption would be higher. Zinc consumption was reduced at lower pH values and a reasonable level of electro-catalytic activity was attained in saturated calcium carbonate. This suggests that a zinc CP anode may be most successful when applied to concrete of low alkalinity, such as a carbonated surface or a concrete containing pozzalanic cement replacements.

The action of rapid stirring appears to have produced more aggressive testing conditions than for the still conditions adopted by others (Sergi *et al*, 1985), as corrosion product accumulation was minimised. This may account for the high current densities observed. Galvanostatic anodic polarisation tests results have indicated that zinc passivation was controlled by diffusion (Sergi *et al*, 1985). It is likely that the kinetics of passive film development and disruption would be modified for a zinc CP anode applied to concrete owing to diffusional restraints.

#### **4.4.2. Anode T**

The polarisation curves are shown in figures 4.7 to 4.10 and experimental data summarised in table 4.6. The mixed metal oxide coating appeared to be continuous and in good condition for all specimens both before and after testing. The polarisation curves do not show the passivating behaviour observed for other anodes, suggesting that the anode remains inert in the electrolytes used and in addition, the maximum potentials cannot indicate any trends.

Table 4.6 shows that the value of  $E_{\text{corr}}$  tended to increase with decrease in pH, as may be expected from the slope of the oxygen evolution line of the Pourbaix diagram for water, and was not influenced by chlorides. The value for  $i_{\text{corr}}$  was low and relatively independent of pH and chloride ion concentration, which confirms that the anode surface remained inert.



The maximum current density was significantly influenced by chlorides in alkaline solutions, with very high current densities under the experimental conditions. In chloride free electrolytes, the current density was lower by two orders of magnitude for the solutions N9 and N7 than for solution N12. In hydrochloric acid there was little influence in increased chloride. Each polarisation curve will be analysed in detail to determine probable reactions.

#### 4.4.2.1. Specimens C12T and N12T

Figure 4.7 shows that the polarisation curves for C12T and N12T were similar. In saturated calcium hydroxide, the only thermodynamically possible reaction was oxygen evolution. Table A4.1 indicates a theoretical equilibrium electrode potential value of  $E_0=240$  mV for oxygen gas evolution for electrolyte N12. The initial part of the anodic curve is steep and unstable up to a current density of around  $30 \mu\text{A}/\text{cm}^2$  and potential of 550 mV. A Tafel slope of  $\beta_a=66$  was then observed which probably related to oxygen gas formation, followed by increasing concentration polarisation. Specimen C12T similarly showed low activity up to 540 mV, followed by oxygen gas evolution at the lower Tafel slope of  $\beta_a=56$  mV/decade, which with a final higher current density suggests that hypochlorite evolution also occurred, as this was thermodynamically possible at potentials exceeding 764 mV (SCE).

#### 4.4.2.2. Specimens C9T and N9T

Figure 4.8 shows the difference in activity for specimens C9T and N9T. Specimen C9T has a similar curve to C12T, but with several deviations. Activity was low up to around 470 mV, which was followed by an unstable region with the current density varying between  $0.01$  to  $20 \mu\text{A}/\text{cm}^2$ . This corresponded closely to the theoretical oxygen discharge potential of  $E_0=471$  mV (SCE) for calcium carbonate (Table A4.1), although carbon dioxide gas evolution was thermodynamically possible in small quantities. A Tafel slope of  $\beta_a=95$  mV/decade was observed from a potential of 1030 mV. Table A4.1 shows that evolution of small quantities of chlorine gas were thermodynamically possible from 965 mV (SCE), although hypochlorite ion formation was theoretically favoured from 1079 mV(SCE). Chlorine odour was noted at the anode, suggesting that chlorine evolution was favoured,

and that the anode solution pH decreased during electrolysis. The cathode became encased in a white precipitate during the electrolysis, which was probably due to precipitation of calcium hydroxide in the increasingly alkaline cathode solution. In contrast, the curve for specimen N9T showed a marked reduction in activity, with an unstable region up to 710 mV followed by a slight increase in slope. The slope was linear over a current decade, although the slope of 650 mV/decade does not correspond to Tafel behaviour. It would appear that oxygen was evolved with difficulty. Evolution of small amounts of carbon dioxide were also thermodynamically possible from dissolved bicarbonate (Pourbaix, 1966).

#### 4.4.2.3. Specimen C7T and N7T

Figure 4.9 shows that specimen C7T performed similarly to specimen C9T, with relatively low, unstable activity up to a potential of 1050 mV and current density of 100  $\mu\text{A}/\text{cm}^2$ , probably relating to oxygen evolution. The Tafel region with  $\beta_a=63$  was probably due to chlorine gas evolution, which became theoretically possible from 965 mV (SCE). Again, the cathode became covered by a white precipitate, which appeared in this case to limit and reduce the current density from 1250 mV. Specimen N7T showed similar behaviour to specimen N9T, with a steep slope from 270 mV indicating oxygen evolution.

#### 4.4.2.4. Specimens C2T and N2T

The curves for specimens C2T and N2T shown in figure 4.10 are essentially similar to the curves for specimens C9T and C7T. The current density appears more stable at lower potentials than in the more alkaline solutions and was probably due to oxygen evolution. Chlorine gas evolution became thermodynamically possible at potentials more noble than about 915 mV (SCE), and Tafel behaviour was observed from around 1090 mV with  $\beta_a=65$  to 85 mV/decade. A strong chlorine smell was noted for each specimen, the electrolyte of specimen C2T attaining a yellow colour.

#### 4.4.2.5. Discussion: Anode T

The results confirm that while being thermodynamically possible, the gaseous evolution of oxygen on anode T was kinetically difficult in the electrolytes used in this study, other than in saturated calcium hydroxide, where oxygen evolution appeared to predominate over



chlorine evolution. At low potentials, the evolution of oxygen appeared to be associated with low current densities. At a potential positive enough for chlorine evolution to become thermodynamically possible, this reaction occurred readily with relatively high associated current densities which became limited by concentration polarisation effects as the electrode potential increased.

#### **4.4.3. Anode E**

A glance at table 4.7 indicates that anode E showed much the same behaviour as anode T. The coating of anode E appeared variable in thickness, as judged by variation in deepness of colour, and had small surface scratches. This may have affected results, as the maximum current densities passed were generally lower in each solution than for anode T. The low  $i_{\text{corr}}$  values were comparable to those for anode T. Again, the  $E_m$  values were a function of the  $E_{\text{corr}}$  values, which tended to increase with decrease in pH.

##### 4.4.3.1. Specimens C12E and N12E

Figure 4.11 for specimens C12E and N12E indicates that electrolysis proceeded with some difficulty up to a potential of around 550 mV, where gaseous oxygen evolution became possible. The Tafel slope for C12E of  $\beta_a=110$  was steeper than that for N12E, with  $\beta_a=75$ , indicating that a chloride based reaction may also have occurred simultaneously. Hypochlorite formation was theoretically possible at potentials exceeding 764 mV (SCE). The region from 250 mV to 550 mV was more stable for N12E than C12E, a feature which was also be observed for anode T. The significance of this was not clear.

##### 4.4.3.2. Specimens C9E and N9E

Figure 4.12 shows that the electrolytic activity was much reduced for specimen N9E. Tafel behaviour was not observed over the potential range measured and the current density was variable up to around 500 mV. A reduction in slope occurred at 750 mV, which may have been due to carbon dioxide evolution from bicarbonate in preference to dissolved oxygen evolution. The curve for specimen C9E was similar to that for C9T, with chlorine evolution being likely at potentials exceeding 965 mV (SCE), and the magnitude of maximum current densities passed for each were 8 mA/cm<sup>2</sup> and 7 mA/cm<sup>2</sup> respectively.

#### 4.4.3.3. Specimens C7E and N7E

Figure 4.13 similarly shows the low activity of specimen N7E, with an unstable region up to around 630 mV and a reduction in slope at 850 mV. The only possible reaction was the oxidation of water and changes in the slope may be related to small variations in the pH shifting the theoretical potential for oxygen evolution positively. The curve for specimen C7E was slightly different to others in that the current density remained close to the  $i_{\text{corr}}$  value up to a potential of 880 mV, and then appeared to exhibit Tafel behaviour up to a potential of 1040 mV, but low current density of  $0.02 \mu\text{A}/\text{cm}^2$ . This was followed by a rapid increase in current density to  $50 \mu\text{A}/\text{cm}^2$ , where Tafel behaviour was again observed with  $\beta_a=75$ . This latter slope was probably due to chlorine gas evolution. The reason for the virtually passive behaviour is not clear.

#### 4.4.3.4. Specimens C2E and N2E

Figure 4.14 shows the polarisation curves for anode E in the N2 and C2 solutions. The current density was low and variable up to a potential of around 1000 mV. This was in contrast to the curves for anode T in figure 4.10, where the lower regions of the curve were reasonably linear, and values for  $E_{\text{corr}}$  higher. Titanium has a thermodynamic tendency to corrode in dilute, oxygen free hydrochloric acid (Fontana, 1986), which corresponds to the initial condition for solutions N2 and C2. Considering the imperfect coating of anode E, it is likely that specimens N2E and C2E may have undergone a degree of corrosion until the oxygen content increased sufficiently during electrolysis for repassivation. This may account for the lower  $E_{\text{corr}}$  values. Specimen C2E displayed Tafel behaviour which was probably due to chlorine gas evolution. Specimen N2E however did not show Tafel behaviour, with an active curve at potentials exceeding approximately 1125 mV which appeared to be influenced by concentration polarisation. The maximum current density was lower by a factor of three than for specimen C2E. Chlorine evolution was still the probable reaction for specimen N2E at the higher current densities.

#### 4.4.3.5. Discussion: Anode E

Perhaps not surprisingly, the polarisation curves for anodes E and T had similar features. A comparison between the values for  $E_n$  in tables 4.6 and 4.7 indicate that the reactions



occurring were independent of the specific mesh oxide coatings, being controlled by the electrolyte composition and the experimental set-up. The higher variation and lower current densities for anode E were probably due to the apparently lower quality of the oxide coating and surface scratches. The lower activity of anode E was further indicated by the smaller increases in cathode electrolyte pH for solutions C9E and C7E, which also accounts for the lack of white precipitate on the cathode in these specimens, as was found with specimens C9T and C7T.

The polarisation curves described in the review of previous work for mixed metal anodes embedded in concrete will be reconsidered with respect to the results for anodes E and T in saturated calcium hydroxide. The value for  $E_{\text{corr}}$  of -100 mV (SCE) for a mesh embedded in concrete (Tvarusko and Bennett, 1987), was more positive than the  $E_{\text{corr}}$  values recorded for anodes E and T in deoxygenated solutions, possibly due to a higher oxygen content in the concrete, although the  $i_{\text{corr}}$  values were similar. The current densities at the potentials relating to possible gaseous oxygen evolution, that is from around 550 mV, for anodes E and T in solution were of the same order of magnitude as for the various meshes in concrete at similar potentials. However, the linear slopes of the curves for meshes in concrete exceeded 150 mV/decade, the limiting value for Tafel behaviour, possibly due to concentration polarisation effects in the concrete. The results suggest that the likely anode reaction for an activated titanium mesh in alkaline OPC concrete was oxygen evolution, as claimed by the respective workers.

#### **4.4.4. Anode P**

Changes to the surface of the paint anodes could not be detected visually after electrolysis in any of the electrolytes used. Figures 4.15 to 4.18 show that passivation type behaviour was observed in the majority of specimens. Although this passivating behaviour has not been highlighted in the reviews of carbon electrochemistry studied by the author, it was shown to occur for graphite in calcium hydroxide/sodium chloride solution (Slater *et al*, 1976). Table 4.9 tabulates data taken from this polarisation curve for comparison purposes in the discussion.

$E_{\text{corr}}$  values given in table 4.8 show the general trend, observed for the other anodes, of becoming more positive with decreasing pH. As for the mesh anodes, the  $i_{\text{corr}}$  values were similarly low, indicating the relative inertness of carbon in the electrolytes used and that the oxygen evolution reaction was slow. The maximum current densities were relatively low over the potential range used, although the polarisation curve for specimen C2P in figure 4.18 indicates that higher current densities were possible at more noble potentials. Lower maximum current densities were observed for chloride free electrolytes at each pH level.

#### 4.4.4.1. Specimens N12P and C12P

The polarisation curves for specimens N12P and C12P are shown in figure 4.15. The Pourbaix diagram for the carbon-water system indicates that for solution N12, carbonate formation was thermodynamically possible from -886 mV (SCE), and the lower region of the curve may be due to the oxidation of carbon at a low rate. Table A4.1 indicates that gaseous oxygen evolution became possible from 240 mV (SCE), which may account for the Tafel region observed from 230 mV, with  $\beta_a=125$ . Concentration polarisation led to a small passive loop. An active curve from 710 mV showed linearity over a short length, possibly relating to further gaseous oxygen formation, followed by concentration polarisation. Specimen C12P similarly showed a Tafel region at low current density with  $\beta_a=135$ , over which the probable reactions were carbonate and oxygen evolution followed by concentration polarisation up to a potential of 680 mV. The curve then approximately followed the curve of specimen N12P. Table A4.1 shows that hypochlorite formation from chlorides in solution was thermodynamically possible from a potential of 764 mV (SCE). Although chlorides have clearly influenced the polarisation curves, it is not clear from the thermodynamic data by what mechanism, since the passive loop occurred at a potential below that at which hypochlorite became stable. It would appear that chlorides at the concentration used did not greatly influence the anodic reactions.

#### 4.4.4.2. Specimens N9P and C9P

Figure 4.16 shows that the polarisation curve for specimen N9P was similar to that of specimen C12P in that a passive loop was not observed. However, Tafel behaviour was



not observed and the anode activity was low. The current density increased rapidly to  $0.5 \mu\text{A}/\text{cm}^2$  at 480 mV, followed by a slightly unstable concentration polarisation up to a potential of 820 mV. This was followed by a stable curve indicating a second concentration polarisation controlled reaction. The electrolyte N9 was saturated with bicarbonate, which may have inhibited the formation of carbonate from carbon within the paint. The Pourbaix diagram for carbon-water indicates that carbon dioxide evolution can be predicted using the thermodynamic equation for oxygen evolution, taking into account the solubility of carbon dioxide in alkaline solutions, hence table A4.1 indicates that carbon dioxide evolution was also thermodynamically possible from a potential of 471 mV (SCE) for specimen N9. This suggests that the current increase at 480 mV may be due to oxygen and/or carbon dioxide formation. The polarisation curve for specimen C9P shows a significant passive loop at an  $E_{pp}$  of 915 mV. The activity was again very low from the  $E_{corr}$  value up to 470 mV. The transition at 730 mV to Tafel behaviour with  $\beta_a=120$  was similar to the curve for specimen N12P and was probably due to faster gas evolution. Table A4.1 indicates that chlorine evolution became thermodynamically possible at potentials in the range 965 to 1080 mV. This relatively fast reaction may be expected to significantly increase the current density, hence chlorine formation seems unlikely. The slope of the subsequent curve and the low ultimate current density indicate that gas evolution resumed, and that the current reduction may be related to gaseous concentration polarisation.

#### 4.4.4.3. Specimens N7P and C7P

The polarisation curve for specimen N7P indicates that formation of bicarbonate was very slow in deionised water up to a potential of 450 mV and that the specimen was relatively electrically inactive. Table A4.1 indicates that carbon dioxide evolution was possible from 494 mV (SCE), and the gradual increase in current density was followed at 750 mV by a rapid increase, followed by a short Tafel region with  $\beta_a=136$  and a small passive loop which terminated at around 1210 mV. The polarisation curve for specimen C7P was more complex, with several changes in slope up to a potential of 725 mV, where Tafel behaviour was observed with  $\beta_a=135$ . This was followed by a passive loop similar to that of specimen N7P, with a transition to active behaviour at 1120 mV. The variations in activity

at lower potentials are difficult to analyse, but probably relate to carbonic acid formation. It is likely that chlorine formation also occurred at higher potentials in the slightly acidic solution, increasing the current density .

#### 4.4.4.4. Specimens C2P and N2P

Figure 4.18 shows that the polarisation curves for specimens N2P and C2P. Both specimens exhibited low activity up to 710 mV, in a similar manner to the other specimens, followed by a Tafel region with  $\beta_a=80$  and  $\beta_a=105$  respectively. The unstable low current densities may be due to corrosion of the carbon to carbonic acid. The theoretical potential for carbon dioxide evolution in hydrochloric acid is difficult to determine, since the chloride ion will influence the equilibrium parameters for oxygen gas evolution from water, and may be less than the value 907 mV (SCE) indicated in table A4.1. Specimen N2P formed a large passive loop which terminated at around 1365 mV while that of specimen C2P terminated at the lower potential of 1125 mV and was followed by a second smaller passive loop. The reason for the differences are not clear from the thermodynamic data, which indicates that chlorine evolution was possible in the range 913 to 1416 mV (SCE). It seems likely that the passive loops were due to carbon dioxide formation. A second Tafel region was observed at around 1665 mV with  $\beta_a=70$ , followed by concentration polarisation for specimen C2P. This may have been due predominantly to chlorine evolution, bearing in mind the increased overpotential for chlorine evolution on carbon from that for an inert electrode, and the potentials at which the mesh anodes appeared to evolve chlorine.

#### 4.4.4.5. Discussion: Anode P

The polarisation curves for the carbon based paint were more difficult to analyse than for the other systems due to the multiplicity of possible reactions and the limitations of the thermodynamic equilibria. The electrical activity appeared to be lower over the potential range used than for the other anode specimens. The polarisation curves appear to confirm the theoretical reactions outlined in the introduction. For specimens in alkaline calcium hydroxide, slow carbonate formation was followed by oxygen evolution. For the remaining solutions it is probable that slow carbon consumption as bicarbonate or carbonic acid formation occurred at low overpotentials, followed by carbon dioxide evolution,



associated with an unexplained passivating mechanism. Chlorides appeared to increase the electrical activity, suggesting that chlorine evolution as hypochlorite may have occurred in parallel with other reactions. Results for specimen C2P showed that gaseous chlorine evolution was possible from relatively high overpotentials under the experimental conditions used.

Concerning the passivation type behaviour, the potential at which “passivation” occurred,  $E_{pp}$ , increased with decreasing pH, as summarised in table 4.8.  $E_{tp}$  values similarly increased for N12, N7 and N2 specimens, but remained roughly the same at 1120 mV for specimens C9P, C7P and C2P. Although values of  $i_{crit}$  were within a narrow range of 10 to 25  $\mu\text{A}/\text{cm}^2$  for all specimens, they increased with decreasing pH for N12, N7 and N2 specimens but decreased with decreasing pH for specimens C9P, C7P and C2P. The initiation of passivation would therefore appear to be strongly related to oxygen evolution, whilst reactivation was clearly influenced by the chlorine evolution. However, the full significance of these interesting observations was not clear and a more detailed investigation was beyond the scope of this study.

As far as results can be compared with those shown in table 4.9 for graphite in saturated calcium hydroxide plus 1 M sodium chloride, considering the different experimental conditions, the values for  $E_{corr}$  were in general agreement at around -200 mV (SCE). The graphite appeared more active than the carbon paint with an  $i_{corr}$  of 1  $\mu\text{A}/\text{cm}^2$  compared to  $1 \times 10^{-3}$   $\mu\text{A}/\text{cm}^2$ , and exhibited a low Tafel slope leading to a passive loop at an  $E_{pp}$  of -90 mV (SCE). Of interest, the second passive loop terminated at an  $E_{tp}$  of around 1100 mV (SCE) as was found above for chloride electrolytes.

Returning to the polarisation curves for carbon in concrete reviewed in the introduction, the polarisation curves for the carbon paint in deoxygenated saturated calcium hydroxide solution were resembled by the curve for carbon in concrete (Bennett and Martin, 1987). The anode area for this curve was not reported hence comparisons of current density cannot

be made. The  $E_{\text{corr}}$  values were of the same order and the electrical activity increased under concentration polarisation control. The slope of the curve did not suggest that chlorine evolution occurred during the test, and carbon dioxide evolution would not be expected from thermodynamic considerations. The polarisation curve for carbon in concrete with 2% chloride (Mussinelli *et al*, 1987) appeared to be a steeper version of the curve published by Bennett and Martin (1987).

#### **4.5. Conclusions**

The results demonstrated that the electrochemical behaviour of each anode material was influenced by the composition of the electrolyte, and reactions which were assumed from thermodynamic considerations may have been kinetically inhibited. General trends observed for anodes T, P and E were for the overpotential relating to oxygen evolution to become more positive with decreasing alkalinity, as may be expected from thermodynamic considerations. Increased electrolytic activity was observed for all anodes in chloride electrolytes.

The activity of zinc anodes was due to metallic dissolution and was controlled by the formation and disruption of passive layers, which in turn depended on the pH and chloride ions. The rapid stirring of electrolytes resulted in higher maximum current densities than for anode P, but also greater anode degradation. The results were in general agreement with previous work on zinc coatings in electrolytes. For chloride free electrolytes, passivation limited the current density, which was greatest in the more aggressive calcium hydroxide. Chlorides inhibited passivation and destabilised passive films which formed, with consequently higher current densities. Possibly as a result of hydrolysis, in which chlorides depress the pH of an electrolyte, specimens actively corroded in solutions of pH 9.2 or less, with current densities approaching those observed for the more efficient mesh anodes.



Anodes E and T exhibited similar electrical behaviour in each electrolyte, anode T exhibiting greater activity. For both anodes in calcium hydroxide solution, oxygen evolution appeared to predominate at an overpotential of around 550 mV (SCE), whilst in less alkaline solutions, significant current was only passed if chlorine evolution from chlorides in solution could take place, at an overpotential of approximately 1030 mV (SCE).

The carbon paint showed a lower activity than for the two mesh anodes at similar overpotentials. Oxygen and carbon dioxide evolution appeared to predominate in the electrolytes used and chlorine evolution was only observed at a high overpotential in an acidic solution. A passivation phenomenon was noted which was more apparent in the less alkaline solutions, although the mechanism was not clear and would require further investigation.

## 5. Chapter Five. Ionic migration in cement paste prisms during cathodic protection.

### **5.1. Introduction**

Early work on the electrolysis of concrete at very high current densities up to 50 A/m<sup>2</sup> demonstrated the phenomena of migration of soluble alkalis towards a cathode and sulphate towards an anode, the magnitude of current density influencing the concentrations generated (Rosa *et al*, 1913). In itself, the passage of high electric current through concrete was not shown to influence the strength of concrete, as determined by crushing tests.

The concept of ionic movement in concrete under the influence of an applied electric field underlies the realkalisation/desalination technique, which was outlined in chapter 1. Negatively charged chloride and hydroxyl ions migrate towards an anode and positively charged sodium and potassium ions migrate towards a cathode. A similar movement of ions during CP seems likely and would facilitate repassivation of steel reinforcement by reducing chloride activity adjacent to embedded reinforcement. It has been suggested that under steady conditions, the ionic species would reach a certain balance between a tendency to migrate and to diffuse back to restore ionic equilibrium (Lewis and Boam, 1987). In effect, a concentration gradient may develop and under steady conditions the net migration would become zero. The influence of current density and anode material on this process of ionic migration and back diffusion is little understood and recent research has been directed towards elucidating the migration of various ionic species during cathodic protection.



## 5.2. Previous work

### 5.2.1. Ionic profiles from HCP dissolved in acid

#### 5.2.1.1. Chlorides

One study specifically investigated the migration of chlorides in concrete under external and laboratory conditions both during CP and after current interruptions (Polland and Page, 1988). Current densities of 10, 50 and 222 mA/m<sup>2</sup> (concrete area) were applied to small scale mortar and reinforced concrete specimens of area 0.09 m<sup>2</sup>, utilising a conductive paint anode for a period of 469 days. Acid soluble chloride profiles over the 50 mm cover depth were obtained by drilling of the specimens in increments of between 2 to 10 mm. The results can only be viewed qualitatively as the specimens were poorly characterised and were modified by placing wet sponges on the conductive coatings during CP in order to reduce the system voltage. The specimen design was flawed, consisting of a chloride free lower layer and an upper layer with a variable proportion of admixed chloride. This introduced an unknown factor of diffusion between the different layers and the initial profiles were uneven.

The total chloride profiles reported indicated that little chloride migration occurred at low current densities of 10 mA/m<sup>2</sup>, whilst migration away from the cathode and general chloride depletion were observed at 50 mA/m<sup>2</sup> and more so at 222 mA/m<sup>2</sup>. Progressive reduction of surface chloride was indicative of chlorine evolution and the general depletion of total chlorides in the specimens suggested that a steady flux of chlorides towards the anode may have occurred. Back diffusion of chloride ions after a six month period was reported within 10 mm of the cathode for mortar specimens in 90% relative humidity, both on full removal of CP and on current reduction from 222 mA/m<sup>2</sup> to 1 mA/m<sup>2</sup>. Since ionic diffusion is largely controlled by moisture content, these conditions would appear to be favourable for re-migration, which was therefore unsurprising and would be expected to be slower under practical exposure conditions.

Chloride ion migration was noted during application of CP to concrete specimens using an activated titanium mesh anode at current densities in the range 0.1 to 2 A/m<sup>2</sup> (Mussinelli *et al*, 1987), with chloride depletion within 10 mm of the cathode and chloride accumulation within 10 mm of the anode. However, no information was given of which specimens were tested.

#### 5.2.1.2. Chloride and metal ions

A recent study analysed the variation of total chlorides and metal ions during CP of reinforced concrete (Ali *et al*, 1992). Specimens consisted of small concrete blocks of approximate area 0.043 m<sup>2</sup>, of a well characterised mix, containing a single steel bar with a cover of 63 mm. Constant currents of approximately 10, 30, 50 and 130 mA/m<sup>2</sup> (concrete area) [3, 10, 20 and 50 mA/ft<sup>2</sup> steel area] were applied for 14 months using an activated titanium mesh anode, embedded 12 mm from the surface. Chloride was admixed as sodium chloride in concentrations of approximately 0.4% and 1.5% (wt. cement) (0.05% and 0.2% wt. concrete). Powdered samples were obtained by drilling at relatively coarse increments, adjacent to the anode and cathode and midway between the two, and dissolved in acid before analysis for chlorides and metal cations.

The results were in agreement with general expectations of long term ionic movement as a result of CP. The total chloride content decreased at the cathode and increased at the anode. The latter result indicates that chlorine evolution did not occur at the mesh anode. The variations were insignificant at the lowest current density but then increased with increasing current density and with chloride content. Potassium and sodium ion concentrations similarly increased at the cathode and decreased at the anode. Where initial concentrations of sodium and potassium were similar, as for the 0.4% sodium chloride addition, potassium ion accumulation at the cathode was greater than for sodium ions, indicating greater potassium ion mobility. Calcium ion concentrations increased slightly with increasing current density adjacent to the cathode. However, the calcium ion results were questionable since the limestone coarse aggregate used may have contributed calcium ions when dissolving powdered samples. No discernible trends were apparent for magnesium ions.



These studies of the impact of CP on ionic profiles, as determined by acid dissolution of concrete and cement pastes, were clearly valuable in establishing long term changes at the anode and cathodes. However, such changes would be expected to be slow and the profiles do not make clear the movement of free ions in relation to the applied current. To do this, it is necessary to analyse pore solution expressed from the cement paste of polarised specimens.

#### **5.2.2. Charge balance in cement pastes**

Charge balance of anions and cations was shown to control diffusion rates through cement paste discs (Sergi, 1986). Hydroxyl ions appeared the most mobile, and chloride ions diffused faster than associated cations when the ionic charge balance was maintained by the counter diffusion of hydroxyl ions. Diffusion rates of anions and cations were shown to be the same in carbonated pastes, where free hydroxyl ions were not available. Disruptions to the ionic equilibria within a cement paste resulted in the release or complexing of ionic species, followed by ionic redistribution within the paste to restore charge equilibrium. Hence chloride ion removal by complexing resulted in the release of hydroxyl ions, increasing the pore solution pH. This work showed that it was important to consider ionic migration as a complex system of ion movements, rather than as single ionic species moving in isolation.

#### **5.2.3. Hydroxyl ion migration**

Hydroxyl ion generation during cathodic protection was studied by analysing pore solution expressed from chloride contaminated mortars which were subjected to CP under potential control for 5 weeks (Hardon, 1989). Mortar prisms of w/c ratio 0.5 were placed in saturated air and CP applied to embedded mesh using an anode of stainless steel, sandwiched in sodium chloride soaked cotton wool. Material up to 4 mm from either side of the cathode mesh, obtained by crushing the mortar prism, was used in the determination. The hydroxyl ion concentration at the cathode was observed to increase from 550 to 830 mM/l during the test period, independent of the polarisation potential which varied from -

700 to -1150 mV (SCE). This indicated that hydroxyl ion generation was controlled by a rate limiting oxygen diffusion step in the near saturated specimens.

#### **5.2.4. Ionic profiles from expressed pore solution**

Anion and cation concentration profiles were measured as part of a study into the initiation of alkali silica reaction during CP (Sergi and Page, 1992). Specimens consisted of saturated hardened cement paste blocks, subdivided into 4 connected prisms of dimensions 35 x 35 x 150 mm. A mixed anode of activated titanium mesh/carbon paint was applied to either end of each block and current passed to steel plates placed centrally in each prism. This eliminated both the unknown effect of migration from the bulk of the sample and uneven current distribution. The distance of 75 mm between anode and cathode allowed detailed ionic concentration profiles to be determined as changes in concentration occurred within short distances of the anode or cathode. Specimens were polarised over a period of 100 days, some potentiostatically to -850 mV (SCE) and -700 mV (SCE) whilst others were polarised galvanostatically at 5 mA/m<sup>2</sup> and 20 mA/m<sup>2</sup>. Pore solution was obtained from slices of the blocks and analysed for hydroxyl, chloride, sodium and potassium ions. The use of hardened cement paste facilitated pore liquid extraction. In addition, the total chloride concentration (acid soluble) was obtained from crushed material and the moisture content determined, allowing plotting of profiles for the free and bound chloride ion concentrations.

The results showed that charge balance was maintained throughout specimens under cathodic protection, up to a short distance from the electrodes. It was suggested that the apparent loss of anions at the anode was due to migration of sulphates, which were not analysed for. In general, S-shaped ionic profiles developed, with sharp ionic depletions/increases within 20 mm of the anode and cathode. Free and bound chloride ion concentrations were observed to decrease at both the cathode due to migration and at the anode due to apparent chlorine evolution.

Hydroxyl and sodium ion concentrations increased at the cathode and decreased, generally to a greater extent, at the anode. Potassium ion migration was generally negligible.



Differences between the theoretical level of hydroxyl ions produced at the cathode and measured levels suggested that hydroxyl ions which formed at the cathode migrated quickly to the anode, to be consumed in the anodic reaction. Increased hydroxyl ion concentrations at the cathode were related by the authors to the cation concentration levels. Since cations could not be consumed at the cathode, the cation concentration profile would depend on the strength of the applied electric field, which was related to current density. This suggested that ionic profiles in pore solution were primarily influenced by the magnitude of current density at the time of current interruption/specimen analysis rather than by the total charge passed.

Whilst potentiostatic control appeared to halt corrosion of embedded steel, the current densities varied greatly between samples, generally in the range 0.2 to 2 A/m<sup>2</sup> for short periods and decreasing thereafter. This made comparisons between specimens difficult, hence the later adoption of constant current, under which the cathodic potentials were observed to become progressively more negative with time.

Concentration profiles for galvanostatically controlled specimens indicated lower alkali accumulation at the cathodes than for potentiostatically controlled specimens and relatively insignificant chloride migration. This may confirm the theory of ionic concentration profile being related to absolute current density, however, the constant current tests were run for relatively short time periods and it is possible that significant changes under these conditions would only become evident later.

A complementary study was performed where CP was applied to concrete prisms containing marginally reactive calcined flint aggregate for two years and acid soluble profiles were obtained for sodium, potassium and chloride ions. The resulting profiles generally showed the characteristic S-shape and indicated that sodium and potassium ion concentrations increased to a far higher degree than for the paste specimens. This suggested that the sodium and potassium ions were complexed out of the pore solution by the concrete

adjacent to the cathode in some way. The results for 0 and 1% chloride (wt. cement) were similar to those of Ali *et al* (1992), in that the cation concentrations increased to a greater extent at the cathode than at the anode. In addition, for specimens with no sodium chloride addition, potassium ion accumulation at the cathode was again greater, by a factor of 2, than that for sodium ions. Where sodium was admixed, the ionic profiles reflected this with greater sodium migration. At high chloride levels of 2% (wt. cement), more complex profiles developed due to excess free chlorides apparently being complexed whilst migrating towards the anode.

Theoretically, where chloride evolution forms an anodic reaction, the total quantity of hydroxyl ions evolved at the cathode would exceed the total quantity consumed at the anode, leading to an increase in the total hydroxyl ion concentration. The release of bound chlorides due to chloride depletion would also be expected to lead to a steady increase of hydroxyl ions in the pore fluid, related to current density. Although conclusive evidence was not found to confirm these related phenomena in the cement paste study above, ASR enhancement which was observed during CP of chloride containing concrete prisms was attributed to increased hydroxyl ion levels.

The work of Sergi and Page was directed at the cathode area and the anode interface was poorly characterised, with a mixture of activated titanium mesh, cement paste and conductive paint. It was proposed that chloride ion removal at an anode would influence the hydroxyl ion concentration profile within the pore solution. Considering the claims of oxygen specificity for certain anode materials, as outlined in chapter 4, it was of interest to conduct similar experiments using the four anode materials adopted for this study.



### **5.3. Experimental**

#### **5.3.1. Introduction**

This chapter concerns the effect of ionic migration during cathodic protection of hardened cement paste (HCP), concentrating on the anodic region. The experiments also shed light on the durability of lightweight anode materials in high relative humidities.

Briefly, cathodic protection was applied to steel plates embedded in HCP blocks, which were then sectioned so that pore fluid could be obtained for chemical analysis. It was anticipated that the ionic concentration profiles thus determined would be influenced by the anode material and the occurrence of chlorine evolution. Dissolved zinc ions were expected to migrate towards the cathode in a similar manner to other cations. In addition, it was intended to determine the influence of a low constant current density, applied over a long time period, on hydroxyl ion concentration levels in pore solution.

#### **5.3.2. Experiment design**

Galvanostatic polarisation, rather than potentiostatic polarisation, was applied to specimens to provide a constant current density of  $50 \text{ mA/m}^2$  over a period of approximately two years. In addition, specimens were energised for shorter periods of 4 months to 6 months at current densities of  $50 \text{ mA/m}^2$  and  $20 \text{ mA/m}^2$  to elucidate the influence of time and current density on the profiles determined. Specimen details and reference numbers are given in table 5.1.

HCP was used in the work to facilitate rapid production of multiple pore fluid samples. In particular, HCP was relatively easy to dry cut and expression of pore fluid from saturated HCP sections maximised yield and was quickly accomplished. Specimen design was based on the multiple prism cement paste block developed by Sergi and Page at Aston University. Some of the geometric advantages of this design were described above. The distance of 75 mm between anode and cathode provided high definition ionic profiles. In addition, the paste block was easily split into the individual prisms of cross section  $35 \times 35 \text{ mm}$  which were of suitable dimensions for sectioning and placing into the pore press.

Cement of high  $C_3A$  content was used by Sergi and Page in order to manipulate the pore solution alkali level by adding varying levels of chloride, which would then be removed by complexing. However, this influenced the free chloride available at any time and the results would not be directly comparable with ordinary portland cements. Control of initial alkali levels was of no concern in this study hence an OPC was used which would allow comparisons to be made with work as described in Chapter 8. Studies of general ionic migration have added chloride to specimens as sodium chloride (Sergi and Page, 1992, Ali *et al*, 1992), which influenced the sodium and potassium ion migration profiles. To prevent this effect, chloride was added as calcium chloride.

It was convenient to use the same moulds as for the previous study to make specimens suitable for application of the conductive paint and zinc coatings, as shown in figure 5.1. Sergi and Page fixed titanium mesh to each end of the paste block using a thin layer of cement paste. However, this was deemed unsuitable for this study, since in practice CP mesh would be embedded in mortar or concrete, and ionic migration in the region of the anode was of particular interest. Embedding the mesh in a mortar or cement paste, cast onto the ends of a hardened paste block, was rejected due to the heterogeneity that this would induce at the interface between the two materials. To ensure homogeneity between anode and cathode, an extended mould was made which allowed a compressed mesh anode to be placed 75 mm from the cathode plates, with 15 mm cover to the end surface, as shown in figure 5.2.

The cement paste blocks measured 150 x 35 x 150 mm and 150 x 35 x 180 mm. Four steel plate cathodes were placed centrally in each prisms, with an agar salt bridge adjacent to one to allow potential measurements. Identical control specimens were prepared and placed within a high humidity environment without applied current.



### 5.3.3. Specimen preparation

#### 5.3.3.1. Cathode plates

The 4 mild steel central cathode plates each measured 2.3 cm by 2.5 cm, giving a total cathode area of 46 cm<sup>2</sup>. A short stub bar, of 2 mm diameter, was fixed to each plate using a sawn slot and spot welding. The bars allowed external electrical connections between plates and performed the secondary function of locating plates in the mould during casting. Completed cathodes were degreased using acetone and de-rusted by acid pickling as outlined in chapter 3. The stub joint was protected from crevice corrosion by application of two coats of a cement/SBR polymer slurry mixed, in the ratio 1:1 and cured for 3 days in a humidity box<sup>5</sup>. The joint was then coated with epoxy resin.

#### 5.3.3.2. Mesh anodes

Anode E and T electrodes were similarly prepared by cutting an area of mesh and collapsing the diamonds to give a narrow, condensed surface of depth 1 mm. Small off-cuts were used to secure the mesh at the ends and the central tie was kept long to act as an external electrical connector after casting. As far as possible, the mesh and ties were compressed between sheets of paper in a vice to give a plane surface, parallel to the cathodes and hence some surface coating scratching was unavoidable. The area of mesh E was made up from 16 diamonds and mesh T from 12 diamonds, due to differences in mesh geometry. These areas were the maximum which could be fitted within the confines of the specimen geometry and were higher than the total specimen cross sectional area, as shown in table 5.2, with the intention of providing an even current distribution. Examples of prepared mesh anodes and steel plate cathodes are shown in plate 5.1.

#### 5.3.3.3. Casting

Each mix used Northfleet OPC with 2% calcium chloride by weight and water/cement ratio of 0.48. This relatively high w/c ratio was intended to produce a permeable paste and facilitate pore water expression.

---

<sup>5</sup> This maintained a very high humidity and consisted of a perspex box which had a reservoir of water filling its lower volume and an atmospheric seal, provided by the lid resting in a water filled lip. Specimens were placed above the water on free standing, perforated perspex platforms.

Plastic coated wooden moulds were used with built in perspex ridges on the base and lid to form the individual, connected prisms and petroleum jelly was used as mould release agent. Moulds were fully assembled with cathodes in place and mesh located in slots, sawn into the perspex ridges, as appropriate. A side piece was left off to allow placement of the cement paste. A void was formed for the agar bridge, adjacent to a central cathode plate, using a short length of flexible tubing. Cement paste was prepared in a forced action mixer and emptied into the mould and air bubbles removed by vibration. The final side piece was then carefully screwed into position. Specimens were cured in the mould for three days, then demoulded and stored for the duration of the study in humidity boxes.

#### 5.3.3.4. Anode coatings application

Specimens to be coated were allowed to cure for 7 days in the high humidity environment. The paste surface was roughened using a wire brush and primary anodes were fixed to the surface with epoxy resin. These consisted of metal strips, of dimensions 50 x 5 x 0.7 mm, with a 2 mm diameter hole in the free end for electrical connections. Titanium was used for the carbon paint with carbon fibre strands to form a secondary current distributor and brass was used for the zinc anode. Anode coatings were applied as described in chapter 3 and the specimens returned to the high humidity environment.

#### 5.3.3.5. Connections

Electrical connections between cathode plates were made by soldering a copper/nickel wire between exposed steel stubs. Connections between the electrodes and galvanostat used standard electrical connectors which were subsequently coated in lacquer to protect against corrosion. The galvanostat was able to provide current up to 1 amp per circuit. Current density was calculated with respect to the concrete surface area to allow direct comparisons to be drawn between specimens. However, the current densities at the mesh surfaces were lower than for the coatings due to smaller surface areas, as shown in table 5.1. Agar salt bridges were formed using flexible polythene tubing and placed in the pre-formed holes adjacent to the cathode, with the free ends placed in potassium nitrate solution. Four blocks were placed in each humidity box. The experimental arrangement is shown in plate 5.2.



#### 5.3.3.6. Moisture conditioning

To provide an optimum moisture condition in the test samples and to facilitate pore solution extraction, the samples underwent a process of re-saturation after electrical connections had been made. Re-saturation was achieved by wrapping each sample in absorbent paper towels and providing a regular soaking with de-ionised water. The samples were stored in a humidity box. In order to ensure full re-saturation had been achieved, the control specimens were weighed at intervals. The results in figure 5.3 show that there was a significant early uptake of water by the samples and steady conditions were approached slowly thereafter. A small weight increase with time may be due to continuing cement hydration. Following this procedure, the specimens were unwrapped and polarised.

#### **5.3.4. Testing**

##### 5.3.4.1. Electrical measurements

Linear polarisation measurements and  $E_{\text{corr}}$  values were obtained before energising each paste block, as described in chapter 3. The cathode potentials were measured via the agar salt bridge and the anode potentials initially measured within 5 mm of the anode edge or directly above the mesh anode, with the current switched on. After a time, as a result of anode Z corrosion products, it was necessary to measure some anode potentials through the agar bridge. It was considered that any error due to IR-drop along the paste block would be small since the specimens were maintained in a saturated state and contained a significant level of chloride. This was checked by regularly measuring anode potentials by both methods for each anode. The apparent IR-drop varied in the range 10 to 40 mV and was observed in all specimens, hence the induced error was considered relatively constant. The  $E_{\text{corr}}$  and  $i_{\text{corr}}$  values given in table 5.3 indicate that each specimen was corroding at a significant rate before the application of CP. This was confirmed by breaking open a spare specimen and observing copious corrosion products, concentrated at the plate edges.

##### 5.3.4.2. Analysis of specimens

On disconnection from the galvanostat, each specimen was inspected for cracks. Lines corresponding to saw cuts were drawn perpendicular to the length of the prisms to ensure the accuracy of saw cuts, as shown in figure 5.4. The mesh anodes were sawn through by

hacksaw at the three connection locations to allow prisms to be separated. Anode coatings and primary anodes were removed. Individual prisms were then split in two at the cathode plate, which was inspected for corrosion, and stored in sealed polythene bags. Five half prisms were selected and sectioned by mechanical hacksaw, with careful cleaning of the blade in between cuttings to prevent contamination between samples. This dry cutting method was shown to limit any increase in sample temperature (Sergi, 1986). The dust from sawing was collected for later analysis of acid soluble chlorides. Groups of slices, cut at the same location, were stored in sealed polythene bags and placed in an airtight container before pore pressing. This was carried out directly in order to yield the greatest pore solution. The pore fluid was analysed for hydroxyl ions immediately following extraction and subsequently for chloride, sodium and potassium ions. Pore fluid from zinc coated specimens was also analysed for zinc ions. Control specimens were similarly sectioned and analysed.

Carbonation depths and the alkalinity of the cathode plates were measured by applying phenolphthalein indicator solution to the freshly broken paste surface. Unpressed sections were analysed for evaporable water and non-evaporable water, as described in chapter 3.

## **5.4. Results**

### **5.4.1. Introduction**

A number of unanticipated experimental difficulties and errors occurred during the work, as will be identified in this section, and the results should not be viewed as reliable. Consequently, it was difficult to draw definitive conclusions.

Cathodic protection of the steel plates was indicated by the conversion of brown rust to black magnetite due to oxygen depletion, as was found to occur by other investigators (Sergi and Page, 1992). Typical protected cathodes are shown in plate 5.3. All of the HCP specimens were observed to have hairline cracks around part of the cathode, possibly due to shrinkage or corrosion products. Only one of the control specimens, E:0, cracked



open at the cathode plates. It is possible that corrosion was restricted by low dissolved oxygen availability in the saturated specimens. Localised corrosion of the exposed stub may have provided cathodic protection to the large cathode embedded in a low dissolved oxygen, alkaline environment. Carbonation depths up to 4 mm were noted adjacent to the central cathode bar connection but were less than 0.5 mm elsewhere.

#### **5.4.2. Durability of powered specimens**

The high humidity environment proved very aggressive. Anode and cathode connections required replacement after 6 and 14 months, despite the anti-corrosion measures. The zinc coatings suffered severe surface corrosion. After a number of months it became apparent that electrical shorts occurred between specimens through moisture films on supporting surfaces and through the agar salt bridges, which were initially placed into common electrolyte containers. To minimise these effects, specimens were supported on polythene tubing and agar salt bridges placed in individual containers. However, these phenomena meant that the precise level of current supplied to each specimen was no longer known.

No anodic degradation was observed for anodes E and T and the cathodes appeared protected. The paste between anode strands for specimens E:50a and T:50a were observed to be a lighter grey than adjacent paste, possibly due to dehydration, but appeared completely intact. The micrograph in plate 5.4 shows a mesh strand in rectangular cross section, with dark brown paste adjacent indicating that no neutralisation of the cement paste occurred. The blue areas in the micrograph are resin filled voids from the thin section preparation, which was made difficult by the high density of mesh strands.

Specimen P:50a developed a crack at the cathode, 400  $\mu\text{m}$  in width, shortly before testing and on breaking open, the two central cathode plates showed significant corrosion. The paint anode had bubbled and on removal, adhesion to the substrate appeared low compared to the unpolarised control. Problems with the primary anode occurred during the work as the titanium strip debonded from the coating and epoxy resin, which suffered softening. This connection was repaired after 14 months by removing loose paint and epoxy resin and

reinstating the primary and secondary anodes as for the initial application. The relative ease with which the primary and secondary anodes were removed from specimen P:50a is indicated by the bare central area in plate 5.5.

A white corrosion product developed at the interface between the zinc and cement paste and the coating was difficult to remove from the control specimen, with paste pieces adhering to removed zinc. However, the white product was more copious for Z:50 specimens and although the zinc coating did not debond, the majority of it lifted off easily, leaving a layer of corrosion product adhering strongly to the cement paste, as shown in plate 5.6. Some what surprisingly, the cathode plates appeared to be protected for all zinc coated specimens.

#### **5.4.3. Electrical data**

Table 5.1 shows the total charge passed for each specimen, assuming accurate current control by the galvanostats used. However, as outlined above, absolute control of current to specimens proved difficult due to the very high humidity environment and the measured current could drift by  $\pm 5\%$  for mesh anode specimens and by up to  $\pm 25\%$  for coated specimens. In addition power was suspended for short periods during maintenance. The total charge passed for specimens generally exceeded the total charge passed in the work of Sergi and Page, where the maximum of 2550 Coulombs was measured for 2% chloride specimens held at -850 mV (SCE).

Figures 5.5 to 5.16 show variations of the anode ( $E_a$ ) and cathode ( $E_c$ ) potentials for specimens with time. The system voltage comprised of the sum of the two and is not shown. The  $E_c$  values dropped immediately to around -1150 mV (SCE) for the majority of specimens, independent of applied current density. This value is indicative of hydrogen evolution and may be related to the availability of oxygen at the cathode in the fully saturated specimens. The exception was specimen E:20, where the  $E_c$  value was approximately -550 mV, occasionally falling to around -1000 mV as shown in figure 5.10. Specimen E:50b also showed some early variability in figure 5.9. It was noted that the top surface of these specimens were often dry due to uncontrollable variations within the humidity cabinet. As



the test proceeded, all of the  $E_c$  values underwent some variation after around 150 days. This may be partly related to the increased temperature within the humidity cabinets during the summer months, as shown in figure 5.17. The minimum  $E_c$  value recorded for the mesh specimens during this period was around -550 mV and then more negative potentials resumed, as shown in figures 5.5 and 5.8. The  $E_c$  values for anode specimens P and Z followed similar trends initially, but longer term values became less negative as shown in figures 5.11 and 5.14, suggesting that the CP had become less effective.

Figures 5.5 to 5.7 show that the  $E_a$  values for anode T were steady at around  $515 \text{ mV} \pm 10 \text{ mV}$  (SCE) and not influenced by apparent moisture variations or applied current density. Figures 5.8 to 5.10 show similar trends for anode E, with higher  $E_a$  values of  $610 \text{ mV} \pm 20 \text{ mV}$ . Figures 5.5 and 5.8 show that  $E_a$  increased in the long term to  $550 \text{ mV} \pm 30 \text{ mV}$  for specimen T:50a and to  $800 \text{ mV} \pm 50 \text{ mV}$  for specimen E:50a. These results indicate that similar anodic reactions occurred at each anode. The lower  $E_a$  values for anode T may be due to its lower anode current density, as shown in table 5.1, other factors being constant.

Figures 5.11 and 5.12 show that  $E_a$  for anode P specimens gradually increased from 750 mV to around 1200 mV over 200 days and proceeded to increase up to around 1600 mV over the next 200 days, with some large variations up to around 3 V. Subsequent potentials were extremely erratic. A significant proportion of the later values was due to increased resistance as the anode connections deteriorated and it was not possible to obtain reliable readings. The reduced effectiveness of the paint coating was indicated in the more positive  $E_c$  values and the cathode plate corrosion of specimen P:50a. However, the paint appeared to provide adequate protection at an anode potential around 1200 mV (SCE) during the initial experimental period.

For clarity,  $E_a$  and  $E_c$  values for anode Z specimens are plotted separately. Figures 5.13 and 5.15 show anode potentials measured both adjacent to the anode surface and via the agar salt bridge. It is clear that the  $E_a$  values quickly became erratic due to high resistance at

the anode interface. Potentials obtained by both methods were shown to vary from -600 mV to +600 mV over the first two months, followed by a general increase to around  $2\text{ V} \pm 1\text{ V}$ . Values after 500 days approached 17 V and are not given for clarity. The excessive voltage requirement due to the high anode resistance caused failure of the galvanostat and made current control impossible.

#### **5.4.4. Ionic concentration profiles**

The ionic concentration profiles shown in figures 5.18 to 5.60 indicate that ionic migration occurred as a result of cathodic protection. However, quantitative conclusions cannot be drawn in the majority of cases due to an unforeseen experimental error, the magnitude of which was not fully appreciated until the final 2 year analysis. An examination of figures 5.27, 5.39, 5.48 and 5.57 for the un-polarised control specimens after 2 years indicates that the hydroxyl ion concentration levels were considerably lower than values observed by others workers (Hardon, 1989) and lower than would be expected from a consideration of the cement alkali content<sup>6</sup>. The only probable explanation for this large discrepancy was that considerable ionic leaching occurred from the bulk of each block as a result of the long exposure in the very high humidity cabinets. Droplets of water forming by condensation on a block surface absorbed ions, which were subsequently removed as excess water dropped into the reservoir of water. An alternative mechanism may have been ionic migration through continuous moisture films. The originally neutral water reservoir had attained a pH of around 13, as measured by indicator paper. This unexpected phenomenon clearly had a great impact on all of the results, reducing their quantitative value, and was unavoidable in the high humidity cabinets used. Suggestions for improving the experimental procedure are given in the discussion. It had incorrectly been assumed that ionic concentration reductions at 120 and 260 days were entirely due to CP effects since controls specimens were not analysed at these times. The ionic profiles will be discussed in the light of the progressive leaching; Ionic levels at 720 days for polarised specimens may still be related to the un-

---

<sup>6</sup>The total alkali content of the OPC of 0.50 % ( $\text{Na}_2\text{O}$  Equivalent), (calculation is given in Appendix 5.1), can be equated to a hydroxyl ion concentration of around 360 mM/l for a HCP of w/c ratio 0.5, from the results of Nixon and Page (1987)



polarised controls and specimens analysed at 120 and 260 days may be compared with one another.

#### 5.4.4.1. Anode T

The ionic profiles for the 260 day specimens, T:20 and T:50b will be compared first. The hydroxyl ion concentration for both specimens was around 200 mM/l at the cathode, as shown in figures 5.18 and 5.21, and appeared to decrease linearly towards the anode for specimen T:50a, possibly indicating that hydroxyl ion evolution exceeded the rate of consumption at the higher CD but not at the lower CD. The free chloride ion concentrations in these figures were observed to increase from the cathode towards the anode, and a particularly high concentration in the outer 20 mm may have been due to ions 'trapped' there by the applied field. The free chloride levels were lower for specimen T:50b, as were the total chloride levels as shown in figures 5.19 and 5.22. These results suggest that at 20 mA/m<sup>2</sup>, anode T was evolving anodic oxygen at the same rate as cathodic hydroxyl ion formation, and chlorine migration had reached a steady state with some redistribution of bound chlorides. At 50 mA/m<sup>2</sup>, chlorine evolution may also have occurred, leading to a lower total chloride content in the anode region and in the sample bulk. Anodic chlorine evolution may also have caused the hydroxyl ion gradient to form. Alternatively, the hydroxyl gradient may have developed to maintain charge balance with the slightly higher cathode potassium ion concentration in figure 5.21.

Figure 5.24 shows that the free ion profiles trends for specimen T:50a were similar to those for specimen T:50b in figure 5.21, although the overall concentration of ionic species had decreased. Accepting that ionic leaching had occurred, the hydroxyl ion concentration for T:50a shows a significant increase towards the cathode from the base level around 100 mM/l to 200 mM/l when compared to the control in figure 5.27. The free chloride ion profile for T:50a in figure 5.24 displays a general increase from around 130 mM/l at the cathode to 200 mM/l at the anode, compared to an even concentration around 150 mM/l for T:0 in figure 5.27. The reduction of bound chloride at the anode of T:50b was not observed in T:50a. However, the total chloride concentration was lower in T:50a than in the control

T:0, particularly in the cathode region.. It is not entirely clear therefore whether chlorine evolution continued at this current density. On the assumption that it did not, the most probable explanation for the hydroxyl ion gradient is that it developed to maintain charge balance with the potassium ions in solution. Such a relationship was reported in the literature review from the work of Sergi and Page (1992).

Potassium ion concentrations were approximately three times greater than the sodium ion concentrations, which were not observed to migrate. The potassium ion profile in figure 5.18 appeared level whilst the profiles for 50 mA/m<sup>2</sup> specimens in figures 5.21 and 5.24 appeared to increase in the cathode and anode regions compared to the central region. The anodic increase appeared to be related to high free chloride concentration in the anode region whereas the cathodic increase appeared to be related to the current density. It can be seen that the quantities of hydroxyl ion were influenced by the quantities of free alkali metal ions.

#### 5.4.4.2. Anode E

The ionic profiles for specimens E:20 and E:50a, as shown in figures 5.30 to 5.35, were obtained after 120 days. The free chloride ion profiles in these figures should be viewed with caution since the spectrometer apparatus was performing erratically at the time the results were obtained and the sum of ions in these figures show some variation. However, the trends in the figures resemble those described for anode T specimens T:20 and T:50b in figures 5.18 to 5.23, which suggests similar anodic behaviour. Of interest, the similar hydroxyl ion concentrations for E:20/T:20 and E:50b/T:50b, obtained approximately 140 days apart, suggests that the majority of ionic leaching occurred at an early stage of the experiment, possibly during the re-saturation procedure.

The chloride and hydroxyl ion concentrations for E:50a in figure 5.36 appear lower than those for T:50a in figure 5.24. The gradients of the ionic profiles also differ, the chloride profile appearing steeper and the hydroxyl profile more shallow. A comparison of the bound chlorides in figures 5.37 and 5.34 indicates that, as for anode T, anode E did not show a reduction of bound chloride adjacent to the anode after 720 days as was apparent at



120 days, rather it displayed a slight increase compared to the cathode region. A comparison of the total chloride levels in figures 5.37 and 5.40 indicates that the total chloride content of E:50a was higher than would have been expected, considering the low levels of free chloride. The results indicate that significant chlorine evolution did not form an anodic reaction in specimen E:50a at the time of analysis.

The potassium ion concentration tended to increase towards the anode in specimens E:20 and E:50b. The profile for specimen E:50a was level in the bulk of the specimen, increasing sharply at the anode, presumably related to the similar sharp chloride ion increase. This may account for the shallow hydroxyl ion profile.

#### 5.4.4.3. Anode P

Figure 5.42 shows that the ionic concentration of specimen P:50b at 126 days was considerably lower than for the anode E and T specimens of similar age, but chloride, potassium and hydroxyl ion profiles displayed similar trends. Comparison of figures 5.19 and 5.43 shows that the total chloride concentration profile was similar to that of specimen T:20. These results suggest that similar anodic processes occurred as for the mesh anodes at the lower current density 20 mA/m<sup>2</sup>.

Figure 5.45 gives the ionic profiles for specimen P:50a. The sodium and potassium concentrations were lower than the control P:0 in figure 5.48, and both increased towards the cathode. The hydroxyl ion levels reflected the reduced alkali metal levels; The hydroxyl ion concentration adjacent to the anode was 40 mM/l, which equates to a pH of 12.6, that is the buffering pH of calcium hydroxide. This increased steadily to a plateau of 70 mM/l at the cathode, a pH of 12.9, which was about the pH observed in the control specimen in figure 5.48. The free chloride ion profile had a negative gradient, tending to decrease towards the cathode from an anode level around 100 mM/l. The total chloride ion profile shown in figure 5.46 forms an S-shape, indicating that the bound chloride became redistributed with decreased chloride complexes adjacent to the cathode and increased

complexes at the anode. These results also suggested that the chloride ions were not involved in the anodic reactions.

#### 5.4.4.4. Anode Z

Figure 5.51 shows the ionic profiles for specimen Z:50b after 246 days. The hydroxyl ion profile fell in between those of specimen T:50b in figure 5.21, and specimen P:50b in figure 5.42, and appeared to be related to the potassium ion profile. The free chloride concentration appeared lower immediately adjacent to the cathode and was level otherwise. The total chloride concentration in figure 5.52 appeared to be comparable with levels shown in figures 5.22 for anode T.

The ionic profiles for the 720 day specimen are given in figure 5.54. The potassium ion concentration was lower than that of the control in figure 5.57 and displayed a slight increase from anode to cathode. The hydroxyl ion concentration was at a similar level to the control Z:0 adjacent to the cathode, reducing in the anode region. The relatively even alkali profile indicates that the CP circuit had reduced in its effectiveness. The free chloride ion concentration showed a slightly negative profile gradient and the total chloride profile in figure 5.55 displayed a shallow S-shape, indicating that chlorides were redistributed by the applied current rather than participate in the anodic reactions.

The corrosion products at the interface between the zinc and HCP were not analysed but would be expected to be various forms of zinc hydroxide. The distribution of soluble zinc ions within specimen Z:50b at 246 days and specimens Z:0 and Z:50a at 720 days are shown in figure 5.60. Considering the latter specimens first, the zinc ion concentration of specimen Z:0 decreased from around 0.03 mM/l at the anode to approximately 0.01 mM/l in the remaining paste. This demonstrates that a small proportion of soluble zinc ions passed into the HCP by normal diffusion processes. The profile for specimen Z:50a displayed a similar low zinc concentration up to the cathode, where it increased significantly to 0.16 mM/l. Although insufficient pore solution was obtained from paste slices adjacent to the cathode of Z:50b for analysis, the shape of the profile for Z:50b suggests that a similar or



greater increase would have been measured at the cathode. These results indicate that zinc migration was enhanced by CP and that zinc ions accumulated in the HCP adjacent to the cathode.

A comparison of the profiles indicates that the soluble zinc content within the specimens decreased with time. It could be postulated that this decrease, and the concentration of zinc ions at the cathode, were related to zincs' increased solubility in alkaline solutions, since the alkalinity was higher in the cathodic region in both specimens and decreased with time as shown in figures 5.51 and 5.54. The hydroxyl concentration for specimen Z:50a ranged from 58 to 105 mM/l. The minimum theoretical solubility of bizincate ions in these solutions is 0.12 mM/l and 0.22 mM/l respectively (calculation is given in appendix 5.2), which exceed the measured zinc concentrations at corresponding locations. This suggests that the measured zinc ion concentration in the alkaline pore solution was not limited by low solubility in the bulk of the specimen, that is, zinc hydroxide precipitation in pores did not occur. The situation adjacent to the cathode is less clear and it is possible that the quantity of zinc in solution was limited by the decreasing alkalinity, that is, it is possible that precipitation occurred. Such precipitation may cause pore blocking and reduce the access of oxygen to the cathode. Such a mechanism may account for the apparent protection from corrosion, as indicated from a visual inspection of cathode plates, for the Z anode specimens after the anode had apparently failed.

#### **5.4.5. Discussion**

It was pointed out in the results above that excessive leaching occurred during the experiment. The two possible causes of this were the re-saturation procedure and the experimental set-up itself, where moisture condensed on specimen surfaces and then ran off. The only way of avoiding such loss of ions, whilst maintaining specimens in a saturated state, would be to change the experimental set up. A possible alternative would be to wrap each specimen in absorbent paper, which would be kept permanently moist using distilled water, and to cover a number of such specimens with polythene sheeting to limit moisture loss. This is similar to the method used to re-saturate the specimens. Such an

arrangement appears to have been used successfully in recent studies of CP induced ASR (Sergi and Page, 1992). It would be necessary to support each specimen to prevent short circuiting along the specimen underside and care would be required to prevent short circuits between the cathode and anodes. A degree of leaching into the absorbent paper would be unavoidable, but this could be minimised with care. It may be advantageous to place trays beneath each supported specimen so that the amount of any alkali loss could be quantified.

A second experimental error was the inability to control the applied current for significant periods, again partly caused by conditions within the humidity cabinets and partly due to deterioration of the coated anodes. In this respect, the mesh anodes appeared the more durable and able when operating in a very high humidity. The compressed mesh performed a reinforcing role for the paste blocks, which were susceptible to breaking at the crack-inducers as a result of mishandling during the experimental set-up. Generally, the mesh anode specimen design appeared to be suitable for further studies of ionic migration although the electrical connections would require greater corrosion protection.

An examination of the results indicates an absence of the characteristic S-shaped ionic profiles, as observed by Sergi and Page (1992). The profiles tended to exhibit gradients across the entire specimen rather than adjacent to the anode and cathode. The reduced alkalinity of the cement pastes may partly account for this, since a lower proportion of free ions were available for charge transport.

Owing to the uncertainty induced by the apparent leaching effect, the accuracy of bound chloride levels was questionable, as the calculation relied on the free chloride concentrations. More confidence was placed in the total chloride profile trends as it was thought that leaching would influence chloride levels evenly throughout a specimen, as was generally indicated in the control specimens. The total chloride levels of between 0.35 to 0.45 mM/g cement appeared reasonable when compared to the variation of bulk chloride concentration results of Sergi and Page (1992): the total chloride contents for high C<sub>3</sub>A



(high complexing capacity) cement specimens containing 2% added chloride was in the range 0.47 to 0.55 mM/g cement. Previous studies have deduced the occurrence of chlorine evolution from a reduction of both bound and free chlorides in the anode region. This was not generally observed in specimens other than T:50b and E:50b, where the total chloride level appeared to decrease in the anode region, yet the free chloride level did not. It was not clear from these results, therefore, whether the mesh anodes evolved chlorine at the higher current density.

Net increases in hydroxyl ion concentration within the bulk of a specimen have been attributed to charge consumption by the chlorine evolution reaction at the anode (Sergi and Page, 1992). Clearly, any possible increase of hydroxyl ion concentration in the pore solution due to greater production at the cathode than anode in these tests was masked by the loss of ions from leaching. Hydroxyl ion gradients, increasing towards the cathode, developed in all specimens held at 50 mA/m<sup>2</sup> but not in the mesh anode specimens held at 20 mA/m<sup>2</sup>. This difference can not be related to the cathode polarised potentials, which had appeared to be influenced by the specimen moisture condition rather than by the current density. In the absence of chlorine evolution the development of a positive hydroxyl ion profile slope can only be related to the maintenance of charge balance with the alkali metal ions. It was noted in the results that the hydroxyl levels were relatively even throughout specimens in which the potassium ion levels were also even, namely mesh specimens held at 20 mA/m<sup>2</sup>. The results therefore appear to support the model proposed by Sergi and Page (1992) whereby the magnitude of the applied current density controlled the gradient of alkali ions near to the electrodes and hence the hydroxyl ion profile.

It was clear from the results that potassium ions were significantly more mobile than sodium ions, as was observed by Ali *et al* (1992), possibly because the concentration of potassium ions was approximately three times higher than that of sodium ions. The ions of both metals were present in low concentrations since neither was added as an admixture. Although it has been pointed out that alkali metal ions can not be consumed in an

electrochemical reaction, their levels appeared to decrease in polarised specimens compared to the controls, which suggest that they may have become complexed by the cement paste. Such complexing of potassium and sodium ions in the cathode region of polarised concrete prisms was apparent in the Sergi and Page study. As the alkali metal concentrations decreased, the hydroxyl ion concentration similarly decreased. Perhaps as a result of the low ionic content of the pore water, the potassium ion profiles appeared to reflect ionic migration due to the direction of the applied field and due to a requirement to balance chloride ion negative charges.

The  $E_a$  data appeared to reflect the different mesh anode surface current densities. It would be advantageous in a future experiment to ensure that each anode surface area was approximately equal. As the chemical nature of the specimens changed with time, the  $E_a$  values tended to increase, suggesting a deterioration in the efficiency of the anodic reactions. This increase in anodic overvoltage with ion depletion was in agreement with trends in Chapter 4 results, where electro-catalytic activity decreased with decreasing electrolyte chloride concentration and with decreasing pH. However, the pH of paste specimens did not decrease below 12.6, the maximum pH adopted in the solution work. The mesh anode  $E_a$  values were in good agreement with the oxygen evolution overpotential value of 550 mV (SCE) for the anodes in saturated calcium hydroxide solution. This supports the ion profile evidence that the mesh anodes evolved oxygen rather than chlorine. The initial  $E_a$  values of around -600 mV for anode Z specimens were also in general agreement with the active portion of the polarisation curves in figure 4.4. However, the apparent  $E_a$  value increased subsequently due to the increasing corrosion at the zinc interface. Similarly, the initial  $E_a$  values for anode P specimens could be related to the more active part of the polarisation curves in figure 4.15.

No attempt was made in the study to control the temperature of specimens. The elimination of this extra variable factor in further work would enable variations of  $E_c$  to be related to changes in cathode processes.



## 5.5. Conclusions

Hardened cement paste prisms were polarised for a two year period and evidence of ionic migration due to the applied current was obtained by analysing expressed pore water. It was only possible to view the results qualitatively owing to unforeseen experimental errors related to the high humidity environment in which specimens were kept. The results appeared to support the ionic migration model proposed by Sergi and Page (1992) in which the hydroxyl ion concentration profile is influenced by the free alkali metal ion profile, which is controlled by the electric field strength. The alkalinity of the anode region was equal to or exceeded pH 12.6 in all specimens. The ionic profiles indicated that it was unlikely that chlorine evolution had occurred in any of the specimens in this highly alkaline environment. This was in agreement with the anodic polarisation study in Chapter 4. The anodic overvoltage for each anode appeared to increase in the long term due to a reduction of the pore water ionic species. The mesh anodes proved more able to operate in the very high humidity environment than the lightweight coating anodes. Zinc ion migration was observed for sprayed zinc specimens which was greatly accelerated by the applied CP. Zinc ions accumulated adjacent to the cathode and the results suggested that the measured zinc concentration levels may have been limited by the solubility of bizincate ions in the pore water, and that zinc precipitation in the cathode region was possible.

## **6. Chapter Six. CP trial: The physical performance of lightweight anodes.**

### **6.1. Introduction**

It was noted in Chapter 2 that some anode manufacturers have not readily provided comprehensive information regarding their products which would enable cathodic protection engineers to make a rational assessment of the life expectancy and performance of various systems. This delayed the adoption of novel CP technology outside the USA and several independent laboratory and full scale trials were established to generate the required information and confidence in the new materials, as previously reviewed. It is generally accepted that degradation to an anode system is likely and that some anodes may require periodic maintenance or replacement during service. What have not been established, or perhaps published, are the probable mechanisms of anode failure and the influence of operating procedures or concrete substrate on these. It was clear that the major influence on anode system durability was the magnitude of the applied current density. In addition, the chloride content of the concrete substrate appeared to accelerate anodic degradation for paint coatings and for an anode mesh/overlay combination.

This chapter and the following associated chapters 7 and 8 describe an eighteen month study of the performance of lightweight anodes which were applied to well characterised reinforced concrete slabs and exposed out of doors. The primary aim of the work was to relate any progressive anodic deterioration to the experimental variables, identify anodic products and subsequently to elucidate failure mechanisms. The study generated general operating information for CP systems and allowed a quantitative study of “instant off” potentials. In addition, the influence of CP on the concrete substrate and ionic migration was investigated and appropriate tests for anode appraisal under field and laboratory conditions were identified. The anode performance results were compared with those obtained in the laboratory experiments of Chapters 4 and 5.



## **6.2. Experimental design**

A schedule for the various tests undertaken during the CP trial, arranged by chapter order, is given in Appendix 6.1. The calendar month is given numerically in the table, so that “4” represents April, and so on. Time is generally referred to in terms of days or months from the initial polarisation of specimens.

### **6.2.1. Current density**

It is important to specify how current density is calculated: by reinforcement surface area; by concrete surface area; or by anode surface area. The level of applied current for a structure is fundamentally influenced by the area of steel reinforcement to be protected and by the intensity of the corrosion current to be reversed. Design considerations concerning structural geometry are given elsewhere (Concrete Society TR36, 1989).

CP systems are generally operated at current densities of 10 to 20 mA/m<sup>2</sup> (reinforcement area) (ICI, 1989, McKenzie, 1990). Whilst these values reflect the average current density, the initial current density at specific locations may vary by an order of magnitude either side, depending on the chloride ion concentration and the initial output is sometimes increased by up to 50 % to ensure polarisation (John and Messham, 1989). After a period, the structure becomes polarised and the current demand becomes reduced. This has been related to the migration of chlorides away from the reinforcement (Wyatt and Irvine, 1987).

A maximum anode current density of 108 mA/m<sup>2</sup>, often specified by anode manufacturers, was derived empirically for a slotted anode using graphite filled polymer grout to limit acid degradation to surrounding concrete (Clear, 1984). Both anodes and concrete can be prone to acid induced degradation. It was recommended that conductive paints operate in the range 2-20 mA/m<sup>2</sup>, subject to a maximum short term current density limit of 30 mA/m<sup>2</sup> (Concrete Society TR36, 1989). Similar guide-lines were proposed for sprayed zinc anodes.

Owing to the smaller surface area, the average current density for mesh anodes embedded in an overlay can reach around 100 mA/m<sup>2</sup> (anode s.a.), equivalent to approximately 20 mA/m<sup>2</sup> (concrete s.a), at typical protection levels (Kotowski *et al*, 1989). However, some mesh manufacturers recommend a maximum anodic current density of 400 mA/m<sup>2</sup> in the short term and 200 mA/m<sup>2</sup> in the long term, limited by the performance of the cementitious overlay rather than the anode (ICI, 1989), although test results have yet to be published.

#### **6.2.2. Accelerated testing**

Several studies have adopted high levels of current density over short time periods in an attempt to simulate long term operating data (Apostolos, 1984, Mussinelli *et al*, 1987, Kramer, 1989). The result of an accelerated test is uncertain as the test does not represent real operating conditions. It may be that the system operates in a completely different way at low current densities than at the accelerated high current densities. One must determine if the accelerated test results are valid in predicting long term performance, and if any deleterious physical effects are a function of accumulative current or of short term high current. A study of loss of reinforcement bond due to applied current density indicated that cumulative current density was the critical factor (Vrable, 1977), and an accelerated test in this case may be valid. However, as was demonstrated in Chapter 4, the anodic overvoltage is significantly affected by the current density hence it is likely that greater acid generation would occur at high anode current densities due to preferential oxygen evolution.

For this work, it was decided to use current densities which would allow test results to be related to actual cathodic protection systems. Consequently, 20 mA/m<sup>2</sup> (concrete area) was adopted as a realistic average value and 50 mA/m<sup>2</sup> was adopted as a current density which could reasonably be expected to be occur due to preferential current paths. By applying the same current density by concrete area to all specimens, similar levels of polarisation were anticipated although the current density at the mesh anode surfaces became much higher by default, as seen in table 6.1. Additional current variation was introduced due to unavoidable differences in mesh geometry during the mesh application procedure. It was felt that the high values would provide a test of the higher current density limits proposed by the mesh



manufacturers. Owing to the relatively small cathode area, the application of these current densities resulted in cathode current densities significantly higher than would be normal, and some over-protection of the reinforcement was expected.

#### **6.2.3. Chloride content**

A number of CP laboratory trials have used concrete with an admixed chloride content of 2% (weight cement) to represent concrete with a high risk of corrosion (Pedefferri *et al*, 1989, Humphrey and Lambe, 1989) and the threshold level for corrosion initiation is around 0.4% for admixed chloride. Chloride was therefore added at concentrations of 0.4% and 2% calcium chloride dihydrate by weight of cement, for convenience abbreviated to 0.4 % chloride and 2% chloride. In addition, control specimens containing zero chloride and 4% chloride were produced, one of the latter slabs being energised at a low current density in a speculative determination of the influence of very high chloride on mesh anode performance. The zero chloride slab was conceived as a control for use with the polymer anode and became largely obsolete with the sudden withdrawal of that material.

#### **6.2.4. Specimen geometry**

The overall dimensions of the concrete slabs were limited to 0.5 m by 0.5 m wide by 0.08 m deep to facilitate handling. Similar sized slabs have been used in another CP trial (Humphrey and Lambe, 1989). The reinforcement cover depths of 20, 30 and 40 mm were intended partly to represent variation which may be expected in actual structures and partly to determine if small variations in bar depth induced preferential current distribution. Bar spacing was set at a value which would similarly be expected to induce current concentration effects, with the aim of inducing anodic degradation within the time scale of the study.

#### **6.2.5. Mix design**

The concrete mix was designed by Taywood Engineering and was based on the control mix adopted in a BRITE investigation into the corrosion of reinforcement in concrete (Bamforth and Pocock, 1990), adjusted for a reduced maximum aggregate size, as detailed in table 6.2. The maximum aggregate size of 10 mm was adopted since the minimum cover was

20 mm and the W/C ratio of 0.64 allowed for the increased aggregate specific surface area to give a workable mix. The design strength was 30 N/mm<sup>2</sup>.

#### **6.2.6. Curing**

Trials of CP anodes when applied to corroding structures have had the disadvantage of poor characterisation of the substrate, with the resulting uncertainty of causes and effects of anodic degradation. It was decided therefore to produce concrete substrates of well defined permeability in order to determine any influence of this property on anode behaviour. This was achieved by using two curing methods. The majority of specimens were allowed to dry indoors following demoulding, to represent poor curing. The remainder were covered in hessian, thoroughly wetted down and then covered with polythene sheet for three days, in accordance with BS 8110.

### **6.3. Specimen fabrication**

#### **6.3.1. Concrete slabs production**

##### 6.3.1.1. Formwork

Formwork consisted of a wooden mould which produced six slabs to dimensions as shown in figure 6.1. Oversize 15 mm holes, to accommodate the increased bar cross section due to the end treatment, were drilled into the base to locate the bars accurately with the upper bar ends being fixed by wood spacer blocks. A proprietary mould release agent was used for each concrete batch.

##### 6.3.1.2. Reinforcement preparation

Specimen reinforcement comprised 10 mm diameter mild steel hot rolled bars. Three bars were placed in each specimen slab at 170 mm centres. Electrical connections were achieved by placing mild steel self tapping screws in one end of each bar prior to casting. Bars were obtained in 600 mm lengths, each being straightened manually as required and deformed ends trimmed by up to 8 mm. The bars were degreased in an acetone bath and rust scale removed by the acid pickle process, as outlined in chapter 3.



A standard methodology for masking bars ends was adopted to protect against corrosion and crevice effects, based on a previous duplex system of cement paste overlaid with an epoxy resin (Lambert, 1983), as shown in figure 6.2. This also ensured that each specimen had a standard area of protected reinforcement, or cathode area. Cling film provided protection to the cleaned bar surface during masking. A two part, proprietary polymer modified cement incorporating corrosion inhibitors was used to provide a layer of high alkalinity and impermeability and applied to the manufacturers instructions. After application and curing of the epoxy coating, the protective cling film and selotape were removed and the polymer cement edges made even. The bars were stored in a desiccator before casting.

#### 6.3.1.3. Casting procedure

The casting schedule is given in table 6.3. One batch was sufficient to cast 3 slabs and two 100 mm concrete cubes. The moulds were assembled, any debris blown clear and mould release agent applied. Dry constituents were pre-weighed and stored in sealed PVC sacks. The prepared steel bars were inspected for signs of corrosion and all were found to be defect free. The dry materials were placed in 250 Kg forced action mixer and blended for 1 minute, water added and mixing continued for 2 minutes until an even consistency was achieved. The concrete was placed evenly into the mould and compacted by vibrating table with secondary compaction by a one inch poker vibrator. It was noted that the mix stiffness increased with increased addition of calcium chloride accelerator. The top concrete surface was finished by hand trowel and the moulds covered with polythene and cured overnight. The slabs were then demoulded and cured as required by the casting schedule.

#### **6.3.2. Anode application**

After manufacture the concrete slabs were stored indoors for a period of 4 months to allow corrosion initiation. Anodes E, T and P were then applied in a laboratory and anode Z in an air conditioned room to ensure ideal conditions and a dry concrete surface. The laboratory air temperature and relative humidity were measured during anode application by mercury thermometer and by a whirling hygrometer respectively and were within respective manufacturers recommendations for the application of their materials, as shown in table 6.4.

Trends in reinforcement potentials during cathodic protection have provided evidence of preferential current paths adjacent to primary anodes (Das and Geoghegan, 1984). Current codes of practice specify the electrical insulation of primary anodes from the concrete surface to prevent high local current drain (Concrete Society TR36, 1989). Consequently, conductive coating primary anodes were fixed to the concrete substrate using an insulating bed of epoxy resin. Primary anodes for the meshes did not come into direct contact with the concrete substrate and so were not shielded.

#### 6.3.2.1. Surface preparation

The slabs were grit blasted to remove surface laitance prior to application of anode materials. The reinforcement bar ends were protected during this operation by wrapping them in a heavy duty masking tape and surplus grit blown free by compressed air.

#### 6.3.2.2. Flame sprayed zinc application

Primary anode brass discs of thickness 0.5 mm and diameter 50 mm with a brazed brass stud for electrical connections were manufactured and fixed with epoxy resin on to the grit blasted concrete surfaces. The smooth brass surface was roughened with emery paper prior to the flame spraying operation, which was performed as described in chapter 3.

#### 6.3.2.3. Paint coating application

Titanium primary anode strips of thickness 1.5 mm and length 70 mm with a 4 mm diameter hole to take a brass screw for electrical connections were manufactured and fixed with epoxy resin on to the grit blasted concrete surfaces. The secondary anode carbon fibre strands of length 500 mm were fixed to the concrete surface, passing over the primary anode titanium strip, using the conductive paint to wet and secure the fibres. The paint was then applied by brush, taking care to work it into any blow holes in the concrete surface, to form a wet film thickness of 400  $\mu\text{m}$  and allowed to dry for 24 hours. A second coat was similarly applied. The wet film thickness was checked with a 100-1200 micron wet film comb gauge. One coating of a masonry paint was then applied by brush to a wet film thickness of 170  $\mu\text{m}$ , allowed to dry and then a second coat applied.



#### 6.3.2.4. Titanium mesh fixing

The application methods for the two titanium based meshes were slightly different due to different recommended primary anodes. The anode E mesh required a titanium metal strip of thickness 0.7 mm and length 175 mm, spot welded at each strand junction. A 4 mm diameter hole was drilled in one end of the strip to take a brass screw for electrical connections. The anode T mesh was supplied cut to size with a 2 mm diameter wire pre-attached by crimping. The anode E mesh was cut to suit from a roll, to within 10 mm of the specimen edges. Placing of the mesh close to the substrate was achieved by stretching it slightly and fixing it to the concrete using standard commercial nylon anchors inserted in drilled holes at each corner. Due to the small specimen area and the natural springiness of the mesh, some difficulty was experienced in ensuring that the mesh was installed tightly against the substrate. It was necessary to deform some of the diamonds and to insert further anchors, resulting in slightly non-standard mesh diamond shapes and profiles. Plate 6.1 shows mesh fixed to a slab prior to overlay application.

The number of diamonds was determined for each slab to allow precise current densities at the mesh surface to be calculated. Although the mesh manufacturers provide information of the anode surface area per square metre of mesh, it was required to know the surface area of an individual anode diamond. This calculation is given in Appendix 6.2 for each anode.

#### 6.3.2.5. Overlay application

The recommended methods of application for the cementitious overlay were by airless spray, pouring or pumping and pouring was adopted owing to the small specimen surface area. Wooden batten formwork was built around each slab to provide an overlay thickness of 15 mm. The powder was added to the liquid and mixed in a drum and paddle mixer. The concrete surface was wetted slightly and the overlay poured on to the specimen, smoothed by trowel to a depth of 7 mm to cover the mesh and allowed to harden for 24 hours. A second layer was similarly placed to a thickness of 5 mm and a third layer applied to make up the required thickness.

#### 6.3.2.6. Pitch tar application

The final step in specimen fabrication was to seal the slab sides and underside against the environment. Significant blow holes were filled with an epoxy cement. A two part, epoxy pitch tar material was used for the application and was supplied in red and black to ensure that the first coating was completely covered by the second coating. Mixing was achieved with a paddle stirrer and the material applied by brush. Each coating was allowed to cure for 24 hours.

#### **6.3.3. Specimen arrangement and numbering**

All specimens were placed horizontally on wooden battens, anode face uppermost, adjacent to a south facing wall. Slabs were numbered according to the specimen schedule in table 6.1 and placed in groups of five to facilitate electrical connections. The slabs were wetted every 7 days in addition to any natural precipitation to off-set drying out effects on circuit resistances. However, this was only marginally successful during hot weather owing to rapid evaporation of any surface water and the fact that the anode coatings were initially relatively impermeable.

#### **6.3.4. Potential measurements**

The slab specimens differed from actual cathodic protection systems in that embedded half cells were not required for current control purposes. It was uneconomical to embed miniaturised half cells in each slab for system polarisation measurements, therefore it was decided to leave a strip uncovered beneath each reinforcement bar to allow potential measurements, which are described in chapter 7.

#### **6.3.5. Power supply and electrical connections**

A constant current power supply was designed by Taywood Engineering for the study and is shown schematically in figure 6.4. Initially the main power supply was 110 volts but it was necessary to change to 240 volts due to unavoidable intermittent disruptions to the 110 volt supply. The slabs specimens were connected in 5 groups of 10 core cables which were routed to the control unit. This was situated in an environmental cabinet which was bolted to a laboratory wall. The applied current was set directly on the panel for each individual specimen and the value checked by connecting a digital volt meter to the appropriate



terminals. The applied voltage was measured in a similar way. The three reinforcement bars were connected together externally with solid 2 mm copper wire and connected via standard electrical connectors to the negative supply cable as shown in figure 6.5. The primary anode was similarly connected to the positive supply cable and the connections protected with silicone grease. The slabs were polarised on 19.4.89. The reinforcement bars of the control slabs were isolated electrically.

#### **6.4. Pre-polarisation tests**

The following tests were performed before polarising the specimens in order to characterise them fully.

##### **6.4.1. Linear polarisation**

Linear polarisation measurements were carried out on selected CP slab specimens to determine the rates of rebar corrosion before polarisation, as described in chapter 3. Steel reinforcement corrosion potentials were also recorded using the Taywood potential wheel. The results in figures 6.6 to 6.9 indicate that the rate of current decay became relatively constant after 30 seconds, indicating that the time constant of 30 seconds proposed in chapter 3 (Andrade *et al*, 1986) was reasonable. It can be seen from table 6.5 that none of the specimens exhibited significant corrosion rates prior to polarisation. Examination of the  $E_{corr}$  values also indicate that the probability of corrosion in each sample was low to medium with regard to published corrosion risks (ASTM, 1978).

The low initial corrosion rates for samples with added chloride suggest that corrosion initiation was slow due to chloride binding by the cement on hydration, an effect observed by other workers (Jafar *et al*, 1990). A second factor may be the bar preparation method: The inclusion of the inhibitor hexamine in the acid pickling process clearly resulted in standardised, rust free bars and may have minimised chloride induced pitting.

#### **6.4.2. Casting data**

The 28 day compressive strength results exceeded 30 N/mm<sup>2</sup>, as shown in table 6.3, indicating that batching and casting was performed satisfactorily, The concrete densities approximate to the design value of 2326 Kg/m<sup>3</sup>.

Two 50 mm dry cores were obtained from each control slab on 17/4/89 to characterise each anode/concrete substrate interface before the passage of CP current. The resulting holes were filled with a readily available high strength concrete, containing pulverised fuel ash and air-entrainment admixture. The cores were stored indoors in dark, dry conditions to allow comparison with anode/concrete condition at the end of the trial.

#### **6.4.3. Permeability**

Water permeability data relating to the 'as cast' surface of the concrete slab specimens was obtained for each mix. Extra specimens without steel reinforcement were cast and two 100 mm cores were taken through these slabs from central locations representing the bulk concrete, 125 mm from the top and bottom edges. The cores obtained were wet cut by diamond blade to provide samples of approximately 40 mm thickness, suitable for use in the water permeability test cell. The test procedure was followed as outlined in chapter 3.

The results in figure 6.10 show that the permeability coefficient, K, was higher when determined by time to penetration than by flow, in agreement with other work (TEL, 1988), and that the two methods gave similar trends. It can be seen that the combination of varied chloride additions and curing produced a wide range of concrete qualities, the values for K obtained from the time to penetration data falling within the range 10<sup>-9</sup> to 10<sup>-12</sup> m/s, which was in general agreement with K values obtained for normal concretes with water-cement ratios in the range 0.45 to 0.75 (TEL, 1988).

The K values in table 6.3 were the averages of two cores, as determined by the time to penetration, and have been arranged in order of increasing permeability. The general trend was for the K value to decrease as the percentage of chloride increased. The air cured



concrete with 4% chloride appeared to be of very low quality, as may be expected for such a high quantity of accelerator which would induce very rapid cement hydration. The lower 2% chloride addition appeared to have minimised the concrete permeability. The influence of moist curing was apparent in all specimens, the K values being between 3 to 107 times higher in the air cured specimens. This was in agreement with previous results, when moist curing was shown to decrease the permeability coefficient by up to three orders of magnitude from that of dry curing (TEL, 1988).

#### **6.4.4. Resistivity**

Resistivity measurements were obtained for all specimens prior to application of anodes, as described in chapter 3. The air temperature was 14°C and the relative humidity was 48% at the time of measurements, which were carried out indoors. Average values were determined for each concrete condition, as shown in table 6.3. It can be seen that the apparent resistivity values fell within the range 5 to 12 kΩcm, indicative of a high risk of corrosion (Figg and Marsden, 1985). The apparent resistivity decreased with increasing chloride content. Factors which decrease permeability are expected to increase resistivity. However, specimens with improved curing appeared to contradict this, with lower resistivities at particular levels of chloride.

### **6.5. Experimental procedures for the determination of anode durability**

#### **6.5.1. Conductive coatings**

##### 6.5.1.1. Adhesive strength/ visual inspection

The pull-off test, described in Chapter 3, was used to assess durability of the conductive coatings. The test determines the plane of greatest weakness in the coating system and the failure mechanism may be complex. It is necessary therefore to consider the nature of the failure surfaces and the way failure occurred to interpret the absolute values of failure load.

Pull-off's previously carried out on paint coatings by Taywood Engineering were analysed by assessing the percentages of four failure modes present on each dolly, i.e. resin/coating,

inter-coating, coating/substrate and substrate (Palmer and Bradley, 1989), and this method was initially adopted. As the study progressed, the classification of failure modes was modified since it became apparent that the morphology of the pull-off interface reflected the level of anodic degradation. In addition, it was felt that the estimation of area percentages was too subjective. A classification system was devised for the zinc coating when a progressive degradation mechanism became apparent. Failures of both coatings tended to occur either gradually or explosively, and this was recorded together with the colour of the substrate and the presence of corrosion products. The location of pull-off sites is shown in figure 6.11. Duplicate tests were undertaken for each specimen.

Regular visual inspection of the coatings indicated whether localised degradation was occurring. Down-coat voltages were obtained for the conductive paint, as described in Chapter 3.

#### **6.5.2. Mesh anodes/cementitious overlay**

##### **6.5.2.1. Ultra-sonic pulse velocity**

Debonding of cementitious overlays is usually assessed by sounding for hollow areas with light blows of a hammer and such debonding is perhaps the last stage of a degradation process. The use of other non-destructive tests (NDT) for the assessment of mesh anode/overlay performance has not been reported. A possible NDT method to detect cracking and overlay debonding was ultra-sonic pulse velocity measurements (USPV), whereby the time for high frequency sound pulses to pass through the concrete from one surface location to another gives a measure of the concrete density. A plot of the time required for a signal to pass between two transducers when moved apart by successive incremental distances can indicate the presence of discontinuities (sound pulses travel through air more slowly than through solid material). A series of measurements was therefore undertaken on mesh specimens after 14 months polarisation using the proprietary "Pundit" apparatus, with the aim of establishing its suitability for the detection of anodic degradation. Both flat and exponential transducer heads were used at an increasing radial separation, using a conductive gel to promote good contact with the overlay, as indicated in



plate 6.2. The results will not be reported in detail since they were inconclusive. The overlay surface was too rough for the accurate use of flat heads, with much data scatter. Exponential heads produced less scatter, as shown in figure 6.12, but did not indicate significant differences within or between specimens, perhaps because no debonding occurred. The technique did not appear sensitive enough to indicate differences due to paste loss around anode strands.

#### 6.5.2.2. Wet coring/ visual inspection

Surface coring through anode materials was shown to be a useful method for the observation of long term anodic performance, although it was noted that only advanced deterioration was detected by this method (Schell and Manning, 1985). Destructive coring was considered to be the only appropriate technique for inspection of progressive deterioration in the anode region. The smallest practical core diameter of 25 mm allowed sampling of material whilst minimising damage to the small specimen area. Cores were obtained along lines parallel to the reinforcement bars, as shown in figure 6.11. An appraisal of a core surface gave an immediate idea of deterioration of the anode region, if an anode strand was present. Several cores were sometimes required to locate an anode strand. Examination by binocular microscopy gave more detailed information, and a thin section made from the core allowed analysis by petrography, as reported in Chapter 8. Core holes were not patched and visual observations were made periodically of the deterioration within the core holes.

#### 6.5.2.3. Adhesive strength

A number of specimens were subjected to adhesive strength testing of the overlay at the end of the test period, using the Limpit method described in Chapter 3.

### **6.6. Results**

The physical performance results for anodes *E* and *T* will be considered together whilst anode *P* and *Z* are considered separately, since the anodic degradation mechanisms for each were significantly different. The analysis of degradation products which were observed are reported within each of the following sub-sections.

### **6.6.1. Anode P**

#### **6.6.1.1. Visual inspection**

The monthly visual inspections, as summarised in figures 6.13 to 6.18 and in tables 6.6 and 6.7, indicated that degradation processes were progressive. Four general forms of degradation were observed:

- i. Micro-bubble clusters formed within the conductive paint (plate 6.3).
- ii. Macro-bubbles formed within the conductive paint which tended to grow with time.
- iii. The weathered top-coat surface became bleached white.
- iv. The surface blackened and blistered with surface cracks.

Surface rust spotting of the specimen surfaces was observed for all specimens to varying degrees. Control specimens displayed minimal signs of degradation during the study. Degradation was low in specimens held at 20 mA/m<sup>2</sup>, other than specimen P:2:20:1, where the primary anode became disbonded from the epoxy adhesive after 6 months, yet remained in contact with the secondary anode. This was eventually repaired and performed satisfactorily. Specimens held at 50 mA/m<sup>2</sup> suffered high local degradation, particularly at the primary and secondary anodes but also at edges and in central locations. Of interest, high degradation for the P:2:50 specimens occurred at approximately the same location, centrally between bars A and B. Plate 6.4 shows highly localised blistering adjacent to a repaired primary region, whilst plates 6.5 and 6.6 indicate the progressive nature of the coating deterioration. It is clear that the surface bleaching effect, probably due to hypochlorite formation, provided an early indication of high coating degradation. From visual inspections, specimens with a high substrate chloride content appeared to exhibit greater deterioration at locations removed from the primary and secondary anodes, at each current density.

On removing specimens P:2:0:1, P:2:20:1 and P:2:50:1 for analysis after 18 months and during the repair of other primary anodes, it was noted that the epoxy adhesive bed beneath the primary anode had softened. The secondary anodes were also examined: The fine



carbon fibres had been only partially coated by the paint, which had been consumed to varying degrees, and the fibres appeared to be unaffected by polarisation.

#### 6.6.1.2. Pull-offs

##### **6.6.1.2.1. Visual inspection of fracture surfaces**

The Taywood classification system and the modified classification system are outlined in table 6.8 for comparison purposes. After examination of a considerable number of pull-off surfaces, only three types of paint morphology were readily identifiable, as indicated in the table. Type 4 failure, where the paint appears relatively smooth and graphite like, was assumed to be the worst case and is illustrated in plate 6.7. Type 4 failures were more prevalent in high CD specimens, yet were observed somewhat randomly. In type 3 failures, the coating fracture surface appeared dull and rough with small adhering paste particles, as illustrated in plate 6.8. This represented the general condition for polarised specimens throughout the study: Table 6.8 demonstrates that within a short period of CP operation, there was little difference between the nature of the pull-off surfaces of polarised specimens. Type 2 failure, as shown in plate 6.9, was always observed for the control specimens and was therefore considered to be indicative of no change. Where the coating failed within itself, it appeared shiny, metallic and crystalline, whilst appearing smooth and matt black at large aggregate interfaces. Large, thin paste pieces which adhered to pull-off surfaces were usually associated with large aggregates close to the substrate surface. The results did not confirm the findings of Palmer (1988), who observed that inter-coat (IC) failures decrease with time whilst topcoat/conductive coat failures increase with time, indeed the latter type of failure was not observed for any specimen in this study.

The surface layer of the substrate of both polarised and un-polarised slabs attained an orange colour, first observed at 3 months (plate 6.10). The substrate surface often appeared orange at pull-off locations where part or all of the failure plane was located precisely at the coating/substrate interface, as indicated in table 6.8. This type of failure was more prevalent in specimens polarised for longer periods. The orange staining appeared to be induced by the application of the conductive paint rather than by anodic reactions and extended to

approximately 200 to 300 microns depth. A second phenomenon, observed infrequently on only a few pull-off fracture surfaces, was white crystalline deposits, as shown in plate 6.11. Although it was not possible to isolate the crystals in order to perform an SEM/EDAX analysis, the most probable composition was considered to be calcium carbonate.

#### **6.6.1.2.2. Adhesive strength**

The adhesive failure loads are presented in figures 6.19 and 6.20 and in table 6.9. The figures indicate that the adhesive strength increased over the first 6 months for all specimens. Un-polarised specimens attained adhesive strengths in excess of 12 Kg/cm<sup>2</sup>. Adhesive strengths for specimens held at 20 mA/m<sup>2</sup> tended to remain above 5 Kg/cm<sup>2</sup>, the apparent minimum design strength (Palmer, 1988), although the results show much scatter. Specimens held at 50 mA/m<sup>2</sup> appeared to display decreasing strengths after around 7 months polarisation. The average adhesive strengths shown in table 6.9 indicate little variation between polarised specimens. This may be a reflection of the localised nature of the coating degradation processes. The findings were in close agreement with previous results for the coating, where the mean strength of polarised coatings was 6.5 Kg/cm<sup>2</sup> and that of unpolarised coatings was 10.8 Kg/cm<sup>2</sup>, whilst coating bond strength increased for around 6 months followed by a decrease under polarisation to around 5 Kg/cm<sup>2</sup> (Palmer and Bradley, 1989).

Table 6.10 summarises the failure modes as an explosive “pop” or progressive lift off. Lift-off failures were observed in all polarised specimens, but not un-polarised specimens, and were associated with adhesive strengths of 4 Kg/cm<sup>2</sup> or less, and with failure within the coating, or at the coating/substrate interface.

#### **6.6.1.3. Examinations of degraded coating sites**

##### **6.6.1.3.1. Bubble site**

A blister/bubble of diameter 2 cm on specimen P:2:50:1 was examined after 9 months of polarisation. An incision was made by scalpel into the bubble and a piece of pH paper,



soaked in de-ionised water, immediately placed between the coating and substrate. The indicated acidity within was pH 4, suggesting the presence of carbonic acid. The coating around the edge of the blister was sound, not brittle and adhered well to the substrate. Cutting away the top of the blister revealed that the coating had been consumed and the paste underneath was soft with some dissolving of the paste around aggregate particles (plate 6.12). Clearly an acidic environment had developed within the blister. Small white deposits of unknown composition were visible both in the substrate and underside of the blister, similar to those shown in plate 6.11.

It was observed that blister areas were difficult to determine visually but were easily pin pointed by lightly moving a finger, or a soft plastic tool handle, over the surface and listening for a "hollow" sound.

#### **6.6.1.3.2. Debonded area**

A sample of paint coating was taken from the edge of specimen P:2:50:1 after 9 months, where it had completely disbonded. The coating had become brittle, but not blistered, and the substrate paste at this location was brown and soft, as indicated in plate 6.6. DTA analysis of a surface paste sample from this region indicated that its main constituents were calcium carbonate and quartz with minimal CSH gel and no calcium hydroxide present (Appendix 6.3). Cement paste adhering to the removed coating appeared beige in colour and fissured (plate 6.13), indicating loss of CSH gel and the larger sand particles were bare of paste. Results of a SEM/EDXA analysis of the fissured paste area and adjacent coating, shown in plate 6.14, are presented in figures 6.21, 6.22 and table 6.11. It should be noted that carbon quantities could not be determined by EDXA and the chlorinated binder masked possible increases of chlorine or reaction products due to chlorine at the paint surfaces. Figure 6.21 indicates a complete absence of any calcium hydroxide or CSH gel in the fissured paste, which comprised similar proportions of chlorine and silicon. The adjacent coating surface appeared flakey and porous, as shown in plate 6.15, the elemental analysis similarly indicating chlorine for the paint and a smaller proportion of silicon for the adhering aggregate particles.

#### 6.6.1.4. Analysis of rust spot and white top coat

The elemental composition of a rust spot was confirmed by SEM/EDXA analysis to mainly comprise of iron, as shown in figure 6.23 and table 6.11. A similar analysis of the masonry paint top coat indicated a high proportion of titanium, with a degree of iron contamination from the adjacent rust spot and silicon from aggregate particles, an unremarkable composition for a masonry paint (figure 6.24).

#### 6.6.1.5. FTIR analyses of paint coating

##### **6.6.1.5.1. Experimental**

A short investigation was undertaken to determine changes to the chlorinated rubber binder due to acidification by the FTIR analytical techniques, as described in Chapter 3. Spectroscopic analysis of samples using the transmission and reflectance modes was unsuccessful owing to the very high carbon loading in the paint. A typical, relatively blank, spectra result is given in figure 6.25. The peaks on the left hand side represent moisture and the small peak in the centre represents carbon dioxide.

An alternative photo-acoustic analysis of the paint, dissolved in xylene, indicated the presence of polyethylene. This was assumed to be a contaminant from the preparation procedure. Consequently, specimens were prepared using a revised methodology, described in chapter 3, and analysed using the horizontal ATR method. Material from a coated microscope slide of area  $8\text{ cm}^2$  was used as a control against material lifted from a  $6\text{ cm}^2$  area blister site of specimen P:2:50:1, which included the masonry paint top-coat. A further three samples were obtained by scalpel from pull-off dollies: P:0.4:0:1 (3 months), P:0.4:20:1 (12 months) and P:0.4:50:1 (3 months).

##### **6.6.1.5.2. Results**

The results are given in figures 6.26 and 6.27. The spectra were matched on the computer display using the integral computer reference library. The control sample matched that of polyvinyl-chloride:ethylene (Hummel Polymers Library), as shown in figure 6.26, whilst the blister sample spectra in figure 6.27 matched that of polyvinyl-acetate:ethylene. The latter result was attributed to the presence of the masonry paint, hence a second sample from



the blister site was obtained without the overcoat and analysed. The resulting spectra is plotted, to the same scale, against the spectra for the control sample in figure 6.28. The spectra appear identical apart from a larger peak at wave number  $1715\text{ cm}^{-1}$  for the blistered area. Peaks in the region  $1700\text{ to }1720\text{ cm}^{-1}$  of the spectra are caused by carbon-oxygen bonds (Williams and Fleming, 1987), so it appears that the blistered paint binder was oxidised by the acidic anodic reaction products. This is in agreement with unpublished work, which found that degradation to the binder during CP at  $100\text{ mA/m}^2$  was similar to degradation caused by placing the conductive paint in 83% sulphuric acid, a powerful oxidising agent (Bingham, 1991).

The results in figures 6.29 to 6.31 for pull-off dollies indicate that oxidation of the paint occurred in the polarised specimens. The larger oxidation peak in figure 6.30 for P:0.4:20:1 from that in figure 6.31 for P:0.4:50:1 indicates that oxidation took place at the lower applied current level and was progressive. The spectra for specimen P:0.4:0:1 in figure 6.29 also displayed a large peak close to the carbon-oxygen bond region. However, it appears sharper than the broad peaks of the polarised specimens and this, together with a large peak in the region of wave number  $1350\text{ cm}^{-1}$ , suggests that this specimen was contaminated by polyvinyl-acetate:ethylene from the masonry paint top-coat.

#### **6.6.1.5.3. Summary: FT-IR spectroscopy**

The work in this section has identified a suitable methodology for analysis of the conductive paint coating, using relatively small samples from the surface of pull-off dollies and horizontal ATR spectroscopy. The main constituent of the paint binder was identified as polyvinyl-chloride:ethylene and that of the masonry top-coat was deduced as polyvinyl-acetate:ethylene. The binder was shown to undergo oxidation both at sites of high degradation and within areas of apparently low degradation, as indicated by broad spectra peaks in the region  $1700\text{ to }1720\text{ cm}^{-1}$ . Further work is required to quantify the effects of time and applied current density on the oxidation processes.

#### 6.6.1.6. Down coating voltage drop measurements

##### **6.6.1.6.1. Introduction**

Voltage drops between the primary anode and specific spot locations, as shown in figure 6.32, were measured at regular time intervals, as described in chapter 3. The results, converted into resistance values, are presented in tables 6.12 to 6.18. The primary anode location varied slightly and the distance between spots and the primary is indicated in the tables. In some cases, values between adjacent locations varied greatly due to the development of localised 'hot spots', and these are highlighted in italics in the tables. The paint was observed to become exceedingly brittle at the hot spot locations and where this affected the measurements, the probe was moved to the nearest area of intact coating. Measurements were also made of specimens which had remained polarised after the final destructive testing programme, at 22 months.

##### **6.6.1.6.2. Results**

To gain an impression of the general increases in coating resistance, an average was determined from all data points, excluding hot spots and locations  $\alpha$  and  $\beta$ , as shown in table 6.18 and plotted to a log scale against time in figure 6.33. An inspection of values over the first 9 months suggests that the coating resistance gradually increased with time for all specimens. The increases were low for 20 mA/m<sup>2</sup> specimens and only one hot spot was observed, at location B3 for specimen P:0.4:20:1. Resistances of 50 mA/m<sup>2</sup> specimens were comparable with 20 mA/m<sup>2</sup> specimens over the first 3 months at around 3 ohms. The resistance at locations  $\alpha$  and  $\beta$  increased significantly for specimens P:2:50:2 and P:0.4:50:1 after 4 and 5 months respectively, as shown in tables 6.16 and 6.17, and this greatly influenced the coating resistance at more distant locations. Hot spots were also more prevalent in these two specimens. When the primary anodes of specimens P:0.4:50:1 and P:2:20:1 were repaired at 10 months, their average coating resistances fell to levels similar to specimens P:2:50:1 and P:0.4:20:2 respectively. This highlighted the significant influence of primary anode degradation on current distribution, even at low current densities. The average resistances appeared to decrease during the period 10 to 16 months for all specimens and then to increase once more. The decrease corresponded to the



summer months, suggesting that the resistance of the coating varied with ambient temperature. In the long term, the average resistance of specimens polarised at 50 mA/m<sup>2</sup> exceeded that of specimens polarised at 20 mA/m<sup>2</sup>.

It was observed that the conductance path along the secondary carbon fibre anode was not greater than at an adjacent coating location. This would be expected if the secondary fibres and surrounding paint were considered to be resistors in series. The carbon fibre maintained its integrity and continued to distribute current when the surrounding coating had failed.

#### **6.6.1.6.3. Discussion of down coating voltage drop results**

The results demonstrated that the sudden increase in resistance associated with hot spots could not be predicted from previous data at a specific locations, supporting previous observations from a full scale trial (Palmer, 1988). However, large increases in the average resistance indicated degradation in the primary anode region and confirmed that the coating/primary anode interface area was particularly sensitive to a high current density. The composition of the substrate did not appear to influence the variation of coating resistance. Environment did appear to influence the coating resistivity, although longer term measurements would be required to confirm this.

Voltage drop measurements allowed overall changes in coating resistance to be determined, as indicated by the results for specimen P:2:50:1 which suffered less anode degradation than the other 50 mA/m<sup>2</sup> specimens and by results for 20 mA/m<sup>2</sup> specimens. It was evident that for 50 mA/m<sup>2</sup> specimens, the resistivity increased with time. It was less clear if the 20 mA/m<sup>2</sup> specimens developed higher resistivities with time, or if variations were due to environmental factors.

Voltage drops measured in a full scale CP trial can be similarly converted to resistances for comparison purposes. Current densities in the range 2.5 mA/m<sup>2</sup> to 10 mA/m<sup>2</sup> were applied to columns of area 40 m<sup>2</sup> in the Woolaston water tower CP trial. Down coat resistances

were in the range 0.25 ohms to around 2.75 ohms over distances of up to 1.5 m from the titanium primary distributor. Coating resistance at hot spots ranged up to 20 ohms, limited by the applied voltage of 5 volts, and these were associated with areas of great paint bubbling and low adhesive strength (Palmer, 1988, Palmer and Bradley, 1989). These values were generally lower than observed in the present study, presumably due to the lower applied current density. Where the coating had failed significantly, the down coating drop could not exceed the maximum available driving voltage, which may account for the lower hot spot resistance values at Woolaston.

#### 6.6.1.7. Discussion: Anode P

Visual observations of anode P surfaces indicated the progressive nature of coating degradation. The results were in agreement with other studies which had observed increased coating degradation with increasing current density and on substrates of higher chloride content (Burns, 1988). Bleaching of the weathered masonry paint top-coat appeared to provide an early warning of acidic degradation and would be associated with hypochlorite formation as the interfacial pH decreased. Sites of degradation generally developed at random locations, with the exception of those adjacent to the primary anode, owing to inadequate design of this connection. Down coating voltage measurements were shown to be sensitive to degradation induced high resistance in the primary anode region and were unable to predict the development of “hot spots”. The measurements, converted into resistance values, indicated lower deterioration of specimens held at 20 mA/m<sup>2</sup> than 50 mA/m<sup>2</sup>. However, pull-off test adhesive strengths and inspection of dolly failure surfaces did not indicate significant differences between specimens held at the two current densities, probably as a result of the test locations. Indeed, the overall deterioration of specimens held at 50 mA/m<sup>2</sup> was remarkably low.

The paint binder was shown to undergo oxidation at normal current densities, possibly accounting for the generally dull appearance of pull-off failure surfaces. Localised acidification resulted in the chemical breakdown of the paint, which became brittle and appeared to release carbon particles, accounting for the blackening of anode surfaces.



Hypochlorite ions are strong oxidising agents and would be expected to increase the rate of coating binder oxidation. This may explain the increased degradation observed for high chloride specimens, since hypochlorite formation would be related to the free chloride ion concentration at the anode surface. However, further work is required to establish whether the degree of binder oxidation can be quantitatively related to the charge passed.

Alkaline phases of the substrate HCP were neutralised and dissolved by the acidic anode products. The subject of neutralisation will be discussed in the following anode E and T section. The distribution of admixed chlorides was expected to be even throughout the specimens and variation of moisture and environment would have been minimal over the small specimen area. The favoured conditions for hot spot formation, as indicated in previous studies (Palmer, 1989), were therefore absent. The most severe degradation, excluding at primary anodes, occurred between bars A and B of specimens P:2:50: and P:2:50:2. A tentative explanation may be that the supply of hydroxyl ions from the cathode to the coating in these areas was lower than to the areas above the reinforcement bars, hence a higher rate of paste consumption. The increased coating resistance at a degraded site would inhibit the flow of current, leading to higher effective current densities elsewhere and further degradation.

#### **6.6.2. Anode Z**

##### **6.6.2.1. Visual inspection**

Visual observations are summarised in figures 6.34 to 6.39 and tables 6.19 to 6.20. Two main features were noted during the trial; One was debonding of the zinc to varying degrees and the other was the formation of dark grey crystalline surface deposits around 6 months after polarisation (Plate 6.16). Owing to their appearance and progressive growth on the zinc surface, these deposits were termed "Warts". It can be seen from tables 6.19 and 6.20 that warts only developed on slabs with 2 % chloride and wart growth was greater on the higher current density slabs. Plate 6.17 and figures 6.34, 6.37 and 6.38 show that wart growth concentrated at slab edges and between reinforcement bars and was greatest (warts

of up to 2 mm diameter) adjacent to the primary anode. By contrast, plate 6.18 indicates the low surface corrosion of 0.4 % chloride specimens.

Debonding occurred on all polarised specimens and was characterised by the formation of a white corrosion layer between the zinc and substrate which ruptured, allowing the zinc to lift away. The zinc coating became permanently deformed with a gap of up to 10 mm between it and the substrate. Debonding appeared to be lower in 2 % chloride specimens. As for paint bubbling, debonded areas were best detected aurally. Isolated areas tended to join up with time and the zinc had totally disbonded, other than at the edges, on specimens held at 50 mA/m<sup>2</sup> after 18 months. Specimen Z:0.4:20:2 also suffered extensive debonding, including the primary anode from the substrate. This specimen was polarised later than the other specimens because the primary anode had been mechanically damaged and required re-fixing and re-spraying with zinc. This may have affected the strength of the zinc/substrate bond around the anode. On examination of specimen Z:2:50:1 after 18 months, the primary anode disc was still adhering strongly to the substrate, although the adjacent zinc coating had disbonded, as indicated in plate 6.19. Control specimens were not observed to debond or to form surface warts.

#### 6.6.2.2. Pull-offs

##### **6.6.2.2.1. Visual inspection of fracture surfaces**

The white rust layer had a significant effect on the pull-off failure mechanism and load. Inspection of pull-off dollies suggested a degradation sequence, which is summarised in table 6.21. Initially, failures were of type 2, where the zinc failure surface appeared shiny and substrate particles were deeply embedded, as shown in plate 6.20. After a short period, influenced by the applied current density, the zinc formed a darker grey oxide/hydroxide layer (type 3), followed by more voluminous white rust at small isolated sites (type 4). The latter two types are illustrated in plate 6.21, where the upper dolly was a type 3 failure and the lower dolly, located above a reinforcement bar, a type 4 failure. The density of zinc corrosion product was generally higher above a bar than adjacent to it. Failure of 50 mA/m<sup>2</sup> specimens progressed rapidly over 2 months of polarisation to type 5 failures, characterised



by a high density corrosion interfacial layer, as shown in plate 6.22. Pull-off tests were terminated for these specimens after 11 months when type 6 failure occurred, since further testing merely measured the strength of the zinc metal film. Failure of 20 mA/m<sup>2</sup> specimens varied from type 2 to type 5, specimen Z:2:20:1 exhibiting the higher proportion of type 5. The control specimens progressed from type 2 to type 3 failure after 6 months (9 months from anode application) and both had exhibited type 4 after 14 months.

#### 6.6.2.2.2. Adhesive strength

Adhesive strengths are plotted in figures 6.40 and 6.41 and given in table 6.22. The bond strength of un-polarised control specimens increased from relatively low values to values exceeding 10 Kg/cm<sup>2</sup>, with average values over the trial period of 9.9 Kg/cm<sup>2</sup> and 11.9 Kg/cm<sup>2</sup> respectively. Failures were explosive pop-off types in each case, as indicated in table 6.23. The development of corrosion products at the zinc/substrate interface appeared to improved the adhesive strength. These values were generally lower than adhesive strengths previously reported for sprayed zinc coatings of around 14 to 20 Kg/cm<sup>2</sup> (Apostolos, 1984) but comparable to others of 7.5 to 22 Kg/cm<sup>2</sup> (Palmer, 1987).

Specimens polarised at 50 mA/m<sup>2</sup> exhibited adequate initial adhesive strengths of 4 to 5 Kg/cm<sup>2</sup> but these decreased with time to around 2 Kg/cm<sup>2</sup>, practically the lower accuracy limit of the instrument. Specimen P:0.4:20:2 displayed similarly low adhesive strengths. The results for this specimen generally were questionable due to the pre-mentioned primary anode repair. In addition, electrical data for this specimen, to be described in Chapter 7, suggested that it was damaged by a short period of excessive current. The other 20 mA/m<sup>2</sup> specimens exhibited higher bond strengths, with similar average values of 7.2 and 7.3 Kg/cm<sup>2</sup> and a higher proportion of pop-off failures. However, specimen Z:2:20:1 displayed a steady increase in bond strength whilst values for specimen Z:0.4:20:1 were highly influenced by the dolly location and displayed great variability, with low values at months 7 and 12 corresponding to a debonded area and a greater proportion of lift-off failures.

### 6.6.2.3. Analysis of corrosion products

#### **6.6.2.3.1. Alkalinity of zinc/substrate interface**

Some locations where the zinc had disbonded were tested for pH at 9 months by slitting the debonded coating by scalpel and sliding in a piece of universal indicator paper, moistened with de-ionised water. Values indicated were around pH=8 to pH=10, which was consistent with the presence of zinc hydroxide complexes.

#### **6.6.2.3.2. White rust**

The micro-crystalline morphology of the white corrosion product is shown in plate 6.23. Examination by SEM indicated particle sizes in the range 2  $\mu\text{m}$  to 500  $\mu\text{m}$  and indicated a varied surface morphology of complex crystal structures (plate 6.24). EDXA analysis of several crystals indicated zinc as the main constituent, as shown in figure 6.42 and table 6.24.

The white zinc corrosion product was analysed by XRD as described in Chapter 3. The XRD trace peaks were of low intensity due to the samples micro-crystalline morphology, making interpretation difficult. The trace exhibited a number of very sharp peaks at reflection angles which, when converted into d spacings, did not appear to correspond to any crystalline compound and hence may represent experimental errors. These d spacing values were ignored. Using the search technique described in Chapter 3, the remaining d values and peak intensities were found to fit the pattern for  $\text{ZnO}/(\text{ZnO})_4\text{H}$  (Zincite/Zincate: Powder Diffraction File reference 5-664), as shown in table 6.25. It is clear that all of the peaks identified in the analysis relate to the standard compound, although the relative intensity values do not agree in all cases. This was due to the low resolution of the trace and the fact that the standard pattern was determined from a synthetically formed compound.

Hence XRD analysis confirmed that the zinc corrosion product was a micro-crystalline, complex form of oxidised zinc hydroxide, or white rust.



#### 6.6.2.3.3. Warts

A visual examination of pull-off dollies indicated that the warts extended through the zinc coating and they were easily broken off at the surface. The larger warts were collected in this way for later analysis. The wart surface appeared dark grey and had a porous, rough structure as shown in plate 6.25. By contrast, the inner surface was a lighter grey and displayed a more crystalline structure, as indicated in plates 6.26 and 6.27. The needle like crystals in plate 6.26 bore some resemblance to those of the white rust, in plate 6.25. However, EDXA analysis of these and similar surfaces indicated a significant proportion of chlorine (figure 6.43), which was not present in the white rust samples (figure 6.42). This suggested that the warts comprised a mixture of zinc hydroxide complexes and zinc/chlorine complexes. EDXA analysis of the outer wart surface indicated a lower proportion of chlorine (figure 6.44).

The grey warts were analysed using the XRD procedure. A strong trace was produced with many large, sharp peaks. An excellent fit was obtained with the standard data for Zinc Chloride Hydroxide Hydrate ( $\text{ZnCl}_2 \cdot 4\text{Zn}(\text{OH})_2$ ), also named Zinc Hydroxide Chloride ( $\text{Zn}_5(\text{OH})_8\text{Cl}_2$ ) and Simonkolleite ( $\text{Zn}_5(\text{OH})_8\text{Cl}_2 \cdot \text{H}_2\text{O}$ ), a mineral, in the Powder Diffraction File reference 7-155, as shown in table 6.26. However, several peaks, or intensities of peaks, did not fit and these are indicated as Unknowns in the table. Examination of the standard file for elemental Zinc (Powder Diffraction File reference 4-831) appeared to account for these discrepancies, as demonstrated in the table. It is likely that the contaminant was pure zinc which was included during sample collection. One small peak of intensity 7 out of 100 and  $dA^\circ$  of 2.342 did not appear to fit either sets of standard data. This peak occurred on the down slope of the preceding peak and may be due to another contaminant of low concentration.

#### 6.6.2.3.4. Examination of section through zinc films

The structure of the zinc coating which had lifted away from the central area of specimen Z:2:50:1 (18 months) was examined by SEM. Samples were also obtained for comparison purposes from a 50 mm dry core of specimen Z:2:0:1 (0 months), a piece of zinc which had

spontaneously debonded from a paste block due to excessive heat during spraying, and a thin zinc film from a microscope slide prepared for polarisation studies in Chapter 4. A cross section of each was made by breaking the film away from a sharp blade held on the film surface, to give a rough fracture. Each new fracture surface was mounted in grooves cut into an aluminium stub to facilitate the SEM examination.

Each specimen exhibited brittle fracture and a typical fracture surface is shown in plate 6.28 for the paste block sample. A lateral crack can be seen which indicates a plane of weakness, possibly induced by the faulty spraying process. A detail of the crack is shown in plate 6.29. No corrosion products are visible on the surface. The upper region is connected to the lower region by a fold of zinc, indicating that the crack opened during sample preparation. The microscope slide coating appeared to be of low porosity and displayed a layered structure, as shown in plate 6.30. An EDXA analysis of the central area in the micrograph indicated a very high purity of zinc at 97% of the total spectrum.

Plate 6.31 gives an overview of the fracture surface of specimen Z:2:50:1. The lower region is the outer surface side of the zinc and the upper region is the more crystalline white interfacial corrosion product. The boundary between the two phases is distinct and highly fissured, as shown in detail in plate 6.32. EDXA analysis of the smooth lower zinc region in this micrograph confirmed its composition as 97% zinc. The white rust particles displayed high porosity and an EDXA analysis indicated a small chlorine contamination (figure 6.45), although the indicated percentage for chlorine was only 1% compared to 95% zinc. Further corrosion products can be seen to be developing at the precise boundary between the two phases.

#### 6.6.2.4. Discussion: Anode Z

Galvanised and galvanealed zinc coatings immersed or embedded in alkaline solutions and OPC concretes have been shown to form complex passive films comprising zinc oxide, zinc hydroxide and calcium hydroxyzincate (BRS Digest 109, 1969, Sergi *et al*, 1985). The results above demonstrated that the sprayed zinc anode formed a zinc hydroxide based



corrosion product at its interface with the alkaline concrete. The rate of corrosion was greatly influenced by the applied current density and to a lesser degree by current concentration effects above reinforcement bars and adjacent to the primary anode. The wide extent of corrosion indicated that current distribution within the zinc was excellent. The zinc to concrete adhesive bond strength improved initially with the formation of zinc hydroxides, but decreased in time when the thickness of this layer exceeded some critical value and created a plane of weakness. Flame spraying appeared to produce a dense, layered structure, which may have contributed to the evolution of lateral failure planes.

Optimum conditions appear to have been present for the production of the “white rust”, with a ready moisture and hydroxyl ion supply, a limited oxygen supply and anodic polarisation. A mechanism for the evolution of the white rust layer can be deduced as follows: The fresh zinc surface reacted with the highly alkaline pore solution where it was in contact with cement paste to form a passive zinc hydroxide layer. Over a long period, this layer hydrolysed to form white rust, as was observed in un-polarised specimens. Polarisation accelerated the process of zinc dissolution and hence hydrolysis. Hydroxyl ions which evolved at the cathodic reinforcement bars migrated to the adjacent zinc surface and increased the aggressiveness of the pore solution in this region, leading to higher rates of zinc coating corrosion.

The unexpected growth of zinc chloride hydroxide/zinc hydroxide “warts” was of great interest. Wart growth was relatively slow and influenced primarily by the substrate chloride content and secondly by the applied current density and current distribution. It was noted that wart growth was minimal above the reinforcement bars of 50 mA/m<sup>2</sup> specimens. This may have been due to the rapid formation of fissured zinc hydroxide complexes above the bars of these specimens which then acted as a physical barrier between the concrete substrate and the outer zinc surface. Wart growth did extend over bars of specimen Z:2:20:1, which suffered less interfacial corrosion.

The conditions under which zinc hydroxide chloride forms on a zinc substrate have been identified by previous workers (Sergi *et al*, 1985). Zinc coatings were immersed in alkaline solutions with chloride additions, in equilibrium with carbon dioxide free air, for 70 days. Platelets of zinc hydroxide chloride and needles of zinc hydroxide formed in chloride solutions of 0.1 M sodium hydroxide and potassium hydroxide (pH=13). Solutions of calcium hydroxide and calcium carbonate (pH=12.6 and pH=9.0) resulted in products which were not influenced by chlorides and were identified as calcium hydroxyzincate and zinc hydride. The 8 primary XRD “d” spacing values for the latter compound are very similar to Zincite/Zincate, identified in this work, and it is probable that this was the actual composition. These results suggested that zinc hydroxide chloride only formed the main corrosion product in solutions within a specific pH range. However, zinc hydroxide chloride has been identified as the major corrosion product of zinc immersed in near neutral sodium chloride solutions by several workers, the critical factor being a sufficiently high chloride concentration (Keddam *et al*, 1992). In addition, zinc hydroxide chloride formation was related to local anode sites and reduced local pH.

The passivating action of calcium hydroxyzincate was investigated in simulated pore solutions and cement mortars by measuring instantaneous corrosion rates (Andrade *et al*, 1987). In chloride free solutions, at pH values greater than 13.3, the calcium hydroxyzincate crystals formed an imperfect layer which prevented passivation. In mortar specimens where the initial pH was in the range 12 to 12.8, a continuous protective layer developed which proved stable on further increase in alkalinity. The effect of chloride ions depended on the complexing action of the cement and the pH, with pitting attack of the calcium hydroxyzincate rather than the zinc substrate, leading to further alkali attack of the zinc. This suggests that wart formation was initiated by chloride induced disruption of the passive zinc hydroxide layer at some critical ratio of chloride:hydroxide ions. Chloride induced disruption of passivity was observed during anodic polarisation scans of zinc in calcium hydroxide solution, as described in Chapter 4.



It is likely that the majority of chlorides at 0.4% contamination were complexed during cement hydration, whereas a greater proportion would remain as free chlorides in the 2% chloride specimens. Significant chloride ion accumulation in the anode region as a result of polarisation would only be expected therefore for 2% specimens, with higher concentrations at higher current densities. Warts were not observed to form in the zinc films applied to 2% chloride content cement paste prisms in Chapter 5, which suggests that at a certain critical chloride concentration, pitting attack of the zinc hydroxide occurred with the formation of zinc hydroxide chloride. With a constant supply of chlorides, the localised attack of the zinc progressed as the disrupted passive layer allowed further alkali access to fresh zinc to form zinc hydroxides, which were attacked in turn by further chlorides. Such a pitting mechanism is consistent with the narrow crystalline tunnels visible on removal of the surface wart and with the evolution of multiple isolated corrosion sites. Wart growth on the outer zinc surface resembled the reported growth of chloride induced pits on the outer surface of a galvanised coating (Andrade *et al*, 1987). However, a rigorous explanation of this development was beyond the scope of this work. The warts' dark grey appearance resulted from surface oxidation of the various hydroxide complexes.

Both visual and pull-off strength results indicated that coating debonding was less in the 2% specimens, particularly at 20 mA/m<sup>2</sup>. A possible explanation for this could be that as a secondary corrosion mechanism, wart formation limited the white rust formation. In any case, the warts did not appear to impair the adhesion of zinc to the substrate.

Debonding had not been reported in other sprayed zinc studies and it was possible that this was a phenomenon related to the relatively high currents used in this work. Consequently, an examination was made of a CP trial comprising a zinc anode, sprayed on to a reinforced concrete slab containing 3% calcium chloride, which had been polarised at 2.5 to 5 mA/m<sup>2</sup> for 3 years. The results are presented in appendix 6.4. Significant white rust had formed at the zinc/cement paste boundaries, although adhesive strengths appeared high and no debonding was apparent. The concrete had a highly revealed aggregate surface, which

made adhesive strength measurements difficult and may have aided adhesion of the zinc coating. Very small zinc warts were visible at isolated locations. The concrete substrate had been subjected to CP prior to application of the sprayed zinc (Broomfield *et al*, 1985, Palmer, 1987) and it is likely that the chloride content was lower than the original 3%, possibly accounting for the low wart occurrence. Electrical results for the specimen indicated that the circuit resistance had been gradually increasing over the trial period (Geoghegan, 1989). The results supported the proposed degradation mechanisms and indicated that significant zinc corrosion was possible at sustained low current densities.

### **6.6.3. Anodes E and T**

#### **6.6.3.1. Visual inspection**

Visual observations are summarised in tables 6.27 to 6.30. Although the cementitious overlay was described as shrinkage compensated by its manufacturer, drying shrinkage cracks were observed in the majority of specimens when the overlay was drying out after becoming saturated, as shown in plate 6.33. Water loss may have occurred by suction from the relatively dry concrete below<sup>7</sup>. After a period, surface cracks became visible in the dry condition as shown in figure 6.46, but these were not observed to propagate or to be related to experimental variables.

There were no significant differences in the physical performance of anodes E and T. Observations of the anode region within open cored holes should be considered cautiously as the conditions at anode strands in contact with external moisture and air were not representative of conditions within the overlay. Various corrosion products were observed around the anodes, as shown in plates 6.34 and 6.35 and described in tables 6.27 to 6.30. White and orange coloured precipitates were observed to form within water filled core holes, particularly after 22 months polarisation, as indicated in figures 6.47 and 6.48. The

---

<sup>7</sup>Plastic shrinkage occurs whilst the cement paste is still plastic and is caused by water loss by evaporation from the surface or by suction from dry concrete below. Where contracting layers are restrained, either by non-shrinking inner concrete or by mesh reinforcement, tensile stress develops and plastic cracking can occur. The volumetric contraction is of the order of 1% of the absolute volume of dry cement, and is greater the larger the cement content (Neville, 1977).



analyses of some of these products are described in the following sections. Slow anodic gassing was observed from time to time on the surface of some anode strands which had been wetted, associated with a chlorine odour. No degradation was apparent in the region of primary anodes.

#### **6.6.3.1.1. 25 mm cores**

A summary of visual inspections of core surfaces is given in table 6.31. As for anodes P and Z, a classification scheme was devised to describe the progressive anodic degradation. These are outlined in the table and typical cases shown in plates 6.36 to 6.39. In type 1, or zero degradation, the cementitious overlay was unchanged, as was the case for control specimens. All of the degradation processes occurred radially, although to a lesser extent in the direction of the substrate, and not necessarily in the order given. Total paste loss occurred up to a distance of around 1 mm from the anode strand, as shown in plate 6.39.

Degradation was primarily influenced by current density and also by current distribution; some cores displayed greater degradation on the side closest to the reinforcement bar. Rapid localised paste loss was apparent for anode T:50 specimens adjacent to bar A after just 3 months polarisation, in particular specimen T:0.4:50:1. This may have been due to the particularly high effective current density at the anode strands for these anodes, as indicated in table 6.32. However, the degradation adjacent to bar C was minimal for the same specimens at 6 months. Clearly, the choice of sampling location influenced the results and the level of degradation observed at one location was not necessarily representative of the whole specimen. Observations of cored holes at 22 months indicated a wide range of degradation was possible in a single specimen, as shown in figures 6.47 and 6.48.

Cement paste adjacent to anode strands exhibited an orange discolouration after 9 months polarisation at 50 mA/m<sup>2</sup> and at varying later periods for some of the specimens polarised at 20 mA/m<sup>2</sup>. This discolouration was held to indicate advanced degradation and its occurrence in all 50 mA/m<sup>2</sup> specimens at 9 months indicated that the substrate composition did not affect anodic degradation at high current densities.

Substrate composition did appear to exert an influence at 20 mA/m<sup>2</sup>, as indicated by the absence of paste loss in 2% chloride specimens until 18 months compared to 9 months for 0.4% chloride specimens in table 6.31. Indeed, no paste loss was observed for the 4% chloride specimen E:4:20:1 during the trial, although an orange discolouration did develop after 18 months polarisation.

#### **6.6.3.1.2. Rust spotting**

Rust spotting was observed on some specimens, as shown in plate 6.33 and indicated in tables 6.27 to 6.30. The occurrence appeared random and could not be related to experimental variables. The movement of orange particles from an aggregate particle towards an anode strand suggested that this was the source of iron (plate 6.37).

#### **6.6.3.2. Examination of anodic products**

On slicing the cored overlay above the plane of the embedded mesh, the white precipitate surrounding anode strands (plate 6.36) was observed to follow the line of the strands (plate 6.40). By chance, a macro-pore filled with the dense, micro-crystalline product was uncovered (plate 6.41) and EDXA analysis indicated the main constituents as 89% calcium and 5% chlorine (figure 6.49 and table 6.33). Similar analysis of the adjacent cementitious overlay (figure 6.50) suggested that the chlorine was a contaminant from the overlay, or possibly a result of chloride accumulation. The SEM examination indicated that the product was calcium carbonate rather than calcium hydroxide, which would be expected to form more defined crystals. This diagnosis was confirmed by XRD analysis, which was undertaken by an external laboratory due apparatus limitations induced by the small sample quantity. More precisely, the product was identified as a mixture of two forms of calcium carbonate, calcite and vaterite.

The orange/beige paste surrounding the anode strands was similarly analysed externally and found to comprise mainly alpha quartz with small amounts of calcite, gypsum and a minor amount of unidentified crystalline material. This was consistent with the consumption of hydrated cement phases such as CSH gel and calcium hydroxide due to acid attack.



A sample of voluminous orange/beige precipitate, obtained from water filled external core holes of specimens E:2:50:2 and T:2:50:2 after 22 months polarisation, was stored in a sealed glass jar. Later, on opening the jar, a strong chlorine odour was detected. The material was allowed to dry out and analysed by EDXA. The result in figure 6.51 shows a varied composition of mainly calcium, with aluminium, iron, silicon and trace amounts of other elements including chlorine, indicating that the degradation product was calcium carbonate with impurities from the breakdown of the cement paste phases. A specific search of the sample for iron pyrites crystals indicated that iron was only present as a general contaminant. It is possible that localised overlay degradation was accelerated within the core hole when the level of rain water exceeded the level of the anode strands. However, the orange precipitate was not observed in specimens E:0.4:50:1 and T:0.4:50:1, which suggests that it was a result of acid attack of the concrete substrate rather than the overlay.

#### 6.6.3.3. Adhesion Test

##### **6.6.3.3.1. Introduction**

A limited examination of the adhesive strength of the mesh anode/cementitious overlay systems was performed at the end of the trial period. The intention was to elucidate the influence of localised anodic degradation on the bond strength and failure mode. Anode E and T specimens of 2% chloride content and air curing were tested at locations indicated in figure 6.52, following the procedure described in Chapter 3. The results are given in full in table 6.34 and summarised in table 6.35. Typical failure modes are illustrated in figure 6.53 and in plate 6.42. Table 6.34 indicates the failure mode, the depth of the failure plane and the distance of the anode strand from the concrete substrate. The latter displayed some variability within specimens from 0.5 to around 6 mm. It was necessary to repeat a number of tests due to early failure of the epoxy adhesive and due to possible operator error. Where possible 5 representative measurements were obtained. Results in brackets in the tables of results were particularly questionable and therefore not included in the averaged results.

#### 6.6.3.3.2. Results

In general, higher adhesive strengths were associated with failures of the concrete substrate than with failures of the overlay, as indicated in table 6.36. Results for anode E specimens in table 6.35 indicate a shift of the failure plane from within the concrete substrate to within the overlay with increasing current density, whilst the corresponding failure loads tended to decrease. Results for anode T specimens were less clear cut as many failures of the epoxy adhesive occurred and the failure plane tended to be variable for each specimen. The overall trend for the average failure load was to decrease with increasing current density.

#### 6.6.3.3.3. Discussion

The overlay manufacturers' technical information indicated an adhesive strength to concrete of 2.3 N/mm<sup>2</sup>. This value was exceeded at 15 % of locations and the average value of 2.02 N/mm<sup>2</sup> for failure by B/f modes indicated that the overlay workmanship was reasonable. A lowest tensile bond strength for cementitious overlays of 1 N/mm<sup>2</sup> has been proposed (John and Messham, 1989). The average results for all specimens after 18 months polarisation exceeded the latter value with the exception of specimen E:2:50:1, which was also the only specimen to fail almost entirely at the overlay/substrate interface.

The results suggested that a reduction of overlay bond strength was induced by CP for both mesh anodes. The magnitude of anodic current density appeared to influence the failure load and mechanism. This was in contrast to a study which reported no loss of bond strength after one years polarisation at a current density of 67 mA/m<sup>2</sup> (anode area) (Humphrey and Lambe, 1989), and the general view that the overlay bond is not influenced by local degradation (Mussinelli *et al*, 1987, Williams, 1989). However, relatively few measurements were made and further testing should be performed on specimens held at lower current densities for longer periods.

#### 6.6.3.4. Discussion: Anodes E and T

The overlay material was withdrawn by its manufacturer for a short period during this CP trial, following tests at high current densities of 860 mA/m<sup>2</sup> (anode area) for 6 months. Severe localised degradation was reported including darkening, cracking, surface cratering,



white and red staining, and the formation of complete annuli around anode strands (Williams, 1989). It was concluded that such testing constituted destructive, rather than accelerated, testing, and that the maximum recommended anodic current density for this material would be  $108 \text{ mA/m}^2$ . Similar anodic degradation products and annuli were observed in the present study, although surface effects were not.

The anodic current densities used in this work ranged from  $107 \text{ mA/m}^2$  to  $391 \text{ mA/m}^2$  (anode area) (table 6.32), hence the overlay was operating in the region of greatest uncertainty regarding accelerated/destructive testing. The high degradation observed at 3 months for anode T specimens held at  $50 \text{ mA/m}^2$  (concrete area), although possibly related to experimental design, leads one to question the similar “commissioning” high current densities proposed by some, as discussed earlier. The results demonstrated that anodic degradation was progressive and directly influenced by the current density. The results for  $20 \text{ mA/m}^2$  (concrete area) specimens supported a deduction in Chapter 2 that anodic degradation was also influenced by the substrate chloride ion concentration. This will be discussed shortly. In addition, sampling location influenced the level of degradation observed, with higher levels towards the reinforcement bars. A chlorine odour was noted during inspections of both anodic products and anode E and T ( $50 \text{ mA/m}^2$ ) specimens, although it was not possible to determine quantitatively whether anode bubble gases were oxygen or chlorine. Gaseous chlorine evolution was only thermodynamically possible in acidic electrolytes, and hence provided an indication of advanced anodic degradation.

The morphology of the discoloured overlay paste surrounding the anode resembled that of unaffected overlay paste, despite the complete loss of CSH gel and calcium hydroxide. This effect was previously noted during studies of the carbonation of CSH gel, which resulted in an unchanged gel structure of composition silicon dioxide gel, calcite and vaterite (Sauman, 1971), similar to the beige pastes’ composition as identified in this study. This suggests that the processes involved in the anodic paste degradation were similar to those of carbonation of HCP. A full account of carbonation processes is given elsewhere (Sergi,

1986). The precipitation of calcium carbonate in macro pores adjacent to the anode was consistent with carbonation type neutralisation processes, as given in footnote 1, chapter 2; Bicarbonate ions migrated away from the acidified region immediately adjacent to the anode strand to more alkaline regions, where precipitation of calcite and vaterite occurred. Precipitation within plastic shrinkage cracks was also observed, as shown in plate 6.39. These observations directly contradict the literature of one mesh anode manufacturer (Kotowski *et al*, 1989). It was clear that significant pore blocking occurred in a region up to 5 mm from anode strands, decreasing the overlay permeability and it may be inferred that the local resistivity would consequently increase (Figg and Marsden, 1985). The overlay appeared to be air-entrained<sup>8</sup>, which would have minimised bursting stresses due to the precipitation.

The simple model of CP, whereby hydroxyl ions which form at the cathode migrate to the anode where they are consumed (Bennett and Martin, 1987), clearly breaks down at the current densities under discussion. Theoretically, progressive paste neutralisation would occur if the rate of anodic hydroxyl ion consumption exceeded the rate of replenishment from the cathode. The rate of cathodic hydroxyl ion formation during CP would reach a limiting value, dependent on the rate of oxygen diffusion to the reaction sites rather than the magnitude of the polarisation potential (Hardon, 1989). Consequently, the supply of hydroxyl ions to the anode would similarly reach a limiting value, also influenced by the rate of diffusion of hydroxyl ions within the concrete substrate and overlay. At current densities exceeding a particular value, excessive anodic acid formation becomes unavoidable.

The resistance of the overlay to neutralisation would depend on its buffering capacity. A study of the neutralisation of HCP was performed by progressively adding nitric acid to a constant volume mixture of powdered HCP and water and monitoring the pH (Sergi,

---

<sup>8</sup>Air entrainment creates a cellular network of discontinuous voids, reducing the continuous capillary porosity (Anderson and Sweeney, 1989).



1986). The pH was observed to decrease in stages, indicating that several components of the cement offered a buffering capacity, of which the greatest by far was calcium hydroxide at pH 12.56, and it was concluded that neutralisation of the CSH phases was progressive. Hence, if the rate of excess anodic acid evolution was roughly proportional to the current density, or charge passed, one would expect the rate of cement neutralisation to exhibit a similar relationship. It was not possible to draw a firm conclusion regarding this from the results, owing to concentration effects above the isolated reinforcement bars which resulted in uneven degradation. The observation that overlay degradation was less directly below the anode strand can be related to the constant arrival of hydroxyl ions to this region from the cathode, which then reinforced the buffering action of the cement phases. Minimisation of degradation in the overlay/substrate interface region would contribute to the maintenance of a good overlay adhesive bond.

Collapse of the acidified overlay gel structure eventually occurred, resulting in large voids around the anode strand. On the assumption that this void filled with pore water, the anode strand effectively operated in an enclosed electrolyte, which would be expected to rapidly attain a very low pH. The anode would become more sensitive to variations in the moisture content of the overlay, since drying out would result in an air gap of high resistance.

Mesh anode reactions would be controlled by the anodic overvoltage induced by a particular combination of electrolyte pH and current density, as indicated in Chapter 4. The results of Chapters 4 and 5 suggested that oxygen evolution was the predominant reaction for anodes E and T in uncarbonated cement paste. However, once the buffering calcium hydroxide adjacent to the anode strand became neutralised, the chlorine evolution reaction would be thermodynamically favoured, depending on the local chloride ion concentration. This would be beneficial since the oxygen evolution reaction is more aggressive to the anodic environment (Shreir and Hayfield, 1986) and the circuit voltage would become lower. With the anode strands in close proximity to the concrete substrate surface, the local anode chloride concentration would be influenced by the migration of free chlorides from the

substrate, which would be greater for substrates containing higher proportions of chloride. The earlier observation that anodic degradation was lower in high chloride specimens indicates that a greater percentage of chlorine based reactions took place as the local chloride concentration increased. At the high current density of 50 mA/m<sup>2</sup>, it is possible that the anodic overpotential would be sufficiently high for oxygen evolution to proceed despite the reduced pH, and chloride migration would be less influential. In the introduction it was suggested that high substrate/overlay chloride contents induced greater anodic degradation. This was based on results for a mesh embedded in concrete with 6% chloride, held at 200 mA/m<sup>2</sup> (anode area) for 12 months (Mussinelli *et al.* 1987). It now seems more likely that the high acidity noted for this specimen resulted from the high current density rather than the substrate chloride content.

## **6.7. Conclusions**

Each generic anode was observed to develop characteristic degradation mechanisms during the study. These were broken down into logical stages, denoted type 1 degradation and so on, which were then used to give an indication of the degree of degradation at the sampling location at any time. Mesh and zinc anode specimens exhibited progressive degradation mechanisms which appeared to be influenced both by current density and the substrate chloride content. The paint anode failure mechanisms were less easy to categorise due to the somewhat random occurrence of degradation over the specimen areas and the tendency for failure to occur adjacent to the primary anode.

The sprayed zinc anode failed within a short period at the 50 mA/m<sup>2</sup> current density when a weak, voluminous zinc hydroxide based corrosion product developed at the concrete/zinc interface and induced coating delamination. Performance was better at the lower 20 mA/m<sup>2</sup> current density, as may be expected, in particular for the higher 2% chloride specimen. This may have been related to the formation of a second corrosion product, zinc hydroxide chloride, which probably evolved by a pitting mechanism as the chloride concentration at the anode/substrate interface reached a critical value.



The chlorinated rubber binder of the paint coating appeared to undergo oxidation at normal current densities. This was accelerated by the passage of high current, leading to break up of the coating, and probably by increased hypochlorite ion formation in high chloride specimens. Localised degradation was first observed as micro-bubbling, bleaching and larger bubble formation, each being related to acidification. The coating's bulk resistance appeared to increase with time, presumably due to progressive oxidation of the binder. The development of isolated degradation sites appeared to be unavoidable at the current densities used in the study and could not be predicted from regular coating voltage drop measurements.

A mechanism of progressive neutralisation above a certain threshold current density was proposed for the mesh anodes embedded in a cementitious overlay, which would also be partly relevant to the paint anode. Degradation was concentrated around the anode strands, as reported by several other workers, and resembled slow neutralisation by carbonation processes. Bicarbonate migrated away from the anode to be precipitated as calcite and vaterite in adjacent pores, decreasing the local porosity. Degradation was lower towards the substrate. Chlorine evolution, which became thermodynamically favoured as neutralisation progressed, appeared to result in a lower rate of anodic degradation. Complete annuli around anode strands were observed, which would change the kinetics of anode reactions and increase the sensitivity of the anode system to environmental variations. Cathodic protection influenced the overlay/concrete substrate adhesive bond, which reduced with increasing current density.

## **7. Chapter Seven. Electrical operating performance of the CP trial.**

### **7.1. Introduction**

This chapter is concerned with the electrical performance of the CP trial described in Chapter 6. Literature is reviewed to establish current practices in this area and the electrical measurements are presented and discussed.

### **7.2. Literature Review**

#### **7.2.1. CP system control**

Control of CP systems can be achieved in two ways: A pre-determined level of constant current, or stabilised voltage, may be applied which is considered sufficient to polarise all locations adequately; Alternatively, embedded reference electrodes may be used to control the current supply and achieve the required polarisation potential. Early systems which adopted the latter approach were often unable to achieve specific criteria at all structural locations. This was partly due to difficulties in polarising large passive areas and partly due to the erratic performance of the half cells in concrete of varying oxygen content (Stratfull, 1983). Stabilised voltage control is not appropriate for above ground CP since variations in concrete resistivity reduce or increase the cathodic current density unpredictably (McKenzie, 1990). Constant current control has therefore become widely adopted due to its relative simplicity. Monitoring of embedded half cells enables adjustments to the applied current to be made as polarisation levels vary. However, the system operator must adopt criteria with which to judge that the CP system is providing adequate protection and the subject of such criteria remains contentious. Some workers have claimed that "cathodic protection can be designed to completely stop corrosion damage regardless of the salt content of the concrete" (Barnhart, 1982), whilst others have noted that it may not be desirable or economical to do this (Stratfull, 1983). Any moderate amount of CP applied to chloride contaminated structures will be beneficial as it encourages chloride ion movement away from the



reinforcement and the re-establishment of alkalinity, thereby reducing the rate of corrosion. However, it is difficult to establish the complete efficacy of CP in the short term.

#### 7.2.1.1. Criteria

Numerous criteria have evolved for making informed judgements of the on-going performance of cathodic protection of reinforced concrete from remotely sensed data. Such data includes absolute potential values (on switching the CP current off), negative potential shifts (due to the application of CP current), positive potential decays (on switching the CP current off) and in addition, the voltage for constant current systems.

##### **7.2.1.1.1. Absolute potential values**

As indicated in Chapter 2, cathodic protection drives the potential of reinforcement more negative with respect to a reference half cell and the change in potential gives some measure of the consequent reduction in corrosion rate.

The criterion for the maximum permitted polarised potential of -1040 mV (CSE) was introduced to prevent a reduction of the steel-concrete bond strength due to sodium and potassium accumulation at the cathode and to reduce current demand (Hausmann, 1967). This criterion was later extended to prohibit cathodic hydrogen evolution from water reduction at the potential of -1050 mV (CSE) (Robinson, 1972) and this value has become adopted in CP specifications (Concrete Society TR36, 1989). Exceeding this level of polarisation during cathodic protection is often termed “over protection”. Hydrogen evolution may also occur as the rate of hydroxyl ion generation is limited by oxygen concentration polarisation. The adsorbed atomic hydrogen produced may dissolve into the metal surface, rendering the normally ductile material brittle in a corrosion process termed hydrogen embrittlement, or may be evolved as hydrogen gas (Hartt, 1990). This is of particular significance with regard to prestressed concrete containing multiple small diameter, high strength steel cables or rods, where the loss of a few tendons can have a serious structural effect. Gaseous hydrogen may form at a faster rate than it can diffuse towards the surface and it has been suggested that the resultant build up of pressure may

cause spalling of the concrete cover (American Concrete Institute, 1985). However, this has not been reported in accounts of reinforced concrete cathodic protection.

Studies of hydrogen production at a steel-cement interface in saturated lime solution indicated that significant hydrogen gas was produced at the potential of -790 mV (SCE), suggesting that the effect of over protection may occur at potentials more positive than -1115 mV (SCE) (Hope and Ip, 1987). It is now generally accepted that whilst hydrogen embrittlement is a potential danger when applying cathodic protection to pre-stressed concrete, detrimental effects to mild steel reinforcement in concrete have not been reported and cannot be avoided in practice (Showan and Wyatt, 1987). Rather hydrogen evolution is wasteful in terms of excess system power consumption.

The minimum protection potential -850 mV (CSE) was generally accepted for pre-stressed concrete pipes in soil (Franquin, 1964). Steel embedded in concrete tends to exhibit corrosion potentials of the order 200 mV to 300 mV more positive than for steel in other aerated media, such as soil, and it is accepted that reinforcement polarised to -770 mV (CSE) is completely protected from corrosion (Concrete Society TR36, 1989). Corroding areas of structures are often related to high local chloride concentrations, with a lower associated resistivity, and have been found to polarise to specified potentials more easily than passive areas (Stratfull, 1983). The successful achievement of cathodic polarisation to at least -770 mV (CSE) over the entire area of a structure was shown to be difficult at normal current densities of up to 32 mA/m<sup>2</sup> (Schell and Manning, 1985), and the application of global minimum potential criteria generally requires excessive currents, leading to overprotection of previously active areas (Stratfull, 1983) and accelerated anode degradation (John and Messham, 1989). For this reason and owing to uncertainties regarding long term accuracy of steel potential measurements, minimum potential criteria are not recommended for use with above ground structures (Concrete Society TR36, 1989).



#### 7.2.1.1.2. Potential shift

The potential shift criterion requires that the reinforcement potential be lowered by a specified value from the initial  $E_{\text{corr}}$  value as a result of CP. It has been shown to be an effective commissioning criterion and the currently recommended shift value is 300 mV (Concrete Society TR36, 1989). By relating the potential shift to a worst assumption for an anodic Tafel slope of 240 mV/decade for corroding steel in concrete, a 300 mV negative potential shift would reduce the corrosion rate by at least an order of magnitude. In practice, the anodic Tafel slope is difficult to determine and varies with time. Whilst proposed values have ranged from 60-240 mV/decade (Preece *et al*, 1983, Bennett and Mitchell, 1990, Funahashi and Bushmann, 1991), it is likely that the values exceeding 150 mV/decade were influenced by concentration polarisation and do not represent true Tafel behaviour. The potential shift principle cannot be applied for subsequent system appraisals as the surface chemistry of the reinforcement is irrevocably altered by the applied cathodic polarisation (John and Messham, 1989).

#### 7.2.1.1.3. Potential decay

Cathodically protected structures have long been shown to behave as charge accumulators: A substantial time was required for full depolarisation of cathodically protected pre-stressed pipes in soil to occur on switching the protection current off (Franquin, 1964). This phenomenon has been observed during CP of reinforced concrete (Heuzé, 1965, Fromm, 1976).

The potential decay criteria are based on the progressive positive shift in reinforcement potential at a location on removal of the applied current. They rely on the assumption that the magnitude of the potential decay, within a certain time period, gives a fair indication of the degree to which the reinforcement has been polarised, or charge accumulated (Ashworth, 1989). The rate of depolarisation is said to depend on the rate of oxygen diffusion back to the reinforcement (Concrete Society TR36, 1989), which is influenced by pore structure, moisture content and depth of cover material, although no theoretical principles have been proposed to support the recognised criteria.

After a certain period of time from current interruption, the influence of the applied current on the polarised potential will have become negligible and the potential will then be influenced by environmental factors. The potential decay measurement is generally easy to obtain and has the advantage of independence from long term variability of the reference electrode used (Lewis and Boam, 1987).

The reinforcement potential is obtained free of IR (ohmic drop) error by switching off the current and is then monitored at arbitrary time periods to determine the potential decay. IR error is created by the passage of current between the half-cell electrode and embedded steel through the high resistance concrete and masks the true cathodic polarisation potential. On switching off the current, the IR error decays almost instantaneously, whilst the reinforcement potential decay is said to be similar to a capacitor discharging with a slow rate (John and Messham, 1989). Inductive effects in the system induce transient potential surges (Broomfield *et al*, 1987) and a minimum time period which is considered by some to give an accurate "instantaneous off" is 0.01 seconds (Bennett and Mitchell, 1990). The maximum time that is allowed for the measurement is the arbitrary value of 1.0 second (Concrete Society TR36, 1989), which is intended to prevent the half cell potential from decaying by too much, hence the term "one second instant-off" is sometimes used.

A period of four hours is commonly quoted in the literature as a practical period before the second potential measurement and a decay value greater than 100 mV is said to indicate adequate protection (Concrete Society TR36, 1989). However, some disagreement remains concerning this criterion. It has been suggested that absolute adherence to it may lead to overprotection in good quality concrete, where the rate of depolarisation may be slow and decrease with time (Kendell and Pithouse, 1988). Conversely, underprotection may occur in very low quality concretes, where depolarisation is likely to be rapid (Ashworth, 1989) and an increased decay to 150 mV has been proposed (Bennett and Mitchell, 1989). In addition, the 100 mV decay in 4 hours criterion may not be achieved in concrete which is



initially at low risk of corrosion due to chlorides and which is therefore more difficult to polarise (Wyatt and Wartecki, 1991).

Proposals have been made to allow some engineering judgement for adjustment of both the time period and acceptable potential decay values in order to overcome these difficulties (John and Messham, 1989). The measured potential may vary during an extended time period due to changes in external factors such as temperature and moisture, thereby influencing apparent decay values where the time period exceeds four hours.

#### 7.2.1.2. System voltage

A common method for assimilating CP system performance is to monitor the voltage required by the system in order to maintain a constant current. The total driving voltage comprises the sum of the anodic polarized potential, the cathodic polarized potential, the potential loss across the electrolyte and potential drops due to resistances in external circuits. The latter two may contribute significantly to the total voltage. The cathodic potential tends to be controlled by oxygen diffusion and would not be expected to show significant variation. The anodic potential is influenced by the overvoltage for oxygen and chlorine evolution hence the anode material and composition of the electrolyte may significantly affect the voltage.

It is desirable for a CP system to exhibit a steady voltage when held at constant current. However, the overall circuit resistance has been shown to be dominated by the anode/concrete interface resistance and CP system voltages vary with changes in environmental conditions. In studies, voltages were lower during summer and higher during winter for mesh/overlay systems (Schell, 1984, Pedferri *et al*, 1989), whilst the opposite was observed for conductive coatings (Schell, 1984, Broomfield *et al*, 1985). These discrepancies are a result of the sometimes opposing phenomena of surface drying out which results in increased resistance and changes in concrete resistivity with temperature, low temperatures also leading to increased resistance. Wetting of dry concrete

was reported to produce an immediate, significant drop in system voltage for conductive coatings (Apostolos, 1984).

On the assumption that voltage variation from a base level reflects changes in the anode to ground resistance, monitoring of system voltage, together with environmental data, may give an early indication of degradation to the interface between anode and concrete which may be expected to induce an additional resistance to the system.

### **7.3. Experimental**

The Taywood potential wheel, a device which semi-automates potential measurements (Broomfield *et al*, 1990), was used initially to obtain comprehensive potential data along each bar. However, this proved inappropriate as it was not possible to obtain instant-off potentials with the potential wheel, precise re-location of spot potentials was difficult and potential readings exhibited low stability due to high concrete surface temperatures which influenced the electrical contact. As an alternative, three locating spots were marked on the underside of each specimen above each bar, as shown in figure 6.3, and cathodic potentials were obtained with a robust hand held silver/silver chloride half cell. The concrete surface and the half cell sponge tip were pre-wetted with tap water prior to each measurement. The composition of the contact fluid between half cell and concrete pore solution is thought to influence the liquid junction potential, and hence the measured potential, due to variations in pH and ionic concentrations (Figg and Marsden, 1985). This influence is considered insignificant compared to other sources of error, such as high surface skin resistance and concrete moisture content, for measurements over a period of time at the same locations and may be considered a measurement constant. Only stable potentials were recorded. It was not possible to obtain potential measurements at surface temperatures below 5°C due to instrument limitations. Potentials were recorded and are presented to a resolution of 1 mV, although 10 mV is recommended for potential surveys due to the magnitude of possible errors (Figg and Marsden, 1985). During the first 6 months polarisation, instant off measurements were made using the questionable method of visual detection of potential



decay as displayed on a hand held DVM, that is approximately one second after current interruption. The freeze-hold apparatus, described in Chapter 3 and Appendices 6.8 and 6.9, was used from month 10 onwards.

Since the slabs were arranged anode face uppermost, it was necessary to lean them against the adjacent wall prior to measurements, taking great care not to damage the thin electrical wire connections, as shown in plate 7.1. In practice, the positive anode wires were very susceptible to corrosion at sites of abrasion to the plastic insulation and required frequent repairs. It is possible that circuit resistances increased at partial corrosion sites. In addition some repairs were required to primary anode connections due to corrosion and accidental damage.

#### **7.4. Results**

To aid interpretation of the following plots, table 7.1 relates the time in days to the date and month of the potential measurements.

##### **7.4.1. Air and specimen temperature**

The variation of air temperature at the time of some of the potential measurements is shown in figure 7.1. Measurements were made at varying times of the day and values do not reflect the average air temperature, although a comparison with average temperature data (from Hankin *et al*, 1985) indicates a general correlation with seasonal variation for the London region. It is likely that the potential measurements were influenced by the specimen temperature, which would vary throughout the day with the fluctuating air temperature. The surface temperature of specimens and the air temperature were recorded at the time of some potential measurements to obtain a qualitative measure of the effect of heat gain in specimens. A flat thermocouple probe, connected to a digital thermometer, was placed on the concrete surfaces and allowed to equilibrate for 30 seconds before obtaining each reading. Table 7.2 indicates that average surface temperatures of the south facing specimens reached over 40°C during the summer. By contrast, the specimens had thawed out to only 5°C by midday during winter months.

#### 7.4.2. $E_{\text{corr}}$ of control specimens

It was established from linear polarisation measurements, reported in chapter 6, that the specimens exhibited low corrosion rates prior to polarisation and the initial  $E_{\text{corr}}$  values reflected this. The  $E_{\text{corr}}$  values for control specimens were monitored throughout the trial and the results in figures 7.2 and 7.3 represent the average values of the central locations A2, B2 and C2. It can be seen that in general, the  $E_{\text{corr}}$  values were slightly lower for 2% chloride specimens and tended to become more positive with time. The latter trend is in agreement with the findings of Lambert *et al* (1991), and reflects progressive binding of free chlorides. The seasonal influence on the corrosion potentials is also apparent, with values tending to become more negative between 300 and 400 days, corresponding to the period January to April, and subsequently becoming more positive again.

#### 7.4.3. Circuit voltages

The circuit voltages for each anode/current density level are plotted against time in figures 7.4 to 7.15. All anode materials were shown to be sensitive to sudden surface wetting, to varying degrees. On some occasions, the specimens were wetted immediately before measurements were obtained, and this is indicated in the figures. The figures also indicate the times when it had been noted that the slabs were wet due to rain, although it was not possible to monitor the specimens from day to day. The general trend observed for all specimens was for the applied voltage to increase in the long term. The pattern for long term variations due to seasonal changes was similar to that for  $E_{\text{corr}}$  of the control specimens, in figures 7.2 and 7.3. In the short term, it can be seen that variation of circuit voltages occurred at the same time for each specimen, which indicates that this was due to environmental changes. In addition, the figures clearly show the influence of current density on the required voltage for all anodes, which in general was roughly double at the higher current density. For a group of specimens held at constant current, variation of the circuit voltage reflected variation of the circuit resistance. Due to inherent differences, each anode material will be considered separately.



#### 7.4.3.1. Anode T

Figure 7.4 shows that the three anode T specimens held at 20 mA/m<sup>2</sup> required the lowest driving voltages, which ranged from 1.2 V to a maximum 3.9 V, of any specimens throughout the trial. The specific values remained similar between specimens, specimen T:0.4:20:1 tending to require slightly higher voltages.

Figure 7.5 for specimens held at 50 mA/m<sup>2</sup> indicates that whilst initially similar, the voltages diverged during the trial from around 2.1 V up to 8.5 V. These specimens can be ranked in order of increasing circuit resistance; T:2:50:2 < T:2:50:1 < T:0.4:50:1.

#### 7.4.3.2. Anode E

Figure 7.6 for anode E specimens held at 20 mA/m<sup>2</sup> indicates that the circuit resistances diverged after around 100 days from 1.7 V to a maximum of 7.8 V. The voltages were comparable with those for T:50 specimens in figure 7.5. The voltage for specimen E:0.4:20:2, plotted separately in figure 7.7 for clarity, attained very high values of up to 26 V, for no apparent reason. In order of increasing circuit resistance, the specimens may be clearly ranked: E:4:20:1 < E:2:20:1 < E:0.4:20:1 < E:0.4:20:2.

However, figure 7.9 indicates no clear trends for anode E specimens held at 50 mA/m<sup>2</sup>; Over the first 200 days, specimen E:0.4:50:1 exhibited a lower voltage at around 4 V than the two 2% chloride specimens, which had similar circuit voltages of up to 13 V during the first 430 days. Against the trend for most specimens, the voltage of specimen E:0.4:50:1 increased to around 13 V during the period 320 to 420 days, whilst that for specimen E:2:50:1 had similarly become high, in excess of 15 V, at 470 days.

#### 7.4.3.3. Anode P

It can be seen from figures 7.9 and 7.10 that the voltage for anode P specimens varied similarly as for the mesh anode specimens, yet by larger orders of magnitude. Peak voltages around 50 days corresponded with high air temperatures, as indicated in figure 7.1.

At 20 mA/m<sup>2</sup>, specimen P:0.4:20:1 was particularly influenced by the high temperature environment around 50 days, but for no obvious reason. The circuit voltages varied from 2.5 V to around 20 V during the trial. From 100 days, specimen P:0.4:20:2 tended to require the highest voltage.

At 50 mA/m<sup>2</sup>, the circuit voltages for specimens P:2:50:1 and P:0.4:50:1 were similar and varied from 5 V to 62 V, the maximum voltage. Specimen P:2:50:2 showed a lower, more steady circuit voltage.

#### 7.4.3.4. Anode Z

Figures 7.11 to 7.15 demonstrate that the circuit voltages of the anode Z specimens followed the general trends of the other specimens, but showed the greatest variation. Each specimen quickly became influenced by the environmental conditions, such that wetting the anode surface reduced the circuit resistance significantly.

The circuit voltage ranged from 1 V to 37 V for specimens Z:2:20:1 and Z:0.4:20:1, as shown in figure 7.11. The circuit voltage was lower in the 2% specimen over the first 60 days, after which it was higher than the 0.4 % specimen. Following the winter period, at around 380 days, or 13 months, the voltages of both specimens became extremely erratic. The results for specimen Z:0.4:20:2 are plotted separately in figure 7.12 for clarity. This specimen was polarised later than the others, as reported in Chapter 6, and the circuit voltage rapidly approached 62 V, reducing on wetting and during the winter months.

Figures 7.13 and 7.14 show that the limiting voltage of around 62 V was attained within 35 days for the 2% chloride specimens and remained around this value during the summer of the first year. The circuit voltage was generally lower for the 0.4% chloride specimen, peaking at 62 V briefly around 80 days and regaining this general value after around 11 months.



As zinc coated specimens attained the limiting voltage, the abilities of the galvanostat were exceeded and the applied current decreased to as low as 0.25 mA, equivalent to a current density of 1 mA/m<sup>2</sup>, as shown in figures 7.16 and 7.17. Figure 7.16 indicates that specimen Z:0.4:20:2 was erroneously held at 50 mA/m<sup>2</sup> (12.5 mA applied current) during the period 100 to 140 days. The excessive voltage during this period, as shown in figure 7.12 can be attributed to this error.

#### **7.4.4. Cathodic potentials**

For the first ten months of specimen polarisation it was only possible to obtain 'on' cathode potentials. It can be seen from a selection of typical results in table 7.3, for specimens T:0.4:20:1 and T:0.4:50:1, that a considerable potential gradient was measured along bars whilst the current was on, and that this affected the overall specimen average potentials. Apparent potentials regularly exceeded -1115 mV(Ag/AgCl), the theoretical hydrogen evolution potential, at locations 1 and 3. A similar variation of potential within an apparently uniform environment was noted in an earlier CP trial (Broomfield *et al*, 1985). The cathode potentials did not appear to be influenced by reinforcement bar depths. This may have been due to specimen geometry and the requirement to leave a strip uncovered on the underside of each bar for measurements, allowing ready oxygen access. Measured potentials incorporating the IR error rarely exceeded 2 V, indicating that the majority of the increase in circuit voltage was due to anodic resistance effects. When quantitative instant-off measurements became possible, it was clear that the excessive potentials measured at the bar ends were due to specimen geometry/edge effects and the actual polarisation was more even, as demonstrated in table 7.4. Consequently, the current "on" potentials plotted in figures 7.18 to 7.25 represent the averages of the central positions A2, B2 and C2. It can be seen in these figures that the majority of specimens were polarised by at least 400 mV from the initial corrosion potential for the duration of the trial. As would be expected, polarisation levels were influenced by the applied current density and by environmental factors. The plots all show random variation of potentials within specimen groups, with greater variation at the higher current density. All specimens held at 20 mA/m<sup>2</sup> show

similar “on” potentials in the approximate range -600 mV to -800 mV, with the exception of specimen Z:0.4:20:2 which was incorrectly polarised for a short period.

Anode Z specimens held at 50 mA/m<sup>2</sup>, which were deemed to have failed completely from visual observation in Chapter 6, were the only specimens where the “on” cathode potentials increased to levels indicative of corrosion during the last 3 months of the trial.

#### **7.4.5. Instant-off potentials**

##### **7.4.5.1. Depolarisation decays**

###### **7.4.5.1.1. 1 month**

The CP current supply was disconnected after one month to determine the depolarisation characteristics of the specimens. The half cell was placed at the most negative location in order to determine whether the instant-off potential exceeded accepted limits and the potential decay was measured at that location at time intervals of 10, 30, 60 seconds and 4 hours. An inspection of typical ‘on’ potentials in table 7.3 indicates that the significant IR error at bar ends had not developed at this stage, hence these spot potentials may be viewed as representative of the state of polarisation within each specimen. For convenience, the results are plotted with time to a log scale, with time ‘zero’ given the value 0.1 seconds, as shown in figures 7.26 to 7.33. It is clear that the instant-off decay was greater at the higher current density and that CP induced polarisation was negligible after 4 hours, that is, the 100 mV decay in 4 hours criterion was easily exceeded. The latter is not surprising, considering the small dimensions of the specimens and it is likely that the short reinforcement cover distance allowed ready oxygen access. The specimens held at 20 mA/m<sup>2</sup> generally displayed similar IR drop free potentials and the potential decay within 60 seconds of current interruption was substantial. Specimen E:4:20:1 displayed a greater initial potential decay (figure 7.28) whilst the decay for Z:20 specimens was less (figure 7.32). The latter effect may have been a result of a small galvanic current from the zinc. At 50 mA/m<sup>2</sup>, the decay plots reflect the different initial polarisation levels. The figures indicate that the rate of depolarisation was lower for specimens with improved curing, as



may be expected if it is accepted that the rate of depolarisation is related to the rate of diffusion of oxygen back to the reinforcement.

#### **7.4.5.1.2. 6 months**

A similar depolarisation procedure was followed after 6 months operation, with potential measurements at the most negative location at 1 second off, followed by nine measurements at 4 hours, 24 hours and 96 hours. Only typical results are given in table 7.4 since the measurements were not considered as representative. Substantial decays were recorded in the first second due to the high IR errors at bar ends, as previously mentioned, and the polarisation due to CP was effectively removed after 4 hours. It can be seen that the potentials of bars following this varied very widely. Similar potential activity observed after polarisation at very negative values was attributed to renewing of the passive film from a bare metal surface condition (Palmer, 1988).

#### **7.4.5.1.3. 18 months**

Instant off, 4 hour and 24 hour potential decays were quantitatively determined at the end of the project, as shown in figures 7.34 to 7.41. The values plotted in this case are averaged between the locations A2, B2 and C2 and the actual decay period of 0.2 seconds is represented by 1 second in the figures, and zero seconds by 0.1, for clarity. The results indicate that the majority of the anodes were successful in polarising the reinforcement to similar levels as shown in figures 7.26 to 7.31 at month 1. Remarkably, figure 7.41 indicates that the Z:50 specimens were still providing a small level of polarisation despite the virtual total disbondment of the zinc, as reported in chapter 6. These specimens also appeared to satisfy the 100 mV in 4 hour decay criterion. Of the Z:20 specimens, Z:2:20:1 was providing the highest level of polarisation (figure 7.40), which was comparable with the best performance of the other anodes materials (figures 7.34, 7.36, 7.38). By contrast, a comparison of figures 7.32 and 7.40 indicates that the performance of specimen Z:0.4:20:1 appeared to have declined since month 1.

As before, the majority of cathodic polarisation was removed within 4 hours. Comparison with figures 7.26 to 7.33 indicates that the IR error free potentials were influenced less by

applied current density after 18 months operation and that specimen composition no longer appeared to influence the rate of depolarisation, excepting anode Z specimens.

#### 7.4.5.2. Current “off” potentials: Months 1 to 18

Figures 7.42 to 7.49 show the current “off”, or instant-off, potential results. As mentioned above, the data point at 190 days (6 months) should be viewed with some caution, since it represents one spot value rather than an average of three and may be unrepresentative. The monthly variations in the plots resemble those of the ‘on’ potentials in figures 7.18 to 7.25. With the exception of the month 1 results, the average “off” cathode potential did not approach the theoretical hydrogen evolution potential of -1115 mV (Ag/AgCl), despite the high current densities used, presumably owing to high oxygen availability. However, “off” potentials in the region of -1000 mV (Ag/AgCl) for Z:50 and P:2:50:2 specimens up to 372 days (month 12) may reflect low oxygen availability for these specimens. The later quantitative results in figures 7.42 to 7.45 for mesh anodes indicated that the extra current at 50 mA/m<sup>2</sup> did not significantly affect cathode polarisation levels. However, the move towards more positive potentials for P:50 specimens in figure 7.47 may be indicative of a reduction in the anode efficiency owing to coating degradation. Similar positive increases can be observed for specimen Z:0.4:20:2 at 500 days in figure 7.48 and for Z:50 specimens from 418 days (month 14).

#### 7.4.5.3. Variation of IR drop (dE) over months 10 to 18

Figures 7.50 to 7.57 show the variation of the magnitude of the average instant-off potential decay with time for the more quantitative month 10 to month 18 results. The IR drop (dE) gives a measure of the concrete resistance. As may be expected, dE was greater at higher current densities. In general, the dE values appeared to be a minimum in months 11 and 12, increasing up to month 18, probably due to general increases in concrete resistivity from drying out. Figures 7.56 and 7.57 indicate that dE values for Z:50 specimens were erratic from 14 months, becoming as low as 10 mV.

The degree of curing had no clear influence on dE values. Increasing chloride content appeared to decrease dE for anode E and T specimens, particularly at the higher current



density. Such trends were less clear for zinc and paint anodes, with no obvious relationships between dE and specimen composition.

#### **7.4.6. Discussion**

The CP specimens experienced a wide range of temperatures and environmental effects during the eighteen month polarisation period, with consequent fluctuations of concrete resistivity. The specimens initially exhibited low corrosion rates and were easily polarised at the applied current densities. The applied voltage tended to increase over the long term for all anodes whilst cathode potentials remained reasonably constant, generally within a 300 mV band at a specific current density, indicating that the anode/concrete or anode/overlay resistance had increased. These trends were also observed in the electrical results of Chapter 5. Surface wetting immediately before electrical measurements were made reduced the circuit voltages, as reported in the literature. However, on the assumption that a CP system would not receive such aid in reducing circuit voltages, conductive coating anodes would appear especially vulnerable during hot spells when operating at 20 mA/m<sup>2</sup> or more.

The similar circuit voltages in figure 7.4 for T:20 specimens indicated that similar anodic processes occurred, unaffected by differences between specimen composition. The results for T:50 specimens in figure 7.5 indicated that the voltage was lower for concrete of higher chloride content. This trend was also shown in the voltages of E:20 specimens, which were of similar magnitude to T:50 specimens. Voltages for E:50 specimens and specimen E:0.4:20:2 were particularly high and it was clear that, other experimental factors being equal, anode E specimens developed much higher anode resistances than anode T specimens. The difference between the operating voltages of the two mesh anodes may be partly explained by the lower apparent catalytic activity exhibited by anode E in the anodic polarisation study of Chapter 4. This would result in a higher anodic overvoltage to maintain the same current density as the more efficient anode T and hence higher initial circuit voltage. The influence of chloride ions in reducing the overvoltage was apparent in Chapter 4 and may similarly explain the lower voltages with high chloride contents for T:50

and E:20 specimens. Subsequent voltage increases may have been induced both by a reduction of alkalinity around anode strands increasing the oxygen evolution potential and by reduced porosity around anode strands from pore blocking, as observed in Chapter 6, which then limited the movement of anodic reactants. The influence of paste loss around anode strands on the sensitivity of the mesh anodes to the environment is clear from the high voltages during the second summer period after around 420 days, or 14 months.

However, the circuit voltages for all specimens appear high when compared to results reported for similar CP trials. Voltages for mesh anodes embedded in various cementitious overlays which were observed to increase from around 1.1 V to 2 V at a current density of 67 mA/m<sup>2</sup> (anode area) over a period of 300 days, were simply attributed to moisture loss (Humphrey and Lambe, 1989). The study used lower current densities than the present study and no degradation was reported. The voltage for a mesh anode embedded in a 2% chloride content concrete and held at 100 mA/m<sup>2</sup> only varied in the range 1.3 to 2.1 volts over 800 days and the seasonal voltage variation was directly opposite to that observed in the present study (Pedferri *et al*, 1989). These anomalies may be due to different experimental arrangements. The study utilised a steel mesh cathode which would have given a more even current distribution, and specimens were sheltered from rain and direct sunlight. Degradation for this specimen was reported to be insignificant and it may be that mesh cast into a concrete performs better than anodes embedded in cementitious overlays of different composition to the original substrate. The overlay moisture permeability may be influential in this.

No clear differences were discernible between the physical performance of the two mesh anodes in Chapter 6, with similar apparent mechanisms and rates of anodic degradation at each current density. This suggests that the dominant anodic reaction was oxygen evolution for both anodes in specimens up to 2% chloride content, with the chlorine reaction being limited by the supply of chlorides. The very low degradation for specimen E:4:20:1, and relatively low circuit voltage, may be attributed to a higher proportion of free chlorides.



Early increases in circuit voltage for anode P indicated that it was far more susceptible to environmental variations than the mesh anodes. The higher initial circuit voltages may again be explained from the Chapter 4 results, which indicated a lower catalytic activity for anode P than for the mesh anodes and in addition indicated that anode P activity was higher in less alkaline, chloride solutions. However, no clear trend could be observed regarding the influence of specimen composition on circuit voltages; Specimen P:0.4:50:1 displayed a higher initial circuit voltage than P:2:50 specimens, but further differences became masked by other sources of resistance. The circuit voltage of specimen P:0.4:50:2 generally resembled that of the P:20 specimens rather than P:50 specimens. The physical results of chapter 6 do not provide any possible explanations for this and a significantly lower average coating resistance was not indicated for specimen P:0.4:50:2 in figure 6.33. Similar circuit voltages, of up to 14 V, have been observed in practice for paint anodes held at 13 mA/m<sup>2</sup> (Schell *et al*, 1984).

Zinc coated specimens quickly developed a high anode/concrete resistance due to the formation of zinc oxide complexes, which resulted in a high voltage demand up to the maximum available of around 62 V. At times the resistance became so high that the galvanostat was unable to meet its constant current requirements, and the circuit current dropped. It should be noted that commercial constant current devices are often designed to a maximum voltage capacity of 5 to 48 V (Concrete Society, 1989). The formation of hydrated zinc oxide layers would fundamentally change the kinetics of reactions at the zinc anode interface, as indicated in the Chapter 4.

Circuit voltages during the first two months for Z:20:1 specimens in figure 7.11 indicated that high chloride substrate contents reduced the anode resistance, yet this trend was then reversed. The former effect was predicted in Chapter 4, where chlorides resulted in lower anodic overvoltages. The reversal may be related to changes to the partially passive layer forming at the anode interface, such as the zinc hydroxide chloride “warts” observed on

specimen Z:2:20:1, in Chapter 6. During the first 12 months polarisation at  $50 \text{ mA/m}^2$ , 2% chloride specimens tended to attain higher voltages than the 0.4% chloride specimen. The zinc wart phenomenon therefore appeared to contribute to an increased anode resistance.

Considering the high anode resistances and general condition of the Z:50 specimens, intermittent wetting appeared remarkably successful in maintaining adequate cathode polarisation levels, as determined from the instant off measurements in figure 7.49. This success may have been aided by the low initial corrosion rates of the reinforcement bars and the short periods of time between wettings preventing corrosion initiation. It is likely that conductance through the insulating white rust films on wetting was aided by the dissolution of bi-zincate ions from the hydroxide complex to provide a conductive medium. Cessation of manual wetting after 14 months resulted in marked anode resistance increases with corresponding current reductions and a consequent reduction of cathodic polarisation. However, potential decays on turning the current off, shown in figure 7.41, indicated that the Z:50 specimens were still providing a low degree of cathodic polarisation which may have still been sufficient to reduce the reinforcement corrosion rates.

The instant-off cathode potentials in figure 7.48 indicate that Z:2:20:1 sustained the best level of protection of the Z:20 specimens at 18 months. This complements the observation in Chapter 6 that this specimen displayed the lowest degradation rate of anode Z specimens. In addition, the high degradation rate noted for specimen Z:0.4:20:2 in Chapter 6 was probably initiated during the 1 month period of high applied current and suggests that the zinc coating was extremely sensitive to even a short period of excessive current density.

The magnitude of potential decay on current interruption was primarily influenced by current density, as may be expected. Quantitative measurement of the IR drop indicated that the magnitude of  $dE$  was also influenced by the chloride content of specimens and seasonal variation, that is, the factors which influence resistivity. The depolarisation results at 1 month indicated that subsequent depolarisation was rapid; at  $20 \text{ mA/m}^2$ , around half of



polarisation was lost within around 60 seconds and the remainder within four hours. This was attributed to the ready availability of oxygen to the reinforcement. Whilst the initial depolarisation was slower at 50 mA/m<sup>2</sup>, the four hour results were similar to the 20 mA/m<sup>2</sup> specimens. The rate of depolarisation was lower in better quality concrete, but this was less apparent after 18 months, when depolarisation rates appeared independent of original specimen composition and current density. This indicates that the cement paste layers surrounding the reinforcement of each specimen attained a similar composition or relative permeability, possibly a result of calcium hydroxide precipitation in this region. More work would be necessary to confirm this supposition. The results support the contention that the decay criteria require engineering judgement rather than an absolute specification.

It is possible that the high concrete surface temperatures measured during the summer may not be observed on deeper concrete elements, which would have a greater capacity to dissipate solar energy from the surface. Consequently, anode performance may be better on actual structures than observed on small laboratory specimens.

## **7.5. Conclusions**

Monitoring of the system voltage in parallel with cathode polarisation and environmental factors appeared to provide adequate data for the appraisal of anode performance. The progressive degradation of all anode systems was apparent from the circuit voltage data, which increased in the long term due to changes in the anode/concrete resistance. The anodic overvoltage appeared to contribute a significant proportion of the circuit voltage and it is possible to rank the anode materials in the same decreasing order of electrical efficiency as was proposed from the ionic migration study in Chapter 5, that is anode T > anode E > anode P > anode Z. From a CP criteria point of view, all of the specimens were adequately polarised during the trial with the exception of Z:50 specimens, which totally disbonded.

From a consideration of the circuit voltages and rates of overlay degradation in Chapter 6, it is concluded that the dominant anode reaction for anodes E and T was oxygen evolution, at

least until the buffering calcium hydroxide had been consumed. The reduced overvoltages and degradation with increasing substrate chloride content suggest that high chloride levels were beneficial with respect to mesh anode performance. The conductive coatings were more susceptible to temperature and moisture fluctuations than the mesh anodes, even relatively early in the trial. The influence of a high chloride content on the circuit resistance of anode P specimens was difficult to determine, whilst the formation of chloride related corrosion products appeared to increase the circuit resistance of anode Z specimens.

A convenient instrument for the accurate determination of “instant-off” potential measurements was developed and used with some success. The rate of potential decay on current interruption became less dependent on specimen composition with time.

Although the results only cover an 18 month period, it is suggested that the current density of 20 mA/m<sup>2</sup> was too great with respect to the long term performance of all the anodes, but in particular to anode Z.



## **8. Chapter Eight. The influence of CP on the concrete substrate.**

### **8.1. Introduction**

Actual measurements of acidity at an anode interface have been reported (Mussinelli *et al*, 1987), as reviewed earlier in Chapter 2. Regular acidity measurements were considered to be difficult under site conditions and prone to error. It was only possible to obtain approximate pH values for coated anodes at blister sites, as reported in Chapter 6. Owing to these difficulties, the development of acidity at the anode interfaces was inferred indirectly from other measurements and observations. Primarily, visual observation of the anode surfaces and of small diameter cores appeared to provide a good indication of acid attack of HCP, as described in Chapter 6. CP induced compositional changes within the concrete were anticipated in the long term, and it was of interest to determine to which depth from the concrete surface these occurred and whether degradation was confined to the overlay, for embedded mesh anodes. Consequently, long term exposure specimens were examined using the established techniques of mercury intrusion porosimetry, differential thermal analysis and thin section petrography. An investigation was also undertaken of ionic concentration profiles around the anode region for comparison with results obtained for HCP prism specimens, as described in Chapter 5. Specimens 1 to 12 in table 6.1 were selected for analysis, that is specimens containing 2% calcium chloride, air curing and current densities of 0, 20 and 50 mA/m<sup>2</sup>.

### **8.2. Sampling methods**

Material for the following investigations was obtained by taking 100 mm diameter cores perpendicular to the anode surface at the central bar location A2, as shown in figure 7.1. The cores were then cut in half, perpendicular to the central bar and the anode surface. One half-core provided material for analysis by MIP, as described in Chapter 3. The second half-core provided material for DTA and ionic concentration profiles, using the profile-grinding technique, as described in Chapter 3. Sample depths were related to the anode/concrete interface as shown in figure 3.4, the depth being taken to the centre of the 2 mm sampling depth.

Material for the thin section analysis was provided by the 25 mm cores taken through various specimens periodically during the study.

### **8.3. Thin sections**

#### **8.3.1. Introduction**

Impregnation with blue resin facilitated observation of voids within HCP pores in the thin sections. The visual observations are summarised in tables 8.1 to 8.5, which also indicate which specimens were examined and the time at which they were obtained after the initial polarisation.

##### 8.3.1.1. General observations

Petrographic examination of the concrete confirmed that the aggregate used consisted of Thames Valley flint with a proportion of glauconite. The latter constituted the source of iron pyrites, accounting for the orange rust staining of the overlay and conductive paint reported in Chapter 6. The cores indicated a highly variable macro porosity over the full depth of the concrete substrate with voids of up to 4 mm diameter. All specimens displayed a degree of carbonation which appeared to vary by up to around 2 mm from the concrete surface, probably as a result of the poor curing regime.

##### 8.3.1.2. Anode P

The paint thickness was observed to vary in the range 200 to 850  $\mu\text{m}$ , depending on surface topography but apparently not with applied current. The paint coating was observed to be in good contact with the substrate in the majority of specimens. A number of lateral micro-cracks were observed in control specimens, as shown in plates 8.1 and 8.2, which may have occurred during specimen preparation. The porosity of HCP immediately adjacent to the paint surface tended to vary from very high to relatively low, as demonstrated in plates 8.3 to 8.5, taken within 3 mm of each other. The carbonation, or cement neutralisation, was similarly variable. The polarised specimens exhibited more coating ruptures than non-polarised specimens, indicating a weaker structure. Significant HCP was lost at the acidified bubble site during slide preparation due to the weakened paste structure. The



remaining paste was highly porous and the underlying aggregate displayed significant cracking, as shown in plate 8.6. Cracked aggregate particles were also observed in other specimens, as indicated in table 8.1.

#### 8.3.1.3. Zinc coating

The sprayed zinc was also in intimate contact with the substrate. Significant cracking of large surface aggregate particles occurred in all specimens as a result of the flame spraying process, as shown in plates 8.7 and 8.8. The zinc coating was of variable thickness and appeared slightly porous, as shown in plates 8.7, 8.9 and 8.12. The substrate porosity appeared low in all specimens. A glassy phase, of variable thickness up to approximately 180  $\mu\text{m}$ , was observed in all polarised specimens adjacent to the zinc. The glassy phase appeared brittle and contained lateral cracks as shown in figures 8.10 to 8.12.

#### 8.3.1.4. Mesh anodes

Petrographic examination indicated that the cementitious overlay aggregate consisted of quartz and ortho and meta phase quartzite. The porosity of the overlay was generally high but varied from sample to sample due to its application as thin layers. Plate 8.13 illustrates typical banding of layers; The lower portion of the micrograph shows higher porosity than the upper region, possibly due to bleeding of capillary water. A narrow, central dark brown band indicates light carbonation at the joint between two layers.

Little difference was observed between anode E and T specimens, hence these will be considered together. The thin sections complemented and confirmed the visual observations and conclusions made of the core surfaces in Chapter 6 which indicated the progressive development of a degradation zone surrounding the anode. An examination of the overlay/substrate interface indicated a good bond and less substrate carbonation in the control specimens, as shown in plate 8.14, possibly due to realkalisation by migration from the highly alkaline overlay. By contrast, polarised specimens tended to exhibit varying depths of carbonated HCP and lateral micro-cracking in specimens polarised to 50 mA/m<sup>2</sup>, as indicated in tables 8.3 to 8.5 and plate 8.15. The cracks were observed after a period of polarisation and in some cases extended through aggregate particles. The overlay remained

alkaline other than adjacent to anodes, hence it is suggested that such cracking was due to electro-osmotic pressures which developed at the high current densities rather than by acidification. Clearly, this effect would require further investigation. A second phenomenon observed after approximately 9 months was crystal formation in macro-pores within a short distance of the anode, as shown in plates 8.16 and 8.17. The needle like crystals resembled ettringite crystals but appeared multi-coloured when observed under crossed polarised light, a characteristic of portlandite (Sibbick, 1992). The sequence of plates 8.18 to 8.21 demonstrates the progressive degradation processes around the mesh anode. In plate 8.18, no degradation was apparent after 20 mA/m<sup>2</sup> for 3 months, whereas after 12 months the same specimen exhibited signs of cement paste neutralisation, as shown in plate 8.19. The porosity of the paste had increased to the upper right and lower left of the strand. Plate 8.20 shows a ring of increased porosity, free of portlandite and surrounded by a narrow carbonated ring after 50 mA/m<sup>2</sup> for 3 months. The sphere of influence had expanded greatly after 12 months, as shown in plate 8.21. The wider neutralisation front for this specimen is shown in plate 8.22.

### **8.3.2. Discussion**

The thin sections provided unambiguous evidence of anodic degradation for each anode and complemented results in Chapter 6. Zinc corrosion products, which were observed to develop from inspection of pull-off stubs in Chapter 6, appeared as a glassy interfacial layer. It was confirmed that surface aggregates were shattered during the flame spraying process, a seemingly unavoidable occurrence. In general, the zinc appeared to adhere intimately with the substrate and the impact of CP on the concrete appeared minimal.

The conductive paint also adhered well in general. Degradation was observed in polarised specimens in highly localised shallow regions of very high porosity, approximately 200 µm deep. Aggregate particles were observed to crack at areas of high acidity although in general, surface particles were not cracked.



The overlay was shown to comprise of layers of variable porosity. The anode of specimen T:2:50:1, which sustained high paste loss, was generally embedded in dense mortar of relatively low porosity, which suggests that the overlay porosity may not have influenced anodic degradation rates. Interfacial lateral cracking which was observed in polarised specimens may have been induced by electro-osmotic pressures between the overlay and substrate. Such cracking may have contributed to the reduced overlay bond strength as reported in Chapter 6. The anodic degradation processes were confined to the overlay and appeared to be related both to the magnitude of applied current and time.

#### **8.4. Variation of pore structure**

##### **8.4.1. Introduction**

Cement paste at the substrate/overlay interface of high current density specimens was considered the most likely to exhibit variation in porosity. Samples from 50 mA/m<sup>2</sup> and related control specimens were prepared and analysed as described in Chapter 3. A summary of the MIP data is given in Appendix 8.1 and results shown in figures 8.1 to 8.8. Values for the percentage of available intrusion volume used in the penetrometer, given in Appendix 8.1, indicate that the measurement efficiency was very low for the concrete specimens and slightly too low for cementitious overlay samples. It was not possible to remove all of the fine aggregate from the concrete samples, and this contributed to the lower relative porosity and efficiency. A penetrometer of lower stem volume would have improved the measurement efficiency for all specimens but was unavailable at the time.

##### **8.4.2. Results**

###### **8.4.2.1. Cementitious overlay**

The results in figures 8.1 to 8.4 confirmed visual evidence that the cementitious overlay had a far coarser pore structure than the concrete substrate, in agreement with previous MIP studies of polymer modified cements (Hardon, 1989). Around 40% to 50% of overlay pores were in the range 0.307  $\mu\text{m}$  to 2.19  $\mu\text{m}$  radius compared to approximately 15% of the concrete pores. Figure 8.1 shows that the pore size distribution (PSD) for the overlays of anode E samples were broadly similar, whilst figure 8.2 shows greater variation for anode

T specimens. This is probably a reflection of the variable layers observed in the previous section.

#### 8.4.2.2. Anodes E and T

Figures 8.3 and 8.4 show that the PSD's for anode E and anode T concrete substrates were virtually unaltered by high applied current. Small variations can be seen in the range 0.115  $\mu\text{m}$  to 3.59  $\mu\text{m}$  for anode E and in the range 0.0702  $\mu\text{m}$  to 0.82  $\mu\text{m}$  for mesh T, probably due to experimental variability.

#### 8.4.2.3. Anode Z

Figure 8.5 indicates that the whilst the PSD was broadly similar for specimens Z:2:0:1 and Z:2:50:1, the overall porosity was slightly lower for specimen Z:2:50:1. This small effect may be due to experimental variation or reflect reduced surface porosity due to increased production of zinc corrosion products.

#### 8.4.2.4. Anode P

Figure 8.6 compares the PSD of the control samples P:2:0:1 and T:2:0:1 and is intended to illustrate that the PSD of specimen P:2:0:1 differed significantly from those of the other control samples, which followed one another closely. Reference to Appendix 8.1 indicates that the bulk density of P:2:0:1 was particularly low compared to the other samples, which indicates poor specimen preparation. The porosity for the sample P:2:50:1 appeared to be significantly lower than the control sample, hence an additional sample was obtained for the depth 6-10 mm and specimen P:2:20:1 was also sampled, at a depth of 0-4 mm. Figure 8.7 is a plot of the results for the surface 0-4 mm depth of specimens P:2:0:1, P:2:20:1 and P:2:50:1 and indicates that the PSD was quite variable. Porosity in the range 0.115  $\mu\text{m}$  to 1.05  $\mu\text{m}$  decreased with increasing applied current. Over the range 0.115  $\mu\text{m}$  to 3.59  $\mu\text{m}$ , the porosity of the polarised specimens was significantly lower than that of the control. Figure 8.8 shows that the PSD for the 6-10 mm depth sample was similar to that of the control T:2:0:1, that is, it was characteristic of unaffected concrete.

The results suggest that the porosity of the surface layer of anode P specimens was reduced by CP reactions and possibly by penetration of the paint binder into the concrete. The



apparent reduction in porosity with current density contradicts an assumption that the porosity would increase as a result of acidification and may reflect a redistribution of carbonates within the surface layer. However, the variability in PSD for surface samples of anode P and the cementitious overlay may be related to the preparation method, involving heating to 105°C. It has been suggested that the presence of organics may induce distortions to the pore structure at this temperature (Hardon, 1989).

#### **8.4.3. Conclusions**

The most obvious differences in porosity were between the concrete and cementitious overlay, the latter exhibiting a more coarse structure which varied as a result of the application method. No significant changes were observed in the PSD of substrate concrete of anode E, T and Z specimens as a result of CP, whilst the surface porosity of anode P specimens appeared to decrease. Petrographic examination of thin sections indicated that anodic effects were limited to a depth of around 2 mm, often considerably less. The sample depth of 4 mm was clearly too coarse for the detection of subtle variations of porosity in the anode region and MIP did not appear to be a suitable method for this purpose. .

### **8.5. Ionic concentration profiles**

#### **8.5.1. Introduction**

Ionic concentration profiles were obtained from powdered samples using the chemical analysis methods described in Chapter 3. The grinding tool diameter of 50 mm was thought to provide a sampling area of sufficient size to have a reasonably constant HCP/aggregate ratio, considering the maximum aggregate size of 20 mm. It has been suggested that in this case, there is generally no need to perform further analyses to determine the cement/aggregate ratio (Wood *et al*, 1989). However, calcium analyses were undertaken using the ICP method as a precaution against questionable results. Since the aggregate used in the concrete was Thames Valley crushed rock and sand, which has a very low calcium content, it was not considered necessary to analyse specimens for silicon content. Magnesium and zinc ion concentrations were also provided automatically by the ICP analysis. Powdered concrete samples of known chloride content were analysed in parallel

to provide a measure of the reliability of the chloride analyses, and these results are given in Appendix 3.4.

Additional tests were performed as follows: The overlay material of specimen T:0:0:1, obtained by 50 mm diameter dry coring before the specimens were energised and stored in a dry indoor environment, was analysed for chloride and alkali metal ions. Since the concrete substrate of this specimen contained zero chloride, it was considered that the results would reflect the original chloride and alkali metal concentrations of the overlay.

To gain a qualitative measure of any change in chloride content of the conductive paint, samples were obtained from an acidified pull-off stub (specimen P:2:50:1) and from paint applied to a glass microscope slide (as described in Chapter 4) and analysed as for cementitious samples.

Results of these additional tests are given in table 8.6. The high concentrations for sodium and chloride ions in the overlay suggest that chloride was added as sodium chloride. Results for the conductive paint indicate that the initial chloride content of the binder was relatively high at around 0.38 mM/g of sample and that a loss of approximately 75% of the chloride was possible as a result of anode operation.

#### **8.5.2. Results**

The results are grouped by specific ion of interest and are displayed in figures 8.9 to 8.36. Ionic concentrations are given as mM/g of sample. Positive distance values relate to the concrete substrate and negative values to the overlay where present.

##### **8.5.2.1. Calcium and magnesium ions**

The results for calcium and magnesium ions are shown in figures 8.9 to 8.12 and 8.13 to 8.16 respectively. It can be seen that the trends in concentration for the two ions followed one another closely, as would be expected if the calcium concentrations were solely indicative of the quantity of hardened cement paste in each sample and where the aggregate had a low calcium content. The calcium content by weight of sample in the concrete



substrate appeared to show some variation at depths greater than 2-4 mm, indicating that the ratio of aggregate to HCP was not constant. Increased calcium levels at the surface 0-2 mm of P and Z specimens, as shown in figures 8.11 and 8.12, suggests that the surface layers may have been richer in cement than in the bulk of the concrete. It can be seen from figures 8.9 and 8.10 that calcium levels in the cementitious overlay were approximately twice those of the concrete by weight of sample, which may reflect a lower cement/aggregate ratio. A certain amount of cross contamination occurred in the 0-2 mm region for these specimens, which was unavoidable due to small heterogeneities in the concrete surface.

#### 8.5.2.2. Chloride ions

A calculation for the expected chloride concentration which assumes a homogeneous mix of the concrete constituents is given in Appendix 3.4. It can be seen from figures 8.17 to 8.20 that the chloride ion concentrations for the control specimens with zero current generally exceeded this calculated value of 0.055 mM/g. In general, the chloride concentrations in the concrete substrate decreased with increasing current density and the profiles tended to be even until the immediate surface was reached at a depth 0-2 mm.

Figure 8.19 shows that the chloride concentration increased sharply at the surface layer for anode P specimens, independent of current density. This increase may have been due to contamination of the surface samples by the conductive paint. Table 8.6 indicates that the chloride content of acidified paint was still high enough to have this effect. Alternatively, the increase may be due to a higher proportion of cement in the surface layer, as indicated by the calcium ion profiles.

The profiles for anode Z specimens in figure 8.20 showed contradictory trends, the chloride concentration for the control specimen Z:2:0:1 decreasing to around 0.03 mM/g, whilst the profiles for specimens Z:2:20:1 and Z:2:50:1 remained level at around 0.05 mM/g. If the cement contents of the surface samples are considered, as indicated by the calcium profile in figure 8.12, the 0.03 mM/g value appears to be erroneous, whilst the chloride concentration

by cement content is lower for specimen Z:2:50:1 than for specimen Z:2:20:1, as shown in a plot of the ratio of chloride/calcium ions in figure 8.21.

The chloride concentration in the overlay of all mesh specimens, as shown in figures 8.17 and 8.18, appears to be significantly lower than for the value shown in table 8.1 for specimen T:0:0:1 of 0.221 mM/g sample. The apparent reduction of chloride in the control specimens T:2:0:1 and E:2:0:1 may be due to a combination of diffusion of chlorides from the high concentration of the overlay to the relatively lower concentration in the concrete and leaching of chloride from the externally exposed specimens. The polarised mesh specimens showed similar chloride profile trends. Chloride accumulated in the region -4 to -2 mm, corresponding to the anode mesh region, at the lower current density of 20 mA/m<sup>2</sup> whereas the chloride levels for specimens held at 50 mA/m<sup>2</sup> were lower than the controls. This suggests that chlorine discharge may have occurred more readily at 50 mA/m<sup>2</sup> than at 20 mA/m<sup>2</sup>.

#### 8.5.2.3. Sodium and potassium ions

Table 3.1 indicates that the quantities of sodium and potassium in the original concrete mix were relatively low.

Figures 8.22 and 8.23 indicate that the sodium ion concentration decreased from around 0.13 mM/g at the anode to around 0.06 mM/g in the concrete bulk for both mesh anodes, independent of current density. It is likely that this was due to the diffusion of excess sodium ions from the overlay. The concentration of sodium and potassium ions in the overlays, as shown in figures 8.22, 8.23, 8.26 and 8.28, were lower than the values given in table 8.6 for the overlay of specimen T:0:0:1, but were generally higher than those determined for the substrate of the Z and P specimens, as shown in figures 8.24, 8.25, 8.28 and 8.29. The sodium ion profiles in figures 8.22 and 8.23 appear to have been “flattened out” by increasing applied current, that is, the sodium ion content in the concrete substrate was higher for polarised specimens than for the unpolarised controls. This may be indicative of increased ionic diffusion from the overlay towards the cathode as a result of



the applied electric field. This effect was less apparent for potassium ions, probably due to the relatively low concentrations in the overlay and concrete.

The sodium and potassium ion concentration profiles in figures 8.24 and 8.28 for anode P show very little variation with depth. The high value of 0.106 mM/g for specimen P:2:0:1 in figure 8.24 appears to be erroneous. Figure 8.25 indicates that the sodium ion concentration decreased with increasing current density for anode Z specimens, presumably due to increasing ionic diffusion towards the cathode. The potassium ion concentration profiles for anode Z in figure 8.29 do not show clear trends, again due to low absolute concentrations.

#### 8.5.2.4. Hydroxide ions

A qualitative determination of the alkalinity of surface samples was undertaken, as described in Chapter 3. The hydroxyl ion concentrations should not be viewed as absolute, but are suitable for comparisons and observation of trends.

The hydroxyl ion concentration profiles are shown in figures 8.30 to 8.33. There was a slight tendency for the alkalinity to increase from the anode interface towards the bulk of the substrate for all specimens, which may be due to carbonation of the concrete surface prior to anode application. The results were in general agreement with values determined for the overlay of the control specimen T:0:0:1 and the powdered HCP sample of chloride content 0.13 %, which are also plotted at the distance of 1 mm on the graphs.

The profiles for mesh specimens given in figures 8.30 and 8.31 appear to be related to the calcium ion profiles rather than the magnitude of applied current density, with an overlay hydroxyl ion concentration approximately twice that of the concrete.

Figure 8.32 indicates that the hydroxyl ion concentration was generally steady within the concrete substrate, and only decreased significantly for specimen P:2:50:1 within the 0 to 2 mm depth. A plot of the ratio of hydroxyl/calcium ions was constructed to eliminate the

— Influence of inert aggregate from the profiles, as shown in figure 8.34. Reduced alkalinity at the surface of specimens P:2:0:1 and P:2:20:1 may be attributed to carbonation. The alkalinity of specimen P:2:50:1 appeared to decrease significantly from a depth of 4 mm to the concrete surface, and it is suggested that this indicates progressive neutralisation of the surface cement paste.

Figure 8.33 indicates that the hydroxyl concentrations decreased from around 1.0 mM/g towards the concrete surface and reached a limiting value of around 0.5 mM/g at the zinc anode interface. A plot of hydroxyl/calcium ions was similarly constructed as for paint specimens, as shown in figure 8.35. It can be seen that the magnitude of applied current density had a minimum impact on the variation of alkalinity in the substrate of the zinc specimens, and that the reduction in alkalinity was restricted to depths up to 4 mm from the concrete surface.

#### 8.5.2.5. Zinc ions

Analyses of non-zinc coated specimens indicated concrete zinc contents of less than 0.005 mM/g. Figure 8.36 shows the variation of zinc ions in the zinc coated specimens. The high value of 0.97 mM/g for Z:2:0:1 at a depth 0 to 2 mm may be due to contamination of the surface sample with pure zinc and it is likely that the polarised specimens would similarly be contaminated by significant amounts of zinc oxides. It is clear that zinc ions penetrated up to a distance of around 6 mm from the surface, and the degree of penetration appeared to decrease with increased current density.

#### **8.5.3. Discussion**

The technique of profile grinding to obtain samples for chemical analysis appeared to provide a reasonable degree of resolution for the ionic concentration profiles. It was only possible to measure ionic profiles for a small number of specimens from the CP trial. Although the number of sample increments was kept to a maximum of 8 across the anode/substrate interface, this resulted in a large number of samples and it was not possible to obtain double or triplicate samples to provide a measure of statistical confidence in the results.



The results provided limited evidence of ionic migration due to applied cathodic protection. The ionic profiles appeared to be influenced by the cement/aggregate ratio of the sampled material, as indicated by the calcium ion concentration and this made analysis of certain profiles difficult.

Movement and removal of chloride ions was apparent for all polarised specimens as the total chloride concentration by sample weight appeared to decrease with increased current density. This consistent reduction of chloride in the anode region was in contrast to the results of chapter 5, in which chlorides tended to accumulate at the anode, and removal by chlorine evolution was not apparent. It would appear that some chlorine evolution occurred for mesh and paint anodes, in agreement with visual observations and odours. Chlorine evolution is thermodynamically impossible at a pure zinc anode, hence chloride removal would necessitate the formation of zinc oxide/chloride complexes. Such complexes were identified by XRD in chapter 6, in which it was noted that copious zinc hydroxide chloride “warts” formed within the zinc coating of specimens containing 2% chloride.

Chloride and sodium profiles for mesh anode specimens were complicated by the apparent addition of sodium chloride to the overlay, with sodium and chloride appearing to diffuse into the adjacent concrete substrate. The reduction of chlorides appeared greater within the overlay than the substrate, indicating that chlorine evolution was significantly higher at 50 mA/m<sup>2</sup> than 20 mA/m<sup>2</sup>. The diffusion of sodium ions from the overlay to the substrate appeared to increase under applied current. Sodium ions appeared to migrate away from the anode of anode Z specimens, increasing with increasing current density. These movements/reductions of alkali metal concentrations in the anode region were in agreement with a previous report of alkali metal depletion in the anode region (Sergi and Page, 1992). The sodium ion levels in anode P specimens were low compared to anode Z specimens and no trends were discernible. Similarly, potassium ions were present in small quantities in all specimens and no clear trends could be observed.

Obtaining pH measurements of powdered HCP, dissolved in water, appeared to be useful for comparisons of alkalinity. The alkalinity of the samples was generally related to the cement content, as indicated by the calcium ion concentration. Plots of the hydroxyl ion concentration, adjusted for the calcium ion concentration, indicated that a significant reduction was observed at the anode interface for specimen P:2:50:1. Current density had a reduced impact on alkalinity reduction within anode Z specimens, rather this appeared to be influenced by zinc oxide formation. Results for the mesh anodes were more difficult to interpret due to the different composition of the overlay and substrate and the apparent cross diffusion of species.

Zinc ion penetration of anode Z specimens decreased sharply with increasing distance from the anode surface, becoming negligible at the depth 6-8 mm, and decreased slightly with increasing current. Insoluble zinc hydroxide complexes forming at the anode interface, in rough proportion to the current density, may have limited penetration of zinc ions. Since the cathode region was not analysed, it was not possible to confirm a conclusion from Chapter 5 which indicated that zinc migration was accelerated by applied current.

## **8.6. Influence of CP on cement phases - DTA**

### **8.6.1. Introduction**

Concrete powder, obtained from profile grinding was analysed by differential thermal analysis, as described in Chapter 3. Two furnaces were used in the work which had different thermal characteristics, resulting in thermograms of differing slope. The magnitude and location of peaks were influenced by the powder packing density and mass of specimen. Although samples were prepared in a standardised way, some variation in peak temperatures was unavoidable. The furnace temperature and temperature variations were recorded by pen plotter which introduced a further margin of error into interpretation of results. Consequently, the actual traces could not be compared directly. The magnitudes of the peaks were determined taking account of the sloping base lines and the results are



summarised in figures 8.37 to 8.48, with average values for the relevant peak temperatures. In some cases, exothermal effects masked endothermal events making interpretation of the curves very difficult and subject to error.

The main peaks of the thermogram for hardened cement paste have been established from numerous studies (Ramachandran, 1969) and are presented in Appendix 3.6. The broad endothermal hump in the region 100-200 °C arises from the dehydration of the cement hydrates CSH and ettringite. The endothermal peak in the region 400-500°C is due to the dehydration of calcium hydroxide. The peak at 578°C is due to a phase transformation in quartz, which was present in the aggregate and a peak in the region of 800°C is due to the decomposition of calcium carbonate to carbon dioxide and calcium oxide. An exothermal trough from 800°C is due to devitrification of glassy phases.

The main intention of the DTA work was to relate possible cement phase changes due to the acid forming anode reactions with depth from the anode/concrete interface.

#### **8.6.2. Results and discussions**

As mentioned in the introduction, the DTA peak temperatures were averaged to remove experimental variability and facilitate results presentation. Positive values represent endothermal events and negative values exothermal events. The peak temperatures which represent CSH gel, calcium hydroxide, quartz, calcium carbonate (calcite) and the glassy phases were 160, 500, 575, 800/830, and 960°C respectively. These were generally observed for all specimens to varying magnitude. Small endothermal bumps at 740/750°C represent other crystalline forms of calcium carbonate, such as vaterite and aragonite, which were observed during neutralisation of cement paste in Chapter 6. The peaks relating to CSH gel tended to be broad humps and were not of great value. Although the specimens contained admixed calcium chloride, the product calcium chloroaluminate was not readily detectable from the DTA traces, possibly due to the dilution effect of the aggregate particles and masking by large exothermal peaks.

The thermograms for each anode material type will be considered separately and peak magnitudes only related by specimen.

#### 8.6.2.1. Anode Z

Figures 8.37 to 8.39 show an endothermal peak, particular to the zinc anodes, which was observed at around 405°C and may be due to the dehydration of a zinc/cement complex. The magnitude of this peak tended to decrease with depth from the surface, and decreased with increasing current density. These trends were in good agreement with the zinc ion profiles in figure 8.36, reported above. The calcium carbonate peaks at 830°C similarly decreased with distance from the surface, whilst the calcium hydroxide peaks at 500°C increased with depth from the surface. The reduction in calcium hydroxide in the surface 2 mm appeared to be independent of applied current and hence may be attributed to the formation of zinc oxide complexes. Peaks at 750°C relating to the vaterite form of carbonate can be seen in figures 8.38 and 8.39 for specimens Z:2:20:1 and Z:2:50:1. The relative intensity and the sample depth to which the peak was observed were greater at the higher current density. This suggests that hydroxyl ion removal destabilised the existing calcite, which underwent a transformation to the more micro-crystalline vaterite form.

#### 8.6.2.2. Anode P

Figures 8.40 to 8.42 indicate that an exothermal peak particular to the paint anodes was observed at around 350°C and may be due to the oxidation of elements of the chlorinated rubber paint. The peak was observed in all specimens and decreased significantly with distance from the surface, suggesting that the paint penetrated a depth of around 4 mm into the concrete surface. The 1 mm sample depth for the specimen P:2:0:1 was particularly affected by contamination of the paint, as indicated by the strong peak at 350°C in figure 8.40. A strong endothermal peak was observed at around 670°C, which appeared to be related to the surface layers of specimens rather than current density, although it was not clear to what event this was related. The calcium hydroxide peak at 500°C decreased towards the surface of the specimen P:2:20:1 and was absent at the surface 1 mm depth of specimen P:2:50:1, confirming that calcium hydroxide was the primary buffer against acidification. This finding correlated well with the low hydroxyl ion concentration for this



sample depth. The calcium carbonate also decreased towards the surface for specimen P:2:50:1, in contrast to the trend for the other paint and zinc specimens. This may also be attributed to progressive neutralisation. Vaterite peaks were not observed in any traces, which may be a reflection of higher acidity levels.

#### 8.6.2.3. Anodes E and T

The results for the mesh anodes will be considered together. Figures 8.43 to 8.48 show a strong exothermal peak at around 390°C which can be attributed to a constituent of the polymer modified overlay. An individual exothermal peak was also observed for specimen T:2:0:1 at 220°C, presumably due to a different constituent of the overlay. The relative intensity of the peaks did not decrease with current density, indicating that the polymer was unaffected by CP. It can be seen that samples at a depth of 1 mm tended to be contaminated by this constituent of the overlay, presumably due to the uneven substrate surface.

Low calcium hydroxide and high calcium carbonate levels in all samples at the 1 mm depth were indicative of carbonation prior to anode application. Calcium hydroxide levels appeared to be lower in the overlay than in the substrate in figures 8.43, 8.46, 8.47 and 8.48, at variance with the hydroxyl ion profiles reported earlier in this chapter. This may be due to the 390°C exothermal event causing error in the interpretation of the thermograms. The carbonate level was higher in the overlay than in the bulk of the substrate concrete and the broadening of the calcite peak in polarised specimens, as indicated by extra peaks at 740°C, was characteristic of neutralisation processes.

#### 8.6.2.4. Weight loss during DTA

Figures 8.49 to 8.52 show the change in sample weights during the DTA test. The trend was for increased weight loss at the anode/concrete interface and in the overlay than in the concrete. This may be related to the different ratios of hydroxide to carbonate material at each depth, as shown in the previous DTA peak summaries. Carbon dioxide which evolved during decomposition of carbonates would be expected to have a greater mass than the water evolved from a similar volume of hydroxides, hence the higher weight loss. However, the variation in weight loss by weight of sample may simply be due to variation

of the cement/aggregate ratio; the calcium ion profiles reported in figures 8.9 to 8.12, which were related to the cement content, displayed similar trends. In addition, the organics present in overlay and anode P samples may have increased weight losses.

### 8.6.3. Conclusions

The thermograms for anode E, T and P specimens were influenced greatly by exothermal events due to oxidation of polymer additives/contaminants. The DTA method was unable therefore to provide a reliable analysis of the anode/substrate interfacial region. However, the DTA results were in general agreement with other results of the degradation processes at the anode interfaces. Carbonation was detected in the surface layer of all samples. Mesh anode CP reactions appeared to change the calcium carbonate structure from calcite to the vaterite form, in agreement with the neutralisation mechanism proposed in Chapter 6.

Various features were noted from the thermograms. The formation of zinc/cement complexes appeared to be characterised by an endothermal peak around 405°C. The quantity of this complex decreased with increasing current density and depth, in agreement with zinc ion profiles. Consumption of hydroxide appeared to destabilise the calcite form of calcium carbonate.

The cementitious overlay polymer content did not appear to be influenced by the applied current. Oxidation of the polymer was characterised by an exothermal peak at around 390°C. The magnitude of the large exothermal event at 350°C attributed to the paint binder indicated that the binder had penetrated the concrete substrate to a depth of around 4 mm, supporting a proposal to this effect in the earlier MIP section. An endothermal peak was observed at around 670°C which appeared to be a surface effect, unrelated to applied current. Specimen P:2:50:1 appeared to have suffered a high degree of acidification, with an absence of calcium hydroxide and reduction of calcium carbonate in the surface 2 mm.



## 8.7. General conclusions

The results set out in this chapter have highlighted the difficulty in obtaining quantitative information of physical/chemical changes which occur over a very short distance at the anode/substrate interface. The results, however, have generally supported the degradation mechanisms set out in Chapter 6.

Chemical and DTA analyses of samples from profile grinding at 2 mm incremental depths provided profiles of reasonable resolution. However, both methods had inherent problems which reduced the reliability of the results and made interpretation more difficult. In DTA, the presence of organics in the cementitious overlay and conductive paint distorted the thermograms. It should be noted that the quantity of overlay polymer did not vary, suggesting a resistance to acidification. This could be confirmed using FT-IR analysis, as described in Chapter 6. Ionic profiles for anodes T and E were complicated by apparent diffusion of various ions from the overlay to the substrate. MIP, which measures the bulk porosity, was shown to be inappropriate for this study since the anodic reactions only affected the immediate interfacial zone, of up to around 2 mm depth.

Petrographic examination of mesh anode thin sections appeared to be a good method for the early detection of anodic degradation surrounding mesh anodes. It was of less use for coating type anodes, where the likelihood of obtaining a section through a degraded region was lower and the main value was the determination of the coating thickness. A more quantitative examination of these specimens would have been achieved by the use of wider thin sections and a digitised image analysis system. A related technique which perhaps would have provided the best results is backscattered electron microscopy with EDXA/image analysis, in which microstructural gradients of porosity and paste composition are readily produced. A polished cross section of interest is placed in the SEM and the backscattered electrons collected and manipulated by computer, contrast being provided by atomic number variations within the sample (Scrivener and Pratt, 1987).

## **9. Chapter Nine. General conclusions and recommendations for further work.**

### **9.1. General Conclusions**

The CP anodes of interest were two activated titanium meshes, flame sprayed zinc and a conductive paint, termed E, T, Z and P respectively. A potentiodynamic polarisation study of each anode in simulated electrolytes, reported in Chapter 4, for which the conductive coatings were applied to glass microscope slides, suggested that the order of decreasing anode efficiency was anode  $T > E > P, Z$ . The mesh anodes T and E mainly evolved oxygen in saturated calcium hydroxide/chloride solutions. However, the oxygen reaction was severely inhibited in less alkaline solutions and significant current only passed by chlorine evolution. Reactions for anode P appeared to be based on oxygen evolution, although chlorides increased the electrical activity. Passivation type phenomena were noted in the less alkaline electrolytes, which could form the basis of further study. Self corrosion of anode Z was controlled by the electrolyte composition and the experimental set-up. Chlorides destabilised passive films, leading to considerably higher current densities.

The preceding results provided an indication of the likely reactions in bulk electrolytes during CP for each anode. For anodes in intimate contact with hardened cement paste, the movement of anodic reactants and products may be restricted by the cementitious pore structure. Concentration polarisation effects may result and the anode reaction products potentially change the electrolyte composition. The influence of anode material on ionic migration within cement during CP was therefore of interest.

The investigation reported in Chapter 5 was based on a previous study which determined ionic profiles within cement paste prisms by the analysis of pore solution obtained from cut sections. Conductive coatings were applied to each end of similar HCP prisms whilst mesh anodes were compressed and cast into modified prisms. Specimens were polarised



for periods of up to 2 years in a saturated state to facilitate later pore water extraction. Only qualitative results were obtained owing to experimental errors which resulted in poor current control and apparent leaching of free ions from the specimens. Characteristic S-shaped ionic profiles were not observed for this reason and chloride ion profiles were ambiguous. The minimum observed alkalinity in specimens was around pH 12.6 in anode regions, the buffering range of calcium hydroxide, hence chlorine evolution was unlikely for anode E and T specimens. The zero degradation observed for paste in contact with mesh anodes held at up to  $36 \text{ mA/m}^2$  (anode area) was unsurprising considering the high paste buffering capacity, whilst the high humidity environment proved too aggressive for the paint and zinc anodes. Increases in anodic overvoltages during the study were attributed to the reduced pH and ionic species concentrations, and suggested the same order of anode electrical efficiency as the potentiodynamic polarisation study. Zinc ions were shown to migrate to the cathode region, where precipitation was possible at the ionic concentrations measured.

The four anodes were applied to concrete substrates of well defined composition in an investigation of operating characteristics and performance, as described in Chapters 6, 7 and 8. A total of 42 concrete slabs were produced with calcium chloride contents of 0%, 0.4%, 2%, and 4 % (weight cement) with two qualities of curing. Of these, 25 slabs were polarised at current densities of  $20 \text{ mA/m}^2$  or  $50 \text{ mA/m}^2$  (concrete area) ( $107$  to  $390 \text{ mA/m}^2$  mesh anode area) and the remainder acted as controls or were used for specimen characterisation. Three reinforcement bars placed at varying depths ensured anode degradation took place within the time scale of the study as a result of current concentration. Anode meshes T and E were embedded in a proprietary cementitious mortar. Specimens were exposed externally with anode face uppermost. The electrical results confirmed the same order of anode efficiency as observed in the two laboratory studies of anode  $T > E > P > Z$ . In all cases, anodic degradation was accelerated at the higher current density, this factor being more influential than any other.

Flame sprayed zinc formed a strong, intimate bond with a lightly grit blasted concrete substrate. A progressive failure mechanism for zinc anodes was deduced, which will be useful in future appraisal of zinc CP systems. With zero CP current applied, very slow corrosion at the zinc/substrate interface occurred with the formation of a complex white crystalline zinc hydroxide based corrosion product, sometimes called white rust. This appeared as a glassy layer approximately 200  $\mu\text{m}$  deep in a thin section and appeared to generate an endothermal peak at around 405°C during DTA. Under CP, the intimate bond between zinc and concrete diminished as white rust formation was accelerated in relation to the applied current, even a short period at 50  $\text{mA}/\text{m}^2$  (concrete area) resulting in accelerated degradation. The white rust behaved as an insulator, significantly increasing the anode resistance and in time caused the zinc to progressively lift away from the substrate. Circuit resistances varied with the coating moisture level such that the galvanostat was unable to supply the required current at the maximum available driving voltage for various periods. Where the zinc was applied to concrete with a high chloride content, in this case 2% calcium chloride (by weight cement), the zinc hydroxide layer was subjected to chloride pitting attack. This resulted in the formation of small grey surface deposits of main composition zinc hydroxide chloride, called “warts” owing to their appearance and mode of growth. Wart growth was influenced by the current density magnitude and distribution, with larger specimens adjacent to the primary anode. The most critical factor however appeared to be the chloride/hydroxyl ion ratio at the anode interface, which was probably enhanced by CP induced chloride ion migration from the cathode. Anodic degradation tended to be confined to the zinc itself, with minimal impact on the concrete substrate. DTA and chemical analyses of profile ground samples indicated that migration of soluble zinc into the substrate was limited to approximately 4 mm depth, although the concentration in the cathode region was not measured. At the lower current density of 20  $\text{mA}/\text{m}^2$ , a high chloride content appeared beneficial to anode operation. However, the trend towards increasing degradation for this specimen and the separate observations of a Taywood specimen in appendix 6.4 indicate that a current density of 20  $\text{mA}/\text{m}^2$  may be too high for the long term durability of zinc coatings to be ensured.



The conductive paint similarly formed a strong bond with concrete which increased with time. The organic paint binder was observed to stain the surface cement layers orange to a depth of around 1 mm, although DTA and MIP results indicated that the maximum binder penetration depth was actually around 4 mm. Coating degradation was observed at discreet locations and particularly adjacent to the primary input and took the form of large surface blisters, micro bubble clusters, blackening and cracking. At these locations the interface environment was acidic with softening and consumption of cement paste, aggregate cracking and reduced coating adhesion. Acidification resembled established carbonation processes with progressive dissolution of cement phases, but to a very shallow depth as indicated by petrography, DTA and alkalinity comparisons. Bleaching of the masonry paint as a result of hypochlorite formation often preceded significant degradation. Damage to the coating was slightly greater on substrates of high chloride content and at the higher 50 mA/m<sup>2</sup> current density, although high primary anode degradation may have shielded other areas. Circuit voltage results were inconclusive owing to high environment induced resistances. Evidence that low current levels altered the paint coating structure was provided by increases of coating resistance and FT-IR spectra which indicated binder oxidation. Specimen surfaces were considered reasonably uniform with regard to chloride and moisture distributions and the random degradation sites could not be predicted from down-coating voltage measurements, or a specific degradation mechanism deduced. However, the chlorine based anode reactions appeared to be more aggressive than self corrosion of the carbon filler, which suggests that a limit on the substrate chloride content to which a paint anode is applied may extend the coatings' life. Micro and macro bubble formation were probably related to coating impermeability. A longer period for solvent evaporation between coating applications than the 24 hours followed in this work would result in a more micro-porous paint and possibly improve gas transport.

Differences between the degradation mechanisms for anodes E and T could not be readily distinguished. Degradation was largely confined to the cementitious overlay around the

anode strand and was influenced by current density, the substrate chloride content and proximity to the cathode bars. As for anode P, the degradation mechanism resembled progressive carbonation with sequential dissolution of cement phases in the order sodium/potassium hydroxide, calcium hydroxide and then CSH gel and other phases. Eventually complete annuli of approximate diameter 3 mm were formed. Calcite and vaterite were precipitated in pores up to 5 mm from anode strands from an early stage in all polarised specimens, decreasing the porosity in this region. Portlandite crystals (calcium hydroxide) were also detected in macro pores within the 5 mm affected zone. Complete annuli were observed after only 3 months at 50 mA/m<sup>2</sup> (concrete area) which suggests that high commissioning current densities are not conducive to long term durability. The bond between the overlay and substrate was reduced by anode degradation, as related to increasing current density, although the lowest measured values exceeded the minimum overlay bond strength suggested by some workers. When considered with visual observations, the circuit voltage results indicated that both mesh anodes evolved oxygen as the main CP reaction so long as the pH of adjacent overlay remained buffered by calcium hydroxide, in agreement with the laboratory study findings. The results demonstrated that although one mesh anode may be more electrically efficient than another, the propensity for oxygen evolution in normally alkaline cement paste meant that the rate of anode degradation was controlled by the applied current density. Theoretically, by increasing the current density, the anodic hydroxyl ion consumption would eventually exceed the rate of hydroxyl ion replenishment and the rate of neutralisation would then be controlled by the overlay buffering capacity. This suggests that the most desirable overlay property is a high alkali content. Chlorine evolution became thermodynamically favoured as acidification progressed and was indicated by reduced chloride levels and detection of the characteristic bleach odour. At 20 mA/m<sup>2</sup>, increasing the substrate chloride content reduced the rate of overlay deterioration, suggesting that the less aggressive chlorine based reactions depended on free chloride availability. Although the overlay had a high total chloride content, it is likely that a significant proportion of this was bound rather than free chloride owing to the high cement content. A high overlay chloride content would seem desirable to improve



conductance and limit anodic oxygen evolution and it may be advantageous to use a cementitious overlay of low  $C_3A$  content to maximise the free chloride levels. Of course, encouragement of chlorine evolution may not be environmentally acceptable, depending on the structure location and purpose.

To summarise, the degree of anodic degradation for mesh and conductive paint anode systems depended on two main factors; the current density, which controlled the rate of acid production; and the buffering capacity of the cementitious overlay or substrate, which controlled the rate of neutralisation. The rate of zinc anode degradation depended primarily on the current density and secondly on the substrate alkalinity and chloride content. Sustained CP at high current densities of  $50 \text{ mA/m}^2$  (anode area) for conductive coatings and more than  $250 \text{ mA/m}^2$  (anode area) for activated titanium mesh anodes led to rapid anodic degradation. However, high degradation rates also occurred at “normal” current densities for some specimens as a result of current concentration or substrate composition. Although the anodes displayed different electrical efficiencies, this did not necessarily translate into different degradation rates and levels of reinforcement polarisation were generally similar.

#### **9.1.1.1. A critique of anode inspection methods**

A close visual inspection was the most successful method for appraisal of anode P specimens and provided useful results for anode Z. The down coating voltage drop measurements for anode P appeared a useful measure of degradation in the primary anode region and located “hot spots” once they had formed. The conductive coating pull-off adhesion strength test appeared reliable and provided convenient failure surfaces for detailed examination. Petrographic examination of thin sections was of less value, other than for an accurate determination of coating thickness. FT-IR analysis of anode P samples appeared promising as a means of quantifying binder oxidation. Small bubbles and delaminations of zinc and paint coatings were detected aurally by lightly brushing the surface.

Visual inspection of mesh anodes was of little use, other than to check for overlay cracking. Non-destructive assessment of anodic degradation using the Pundit apparatus was unsuccessful. Small diameter cores were readily obtained and minimised specimen damage; anode efficiency was not significantly affected due to the meshes high electrical redundancy. The cores obtained were used for more detailed observations and analyses. Petrographic examination of anode mesh thin sections provided the clearest indication of progressive cement paste neutralisation, although care would be required in obtaining representative samples. The Limpit adhesion tester provided a more destructive measure of mesh anode/overlay performance and therefore may not be suitable for regular use.

Techniques such as profile grinding and MIP would probably not be suitable for regular inspection of CP anodes. A more powerful technique for periodic assessment of anode degradation would be back scattered electron microscopy of polished cross sections.

Variation of system voltage, taking into consideration environmental variations, reinforcement polarisation and erroneous sources of high resistance, provided a useful overview of anode performance for a constant current system. In practice, this would become less useful as the groundbed size increased.

## **9.2. Recommendations for further work**

The ionic migration investigation using cement paste prisms was shown to be subject to various experimental errors arising from the requirement for full specimen saturation over a long period. Alternative experimental arrangements were proposed in Chapter 5. Further studies in this area could be directed towards elucidating the current density at which chlorine evolution at an embedded mesh anode becomes significant. In addition, the embedded mesh anode cement prisms would be suitable for an investigation of ionic migration in cement pastes of varied water/cement ratios. This may also provide evidence of anodic concentration polarisation resulting from low porosity cement paste.



The CP trial demonstrated that all of the anode materials suffered degradation by various mechanisms, even at relatively low current densities, and it would seem advantageous to limit the applied current density where possible. Periodic interruption of current to extend anode life was advised by Heuzé (1965) however this idea has not been adopted, other than in the generally accepted view that 7 day depolarisation measurements as a part of system appraisal, or other short term interruptions, do no harm due to the “built in” protection. Perhaps as an extreme example, the zinc specimens held at 50 mA/m<sup>2</sup> in this study (Chapter 6) demonstrated that adequate polarisation could be maintained by periodic wetting. A pulse current cathodic protection system was considered for a tidal situation with discreet anodes supplying current twice a day for the duration of the high tide (Glass, 1991). The advantages would be reduced power consumption, extended anode life and minimisation of over protection. Clearly, it would need to be established that such a system provided adequate protection and a suitable study would accomplish this.

The influence of the original substrate alkalinity on zinc anode corrosion has not been addressed. In the present study, anodes were applied to young concrete with under 2 mm carbonation and therefore high alkalinity reserves near to the substrate/coating interface. CP trials in the US and Canada which report good zinc anode performance (Manning, 1990) may have used significantly carbonated concretes, where the interfacial alkalinity would remain low for a longer period after polarisation, presumably allowing a more stable zinc passive layer to form. In addition, where spalled concrete has been replaced, a substrate may consist of both carbonated/uncarbonated and high chloride/low chloride areas. A suitable study would investigate possible incompatibilities of zinc coatings with repaired substrates and determine the impact of substrate carbonation on zinc anode performance. A related study could investigate the performance of low alloyed zinc-cobalt coatings applied to concrete and in chloride electrolytes. A study of such coatings in alkaline solutions indicated improvements to the stability of the passive film (Bohe *et al*, 1992), which suggests that the durability of zinc coatings applied to uncarbonated concrete could be improved. Little work has been reported on protective coatings for zinc to extend

coating life in aggressive environments. The specification within Concrete Society TR36 (1989) allows for a decorative protective coat but does not indicate clearly how this will affect system performance. Chromate based surface wash treatments have been shown to increase the corrosion resistance of zinc coatings in aggressive environments including concrete (BRS Digest 109, 1969, Longo and Durmann, 1974, Swamy, 1990), hence it would be of interest to determine if such treatments improved zinc CP performance.

FT-IR analyses of conductive paint pull-off surfaces suggested that oxidation of the paint binder occurred at normal current densities. A suitable laboratory study would establish if the degree of oxidation was related to the charge passed and if this was accelerated by other factors such as the substrate chloride content. A standardised methodology could then be developed which would allow more quantitative analyses of pull-off samples than simple visual inspection as a part of a regular inspection procedures. A simpler alternative method could make use of the qualitative observation in Chapter 8 that the chloride content of the paint decreased during CP, that is, decomposition of the binder released chlorides.

Although the conductive paint generally performed well in this study, random degradation appeared unavoidable at normal current densities, in agreement with other CP trials. Modifications to the paint formulation therefore do not appear warranted and attention should be directed to application practices and primary current supply design to minimise coating failures.

The increased sensitivity of mesh anodes to environmental variations after the formation of annuli decreased the system efficiency. For new mesh anode systems it may be advantageous to limit moisture content variations and thermal effects by the application of a suitable coating, such as a masonry paint. Consideration should be given to possible anode repair strategies which fall short of entire replacement of the mesh/overlay system. It was noted that overlay shrinkage cracks filled with precipitated carbonates and it may be possible



to restore anode alkalinity by the application of an alkaline wash solution to the overlay surface, possibly mixed with sodium chloride.

Lateral micro-cracking was observed at the overlay/substrate interface of selected high current density specimens. It was considered that localised degradation of the cementitious overlay was unlikely to cause interfacial strains, rather these may have been induced by electro-osmotic forces. This phenomenon would be worthy of more detailed investigation to determine if it constitutes a risk to long term mesh anode performance at low current densities.

It is likely that a CP system in normal service would be subjected to continued salt contamination. This factor was not included in this study, and its influence on anode performance would be expected to be considerable, with possible improvements to mesh anode performance and deterioration of zinc and paint anode performances.

The durability research was performed on small individual specimens and did not consider mechanical stresses which may be expected for anodes applied to a dynamic structure or other phenomena which may influence anode performance such as freeze/thaw, workmanship during anode application, substrate surface preparation or thermal compatibility. These factors can only be effectively assessed in full scale trials.

## References

- Ali, M.G., Rasheeduzzafar, Al-Saadoun, S., S., "Migration of ions in concrete due to cathodic protection current", *Cement and Concrete Research*, Vol. 22, pp 79-94, 1992
- American Concrete Institute, Corrosion of metals in concrete, ACI 222R-85, Chairman, D. G. Manning, 1985
- Anderson, G. M., Sweeney, P. J., "Concrete deterioration and environmental exposure trials in Dubai, U.A.E", 3rd International conference: Deterioration and repair of reinforced concrete in the Arabian Gulf, Bahrain, Proceedings, Vol 1, pp 337 - 351, 21-24 October 1989
- Andrade, C., Castelo, V., Alonso, C., González, J. A., "The determination of the corrosion rate of steel embedded in concrete by the polarisation resistance and a.c. impedance methods", Editor Chaker, V., Special Technical Publication 906, American Society for Testing and Materials, Philadelphia, pp 43-63, 1986
- Andrade, C., González, J. A., "Quantitative measurements of corrosion rate of reinforcing steels embedded in concrete using polarisation resistance measurements", *Werkstoffe und Korrosion* 29, pp 515-519, 1978
- Andrade, C., Macias, A., Santos, P., Arteaga, A., Vazquez, A. J., "Corrosion behaviour of galvanised steel in concrete", CIRIA 2nd International conference deterioration and repair of reinforced concrete in the Arabian Gulf, Bahrain, Proceedings, Vol 1, pp 395-410, 1987
- Apostolos, J. A., "Cathodic protection of reinforced concrete by using metallized coatings and conductive paints", *Transportation Research Record* No. 962, pp 22-28, 1984
- Arup, H., "The mechanisms of the protection of steel by concrete", Corrosion of reinforcement in concrete construction, Ed. Crane, A. P., Chapter 10, The Society of Chemical Industry, Ellis Horwood Ltd, London, pp 151-157, 1983
- Ashworth, V., "Rebar corrosion and its control", Paper 1, presented at seminar on corrosion in concrete - Practical aspects of control by Cathodic Protection, London Press Centre, pp 1.1-1.15, 11 May 1987
- Ashworth, V., "Some basic design and operating parameters for cathodic protection", Paper 1, presented at Cathodic Protection - theory and practice, 2nd International conference, Moat House Hotel, Stratford upon Avon, England, no pagination, 26th - 28th June 1989
- ASTM, "Standard test method for half-cell potentials of uncoated reinforcing steel in concrete", ANSI/ASTM C876-87, American Society for Testing Materials, Philadelphia, 1987
- Bamforth, P. B., Pocock, D. C., "Minimising the risk of chloride induced corrosion by selection of concreting materials", Corrosion of reinforcement in concrete, Edited by Page, C.L., Treadaway, K. W. J., Bamforth, P. B., Society of Chemical Industry, pp 119-131, 1990
- Barnhart, R. A., Federal Highways Administration Memorandum, Washington, 1982



Benjamin, S.E., Sykes, J. M., "Chloride-induced pitting corrosion of Swedish iron in ordinary portland cement mortars and alkaline solutions: the effect of temperature", Corrosion of reinforcement in concrete, Edited by Page, C.L., Treadaway, K. W. J., Bamforth, P. B., Society of Chemical Industry, pp 59-64, 1990

Bennett, J. E., Martin, B. L., "The Elgard mesh system", Paper No. 5, Seminar on corrosion in concrete- Practical aspects of control by Cathodic Protection, London Press Centre, pp 5.1-5.18, 11 May 1987

Bennett, J. E., Mitchell, T. E., "Depolarization testing of cathodically protected reinforcing steel in concrete", Corrosion 89, Paper No. 373, Houston, Texas: NACE, 1989

Bennett, J. E., Shue, T. J., "Electrochemical chloride removal from concrete", Proc. N.A.C.E. Corrosion 90, Las Vegas, Paper 316, April 1990

Berke, N. S., "The use of Anodic polarisation to determine the effectiveness of Calcium Nitrite as an Anodic inhibitor", Corrosion effect of Stray currents and the techniques for evaluating corrosion of the rebars in concrete, ASTM STP.906; Ed. Chalker, V., American Society for Testing Materials, Philadelphia, pp 78-91, 1986

Biczok, I., "Concrete corrosion and concrete protection", 3rd Edition, Academia Kiado, Budapest, 1964

Bijen, J. M. J. B., "Maintenance and repair of concrete structures", Heron, Vol.34, No. 2, 82 pages, 1989

Bijen, J. M. J. B., "Alternatives for repair of chloride contaminated structures", Proceedings, CIRIA 2nd International Conference , Bahrain, 1987

Bingham, M., personal communication, 30th June 1991

Boam, K., "Impact of cathodic protection on civil engineering", Paper 22, presented at Cathodic Protection - theory and practice, 2nd International conference, Moat House Hotel, Stratford upon Avon, England, no pagination, 26th - 28th June 1989

Bohe, A. E., Vilche, J. R., Jüttner, K., Lorenz, W. J., Kautek, W., Paatsch, W., "An electrochemical impedance spectroscopy study of passive zinc and low alloyed zinc electrodes in alkaline and neutral aqueous solutions", Corrosion Science, Vol. 32, No. 5/6, pp 609-619, 1991

Broomfield, J. P., Geoghegan, M. P., Das, S. C., "Conductive coatings in relation to cathodic protection", Report No. 014H/85/2754, Taywood Engineering Limited, 345 Ruislip Road, Southall, Middlesex, UB1 2QX, England, January 1985

Broomfield, J. P., Langford, P. E., Ewins, A. J., "The use of a "potential wheel" to survey reinforced concrete structures", ASTM STP 1065, Ed. Berke, N.S., Chaker, V., Whiting, D., American Society for Testing Materials. Philadelphia, pp 157-173, 1990

Broomfield, J. P., Langford, P. E., McAnoy, R. M., "Cathodic Protection for Reinforced Concrete: Its application to Buildings and Marine Structures", Paper 142, Corrosion 87, Moscone Centre, San Francisco, California, 9-13 March 1987

Broomfield, J. P., "The determination of rates of highway bridge deterioration, rehabilitation and life cycle costing under the strategic highway research program" presented at Life Prediction of Corrodible Structures, 3rd NACE International Region Management Committee Symposium, Cambridge, UK, 23-26 September 1991



Browne, R. D., Geoghegan, M. P., Baker, A. F., "Analysis of structural condition from durability results", Corrosion of Reinforcement in Concrete Construction, Edited by Crane, A. P., Society of Chemical Industry, Ellis Horwood Ltd, London, Chapter 13, pp 193-222, 1983

BS 1881 Part 4: section 2: 1970 "Tests for compressive strength of test cubes", British Standards Institution

BS 2569 Part 1: 1964 (1988), "Protection of iron and steel by aluminium and zinc against atmospheric corrosion", British Standards Institution

BS 4550 Part 2: 1970, "Methods of Testing Cement", British Standards Institution

BS 4550 Part 2: Section 13.2: 1970, "Loss on ignition", British Standards Institution

BS 4550 Part 3: Section 3.4: 1978, "Strength Tests", British Standards Institution

BS 8110 Part 1: 1985, "Structural use of concrete. Code of practice for design and construction", British Standards Institution

BS, CP 1021: 1973 (1979), "Code of practice for cathodic protection", British Standards Institution

Building Research Station (BRS), "Zinc-coated reinforcement for concrete", Building Research Station Digest 109, HMSO, 8 pages, September 1969

Burns, C., "Effect of concrete moisture conditions on the adhesion of conductive paints and overcoat materials", Report ME-87-13, Ontario Ministry of Transportation and Communications, 1988

Chatalov, A. Y., "Effet du pH sur le comportement electronique des metaux et leur resistance à la corrosion", Doklad. Akad. Nauk S.S.S.R., Vol.86, pp 775-777, 1952

Clear, K. C., "Non-overlay cathodic protection systems", A manual for the corrosion control of bridge decks, Editor R.F. Stratfull, Report No. FHWA-CrEng-1, Chapter 11, pp 103-108, 1984, (Not issued for reasons of commercial bias)

Concrete Society, "Permeability testing of site concrete - a review of methods and experience", Technical Report No.31, August 1988

Concrete Society, "Repair of Concrete damaged by Reinforcement Corrosion- Report of a working party", Technical Report No.26, October 1984

Concrete Society, "Cathodic protection of reinforced concrete", Concrete Society /Corrosion Engineering Association Technical Report No.36, 1989

Concrete Society, "Model specification for cathodic protection of reinforced concrete", Concrete Society /Corrosion Engineering Association Technical Report No.37, 1989

Cox, L. D., "How does the 'spike' affect 'Instant-off' readings?", Materials Performance, Vol. 31, No. 1, pp 18-21, January 1992

Crundwell, R. F., "Sacrificial anodes - old and new", Paper 11, presented at Cathodic Protection - theory and practice, 2nd International conference, Moat House Hotel, Stratford upon Avon, England, no pagination, 26th - 28th June 1989

Das, S. P., Geoghegan, M. P., "Cathodic protection of reinforced concrete bridges: Report No. 1: Assessment of conductive coatings as possible groundbed materials", Report No.



014H/84/2603, Taywood Engineering Limited, 345 Ruislip Road, Southall, Middlesex, UB1 2QX, England, March 1984

Department of Transport, "Inspection and repair of concrete highway structures", Advice Note 35/90, HMSO, 1990

Dhir, R. K., Jones, M. R., McCarthy, M. J., "Measurement of reinforcement corrosion in concrete structures", *Concrete*, Vol. 25, No. 1, pp 15-19, January 1991

Eltech Systems Corporation, "Elgard data sheet- anode mesh", company literature, 1990

Epelboin, I., Gabrielli, C., Keddam, M., Takenouti, H., "The study of the passivation process by the electrode impedance analysis", *Comprehensive Treatise of Electrochemistry*, Vol.4, Electrochemical Materials Science, chapter 3, Ed. Bockris, J. O. , pp 151 - 192, Plenum Press, New York and London, 1981

Evans, T. E., "Mechanism of cathodic protection in sea water", Paper 10, presented at Cathodic Protection - theory and practice, 2nd International conference, Moat House Hotel, Stratford upon Avon, England, no pagination, 26th - 28th June 1989

Ewins, A. J., "Half-cell calibrations", Internal memorandum, Taywood Engineering Limited, 345 Ruislip Road, Southall, Middlesex, UB1 2QX, England, 13 April 1988.

Ewins, A. J., "Resistivity measurements in concrete", *British Journal of Non Destructive Testing*, Vol. 32, No. 3, pp 120-126, March 1990.

Feldman, R. F., "Pore structure damage in blended cements caused by mercury intrusion", *Journal of the American Ceramic Society*, Vol. 62, No. 1, pp 30-33, 1984

Figg, J.W., Marsden, A.F., "Development of inspection techniques for reinforced concrete: A state of the art survey of electrical potential and resistivity measurements for use above water level", *Concrete in the oceans technical report No. 10*, ref: OTH 84 205, Department of Energy, HMSO, 1985.

Fontana, M. G., "Modern theory - Principles", Corrosion Engineering, Third Edition, McGraw-Hill Book Co., Chapter 9, pp 445-504, 1986

Francis, P. E., "The revision of BSI code of practice on cathodic protection CP1021", Paper 7, presented at Cathodic Protection - theory and practice, 2nd International conference, Moat House Hotel, Stratford upon Avon, England, no pagination, 26th - 28th June 1989

Franquin, J., "The corrosion-protection of pre-stressed concrete pipes", pp 1-8, Grampian Press Ltd., December 1964

Funahashi, M., Bushman, J. B., "Technical review of 100 mV polarisation shift criterion for reinforcing steel in concrete", *Corrosion* Vol. 47, No. 5, pp 376-386, May 1991

Geoghegan, M. P., personal communication, 17 May 1989

Glass, G. K., "Cathodic protection", presented at a meeting of the Concrete Society, Birmingham Chamber of Industry and Commerce, Birmingham, England, 22 May 1991

González, J. A., Alonso, C., Andrade, C., "Corrosion rate of reinforcements during accelerated carbonation of mortar made with different types of cement", Corrosion of Reinforcement in Concrete Construction, Edited by Crane, A. P., Society of Chemical Industry, Ellis Horwood Ltd, London, Chapter 11, pp 159-174, 1983



González, J. A., Molina, A., Escudero, M. L., Andrade, C., "Errors in the electrochemical evaluation of very small corrosion rates. Part I: Polarisation resistance applied to corrosion of steel in concrete", Corrosion Science, 25, 1985

Gray, M. J., "Interactions between chlorides and carbon dioxide and reinforced concrete with special reference to City Centre Tower, Perth", Research Report No. 014H/85/2757 draft, Taywood Engineering Limited, 345 Ruislip Road, Southall, Middlesex, UB1 2QX, England, February 1985

Gurusamy, K. N., Geoghegan, M. P., "Corrosion monitoring of steel in concrete: Theory and practice", Corrosion of reinforcement in concrete, Edited by Page, C.L., Treadaway, K. W. J., Bamforth, P. B., Society of Chemical Industry, p 354, 1990

Hanawalt, "Powder Diffraction File, Hanawalt Method Search Manual Inorganic Compounds", 1978.

Hankins, P. J., Treadaway, K. W. J., MacMillan, G. L., "A study of the influence of concrete properties on reinforcement corrosion in Arabian Gulf conditions", 1st International conference, Deterioration and repair of reinforced concrete in the Arabian Gulf, Proceedings, Vol. 2. Bahrain Society of Engineers, Manama, pp 158-182, 1985

Hansson, C. M., "Comments on electrochemical measurements of the rate of corrosion of steel in concrete", Cement and Concrete Research, Vol.14, pp 574-584, 1984

Harco Corporation, "Platinum anodes", A manual for the corrosion control of bridge decks, Report No. FHWA-CrENG-1, Edited by Stratfull, R. F., Chapter 7, pp 72-79, February 1984

Hardon, R., G., "Technology of repair for corroded reinforced concrete", PhD Thesis, Aston University, England, 1989

Harrop, D., "A galvanostatic and potentiodynamic study of the corrosion behaviour of mild steel in saturated calcium hydroxide solution and embedded in mortar, in the presence of chloride ions", Note No. N116/77, Building Research Establishment, Department of the Environment, 1977

Hartt, W. H., "A critical evaluation of cathodic protection for pre-stressing steel in concrete", Corrosion of reinforcement in concrete, Edited by Page, C.L., Treadaway, K. W. J., Bamforth, P. B., Society of Chemical Industry, pp 515-524, 1990

Hausmann, D. A., "Steel Corrosion in Concrete", Materials Performance, No. 6, pp 19-23, Nov 1967

Heuzé, B., "Cathodic protection of steel in prestressed concrete", Materials Protection, Vol. 4, No. 11, pp 57-62, 1965

Hope, B. B., Ip, A. K. C., "Application of cathodic protection to prestressed concrete bridges", Report ME-87-01, Ontario Ministry of Transportation and Communications, March 1987

Humphrey, M. J., Lambe, R. W., "Cementitious overlays for anodes used in cathodic protection of reinforced concrete", CIRIA 3rd International Conference deterioration and repair of reinforced concrete in the Arabian Gulf, Bahrain, Proceedings, Vol 1, pp 289-308, 1989



Hunkeler, F., "Technical/Scientific interim report - Field tests", Swiss Society for Corrosion Protection, Corrosion Commission Seafeldstrasse 301, 1989

ICI Chemicals and Polymers Ltd., "Anode mesh for cathodic protection of steel reinforcement in concrete", company literature, reference CC/18916/1Ed/23/189, 1989

Jafar, M. I., Dawson, J. L., John, D. G., "Cathodic protection studies on steel in concrete", Corrosion of reinforcement in concrete, Edited by Page, C.L., Treadaway, K. W. J., Bamforth, P. B., Society of Chemical Industry, pp 525-536, 1990

John, D. G., Messham, M. R., "Design and specification of cathodic protection for reinforced concrete structures", paper 24, presented at Cathodic Protection - theory and practice, 2nd International conference, Moat House Hotel, Stratford upon Avon, England, no pagination, 26th - 28th June 1989

Keddum, M., Hugot-le-Goff, A., Takenouti, H., Thierry, D., Arevalo, M. C., "The influence of a thin electrolyte layer on the corrosion process of zinc in chloride-containing solutions", Corrosion Science, Vol.33, No.8, pp 1243-1252, 1992

Keer, J. G., Chadwick, J. R., Thompson, D. M., "Protection of reinforcement by concrete repair materials against chloride induced corrosion", Corrosion of reinforcement in concrete, Edited by Page, C.L., Treadaway, K. W. J., Bamforth, P. B., Society of Chemical Industry, pp 420-433, 1990

Kendell, K., Pithouse, K. B., "The Raychem flexible anode system", Seminar on corrosion in concrete- Practical aspects of control by Cathodic Protection, Paper 6, London Press Centre, pp 6.1-6.18, 11 May 1987

Kendell, K., Pithouse, K. B., "Field observations on the depolarisation assessment of C.P. systems for reinforced concrete, with an initial study of concrete in the anode vicinity", Proceedings Federation Europeenne de la Corrosion, 151<sup>eme</sup> Manifestation, Paris, 15 June 1988

King, P., - personal communication during site visit to Midland Links CP trial, Birmingham, UK, G. Maunsell and Partners, 1988

Kotowski, S., Busse, B., Bedel, R., "Cathodic protection of steel in concrete; Instructions for installation of Heraeus-Titanode, Qualification of the installation contractors and special advantages of Titanode from the point of view of the manufacturer", company literature, Heraeus Elektroden GmbH, Industriestrasse 7-9, 6463 Freigericht, Germany, pp 1-16, 1989

Kramer, O. R., "Feasibility of cathodic protection for reinforced concrete deck structure with two layers of reinforcing bar", CIRIA 3rd International Conference deterioration and repair of reinforced concrete in the Arabian Gulf, Bahrain, Proceedings, Vol 1, pp 255-269, 1989

Kroon, D., H., "Waveform analyser/pulse generator technology improves close interval potential surveys", Materials Performance, Vol. 29, No. 11, pp 18-21, November 1990

Lambert, P., "The corrosion and passivation of steel in concrete", PhD. Thesis, Aston University, England, 1983

Lambert, P., Page, C. L., Vassie, P. R. W., "Investigations of reinforcement corrosion. 2. Electrochemical monitoring of steel in chloride-contaminated concrete", Materials and Structures, Vol. 24, pp 351-358, 1991



Laser, D., Ariel, M., "The anodic behaviour of glassy carbon in acid solution. A spectroelectrochemical study", J. Electroanal. Chem., 52, pp 291-303, 1974

Lea, F. M., The chemistry of cement and concrete, Third edition, London, Edward Arnold, pp 727, 1970

Leek, D. S., Poole, A. B., "The breakdown of the passive film on high yield mild steel by chloride ions", Corrosion of reinforcement in concrete, Edited by Page, C.L., Treadaway, K. W. J., Bamforth, P. B., Society of Chemical Industry, pp 65-73, 1990

Lewis, D. A., "Cathodic protection of reinforced concrete - A 1989 view", CIRIA 3rd International Conference deterioration and repair of reinforced concrete in the Arabian Gulf, Bahrain, Proceedings, Vol 1, pp 241-253, 1989

Lewis, D. A., Boam, K. J., "Cathodic protection of reinforced concrete", CIRIA 2nd International Conference deterioration and repair of reinforced concrete in the Arabian Gulf, Bahrain, Proceedings, Vol 1, pp 79-97, 1987

Locke, C. E., Dehghanian, C., Gibbs, L., "Effect of impressed current on bond strength between steel rebar and concrete", paper No. 178, Corrosion 83, Anaheim, California, April 18-22, 1983

Longo, F. N., Durmann, G. J., "Corrosion prevention with thermal sprayed zinc and aluminium coatings", Proc. Int. Congr. Marine corrosions and fouling. 3rd Meeting date October 1972. Edited by Acker. R.F, pp 158-175, 1974

Lynes, W., "Some historical developments relating to corrosion", Journal of the Electrochemical Society, 98, 3C, 1951

Manning, D. G., "Cathodic protection of concrete highway bridges", Corrosion of reinforcement in concrete, Edited by Page, C.L., Treadaway, K. W. J., Bamforth, P. B., Society of Chemical Industry, pp 486-497, 1990

Manning, D. G., Clear, K. C., Schell, H. C., "Cathodic protection of bridge substructures: Burlington Bay Skyway test site, design and construction phases", Transportation Research Record No. 962, pp 29-37, 1984

Martin, B. L., Bennett, J. E., "An activated Titanium mesh anode for the cathodic protection of reinforced concrete", Corrosion/87, Paper 147, NACE, Houston, Texas, 1987

McAnoy, R. P., Broomfield, J. P., Das, S. C., "Cathodic Protection - a long term solution to chloride induced corrosion ?", Proceedings of 2nd International conference on structural faults and repair: Structural faults '85, Ed. Forde, M. C., Topping, B. H. V., pp 349-365, 1985

McAnoy, R. P., Palmer, R.A., Langford, P. E. "Cathodic Protection of Reinforced Concrete Structures - Experience in the UK; Hong Kong and Australia", CIRIA 2nd International conference deterioration and repair of reinforced concrete in the Arabian Gulf, Bahrain, Proceedings, Vol 1, pp 121-137, 1987

McKenzie, M., "Cathodic protection of reinforced concrete bridges", Construction Maintenance and Repair, pp 170-174, July/August 1990

Micrometrics, "Instruction manual, poresizer 9310, V1.05", Micrometrics Instrument Corporation, Georgia, USA, pp II: 4-30, 30 June 1988

Midgley, H. G., Illston, J. M., "The penetration of chlorides into hardened cement pastes", Cement and Concrete Research, Vol 14, pp 546-553, 1984



Moorland, P. J., Howell, K. M., "Impressed current anodes, old and new", Paper 15, presented at Cathodic Protection - theory and practice, 2nd International conference, Moat House Hotel, Stratford upon Avon, England, no pagination, 26th - 28th June 1989

Mussinelli, G., Tettamanti, M., Pedferri, P., "The effect of current density on anode behaviour and on concrete in the anode region", CIRIA 2nd International conference deterioration and repair of reinforced concrete in the Arabian Gulf, Bahrain, Proceedings, Vol 1, pp 99-120, 1987

Naish, C. C., Harker, A., Carney, R. F. A., "Concrete inspection: Interpretation of potential and resistivity measurements", Corrosion of reinforcement in concrete, Edited by Page, C.L., Treadaway, K. W. J., Bamforth, P. B., Society of Chemical Industry, pp 314-332, 1990

National Association of Corrosion Engineers (NACE), "Cathodic protection of reinforcing steel in concrete structures", National Association of Corrosion Engineers, Standard RP0290-90, 1990

National Association of Corrosion Engineers (NACE), "Design considerations for corrosion control of reinforcing steel in concrete structures", Standard RP0187-90, National Association of Corrosion Engineers, 1990

National Association of Corrosion Engineers (NACE), "Maintenance and rehabilitation considerations for corrosion control of existing steel reinforced concrete structures", National Association of Corrosion Engineers, Standard RP0390-90, 1990

National Cooperative Highway Research Program (NCHRP), Report 278, 1985

National Reinforced Concrete Cathodic Protection Association (NRCCPA), "The design, installation, and evaluation of conductive coating cathodic protection systems for reinforcing steel in concrete", guide-line specification, initial issue, Downsview, Ontario, 15 March 1990

Neville, A.M., "Properties of concrete", Pitman, 1977

Nicolet, Theory of fourier transform infra-red spectroscopy, P/N 269-721903, Technical Publications Department, Nicolet Analytical Instruments, 5275-1 Verona Road, PO Box 4508, Madison, USA, July, 1986

Nuiten, P., "Successful cathodic protection of 288 Dutch balcony elements", Construction Maintenance and Repair, July/August, pp 178-181, 1990

Oronzio de Nora S.A., "Lida - activated titanium anode net for cathodic protection of steel in concrete", company literature, 1987

Page, C. L., Lambert, P., "Kinetics of oxygen diffusion in hardened cement pastes", Journal of Material Science, No. 21, 1986

Page, C. L., "Mechanisms of corrosion protection in reinforced concrete marine structures", Nature, Vol 258, No.5535, pp 514-515, 11 Dec 1975

Page, C. L., personal communication, 25 January 1988

Page, C. L., Treadaway, K. W. J., "Aspects of electrochemistry of steel in concrete", Nature, Vol. 297, No. 5862, pp 109-115, 1982



Palmer, R. A., Bradley, S. J., "Woolaston water tower evaluation of coating degradation", Report No. 014H/89/4085, Taywood Engineering Limited, 345 Ruislip Road, Southall, Middlesex, UB1 2QX, England, 11 August 1989

Palmer, R. A., "Mesh and Zinc Anode Trial", Technical note No. 1735, Taywood Engineering Limited, 345 Ruislip Road, Southall, Middlesex, UB1 2QX, England, 26 June 1987

Palmer, R. A., "Woolaston water tower cathodic protection trial: installation, commissioning and initial monitoring", Report No. 014H/86/3030, Taywood Engineering Limited, 345 Ruislip Road, Southall, Middlesex, UB1 2QX, England, 8 August 1986

Palmer, R. A., "Woolaston water tower. Cathodic protection repair. Feasibility study", Report No. 014H/88/3859, Taywood Engineering Limited, 345 Ruislip Road, Southall, Middlesex, UB1 2QX, England, 1 July 1988

PARC, Model 342 Softcorr Corrosion Measurement Software. Preliminary Operating Manual, EG&G, Princeton Applied Research Corporation, 1986

Pedefferri, P., Mussinelli, G. L., Tettamanti, M., "The use of mixed metal oxide activated net for cathodic protection of steel in concrete: Laboratory and field experience", CIRIA 3rd International conference, Deterioration and repair of reinforced concrete in the Arabian Gulf, Bahrain, Proceedings, Vol 1, pp 271-287, 1989

Pitts, J., "The role of petrography in the investigation of concrete and its constituents", Concrete, pp 5-7, July 1987

Polland, J. S., Page, J. A., "Investigation of chloride migration in reinforced concrete under application of cathodic protection", Report No. ME-87-11, Ontario Ministry of Transportation, May 1988

Pourbaix, M. P., Atlas of electrochemical equilibria in aqueous solutions, translated from the French by J. A. Franklin, Pergamon Press, New York, 1966

Pratt, C., "Chloride ingress into concrete", Technical note No. 1811, Taywood Engineering Limited, 345 Ruislip Road, Southall, Middlesex, UB1 2QX, England, 16 August 1988

Preece, C. M., Grønvold, F. O., Frølund, T. "The influence of cement type on the electrochemical behaviour of steel in concrete", Proceedings: Corrosion of reinforcements in concrete construction, Society of Chemical Industry, London, pp 393-417, June, 1983

Pullar-Strecker, Corrosion damaged concrete- assessment and repair, CIRIA, Butterworths, 1987

Ramachandran, V. S., Applications of DTA in cement chemistry, Chemical Publishing Company Inc., New York, 1969

Randin J. P., "Non metallic Electrode Materials", Comprehensive treatise of electrochemistry, Vol.4, Electrochemical materials science, Chapter 10, Ed. Bockris, J. O., pp 473-537, Plenum Press, New York and London, 1981

Roberts, M. H., "Carbonation of concrete made with dense natural aggregates", Information Paper 6/81, Building Research Establishment, Watford, England, April 1981

Robinson, R. C., "Concrete for corrosion control of steel", Proceedings 2nd Western States corrosion seminar, pp 108-120, 1968



Robinson, R.C., "Design of reinforced concrete structures for corrosive environments", *Materials Protection and Performance*, Vol.11, No. 3, pp 15-19, 1972

Rosa, E. B., Mc.Collum, B., Peters, O. S., "Electrolysis in Concrete", *Technologic Papers of the Bureau of Standards*: No.18, Washington Government Printing Office, 19 March 1913

Sagoe-Crentsil, K. K., Glasser, F. P., "Analysis of the steel:concrete interface", Corrosion of reinforcement in concrete, Edited by Page, C.L., Treadaway, K. W. J., Bamforth, P. B., Society of Chemical Industry, pp 74-86, 1990

Sauman, Z. "Carbonization of porous concrete and its main binding components", *Cement and Concrete Research*, Vol.1, No.6, pp 645-662, 1971

Schell, H. C., "Cathodic protection of reinforced concrete highway structures in Ontario", paper presented at U.K. Corrosion '87, Brighton, England, pp 49-72, 26-28 October 1987

Schell, H. C., Manning, D. G., Clear, K.C., "Cathodic protection of bridge substructures: Burlington Bay Skyway test site, initial performance of systems 1 to 4", *Transportation Research Record* 962, pp 38-50, 1984

Schell, H. C., Manning, D. G., "Evaluating the performance of cathodic protection systems on reinforced concrete bridge substructures", Paper 263, *Corrosion 85*, NACE, Sheraton Hotel Hynes Auditorium, Boston, Massachusetts, pp 1-12, 1985

Schell, H. C., Manning, D. G., Pianca, F., "A decade of bridge deck cathodic protection in Ontario", Paper 123, *Corrosion 87*, NACE, Moscone Centre/ San Francisco, California, pp 123/1-123/13, 1987

Scrivener, K. L., Pratt, P. L., "The characterisation and quantification of cement and concrete microstructures", *RILEM 1st International Congress*, Palais des Congrès, Versaille, Paris, pp 61-68, 7-11 September 1987

Sergi, G. Short, N. R., Page, C. L., "Corrosion of galvanised and galvanized steel in solutions of 9.0 to 14.0", *Corrosion*, Vol 41, No. 11, pp 618-628, 1985

Sergi, G., "Corrosion of steel in concrete: cement matrix variables", PhD. Thesis, Aston University, England, June 1986

Sergi, G., Page, C. L., "The effects of cathodic protection on alkali-silica reaction in reinforced concrete", *Transport Research Laboratory Contractor Report* No. CR310, April 1992

Sergi, G., Page, C. L., Thompson, D. M., "Electrochemical induction of alkali-silica reaction in concrete", *Materials and Structures*, Vol. 24, pp 359-361, 1991

Short, N., personal communication, Aston University, Birmingham, England, 9.7.90

Showan, A. M., Wyatt, B. S., "Corrosion damaged concrete; Assessment and Repair", *CCEJV Task Group* E4-9, 1987

Shreir, L. L., "Electrochemical principals of corrosion - a guide for Engineers", Department of Industry, 1982

Shreir, L. L., Hayfield, P. C. S., "Impressed current anodes", Cathodic protection: Theory and practice, Editors: Ashworth, V. and Booker, C. J. L., Chapter 6, pp 94-127, Ellis Horwood Ltd., Chichester, England, 1986



- Sibbick, R. G., personal communication, Aston University, 1992
- Slater, J. E., Lankard, D. R., Moreland, P. J., "Electrochemical removal of chlorides from concrete bridge decks", *Materials Performance*, pp 21-26, Nov 1976
- Stratfull, R. F., "Experimental cathodic protection of a bridge deck", *Transportation Research Record No. 500*, California Department of Transportation, pp 1-15, 1974
- Stratfull, R. F., "Criteria for cathodic protection of bridge decks", Corrosion of reinforcement in concrete construction, Edited by Crane, A. P., Society of Chemical Industry, Ellis Horwood Ltd, London, Chapter 18, pp 287 -332, 1983
- Stratfull, R. F., Noel, E. C., Seyoum, K., "Evaluation of cathodic protection (CP) criteria for the rehabilitation of Bridge decks", FHWA/RD-83/048, 1983
- Stratfull, R. F., "Progress report on inhibiting the corrosion of steel in a concrete bridge", *Corrosion*, 15, (6), 65, pp 331t-334t, 1959
- Swamy, R. N., "Resistance to chlorides of galvanized rebars", Corrosion of reinforcement in concrete, Edited by Page, C.L., Treadaway, K. W. J., Bamforth, P. B., Society of Chemical Industry, pp 586-600, 1990
- Taywood Engineering Limited (TEL), "Combating reinforcement corrosion with electro-chemical methods", Information sheet, Taywood Engineering Limited, 345 Ruislip Road, Southall, Middlesex, UB1 2QX, England, 1991
- Taywood Engineering Limited (TEL), "In-house test method - Measurement of water permeability", Taywood Engineering Limited, 345 Ruislip Road, Southall, Middlesex, UB1 2QX, England, 1988
- Thompson, D. M., "Concrete repair in highway bridges", Paper presented at a one day seminar on corrosion and deterioration in concrete organised by the Institute of Corrosion, Crest Hotel, Bristol, UK, 9 pages, 13 September 1991
- Thompson, D. M., "Effectiveness of repair of reinforcement corrosion in a motorway viaduct", CIRIA 3rd International Conference deterioration and repair of reinforced concrete in the Arabian Gulf, Bahrain, Proceedings, Vol 1, pp 157-171, 1989
- Thompson, M., Walsh, J. N., A handbook of inductively coupled plasma spectrometry, Blackie, Glasgow, 1983
- Treadaway, K. W. J., "The electrochemistry of concrete repair - the role of cathodic protection", Building Research Establishment, 1988
- Treadaway, K. W. J., Russell, A. D., "Inhibition of the corrosion of steel in concrete", *Highways and Public Works*, September 1968
- Tuutti, K., "Corrosion of steel in concrete", Swedish Cement and Concrete Institute, Stockholm, 1982
- Tvarusko, A., Bennett, J. E., "Practical aspects of cathodic protection of steel reinforcement in concrete with a proprietary activated titanium mesh anode" CIRIA 2nd International conference deterioration and repair of reinforced concrete in the Arabian Gulf, Bahrain, Proceedings, Vol 1, pp 139-154 , 1987
- Uhlig, H. H., Corrosion and corrosion control, Second edition, John Willey and Sons, New York, p 214, 1977



Vassie, P. R., "Concrete coatings: Do they reduce ongoing corrosion of reinforcing steel?", Corrosion of reinforcement in concrete, Edited by Page, C.L., Treadaway, K. W. J., Bamforth, P. B., Society of Chemical Industry, pp 456-470, 1990

Vogel, A., A textbook of quantitative inorganic analysis including elementary instrumental analysis, Fourth Edition, revised by Bassett, J., Denney, R. C., Jeffery, G. H., Mendham, J., Longman Scientific and Technical, England, 1978

Vrable, J. B., "Cathodic protection for reinforced concrete bridge decks", NCHRP Report 180, Transportation Research Board, 1977

Wallbank, E. J., "The performance of concrete bridges, a survey of 200 highway bridges", HMSO, London, April 1989

Washburn, E. W., "Porosity I. Purpose of investigation. II. Porosity and the mechanism of absorption", *Journal of the American Ceramic Society*, 4, pp 916-922, 1921

Weyers, R. E., Cady, D., "Cathodic protection of concrete bridge decks", *ACI Journal*, Nov-Dec 1984, pp 618-622, 1984

Whiting, D., Stark, D., "Galvanic cathodic protection for reinforced concrete bridge decks: Field evaluation. NCHRP Report No. 234, Transportation Research Board, National Research Council, Washington, D.C., pp 1-63, 1981

Wilkins, N. J. M., "Cathodic protection of concrete structures", Cathodic protection: Theory and practice, Editors: Ashworth, V., Booker, C. J. L., Chapter 9, Ellis Horwood Ltd., Chichester, England, pp 172-190, 1986

Wilkins, N. J. M., "Resistivity of concrete", Materials Development Division, AERE Harwell, ref: AERE-M3232, January 1982

Williams, D. H., Fleming, I., Spectroscopic methods in Organic Chemistry, 4th Ed., McGraw-Hill, Maidenhead, England, pp 29-62, 1987

Williams, G. D., - Statement regarding the temporary suspension and selective reinstatement of Thorotop CP material, Thoro System Products, 7800 NW 38th Street, Miami, Florida, 33166, 1 November 1989

Willis, A. D., "Cathodic protection of novel offshore structures", Paper 12, presented at Cathodic Protection - theory and practice, 2nd International conference, Moat House Hotel, Stratford upon Avon, England, no pagination, 26th - 28th June 1989

Wood, J. G. M., Wilson, J. R., Leek, D. S., "Improved testing for chloride ingress resistance of concretes and relation of results to calculated behaviour", CIRIA 3rd International Conference deterioration and repair of reinforced concrete in the Arabian Gulf, Bahrain, Proceedings, Vol 1, pp 427-441, 1989

Wyatt, B. S., "Cathodic protection of fixed offshore structures", Cathodic protection: Theory and practice, Editors: Ashworth, V. and Booker, C. J. L., Chapter 8, pp 143-171, Ellis Horwood Ltd., Chichester, England, 1986

Wyatt, B. S., "Anode systems for cathodic protection of reinforced concrete", Paper 23, presented at Cathodic protection - theory and practice, 2nd International conference, Moat House Hotel, Stratford upon Avon, England, no pagination, 26th - 28th June 1989

Wyatt, B. S., Irvine, D. J., "Cathodic protection of reinforced concrete using conductive coating anode systems", Seminar on corrosion in concrete- Practical aspects of control by cathodic protection, Paper No. 4, London Press Centre, pp 4.1-4.26, 11 May 1987

Wyatt, B. S., Wartecki, M., "Cathodic protection of reinforced concrete highway structures", Paper presented at a one day seminar on corrosion and deterioration in concrete organised by the Institute of Corrosion, Crest Hotel, Bristol, UK, 26 pages, 13 September 1991



## Appendix A

### **Appendix 3.1 The adjustment of mix water due to aggregate and admixture moisture content**

#### **1. Adjustment to mix water due to aggregate moisture**

Free water by weight aggregate,  $Y_a = X \times Z/100$

Adjusted value for mass X,  $X_a = X + Y_a$

Free water due to  $Y_a$ ,  $Y_b = Y_a \times Z/100$

Re-adjusted value for mass X,  $X_b = X_a + Y_b$

Total free water, to be subtracted from added water =  $Y_a + Y_b$

where

$Z$  = aggregate moisture content %

$X$  = mass of aggregate - fine or coarse

$Y$  = mass of water

#### Worked example

Sand moisture content (average of 3) = 5.4 %

Batch weight sand = 51.8 Kg (table 6.2)

$Y_a = 51.8 \times 5.4/100 = 2.797$  Kg

$X_a = 54.597$  Kg

$Y_b = 2.797 \times 5.4/100 = 0.151$  Kg

$X_b = 54.748$  Kg

Total free water to be subtracted =  $2.797 + 0.151 = \underline{2.948}$  Kg

#### **2. Adjustment to mix water due to admixtures**

##### Worked example

Atomic mass of  $\text{CaCl}_2 \cdot 2\text{H}_2\text{O} = 147.02$  g (Vogel, 1978)

Atomic mass of  $\text{CaCl}_2 = 111.02$  g

Atomic mass of  $2\text{H}_2\text{O} = 36$  g

For 2%  $\text{CaCl}_2$  (g/g cement)

Mass required =  $21.3 \times 0.02 = 0.426$  Kg

Mass  $\text{CaCl}_2 \cdot 2\text{H}_2\text{O}$  required =  $0.426 \times 147.02 / 111.02 = 0.564$  Kg

Mass of bound water =  $0.426 \times 36 / 111.02 = \underline{0.138}$  Kg

### Appendix 3.2 The calculation of hydroxyl ion concentration $[\text{OH}^-]$ / pH

#### HCP powder dissolved in water (used in Chapter 8)

For specimen Z:2:0:1, sample depth 1mm

$$\begin{aligned}\text{Mass powder} &= 0.487 \text{ g} \\ \text{Mass water added} &= 24.171 \text{ g} \\ \text{measured pH} &= 11.95 \\ \text{concentration}[\text{OH}^-] &= 10^{\text{pH}-14} \\ &= 8.91 \times 10^{-3} \text{ M/l} \\ &= 8.91 \times 10^{-3} \times 24.171 / 0.487 \\ &= \underline{0.44 \text{ mM/g sample}}\end{aligned}$$

#### $[\text{OH}^-]$ in pore solution by acid titration (used in Chapter 5)

For specimen PC, slice 3

$$\begin{aligned}\text{Volume pore solution} &= 0.1 \text{ ml} \\ \text{Molarity of acid} &= 0.01 \text{ M} \\ \text{Volume acid added} &= 0.7 \text{ ml} \\ \text{concentration}[\text{OH}^-] &= \text{Volume acid} \times \text{concentration} [\text{H}^+] / \text{volume of pore solution} \\ &= 0.7 \times 0.01 \times 1000 / 0.1 \\ &= 70 \text{ mM/l} \\ \text{pH} &= \log [\text{OH}^-] + 14 \\ &= \log [70/1000] + 14 \\ &= \underline{12.845}\end{aligned}$$

### Appendix 3.3 The calculation of evaporable and non-evaporable water content

The following equations were used in the determination of evaporable and non-evaporable water contents of hardened cement pastes. The derivation of these equations is given elsewhere (Lambert, 1983).

$$\text{Evaporable Water} = (M_0 - M_{105})(100 - i + a) / M_{950} \quad (\% \text{ g/g of unhydrated cement})$$

$$\text{Non-evaporable water} = (M_{105}(100 - i + a) - M_{950}(100 + a)) / M_{950}$$

where  $M_0$  = original mass of cement  
 $M_{105}$  = mass of cement at 105°C  
 $M_{950}$  = mass of cement at 950°C  
 $i$  = loss-on-ignition (% g/g of unhydrated cement)  
 $a$  = admixture content (% g/g of unhydrated cement)



### Worked example for specimen PC (Chapter 5)

Original mass of sample 2.0815 g  
 Mass of sample at 105°C 1.6669 g  
 Mass of sample at 950 1.3793 g  
 Loss on ignition (i) 0.4 % g/g  
 Addition of CaCl<sub>2</sub> 2.0 % g/g

Evaporable water =  $(2.0815 - 1.6669)(100 - 0.4 + 2.0)/1.3793$   
 = 30.54 %

Non-evaporable water =  $((1.6669(100 - 0.4 + 2.0) - 1.3793(100+2.0))/1.3793$   
 = 20.78 %

Total water =  $30.54 + 20.78$   
 = 51.32 %

ANODE	Ref.	Mass 105°C g	Mass 950°C g	Evaporable water %	Non-evaporable water %	Total water %
anode Z	ZA	1.8416	1.5121	30.23	21.74	51.97
	ZB	1.6221	1.3655	29.22	18.69	47.91
	ZC	1.8183	1.4987	29.80	21.27	51.07
anode T	TA	1.5418	1.2813	29.99	20.26	50.25
	TB	1.556	1.2796	30.03	21.55	51.58
	TC	1.5509	1.2908	27.69	20.07	47.76
	TD	1.7849	1.4703	28.82	21.34	50.16
anode E	EA	1.525	1.258	30.97	21.16	52.14
	EB	1.694	1.3896	30.53	21.86	52.39
	EC	1.6651	1.3797	32.11	20.62	52.73
	ED	1.7009	1.3704	29.89	24.10	54.00
anode P	PA	1.7592	1.4483	31.28	21.41	52.69
	PB	1.661	1.3224	30.78	25.62	56.40
	PC	1.6669	1.3793	30.54	20.78	51.32

**Table A3.3.1** Water contents of saturated HCP specimens (Chapter 5).

### Appendix 3.4 The calculation of chloride ion concentration

A calibration curve was plotted from chloride standards and a polynomial curve fitted to the data points. The equation of the curve was used to compute the chloride concentration using the net absorbance value. The calibration curve used in the calculations is shown in figure A3.4.1.

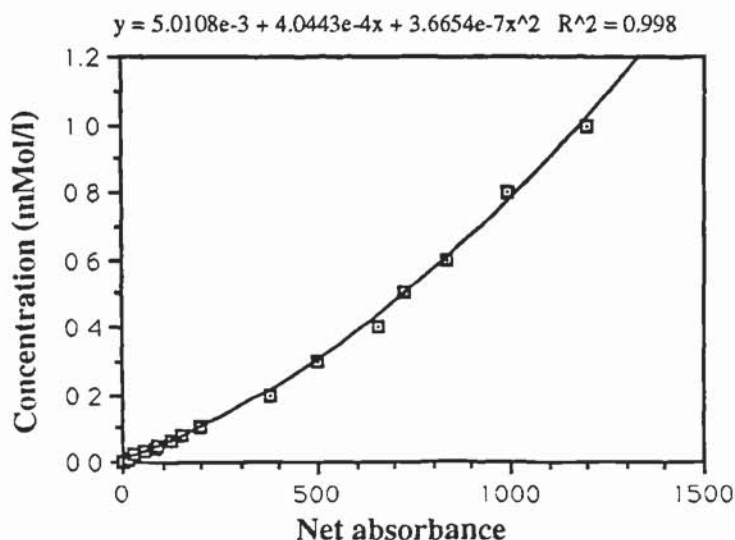


Figure A3.4.1 Chloride calibration curve.

#### Calculation of free chloride from pore solution samples (Chapter 5)

##### 1. Specimen PC, slice 3

Dilution factor = 100  
Absorbance value = 1286  
Blank value = 54  
Net absorbance = 1232

Calculated chloride concentration  $y = 1.05955$  mM/l

Pore solution chloride concentration = 106 mM/l

##### 2. Specimen TC, slice 1

dilution factor = 500  
Absorbance value = 463  
Blank value = 54  
Net absorbance = 409

Calculated chloride concentration  $y = 0.231732$  mM/l

Pore solution chloride concentration = 116 mM/l

#### Calculation of total chloride (acid soluble)

##### Specimen PC, concrete dust from the cutting of slices 3 to 4

Mass of flask = 19.551 g  
Mass of flask + sample = 19.904 g  
Mass of sample = 0.353 g



Need to correct the sample mass to mass at 950°C,

From table A3.3.1,  $M_{105} = 1.6669$   $M_{950} = 1.3793$

Corrected mass,  $M_s = 0.353 \times 1.3793 / 1.6669 = 0.292 \text{ g}$

Mass of acid added,  $M_a = 11.589 \text{ g}$

Dilution factor = 100

Absorbance value = 229

Blank = 53

Net absorbance = 176

Calculated chloride concentration  $y = 8.754 \times 10^{-2} \text{ mM/l}$

Concentration of total chloride/g sample =  $(y \times M_a) / (M_s \times 1000) = 0.347 \text{ mM/g}$

The concentration of chloride in dust from the cutting of slices 4 to 5 and 5 to 6, etc, were similarly computed. The concentrations were then apportioned to individual paste slices:

Dust from slicing	[Cl <sup>-</sup> ] mM/g sample	Slice reference	[Cl <sup>-</sup> ] mM/g sample
3 to 4	0.347	3	= 0.347
4 to 5	0.382	4	$= (0.347 + 0.382) / 2 = 0.364$
5 to 6	0.395	5	$= (0.382 + 0.395) / 2 = 0.388$
etc			
9 to 10	0.368	10	= 0.368

**Table A3.4.1** Computation of total chloride from dust samples.

In some cases the chloride content as a percentage of sample weight was required

Chloride concentration = total chloride x atomic mass Cl x 100/1000

=  $0.347 \times 35.453 \times 100 / 1000$

= 1.231 % sample

### Calculation of bound chloride

Need to convert free chloride from mM/l to mM/g sample

From table A3.3.1, evaporable water content,  $E_w = 30.54 \%$

Free chloride = free chloride x  $E_w / (100 \times 1000)$

=  $105.955 \times 30.54 / 100 \times 1000$

= 0.032 mM/g sample

Bound chloride = total chloride - free chloride

=  $0.347 - 0.032$

= 0.315 mM/g sample

### Calculation of expected chloride concentration [mM/g (concrete sample)]

The expected chloride concentration was calculated for comparison with measured values in Chapter 8 as follows:

### Assumptions

1. The non-evaporable water content ratio is equivalent to the average determined for the same OPC mixed with 2% CaCl<sub>2</sub>, as determined in Appendix 3.3; value = 21.46 %
2. Evaporable water is neglected from the calculation of concrete weight
3. Added CaCl<sub>2</sub> = 2% (wt. cement)
4. Chloride was evenly mixed throughout the cement paste and the cement/aggregate ratio was homogenous throughout the concrete.
5. Concrete composition was as given in table 6.2

### Calculation

$$\text{Added Cl}^- = 2 \times 71 / 111 = 1.28 \%$$

$$\text{Mass of non-evaporable water} = 330 \times 21.46 / 100 = 70.82 \text{ Kg/m}^3$$

$$\text{Mass of concrete (105°C)} = 330 + 980 + 802 + 70.82 = 2182.82 \text{ Kg/m}^3$$

$$\text{ratio mass of cement : mass of concrete (105°C)} = 330 / 2182.82 = 0.151$$

$$\text{chloride concentration} = 1.28 \times 0.151 = 0.194 \% \text{ (wt. concrete)}$$

$$= 0.194 \times 1000/100 \times 35.453 = \underline{0.055 \text{ mM/g}} \text{ (wt. concrete)}$$

### Accuracy of test method

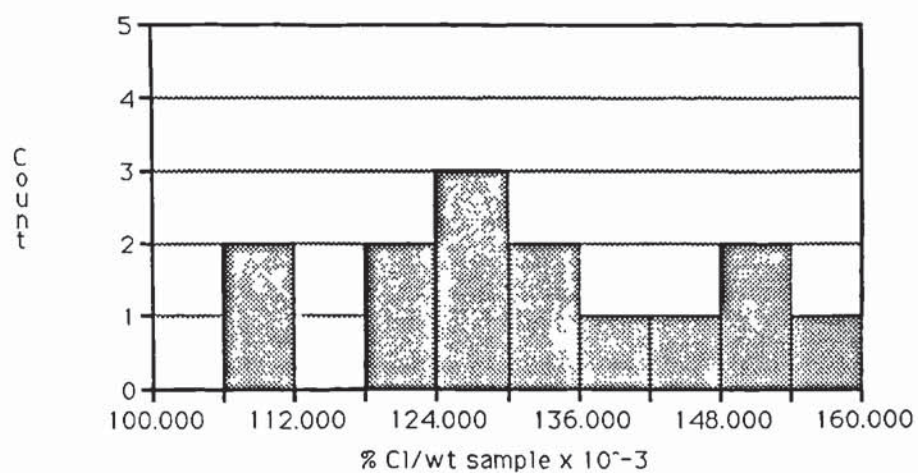
In order to determine the accuracy of the chloride analysis method, control samples were analysed in parallel with the specimens of interest. A powdered hardened cement paste (of known chloride content 0.13 %) was provided by Taywood Engineering Ltd. and used as the control sample.

Table A3.5.2 and the histogram in figure A3.5.2 show that there was a wide spread of values (0.108 % to 0.157 %), indicating relatively low precision. However, the mean of this control sample was 0.131%, that is, virtually identical to the known chloride content of 0.13 %. A t-test confirmed that there was a non-statistically significant difference between the control sample mean and the known value ( $T = 0.3417$ ,  $p > 0.1$ ). This indicates that the methodology used to test the samples of interest was satisfactory. However, the low apparent precision would be expected to influence the reliability of the chloride concentrations determined for concrete specimens in Chapter 8, whose values were only slightly higher than those of the control sample. Chloride concentrations determined for cement paste specimens in chapter 5 were approximately ten times higher than those measured for the control samples and the low precision would be less influential.



Determination number	Total Cl mM/l	Total Cl mM/g sample	Total Cl %/wt sample
1	3.88	0.0419	0.149
2	4.48	0.0432	0.153
3	3.65	0.0355	0.126
4	3.51	0.0363	0.129
5	3.65	0.0384	0.136
6	3.88	0.0416	0.147
7	2.97	0.0304	0.108
8	3.24	0.0372	0.132
9	3.97	0.0443	0.157
10	2.93	0.0340	0.121
11	2.61	0.0307	0.109
12	3.92	0.0373	0.132
13	2.97	0.0332	0.118
14	2.75	0.0349	0.124
<i>mean</i>	<i>3.46</i>	<i>0.0371</i>	<i>0.131</i>
<i>standard deviation</i>	<i>0.55</i>	<i>0.0044</i>	<i>0.016</i>

**Table A3.4.2** Chloride concentration of parallel control determinations.



**Figure A3.4.2** Histogram of control specimen Cl determinations.

## Appendix 3.5 The calculation of metal ion concentrations

### Metal ion concentration by ICP

The ICP apparatus produced a print out of metal ion concentrations in  $\mu\text{g/ml}$ . This value was converted to  $\text{mM/g}$  sample to allow comparisons between samples.

#### Worked example

For specimen Z:2:0:1(Chapter 8), Atomic mass of element calcium,  $A = 40.08 \text{ g}$

ICP value,  $X = 98.5 \mu\text{g/l}$

Volume 0.4 M HCl,  $V = 50 \text{ ml}$

Mass sample,  $M = 0.0548 \text{ g}$

$$\begin{aligned}\text{Concentration of metal (mM/g)} &= X \times V / 1000 \times M \times A \\ &= \underline{2.242 \text{ mM/g sample}}\end{aligned}$$

To establish the precision of the analysis, triplicate samples of the HCP powder of known 0.13 % chloride content and 35.9% CaO content were analysed in parallel with the other specimens:

Concentrations of Ca ( $\text{mM/g}$ ) = 7.18, 6.59, 7.11

Average value = 6.96  $\text{mM/g}$

$$\begin{aligned}\text{Average concentration of Ca (\% g/g)} &= 6.96 \times 40.08 \times 100 / 1000 \\ &= \underline{27.9 \% \text{ g/g sample}}\end{aligned}$$

### Flame spectroscopy

The pore solution contained relatively high alkali metal ion concentrations and it was necessary to determine calibration curves from standard solutions for sodium, potassium and zinc ions, as shown in figures A3.5.1, A3.5.2 and A3.5.3. A polynomial curve was fitted to the data points of each curve and the equation of the curve was used to calculate the ionic concentration from the intensity read from the spectrometer. The concentrations were lower for the acid soluble concrete samples and it was possible to rely on the linearity of the instrument at low concentrations up to 2ppm.

#### Worked examples

##### Pore solution (Chapter 5)

1. Sodium for specimen PC, slice 3

Atomic mass of element sodium,  $A=22.989 \text{ g}$

Maximum intensity 100 = 5 ppm

Dilution = 500

Measured intensity = 52

Concentration,  $y = 2.44 \text{ ppm}$

Metal concentration =  $y \times 500 / A = \underline{53.16 \text{ mM/l}}$



2. Potassium for specimen PC, slice 3

Atomic mass of element potassium,  $A = 39.098 \text{ g}$

Maximum intensity 100 = 20 ppm

Dilution = 500

Measured intensity = 70

Concentration,  $y$  = 12.64 ppm

Metal concentration =  $y \times 500 / A = \underline{161.69 \text{ mM/l}}$

3. Zinc for specimen ZC

Atomic mass of element Zinc,  $A = 65.38 \text{ g}$

Maximum intensity 0.161 = 1 ppm

Dilution = 50

Measured intensity = 0.006

Concentration,  $y$  = 0.04 ppm

Metal concentration =  $y \times 50 / A = \underline{0.03 \text{ mM/l}}$

Acid soluble (Chapter 8)

1. Sodium for specimen Z:2:0:1

Mass of acid = 11.589 g

Mass of sample = 0.93 g

Maximum intensity 40 = 1 ppm

Dilution = 500

Measured intensity = 7

Metal concentration =  $7 \times 1/40 = 0.175 \text{ ppm}$

$= 0.175 \times 500 \times 11.589 / 1000 \times 22.989 \times 0.93$

$= \underline{0.047 \text{ mM/g sample}}$

2. Potassium for specimen Z:2:0:1

Maximum intensity 80 = 1 ppm

Dilution = 500

Measured intensity = 26

Metal concentration =  $26 \times 1/80 = 0.325 \text{ ppm}$

$= 0.325 \times 500 \times 11.589 / 1000 \times 39.098 \times 0.93$

$= \underline{0.052 \text{ mM/g sample}}$

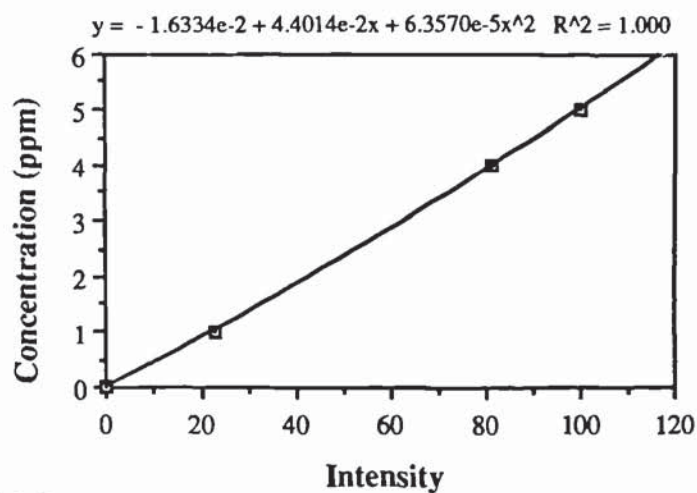


Figure A3.5.1 Calibration curve for sodium ions.

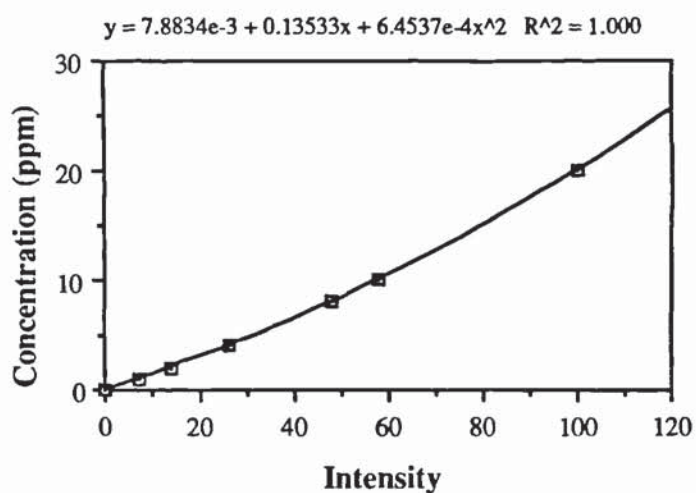


Figure A3.5.2 Calibration curve for potassium ions.

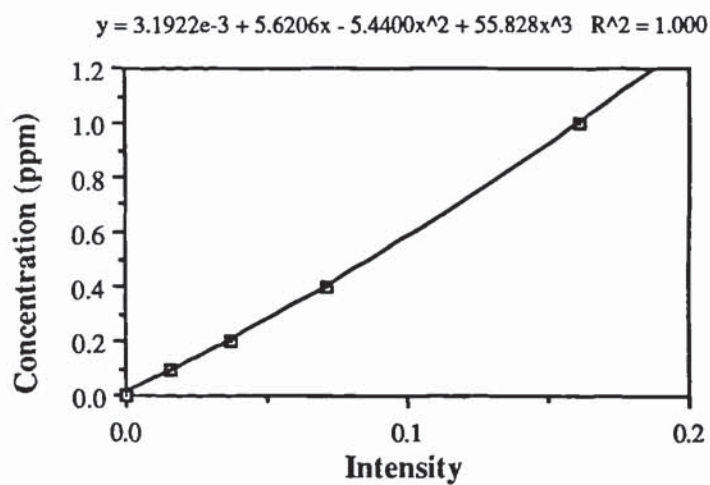
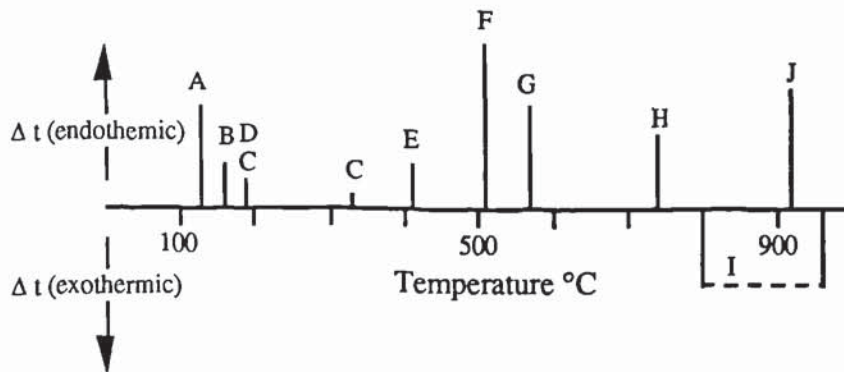


Figure A3.5.3 Calibration curve for zinc ions.



### Appendix 3.6 Characteristic peak temperatures for DTA thermograms



KEY (from Ramachandran, 1969)

A: C-S-H gel, 130°C - 140°C

B: Calcium aluminate trisulphate (Ettringite), 156°C

C: Calcium chloroaluminate, 190°C, 320 °C

D: Calcium aluminate monosulphate, 195°C

E: Zinc , 415°C

F: Calcium hydroxide, 515-590 °C

G: Quartz, 573°C

H: Vaterite, 735°C

I: Devitrification of Glassy phase

J: Calcite, 800°C-920°C

Figure A3.6.1 Schematic representation of characteristic DTA peak temperatures

### Appendix 3.7 Calculation of conductive coating resistance

A value for the conductive coating resistance was derived by dividing the measured voltage drop between the primary anode and an electrical probe by the applied current.

#### Worked examples

1. Specimen P:2:20:1, Month 3, location C1 (table 6.12)

Voltage drop = 16 mV

Applied current = 5 mA

Resistance =  $16 / 5 = \underline{3.2 \text{ ohms}}$

2. Specimen P:2:50:1, month 3, location C1 (Table 6.15)

Voltage drop = 53 mV

Applied current = 12.5 mA

Resistance =  $53 / 12.5 = \underline{4.2 \text{ ohms}}$

## **Appendix 3.8. The development and testing of a freeze-hold voltmeter**

### **Introduction**

This section describes the testing of a practical, hand-held instrument which was developed during this project for the quantitative measurement of transient potentials.

### **Previous Work**

The requirement for instant-off potential measurements was discussed in the literature review in Chapter 7, although little guidance is given in the literature as to the practicalities of the measurement. Large scale CP installations can be remotely controlled by a computer which may have the facility for automatic current interruption and subsequent potential decay monitoring (Ewins, 1990). In some cases, the potential values are obtained during the “off” cycle of the rectifier and this is confirmed with an oscilloscope (Stratfull, 1983). Similar automatic measurements of cathodically protected buried pipelines have been shown to be prone to variable potential spikes which influence the off-measurement (Kroon, 1990, Cox, 1992). However, this facility is often not available in laboratory work, or in the smaller CP trials with basic metering capability of circuit output voltage, output current and reference feedback voltages.

It has been suggested that meaningful measurements can be obtained in these instances by unskilled personnel, visually noting the first or second potential displayed on a hand-held high impedance digital volt meter (DVM) following current interruption by some means (NRCCPA, 1990, Bennett and Mitchell, 1990). Such remarkably crude measurements would appear to be common place in the CP industry and should be questioned regarding their reliability and repeatability. As mentioned in Chapter 7, potential measurements are sensitive to surges, which are related to the efficiency with which the polarizing current is switched off. In practice, operator error would be influential in selecting a potential within the 0.9 second period allowed for the measurement, and the actual time taken could amount to 3 to 5 seconds if power was disconnected manually (Geoghegan, 1989).

More specialised methods have been proposed for buried pipe CP, which may be appropriate for CP of reinforced concrete. Waveform/signal analysers allow the half-cell potential signal to be monitored and after the current is interrupted, the fast decay and potential surges are stored and plotted (Cox, 1992).

### **Experimental**

#### **Preliminary work**

Instant-off measurements using a digital oscilloscope with a store facility at the outdoor location of the CP trial were unsuccessful. The instrument had the capability to download digitised information to a data-logger, which unfortunately was unavailable. An



attempt was made to copy the resulting screen trace onto tracing paper directly, but this proved impossible. In the event, the oscilloscope failed to indicate variation in potential, was difficult to read in the sunny conditions and at best would only allow a measurement accuracy of  $\pm 20$  mV. It was not suitable for use in damp or cold conditions, hence the regularity of measurements was not guaranteed. It was clear therefore that the Taywood research laboratory did not have adequate equipment to allow instant-off potentials to be measured accurately under site conditions during the early part of this project.

In order to fulfill the need of the project for IR error-free potential measurements, an instrument was designed and assembled in-house which could be temporarily incorporated into a CP circuit and enable quantitative measurement of the instant-off potential. Features incorporated into the instrument were as follows:

- A fast, efficient power OFF switch
- An accurate measurement capability
- An ability to measure voltage at specific instants
- An ability to record and display the instant-off potential
- Ease of use and robustness, suitable for outside use
- A data logging facility, capable of down-loading to a PC
- An ability to follow the potential decay in units of milli-seconds, allowing the true decay curve to be measured
- An ability to turn the current back on after the OFF measurement
- An ability to vary the pulse rate for data storage

This work stimulated the development of a second instrument used for practical site measurements of galvanostatic pulse transients, which are used to determine the state of corrosion in reinforced concrete (Gurusamy and Geoghegan, 1990).

#### Investigation of freeze-hold (Instant-off) instrument

Three short investigations were performed to assess the measurement reproducibility and to determine the optimum time delay period. To allow the potential decay to be analysed the instrument was connected to the Taywood data bucket and print outs obtained during test 1. The reader is referred to Chapter 3 and the following Appendix 3.9 for general operational details for the instrument.

##### **Test 1**

This test was designed to investigate the reproducibility of measurement, the influence of waiting time period on voltage drops and the recovery of potential on restoration of current.

### Method

The pulse rate was set to 100/second and the auto-back-on mode selected. The half cell was placed at the centre of specimen Z:0.4:20:1 for a total of 21 measurements. The potential  $E_{on}$  and freeze-hold potential  $E_{off}$  were recorded. The time delay was increased from 0.2 seconds to 1.0 seconds in 0.1 second increments, repeating the measurement for time periods 0.2, 0.7, 0.9 seconds, with rest times between each test of 5 to 60 seconds. The time period was then set to 0.1 seconds to assess the effect of multiple tests over a very short time span of 15 seconds. Finally, the auto-back-on was disabled, the current interrupted and the potential monitored at time intervals of 1, 10, 30 and 60 seconds.

### Results

The results are shown in figures A3.8.1, A3.8.2, A3.8.3, A3.8.4 and table A3.8.1. Inspection of the decay plots in figure A3.8.1 shows the potential surging effect associated with switching the current off and then back on, both effects occurring for a period of about 0.1 seconds. The value  $dt$  is the waiting period before potential measurement, or the "instant". The potential dropped to a certain value and subsequent decay was at a slow rate. On switching back on, the potential generally returned to within 2 mV of the original value. The effect of increasing the off period was to increase slightly the potential drop, as shown in figure A3.8.2. Repeat readings at an off period of 0.1 seconds were within 1 mV of the initial value. Figure A3.8.3 shows that the rate of potential decay decreased over 60 seconds.

### Discussion

The test appeared highly reproducible. Interrupting the current for very short periods did not appear to change the conditions around the cathode, as indicated by the small change in potential throughout the test. The IR element of the measured potential was removed effectively within 0.1 seconds hence there did not appear to be a significant benefit in using a longer current-off period. Shorter periods of current interruption minimised changes to the cathodic polarisation and appeared to allow higher accuracy in subsequent readings. However, 0.1 seconds may not be long enough to remove the IR element from a highly polarised location where the potential drop is an order of magnitude higher.

### **Test 2**

The instrument was used to compare voltage drops for time delays of 0.2 and 1.0 seconds for specimens E:0.4:20:1 and E:0.4:50:1 at the 9 half-cell measurement locations, as shown in figure 6.3.

### Method

The pulse rate was set to 10/second and the auto-back-on mode selected. The data bucket was not required. The standard test method was followed as outlined in Chapter 3 using time delays of 0.2 and 1.0 seconds.



### Results

The results are given in tables A3.8.2. and A3.8.3. For both slabs the voltage drop was slightly greater at 1.0 seconds than at 0.2 seconds. The actual voltage drop values varied greatly with test location, from 68 mV to 807 mV and with higher voltage drops at the higher current density due to a higher degree of polarisation.

### Discussion

The results confirmed those of test 1, with a slightly higher voltage drop at 1 second than at 0.2 seconds. The difference between voltage drops at the two time periods, as shown in the end column of tables A3.8.2. and A3.8.3, appeared to be related to the magnitude of the drops, which were influenced by half-cell location. The lowest potential drops at the central A2, B2 and C2 locations. The differences of around 30 mV, induced for specimen E:0.4:50 at edge locations, indicated that even at high apparent levels of polarisation, the majority of the IR element was effectively removed 0.2 seconds after current interruption.

### Test 3

This test was performed a period of six months after tests 1 and 2 as a more rigorous assessment of the reproducibility of the freeze/hold measurements.

### Method

A total of 99 instant-off values were obtained for specimen T:2:20:1 at the 9 fixed half-cell measurement locations over a period of 30 minutes. The pulse rate was set to 100/second and the auto-back-on mode selected. The test method outlined in Chapter 3 was followed, using increasing time delays of 0.1 seconds up to 1.0 seconds at each spot location. The 'on' potential was allowed to return to its initial value inbetween each measurement. The half cell was placed at each location in the order in which they appear in table A3.8.4, the value of  $E_{on}^i$  being obtained immediately prior to each 0.1 second off measurement. At the end of the multiple measurement sequence, on potentials were checked at each location to assess the influence of multiple current interruptions. These are given as  $E_{on}^f$  in the table.

### Results

It is clear from table A3.8.4 that the majority of the potential decay occurred within 0.1 seconds of the interruption of current, followed by slower decreases similar to the decay from test 1, as shown in figure A3.8.2. Of interest, although the magnitude of the potential decays showed some variability, the instant-off potentials were within a 100 mV band, as shown in figure A3.8.4. It was noted during the test that the time required for the potential to recover after each interruption increased with increasing current-off period. This was especially true after 0.4 seconds and the recovery time was around 15 seconds for a 0.8 second current-off period. The  $E_{on}^f$  values in table A3.8.4 indicate that the reinforcement polarisation levels tended to become more negative during the test. The

variations were relatively small and it is not clear if this was due to the multiple current interruptions or other factors.

### **General discussion**

The specimens in the study exhibited very fast decay characteristics and the IR-error appeared to be removed from the potential measurements within 0.1 seconds. It is likely that a structure under CP for some time may require longer for the transitional potential surge effects to dissipate. For delay periods of between 0.1 to 0.4 seconds, and where the auto-back-on facility was used, the near instantaneous interruption of current minimised cathodic depolarisation. Whilst having a minimal effect on the accuracy of individual IR free potentials, longer delay periods allowed greater cathodic depolarisation. This would influence subsequent measurements made before a full recovery of polarisation. Certainly, significant depolarisation would occur for delay periods exceeding one second for these specimens. Since it was not practical to plot the actual decay trace for every reading to ensure that transient surges had dissipated, a decay period of 0.2 seconds was adopted throughout the study to allow for possible variability in the transients.

### **Conclusions**

1. The optimum waiting period from current interruption to allow for the removal of IR-error before a potential measurement was 0.2 seconds for these laboratory prepared specimens.
2. The freeze/hold test appeared to be highly reproducible over the short term when the "auto-back-on" routine was adopted and environmental conditions were stable.
3. The instrument fulfilled the specified requirements and was deemed suitable for use for the remainder of the trial.



dT (secs)	E <sub>on</sub>	E <sub>off</sub>	dE	Average dE
0.2	-675	-618	57	54
0.2	-672	-618	54	
0.2	-672	-622	50	
0.3	-675	-621	54	54
0.4	-675	-620	55	55
0.5	-676	-621	55	55
0.6	-680	-623	57	57
0.7	-680	-622	58	58
0.7	-681	-623	58	
0.7	-680	-622	58	
0.7	-678	-622	56	
0.8	-678	-620	58	59
0.8	-678	-619	59	
0.9	-678	-619	59	59
0.9	-676	-618	58	
0.9	-675	-617	58	
0.9	-681	-621	60	
1.0	-681	-622	59	59
0.1	-681	-628	53	53
0.1	-681	-629	52	
0.1	-681	-628	53	
1	-678	-620	58	
10		-583	95	
30		-542	136	
60		-506	172	

**Table A3.8.1** Test 1: 0.1 to 1.0 second instant-off potentials/ potential decay for specimen Z:0.4:20:1.

Half cell location	E <sub>on</sub>	E <sub>0.2</sub>	dE <sub>0.2</sub>	E <sub>on</sub>	E <sub>1.0</sub>	dE <sub>1.0</sub>	dE <sub>1.0</sub> -dE <sub>0.2</sub>
A1	-857	-701	156	-859	-688	171	15
A2	-819	-732	87	-817	-732	85	-2
A3	-1168	-771	397	-1170	-750	420	23
B1	-854	-683	171	-853	-671	182	11
B2	-772	-707	65	-765	-697	68	3
B3	-1015	-750	265	-1012	-737	275	10
C1	-906	-662	244	-905	-652	253	9
C2	-770	-667	103	-760	-655	105	2
C3	-1082	-741	341	-1082	-725	357	16

**Table A3.8.2** Test 2: Instant-off results at 0.2 and 1.0 seconds for specimen E:0.4:20:1.

Location	$E_{on}$	$E_{0.2}$	$dE_{0.2}$	$E_{on}$	$E_{1.0}$	$dE_{1.0}$	$dE_{1.0}-dE_{0.2}$
A1	-1321	-995	326	-1321	-973	348	22
A2	-1100	-930	170	-1097	-913	184	14
A3	-1530	-862	668	-1542	-832	710	42
B1	-1097	-749	348	-1091	-741	350	2
B2	-895	-647	248	-876	-630	246	-2
B3	-1583	-811	772	-1572	-765	807	35
C1	-1150	-743	407	-1155	-719	436	29
C2	-950	-711	239	-950	-691	259	20
C3	-1300	-788	512	-1311	-771	540	28

**Table A3.8.3** Test 2: Instant-off results at 0.2 and 1.0 seconds for specimen E:0.4:50:1.

	Half cell locations								
	A1	A2	A3	B1	B2	B3	C1	C2	C3
$E_{on}^i$ (mV)	-815	-685	-874	-910	-770	-953	-878	-738	-955
$E_{off}$									
$E_{0.1}$	-665	-626	-600	-677	-670	-696	-706	-643	681
$E_{0.2}$	-664	626	-598	-673	-666	-690	-704	-643	-678
$E_{0.3}$	-665	-626	-595	-671	-662	-687	-702	-643	-673
$E_{0.4}$	-663	-627	-592	-669	-663	-685	-699	-640	-621
$E_{0.5}$	-663	-625	-591	-665	-661	-682	-698	-643	-669
$E_{0.6}$	-659	-625	-587	-662	-660	-679	-696	-643	-668
$E_{0.7}$	-656	-623	-586	-663	-658	-680	-694	-640	-667
$E_{0.8}$	-654	-622	-583	-660	-658	-677	-693	-639	-666
$E_{0.9}$	-652	-622	-582	-660	-657	-675	-691	-641	-665
$E_{1.0}$	-651	-622	-578	-655	-657	-672	-689	-640	-664
$E_{on}^f$	-850	-689	-900	-940	-774	-970	-881	-775	-950
$d(E_{on}^i - E_{on}^f)$	-35	-4	-26	-30	-4	-17	-3	-37	5
	Potential decay, dE after dt=0.1 seconds								
	A1	A2	A3	B1	B2	B3	C1	C2	C3
$dE_{0.1}$	150	59	274	233	100	257	172	95	274

**Table A3.8.4** Test 3: 'on' potentials and repeat instant-off potentials at 9 half-cell locations for specimen T:2:20:1.



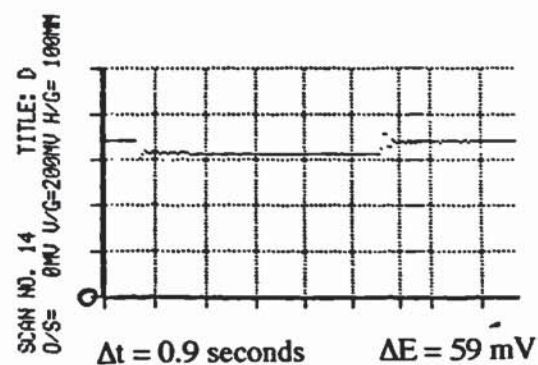
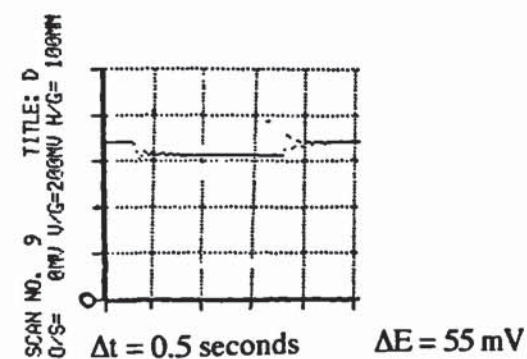
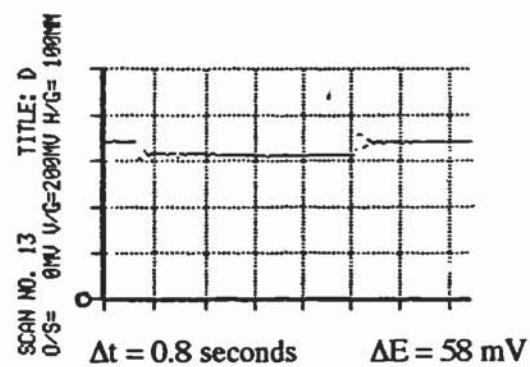
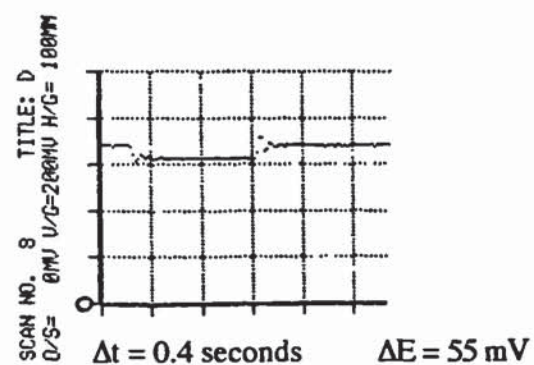
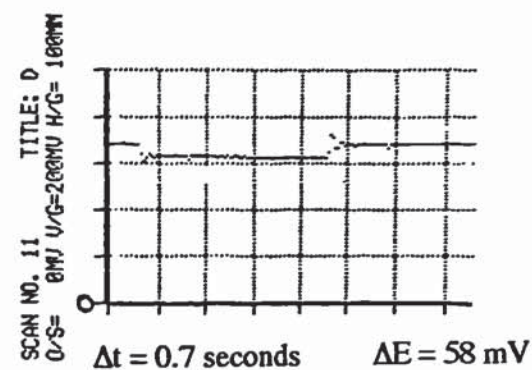
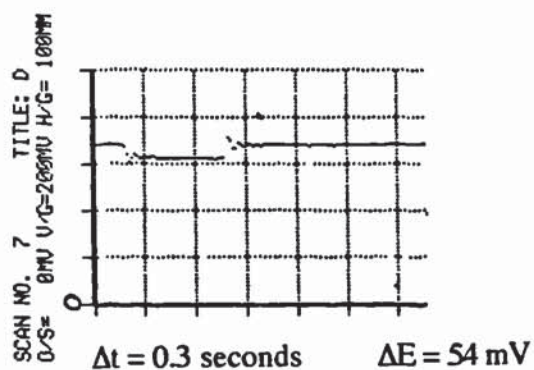
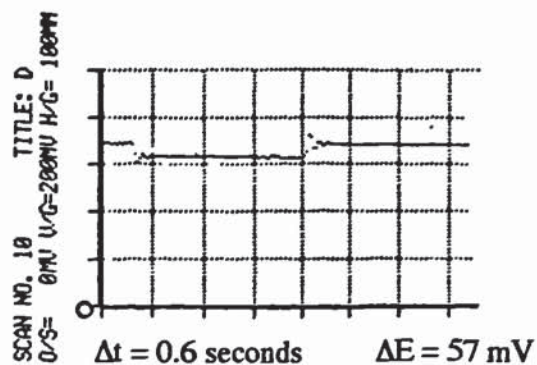
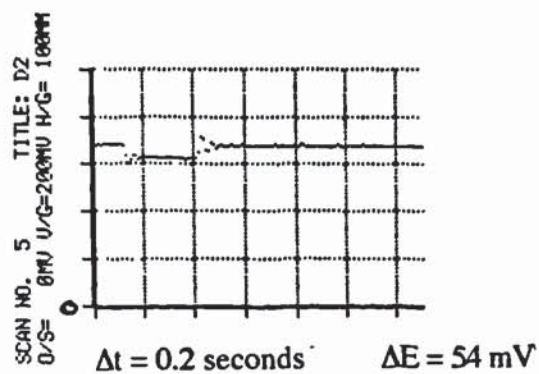


Figure A3.8.1 Potential decay/recovery on current interruption/restoration at increasing time intervals for specimen Z:0.4:20:1.

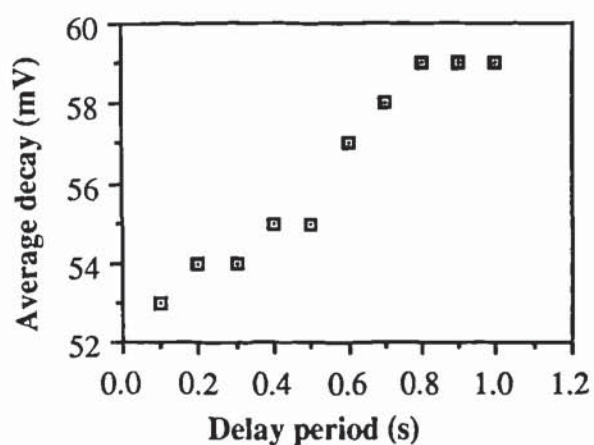


Figure A3.8.2 Variation of potential decay with increasing delay period at a single point for specimen Z:0.4:20:1.

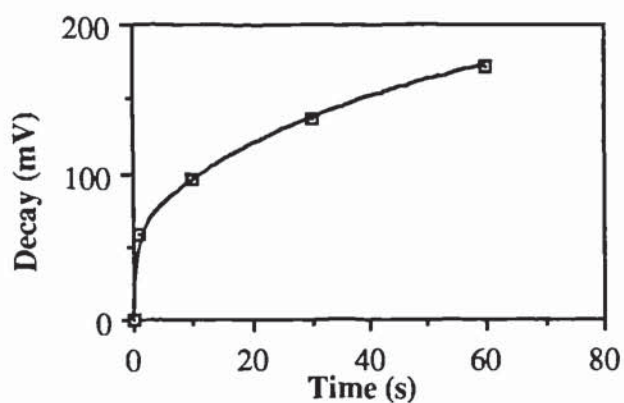


Figure A3.8.3 Potential decay plot over 60 seconds at a single point for specimen Z:0.4:20:1.

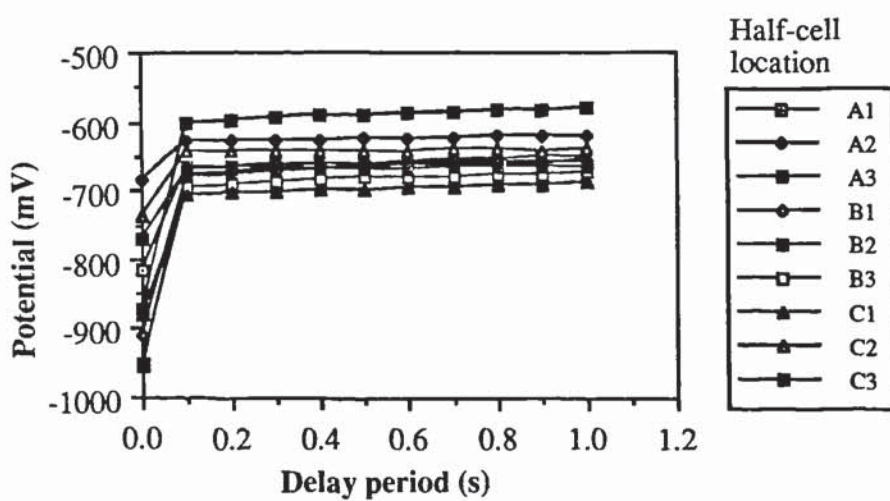


Figure A3.8.4 Variation of potential with increasing delay period at nine half-cell locations for specimen T:2:20:1.



**Appendix 3.9 Copy of a technical note describing the operation of the freeze-hold (instant-off) voltmeter.**

**'One Second Instant-Off' Potential Measurement**

**A REPORT DESCRIBING THE TAYWOOD INSTANT-OFF INSTRUMENT**

**C. J. WEALE, A. LEWINS**

**2/9/90**

**SUMMARY**

A robust, portable instrument for measuring "Instant-Off" potentials for cathodic protection installations has been developed at Taywood Engineering Ltd. The instrument is incorporated into the C.P. circuit and is able to momentarily interrupt the C.P. current over time intervals in the range 0.1 to 1.0 seconds. The potential drop is captured and displayed on the integral Digital Volt Meter. Data may also be stored via the Taywood Data Bucket. Since C.P. current may be restored within 0.1 seconds cathodic depolarisation is minimised and multiple readings are possible.

**Key Words:** Cathodic Protection; Instant-Off; Cathode; Potential

## CONTENTS

1	INTRODUCTION	
2	FEATURES	
		Introduction
	2.1	Sample/Hold Cycle
	2.2	Low Pass Filter
	2.3	Data Display and Storage
	2.4	Auto Back-On
3	OPERATION	
		Introduction
	3.1	Connections
	3.2	Dialling On
	3.3	Time Delay
	3.4	Manual Operation
	3.5	Auto Operation
	3.6	Auto Operation with Data Bucket
	3.7	Auto Back-On
4	APPENDICES	
	4.1	Instrument Sketch
	4.2	Connections Sketch
	4.3	Procedures
		1. Instant-Off Procedure
		2. Dialling On Potential
		3. Operation Of Data Bucket



## **1 INTRODUCTION**

The most widely accepted criteria used to assess the success of a cathodic protection system depend on the decay of potential immediately following abrupt cutting off of the energising current at the steel reinforcement, or cathode.

The one second instant-off measurement involves recording the steel potential at the arbitrary time interval of one second measured from switching the current off. This time-unit value was adopted as it is supposed to prevent potential surges in the system, or ringing effects in the measuring half-cell, affecting the measurement. It is necessary to switch the polarizing potential off in order to remove the significant extra potential drop in the system due to passage of current through the resistive concrete material, which masks the true cathodic polarization potential. A decay value of greater than 100 mV is generally accepted as indicative that the steel has been sufficiently cathodically protected.

The cathodic polarization potential continues to decay whilst the cathodic protection system remains off.

A further measurement of the cathodic polarization potential can be made at, again, the arbitrary time-unit of four hours from switching the current off. The 'four hour' decay is calculated with respect to the measured 'instant-off' potential, and a value greater than 100 mV is said to indicate adequate protection.

The maximum permissible instant-off potential of  $-1.15\text{ V CSE}$  ( $-1.05\text{ V SCE}$ ) is generally stipulated to ensure that possibly deleterious effects due to hydrogen production at the cathode do not occur during normal system operation.

Large scale Cathodic Protection installations can be remotely controlled by a computer which may have the facility for automatic current interruption and subsequent potential decay monitoring. However this facility is often not available in laboratory work, or in the smaller CP trials with basic metering capability of circuit output voltage, output current and reference feedback voltages. The Taywood Instant-Off instrument was developed to allow quantitative measurement of instant-off potentials in these situations.

## **2 FEATURES OF THE TAYWOOD INSTANT-OFF INSTRUMENT**

### **Introduction**

Sketches of the instant-off measurement instrument shows its features (Appendix 4.1) and connection details (Appendix 4.2). The test procedures are outlined in Appendix 4.3. A full technical description of the instrument is not appropriate in this report. The instrument

incorporates a digital voltmeter with a resolution of 1 mV and range of  $\pm 2$  V which draws very little current from the voltage source: less than 1 mV drop for an internal resistance of 1 M $\Omega$ .

### 2.1 Operation of the Sample/Hold Cycle

The instrument monitors an input potential and uses a comparator circuit to detect any voltage drop. On interrupting the C.P. current the input potential decays (drops). The comparator circuit operates within 15 ms upon detection of a voltage drop greater than 20 mV, starting the sample/hold cycle. After the selected delay period the output signal is then captured, i.e. frozen, and displayed by the DVM.

### 2.2 Low Pass Filter

A low pass filter placed between the buffered input signal and the comparator circuit, the display and the analogue output terminal, removes measurement error due to mains interference in the CP circuit. The filter introduces a ringing effect. For voltage drops of up to 200 mV the ringing decays to insignificance within 0.1 s and for a voltage drop of 1000 mV within 0.2 s. Hence for voltage drops reasonably expected during instant-off measurement of CP systems, it is possible to obtain a good reading of input signal within 0.1 s of the voltage drop occurring. The accuracy of any frozen output after 0.1 s will depend on the decay rate of the input signal.

### 2.3 Data Display and Storage

When the operator switch is set to position O, the instrument behaves as a DVM and the system potential and instant-off value can be read directly. The output signal can also be directed to the Taywood data-bucket (part of the Taywood Potential Wheel measurement system). The data bucket stores the output signal at a rate of 10, 100 or 1000 readings per second, which may then be plotted directly, allowing inspection of the potential decay curve, or down loaded to a PC for subsequent analysis. The data bucket has a range of 2 Volts with a resolution of 8 mV and is capable of storing 16000 bytes of data. The operator must select the appropriate pulse rate which will allow determination of the decay characteristics bearing in mind the memory storage available and the number of measurements required:

Pulse Rate	Total storage time available (seconds)
10 /sec	1600
100 /sec	160
1000 /sec	16



It is anticipated that the data bucket would be used in the event that one second is insufficient time to monitor the potential decay or to analyse the potential decay and recovery curve.

## **2.4 Auto Back-On**

This optional facility automatically switches the C.P. current back on 100 ms after the sample-hold cycle is completed and is used in conjunction with the Auto Operation mode. Auto Back-on allows repeat readings, or multiple measurements to be taken over an element since the potential drop associated with removal of C.P. current for 1 second is quickly recovered. This facility should not be selected when the decay is slow or for a "4 hour off" measurement.

# **3 OPERATION OF THE TAYWOOD INSTANT-OFF INSTRUMENT**

## **Introduction**

The sample/hold cycle may be initiated by the operator directly at the instrument (Auto operation) or remotely by disconnecting the C.P. system power (Manual operation). The operator connects the instrument into the C.P. circuit and manually sets the instrument internal potential to within 20 mV of the measured half-cell potential. The operator selects the time delay period for the freeze-hold cycle from 0.1 s to 1.0 s, in 0.1 s increments.

## **3.1 Connections**

The apparatus electrical connections are made to sockets on the front panel and are shown in the CONNECTIONS sketch (Appendix 4.2)

### Input

By convention the Half cell is connected to the positive terminal and the rebar connection is to the negative. This results in negative potentials being displayed as positive and vice versa.

### Output

A three pin connection is provided for connection to the Taywood data bucket.

### Circuit

A three pin connection is provided to enable the apparatus to be connected into the C.P. circuit via normally open (black) or normally closed (red) and common (blue) leads. In practice the normally open is not used and should be clipped back onto itself. The apparatus should be connected to the anode supply cable at two locations such that a break may be made between the connection points, or a switch assembly installed.

## **3.2 Dialling On Potential**

The instrument internal potential is set to equal the input potential by a dial control, which is graduated to display from 0.00 to 10.00. Since the potential range is 2 volts, a potential

of 602 mV would be indicated by 3.01. An LED indicates when the internal potential is within 20 mV of the input potential.

### **3.3 Time Delay Period**

The time delay period is set by the Operator on the control panel. The display ranges from 0 to 9 and represents tenths of a second.

Hence: 1 = 0.1 seconds

4 = 0.4 seconds

0 = 1.0 seconds

### **3.4 Manual Operation**

Manual operation is initiated by pressing the operating switch pressed to the upper position (position M). The sample-hold cycle is then initiated by the operator manually interrupting the current by disconnecting the power. The current remains off until the power is reconnected.

### **3.5 Auto Operation**

Auto operation is initiated by pressing the operating switch to the lower position (position A). At this instant, current continues to flow. The instrument delays switching the current off by 100 ms, upon which the voltage will drop, triggering the sample/hold cycle. The current remains off until the operator switch is pressed back to the middle position (position O).

### **3.6 Auto Operation with Data Bucket**

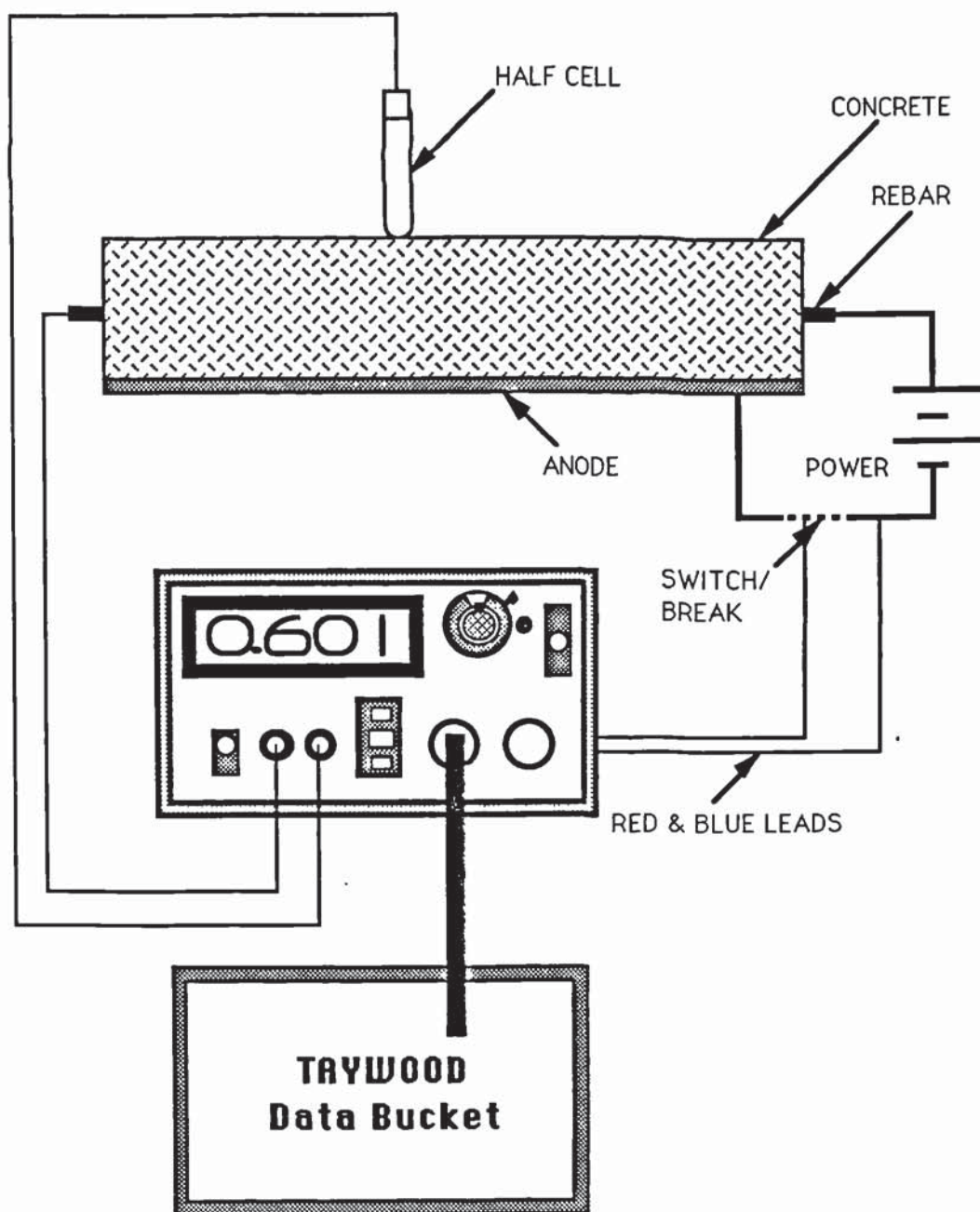
When the instrument is connected to the data bucket, switching to position A initiates the pulse train. The input potential is measured and stored at the instant of switching and subsequently at the pre-selected rate. The operator terminates the pulse train using the data bucket terminal.

### **3.7 Auto Back-On**

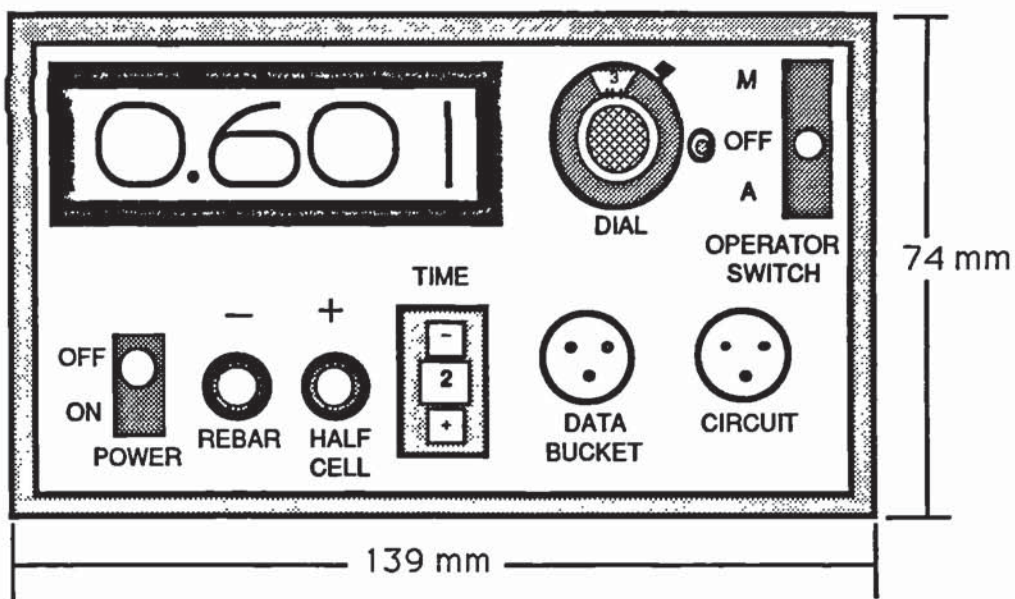
Auto Back-on is selected at the rear panel.



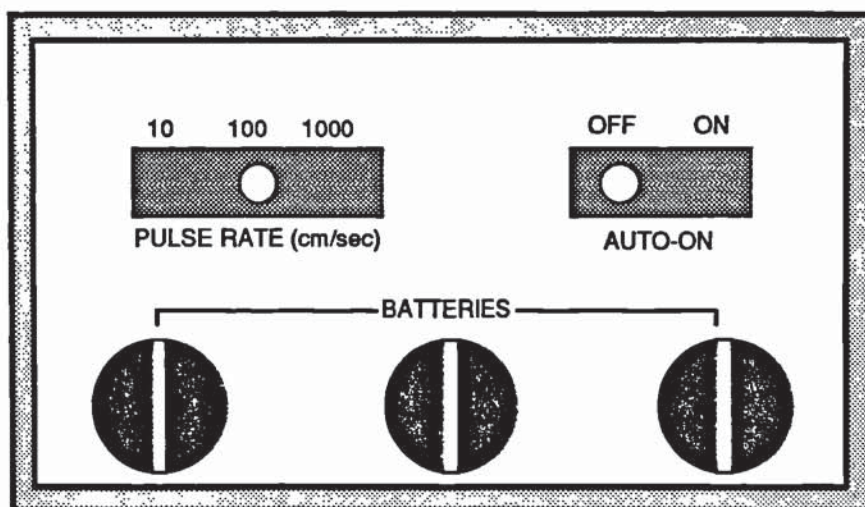
## APPENDIX 4.2: CONNECTIONS



## APPENDIX 4.1 INSTANT-OFF Instrument



FRONT PANEL



REAR PANEL



## APPENDIX 4.3

### 1. INSTANT-OFF PROCEDURE

- 1 Make pre-test decisions: Pulse Rate (100 /second)  
Time Delay (0.2 s)  
Auto Back On: on/off
- 2 Make connections as per connection diagram (appendix 4.2)
- 3 Turn Instrument ON
- 4 Set up Data Bucket sequence if required
- 5 Dial on potential- LED 'just' on
- 6 Record value  $E_{(on)}$

#### **Auto Operation:**

- 7a Interrupt primary circuit  
between instrument connections
- 8a Switch to Auto Operate
- 9a Record  $E_{(off)}$  from DVM
- 10a Switch back to ON
- 11a To Repeat, goto(4), else(12a)
- 12a Reconnect power circuit
- 13 Disconnect instrument
- 14 Print out from data bucket if required
- 15 NEXT READING/TEST, Goto (1)

#### **Manual Operation:**

- 7b Switch to Manual Operate
- 8b Interrupt Current manually
- 9b Record  $E_{(off)}$  from DVM
- 10b Switch back to ON
- 11b Reconnect power circuit
- 12b To Repeat, goto(4), else(13)

### 2. DIALLING ON POTENTIAL

1. Operate the dial until the LED lights.
2. Turn dial clockwise ( increases potential) until the light just goes off.
3. Slowly turn dial anti clockwise ( decreases potential) until LED just comes on.
4. Instrument is now ready for use.

### 3. OPERATION OF DATA BUCKET

1. Select Program 1
2. Calibration and Offset must be set to zero
3. Set C/SPAC to 5
4. Row spacing is irrelevant and may be any value
5. Set FSD = 2000 mV, check setting on data bucket also
6. Proceed through set up routine to STORE
7. Activating 'Auto Operate' switch stores data
8. Stop data storage by selecting CTRL
9. Use the data bucket routines to print data / down load data to PC
10. Always write down Input and Frozen potentials for reference

**Appendix 4.1 Potentiodynamic polarisation program variables, taken from the PARC programme set-up menu**

---

RUN PARAMETERS	PAGE 1
----------------	--------

---

	TECHNIQUE	POTENTIODYNAMIC
<0>	EXP NAME	C12P
<1>	INITIAL E (MV)	-250 VS E
<2>	FINAL E (MV)	1500 VS E
<3>	SCAN RATE (MV/S)	0.5
<4>	CONDITION E (MV)	PASS
<5>	CONDITION T (S)	PASS
<6>	INIT DELAY (MV/S OR S)	1.5 M
<7>	PLOT MAX I RANGE	1 MA
<hr/>		
	<R> RUN EXPERIMENT	
	<S> SETUP/RUN MENU	
	<M> MAIN MENU	
	<N> NEXT PAGE	

---



---

SAMPLE PARAMETERS	PAGE 2
-------------------	--------

---

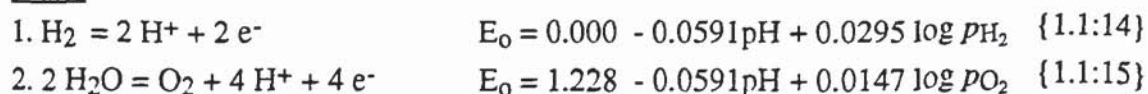
	AREA (CMS^2)	8.05
<1>	EQ WT (GM)	PASS
<2>	DENSITY (GM/CM^3)	PASS
<3>	CATHODIC TAFEL (MV)	PASS
<4>	ANODIC TAFEL (MV)	PASS
<5>	LINE SYNC (Y/N)	PASS
<6>	CURRENT INTERRUPT (S)	PASS
<hr/>		
	<R> RUN EXPERIMENT	
	<S> SETUP/RUN MENU	
	<M> MAIN MENU	

---

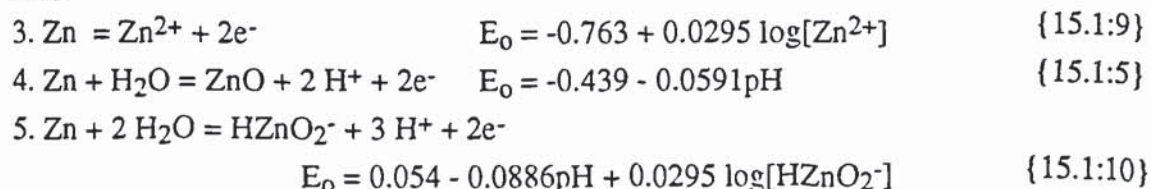


## Appendix 4.2 Thermodynamic equations used in Chapter 4

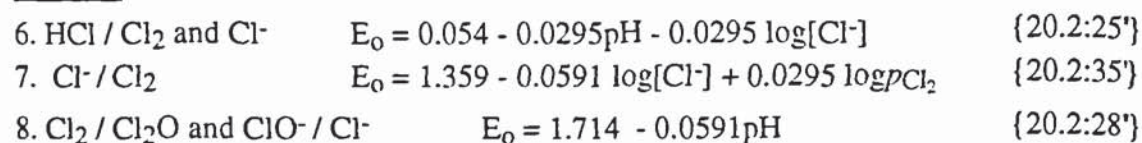
### Water



### Zinc



### Chlorine



### NOTES

1. All thermodynamic equations including references are taken from Pourbaix, 1966, Chapter 4. Reference numbers refer to {section number:equation number}.
2. Values of  $E_0$  determined from these equations relate to the Standard Hydrogen Electrode (SHE) scale, and require conversion to Standard Calomel Electrode (SCE) scale.
3. The following values have been used in the calculations:  
C12, C9, C7, C2  $[\text{Cl}^-] = 0.4 \text{ M}$ ; N2  $[\text{Cl}^-] = 0.05 \text{ M}$ .  
 $\log [\text{Zn}^{2+}]$ ,  $\log [\text{HZnO}_2^-] = -6$ ;  $\log p \text{H}_2$ ,  $\log p \text{O}_2 = 0$ ;  $\log p \text{Cl}_2 = -6$ .
4. Figures in brackets are approximate as  $\text{Cl}^-$  ions may influence the thermodynamic equilibria. Some  $E_0$  values have not been computed for chloride containing solutions for this reason.

solution	pH	$E_0$ Eq'n 1	$E_0$ Eq'n 2	$E_0$ Eq'n 3	$E_0$ Eq'n 4	$E_0$ Eq'n 5	$E_0$ Eq'n 6	$E_0$ Eq'n 7	$E_0$ Eq'n 8
C12	12.02								764
N12	12.64	-988	240			-1484			
C9	6.68							965	1079
N9	8.73	-757	-757		-1196				
C7	5.20							965	1167
N7	8.34	-734	-734	-1181					-
C2	0.98	(-299)	(-299)				915		1416
N2	1.36	(-321)	(-321)	(-1181)			930		1394

**Table A4.1.1** Theoretical equilibrium electrode potential ( $E_0$ ) values mV (SCE)

## Appendix 5.1 The calculation of cement total alkali content

The total alkali content of anhydrous cements is usually expressed as the percentage sodium oxide content, hence it is necessary to convert the percentage of alkali due to potassium oxide to an equivalent sodium oxide content.

Atomic weight of compounds (from Vogel, 1978):

$$\text{Na}_2\text{O} = 61.979 \text{ g}$$

$$\text{K}_2\text{O} = 94.1954 \text{ g}$$

$$\text{Conversion factor} = \text{mass Na}_2\text{O} / \text{mass K}_2\text{O} = 0.658$$

$$\text{Total alkali} = \text{Na}_2\text{O} + 0.658 \text{ K}_2\text{O}$$

From the OPC analysis in table 3.1,

$$\text{Total alkali} = 0.23 + 0.658 \times 0.41$$

$$= \underline{0.50 \text{ g/100g cement}}$$

## Appendix 5.2 Calculation of the minimum solubility of bizincate ions

Solubility of solid ZnO (from Pourbaix, 1966, Ch IV. Section 15.1 p408)



$$1. (\text{OH}^-) = 58 \text{ mM/l}$$

$$\text{pH} = 10^{0.058} + 14 = 12.76$$

$$\log(\text{HZnO}_2^-) = -16.68 + 12.76 = -3.92$$

$$(\text{HZnO}_2^-) = \log^{-1}(-3.92) = \underline{0.12 \text{ mM/l}}$$

$$2. (\text{OH}^-) = 105 \text{ mM/l}$$

$$\text{pH} = 10^{0.105} + 14 = 13.02$$

$$\log(\text{HZnO}_2^-) = -16.68 + 13.02 = -3.66$$

$$(\text{HZnO}_2^-) = \log^{-1}(-3.66) = \underline{0.22 \text{ mM/l}}$$



## Appendix 6.1 Schedule of experimental tests/chapter for the external CP trial

Chapter	Month	0	1	2	3	4	5	6	7	8	9	10	11	12	14	16	18	22
	Date	4	5	6	7	8	9	10	11	12	1	2	3	4	6	8	10	2
6	Specimen characterisation																	
	Linear polarisation	*																
	Resistivity	*																
	Water permeability	*																
	Cube strength	*																
	50 mm dry cores	*																
	Physical performance																	
	Visual Inspection	*	*	*	*	*	*	*	*	*	*	*	*	*	*	*	*	*
	25 mm wet cores:																	
	Binocular microscopy				*			*			*			*			*	
	Adhesion tests (Coatings)	*		*	*	*	*	*	*	*	*		*	*	*		*	
	Down coating voltage (Paint)		*	*	*	*	*	*	*	*	*		*	*	*	*	*	*
	Supplementary investigations																	
	Adhesion test (Overlay)																*	
	Pundit USPV (Overlays)															*		
	FT-IR (Paint)				*						*			*				
	SEM (corrosion products)	Ongoing																
	XRD (corrosion products)	Ongoing																
7	Electrical performance																	
	Current / voltage	*	*	*	*	*	*	*	*	*	*	*	*	*	*	*	*	*
	Temperature	*	*	*	*	*	*	*	*	*	*	*	*	*	*	*	*	*
	Cathode potentials	*	*	*	*	*	*	*	*	*	*	*	*	*	*	*	*	*
	Instant-off potentials		*					*				*	*	*	*	*	*	*
8	Effect of CP on concrete																	
	Petrographic thin sections from 25 mm wet cores				*			*			*			*				
	100 mm wet cores:																*	
	MIP																*	
	Ionic concentration profiles																*	
	DTA																*	

Table A6.1.1 Schedule of experimental tests/chapter for the external CP trial

## Appendix 6.2 Calculation of mesh anode surface areas

Assumptions: The mesh has a square cross section  
Each diamond has equal side lengths

### Anode T

Anode surface area / square metre mesh  $m^2 = 0.16 m^2$  (Company literature)  
Strand width/ material thickness = 1 mm  
Diamond dimensions = 100 x 50 mm  
Number of diamonds /  $m^2 = 1/0.1 \times 1/0.05 = 200$   
Surface area of one diamond =  $0.16 / 200 = 8 \times 10^{-4} m^2$

### Anode E

The manufacturer does not indicate the anode surface area / square metre mesh, hence the individual anode diamond surface area is calculated from first principles.

Mesh dimensions = 76 x 34 mm (Company literature)  
Density of titanium =  $4500 \text{ Kg/m}^3$ , assume that the coating has the same density  
Mesh weight =  $0.13 \text{ Kg/m}^2$

Length of one side of diamond,  $L = (0.038^2 + 0.017^2)^{1/2} = 0.041629 \text{ m}$

Number of diamonds /  $m^2$ ,  $N = 1 / (0.076 \times 0.034) = 387$

Volume of 1  $m^2$  of mesh,  $V = 0.13 / 4500 = 0.029 \times 10^{-3} m^3$

Cross sectional area of a diamond strand of unit area =  $V / (4L \times N) = 4.5 \times 10^{-7} m^2$

Thickness of single strand,  $t = (4.5 \times 10^{-7})^{1/2} = 6.708 \times 10^{-4} m$

Surface area of one diamond =  $4 \times t \times 4 \times L = 4.4682 \times 10^{-4} m^2$

### Check accuracy of calculation by re-calculating the surface area of anode T

Mesh weight =  $0.16 \text{ Kg/m}^2$

$L = (0.05^2 + 0.025^2)^{1/2} = 0.0559017 \text{ m}$

$V = 0.16 / 4500 = 0.0356 \times 10^{-3} m^3$

Cross sectional area of a diamond strand of unit area =  $7.95 \times 10^{-7} m^2$

Thickness of single strand,  $t = (7.95 \times 10^{-7})^{1/2} = 8.9165 \times 10^{-4} m$

Surface area of one diamond =  $4 \times t \times 4 \times L = \underline{7.975 \times 10^{-4} m^2}$

Apparent % error =  $(8.00 - 7.975) \times 100 / 8 = \underline{0.31 \%}$

The assumptions made in the calculation appear reasonable and some confidence can be placed on the result for anode E.



### Appendix 6.3 DTA analysis of acidified paste, specimen P:2:50:1, 9 months

	CSH	Organics	Ca(OH) <sub>2</sub>	Quartz	Vaterite	CaCO <sub>3</sub>	Devitri- fication
Temperature °C	160	350	500	575	670	870	920
Endothermal peak	4		-	24	24	120	
Exothermal peak		201					8

**Table A6.3.1** DTA: relative intensities of peak temperatures for acidified paste from Specimen P:2:50:1 at 9 months.

(Refer to Chapter 3 for a full description of the DTA analysis method and Chapter 8 for a discussion of experimental error and background relating to the peak temperatures.)

### Appendix 6.4 Examination of Taywood Engineering Ltd. Zinc CP Trial

It was of interest to examine a sprayed zinc CP trial which had been under polarisation for a period of 3 years at an applied current density of around 5 mA/m<sup>2</sup>, full details of which are reported elsewhere (Palmer, 1987). A visual inspection of the zinc surface identified clusters of very small warts at discreet locations. White rust was also visible at the edges of surface voids and at breaks in the coating. The overall integrity of the coating appeared excellent.

Pull-off tests were conducted on 27/4/90 at two locations adjacent to an embedded reference electrode and primary power input. The concrete slab had a highly revealed aggregate surface with maximum aggregate size of 30-40 mm. The highly uneven surface made the pull-off test difficult and the failure mode was variable, with values of at least 4 Kg/cm<sup>2</sup> where failure occurred adjacent to paste and values of at least 8 Kg/cm<sup>2</sup> where the substrate was largely aggregate, as indicated in table A6.4.1.

Location	Failure load Kg/cm <sup>2</sup>	Failure type (See table 6.21)	Failure mode
Power 1	4	5	L
	-	1	-
Power 2	8	1	P
	9	5	P
Reference 3	9	1	P
	10	1	P
Reference 4	-	1	-
	4	5	P

**Table A6.4.1** Summary of pull-off tests of Taywood Engineering Ltd. Zinc CP trial

A dense, amorphous white zinc corrosion product was observed at pull-off sites where the zinc was in contact with cement paste, equivalent to a type 5 failure as indicated in Chapter 6. Examination by SEM confirmed the micro-crystalline nature of the zinc product and an EDXA analysis indicated the main composition comprised 94% Zn with negligible impurities.

## Appendix 8.1 Summary of MIP results

Specimen	Depth mm	Int'n Vol cc/g	P A m <sup>2</sup> /g	MPD (Vol) $\mu$ m	MPD (Area) $\mu$ m	APD $\mu$ m	Bulk $\rho$ g/cc	AS $\rho$ g/cc	% Capillary
Z:2:0:1	0-4	0.056	11.3	0.034	0.0100	0.0198	0.326	0.332	7.9
E:2:0:1	0-4	0.073	15.9	0.032	0.0083	0.0183	0.412	0.425	13.3
P:2:0:1	0-4	0.071	12.4	0.048	0.0095	0.0229	0.207	0.210	6.4
T:2:0:1	0-4	0.062	14.7	0.030	0.0072	0.0169	0.342	0.349	9.2
P:2:20:1	0-4	0.075	19.6	0.025	0.0073	0.0153	0.409	0.422	13.4
Z:2:50:1	0-4	0.064	17.5	0.024	0.0069	0.0146	0.410	0.421	11.6
E:2:50:1	0-4	0.071	16.8	0.029	0.0081	0.0170	0.391	0.402	12.1
P:2:50:1	0-4	0.058	14.1	0.029	0.0072	0.0164	0.347	0.354	8.8
P:2:50:1	6-10	0.061	17.0	0.023	0.0065	0.0143	0.408	0.418	10.7
T:2:50:1	0-4	0.071	15.4	0.032	0.0084	0.0185	0.407	0.419	12.6
E:2:0:1 Overlay	0-4	0.099	13.5	0.459	0.0069	0.0293	0.383	0.398	16.5
E:2:50:1 Overlay	0-4	0.096	12.4	0.377	0.0072	0.0309	0.409	0.425	17.1
T:2:0:1 Overlay	0-4	0.111	13.8	0.566	0.0062	0.0322	0.408	0.427	19.7
T:2:50:1 Overlay	0-4	0.128	20.7	0.363	0.0059	0.0247	0.413	0.436	23.0

**Table A8.1.1** Summary of MIP data

Key (from Micrometrics, 1988)

**Int'n Vol: Total intrusion volume**

- the maximum volume of mercury intruded into the pores at the maximum pressure

**PA: Total pore area**

- the area of pores based on the assumption of cylindrical geometry and summed up over the pressure range

**MPD: Median pore diameter** (from the volume or area distribution curves)

- the 50% (percentile) value

**APD: Average pore diameter**

- assumes all pores are right cylinders;  $APD = 4 \times \text{total pore volume} / \text{total pore area}$

**Bulk  $\rho$ : Bulk density**

- calculated from sample weight and volume at initial mercury filling pressure

**AS  $\rho$ : Apparent (skeletal) density**

- bulk density, adjusted for pore volume measured at maximum pressure attained.

**% Capillary**

- the percentage of the available intrusion volume used in the penetrometer. (Preferably in the range 25% to 90%)



## **Appendix B. Plates**



**Plate 3.1** Elecometer pull-off instrument, positioned above an aluminium dolly.

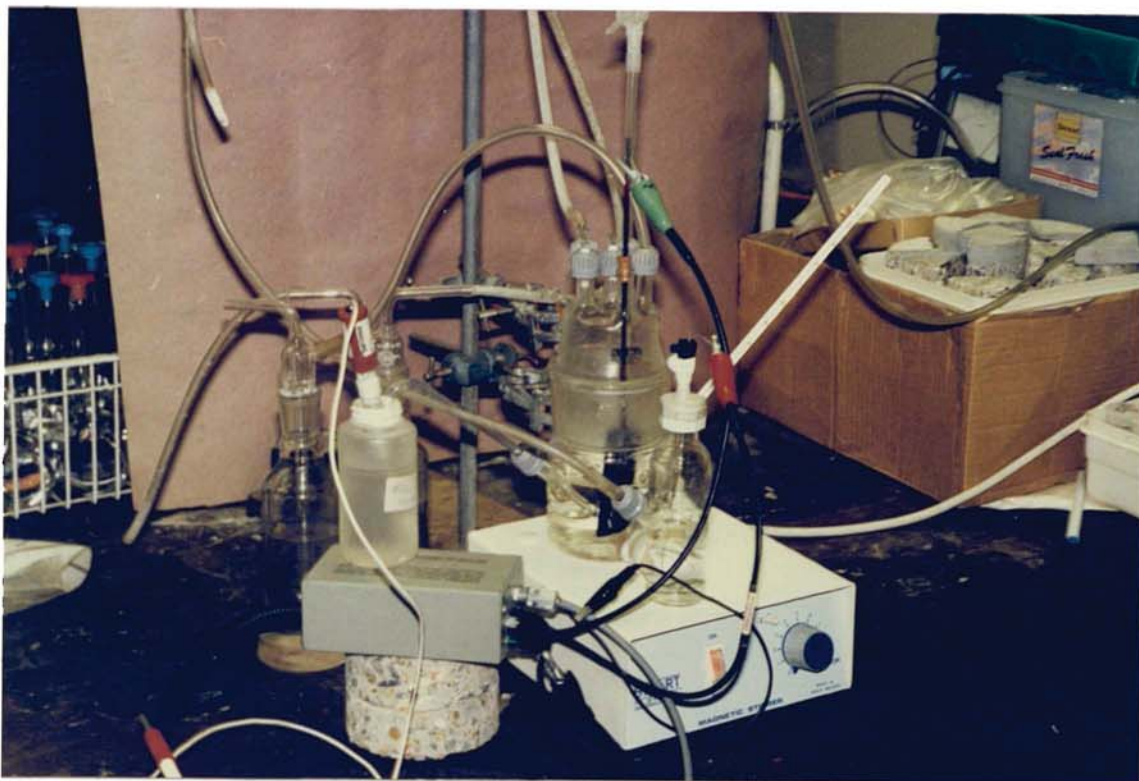


**Plate 4.1** Pyrex corrosion cell, set up for an anode P specimen.



**Plate 4.2** Potentiostat during an experiment; Nylox deoxygenator in the background.



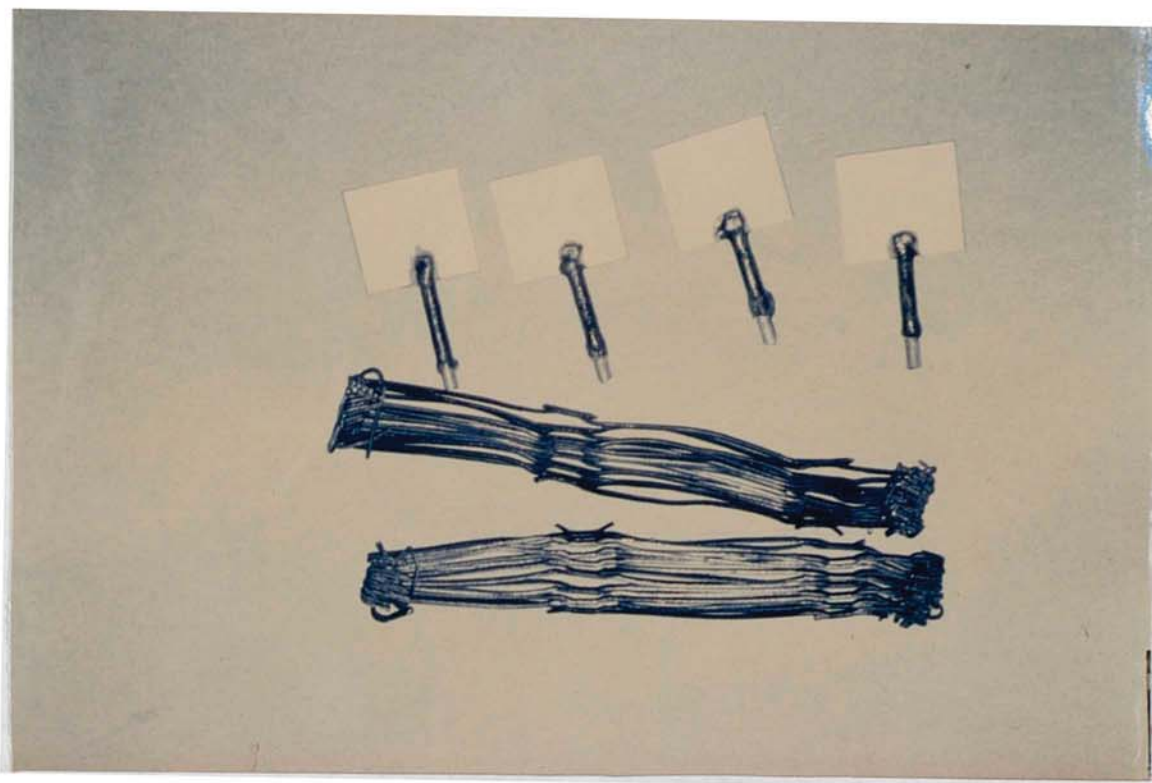


**Plate 5.1** Compressed mesh anode and plate cathodes of paste block specimens.

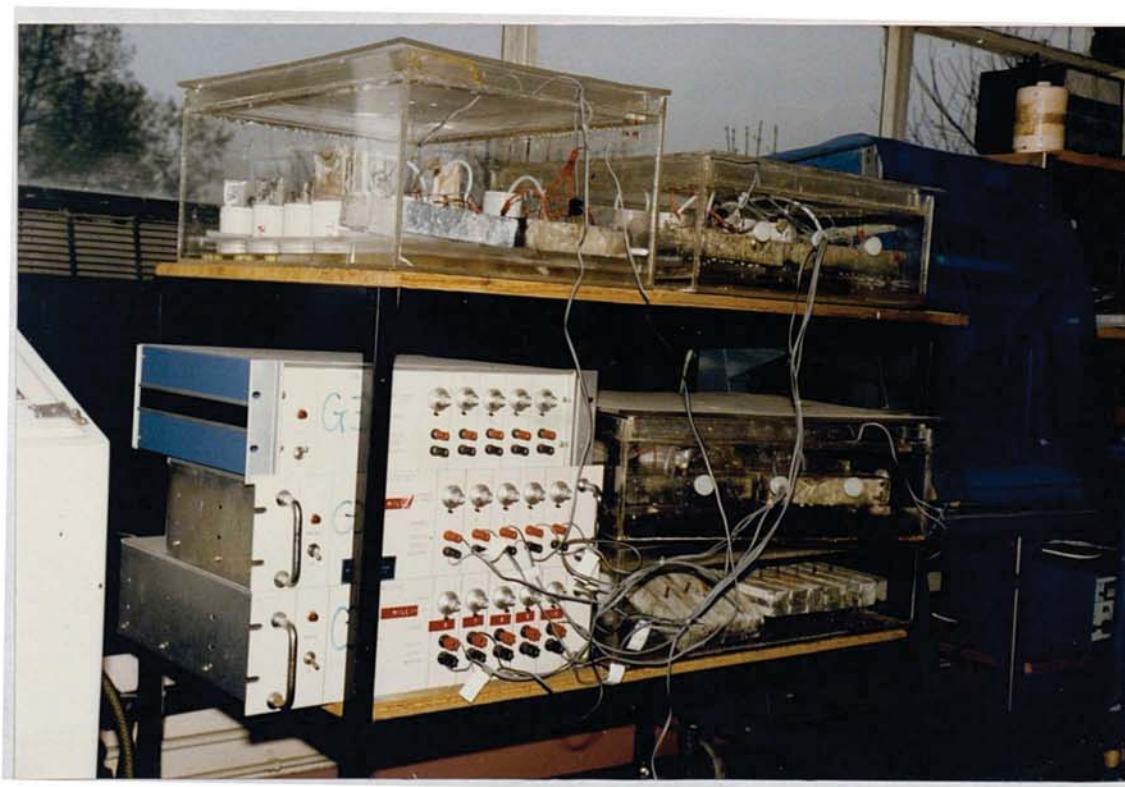


**Plate 5.2** Experimental arrangement of specimens in humidity boxes.

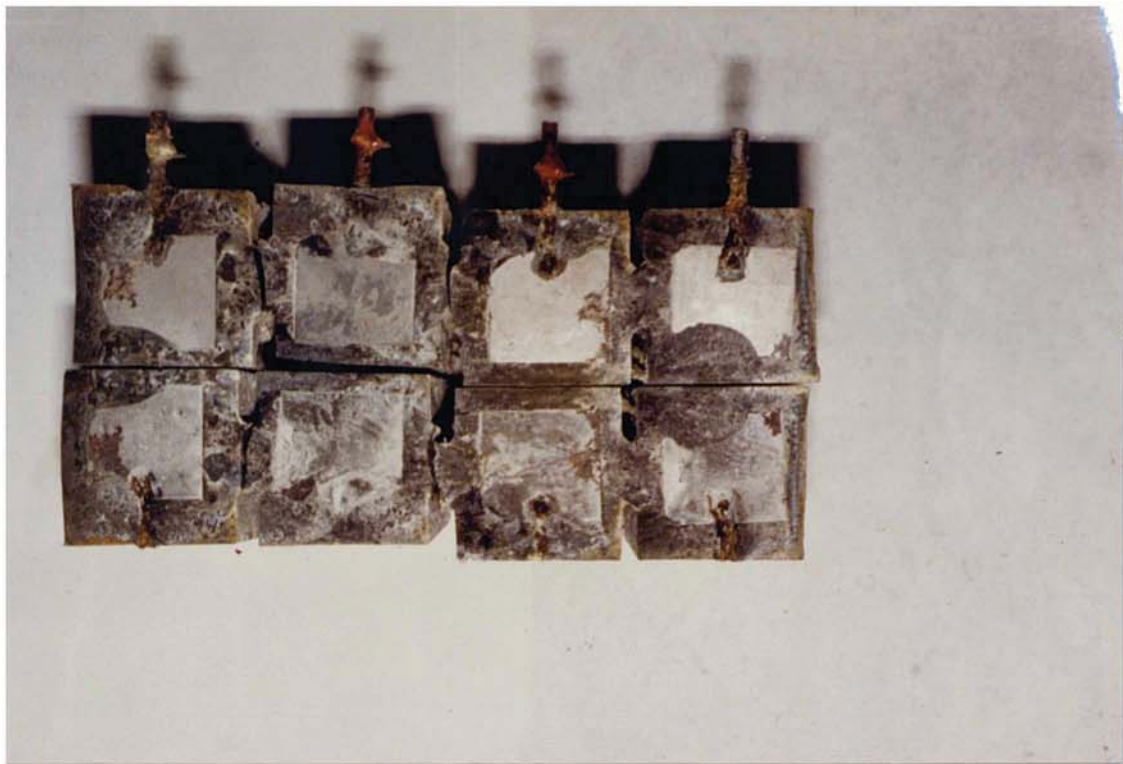


**Plate 5.3** Specimen T:50a paste prism, broken in half at the cathode plates which appear shiny. Black magnetite can be seen at plate edges.

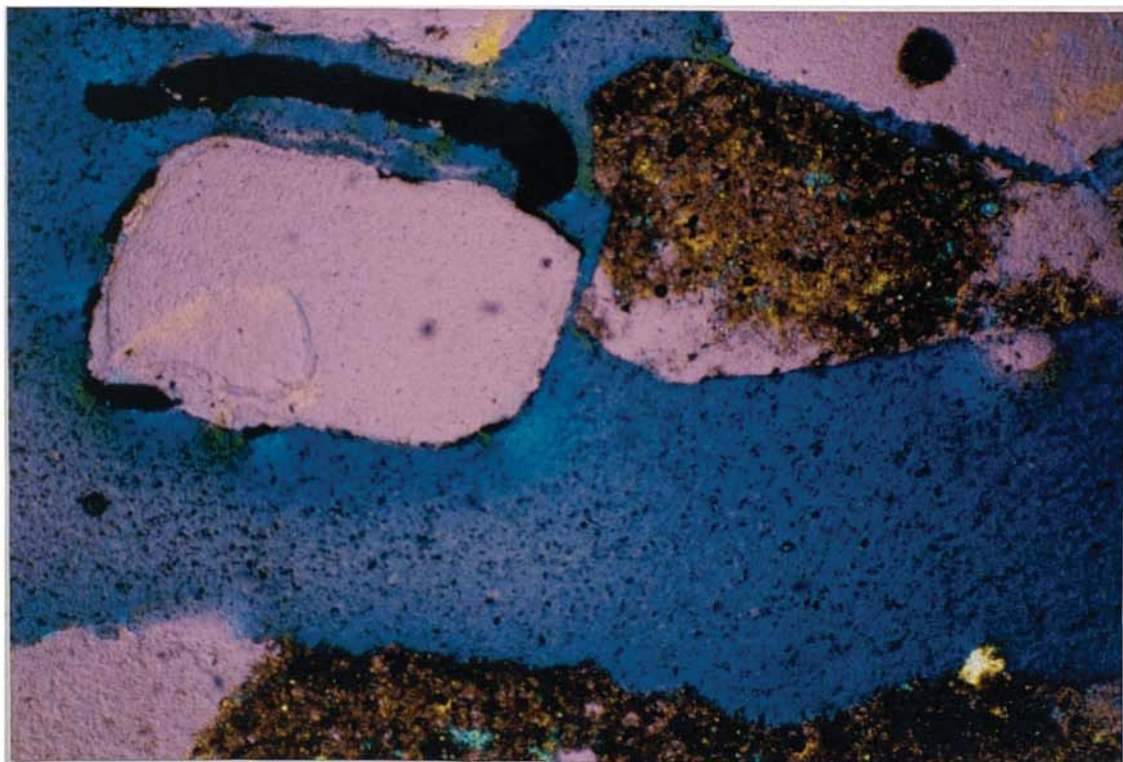


**Plate 5.4** Micrograph of specimen E:50b, interface between mesh (left of central, purple) and cement (right and bottom, brown/purple), crossed polarised light. (XP)(scale 10 mm = 171  $\mu\text{m}$ )



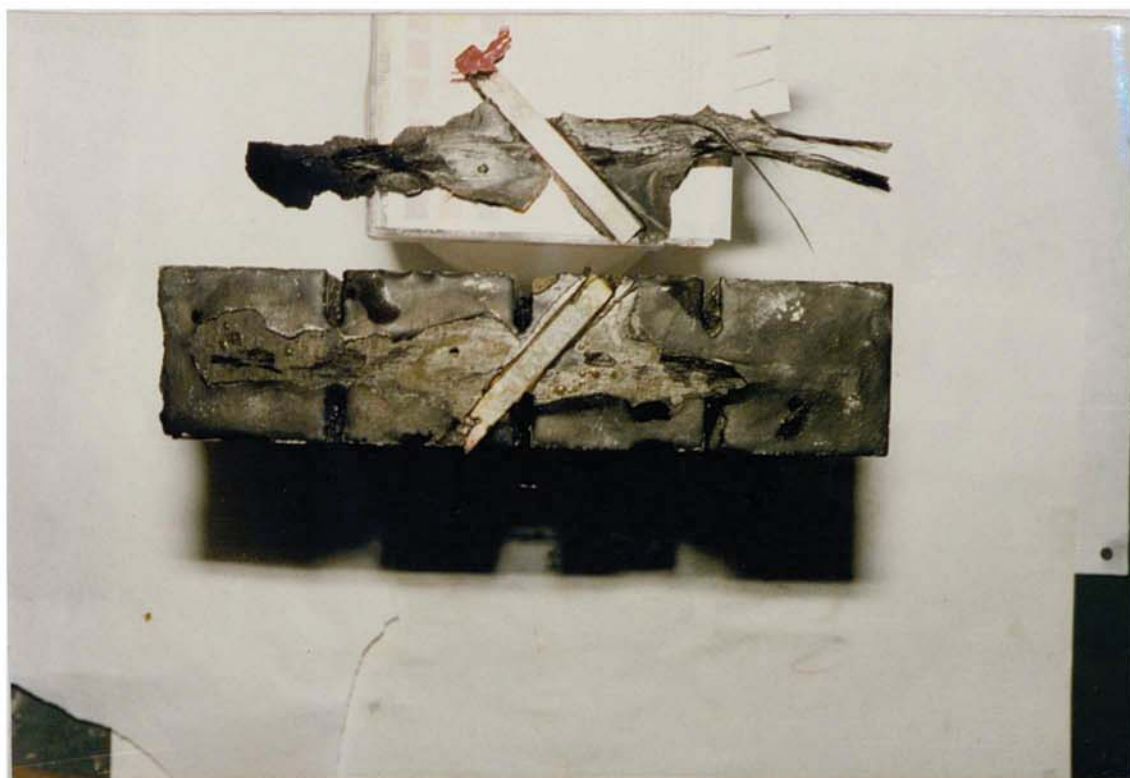


**Plate 5.5** Specimen P:50a before analysis, showing the removed primary and secondary anodes.

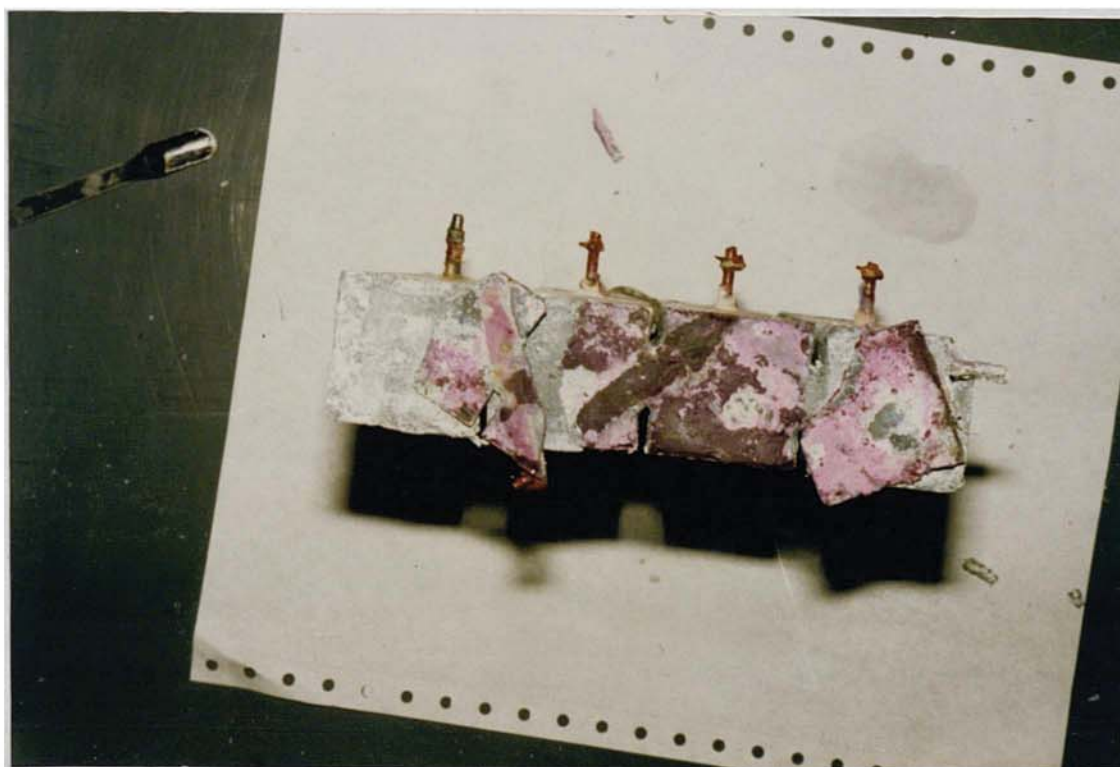


**Plate 5.6** Specimen Z:50a before analysis, showing the alkaline zinc corrosion products on the outer and inner zinc surfaces and paste surface (centre).



**Plate 6.1** Mesh anode fixed to a concrete slab before the application of cementitious overlay.



**Plate 6.2** Specimen E:2:50:2: location of USPV (Pundit) measurements using flat transducer heads.





**Plate 6.3** Specimen P:2:50:2, 8 months: Micro-bubbling, cracking and bleaching of the surface.



**Plate 6.4** Specimen P:0.4:50:1, 18 months: Repaired anode region, degradation has spread further. Majority of the surface is unaffected. Low rust spotting.





**Plate 6.5** Specimen P:2:50:1, 8 months: Heavy rust spotting, bleaching, few micro and macro bubble sites.

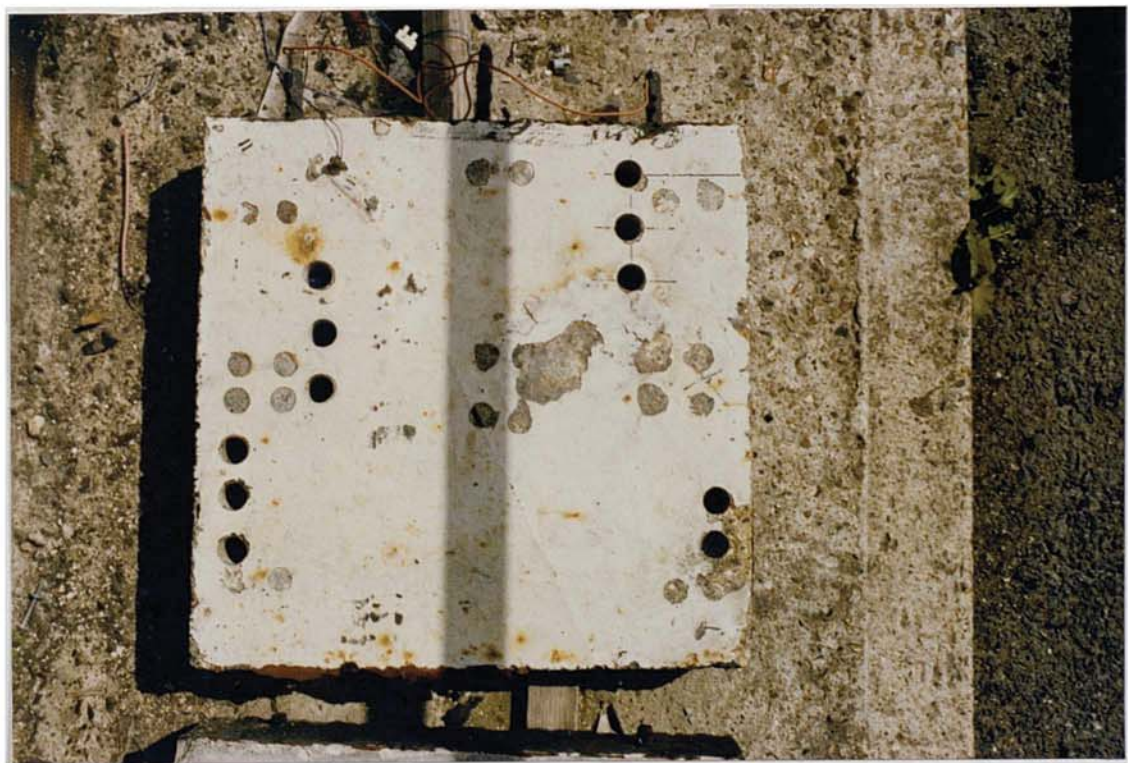


**Plate 6.6** Specimen P:2:50:1, 18 months: Severe localised degradation.





**Plate 6.7** Specimen P:0.4:20:1, 18 months: Anode P, type 4 failure.



**Plate 6.8** Specimen P:2:20:1, 18 months: Anode P, type 3 failure.





**Plate 6.9** Specimen P:0.4:0:1, 18 months: Anode P, type 2 failure.

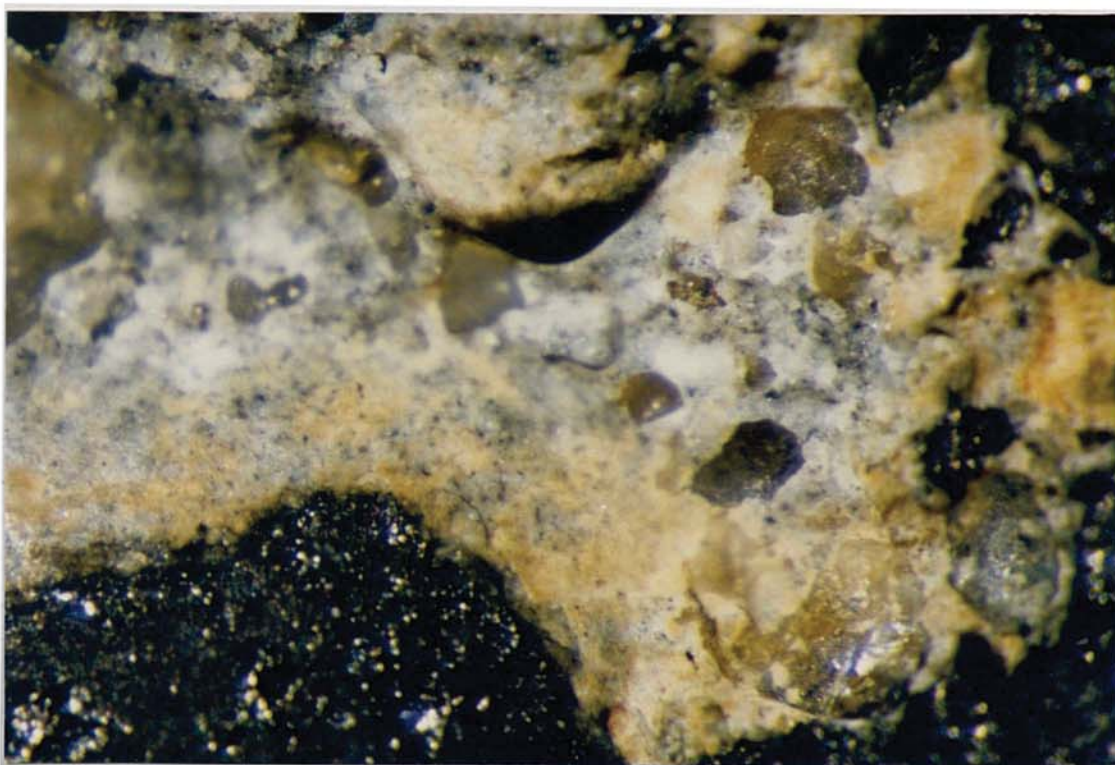


**Plate 6.10** Specimen P:0.4:0:1, 2 months: Orange staining of substrate paste. (scale 10 mm = 0.28 mm)



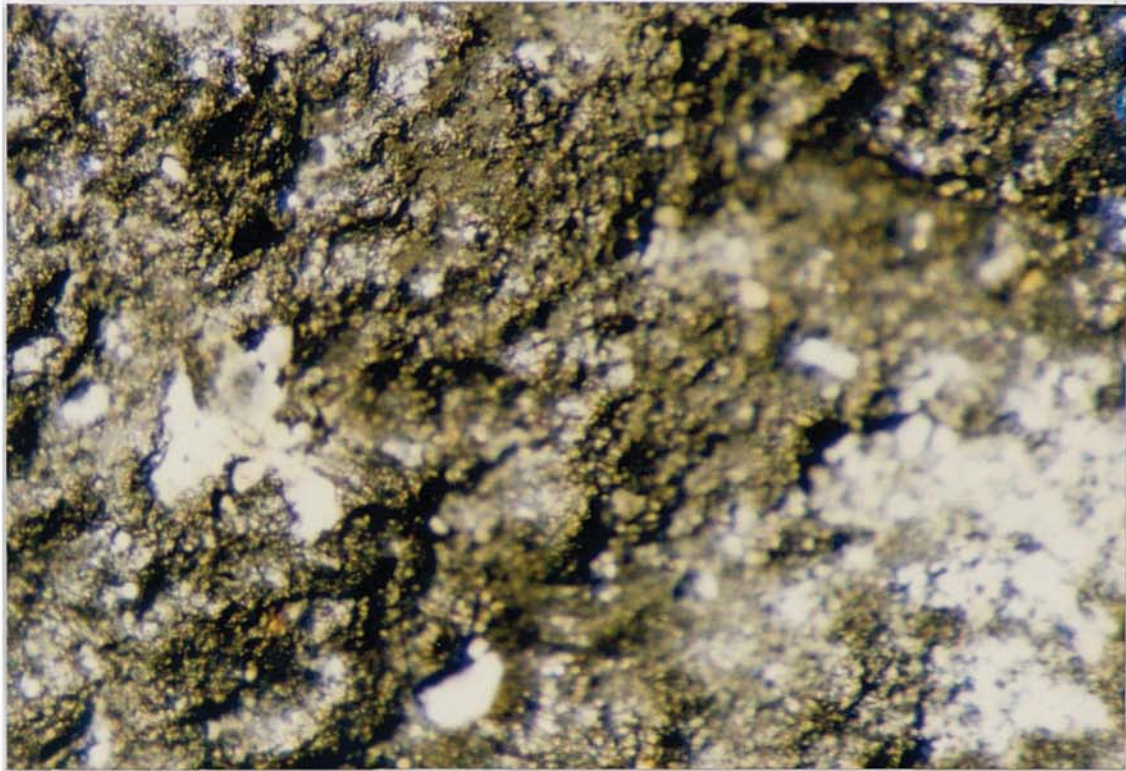


**Plate 6.11** Specimen P:2:50:2, 2 months: White crystalline deposit at coating/substrate interface. (scale 10 mm = 0.28 mm)



**Plate 6.12** Specimen P:2:50:1, 9 months: View of a cored bubble site, with bubble removed. (scale 10 mm = 1.07 mm)





**Plate 6.13** Specimen P:2:50:1, 9 months: View of acidified cement paste adhering to disbonded coating. (scale 10 mm = 1.07 mm)



**Plate 6.14** Specimen P:2:50:1, 9 months: SEM micrograph of similar area as that shown in plate 6.13.



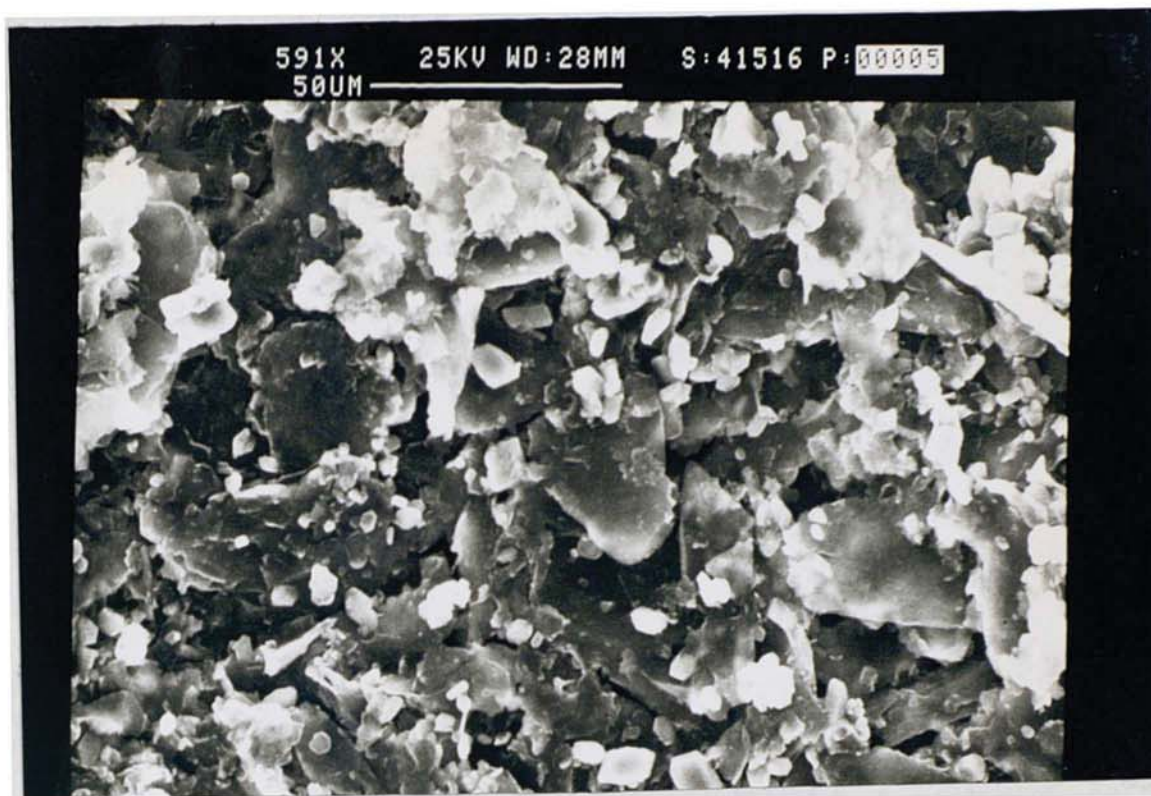


**Plate 6.15** Specimen P:2:50:1, 9 months: SEM micrograph showing open morphology of acidified coating, with adhering substrate surface particles.



**Plate 6.16** Specimen Z:2:50:1, 8 months: Surface "warts" and "white rust" formation over zinc pull-off sites.



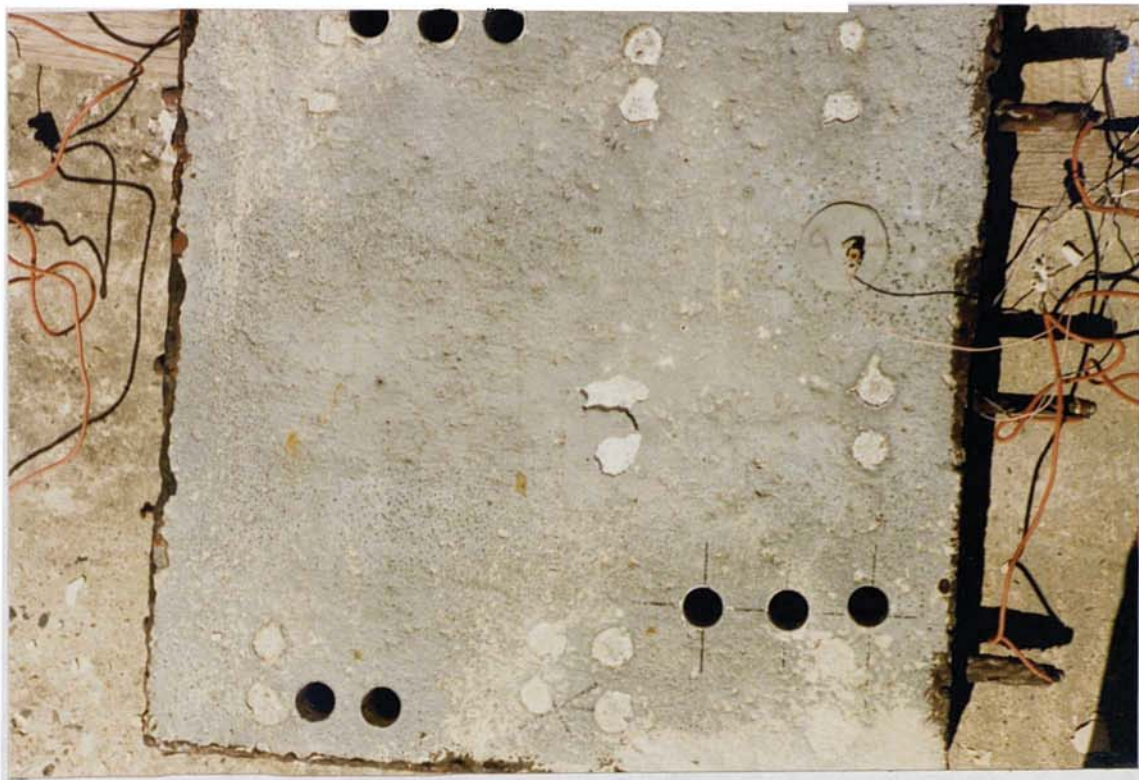


**Plate 6.17** Specimen Z:2:50:1, 12 months: Variation of zinc surface degradation.

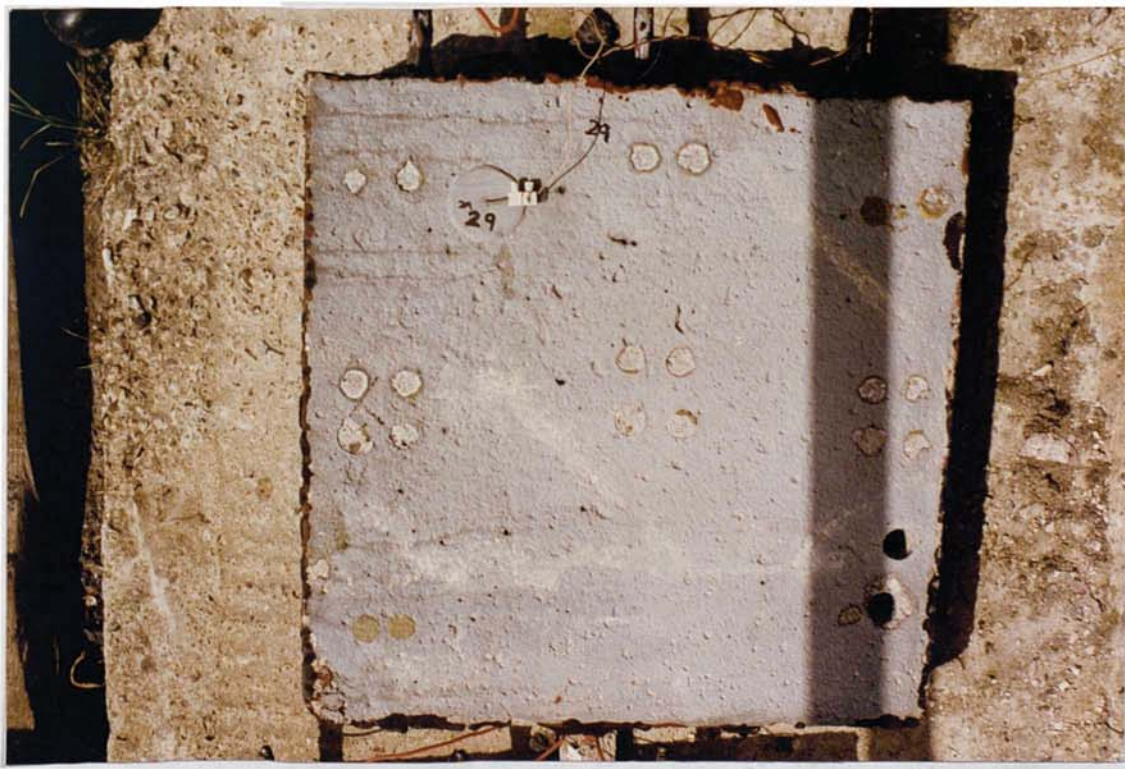


**Plate 6.18** Specimen Z:0.4:20:1, 12 months: Low zinc surface corrosion.





**Plate 6.19** Specimen Z:2:50:1, 18 months: Central area has debonded, good primary anode/epoxy resin/substrate bond. Brown dust from previous coring.



**Plate 6.20** Specimen Z:2:0:1, 4 months: Type 2 failure: zero degradation case. (10 mm = 1.07 mm)





**Plate 6.21** Specimen Z:0.4:20:2, 8 months: Type 3 failure (upper dolly) and type 4 failure (lower dolly).



**Plate 6.22** Specimen Z:2:50:1, 4 months: Type 5 failure. (10 mm = 1.07 mm)



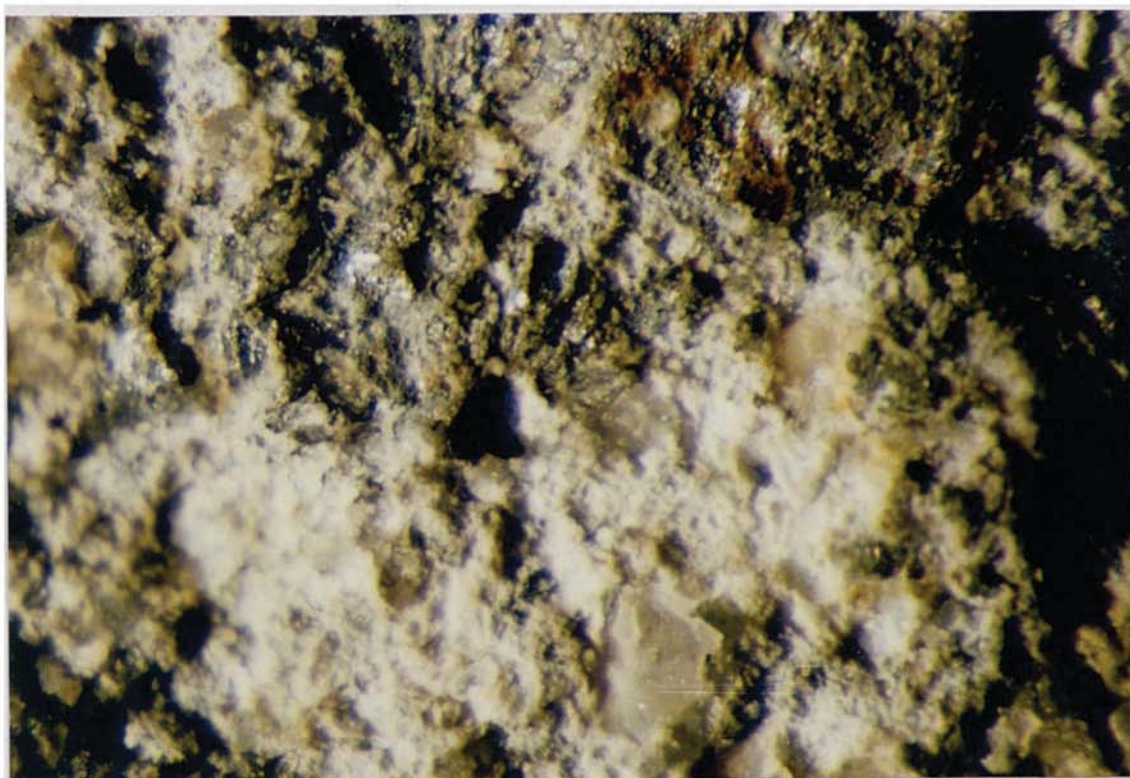


**Plate 6.23** Specimen Z:2:50:2, 4 months: Type 5 failure, amorphous 'white rust' /dull zinc surface. (10 mm = 0.28 mm)

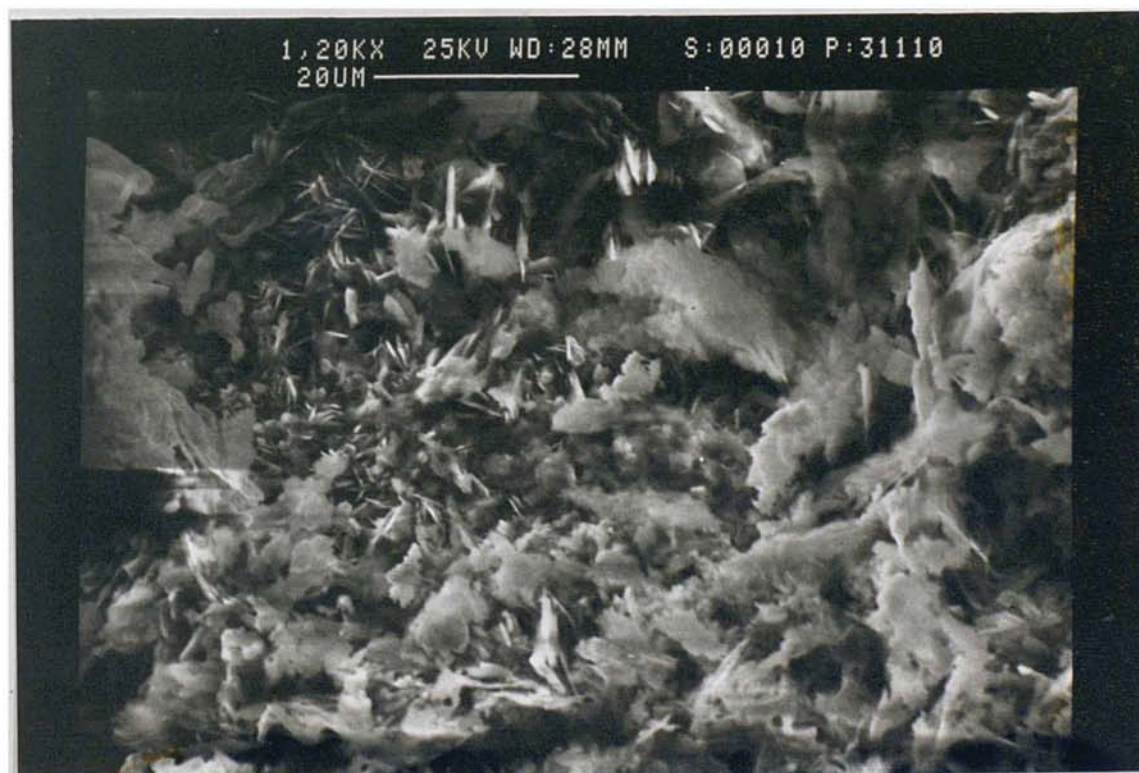


**Plate 6.24** SEM Micrograph of white zinc corrosion product.



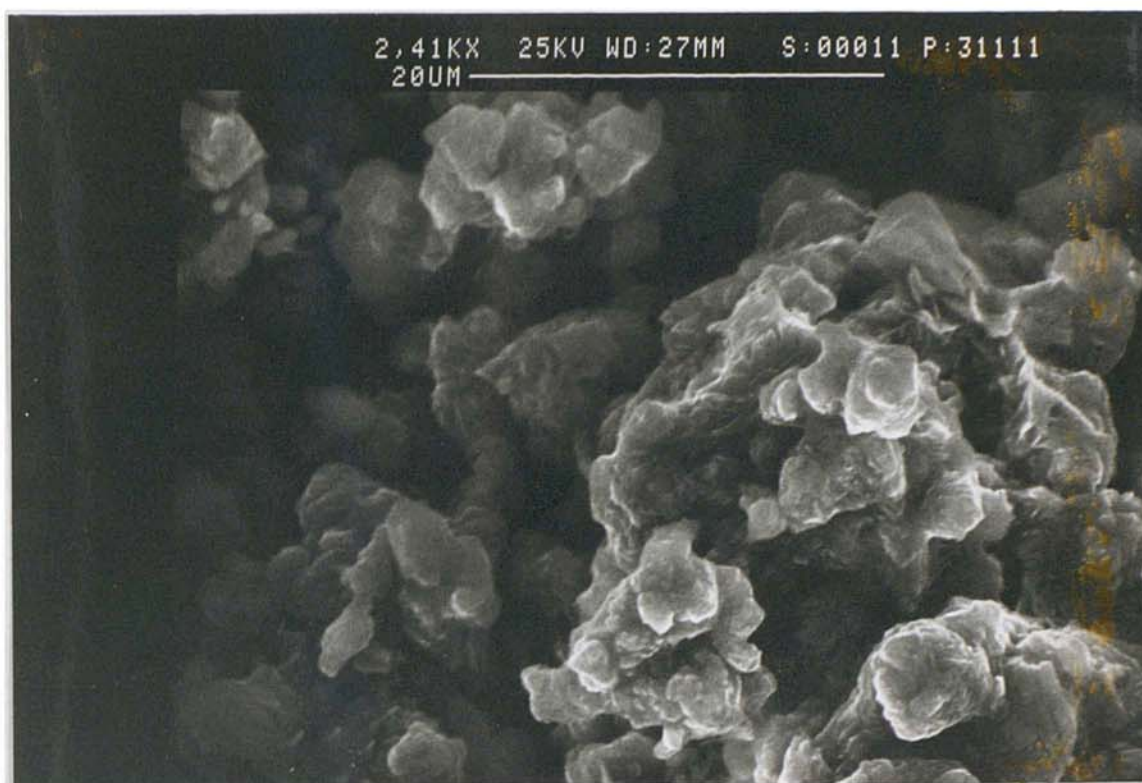


**Plate 6.25** SEM micrograph of zinc wart corrosion product, outer surface.



**Plate 6.26** SEM micrograph of zinc wart corrosion product, inner surface.





**Plate 6.27** SEM micrograph of zinc wart corrosion product, inner surface.



**Plate 6.28** SEM micrograph of zinc fracture surface, sample from paste block.

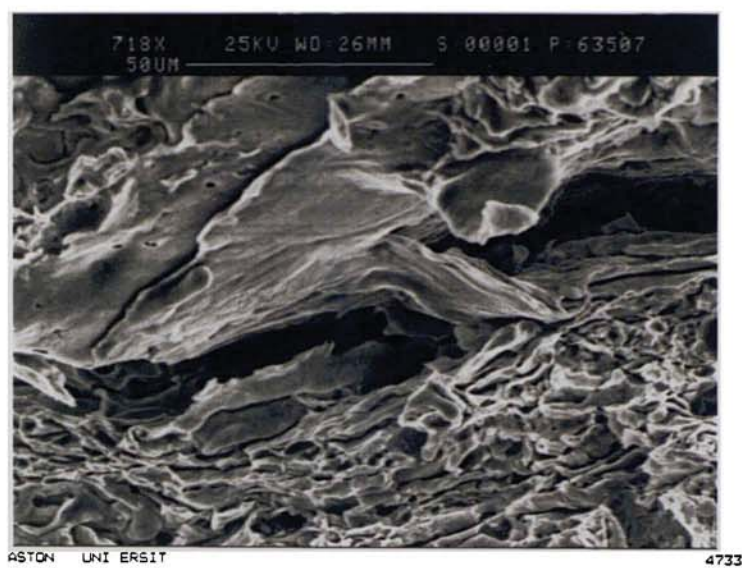


**Plate 6.29** SEM micrograph , detail of lateral crack observed in plate 6.28.

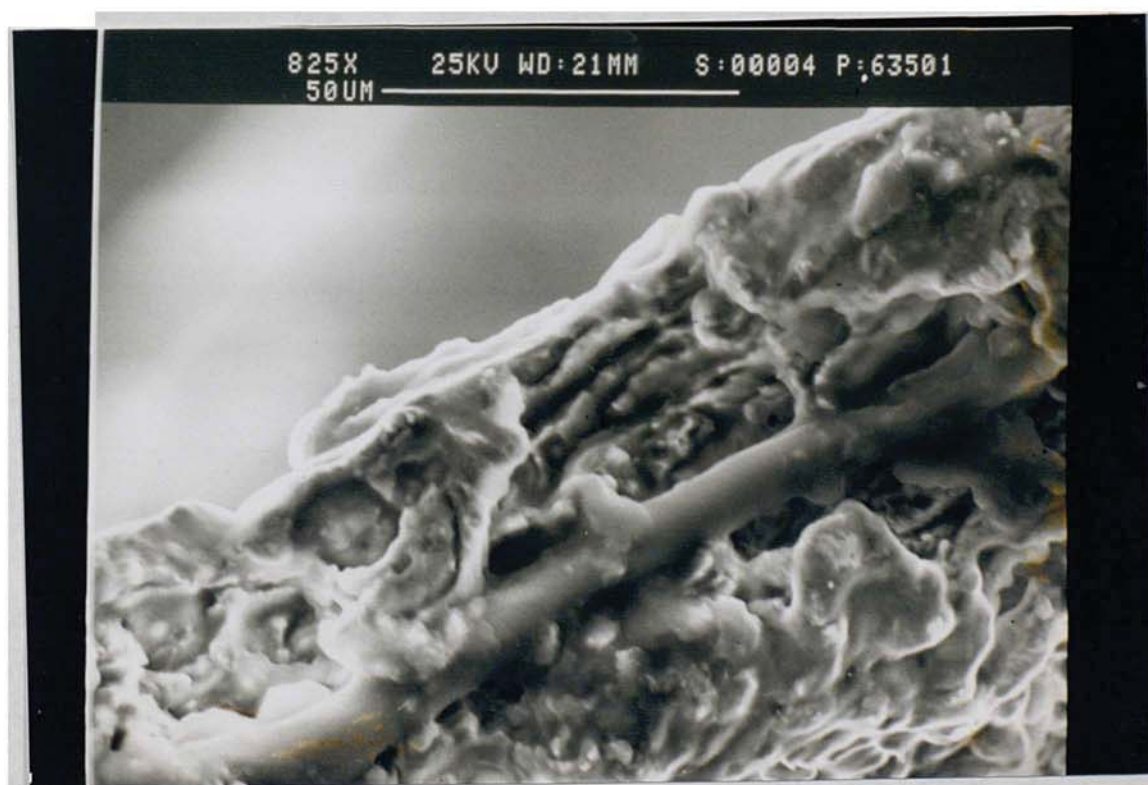


**Plate 6.30** SEM micrograph of zinc fracture surface, sample from zinc sprayed onto a microscope slide.





**Plate 6.31** SEM micrograph of zinc fracture surface, specimen Z:2:50:1.

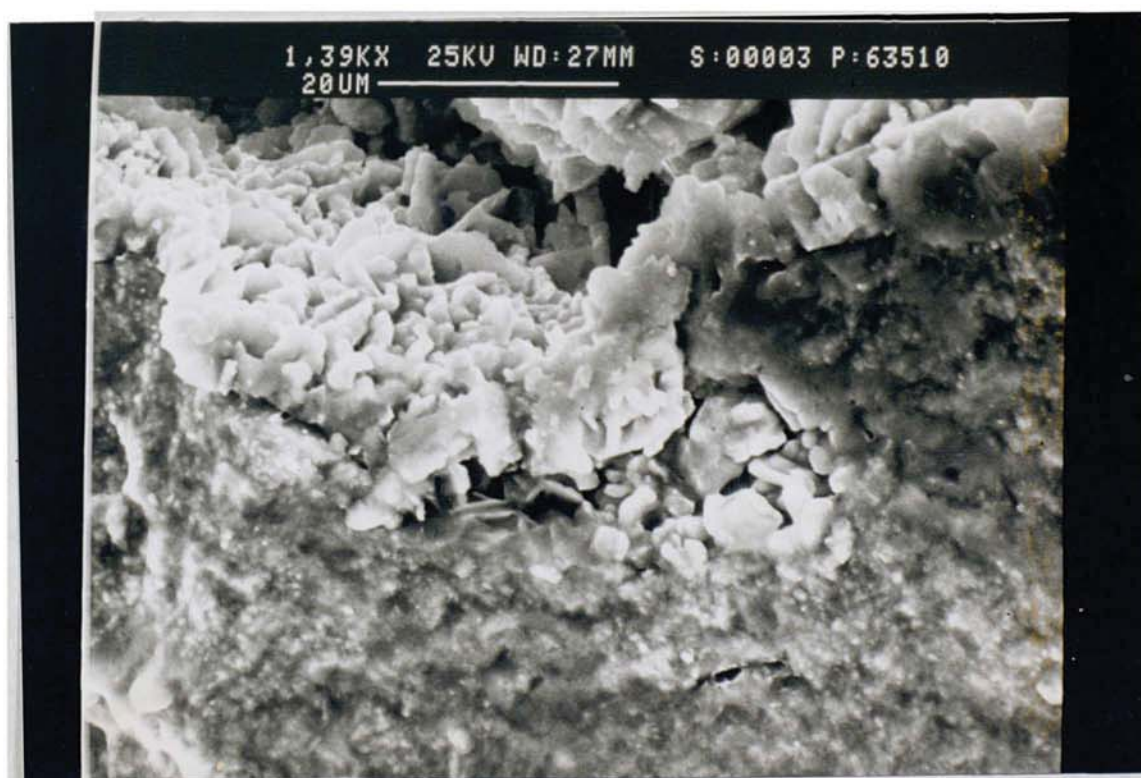


**Plate 6.32** SEM micrograph, detail of plate 6.31, interface of zinc corrosion site and zinc film.





**Plate 6.33** Specimen E:2:50:1, 8 months. Drying shrinkage cracking of cementitious overlay and light rust spotting.



**Plate 6.34** Specimen E:0.4:20:2, 8 months. Corrosion products surrounding an anode strand.





**Plate 6.35** Specimen E:2:50:2, 22 months. Carbonate precipitation within cored hole.



**Plate 6.36** Specimen E:4:20:1, 9 months. Type 2/3 degradation, reduced porosity in anode strand region. (10 mm = 1.07 mm)





**Plate 6.37** Specimen T:2:50:1, 9 months. Type 4/5 degradation, rust staining of paste on left associated with aggregate. (10 mm = 1.07 mm)



**Plate 6.38** Specimen E:2:50:1, 9 months. Type 5 degradation in cored specimen. (10 mm = 1.07 mm)





**Plate 6.39** Specimen E:2:50:1, 12 months. Type 6 degradation, crack extending from anode to surface is partially filled by a precipitate. (10 mm = 1.07 mm)



**Plate 6.40** Specimen T:2:50:1, 12 months. White crystalline product which precipitated along line of anode strand and within macro void. (10 mm = 1.07 mm)



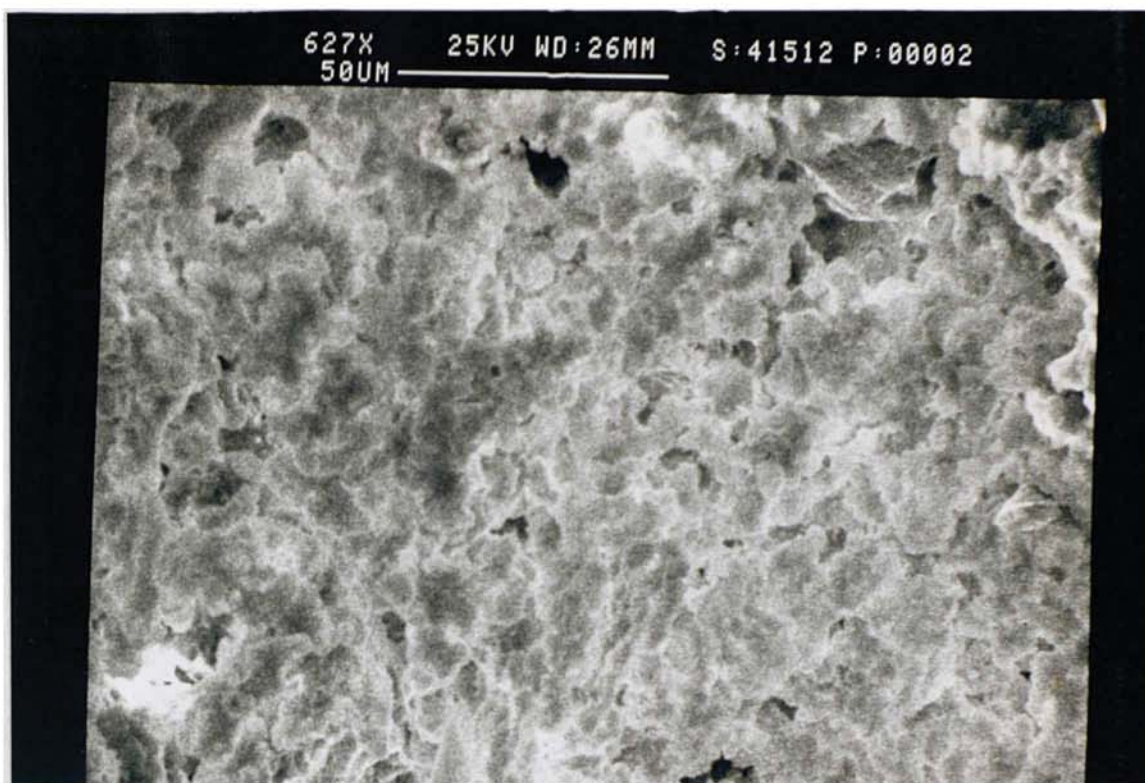


**Plate 6.41** SEM micrograph of crystalline precipitate shown in plate 6.40.



**Plate 6.42** Specimen E:2:50:1, 18 months. Overlay adhesion test (Limpit), failure at the overlay/substrate interface.





**Plate 7.1** Arrangement of slabs during cathode potential measurements.

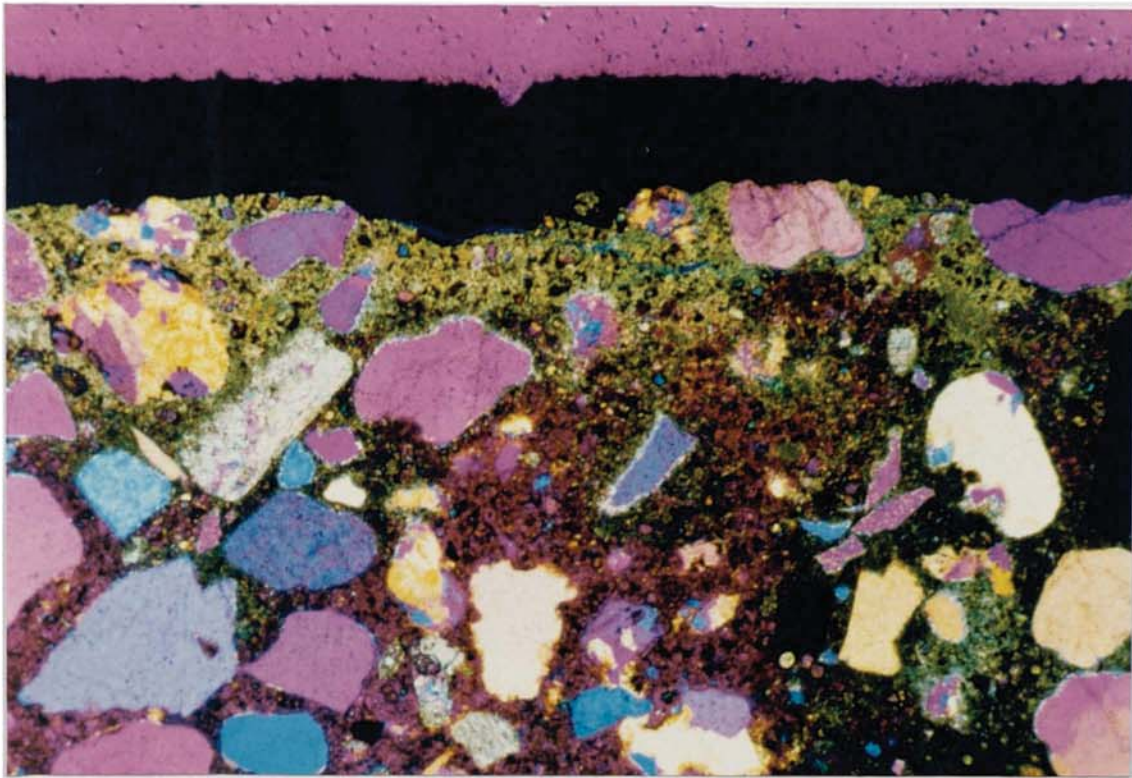


**Plate 8.1** Specimen P:2:0:1, 6 months, coating thickness  $\approx 250 \mu\text{m}$ , carbonation depth  $\approx 250 \mu\text{m}$  (light brown area), low porosity, surface cracking. Solid/mixed colours are small aggregates particles. Purple/black/brown areas are alkaline cement paste. (XP) (scale 10 mm = 171  $\mu\text{m}$ )

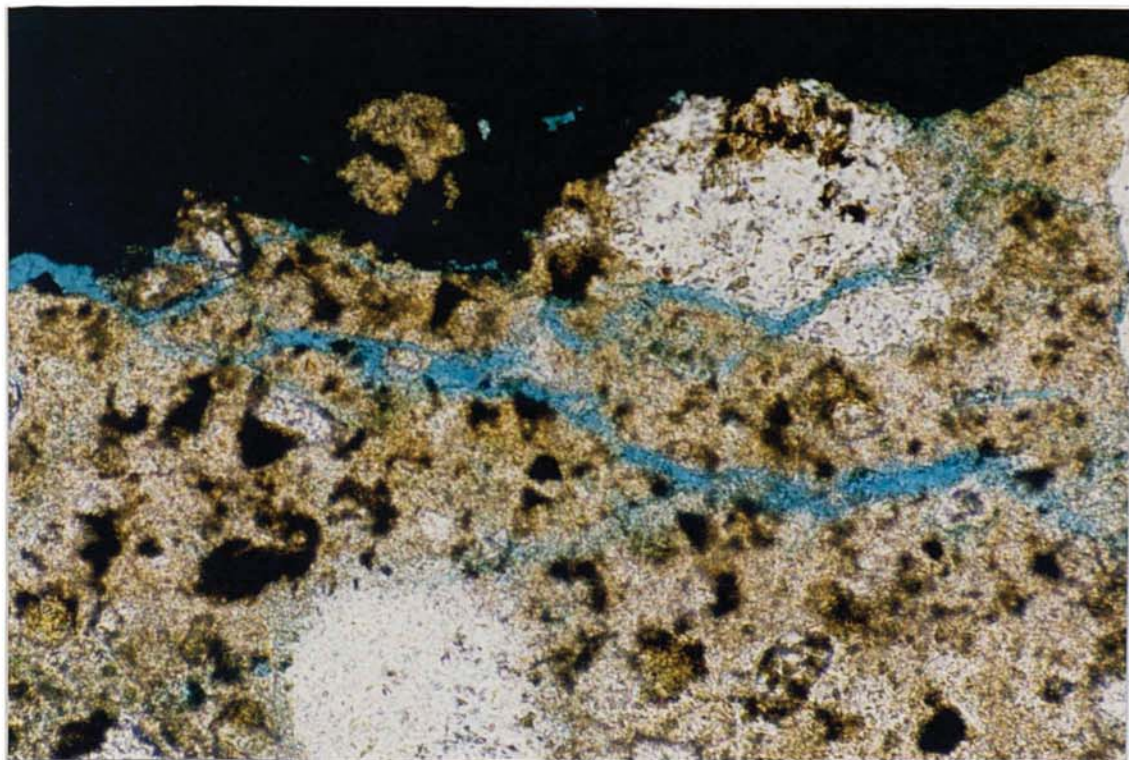


**Plate 8.2** Specimen P:2:0:1, 6 months, enlarged detail of cracked area. (scale 10 mm = 34  $\mu\text{m}$ )



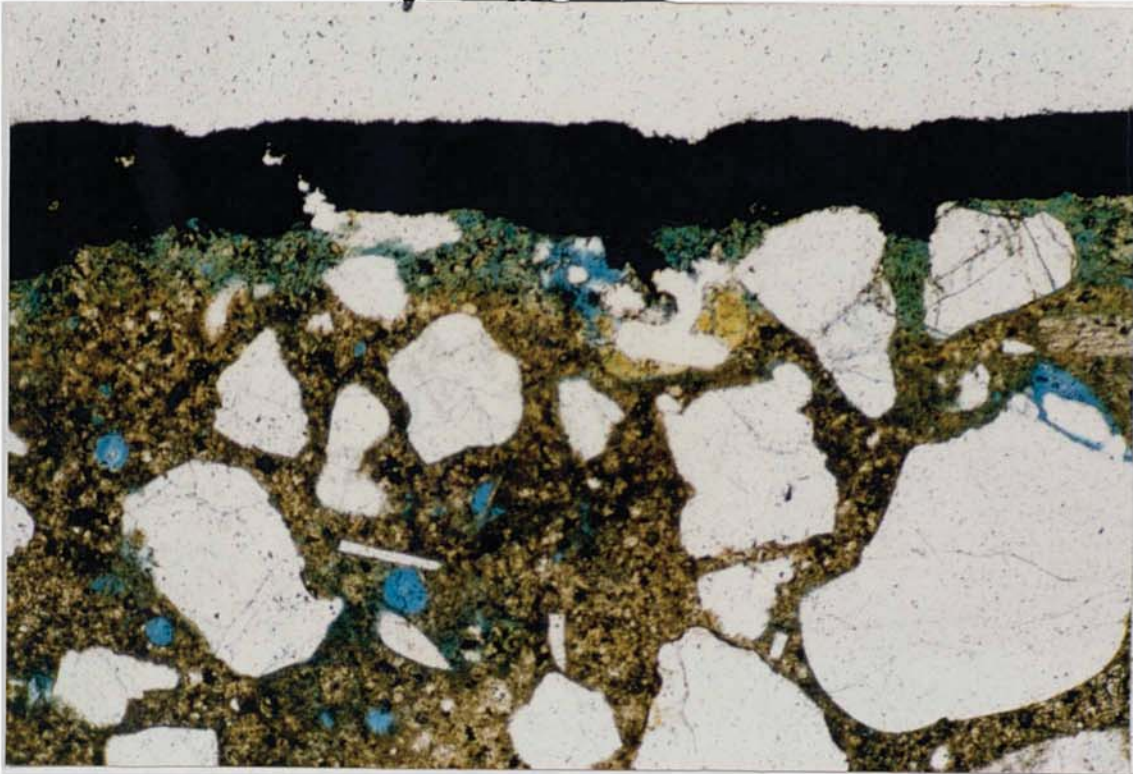


**Plate 8.3** Specimen P:2:50:1, 12 months, coating thickness  $\approx 200\ \mu\text{m}$ , very high surface porosity layer  $\approx 170\ \mu\text{m}$ . (scale 10 mm = 171  $\mu\text{m}$ )

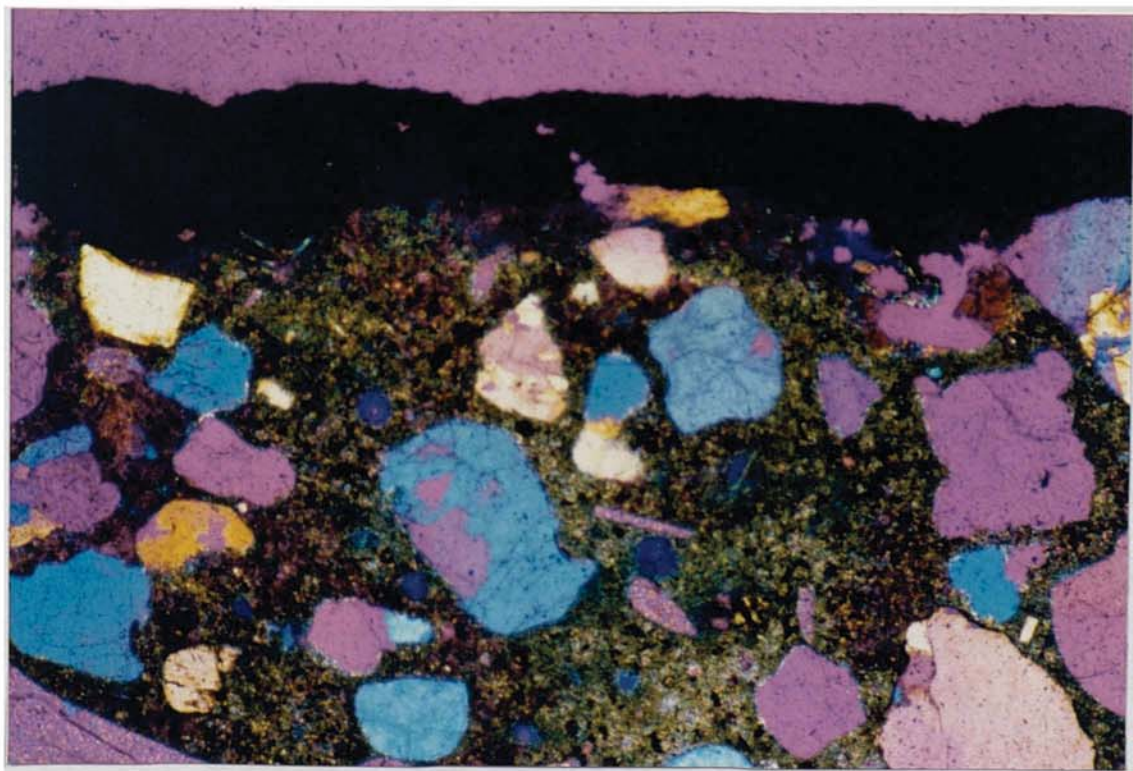


**Plate 8.4** Specimen P:2:50:1, 12 months, same area as plate 8.3, low alkalinity HCP to  $\approx 4\ \text{mm}$ . (XP)(scale 10 mm = 171  $\mu\text{m}$ )



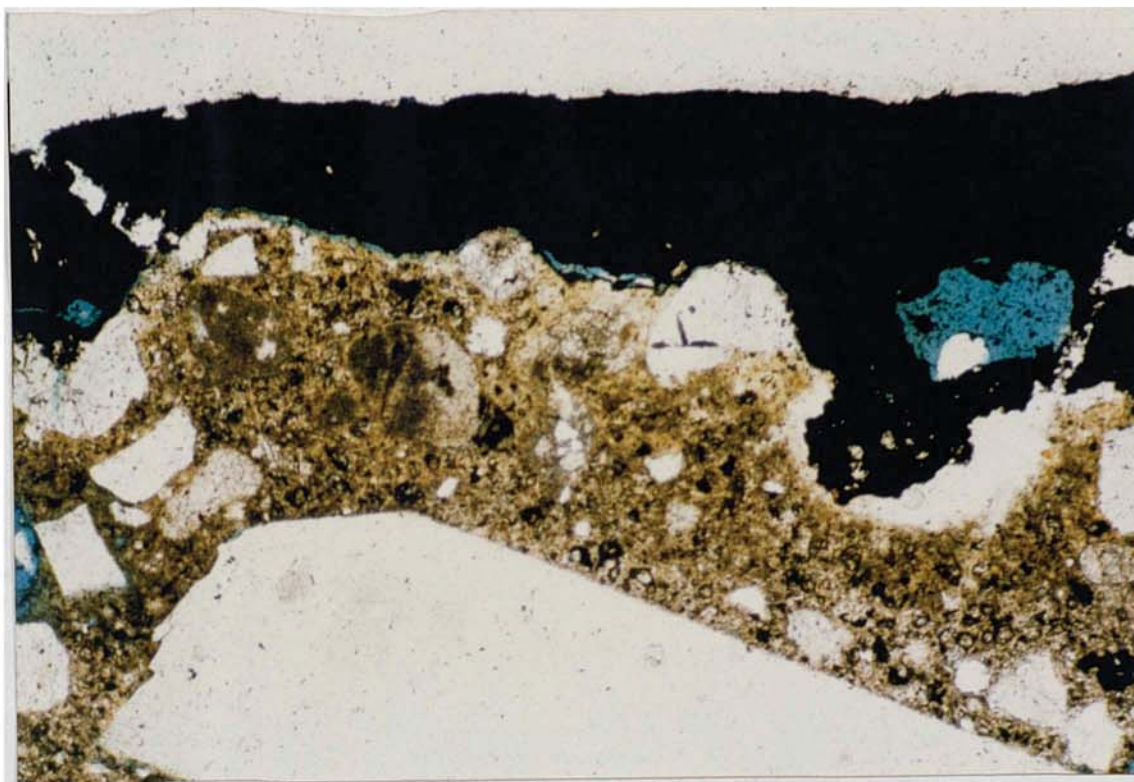


**Plate 8.5** Specimen P:2:50:1, 12 months, area adjacent to plate 8.3, low porosity, crack at interface, paint thickness 200 to 850  $\mu\text{m}$ , discontinuities in paint film. (scale 10 mm = 171  $\mu\text{m}$ )

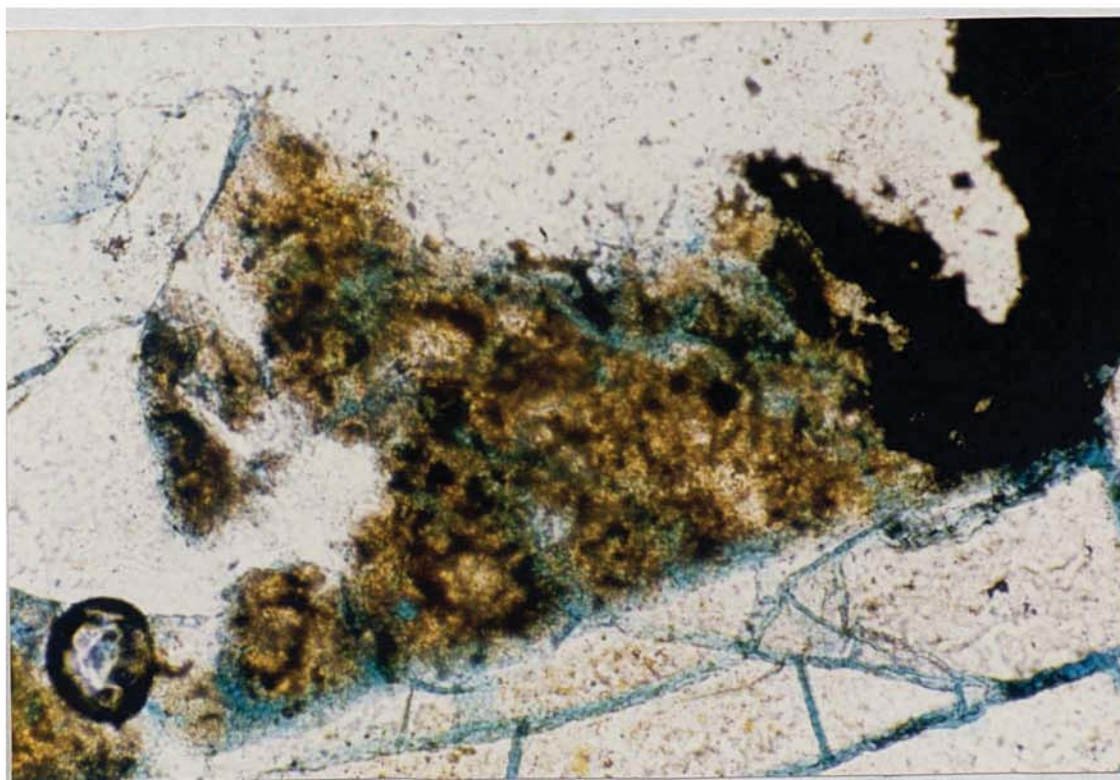


**Plate 8.6** Specimen P:2:50:1, 9 months, acidified bubble site, very high surface porosity, cracks in underlying aggregate, paint loss above site. (scale 10 mm = 34  $\mu\text{m}$ )





**Plate 8.7** Specimen Z:2:50:1, 3 months, shattered surface aggregate, zinc thickness  $\approx 340$   $\mu\text{m}$ . (scale 10 mm = 171  $\mu\text{m}$ )

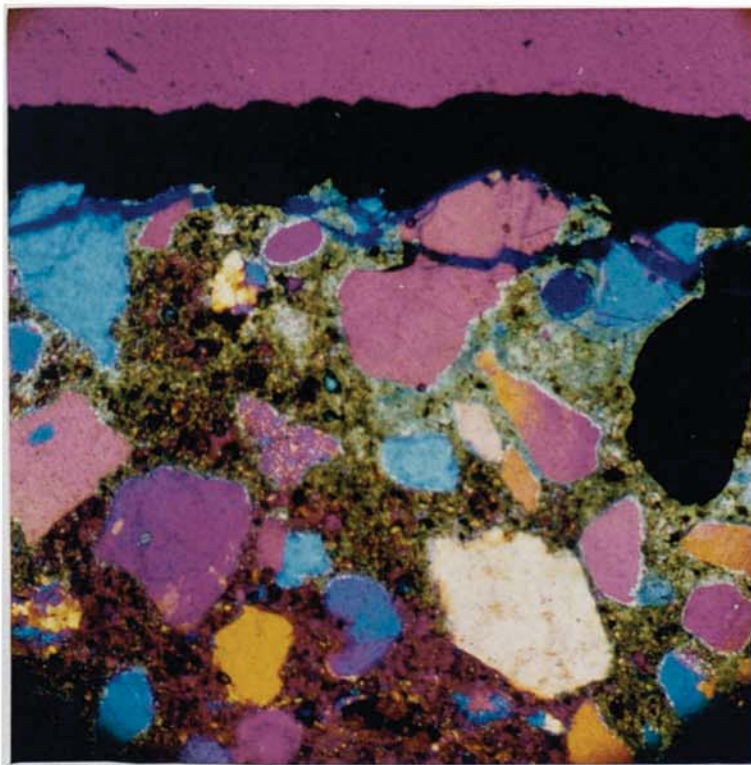


**Plate 8.8** Specimen Z:2:0:1, 3 months, shattered aggregate/surface cracking, zinc thickness  $\approx 170$   $\mu\text{m}$ , carbonation depth to 1.3 mm. (XP)(scale 10 mm = 171  $\mu\text{m}$ )



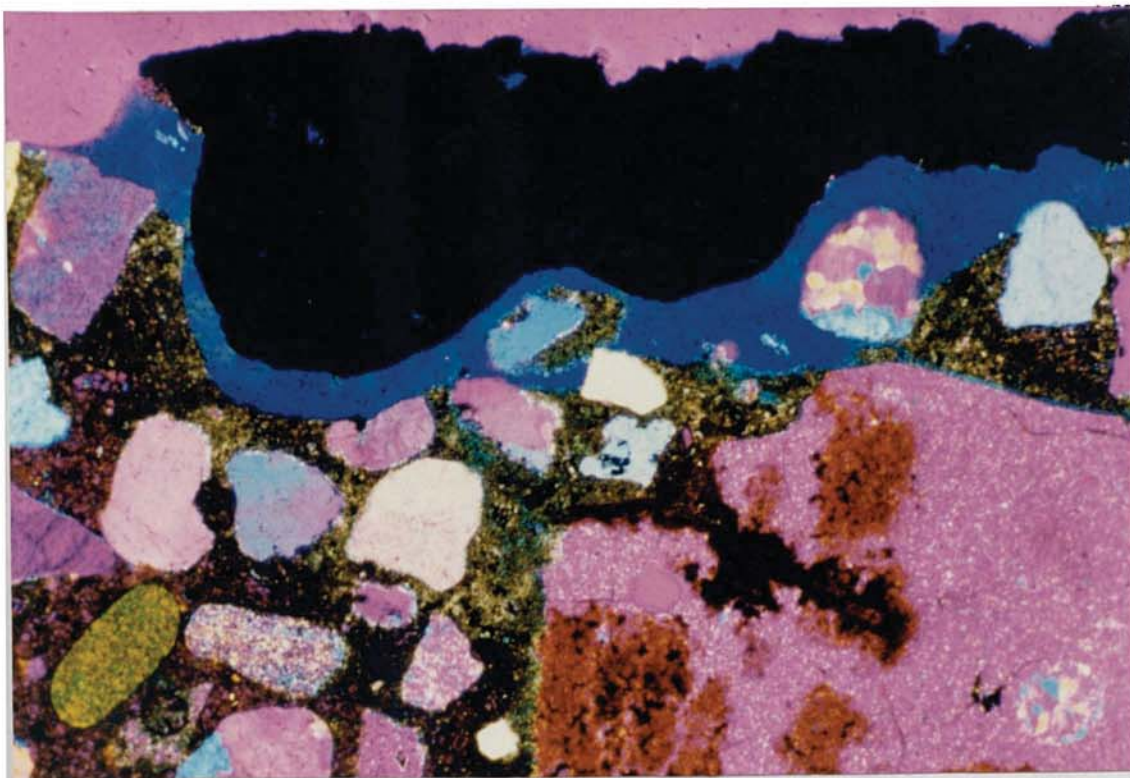


**Plate 8.9** Specimen Z:2:0:1, 6 months, zinc thickness 200 to 750  $\mu\text{m}$ , light carbonation to approximate depth 170  $\mu\text{m}$ , low porosity. (XP)(scale 10 mm = 171  $\mu\text{m}$ )

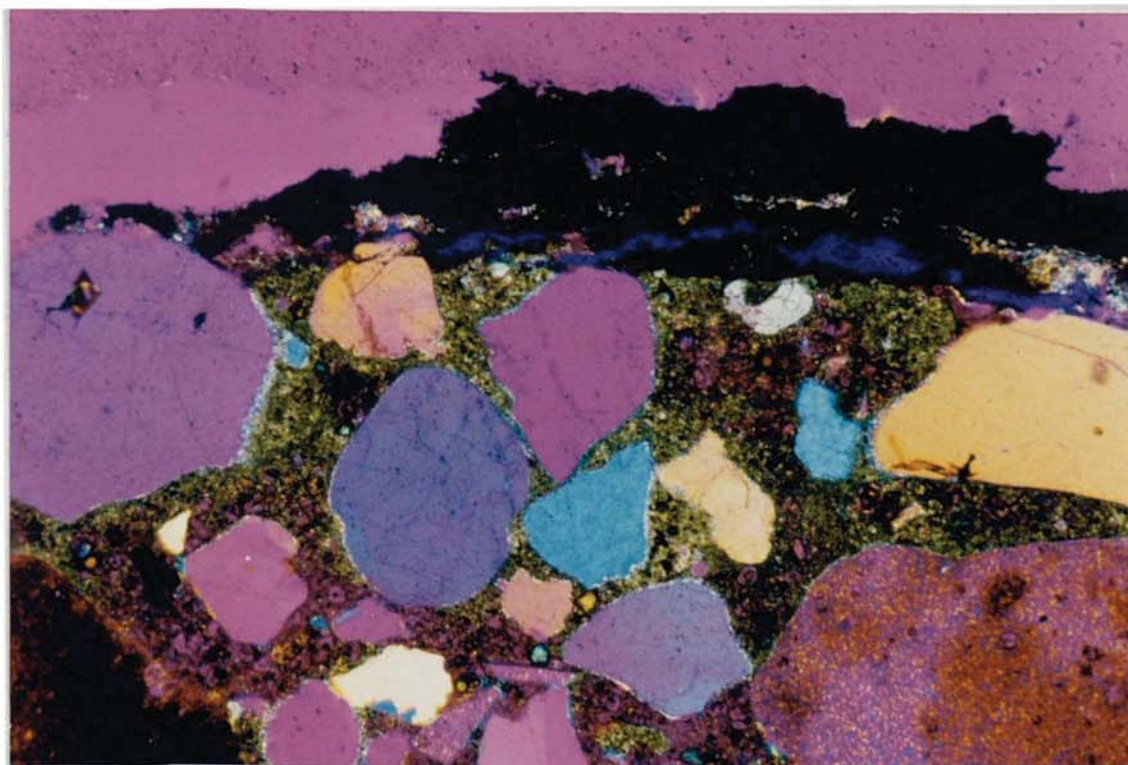


**Plate 8.10** Specimen Z:2:50:1, 9 months, zinc thickness  $\approx 100 \mu\text{m}$ , carbonation 850  $\mu\text{m}$ , low porosity, glassy phase adjacent to zinc with crack. (XP)(scale 10 mm = 171  $\mu\text{m}$ )



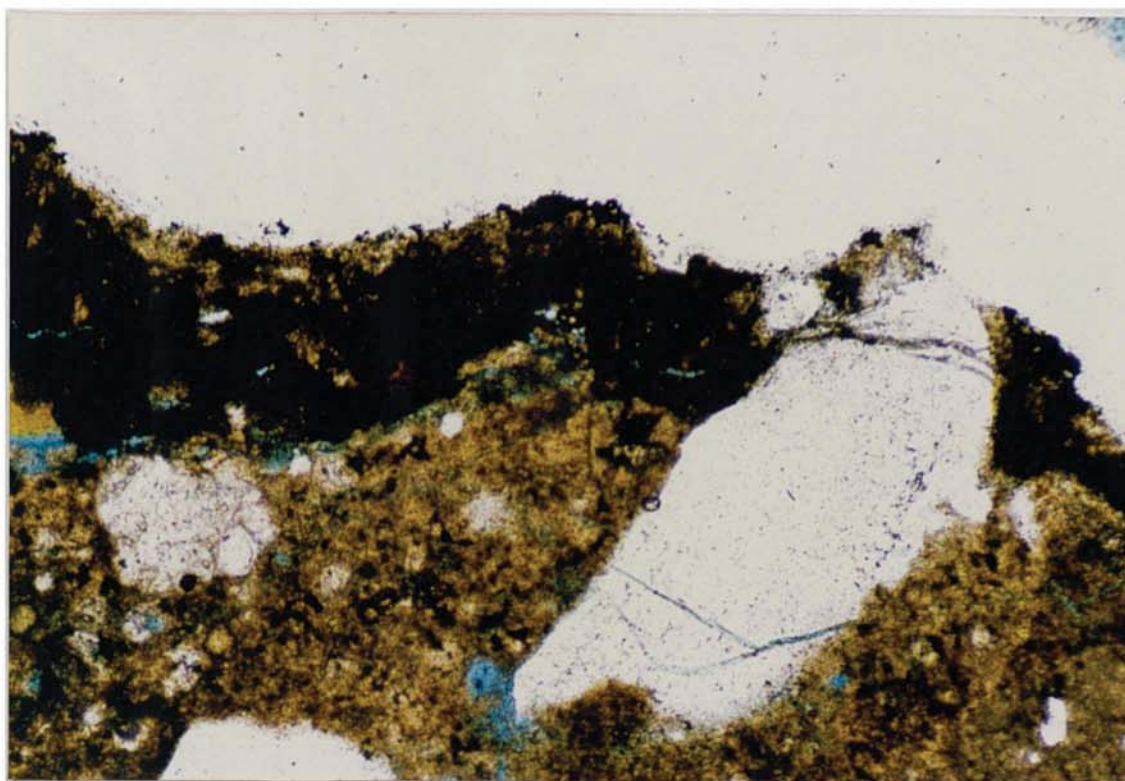


**Plate 8.11** Specimen Z:2:50:1, 9 months, detail of glassy phase at site where zinc has lifted, thickness 50 to 180  $\mu\text{m}$ . (scale 10 mm = 69  $\mu\text{m}$ )

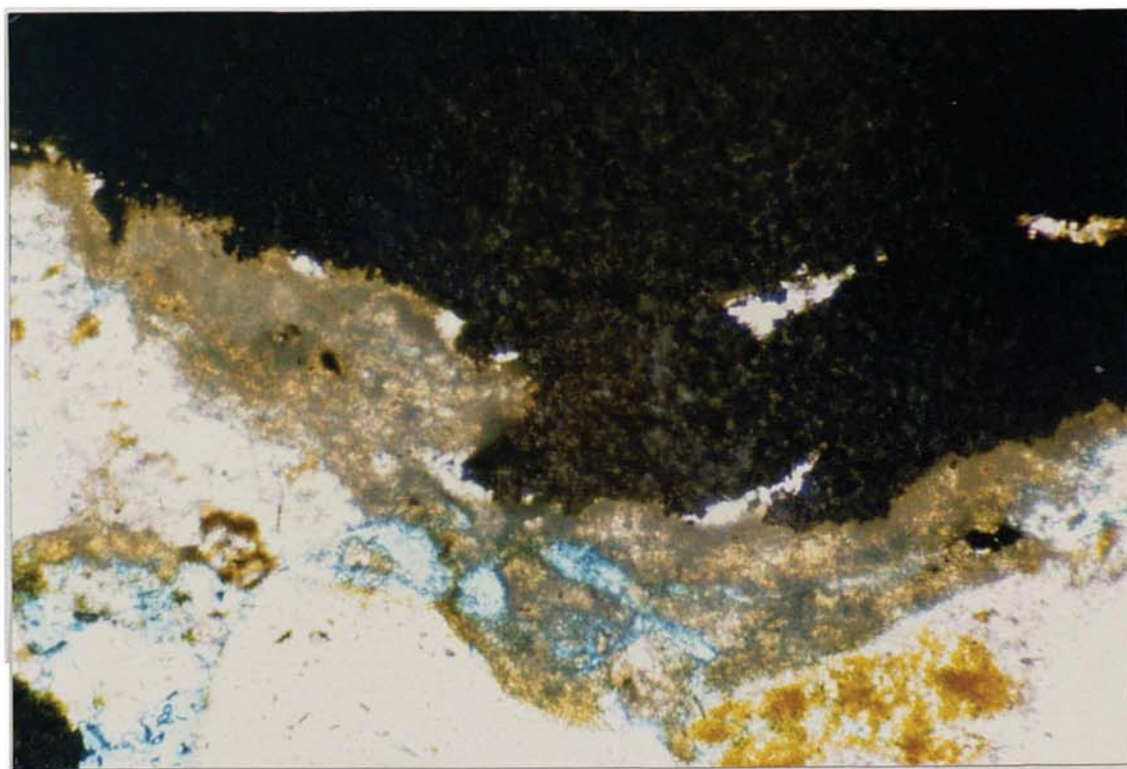


**Plate 8.12** Specimen Z:2:50:1, 3 months, detail of glassy phase/zinc boundary, porosity variable, thickness 50 to 90  $\mu\text{m}$ , lateral tears in zinc coating. (scale 10 mm = 34  $\mu\text{m}$ )



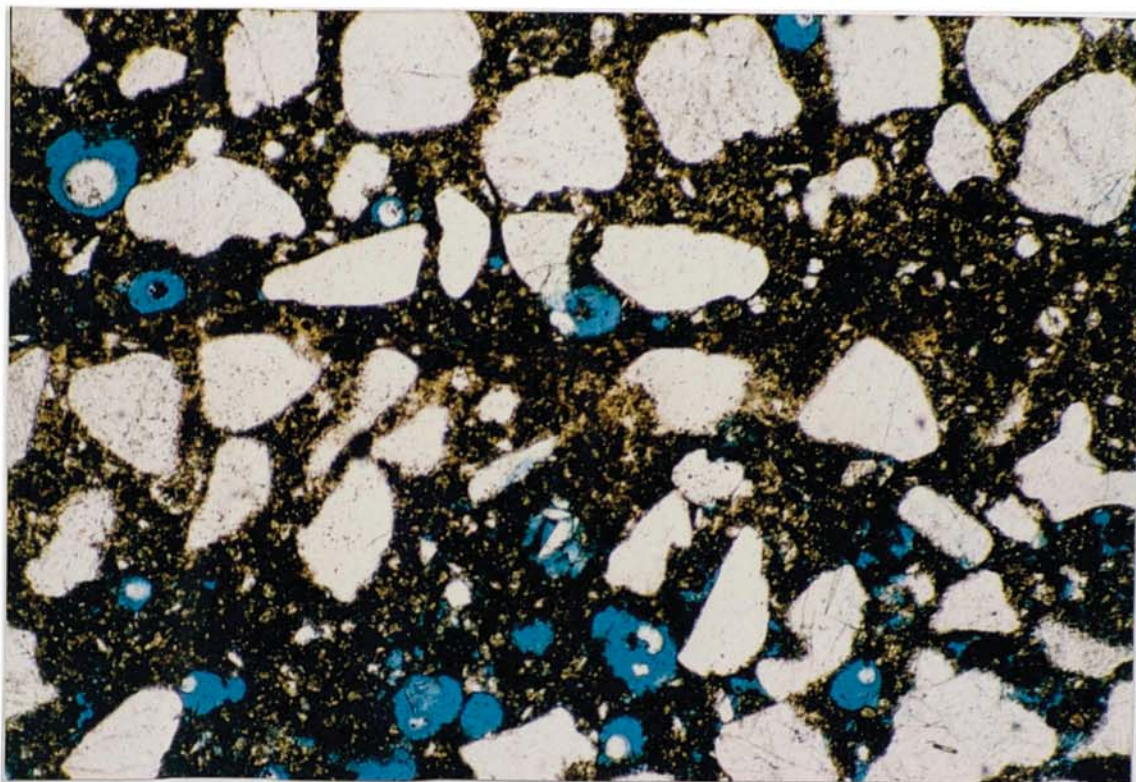


**Plate 8.13** Specimen E:2:50:1, 6 months, cementitious overlay, showing porosity banding due to the application methodology. (scale 10 mm = 171  $\mu\text{m}$ )

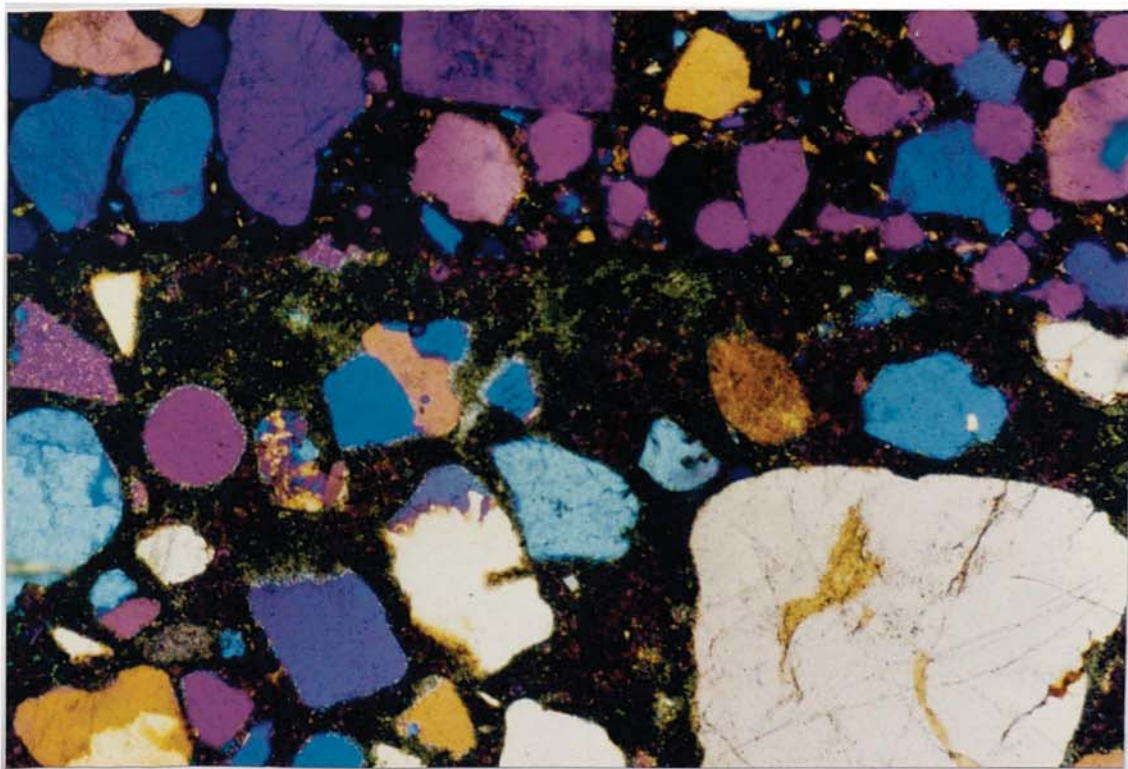


**Plate 8.14** Specimen T:2:0:1, 6 months, overlay/substrate boundary, light carbonation of substrate, intimate interface( $\frac{1}{3}$  from top). (XP)(scale 10 mm = 171  $\mu\text{m}$ )



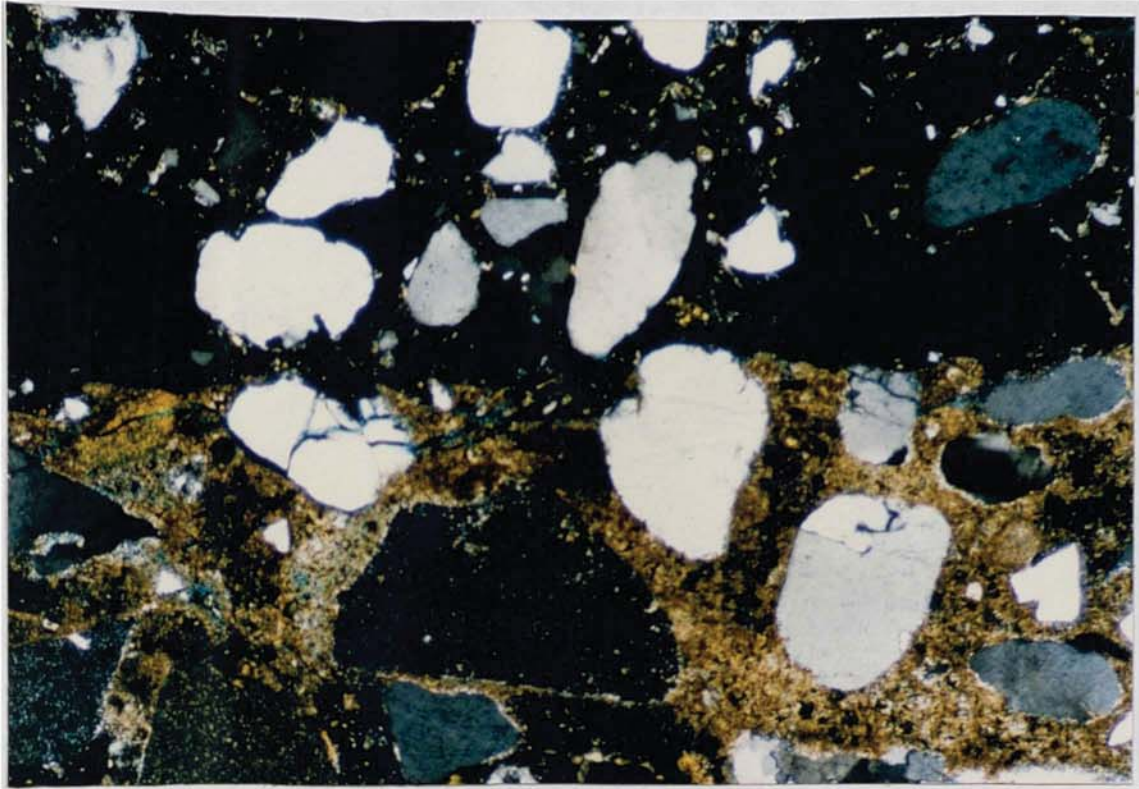


**Plate 8.15** Specimen T:2:50:1, 12 months, overlay (upper) / substrate (lower) boundary, crack along boundary passes through aggregate, light brown paste is carbonated. (polarised light)(scale 10 mm = 171  $\mu$ m)

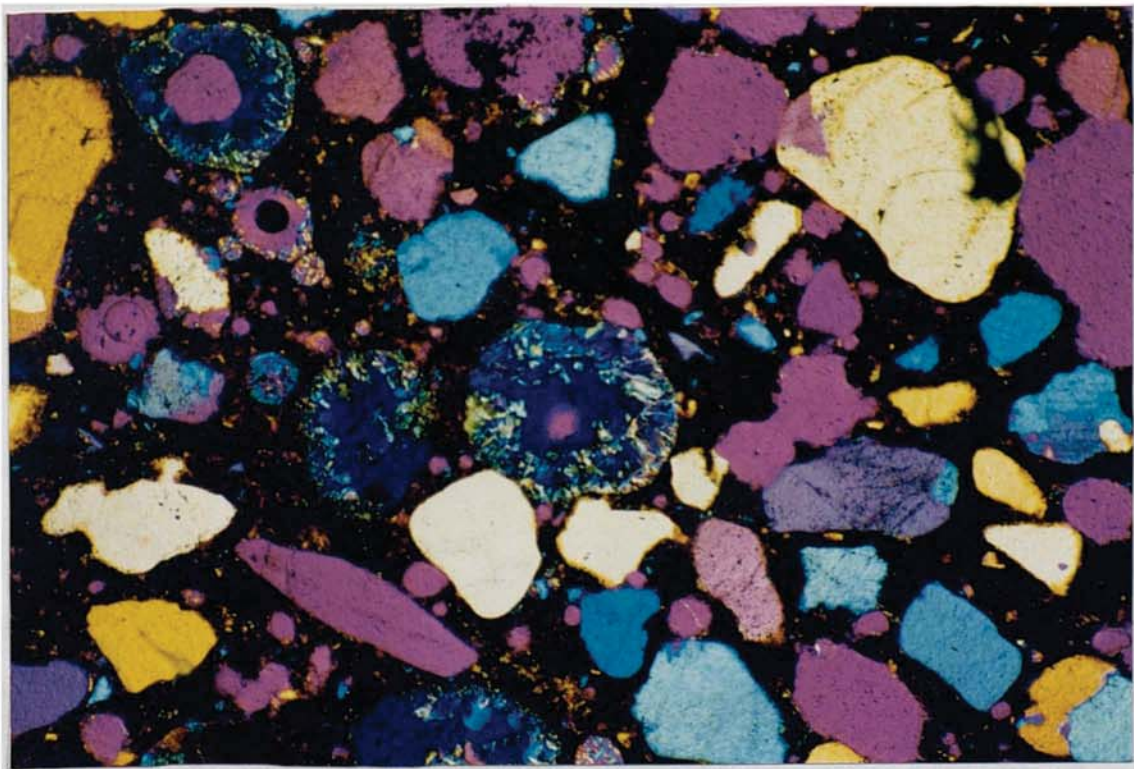


**Plate 8.16** Specimen T:2:50:1, 9 months, macro voids in overlay containing needle portlandite crystals at edges(appear multi coloured). (XP)(scale 10 mm = 171  $\mu$ m)



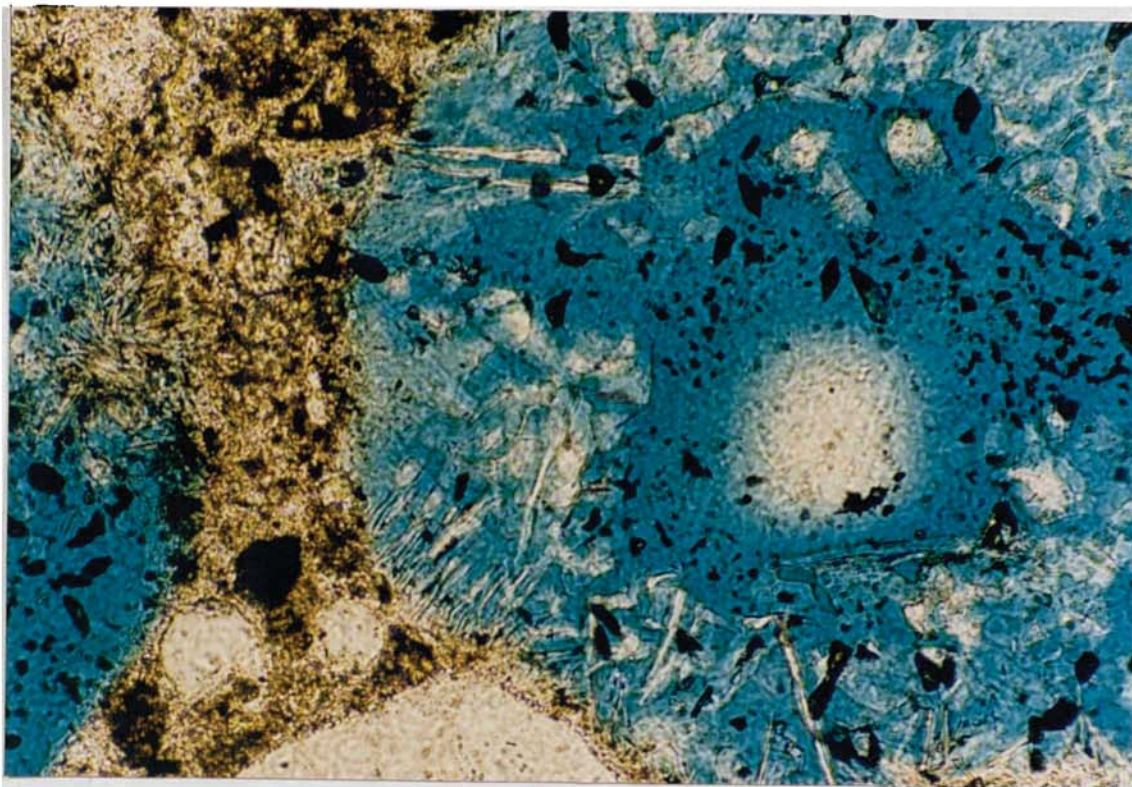


**Plate 8.17** Specimen T:2:50:1, 9 months, detail of needle portlandite crystals in plate 8.16. (scale 10 mm = 34  $\mu$ m)

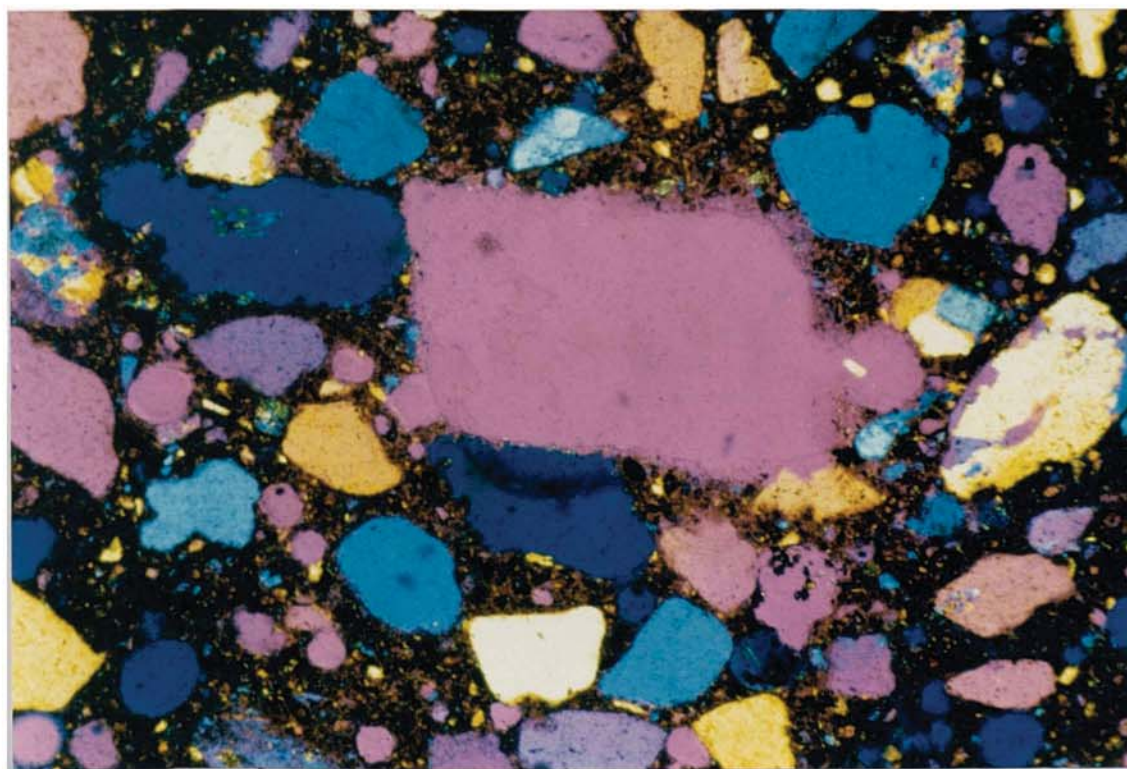


**Plate 8.18** Specimen T:4:20:1, 3 months, cross section of anode mesh with no apparent degradation to surrounding paste. (XP)(scale 10 mm = 171  $\mu$ m)



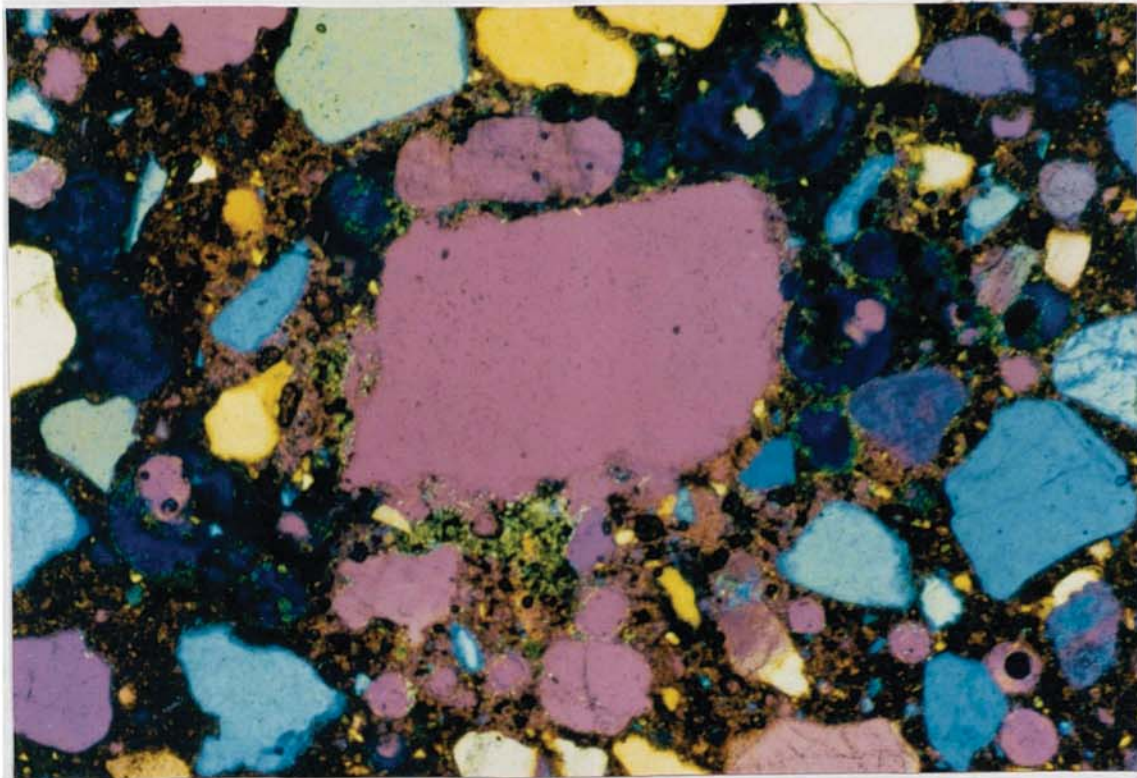


**Plate 8.19** Specimen T:4:20:1, 12 months, cross section of anode mesh with neutralisation of lower paste area up 50  $\mu\text{m}$ /modification to upper corner region. (XP)(scale 10 mm = 171  $\mu\text{m}$ )

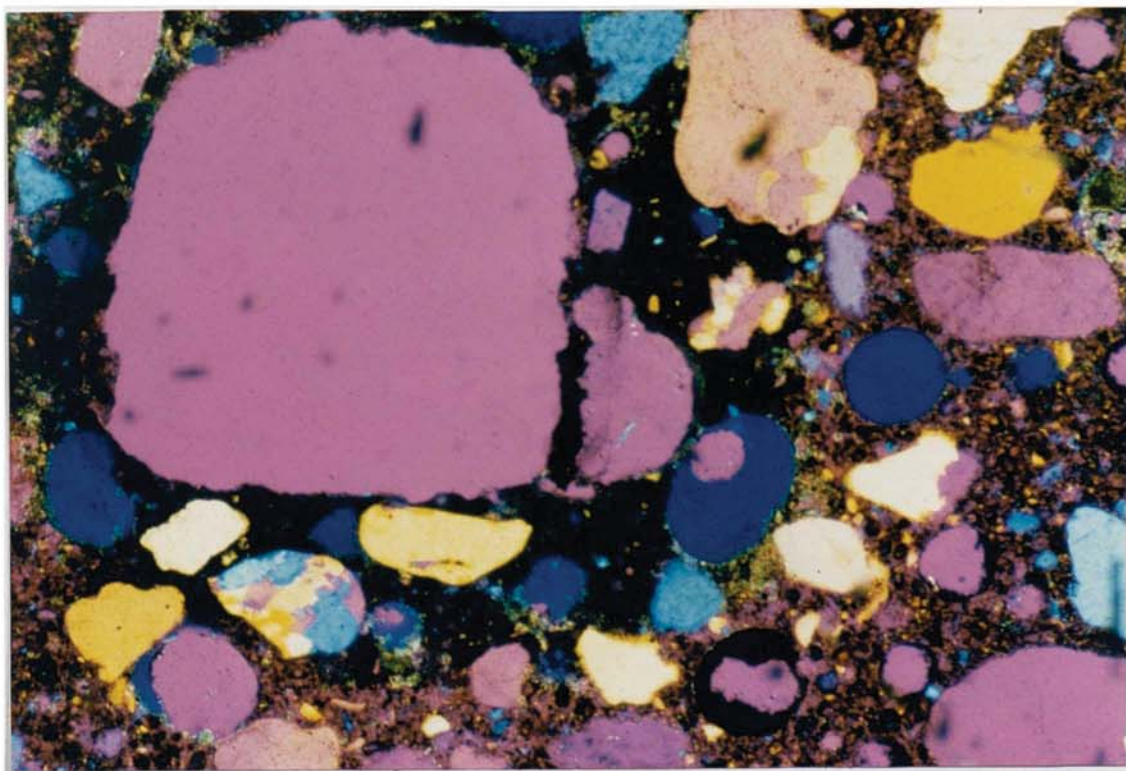


**Plate 8.20** Specimen T:2:50:1, 3 months, cross section of anode mesh with modification of paste up to 0.5 mm from anode. Paste neutralisation at limit of this modification. (XP)(scale 10 mm = 171  $\mu\text{m}$ )



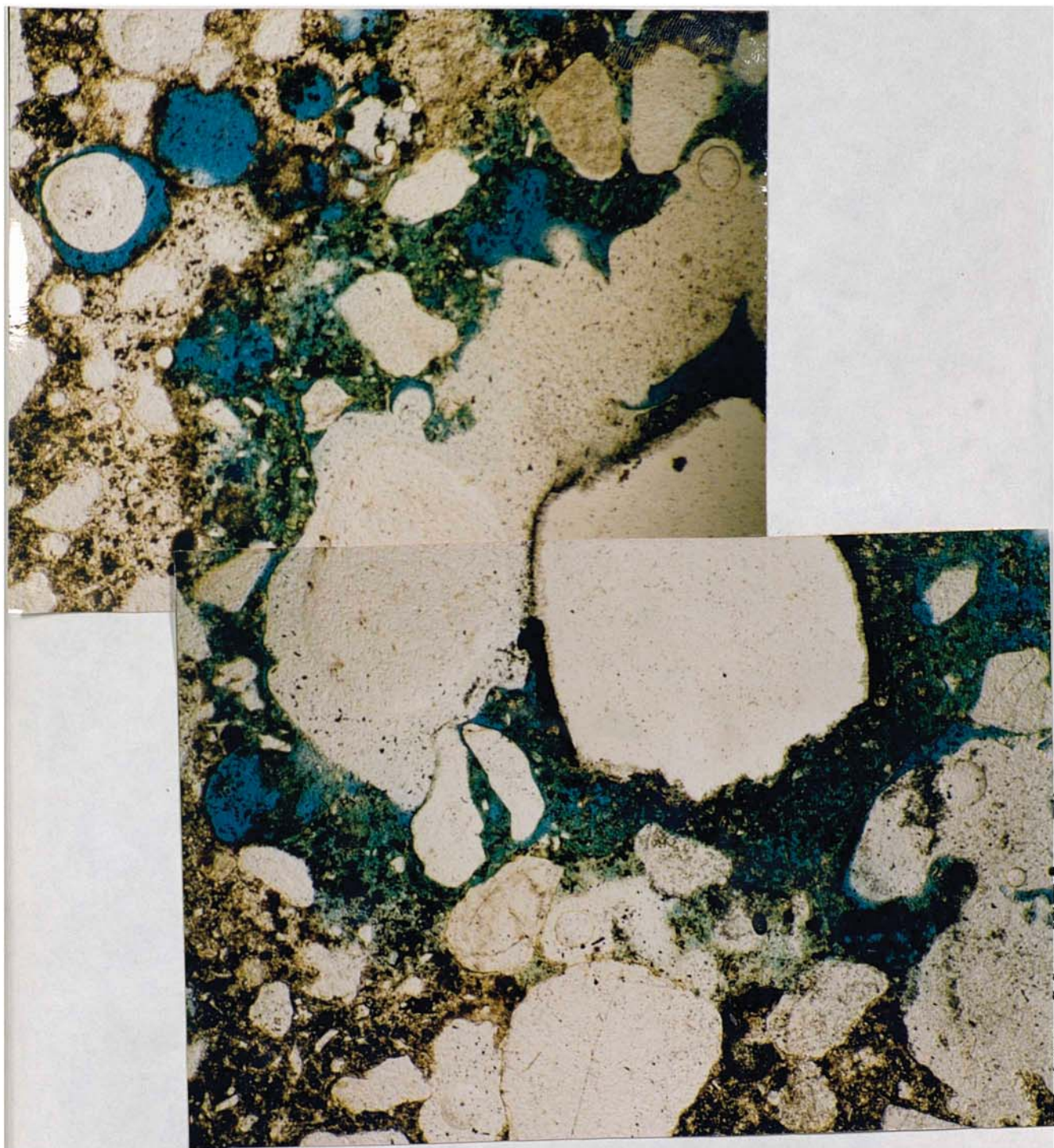


**Plate 8.21** Specimen T:2:50:1, 12 months, cross section of anode mesh. Significant modification of paste up to 1.1 mm from anode, no portlandite in very high porosity ring, clear area adjacent to the anode is an aggregate particle. (scale 10 mm = 171  $\mu$ m)



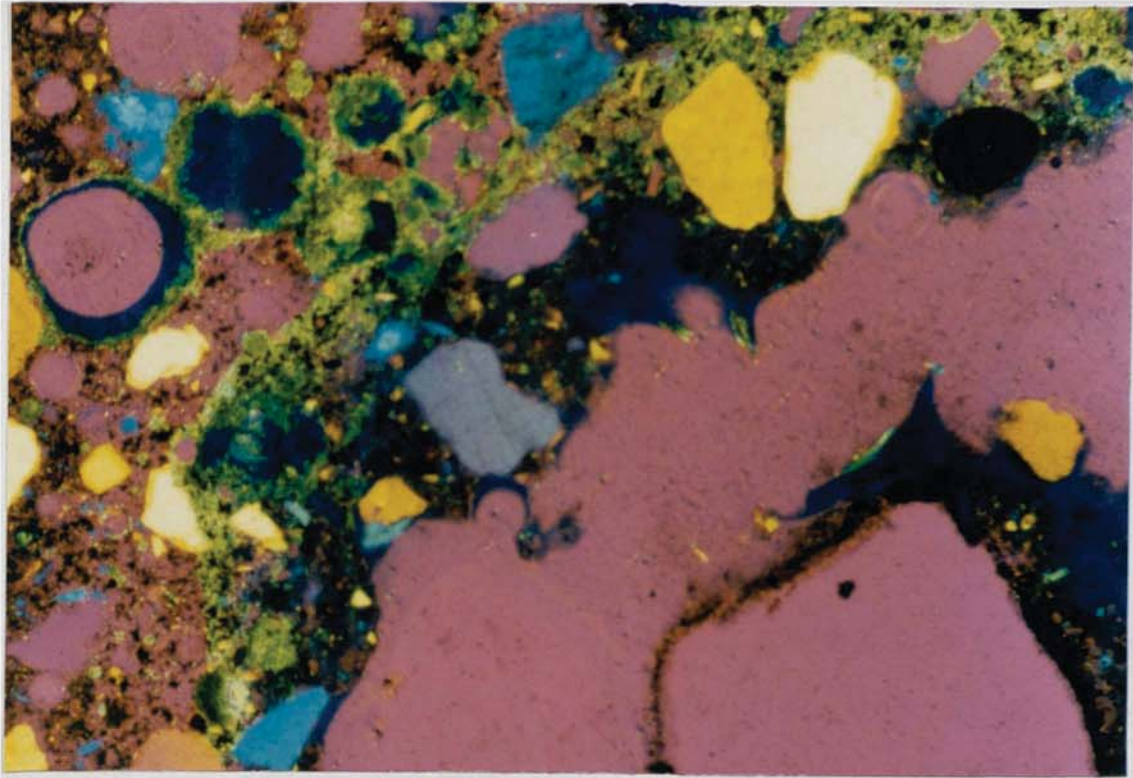


**Plate 8.22** Specimen T:2:50:1, 12 months, upper area of plate 8.21. Outer ring of neutralised paste, extends up to 0.5 mm from high porosity zone. (XP)(scale 10 mm = 171  $\mu$ m)

## Appendix C. Tables

CaO	SiO <sub>2</sub>	Al <sub>2</sub> O <sub>3</sub>	Fe <sub>2</sub> O <sub>3</sub>	SO <sub>3</sub>	MgO	Na <sub>2</sub> O	K <sub>2</sub> O	Acid Insoluble Residue
64.14	20.63	5.36	2.90	2.88	1.33	0.23	0.41	0.29

**Table 3.1** Chemical analysis of OPC cement

Saturated calomel electrode	E = + 0.241 V (SHE)
Hand held silver/silver chloride	E = + 0.236 V (SHE)
Copper/saturated copper sulphate	E = + 0.340 V (SHE)

**Table 3.2** Standard half cell potentials at 25°C

	Zinc	Paint	Anode E	Anode T
Area cm <sup>2</sup>	8.05	8.05	8.00	8.80

**Table 4.1** Anode electrode areas

Scan rate (mV/s)	Media	Investigator
10	saturated Ca(OH) <sub>2</sub>	Slater <i>et al</i> , 1976
0.5	saturated Ca(OH) <sub>2</sub> & OPC	Harrop, 1977
1.0	saturated Ca(OH) <sub>2</sub> & OPC	Page and Treadaway, 1982
25.0	saturated Ca(OH) <sub>2</sub> / NaOH & KOH (0.01M, 0.1M, 1.0M)	Sergi <i>et al</i> , 1985
0.056	saturated Ca(OH) <sub>2</sub> (de-aerated)	Berke, 1986
0.167	OPC/saturated Ca(OH) <sub>2</sub>	Naish <i>et al</i> , 1989

**Table 4.2** Potentiodynamic scan rates and media

Electrolyte	Ref.	pH	pH	pH
		theoretical	meter	indicator paper
saturated Ca(OH) <sub>2</sub>	N12	12.6	12.64	12.5
saturated Ca(OH) <sub>2</sub> + 0.4 M Cl <sup>-</sup> (as CaCl <sub>2</sub> )	C12		12.02	12
saturated CaCO <sub>3</sub>	N9	9.2	8.73	6
saturated CaCO <sub>3</sub> + 0.4 M Cl <sup>-</sup> (as CaCl <sub>2</sub> )	C9		6.68	5
H <sub>2</sub> O (deionised water)	N7	7	8.34	5
0.4 M Cl <sup>-</sup> (as CaCl <sub>2</sub> )	C7		5.20	5
0.05 M HCl	N2	1.30	1.36	0
0.05 M HCl + 0.4 M Cl <sup>-</sup> (as KCl)	C2		0.98	0

**Table 4.3** pH values of test electrolytes



Anode	Reference	Cations	[Cl <sup>-</sup> ] M/l	pH
Zinc	C12Z	Ca	0.4	12.02
	N12Z		0	12.64
	C9Z	Ca	0.4	6.68
	N9Z		0	8.73
	C7Z	Ca	0.4	5.20
	N7Z		0	8.34
Paint	C12P	Ca	0.4	12.02
	N12P		0	12.64
	C9P	Ca	0.4	6.68
	N9P		0	8.73
	C7P	Ca	0.4	5.20
	N7P		0	8.34
	C2P	K	0.4	0.98
	N2P		0	1.36
Anode E	C12E	Ca	0.4	12.02
	N12E		0	12.64
	C9E	Ca	0.4	6.68
	N9E		0	8.73
	C7E	Ca	0.4	5.20
	N7E		0	8.34
	C2E	K	0.4	0.98
	N2E		0	1.36
Anode T	C12T	Ca	0.4	12.02
	N12T		0	12.64
	C9T	Ca	0.4	6.68
	N9T		0	8.73
	C7T	Ca	0.4	5.20
	N7T		0	8.34
	C2T	K	0.4	0.98
	N2T		0	1.36

**Table 4.4** Schedule of polarisation curves

Ref.	$E_{corr}$ $E_m$ mV	$i_{corr}$ $i_m$ $\mu A/cm^2$	$E_{pp}$ mV	$i_{crit}$ $\mu A/cm^2$	$E_{tp}$ mV	$i_l$ $\mu A/cm^2$	$\Delta t$ °C	$\Delta$ $pH_a$	$\Delta$ $pH_c$	$\beta_a$ mV/ dec	Notes
C12Z	-1350 -660	10 $7 \times 10^3$	-1170 -660	$1.8 \times 10^3$ $7 \times 10^3$	-840 -260	440 $1.6 \times 10^3$	+5	0	0	85	2 passive loops
N12Z	-1325 -1200	4 400	-1200	400		170	+2	0	0	100	passivation
			$E_n$	$i_n$	$E_t$	$i_t$					
C9Z	-1150 -220	0.2 $50 \times 10^3$	-1100	100	-1040	$1 \times 10^3$	+2	0	+6	60	active dissolution
N9Z	-1080 480	$0.1 \times 10^{-3}$ 270			-940	2	0	0	0		passivation
C7Z	-1080 -190	0.1 $70 \times 10^3$	-1010	300	-980	$1 \times 10^3$	+7	0	+6	20	active dissolution
N7Z	-850 600	$0.4 \times 10^{-3}$ 50			-810	0.1	+2	0	+2		passivation

**Table 4.5** Potentiodynamic anodic polarisation results for anode Z

Ref.	$E_{corr}$ $E_m$ mV	$i_{corr}$ $i_m$ $\mu A/cm^2$	$E_n$ mV	$i_n$ $\mu A/cm^2$	$E_t$ mV	$i_t$ $\mu A/cm^2$	$\Delta t$ $^{\circ}C$	$\Delta$ $pH_a$	$\Delta$ $pH_c$	$\beta_a$ mV/ decade
C12T	-230 1440	$1 \times 10^{-3}$ $65 \times 10^3$	540	30	625	$1 \times 10^3$	+3	0	0	56
N12T	-230 1425	$0.1 \times 10^{-3}$ $37 \times 10^3$	550	30	650	$1 \times 10^3$	+3	0	0	66
C9T	100 1710	$1 \times 10^{-3}$ $70 \times 10^3$	1030	100	1125	$1 \times 10^3$	+7	0	+8	95
N9T	40 1600	$3 \times 10^{-3}$ 200					+1	0	0	
C7T	115 1250	$1 \times 10^{-3}$ $30 \times 10^3$	1050	100	1175	$10 \times 10^3$	+5	0	+7	63
N7T	50 1675	$4 \times 10^{-3}$ 170					+1	0	+1	
C2T	410 2040	$0.5 \times 10^{-3}$ $42 \times 10^3$	1070	50	1180	$1 \times 10^3$	+4	0	0	85
N2T	420 2060	$1 \times 10^{-3}$ $50 \times 10^3$	1125	70	1200	$1 \times 10^3$	+2	0	0	65

**Table 4.6** Potentiodynamic anodic polarisation results for anode T

Ref.	$E_{corr}$ $E_m$ mV	$i_{corr}$ $i_m$ $\mu A/cm^2$	$E_n$ mV	$i_n$ $\mu A/cm^2$	$E_t$ mV	$i_t$ $\mu A/cm^2$	$\Delta t$ $^{\circ}C$	$\Delta$ $pH_a$	$\Delta$ $pH_c$	$\beta_a$ mV/ decade
C12E	-194 1310	$1 \times 10^{-3}$ $30 \times 10^3$	550	6	800	$1 \times 10^3$	+3	0	0	110
N12E	-220 1230	$1 \times 10^{-3}$ $7 \times 10^3$	540	4	645	100	+2	0	0	75
C9E	-17 1480	$1 \times 10^{-3}$ $8 \times 10^3$	1070	50	1140	500	+1	0	+3	70
N9E	-216 1250	$0.1 \times 10^{-3}$ 50					0	0	0	
C7E	-60 1450	$1 \times 10^{-3}$ $7 \times 10^3$	880 1075	$1 \times 10^{-3}$ 50	1040 1170	0.02 700	+3	0	+6	122 83
N7E	31 1530	$1 \times 10^{-3}$ 150					+2	0	0	
C2E	120 1580	$1 \times 10^{-3}$ $30 \times 10^3$	1030	10	1130	$1 \times 10^3$	+7	0		50
N2E	84 1580	$1 \times 10^{-3}$ $10 \times 10^3$			1125	20	+2	0	0	

**Table 4.7** Potentiodynamic anodic polarisation results for anode E



Ref.	$E_{corr}$ $E_m$ mV	$i_{corr}$ $i_m$ $\mu A/cm^2$	$E_{pp}$ mV	$i_{crit}$ $\mu A/cm^2$	$E_{tp}/$ $E_n$ mV	$i_l /$ $i_n$ $\mu A/cm^2$	$E_t$ mV	$i_t$ $\mu A/cm^2$	$\Delta t$ $^{\circ}C$	$\Delta$ $pH_a$	$\Delta$ $pH_c$	$\beta_a$ $mV/dec$
C12P	-115 1420	$1 \times 10^{-3}$ 400			-30 680	0.01 10	240	1		0	0	135
N12P	-220 1330	0.01 250	540	10	230 710	0.3 8	355	3		0	0	125
C9P	-150 1460	$1 \times 10^{-3}$ 60	915	17	730 1100	1 7	850	10	+2	0	+1	120
N9P	355 1590	$1 \times 10^{-4}$ 50			820	2			+1	0	-1	
C7P	-40 1530	$1 \times 10^{-3}$ 150	930	15	725 1120	1 8.5	860	10	+2	0	+2	135
N7P	0 1490	$5 \times 10^{-3}$ 25	1030	13	845 1210	2 100	940	10	+3	0	0	136
C2P	375	$1 \times 10^{-3}$	1030 1375	11 18	735 1125	0.05 5	840	5	+3	0	0	105
	2040	$3 \times 10^{-3}$			1460 1665	15 50	1735	500				70
N2P	215 1710	$1 \times 10^{-3}$ 40	950	25	710 1365	0.1 3	870	10	0	0	0	80

**Table 4.8** Potentiodynamic anodic polarisation results for anode P

$E_{corr}$ $E_m$ mV	$i_{corr}$ $i_m$ $\mu A/cm^2$	$E_{pp}$ mV	$i_{crit}$ $\mu A/cm^2$	$E_{tp}$ mV	$i_l$ $\mu A/cm^2$	$E_t$ mV	$i_t$ $\mu A/cm^2$	$\beta_a$ $mV/decade$
-270 2000	1 $4 \times 10^3$	-90 940	200 $1 \times 10^3$	270 1100	110 970	-230	100	20

**Table 4.9** Potentiodynamic anodic polarisation results for graphite in sat.  $Ca(OH)_2$  + 1 M NaCl (after Slater *et al*, 1976)

ANODE	Ref.	C.D. (paste) mA/m <sup>2</sup>	I App mA	CD (anode) mA/m <sup>2</sup>	Time days	Charge Coulombs
Zinc	Z:50a	50.00	0.513	50.00	727	32223
	Z:50b	50.00	0.513	50.00	246	10904
	Z:0	0.00	0.00	0.00	716	0
Mesh T	T:50a	50.00	0.513	26.72	722	32001
	T:50b	50.00	0.513	26.72	259	11480
	T:0	0.00	0.00	0.00	715	0
	T:20	20.00	0.205	10.69	261	4627
	E:50a	50.00	0.513	36.43	728	32267
	E:50b	50.00	0.513	36.43	122	5407
Mesh E	E:0	0.00	0.00	0.00	721	0
	E:20	20.00	0.205	14.57	118	2092
	P:50a	50.00	0.513	50.00	723	32046
Paint	P:50b	50.00	0.513	50.00	126	5585
	P:0	0.00	0.00	0.00	713	0

**Table 5.1** Paste block specimen schedule

	Area cm <sup>2</sup> /slab		
Anode area	102.60	Steel/Anode ratio	0.45
Cathode area	46.00	Steel/Mesh E ratio	0.33
Mesh E area	140.80	Steel/Mesh T ratio	0.24
Mesh T area	192.00		

**Table 5.2** Electrode Areas

ANODE	Reference	E <sub>corr</sub> mV (SCE)	i <sub>corr</sub> ( $\mu$ A/cm <sup>2</sup> )
Zinc	Z:50a	-524	0.306
	Z:50b	-462	0.305
	Z:0		
Mesh T	T:50a	-542	0.539
	T:50b	-619	1.170
	T:0		
	T:20	-587	0.882
	E:50a	-416	0.152
	E:50b	-454	0.101
Mesh E	E:0		
	E:20	-520	0.209
	P:50a	-468	0.299
Paint	P:50b	-392	0.125
	P:0		

**Table 5.3** E<sub>corr</sub> and i<sub>corr</sub> values for paste specimens before polarisation



Slab No.	Circuit No.	Specimen reference Anode: Cl: CD: Curing				A s.a. m <sup>2</sup>	C s.a. m <sup>2</sup>	I app mA	CD wrt A s.a. mA/m <sup>2</sup>	CD wrt C s.a. mA/m <sup>2</sup>	Notes
		Anode	Cl % /cement	CD mA/m <sup>2</sup>	Curing						
1	N/A	Z	2	0	1	0.250	0.046	0	0	0	Control
2	N/A	E	2	0	1	0.044	0.046	0	0	0	Control
3	N/A	P	2	0	1	0.250	0.046	0	0	0	Control
4	N/A	T	2	0	1	0.032	0.046	0	0	0	Control
5	1	Z	2	20	1	0.250	0.046	5.0	20	108	Typ. CD
6	2	E	2	20	1	0.044	0.046	5.0	115	108	Typ. CD
7	3	P	2	20	1	0.250	0.046	5.0	20	108	Typ. CD
8	4	T	2	20	1	0.032	0.046	5.0	156	108	Typ. CD
9	13	Z	2	50	1	0.250	0.046	12.5	50	271	High CD
10	14	E	2	50	1	0.047	0.046	12.5	266	271	High CD
11	15	P	2	50	1	0.250	0.046	12.5	50	271	High CD
12	16	T	2	50	1	0.032	0.046	12.5	386	271	High CD
13	17	Z	2	50	2	0.250	0.046	12.5	50	271	Curing
14	18	E	2	50	2	0.044	0.046	12.5	287	271	Curing
15	19	P	2	50	2	0.250	0.046	12.5	50	271	Curing
16	20	T	2	50	2	0.032	0.046	12.5	391	271	Curing
17	N/A	N/A	2	N/A	1	N/A	N/A	N/A	N/A	N/A	Diff'n test
18	N/A	N/A	2	N/A	2	N/A	N/A	N/A	N/A	N/A	Diff'n test
19	N/A	T	0	0	1	0	0.046	0	0	0	Control
20	N/A	N/A	0	N/A	1	N/A	N/A	N/A	N/A	N/A	Diff'n test
21	N/A	N/A	0	N/A	2	N/A	N/A	N/A	N/A	N/A	Diff'n test
22	5	E	4	20	1	0.044	0.046	5.0	115	108	High Cl
23	N/A	N/A	4	N/A	1	N/A	N/A	N/A	N/A	N/A	Diff'n test
24	N/A	N/A	4	N/A	2	N/A	N/A	N/A	N/A	N/A	Diff'n test
25	N/A	Z	0.4	0	1	0.250	0.046	0	0	0	Control
26	N/A	E	0.4	0	1	0.044	0.046	0	0	0	Control
27	N/A	P	0.4	0	1	0.250	0.046	0	0	0	Control
28	24	T	0.4	50	1	0.034	0.046	12.5	368	271	High CD
29	6	Z	0.4	20	1	0.250	0.046	5.0	20	108	Typ. CD
30	7	E	0.4	20	1	0.044	0.046	5.0	115	108	Typ. CD
31	8	P	0.4	20	1	0.250	0.046	5.0	20	108	Typ. CD
32	9	T	0.4	20	1	0.031	0.046	5.0	163	108	Typ. CD
33	21	Z	0.4	50	1	0.250	0.046	12.5	50	271	High CD
34	22	E	0.4	50	1	0.038	0.046	12.5	333	271	High CD
35	23	P	0.4	50	1	0.250	0.046	12.5	50	271	High CD
36	N/A	T	0.4	0	1	0.029	0.046	0	0	0	Control
37	25	Z	0.4	20	2	0.250	0.046	5.0	20	108	Curing
38	10	E	0.4	20	2	0.047	0.046	5.0	107	108	Curing
39	11	P	0.4	20	2	0.250	0.046	5.0	20	108	Curing
40	12	T	0.4	20	2	0.031	0.046	5.0	163	108	Curing
41	N/A	N/A	0.4	N/A	1	N/A	N/A	N/A	N/A	N/A	Diff'n test
42	N/A	N/A	0.4	N/A	2	N/A	N/A	N/A	N/A	N/A	Diff'n test

Table 6.1 CP trial specimen schedule.

	Batch proportions by weight Kg	Batch weights (uncorrected)	Batch weights (corrected)
OPC cement	330	21.3	21.3
10 mm T.V. aggregate	980	63.3	65.6
Sand	802	51.8	54.75
Water	211	13.62	7.94
Total	2323	150.02	150.04

**Table 6.2** Concrete batch quantities.

Date cast	Slabs	% chloride*: curing <sup>^</sup>	Strength N/mm <sup>2</sup>	Density Kg/m <sup>3</sup>	Resistivity KΩcm	Permeability K m/s (penetration)
27/9/89	13-18	2:2	59.5	2337	5.57	2.02E-12
16/9/89	22-24	4:2	48.5	2306		4.67E-12
23/9/89	1-12	2:1	58.0	2329	7.76	8.23E-12
29/9/89	37-42	0 4:2	53.0	2339	8.13	9.22E-12
16/9/89	25-36	0 4:1	54.4	2339	9.51	2.65E-11
16/9/89	19-23	0:2	44.5	2304		2.89E-11
16/9/89	22-24	4:1	48.5	2306	5.6	4.98E-10
16/9/89	19-23	0:1	44.5	2304	11.78	6.76E-10

\* calcium chloride dihydrate by weight of cement

<sup>^</sup> 1 = air curing, 2 = 3 days moist curing

**Table 6.3** Casting and concrete characterisation data.

Date	Relative humidity %	Temperature °C (24 hrs)
26.1.89	48	5 -16
27.1.89	56	5- 15

**Table 6.4** Relative humidity and temperature during anode application.

Reference	R <sub>p</sub> Ω cm <sup>2</sup>	i <sub>corr</sub> μA/cm <sup>2</sup>	E <sub>corr</sub> mV (SCE)
Z:2:20:1	5.07E+05	0.051	-40
E:2:20:1	5.32E+05	0.049	-47
P:2:20:1	2.75E+06	0.009	-47
T:2:20:1	5.24E+05	0.050	-200
E:4:20:1	4.52E+05	0.058	-200
Z:2:50:1	1.74E+06	0.015	-40
E:2:50:1	1.27E+06	0.020	-75
P:2:50:1	2.36E+06	0.011	25
T:2:50:1	1.43E+06	0.018	-200
Z:2:50:2			-35
E:2:50:2	1.57E+06	0.017	-60
P:2:50:2	2.75E+06	0.009	-150
T:2:50:2	1.74E+06	0.015	-90

**Table 6.5** Initial corrosion rates of CP trial specimens.



Month	P:2:20:1	P:0.4:20:1	P:0.4:20:2	P:0.4:0:1
1	acrylic torn in blow holes	one acrylic tear, few rust spots	no degradation	few rust spots
6	large bubbles by primary, primary almost disbonded from epoxy bed	many rust spots	few rust spots	no change
7	bubble area increased	few micro bubbles	no change	no change
8	no change	no change	few micro bubbles	no change
9	bubble area increased, primary had disbonded	micro bubbling and blistering on line of secondary fibre	cracks in paint by primary	no change
10	primary repaired	no change	no change	no change
11	no change	no change	no change	no change
12	micro bubbling by cored area, bleaching	bleaching, blackening/crack at primary	bleaching & crack along primary=30 mm	no change
16	repair ok, few rust spots, 1 blister on secondary, 1 on slab	medium rust spotting & bleaching, blisters along secondary, ok elsewhere	few rust spots, 3 blisters, ok elsewhere	slight weathering of top coat
18	no change	no change	no change	no change
Rust spotting	minimal	light	minimal	minimal
Degradation	primary failed, low elsewhere	low	low	nil

**Table 6.6** Summary of visual inspections anode P surfaces at 20 mA/m<sup>2</sup>.

Month	P:2:50:1	P:2:50:2	P:0.4:50:1	P:2:0:1
1	many rust spots	many rust spots	no degradation	few rust spots
6	increased rust spots, bleaching, bubbling /debonding, bubble 100 x 50 mm area	much micro/macro bubbling, bleaching	micro bubbling, blackening/blistering around primary	no change
7	increased staining, bubble area=10%	bubbles isolated =5%area	no change	no change
8	150 mm central bubble, micro bubbling	large areas bubbled/blistered	increased blistering by primary	no change
9	debonded area increased	increased bubbling, blisters cracking	blistering increased, blackened along secondary	no change
10			repair primary	
11	debonded area increased	bubbled areas joined up	increased blackening along secondary	no change
12	material loss surface of primary, 30 mm crack along edge	bubble area cracking up	blackening at slab edges	no change
16	many rust spots, large blister / blackened / bleached area, edges degrade, general integrity still ok	minimal rust spots, many local blisters, edge degradation, in general many areas ok	minimal rust spots, blisters along secondary, severe degradation at primary and at edge, in general many areas ok	no change
18	no change	no change	no change	no change
Rust spotting	heavy	light	minimal	minimal
Degradation	very high locally, medium to low elsewhere	high locally, medium to low elsewhere	very high around primary and at edge, low elsewhere	nil

**Table 6.7** Summary of visual inspections anode P surfaces at 50 mA/m<sup>2</sup>.

Month	0	2	3	4	5	6	7	8	9	11	12	14	18
P:2:20:1		2	3	3	3/4	3	3	3	3	3/O	3/O	3/4	3/O
P:0.4:20:1		2	3	2	3	3	3/O	3	3	3/O	3/O	3	4
P:0.4:20:2		3	3	3	3	3	3/O	3	3/O	3	3/4/O	3/O	3
P:0.4:0:1	1	2	2	2	2	2	2	2	2	2	2/O	2/O	2
P:2:50:1		4	3	3/O	3	3	3	3	3	4/O	3/O	4	3/O
P:2:50:2		3	3	3	3	3	3	3	3/O	4/O	4/O	4	2/3/O
P:0.4:50:1		3	3	3	3	3	3	3	3/O	3/O	3/O	2/3/4	2
P:2:0:1	1	2	2	2	2	2	2	2	2	2	2/O	2	2

New Classification		Closest equivalent Taywood classification	
CODE	INTERPRETATION (Anode P)		INTERPRETATION
1	Pull-off failure: occurs in epoxy resin or decorative top coat	RD	Dolly is pulled out of adhesive without disrupting the coating
2	Pull-off failure: occurs both within coating and substrate paste. The coating is shiny and crystalline (zero degradation case)	CS	Failure of concrete below the conductive coating
3	Pull-off failure: occurs mainly at interface of coating/substrate. The coating is dull grey or matt black, crystalline, rough, with minimal adhesion of paste particles	CC	Failure of the coating at the interface with the concrete
3/O	Substrate is deep orange colour at the instant of pull-off (mainly CC type failure)		
4	Pull-off failure: occurs mainly at interface of coating/ substrate. Coating is smooth, graphite grey, adhering paste particles may be brown/orange/fissured	IC	Failure by delamination of the coating, leaving coating on both concrete surface and dolly

**Table 6.8** Summary of visual inspections of anode P pull-off dolly surfaces.

Month	0	2	3	4	5	6	7	8	9	11	12	14	18	ave
P:2:20:1		5	3.5	5	5.5	6.5	17	7.5	8	7	6	6	9.5	7.2
P:0.4:20:1		5.5	4.5	5	9	7.5	9	12	12	5	4	5.5	3	6.8
P:0.4:20:2		3.5	2	4	3	4	9	8	4.5	8	3	6	7.5	5.2
P:0.4:0:1	4	5	5.5	8.5	13	11	18	13	15	14	15	13	14	11.3
P:2:50:1		3	0.5	5	5	7.5	12	6	7	4	5.5	3	8	5.5
P:2:50:2		2.5	3.5	3.5	8.5	10	7.5	7	6	5	5	5.5	5	5.8
P:0.4:50:1		3.5	5	4	5.5	13	9	9	5.5	7	3	3.5	4	6.0
P:2:0:1	4	6	7	12	18	18	18	13	17	15	14	16	14	13

**Table 6.9** Adhesion failure loads ( $\text{Kg/cm}^2$ ): Anode P.



Month	0	2	3	4	5	6	7	8	9	11	12	14	18
P:2:20:1			P/L	P	P	P	P	P	P	P	P	P	P
P:0.4:20:1			P	P	P	P	P	P	P	P	L	P	L
P:0.4:20:2			L	P/L	L	P/L	P	P	P/L	P	L	P	P
P:0.4:0:1			P	P	P	P	P	P	P	P	P	P	P
P:2:50:1		L	L	P	P	P	P	P	P	P	P	P/L	P
P:2:50:2		L	L	P	P	P	P	P	P	P	P/L	P	P
P:0.4:50:1		P/L	P	P/L	P	P	P	P	P	P	L	P/L	P
P:2:0:1			P	P	P	P	P	P	P	P	P	P	P

CODE	INTERPRETATION
P	Pull-off failure: explosive pop-off
L	Pull-off failure: progressive lift-off

**Table 6.10** Summary of pull-off failure modes for anode P

Element	Acidified paste % Total (ave of 4)	Acidified paint % Total (ave of 2)	Rust spot % Total (ave of 2)	Masonry paint % Total (ave of 2)
Na	1	1	0	0
Mg	0	0	0	0
Al	0	0	1	0
Si	42	10	8	14
P	0	1	3	1
S/Mo	0	0	1	1
Cl	49	84	8	5
K	0	0	1	1
Ca	1	1	1	0
Ti	1	0	11	34
V	1	1	2	5
Cr	0	1	0	0
Mn	0	0	0	0
Fe	4	0	64	37
Ni	1	0	0	1
Cu	0	1	0	0
Zn	0	0	0	2
Total	100	100	100	100

**Table 6.11** Summary of EDXA data for anode P.

Loc.	Distance mm	Month											
		3	4	6	7	8	9	10	11	12	14	16	18
C1	4	3.2	3.6	1.9	3.3	3.6	4.5	-	1.8	1.3	1.1	0.8	1.0
C2	18	2.6	3.0	2.1	3.5	4.0	5.0	-	2.8	2.3	2.1	1.6	1.9
C3	37.5	2.5	3.2	2.7	4.0	4.6	5.7	-	3.5	3.0	2.6	2.1	2.5
B1	8.5	1.8	1.6	2.2	3.7	3.9	4.9	-	2.7	2.0	2.0	1.3	2.0
B2	19	1.7	1.7	2.3	3.6	4.1	5.0	-	3.1	2.6	2.5	1.8	2.2
B3	39	1.9	2.1	2.7	5.6	4.5	5.5	-	3.5	3.1	2.8	2.1	2.6
A1	25	0.9	0.8	3.3	4.6	5.1	6.2	-	4.0	3.2	3.1	2.2	2.8
A2	30.5	1.4	1.4	3.4	4.6	5.3	6.5	-	4.3	3.6	3.3	2.3	2.9
A3	45	1.8	1.8	4.1	5.2	6.0	7.2	-	5.0	4.4	3.9	2.4	3.3
A	54	2.5	3.4	4.2	5.4	6.2	7.6	-	5.3	4.6	4.0	2.5	3.4
B	44	2.0	2.2	2.8	4.2	4.9	6.1	-	3.6	3.1	2.6	2.1	2.5
C	12	1.4	3.8	3.6	5.5	6.3	10.0	-	2.4	1.6	1.3	1.0	1.2
D	34	3.4	3.1	3.7	4.9	5.3	6.4	-	4.3	3.5	3.2	2.2	3.0
$\alpha$	0.5	0.4	0.4	1.6	2.8	3.3	4.2	-	0.5	0.4	0.4	0.4	0.5
$\beta$	1	0.3	0.5	1.6	2.9	3.3	4.1	-	0.8	0.6	0.6	0.5	0.6

**Table 6.12** Specimen P:2:20:1 voltage drops from primary anode (calculated as resistance  $R=V/I$  ohms).

Loc.	Distance mm	Month												
		3	4	6	7	8	9	10	11	12	14	16	18	22
C1	3	2.8	2.6	1.2	1.3	1.4	303	2.9	2.9	2.1	1.5	1.1	1.4	2.8
C2	19	3.0	3.0	2.8	2.9	3.2	4.4	5.0	5.0	4.0	3.2	2.5	3.1	4.9
C3	39	3.4	4.0	4.1	4.0	5.2	6.4	7.0	6.4	5.3	4.2	3.2	4.0	6.4
B1	9.5	2.0	1.8	2.0	2.1	2.3	3.5	4.0	4.0	3.1	2.4	2.0	2.2	3.6
B2	20.5	2.6	2.4	3.1	3.2	3.4	4.6	5.3	5.3	4.4	3.6	2.8	3.3	5.4
B3	40	3.0	3.2	233	45	300	440	140	9.5	5.9	75	7.0	5.0	8.2
A1	26.5	1.4	1.1	2.8	3.0	3.2	4.5	4.9	5.1	4.0	3.2	2.6	2.9	5.0
A2	32.5	2.3	2.1	3.3	3.5	3.8	5.3	5.8	5.8	4.8	4.0	3.3	3.6	5.6
A3	47	2.8	2.9	4.4	4.5	5.1	6.9	7.2	7.2	6.3	5.6	4.6	5.4	8.6
A	55	3.4	4.0	4.4	4.6	5.1	6.4	7.2	7.3	6.3	5.6	4.5	5.4	8.4
B	45	3.0	3.0	4.2	4.1	4.7	5.7	6.4	6.5	5.3	4.4	3.3	4.2	6.4
C	10	1.8	1.4	1.7	1.7	1.9	2.9	3.4	3.5	2.6	1.8	1.3	1.8	3.2
D	35	2.9	2.8	3.0	3.1	3.4	4.7	5.1	5.2	7.6	3.3	2.7	3.0	4.8
$\alpha$	0.5	1.0	0.5	0.6	0.6	0.6	1.5	2.0	2.0	1.3	0.8	0.6	0.8	1.9
$\beta$	1	0.8	0.7	0.7	0.7	1.1	1.6	2.1	2.1	1.5	0.9	0.7	0.9	1.9

**Table 6.13** Specimen P:0.4:20:1 voltage drops from primary anode (calculated as resistance  $R=V/I$  ohms).



Loc.	Distance mm	Month												
		3	4	6	7	8	9	10	11	12	14	16	18	22
C1	2.5	2.5	2.3	0.6	0.7	0.8	1.0	1.0	1.1	1.1	1.0	0.6	1.0	320
C2	17.5	2.5	2.4	1.7	1.7	2.1	2.4	2.7	2.8	2.5	1.9	1.5	1.7	2.4
C3	37	2.8	2.7	2.2	2.2	2.5	3.0	3.3	3.4	3.1	2.7	2.0	2.3	3.0
B1	10	1.7	1.5	1.4	1.4	1.6	2.1	2.2	2.2	2.0	1.7	1.4	1.5	2.0
B2	20	2.1	1.8	1.7	1.7	1.9	2.3	2.5	2.6	2.3	1.9	1.6	1.7	2.4
B3	38.5	4.9	2.1	2.0	1.6	2.2	2.6	2.8	3.0	2.6	2.2	2.0	1.9	2.7
A1	27	0.6	0.6	2.3	2.5	2.6	3.2	3.2	3.3	2.9	2.5	2.2	2.5	6.2
A2	32	1.9	1.7	2.2	2.2	2.4	3.0	3.1	3.1	2.7	2.3	1.9	2.1	3.0
A3	46	2.6	2.3	3.0	2.8	3.1	3.8	3.9	3.8	3.4	2.8	2.5	2.6	4.8
A	54.5	2.8	2.9	2.9	2.9	3.3	3.9	4.1	4.0	3.5	2.8	2.5	2.7	4.5
B	45	2.8	2.4	2.4	2.4	2.7	3.3	3.7	3.8	3.5	3.0	2.1	2.4	3.9
C	11	1.2	1.1	1.6	1.7	2.2	2.7	2.9	3.2	3.0	2.5	1.4	3.1	44
D	35	2.6	2.5	2.5	2.7	2.8	3.3	3.3	3.4	3.0	2.7	2.3	2.5	3.4
$\alpha$	0.5	0.4	0.3	0.3	0.7	0.3	0.5	0.5	0.5	0.5	0.5	0.3	0.4	0.5
$\beta$	1	0.2	0.4	0.4	1.7	0.5	0.7	0.7	0.7	0.8	0.6	0.4	0.6	0.7

**Table 6.14** Specimen P:0.4:20:2 voltage drops from primary anode (calculated as resistance  $R=V/I$  ohms).

Loc.	Distance mm	Month											
		3	4	6	7	8	9	10	11	12	14	16	18
C1	1.5	4.2	3.3	2.0	2.5	3.2	5.3	6.8	5.6	5.1	4.6	4.4	8.4
C2	19	4.5	3.8	3.6	4.1	5.4	8.0	9.0	7.7	7.0	6.5	6.8	13.0
C3	39	3.8	3.9	4.3	4.9	6.2	9.1	9.9	8.7	7.7	7.0	7.3	14.4
B1	12	2.8	2.3	3.4	4.0	5.2	8.2	9.8	8.3	7.5	6.6	6.6	14.5
B2	22.5	3.1	2.8	4.2	4.9	6.0	8.9	10.5	8.7	7.4	6.6	7.0	14.0
B3	41	3.4	3.3	4.5	5.1	6.3	9.1	10.0	8.7	7.7	7.0	7.5	14.4
A1	29	1.1	1.2	4.6	5.4	6.5	9.6	12.1	10.7	9.4	7.9	7.4	16.1
A2	35	2.5	2.5	5.3	6.1	7.5	10.9	12.3	10.8	9.1	7.9	7.8	15.4
A3	49	3.1	3.2	5.3	5.9	7.2	10.3	11.0	10.0	8.6	7.7	8.1	15.4
A	56.5	4.0	4.7	4.0	6.2	8.2	14.6	11.9	10.9	9.0	7.9	8.3	16.8
B	45	3.1	3.4	4.8	5.4	8.1	10.5	10.3	9.0	7.9	7.1	7.3	14.8
C	8	1.7	3.0	5.7	3.5	6.4	9.2	8.3	7.8	8.0	5.2	5.0	11.4
D	37	4.4	3.4	4.8	5.7	6.8	10.2	12.4	11.1	9.6	8.1	7.6	16.4
$\alpha$	0.5	0.8	0.6	1.1	1.5	1.9	3.6	5.6	4.4	4.0	3.6	3.5	5.6
$\beta$	1	0.6	0.8	1.3	1.8	2.3	4.1	5.9	4.7	4.2	3.9	3.8	6.4

**Table 6.15** Specimen P:2:50:1 voltage drops from primary anode (calculated as resistance  $R=V/I$  ohms).

Loc.	Distance mm	Month												
		3	4	6	7	8	9	10	11	12	14	16	18	22
C1	4.5	2.1	2.6	4.2	7.2	14.9	48.6	26.6	26.0	20.8	12.6	6.9	13.3	166
C2	19	2.2	2.8	4.1	7.6	13.3	35.4	24.2	23.1	18.6	12.8	7.6	13.8	50.0
C3	39	2.2	2.8	4.6	7.8	13.4	33.6	23.9	22.8	18.4	12.7	7.7	13.7	48.2
B1	10	1.6	2.0	3.2	6.4	10.9	27.2	17.8	17.0	13.8	9.6	5.2	9.1	28.8
B2	20.5	1.9	2.4	3.8	7.1	12.2	32.9	21.3	20.3	16.8	11.8	6.7	11.9	36.6
B3	40	2.1	2.7	4.1	7.4	12.8	33.6	22.8	21.8	17.5	12.2	7.3	12.9	44.3
A1	27	2.7	2.2	4.1	7.4	12.3	32.0	20.9	20.0	16.2	11.5	6.6	11.7	37.4
A2	32.5	1.7	2.7	4.4	52.3	12.8	32.5	21.8	21.0	17.0	12.1	7.0	12.4	40.2
A3	47	2.2	3.2	4.4	7.6	13.0	32.9	22.7	21.8	17.6	12.3	7.3	12.9	43.2
A	55	2.2	2.9	4.6	7.8	13.2	33.7	22.9	21.9	17.7	12.4	7.3	12.9	43.4
B	45	3.1	3.6	5.9	9.3	16.3	41.6	28.0	25.6	20.4	13.3	7.7	13.9	50.5
C	11	1.8	2.2	3.6	7.2	132	36.6	25.3	23.8	18.9	12.4	6.8	13.3	49.9
D	34	2.1	2.6	4.1	7.4	20.6	30.9	20.8	20.0	16.2	11.5	6.6	11.6	37.0
$\alpha$	0.5	0.8	74	642	40	104	234	27.2	28.0	10.0	6.9	2.6	4.6	7.0
$\beta$	1	0.7	124	112	139	104	272	97.6	46.4	10.5	6.8	2.8	5.1	9.9

**Table 6.16** Specimen P:2:50:2 voltage drops from primary anode (calculated as resistance  $R=V/I$  ohms).

Loc.	Distance mm	Month												
		3	4	6	7	8	9	10	11	12	14	16	18	22
C1	9.5	1.8	2.8	9.2	48.8	115	844	-	7.8	6.6	8.5	4.9	29.1	219
C2	20.5	1.9	3.1	11.4	52.6	119	856	-	10.2	8.5	11.0	6.5	29.3	219
C3	38.5	2.3	3.4	11.8	18.4	102.6	848	-	10.9	9.0	11.9	6.8	29.8	220
B1	4.5	1.1	1.7	8.2	48.0	97	844	-	7.7	6.8	8.2	4.3	16.6	205
B2	16.5	1.6	3.0	11.5	52.8	102	844	-	10.4	8.6	11.2	6.6	29.2	219
B3	36.5	2.1	3.5	11.8	53.1	103	841	-	11.0	9.2	12.3	7.7	29.8	220
A1	20.5	1.2	2.0	11.0	53.6	102	843	-	10.8	9.2	12.1	6.7	27.8	218
A2	26	1.7	2.8	11.5	54.1	102	844	-	11.2	9.4	12.5	6.9	29.6	221
A3	42	2.0	3.3	12.2	54.6	102	843	-	12.4	10.2	13.3	7.1	30.5	790
A	49.5	2.7	4.1	24.4	264	320	1560	-	80.0	19.5	19.6	7.3	72.0	1040
B	45	2.1	3.5	12.0	54.2	125	840	-	11.1	9.2	12.1	6.8	29.9	222
C	17	1.3	1.8	9.7	50.6	120	840	-	8.3	7.1	9.0	5.2	29.2	219
D	28.5	1.9	2.8	11.2	52.6	123	832	-	10.9	9.2	12.1	6.6	27.5	218
$\alpha$	0.5	0.8	0.6	4920	2160	1080	2280	-	0.9	0.9	1.4	0.8	2.4	7.8
$\beta$	1	0.5	1.4	4800	1600	1160	2200	-	1.0	1.0	1.5	0.9	2.8	20.0

**Table 6.17** Specimen P:0.4:50:1 voltage drops from primary anode (calculated as resistance  $R=V/I$  ohms).



Month	P:2:20:1	P:0.4:20:1	P:0.4:20:2	P:2:50:1	P:2:50:2	P:0.4:50:1
3	2.1	2.6	2.4	3.2	2.2	1.8
4	2.4	2.6	2.0	3.1	2.7	2.9
6	3.0	3.1	2.0	4.3	4.2	12.0
7	4.5	3.2	2.1	4.9	7.5	49.4
8	4.9	3.6	2.3	6.4	13.8	109.2
9	6.2	5.0	2.8	9.1	34.7	843.3
10		5.3	3.0	10.3	23.0	
11	3.6	5.7	3.1	9.1	21.9	10.2
12	3.0	4.7	2.7	8.0	17.7	8.6
14	2.7	3.6	2.3	6.9	12.1	11.2
16	1.9	3.1	1.8	7.0	7.0	6.4
18	2.4	3.5	2.2	14.2	12.6	28.2
22		5.6	3.5		42.5	218.3

**Table 6.18** Average values of voltage drops from primary anode (calculated as resistance  $R=V/I$  ohms) for Anode P specimens.

Month	Z:2:20:1	Z:0.4:20:1	Z:0.4:20:2	Z:0.4:0:1
1	no degradation	no degradation	no degradation	no degradation
6	white product at edges of torn holes	white product at edges of torn hole by primary	white product at edges of torn holes	no change
7	warts $\approx$ 10% area	no change	no change	no change
8	increased warts	no change	no change	no change
9	no change	no change	no change	no change
11	increased warts $\approx$ 30% area	debonding by primary	no change	no change
12	no change	increased debonding	debonded around anode	no change
16	isolated debonding	no change	increased debonding	no change
18	no change	white rust in surface pores	no change	no change
Warts	30%	nil	nil	nil
Debonding	3%	20%	35%	nil

**Table 6.19** Summary of visual inspections anode Z surfaces at 20 mA/m<sup>2</sup>.

Month	Z:2:50:1	Z:2:50:2	Z:0.4:50:1	Z:2:0:1
1	no degradation	no degradation	water run-off stain	no degradation
6	warts at edges, white rust at all exposed edges	white rust at all exposed edges and blow holes	white rust at torn hole edges	no degradation
7	warts $\approx$ 60% area, bigger near primary, white rust covers pull-off sites, zinc lifting off	warts $\approx$ 70% area, bigger near primary, white rust covers pull-off sites, zinc lifting off	no change	no change
8	warts growing, debonded area $\approx$ 10%	warts growing, debonded area $\approx$ 15%	zinc debonded $\approx$ 70% area, white rust on surface low	no change
9	increased debonding	increased debonding	increased white rust	no change
11	warts over entire area except central debonded area	warts increased	no change	no change
12	no change	no change	no change	no change
14	80 % debonded, primary ok	70 % debonded, primary ok	primary debonded	no change
16	no change	80 % debonded, primary ok	90 % debonded	no change
18	no change	no change	no change	no change
Warts	60%	70%	nil	nil
Debonding	80%	80%	90%	nil

**Table 6.20** Summary of visual inspections anode Z surfaces at 50 mA/m<sup>2</sup>.



Month	0	1	2	3	4	5	6	7	8	9	11	12	14	18
Z:2:20:1		2	4	3	3	5	5	4	2	5	5	5	4	3
Z:0.4:20:1		2	4	4	5	4	4	4	4	4	4	5	4	2
Z:0.4:20:2		2	3	3	4	4	4	4	3	3	4	5	4	3
Z:0.4:0:1	2	2	2	2	2	2	2	3	3	3	3	4	2	4
Z:2:50:1		3	5	5	5	5	5	5	4	5	6			
Z:2:50:2		5	4	3	5	5	5	4	4	4	6			
Z:0.4:50:1		2	5	4	5	4	5	5	3	5	6			
Z:2:0:1	2	2	2	2	2	2	2	3	2	3	3	3	4	3

CODE	INTERPRETATION (Anode Z)
1	Pull-off failure: occurs in epoxy resin
2	Pull-off failure: occurs within substrate paste and at the shiny zinc surface (zero degradation case)
3	Pull-off failure: occurs at a dull zinc (oxidised) surface/substrate paste mixed interface
4	Pull-off failure: occurs at a dull zinc (oxidised) surface with isolated white rust particles/substrate paste mixed interface
5	Pull-off failure: occurs at a dull zinc (oxidised)/white rust particles/substrate paste mixed interface
6	Pull-off failure: occurs entirely within the plane of white rust product

**Table 6.21** Summary of visual inspections of anode Z pull-off dolly surfaces.

Month	0	2	3	4	5	6	7	8	9	11	12	14	18	ave
Z:2:20:1		5	5.5	6	7	6	9	8.5	7	9	4.5	9	10	7.2
Z:0.4:20:1		5	4.5	3.5	9.5	14	6	18	9.5	5	2	8.5	2	7.3
Z:0.4:20:2		3.5	6	2.5	3	4	4	4	3	3	3	3.5	5	3.7
Z:0.4:0:1	3	9.5	4.8	5	11	14	12	13	15	14	10	26	19	11.9
Z:2:50:1		4.5	3.8	4	7	2.5	3	5.5	3	2	-	-	-	3.9
Z:2:50:2		4	3	3.5	3	4	2.5	1	2.5	2	-	-	-	2.8
Z:0.4:50:1		4.5	4.5	3.5	3	2	3	2	2	2	-	-	-	2.9
Z:2:0:1	5	7.5	4.8	7.5	9.5	11	10	16	11	11	11	15	11	9.9

**Table 6.22** Adhesion failure loads ( $\text{Kg/cm}^2$ ): Anode Z.

Month	0	1	2	3	4	5	6	7	8	9	11	12	14	18
Z:2:20:1				P	P	P	P	P	P	P	P	L/P	P	P
Z:0.4:20:1				P	P/L	P	P	P	P	P/L	P	L	P	L
Z:0.4:20:2				P	L	P	L	P/L	L	L	P	L	P/L	P
Z:0.4:0:1			P	P	P	P	P	P	P	P	P	P	P	P
Z:2:50:1			L	L	L	P	P/L	P/L	P	L	L			
Z:2:50:2			L	L	L	L	L	L	L	L	L			
Z:0.4:50:1			P/L	L	P	L	L	L	L	L	L			
Z:2:0:1			P	P	P	P	P	P	P	P	P	P	P	P

CODE	INTERPRETATION
P	Pull-off failure: explosive pop-off
L	Pull-off failure: progressive lift-off

**Table 6.23** Summary of pull-off modes for anode Z.

Atomic element	White rust % Total (ave of 6)	Outer surface of wart % Total (1 test)	Inner surface of wart % Total (ave of 11)	White rust(fracture) % Total (1 test)
Na	2	1	4	0
Mg	0	0	0	0
Al	0	0	1	0
Si	0	0	1	0
P	0	0	0	0
S/Mo	0	0	1	0
Cl	0	3	8	1
K	0	0	0	0
Ca	0	0	0	0
Ti	0	1	0	0
V	0	0	0	0
Cr	0	0	0	0
Mn	0	0	0	0
Fe	0	0	1	0
Ni	0	1	0	1
Cu	1	0	0	0
Zn	95	94	85	96
Total	100	101	100	100

**Table 6.24** Summary of EDXA data for anode Z.

2 $\theta$	White zinc corrosion product		ZnO (Zincite): Powder Diffraction File No. 5-664	
	d A°	RI	d A°	RI
31.3	3.316	25		
37.1	2.812	50	2.816	71
40.3	2.597	62.5	2.602	56
42.5	2.468	100	2.476	100
56	1.905	25	1.911	29
67	1.621	62.5	1.626	40
74.7	1.474	62.5	1.477	35
79.1	1.405	12.5	1.407	6
81	1.377	37.5	1.379	28
82.2	1.361	25	1.359	14

**Table 6.25** Anode Z: XRD analysis for white zinc corrosion product.



2- $\theta$	Wart		ZnCl <sub>2</sub> ·4 Zn(OH) <sub>2</sub> PDF No.7-155		RI <sub>w</sub> - RI	Unknowns		x/0.59	Zn/Zinc PDF No.4-831	
	dA°	RI <sub>w</sub>	dA°	RI		dA°	RI	RI'	dA°	RI
13	7.871	100	7.870	100	0					
19	5.350	15	5.350	20	-5					
26	4.014	20	4.020	20	0					
26	3.924	10	3.940	8	2					
29	3.573	23	3.580	25	-2					
33	3.168	26	3.170	35	-9					
35	2.942	26	2.940	30	-4					
36	2.879	33	2.878	25	8					
38	2.730	43	2.725	55	-12					
39	2.676	56	2.672	65	-9					
40	2.606	20	2.601	20	0					
			2.488	4	-4					
42	2.474	23	2.470	10	13	2.474	13	22	2.473	53
44	2.378	34	2.374	35	-1					
45	2.342	7			7	2.342	7	12		
46	2.308	15			15	2.308	15	25	2.308	40
49	2.165	5	2.174	6	-1					
51	2.089	59				2.09	59	100	2.091	100
51	2.065	7	2.067	8	-1					
53	2.022	23	2.023	20	3					
53	2.008	13	2.012	10	3					
54	1.969	8	1.971	4	4					
54	1.957	16	1.957	10	6					
56	1.899	8	1.900	8	0					
59	1.828	7	1.830	4	3					
60	1.790	7	1.792	8	-1					
60	1.784	10	1.782	6	4					
61	1.770	16	1.768	14	2					
64	1.700	16	1.699	14	2					
64	1.692	26	1.693	12	14	1.692	14	24	1.687	28
65	1.674	3	1.674	2	1					
65	1.661	3	1.660	4	-1					
69	1.585	38	1.585	35	3					
70	1.554	20	1.554	16	4					
72	1.515	20	1.517	14	6					
73	1.500	10	1.502	8	2					
74	1.479	3	1.475	6	-3					
75	1.471	3	1.471	4	-1					
76	1.448	5	1.449	4	1					
77	1.438	7	1.439	4	3					
80	1.389	7	1.388	6	1					
			1.369	8	-8					
84	1.342	7			7	1.342	7	12	1.342	25
84	1.334	7			7	1.334	7	12	1.332	21
93	1.236	7			7	1.236	7	12	1.237	2

Table 6.26 Anode Z: XRD analysis for zinc "wart" corrosion product

Month	E:2:20:1	E:0.4:20:1	E:0.4:20:2	E:0.4:0:1	E:4:20:1
1	no degradation	no degradation	no degradation	no degradation	no degradation
6	no change	no change	no change	no change	no change
7	no change	no change	yellow/white product within wet core hole, rust spotting	no change	no change
8	darkening around anode in core holes	no change	paste loss/orange anode ring within cored hole	no change	darkening around anode in core holes
11	no change	no change	no change	no change	white anode ring
12	no change	darkening around anode in core holes	no change	no change	no change
18	no change	no change	no change	no change	no change
(22)		paste loss/orange anode ring, white precipitate in base of wet core hole, anode gassing	white precipitate in base of wet core hole	no change	white precipitate in base of wet core hole, anode gassing
Rust spotting	no	no	no	no	no
Localised degradation	low	high	high	nil	medium

Table 6.27 Summary of visual inspections of anode E surfaces at 20 mA/m<sup>2</sup>.

Month	E:2:50:1	E:2:50:2	E:0.4:50:1	E:2:0:1
1	no degradation	no degradation	no degradation	no degradation
6	few rust spots	few rust spots, stain in drill hole, narrow surface cracks	concrete substrate cracked across entire corner location A1 to 30mm depth due to handling	no change
7	increased rust spotting	no change	no change	no change
8	white ring around anode in core hole	10 mm surface crack, white ring around anode in core hole	paste loss/white ring around anode in core hole	no change
9	narrow surface cracks, paste loss/orange ring around anode in core hole	orange anode ring/increased paste loss in cored hole	narrow surface cracks, orange ring around anode in core hole	no change
11	increased paste loss in core holes	no change	no change	no change
12	voluminous product at anode in wet core hole	voluminous product at anode in wet core hole	increased paste loss in core holes	no change
18	no change	no change	no change	no change
(22)		considerable orange precipitate in core hole	high paste loss around anode in core hole, gas bubbling	no change
Rust spotting	yes	yes	no	no
Localised degradation	very high	very high	very high	nil

Table 6.28 Summary of visual inspections of anode E surfaces at 50 mA/m<sup>2</sup>.



Month	T:2:20:1	T:0.4:20:1	T:0.4:20:2	T:0.4:0:1	T:0:0:1
1	no degradation	no degradation	no degradation	no degradation	no degradation
6	no change	no change	rust spots	no change	no change
7	no change	no change	no change	no change	no change
8	darkening around anode in core holes	darkening around anode in core holes	orange anode ring within cored hole	no change	no change
9	no change	no change	no change	no change	no change
11	paste loss around anode in core hole	paste loss around anode in core hole, narrow surface cracks	paste loss around anode in core hole	no change	no change
12	no change	no change	rust spotting	no change	no change
18	no change	no change	no change	no change	no change
(22)		orange anode ring within cored hole	white precipitate in base of 1 wet cored hole	no change	no change
Rust spotting	no	no	yes	no	no
Local ised degradation	high	high	high	nil	nil

Table 6.29 Summary of visual inspections of anode T surfaces at 20 mA/m<sup>2</sup>.

Month	T:2:50:1	T:2:50:2	T:0.4:50:1	T:2:0:1
1	no degradation	no degradation	no degradation	no degradation
6	many rust spots	cement darkening at anode in drill hole	no degradation	no degradation
7	no change	gas evolution observed at anode within cored hole, chlorine odour	white products observed at anode within wet cored hole	no change
8	paste loss/orange ring around anode in core hole	10 mm surface crack paste loss around anode in core hole	paste loss/orange ring around anode in core hole	no change
9	no change	orange anode ring in cored hole	no change	no change
11	increased paste loss in core holes	increased paste loss in core holes	no change	no change
12	no change	no change	no change	no change
18	no change	no change	no change	no change
(22)		considerable orange precipitate in core hole	no change	no change
Rust spotting	yes	no	no	no
Local ised degradation	very high	very high	very high	nil

Table 6.30 Summary of visual inspections of anode T surfaces at 50 mA/m<sup>2</sup>.

Month	3	6	9	12	18
E:2:20:1	1		2	1, 2	4
E:0.4:20:1	2		4	3, 4, 5	4
E:0.4:20:2	1		2	3, 5	3, 4
E:0.4:0:1	1	1	1	1	1
E:4:20:1	1		2, 3	2, 3	3, 5
E:2:50:1	1	3, 4	3, 5, 6	3, 6	5, 6
E:2:50:2	2	2	5, 6	2, 5, 6	4, 5
E:0.4:50:1	2	1	5	4, 6	4, 5
E:2:0:1	1	1	1	1	1

Month	3	6	9	12	18
T:2:20:1	1		2	2, 3	4, 5
T:0.4:20:1	2		4	3, 6	5
T:0.4:20:2	1		4	3, 4	4
T:0.4:0:1	1	1	1	1	1
T:0:0:1	1		1	1	1
T:2:50:1	3, 4	2	5	4, 5, 6	6
T:2:50:2	3, 4	1	5	4, 5	5
T:0.4:50:1	6	1	5	4, 5	5
T:2:0:1	1		1	1	1

CODE	INTERPRETATION (Anodes E and T)
1	No degradation detected
2	Grey cement paste darkens in a ring around anode strand
3	White crystals observed in pores adjacent to anode strand, porosity decreases up to 5 mm from anode strand
4	Detectable paste loss adjacent to anode strand
5	Paste adjacent to anode strand attains a beige/orange colour
6	Paste loss around the full circumference of anode strand

**Table 6.31** Summary of visual inspections of anodes E and T core surfaces.

Specimen	Anodic current density mA/m <sup>2</sup>	Specimen	Anodic current density mA/m <sup>2</sup>
E:0.4:20:2	107	E:2:50:1	266
E:0.4:20:1	115	E:2:50:2	287
E:2:20:1	115	E:0.4:50:1	333
E:4:20:1	115	T:0.4:50:1	368
T:2:20:1	156	T:2:50:1	386
T:0.4:20:1	163	T:2:50:2	391
T:0.4:20:2	163		

**Table 6.32** Summary of mesh anodic current densities.



Element	White precipitate % Total (ave. of 7)	Cementitious overlay % Total (ave. of 3)	Coloured precipitate % Total (1 test)
Na	0	0	0
Mg	0	0	1
Al	1	0	5
Si	1	37	1
P	1	0	1
S/Mo	0	1	1
Cl	5	4	1
K	0	0	0
Ca	89	54	88
Ti	0	0	0
V	0	0	0
Cr	0	0	0
Mn	0	0	0
Fe	1	2	2
Ni	0	0	0
Cu	0	0	0
Zn	0	1	0
Total	100	100	100

**Table 6.33** Summary of EDXA data for anodes E and T.

Specimen	loc.	Load N/mm <sup>2</sup>	Mode	Depth failure D mm	Anode distance d mm	Notes
E:2:0:1	1	1.83	B	4 to 14	4	
	2	1.78	B	0 to 7	2.5	
	3	2.03	B/f	0 to 9	2	
	7	1.60	B/f	0 to 3	1.5	
	8	1.54	B	7 to 13	4.5	
E:2:20:1	1	2.57	B	2 to 12	0.5-6	
	2	1.98	B/f			
	3	2.41	B/f	0 to 8	3-6	
	7	1.19	f	0 to 1	1.5	
	8	1.16	f	0 to 1	2.5	
E:2:50:1	1	(0.44)	o	-4 <sub>0</sub>		fail in overlay
	2	0.76	f	0 to 1	2	
	3	0.68	f	0 to 1	1.5	
	6	0.73	f	0 to 1	0.5	i/f brown. chlorine odour
	7	0.84	f	0 to 1	2	
	8	0.83	f	0 to 1	2	
T:2:0:1	1	0.8	e	-		
	1	2.67	B/f	0 to 3	4.5	
	2	1.46	e	-	-	
	3	0.97	o	-6 <sub>0</sub>	-	fail in overlay
	4	2.16	e	-	-	
	5	2.05	o	-5 <sub>0</sub>	-	fail in overlay
T:2:20:1	8	1.84	B/f	0 to 8	0.5-4	
	1	2.40	B/f	0 to 1	0.5-3	
	3	1.09	f	0 to 3	2.5	
	6	0.66	e	-	6	
	7	1.63	e	-		
	8	1.60	B/f	0 to 5	7	
T:2:50:1	9	1.00	B/f	0 to 3	4	
	1	1.03	e/o	0 to 2		
	1	2.75	B	0 to 9	3	
	2	1.12	e	-		
	2	-	B/f	0 to 5	2	sheared off
	3	1.34	f	0 to 1	0-1	level of strand
	5	0.87	f	0 to 1	3	
	7	(0.42)	e			wet substrate
	8	(0.22)	e			wet substrate
	9	(0.46)	e			wet substrate

(To be read with figures 6.52 and 6.53)

**Table 6.34** "Limpit" adhesive strength measurements for anodes E and T.



Specimen	Mode	% of failures	Average load N/mm <sup>2</sup>	Ave load all N/mm <sup>2</sup>
E:2:0:1	B, B/f	100	1.76	1.76
E:2:20:1	B, B/f	60	2.39	1.79
	f	40	1.18	
E:2:50:1	f	83	0.77	0.77
	o	17	(0.44)	
T:2:0:1	e	42	1.47	1.77
	B/f	29	2.26	
	o	29	1.51	
T:2:20:1	B/f	51	1.67	1.30
	f	17	1.09	
	e	34	1.15	
T:2:50:1	e	44	1.08	1.15
	B, B/f	22	1.38	
	f	22	1.11	
	o	11	1.03	

(To be read with figure 6.53)

**Table 6.35** Summary of overlay adhesive strengths for anodes E and T.

Mode	B	B/f	f	o	e
	1.83	2.03	1.19	0.94	0.80
	1.78	1.60	1.16	2.05	1.46
	1.54	2.67	1.09	(0.44)	2.16
	2.57	1.84	0.76	1.03	0.66
	2.75	1.98	0.68		1.63
		2.41	0.73		1.12
		2.40	0.84		(0.42)
		1.60	0.83		(0.22)
		1.00	1.34		(0.46)
			0.87		
Average	2.09	1.95	0.95	1.34	1.31

(To be read with figure 6.53)

**Table 6.36** Average overlay adhesive strengths by failure mode.

MONTH	DATE	MONTHS	DAYS
Apr	19/4/89	0	0
May	14/5/89	1	25
Jun	13/6/89	2	54
Jul	11/7/89	3	83
Aug	14/8/89	4	116
Sep	20/9/89	5	154
Oct	26/10/89	6	190
Dec	18/12/89	8	242
(Jan)	1/2/90	9	287
(Feb)	1/3/90	10	316
Mar	20/3/90	11	334
Apr	27/4/90	12	372
Jun	12/6/90	14	418
Aug	14/8/90	16	481
Sep	24/9/90	17	522
Oct	10/10/90	18	538

**Table 7.1** Dates/times of the electrical potential measurements.

Month	Time	Weather	Average temperature °C			
			air	Anode T	Anode P	Anode Z
1	2 pm	sunny	26	37.8	39.6	40.3
2	2 pm	sunny	28.7	32.2	33.1	29.6
3		dry	19.1	19.2	19.5	20.7
4	11.45 am	sunny	23	25.2		
5	3.40 pm	sunny	25.3	30.0		
6	2 pm	rain	14	14.4		
7	9 am	dry	2.2	0.2		
	12 pm		9	5.4		

**Table 7.2** Air/specimen surface temperatures at the times of some potential measurements.



Specimen T:0.4:20:1								
Month	0	1			2	3	4	5
LOCATION	E <sub>corr</sub>	E <sub>on</sub>	E <sub>off</sub>	E <sub>off</sub>	E <sub>on</sub>	E <sub>on</sub>	E <sub>on</sub>	E <sub>on</sub>
			1 sec	4 hrs				
A1	-99	-708			-769	-952	-797	-772
A2	-102	-686			-707	-807	-713	-646
A3	-111	-665			-975	-1050	-927	-877
B1	-103	-740			-715	-929	-820	-776
B2	-101	-730			-732	-909	-805	-765
B3	-97	-670			-888	-1103	-1007	-989
C1	-122	-810	-660	-130	-732	-915	-812	-754
C2	-131	-776			-741	-903	-864	-781
C3	-123	-743			-940	-1111	-1095	-989
Ave A1-C3	-110	-725			-800	-964	-871	-817
Ave A2,B2, C2	-111	-731			-727	-873	-794	-731
Specimen T:0.4:50:1								
Month	0	1			2	3	4	5
LOCATION	E <sub>corr</sub>	E <sub>on</sub>	E <sub>off</sub>	E <sub>off</sub>	E <sub>on</sub>	E <sub>on</sub>	E <sub>on</sub>	E <sub>on</sub>
			1 sec	4 hrs				
A1	-110	-982			-831	-926	-932	-908
A2	-105	-992			-702	-624	-708	-660
A3	-101	-886			-1105	-1191	-1213	-1199
B1	-112	-998			-891	-1024	-1050	-1038
B2	-109	-1025			-785	-793	-841	-870
B3	-103	-881			-1074	-1244	-1264	-1271
C1	-210	-1225	-980	-153	-810	-1013	-1045	-1048
C2	-216	-1232			-834	-940	-944	-918
C3	-204	-1190			-1107	-1354	-1380	-1432
Ave A1-C3	-141	-1046			-904	-1012	-1042	-1038
Ave A2,B2, C2	-143	-1083			-774	-786	-831	-816

Table 7.3 Various cathode potentials for selected anode T specimens.

Specimen T:0.4:20:1											
Month	6					10			11		
LOCATION	E <sub>on</sub>	E <sub>off</sub>	E <sub>off</sub>	E <sub>off</sub>	E <sub>off</sub>	E <sub>on</sub>	E <sub>off</sub>	dE	E <sub>on</sub>	E <sub>off</sub>	dE
		1.0 s	4 hrs	24 hrs	96 hrs		0.2 s	0.2 s		0.2 s	0.2 s
A1	-882		10	610	58	-722	-607	115	-694	-597	97
A2	-791		245	590	-90	-704	-651	53	-677	-630	47
A3	-1163		80	664	-116	-874	-650	224	-794	-618	176
B1	-991		-92	-79	-72	-721	-588	133	-676	-520	156
B2	-965		-114	-74	-72	-706	-611	95	-686	-610	76
B3	-1281		-90	25	-48	-942	-668	274	-844	-632	212
C1	-1000		-128	-256	-62	-780	-638	142	-735	-619	116
C2	-962		-150	-244	-53	-726	-618	108	-719	-626	93
C3	-1294	-838	-160	-252	-39	-974	-685	289	-903	-675	228
Ave A1-C3	-1037		-44	109	-55	-794	-635	159	-748	-614	133
Ave A2,B2, C2	-906		-6	91	-72	-712	-627	85	-694	-622	72
Specimen T:0.4:50:1											
Month	6					10			11		
LOCATION	E <sub>on</sub>	E <sub>off</sub>	E <sub>off</sub>	E <sub>off</sub>	E <sub>off</sub>	E <sub>on</sub>	E <sub>off</sub>	dE	E <sub>on</sub>	E <sub>off</sub>	dE
		1.0 s	4 hrs	24 hrs	96 hrs		0.2 s	0.2 s		0.2 s	0.2 s
A1	-1093		667	18	-25	-1018	-821	197	-933	-777	156
A2	-885		540	117	296	-1067	-937	130	-888	-794	94
A3	-1663		749	92	859	-1531	-887	644	-1241	-787	454
B1	-1234		-94	-64	-20	-1076	-776	300	-947	-728	219
B2	-1054		-132	-88	-143	-967	-742	225	-846	-690	156
B3	-1758	-898	-9	-55	-174	-1498	-788	710	-1222	-725	497
C1	-1343		-296	-102	-242	-1089	-739	350	-959	-714	245
C2	-1181		-287	-97	-245	-1036	-796	240	-926	-758	168
C3	-1962		-309	-121	-270	-1682	-876	806	-1356	-805	551
Ave A1-C3	-1353		92	-33	4	-1218	-818	400	-1035	-753	282
Ave A2,B2, C2	-1040		40	-23	-31	-1023	-825	198	-887	-747	139

**Table 7.4** Instant-off cathode potentials for selected anode T specimens.



Month	Specimen P:2:0:1	Specimen P:2:50:1
3	Insignificant micro-cracks in HCP parallel to surface, intimate contact, carbonation even, medium porosity.	Much lateral cracking at interface, some passing through aggregate, variable porosity, generally intimate contact, carbonation up to 1mm.
6	Low porosity, uneven carbonation $\approx 250 \mu\text{m}$ , intimate contact, insignificant micro-cracks in HCP parallel to surface, isolated coating rupture.	Continuous micro-cracking at interface, some passing through aggregate, variable porosity, generally intimate contact, uneven carbonation
9		High porosity/carbonated surface layer, lateral micro-cracking to depth $\approx 0.4 \text{ mm}$ . Acid bubble site, much material lost during slide preparation, aggregates cracked, paste highly porous.
12		Localised region very high porosity $\approx 170 \mu\text{m}$ deep extending across 5.2 mm, elsewhere low interfacial porosity/lateral micro-cracks. Carbonation type zone extending up to 4 mm into HCP. Several ruptures of coating.

**Table 8.1** Summary of thin section examination: Specimens P:2:0:1 & P:2:50:1.

Month	Specimen Z:2:0:1	Specimen Z:2:50:1
3	Cracking of surface aggregate, generally intimate contact between zinc and substrate, 2-3 mm carbonation.	Brittle glassy phase at interface, interfacial cracking.
6	Cracking of surface aggregate, zinc separate from substrate, 200-800 $\mu\text{m}$ carbonation.	Glassy phase at interface, interfacial cracking.
9		Glassy phase at interface, interfacial cracking.
12		Zinc removed during preparation, glassy phase at interface, interfacial cracking..

**Table 8.2** Summary of thin section examination: Specimens Z:2:0:1 & Z:2:50:1.

Month	Specimen T:2:0:1	Specimen T:2:50:1
3	Substrate/overlay bond good, substrate carbonation negligible, up to $\approx 70 \mu\text{m}$ , no anodic degradation. Overlay porosity high.	Substrate/overlay good bond, variable carbonation. Degradation zone extending $\approx 0.5 \text{ mm}$ from anode surface, inner ring increased porosity, no portlandite, outer narrow carbonation ring $\approx 50 \mu\text{m}$ .
6	Substrate/overlay bond good, substrate carbonation up to $\approx 0.5 \text{ mm}$ , no anodic degradation. Overlay porosity high.	No mesh in sample, Overlay/substrate bond good, substrate carbonated.
9		Overlay/substrate bond good, substrate carbonated. Overlay degradation in very high porosity ring up to 3mm diameter, paste devoid of portlandite, outer ring of solid carbonated paste up to $\approx 250 \mu\text{m}$ . Significant portlandite crystallisation in macro pores in alkaline areas adjacent to the anode.
12		Overlay/substrate lateral micro-cracking, passes through aggregate particles. Partly carbonated crack from surface of overlay to substrate, 5 mm from anode. Substrate carbonated up to 1.6 mm. Overlay degradation in very high porosity ring up to 3mm diameter, paste devoid of portlandite, outer ring of solid carbonated paste up to $\approx 250 \mu\text{m}$ . Porosity elsewhere as for controls. Limited portlandite crystallisation in macro pores.

**Table 8.3** Summary of thin section examination: Specimens T:2:0:1 & T:2:50:1.

Month	Specimen E:2:0:1	Specimen E:2:50:1
3	Substrate/overlay bond good, substrate carbonation negligible, up to $\approx 70 \mu\text{m}$ , no anodic degradation. Overlay porosity high.	No mesh in sample, Overlay/substrate bond good, substrate carbonated.
6	Substrate/overlay bond good, substrate carbonation up to $\approx 0.5 \text{ mm}$ , no anodic degradation. Overlay porosity high.	No mesh in sample, Overlay/substrate lateral micro-cracking passes through aggregate particles, substrate carbonated.
9		Overlay/substrate lateral micro-cracking, passes through paste, substrate carbonated. Overlay degradation in very high porosity ring up to 3mm diameter, paste devoid of portlandite, outer ring of solid carbonated paste up to $\approx 100 \mu\text{m}$ .
12		Overlay/substrate lateral micro-cracking, passes through aggregate particles. Substrate carbonated. Overlay degradation in very high porosity ring up to 3.5 mm diameter, paste devoid of portlandite, outer ring of solid carbonated paste up to $\approx 100 \mu\text{m}$ , extends to substrate. Porosity elsewhere as for controls. Significant portlandite crystallisation in macro pores.

**Table 8.4** Summary of thin section examination: Specimens E:2:0:1 & E:2:50:1.



Month	Specimen T:0:0:1	Specimen E:4:20:1
3	No mesh in sample, substrate/overlay bond good, substrate carbonation negligible. Overlay porosity high.	Overlay/substrate bond good, substrate carbonation negligible. no apparent anodic degradation
6	Substrate/overlay bond good, carbonation negligible. No anodic degradation. Overlay porosity high.	No mesh in sample, Overlay/substrate bond good, substrate carbonation negligible.
9		Overlay/substrate bond good, substrate carbonated. Overlay degradation with increased porosity on substrate side of anode up to $\approx 700\ \mu\text{m}$ from anode, some portlandite loss/ partial carbonation.
12		Overlay/substrate bond good, substrate carbonated. Partial overlay degradation, portlandite loss, increased porosity up to $\approx 0.5\ \text{mm}$ from anode.

**Table 8.5** Summary of thin section examination: Specimens T:0:0:1 & E:4:20:1.

	Cl (mM/g sample)	Na (mM/g sample)	K (mM/g sample)
Overlay T:0:0:1	0.221	0.303	0.084
Acidified paint	0.099		
Paint control	0.382		

**Table 8.6** Ionic concentrations of non-standard specimens.

## Appendix D. Figures

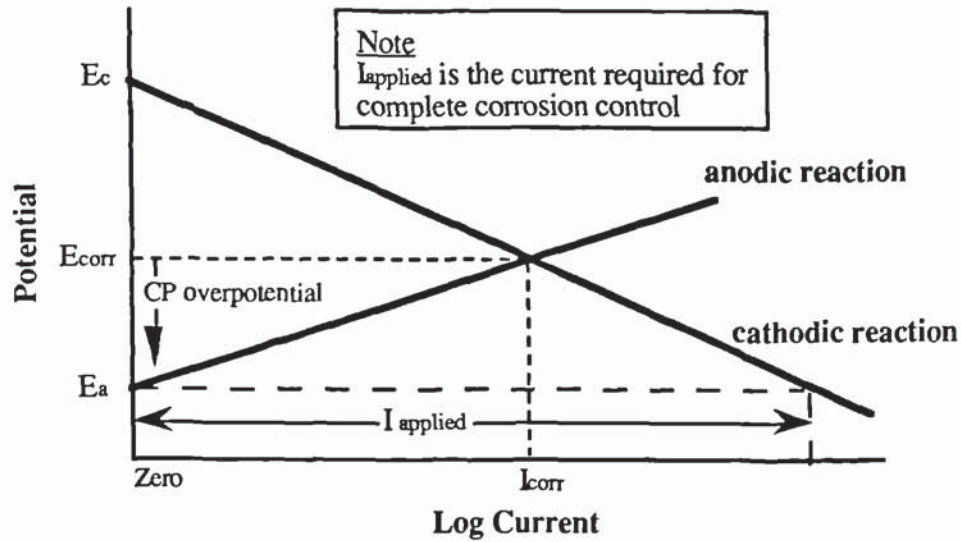


Figure 2.1 Simplified Evans diagram demonstrating the principle of cathodic protection

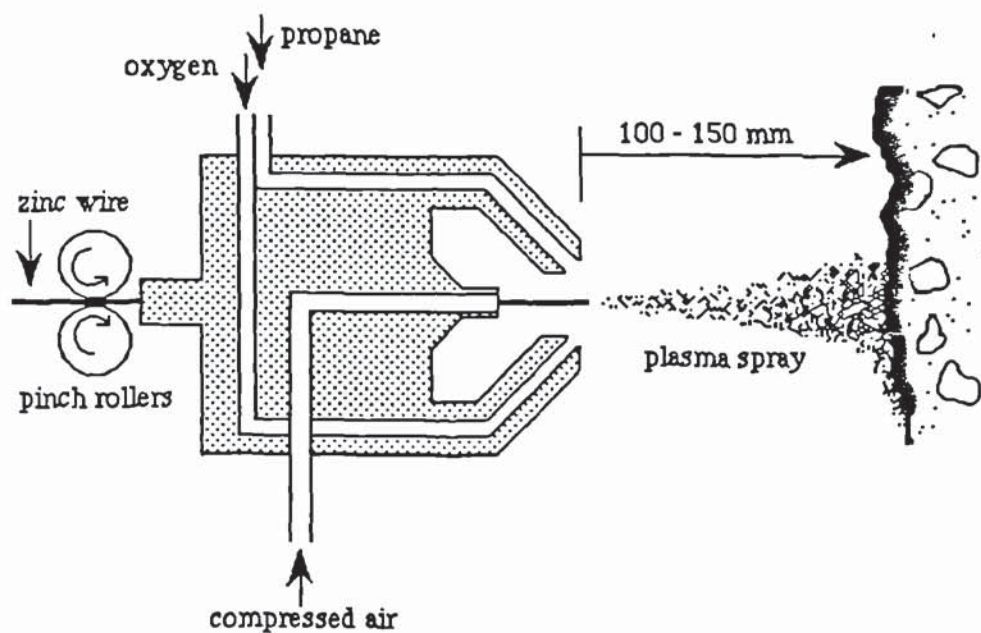


Figure 3.1 Schematic illustration of flame spraying operation.



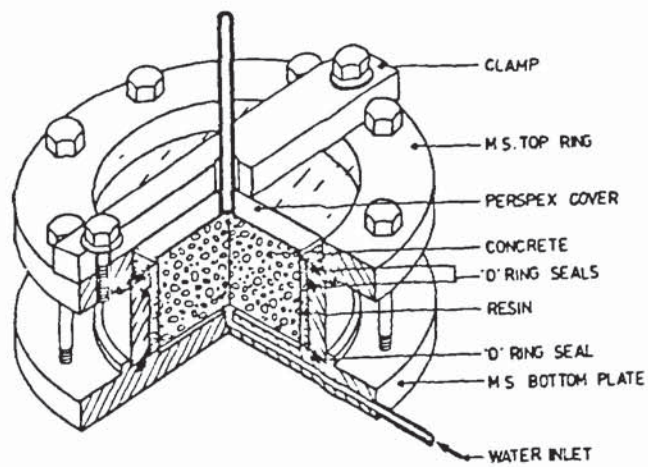


Figure 3.2 Water permeability test rig.

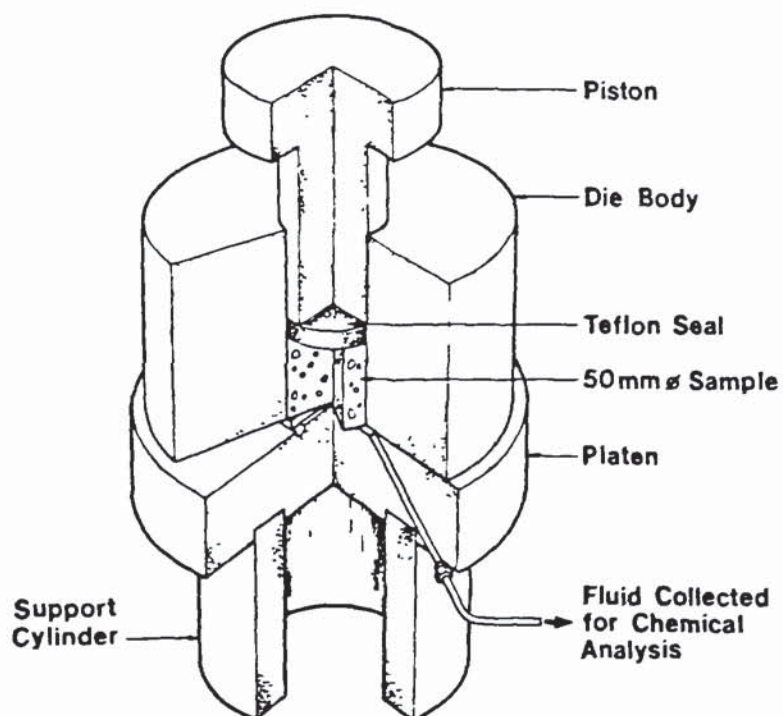


Figure 3.3 The pore solution expression pressure vessel.

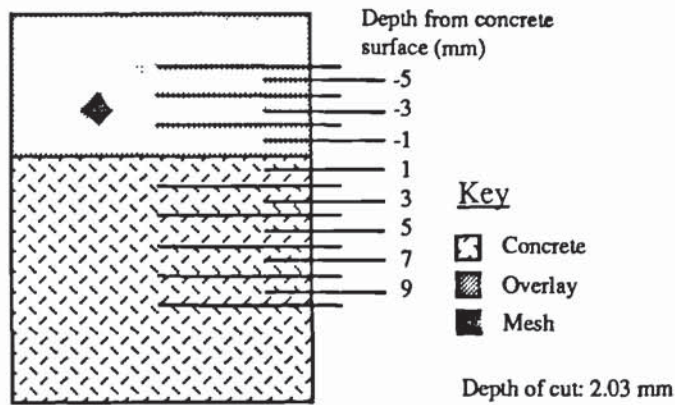


Figure 3.4 Schematic illustration of profile grinding of cored concrete samples.

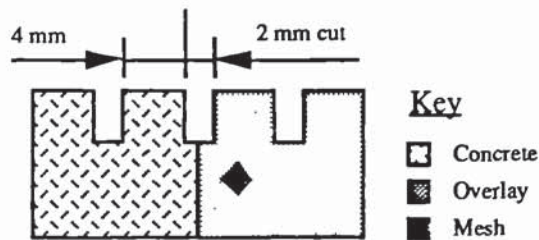


Figure 3.5 Schematic illustration of sampling for MIP.

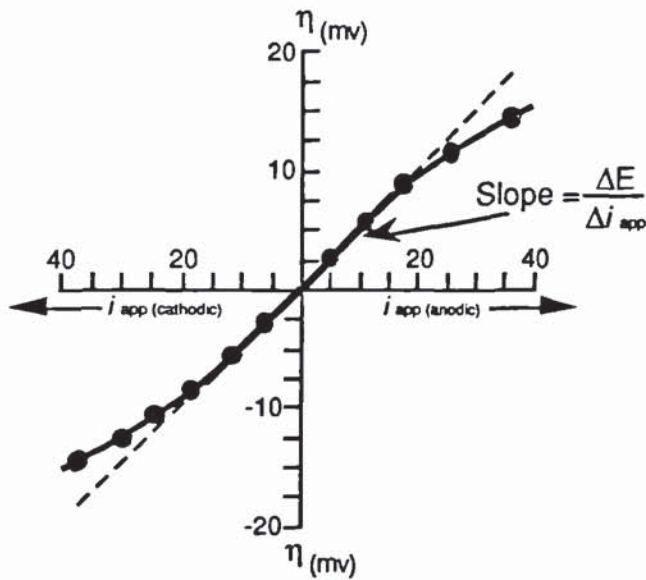


Figure 3.6 Applied-current linear polarisation curve (after Fontana, 1986).



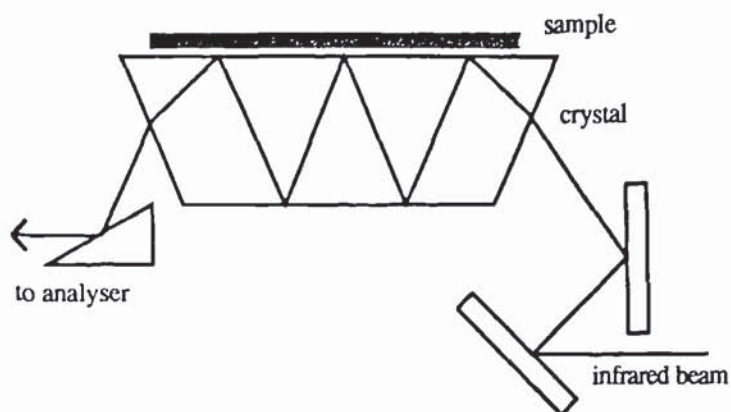


Figure 3.7 Schematic illustration of Horizontal ATR.

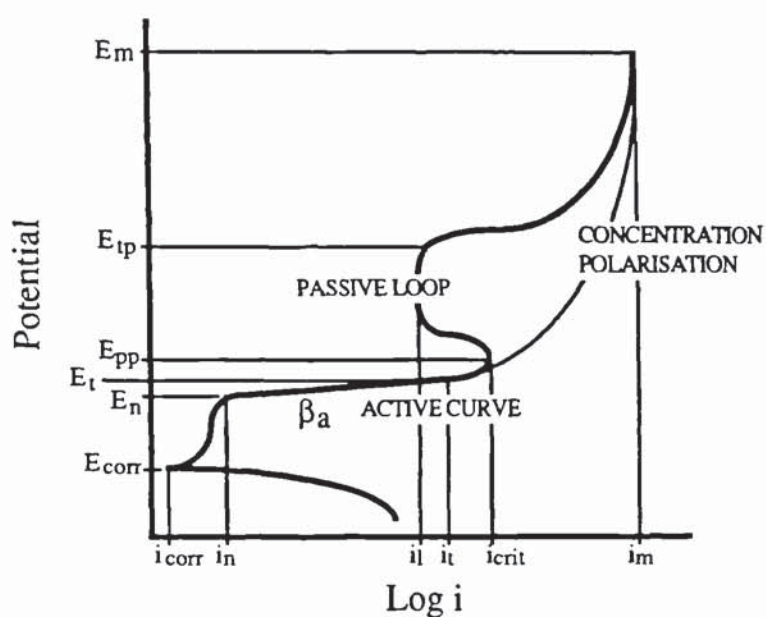


Figure 4.1 Idealised anodic polarisation curve showing an active curve and passive loop.

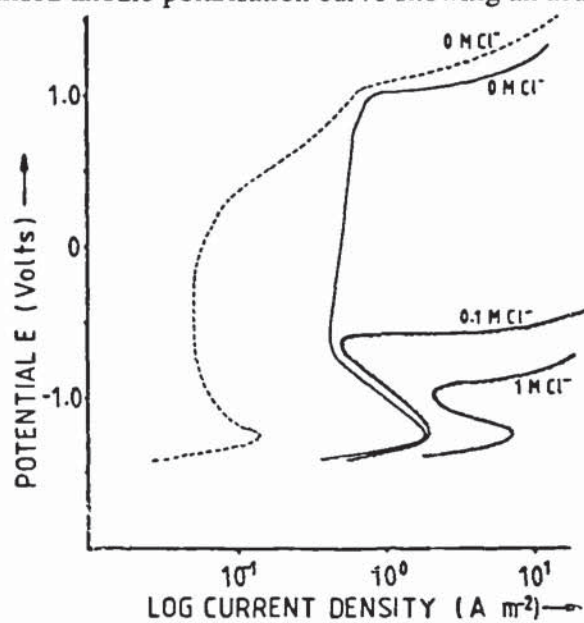


Figure 4.2 Polarisation curve for zinc in 0.01M KOH (after Sergi *et al*, 1985)

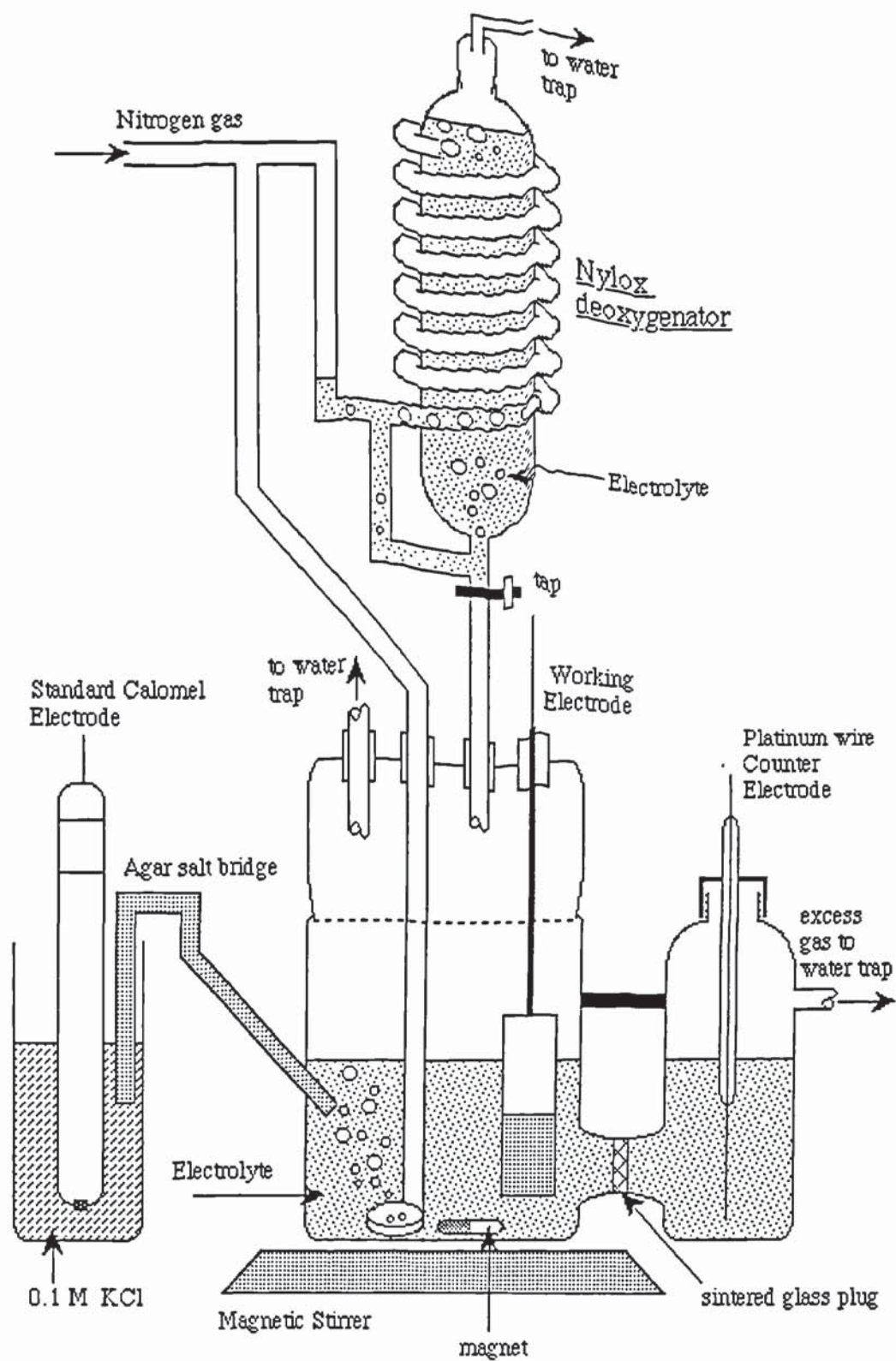


Figure 3.4 Corrosion cell arrangements



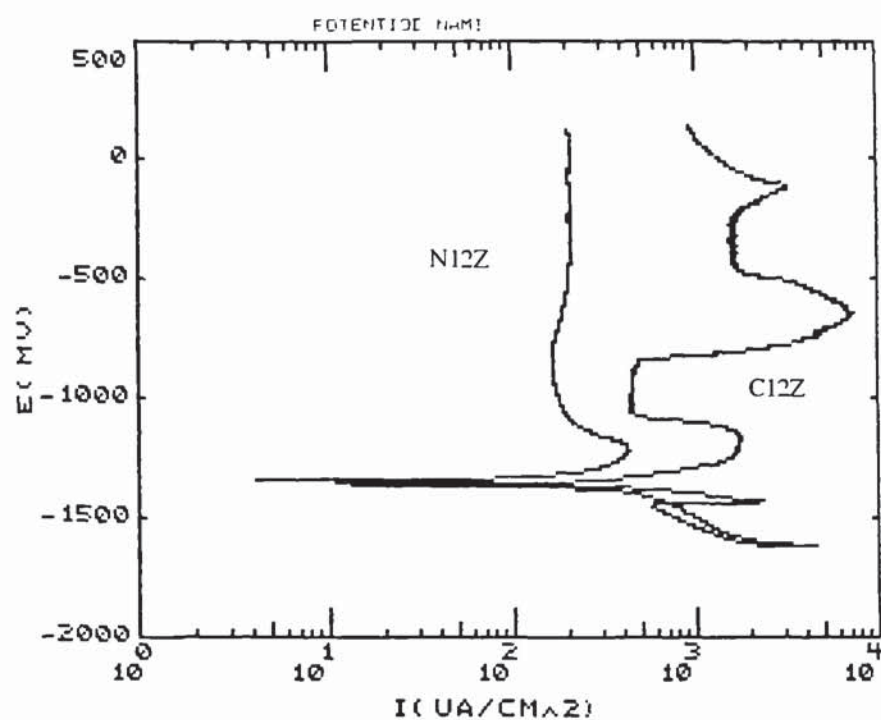


Figure 4.4 Polarisation curves for 12Z specimens.

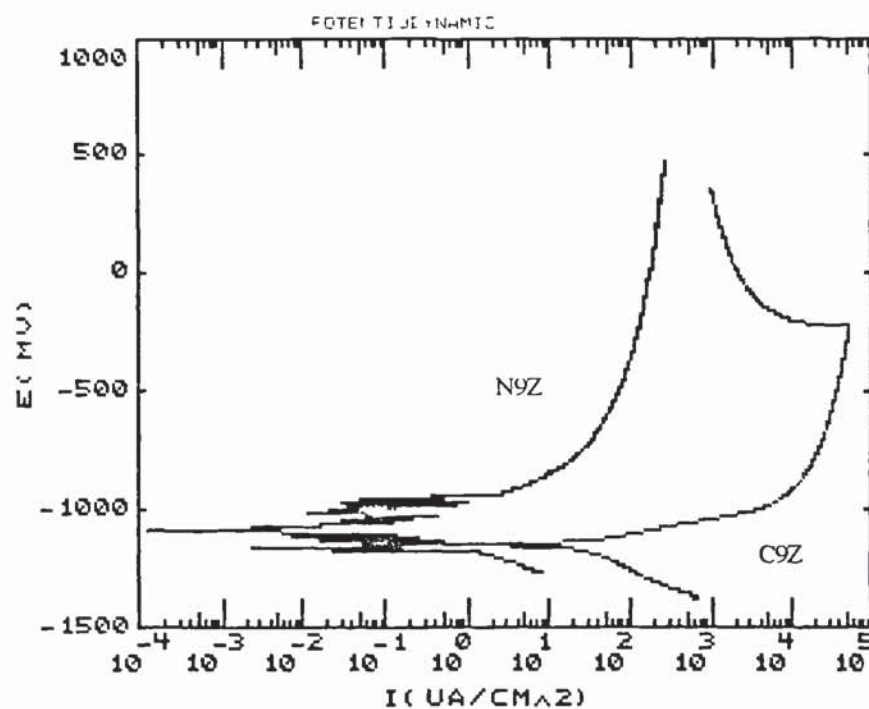


Figure 4.5 Polarisation curves for 9Z specimens.

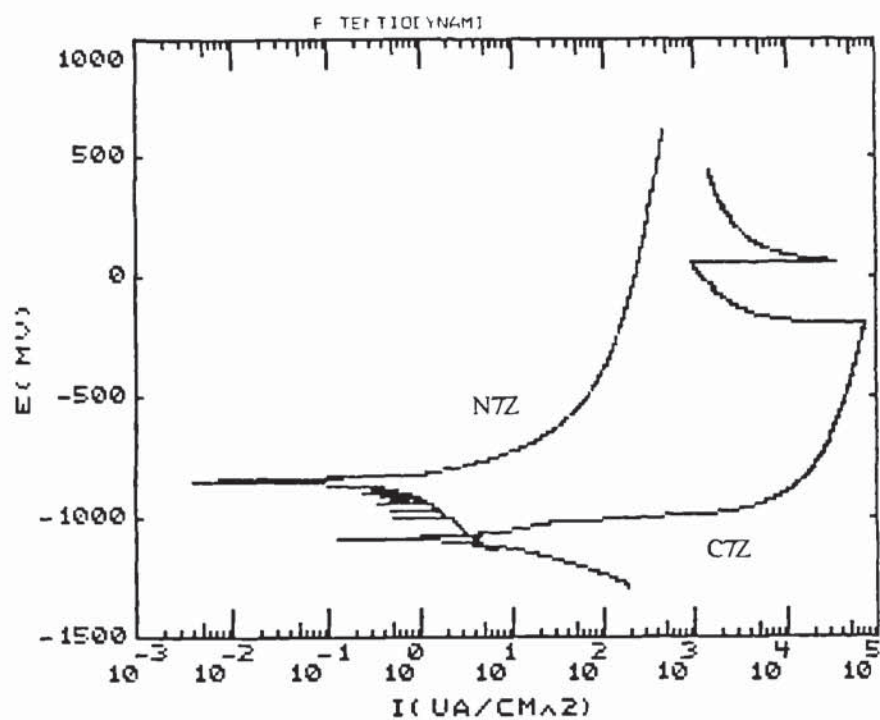


Figure 4.6 Polarisation curves for 7Z specimens.

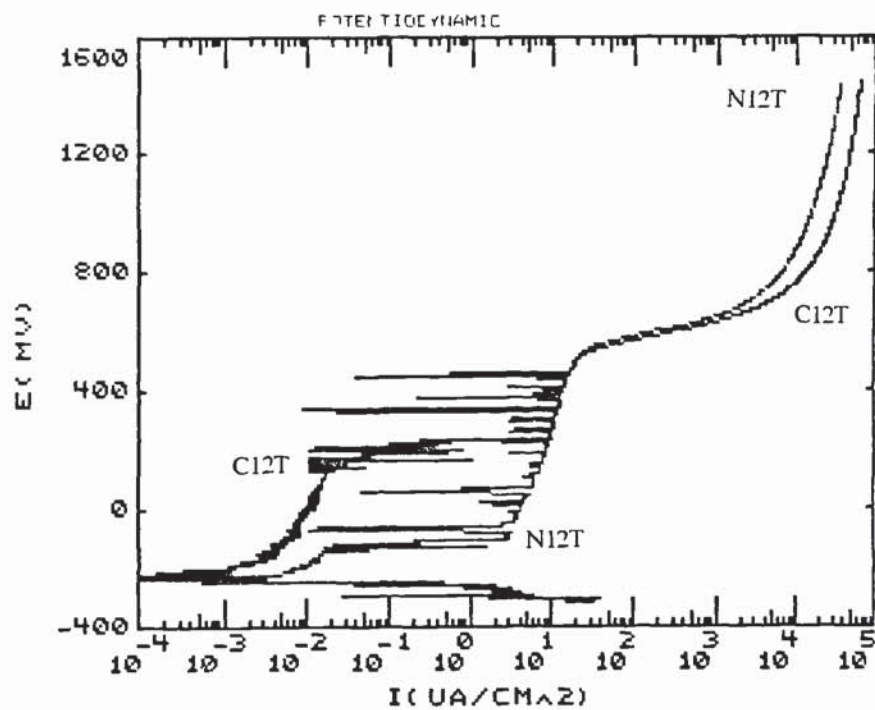


Figure 4.7 Polarisation curves for 12T specimens.



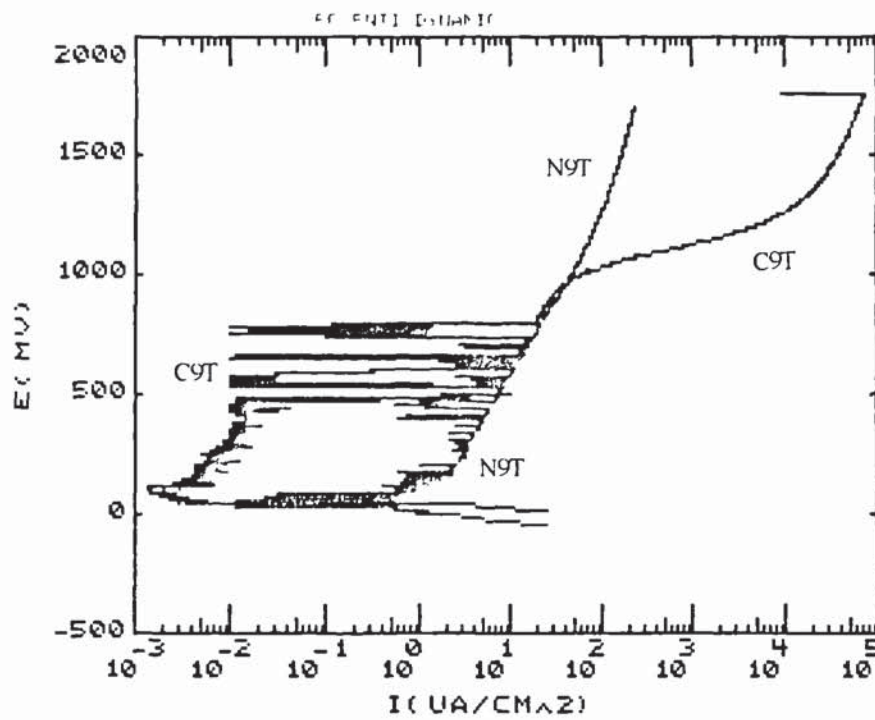


Figure 4.8 Polarisation curves for 9T specimens.

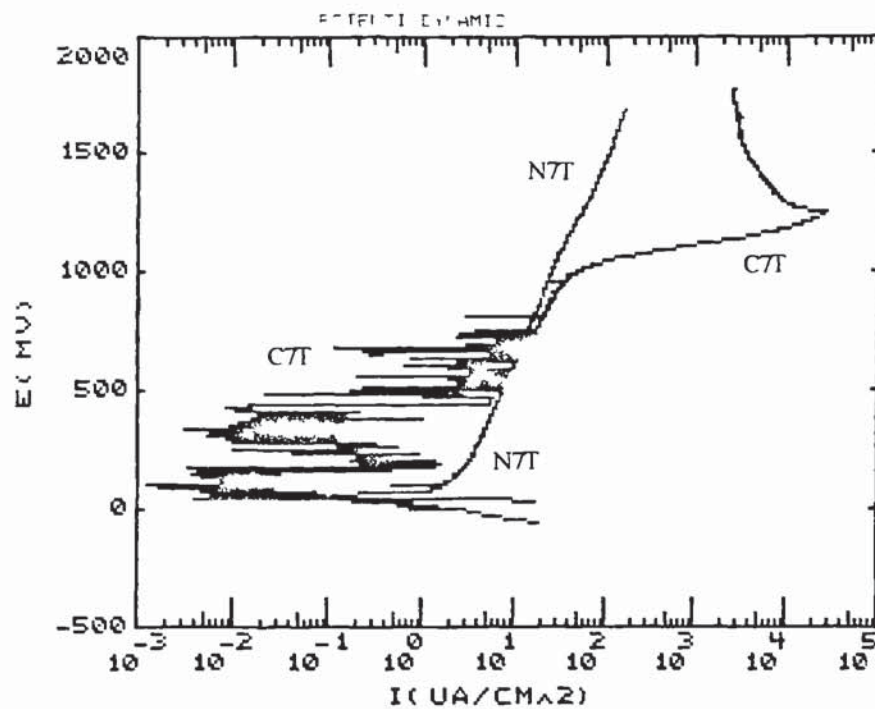


Figure 4.9 Polarisation curves for 7T specimens.

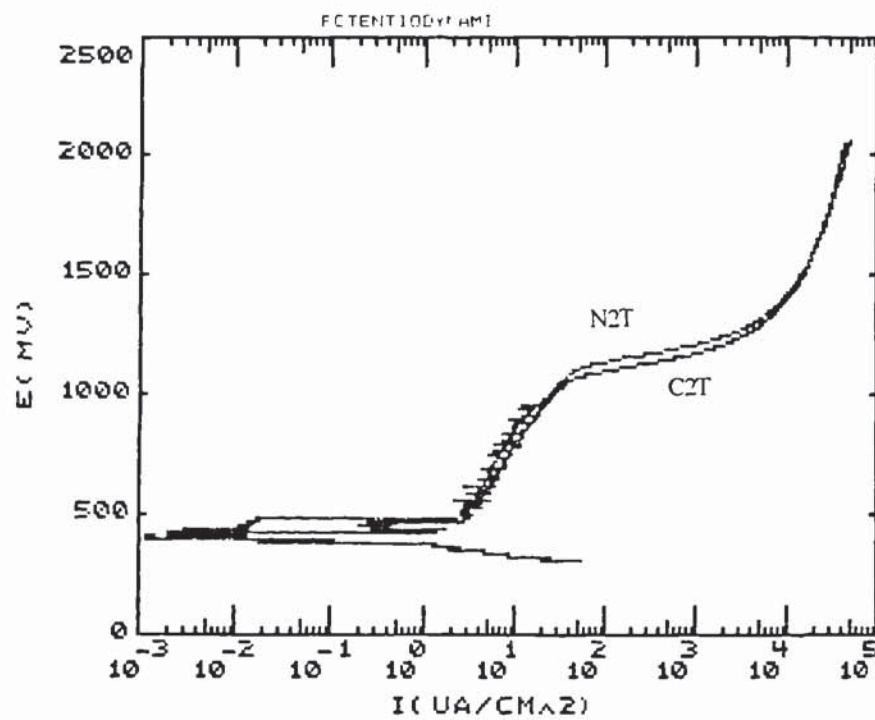


Figure 4.10 Polarisation curves for 2T specimens.

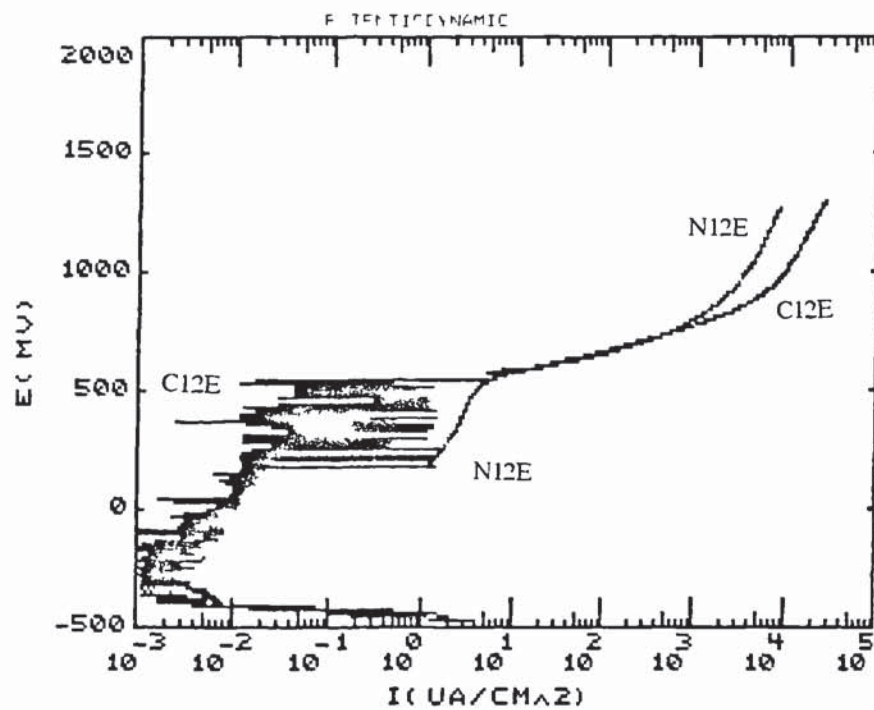


Figure 4.11 Polarisation curves for 12E specimens.



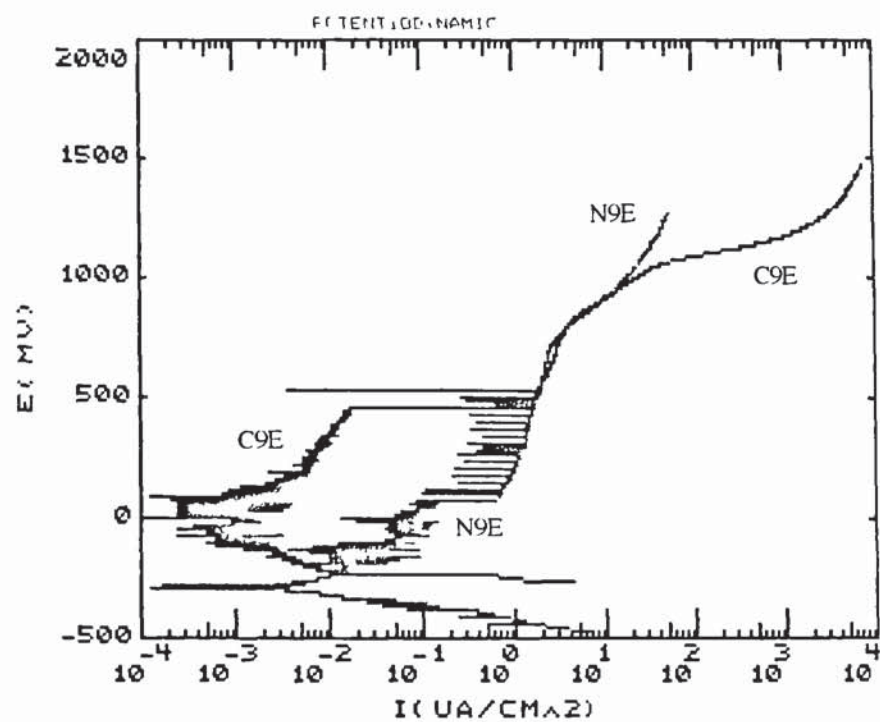


Figure 4.12 Polarisation curves for 9E specimens.

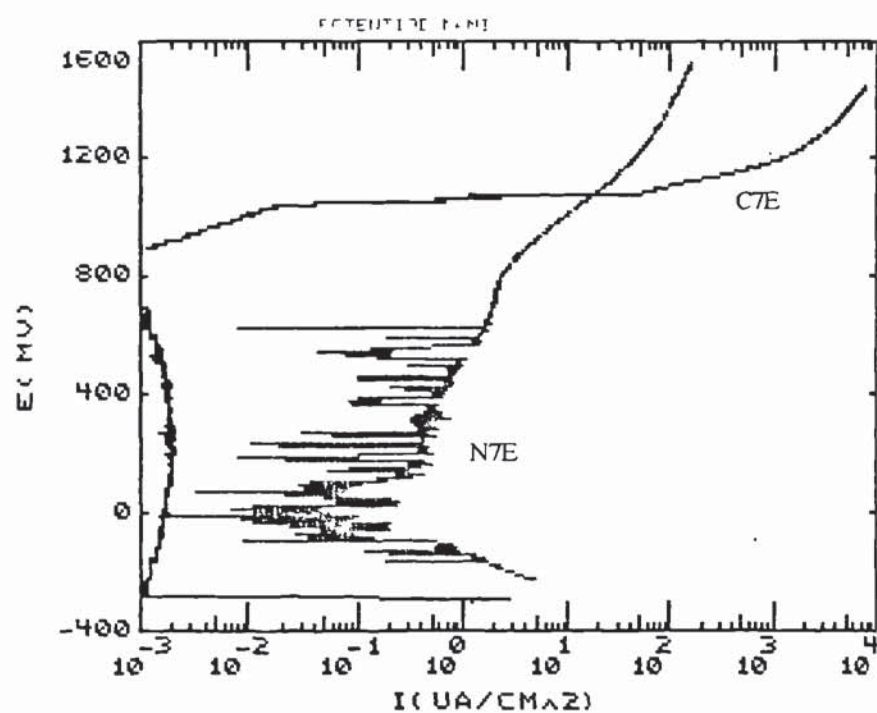


Figure 4.13 Polarisation curves for 7E specimens.

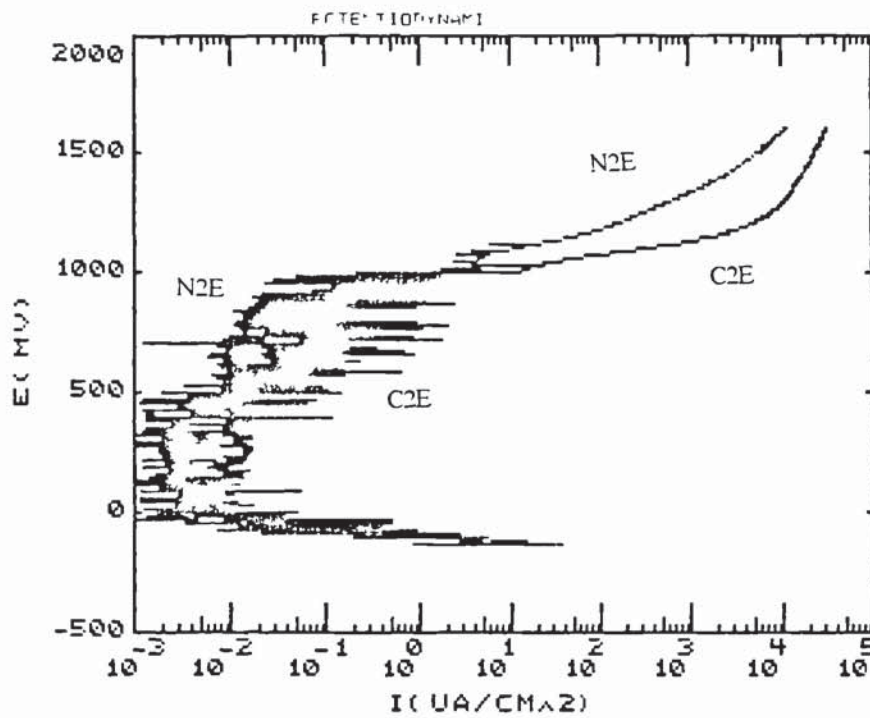


Figure 4.14 Polarisation curves for 2E specimens.

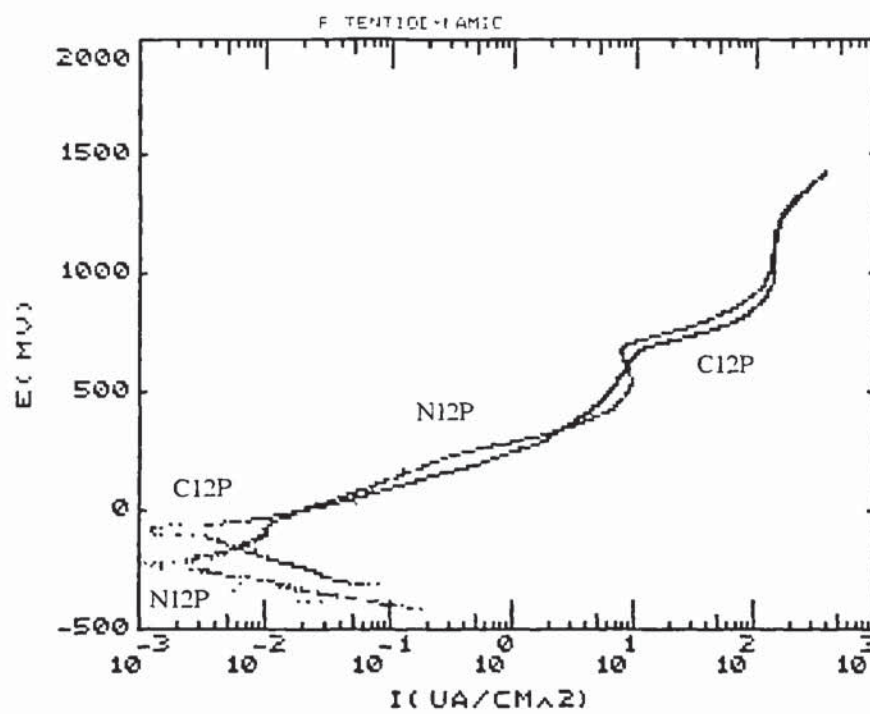


Figure 4.15 Polarisation curves for 12P specimens.



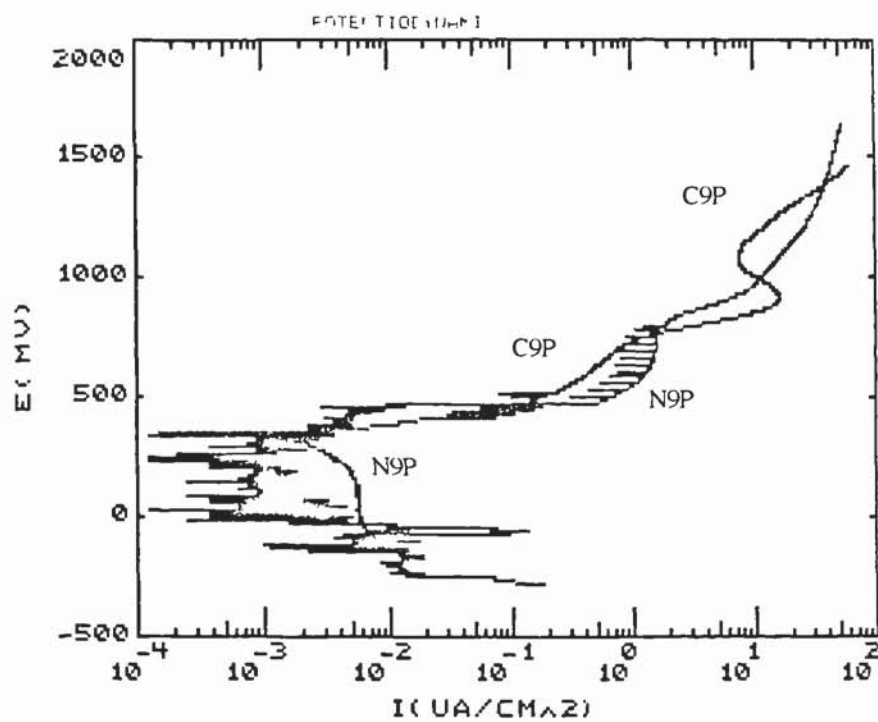


Figure 4.16 Polarisation curves for 9P specimens.

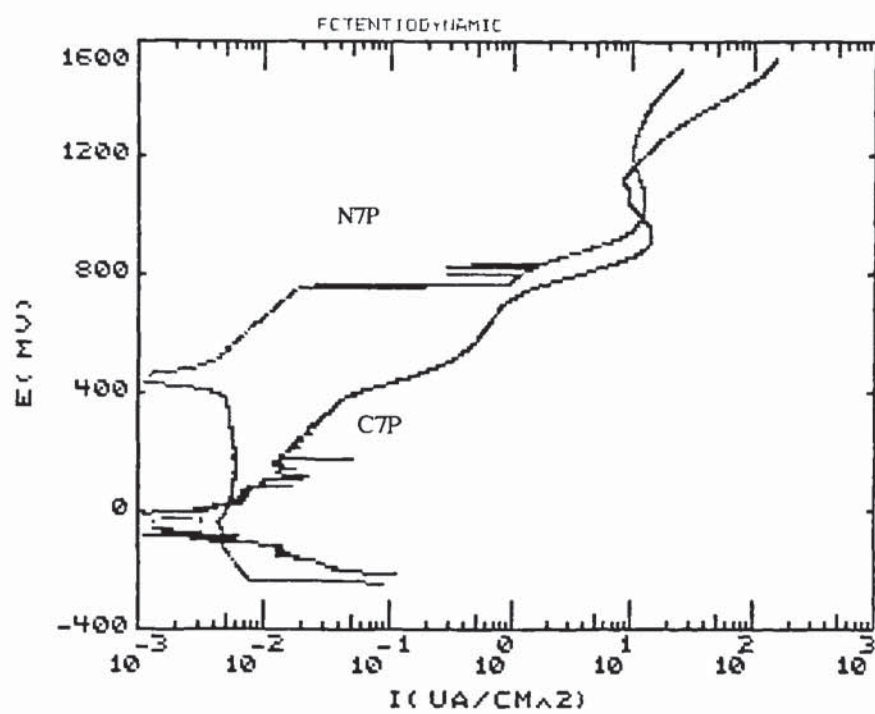


Figure 4.17 Polarisation curves for 7P specimens.





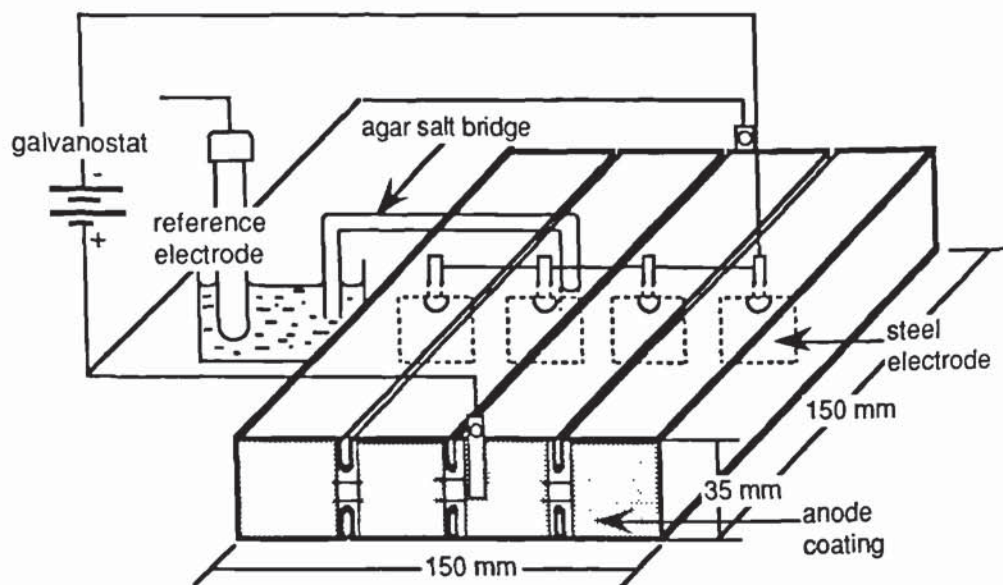


Figure 5.1 Coated anode HCP prism connected to the galvanostat

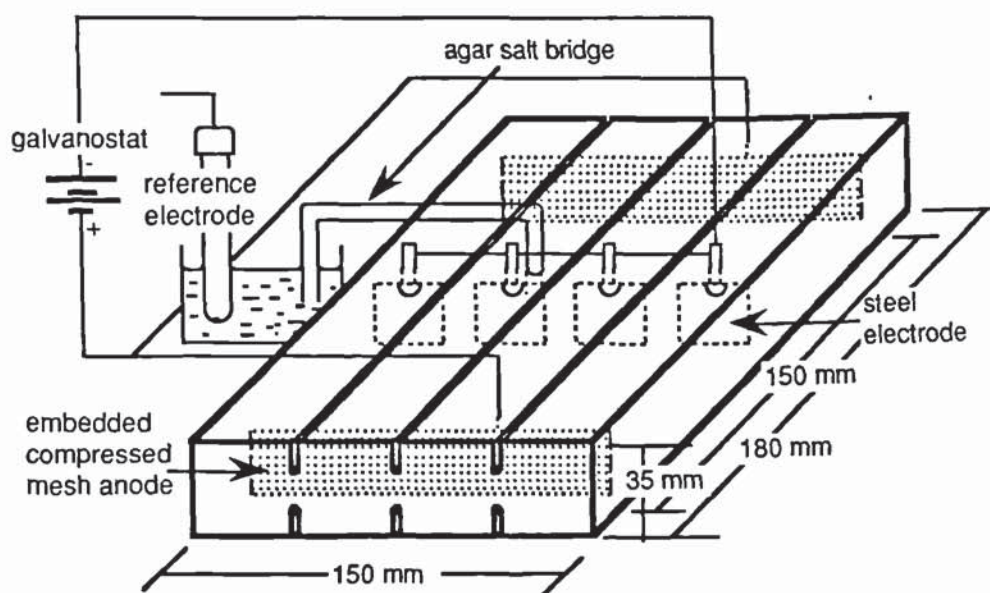


Figure 5.2 Mesh anode HCP prism connected to the galvanostat

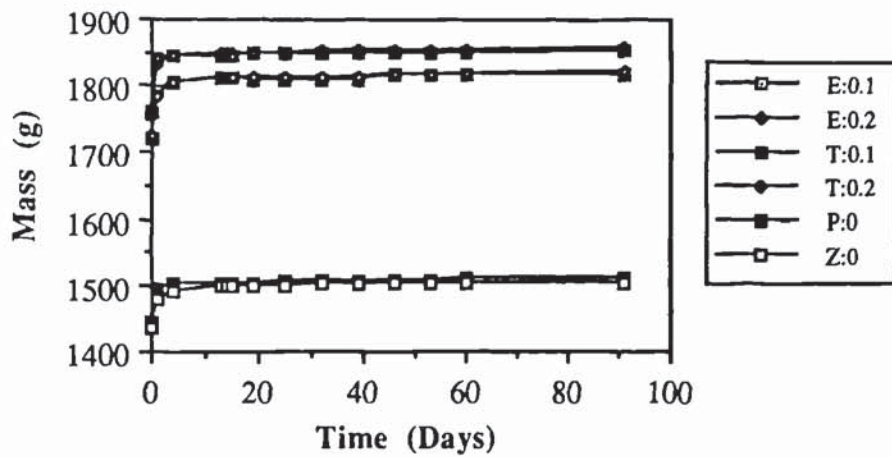


Figure 5.3 Re-saturation weight gains for control cement paste prisms.

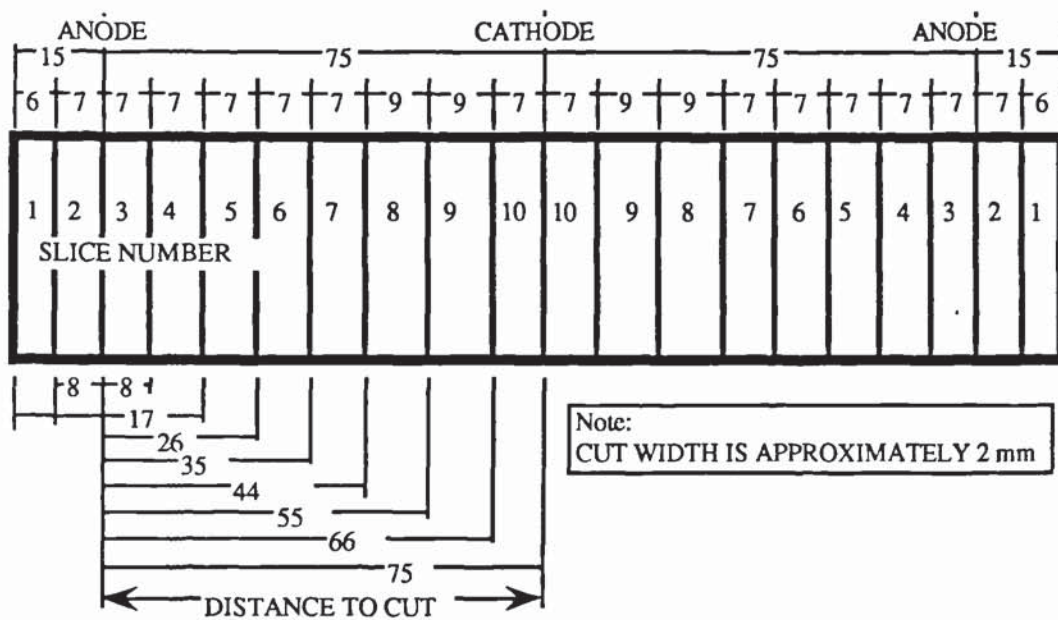


Figure 5.4 Cement paste prism sectioning detail.

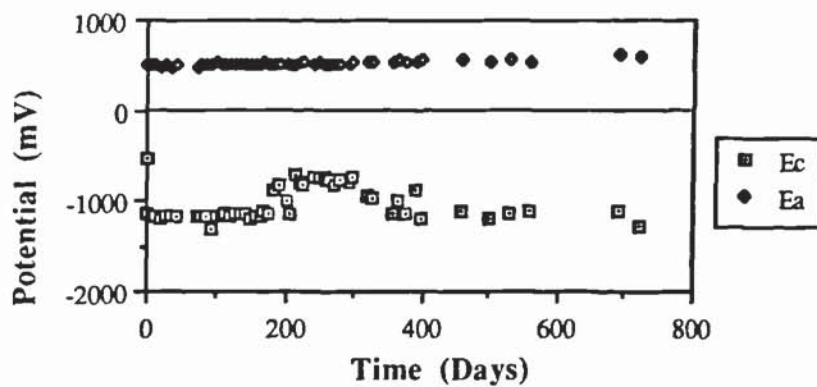


Figure 5.5 Variation of potential / time for specimen T:50a.



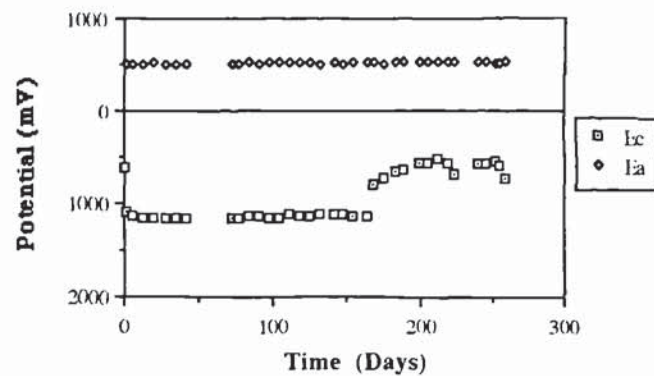


Figure 5.6 Variation of potential/time for specimen T:50b

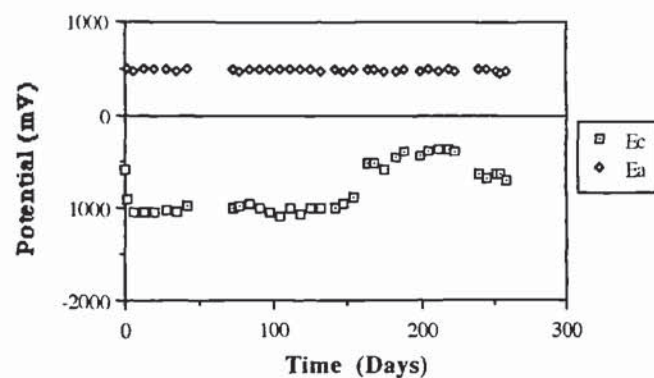


Figure 5.7 Variation of potential time for specimen T:20

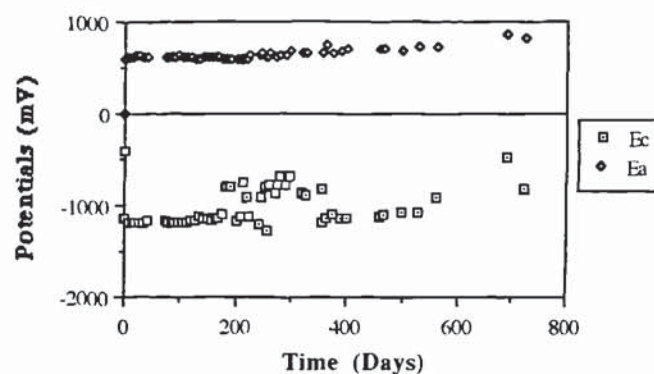


Figure 5.8 Variation of potential time for specimen E:50a

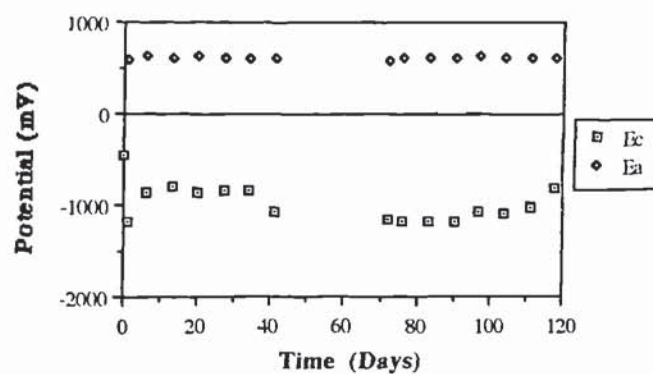


Figure 5.9 Variation of potential/time for specimen E:50b

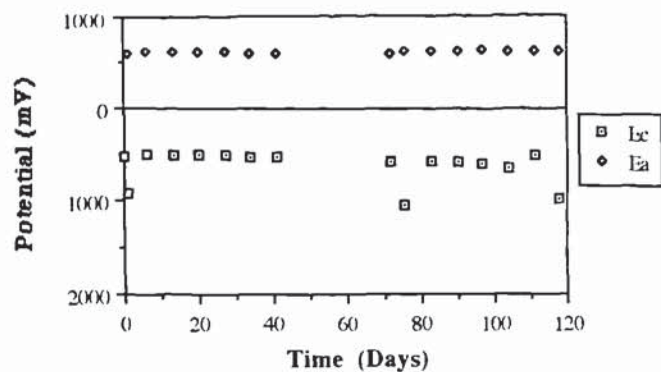


Figure 5.10 Variation of potential/time for specimen E:20

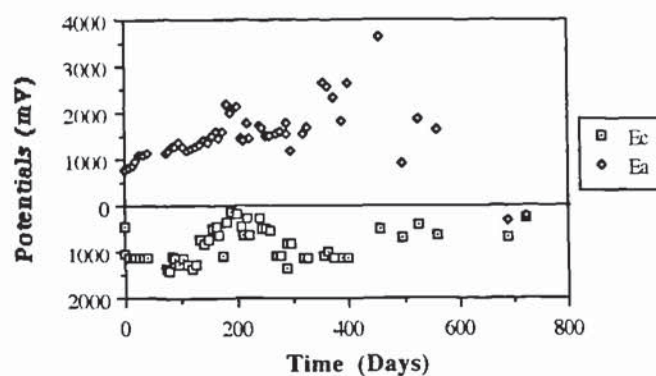


Figure 5.11 Variation of potential time for specimen P:50a

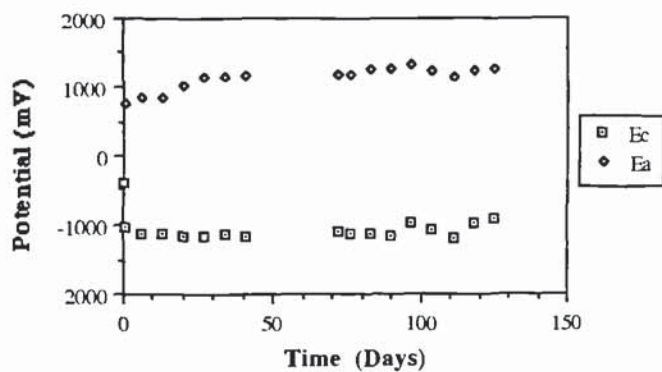


Figure 5.12 Variation of potential/time for specimen P:50b

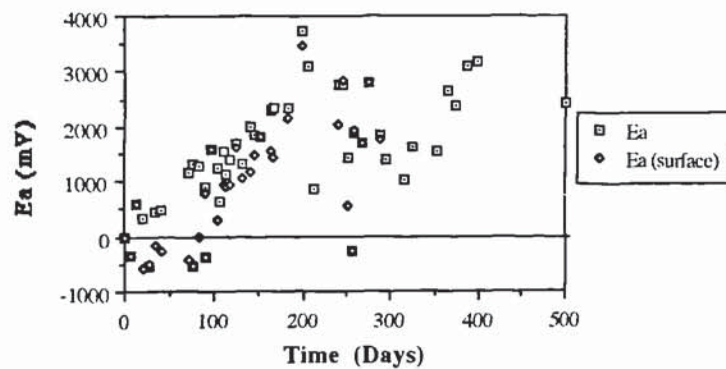
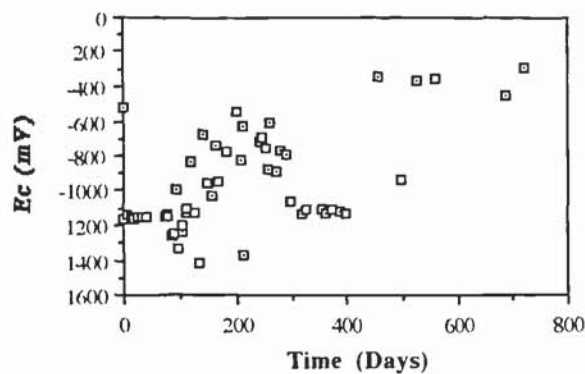
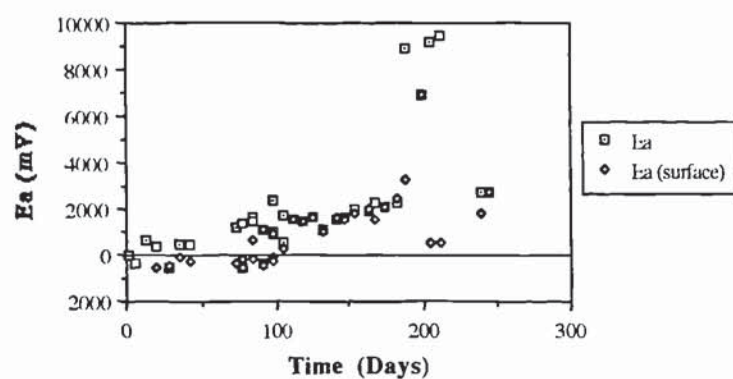


Figure 5.13 Variation of anode potential/time for specimen Z:50a





**Figure 5.14** Variation of cathode potential/time for specimen Z:50a



**Figure 5.15** Variation of anode potential/time for specimen Z:50b

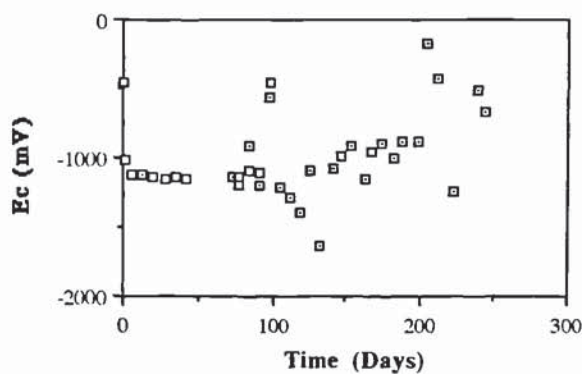


**Figure 5.16** Variation of cathode potential time for specimen Z:50b

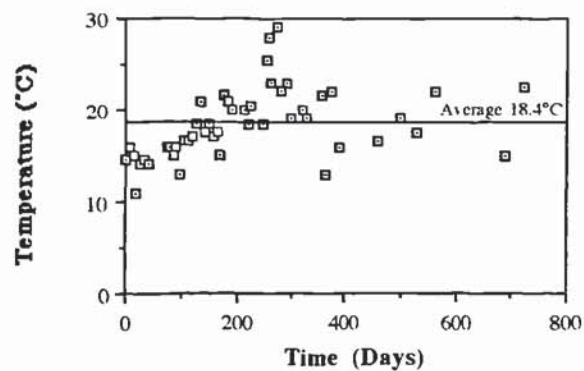


**Figure 5.17** Variation of laboratory temperature/time during the paste block trial

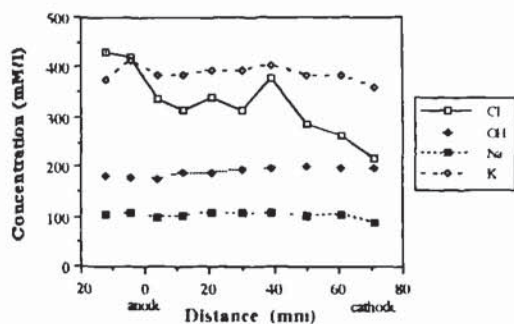


Figure 5.18 Na, K, Cl and OH concentration profiles for specimen T.20

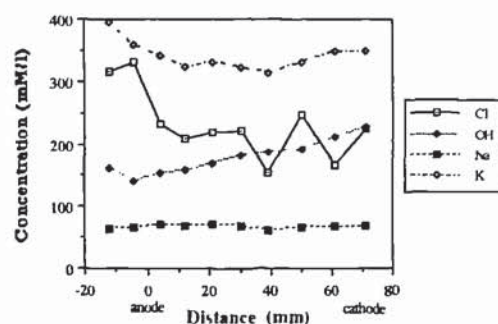


Figure 5.21 Na, K, Cl and OH concentration profiles for specimen T.50b

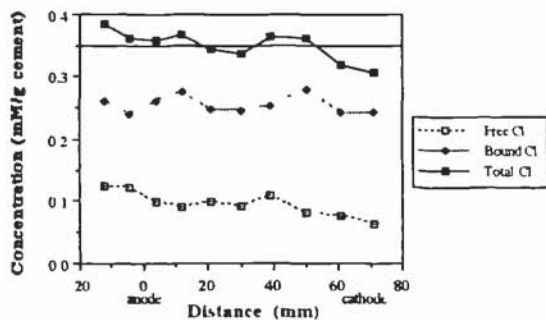


Figure 5.19 Chloride ion concentration for specimen T.20

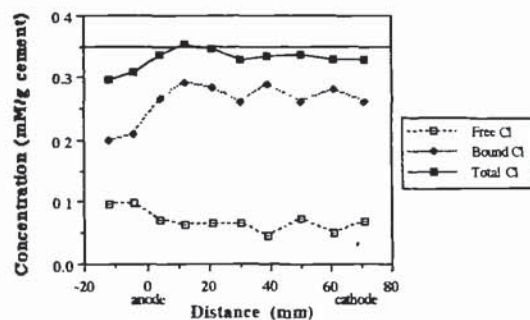


Figure 5.22 Chloride ion concentration for specimen T.50b

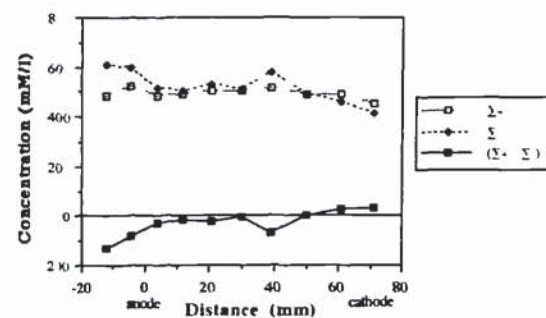


Figure 5.20 Summation of positive negative ion profiles for specimen T.20

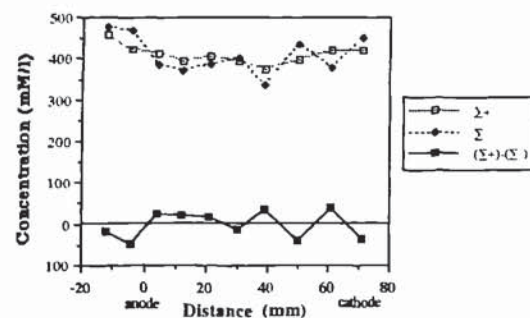


Figure 5.23 Summation of positive negative ion profiles for specimen T.50b



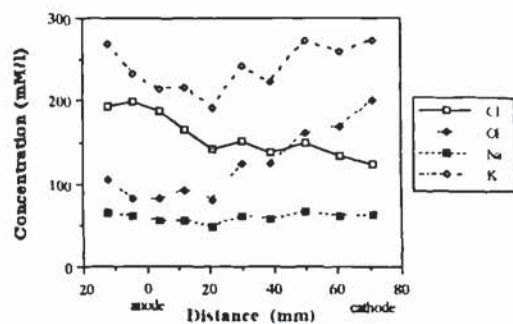


Figure 5.24 Na, K, Cl and OH concentration profiles for specimen T 50a

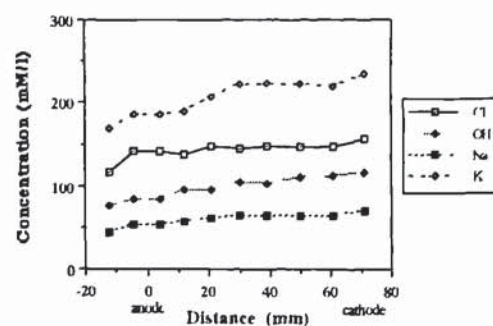


Figure 5.27 Na, K, Cl and OH concentration profiles for specimen T 0

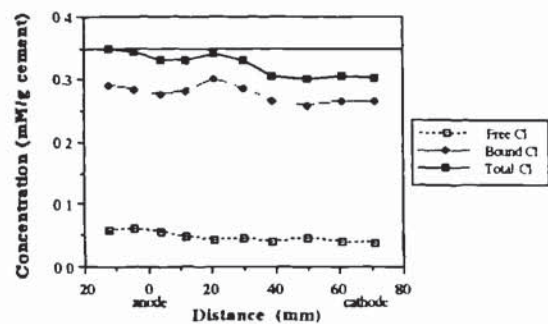


Figure 5.25 Chloride ion concentration for specimen T 50a

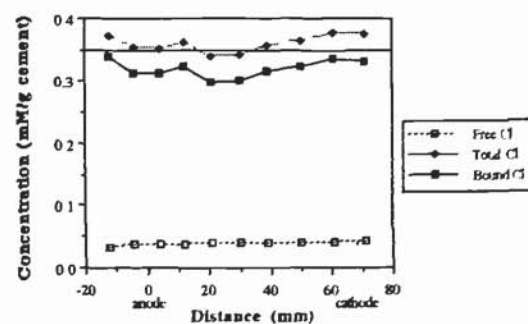


Figure 5.28 Chloride ion concentration for specimen T 0

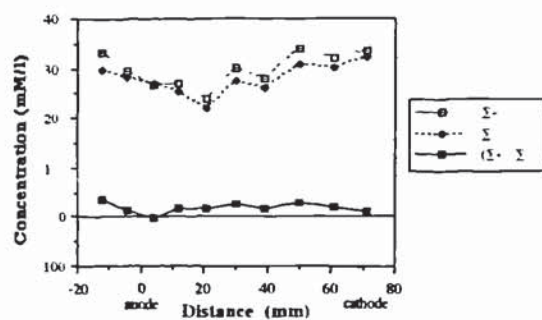


Figure 5.26 Summation of positive negative ion profiles for specimen T 50a

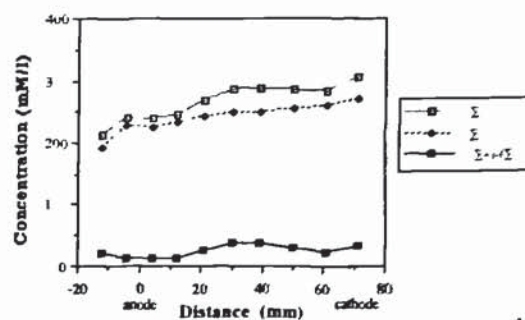


Figure 5.29 Summation of positive negative ion profiles for specimen T 0

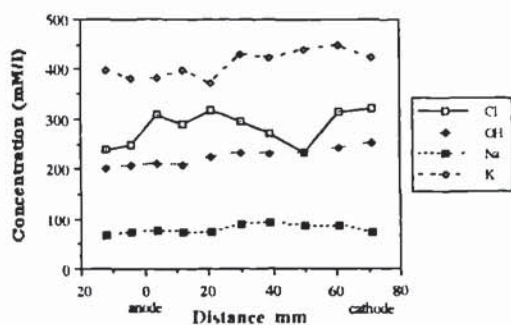


Figure 5.30 Na, K, Cl and OH concentration profiles for specimen E 20

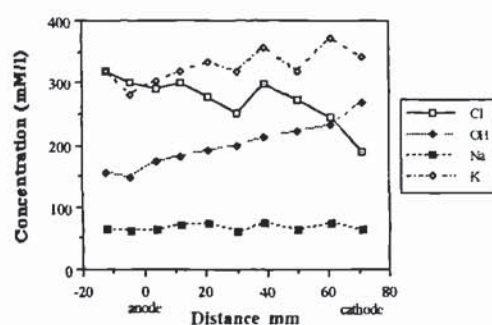


Figure 5.33 Na, K, Cl and OH concentration profiles for specimen E 50b

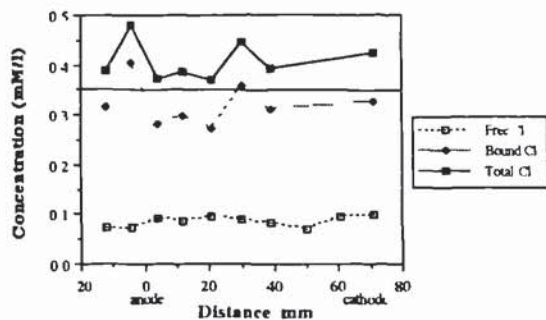


Figure 5.31 Chloride ion concentration for specimen E 20

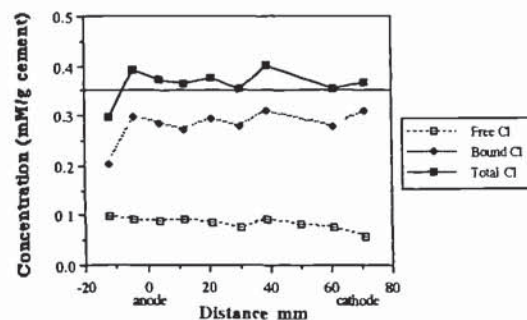


Figure 5.34 Chloride ion concentration for specimen E 50b

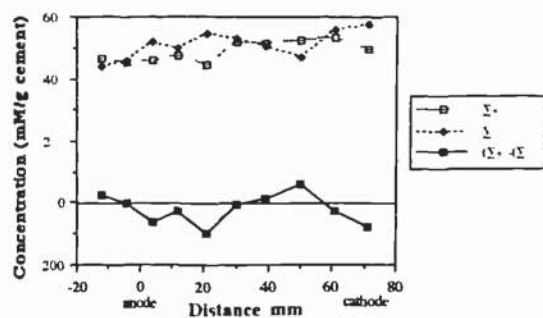


Figure 5.32 Summation of positive/negative ion profiles for specimen E 20

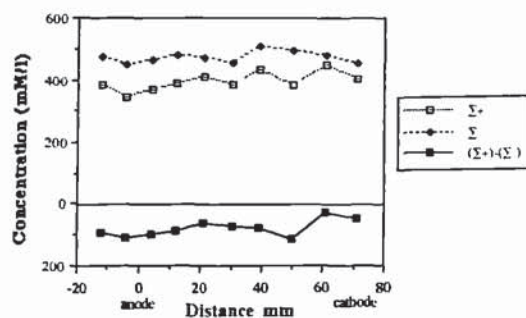


Figure 5.35 Summation of positive/negative ion profiles for specimen E 50b



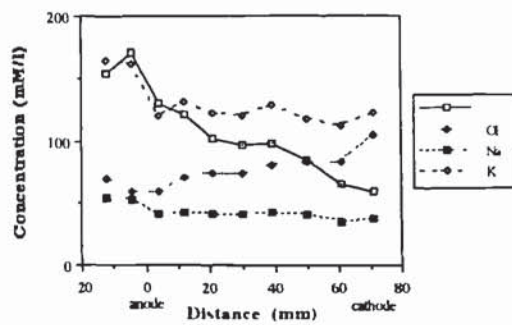


Figure 5.36 Na, K, Cl and OH concentration profiles for specimen E-50a

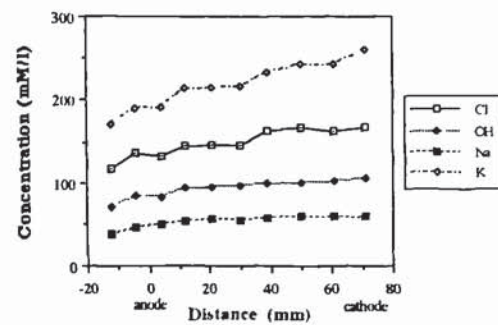


Figure 5.39 Na, K, Cl and OH concentration profiles for specimen E-0

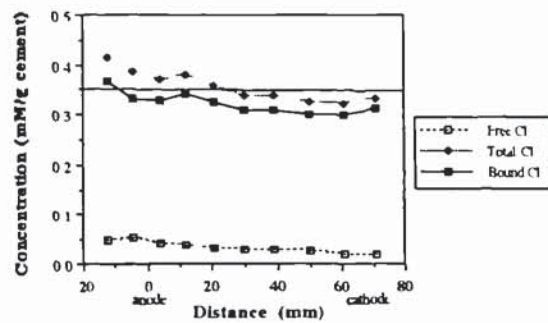


Figure 5.37 Chloride ion concentration for specimen E-50a

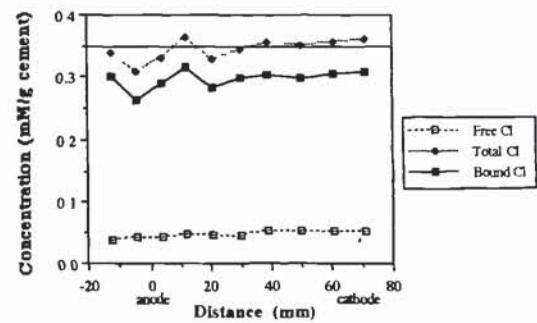


Figure 5.40 Chloride ion concentration for specimen E-0

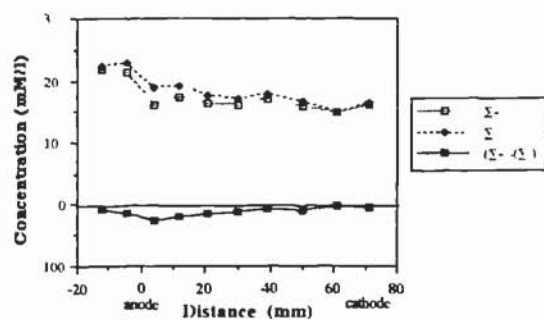


Figure 5.38 Summation of positive negative ion profiles for specimen E-50a

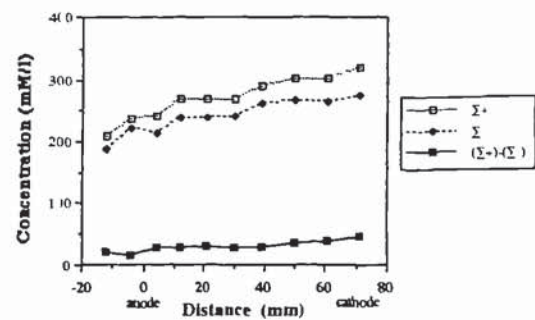


Figure 5.41 Summation of positive negative ion profiles for specimen E-0

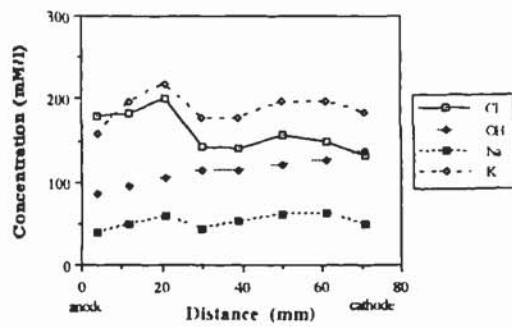


Figure 5.42 Na, K, Cl and OH concentration profiles for specimen P-50b

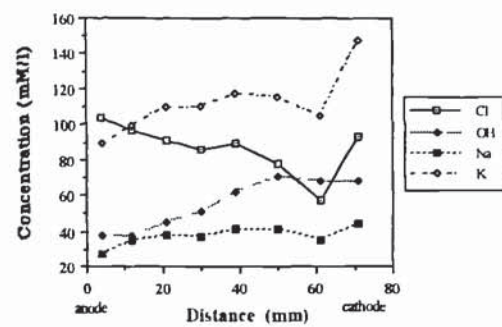


Figure 5.45 Na, K, Cl and OH concentration profiles for specimen P-50a

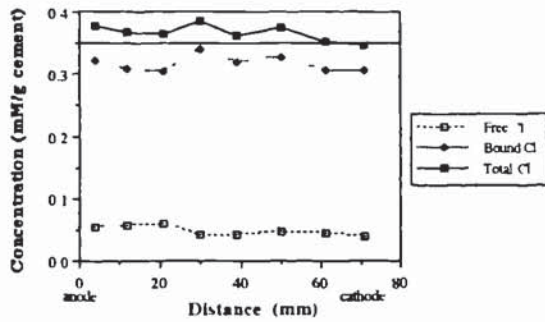


Figure 5.43 Chloride ion concentration for specimen P-50b

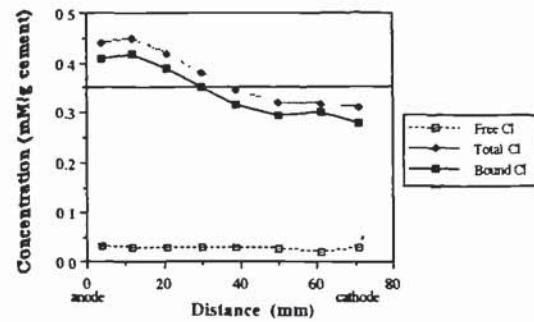


Figure 5.46 Chloride ion concentration for specimen P-50a

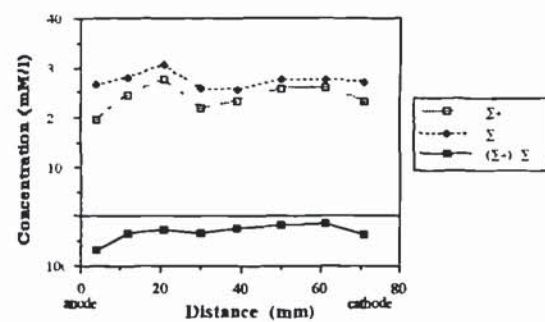


Figure 5.44 Summation of positive negative ion profiles for specimen P-50b

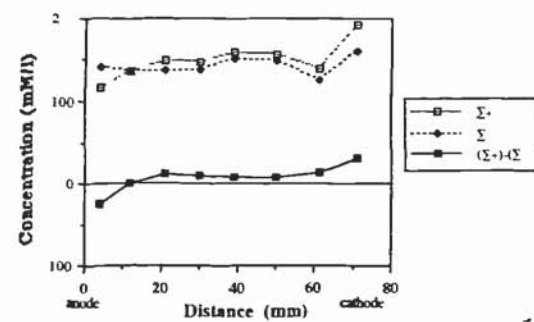


Figure 5.47 Summation of positive negative ion profiles for specimen P-50a



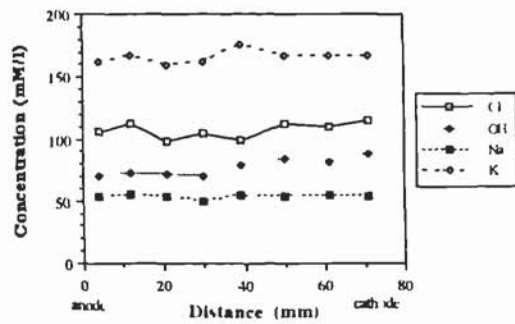


Figure 5.48 Na, K, Cl and OH concentration profiles for specimen P-0

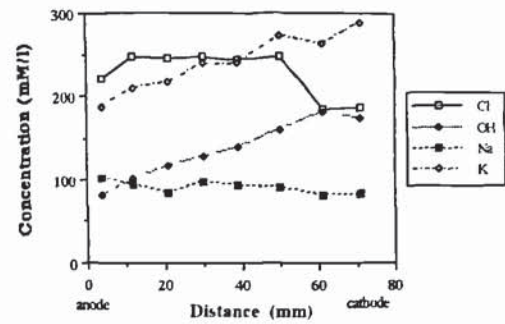


Figure 5.51 Na, K, Cl and OH concentration profiles for specimen Z-50b

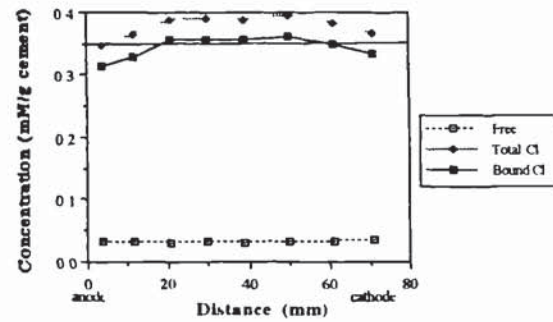


Figure 5.49 Chloride ion concentration for specimen P-0

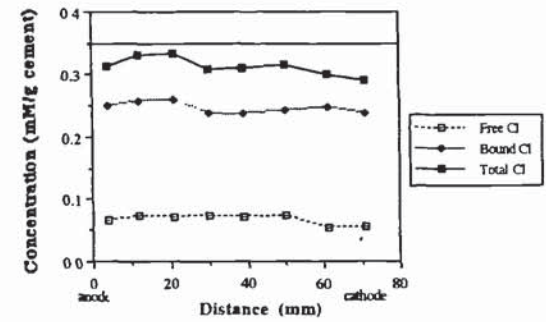


Figure 5.52 Chloride ion concentration for specimen Z-50b

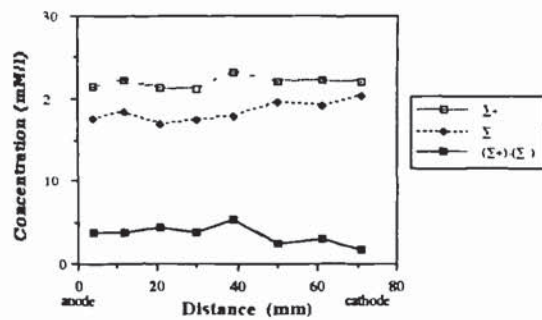


Figure 5.50 Summation of positive negative ion profiles for specimen P-0

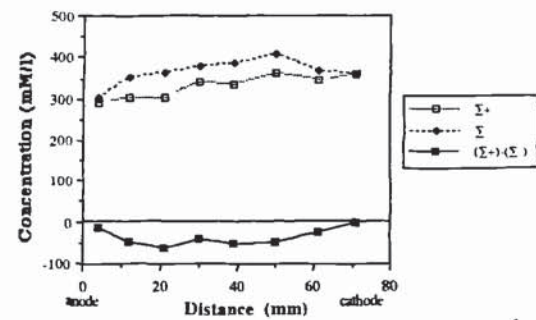


Figure 5.53 Summation of positive negative ion profiles for specimen Z-50b

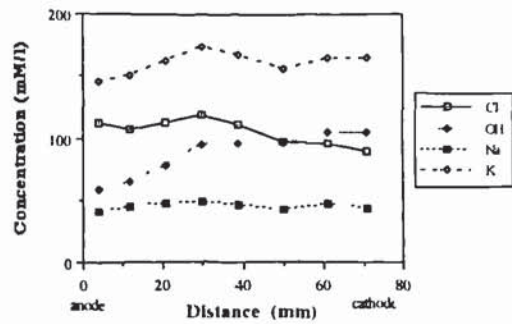


Figure 5.54 Na, K, Cl and OH concentration profiles for specimen Z 50a

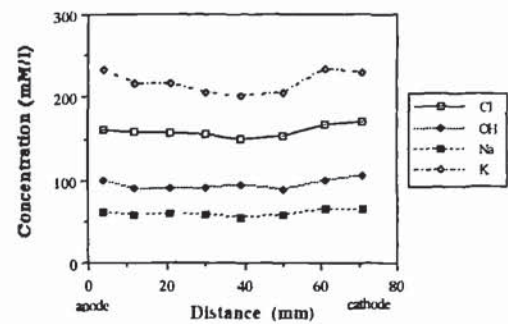


Figure 5.57 Na, K, Cl and OH concentration profiles for specimen Z:0

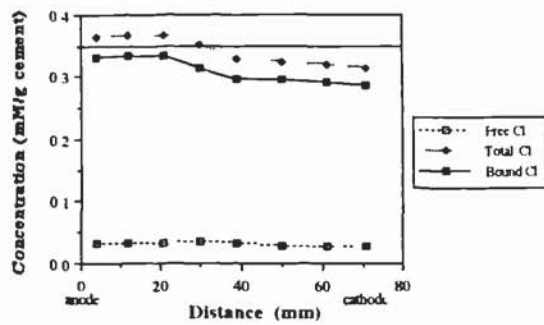


Figure 5.55 Chloride ion concentration for specimen Z 50a

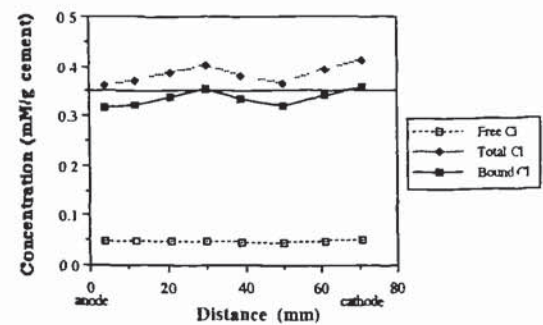


Figure 5.58 Chloride ion concentration for specimen Z:0

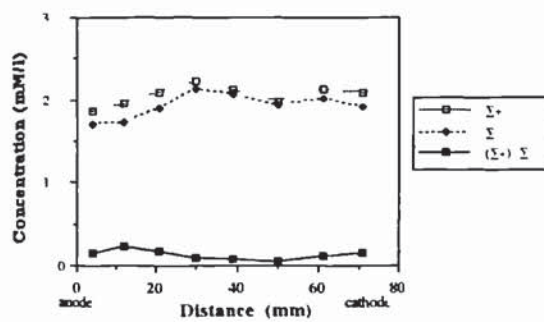


Figure 5.56 Summation of positive negative ion profiles for specimen Z 50a

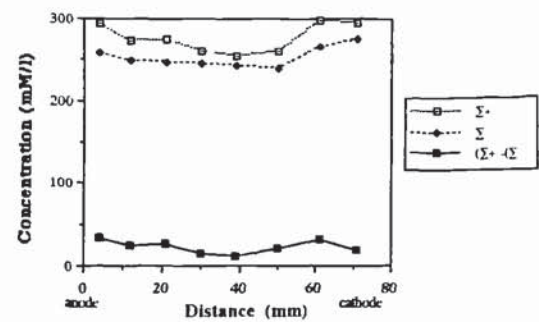


Figure 5.59 Summation of positive negative ion profiles for specimen Z:0

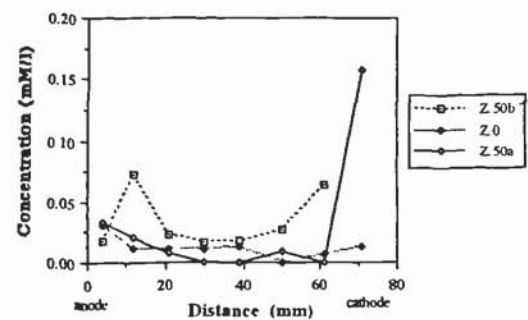


Figure 5.60 Zinc ion concentration for Z anode specimens



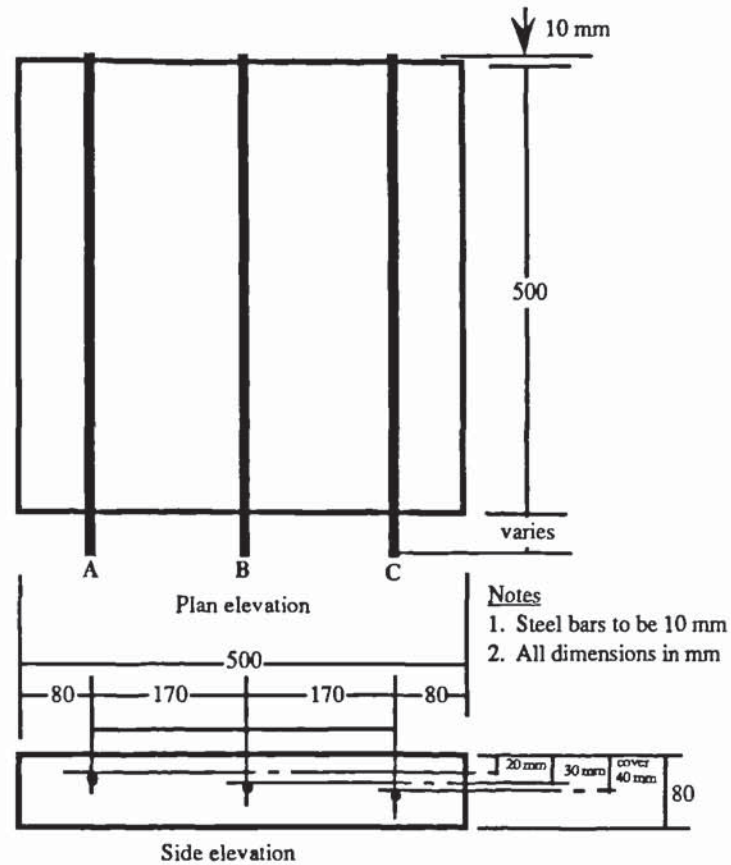


Figure 6.1 Sketch of CP trial concrete slab.

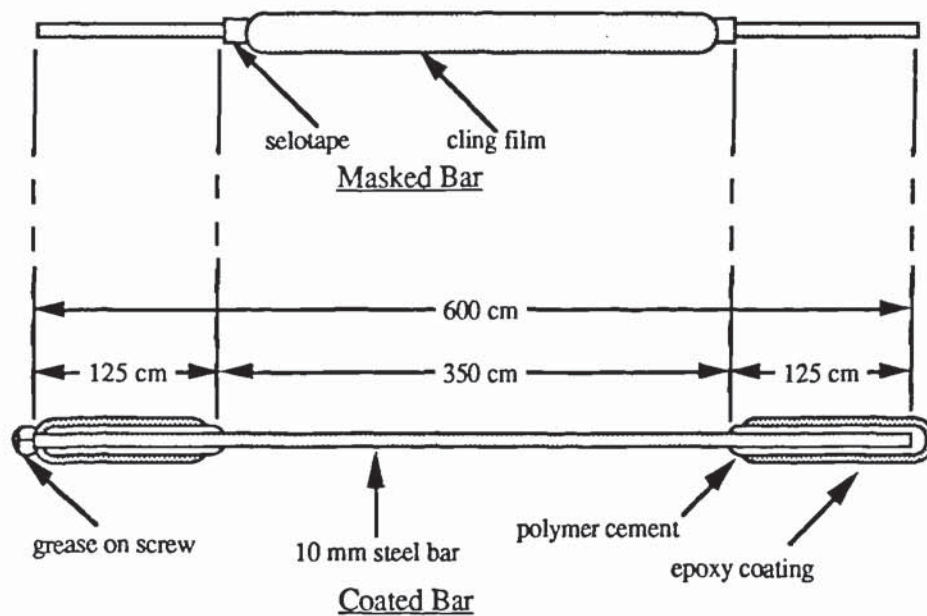


Figure 6.2 Steel reinforcement bar preparation.

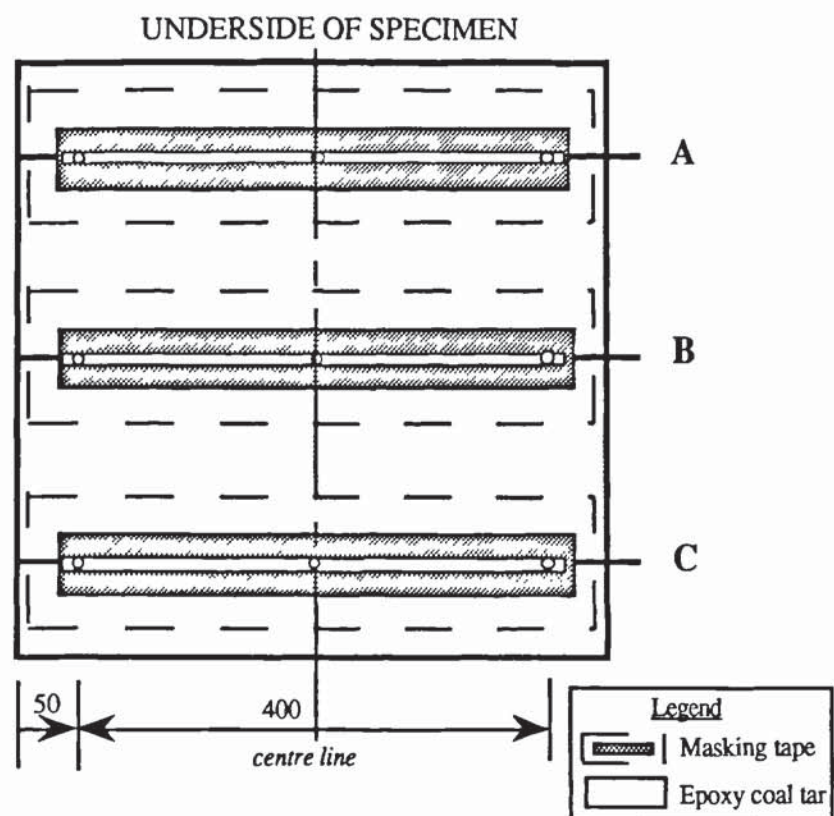


Figure 6.3 Location of half cell measurement positions.



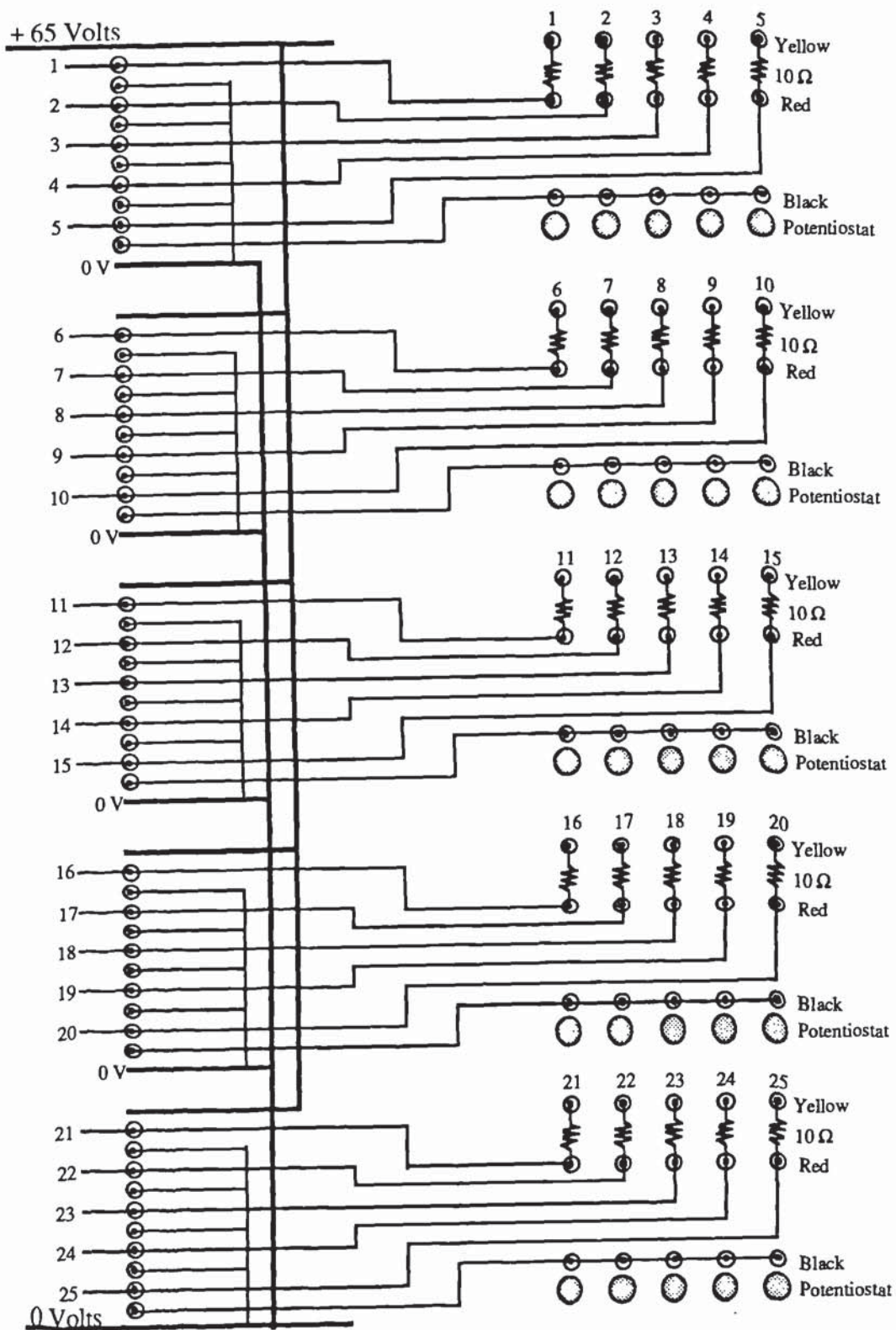


Figure 6.4 Circuit diagram of 3 terminal, variable constant current source.

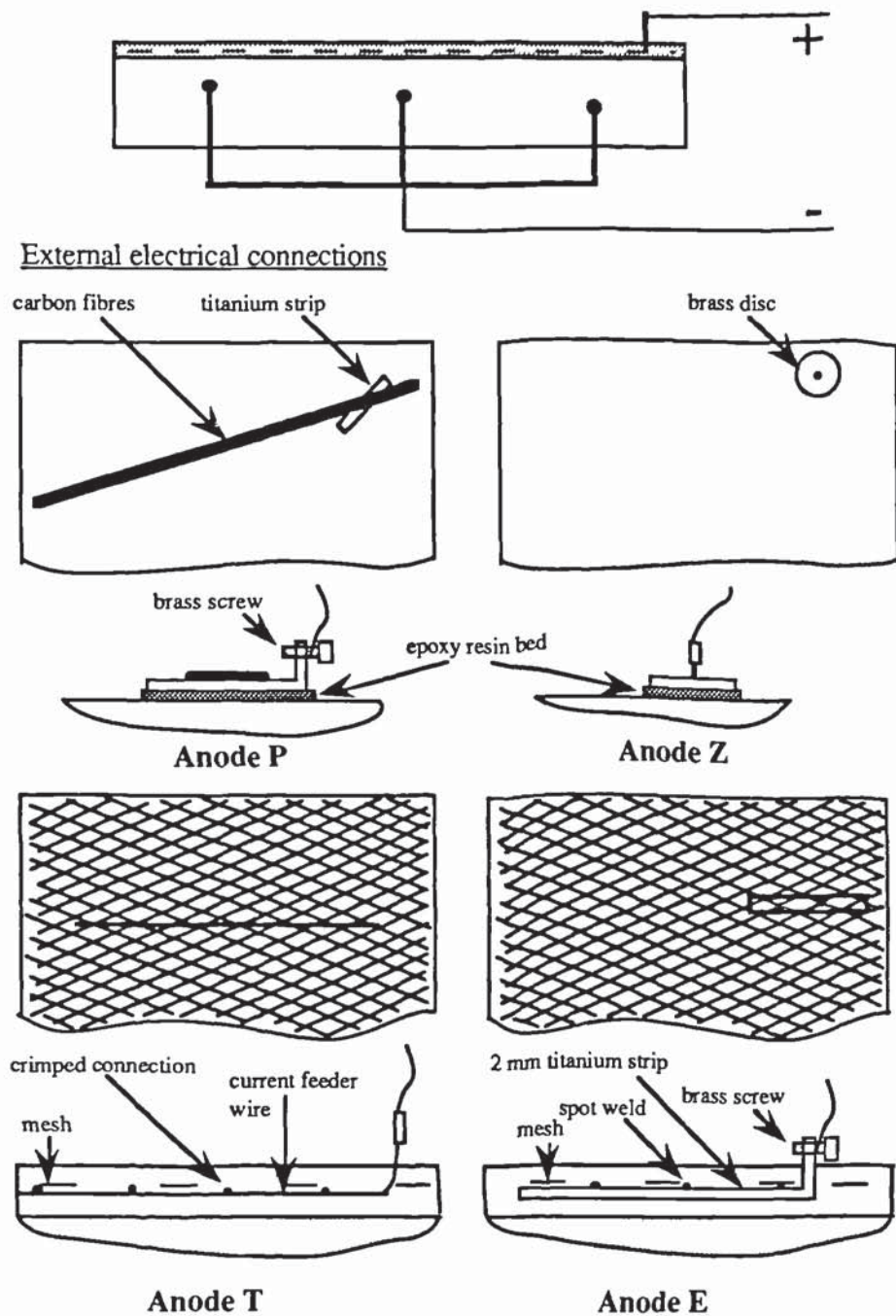


Figure 6.5 Sketches of primary anodes and external electrical connections.



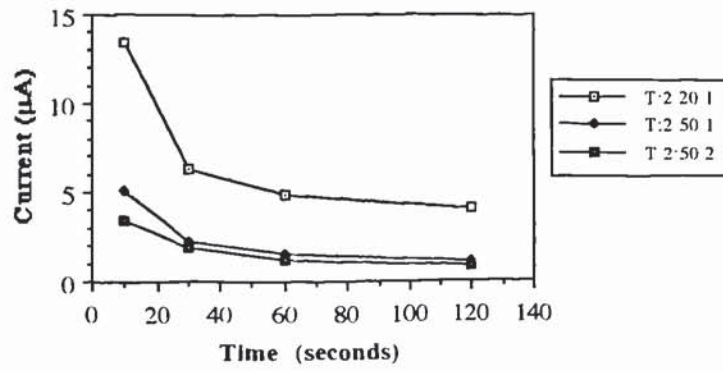


Figure 6.6 Linear polarisation decay curves for anode T specimens

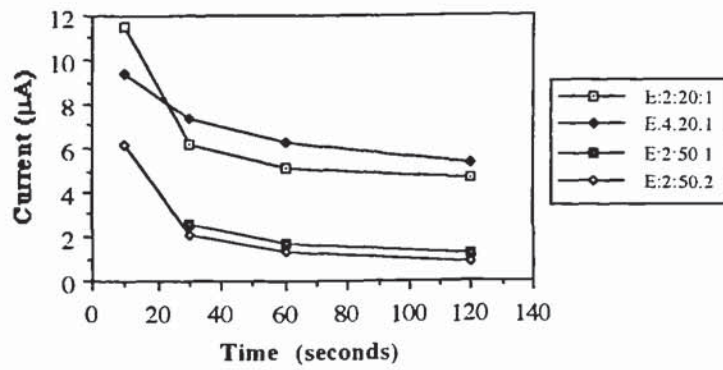


Figure 6.7 Linear polarisation decay curves for anode E specimens

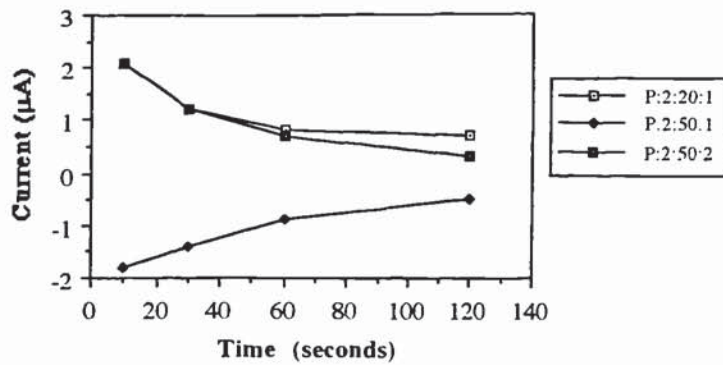


Figure 6.8 Linear polarisation decay curves for anode P specimens

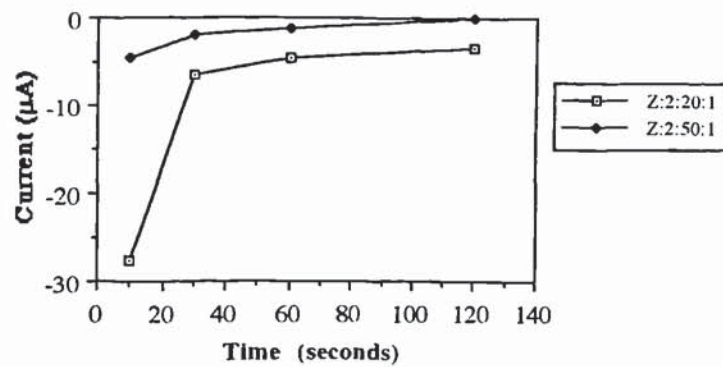


Figure 6.9 Linear polarisation decay curves for anode Z specimens

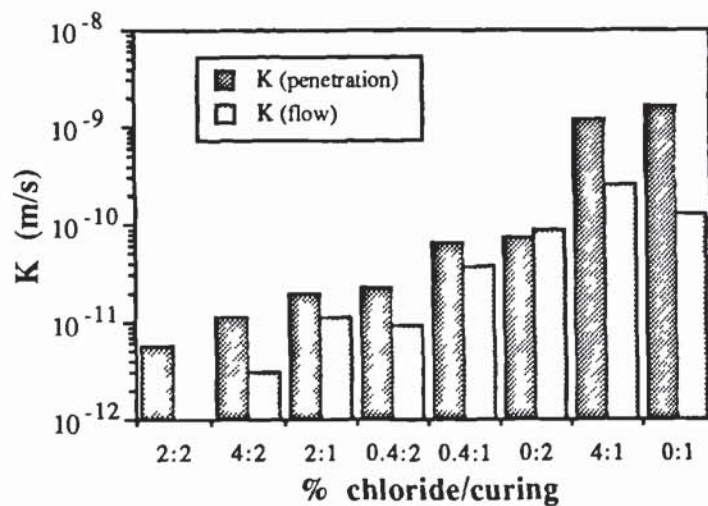


Figure 6.10 Permeability coefficients vs. % chloride content: specimen curing.

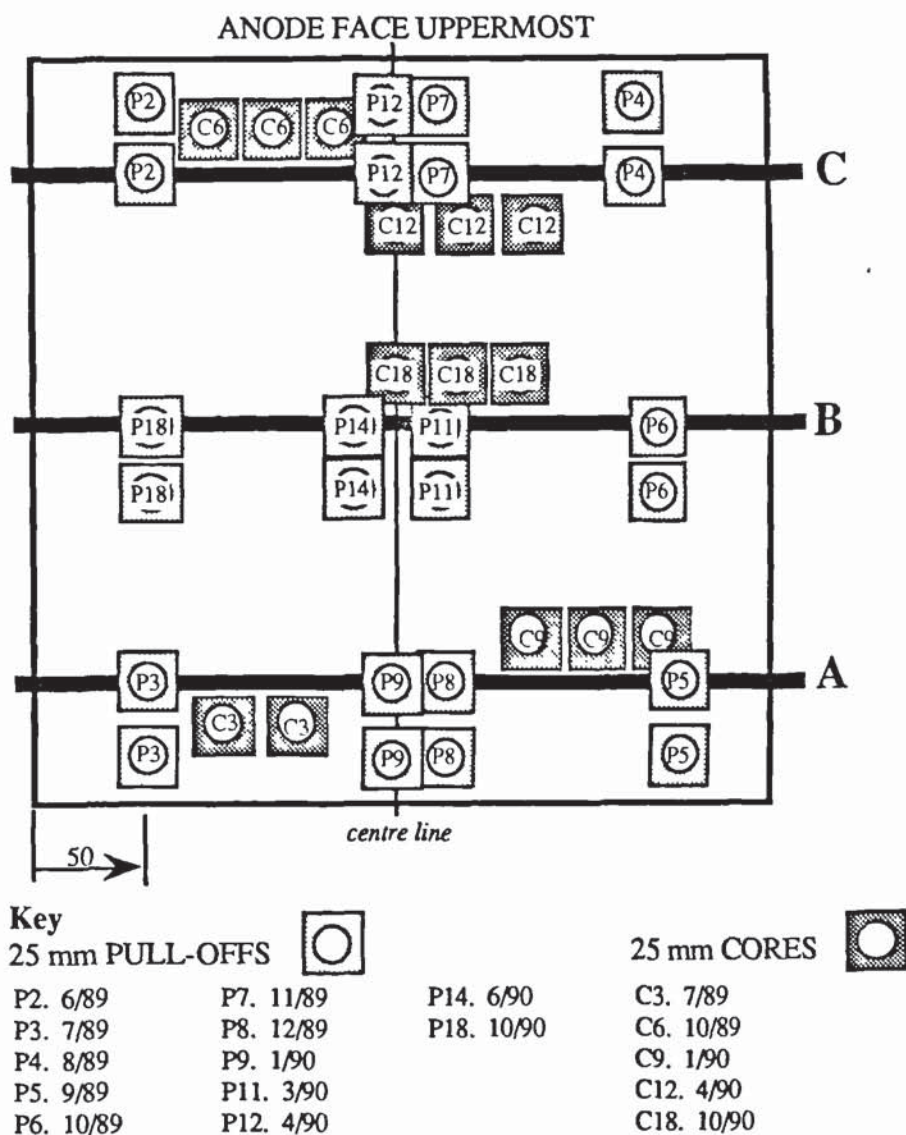
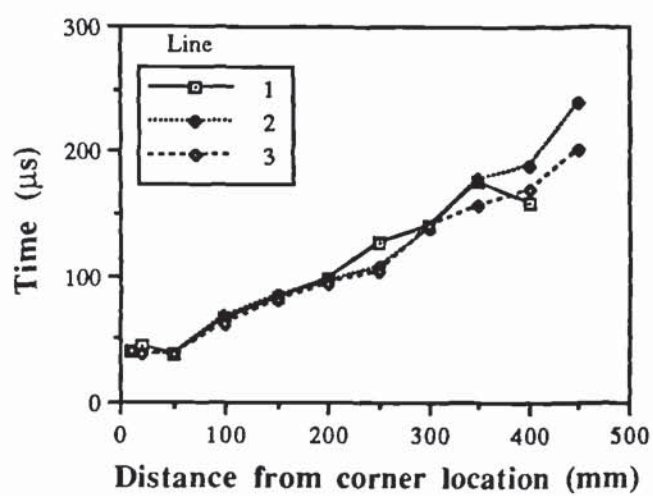
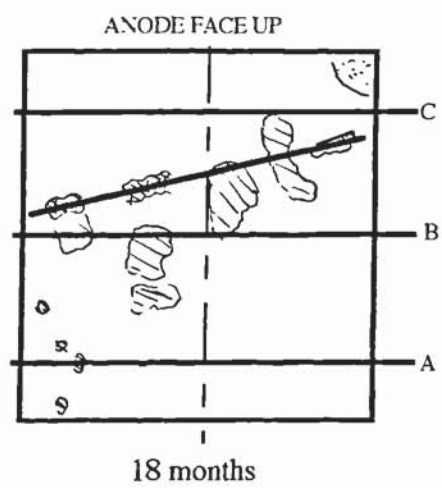
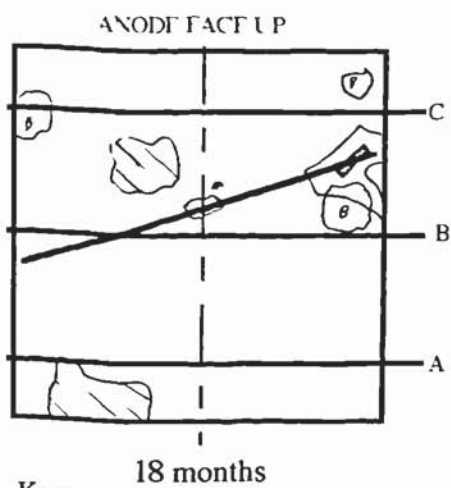
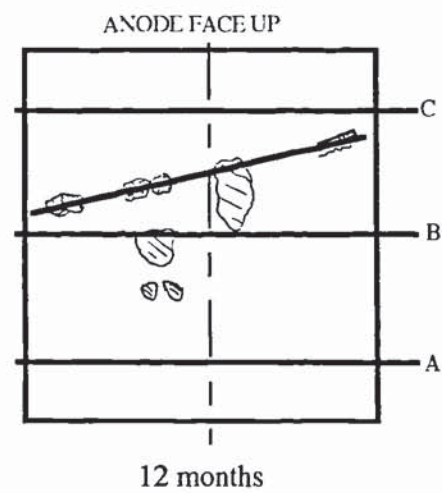
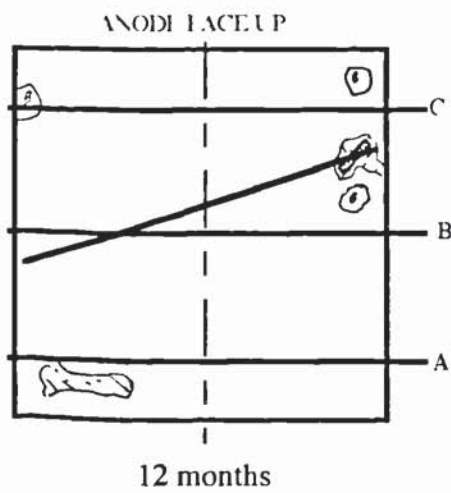
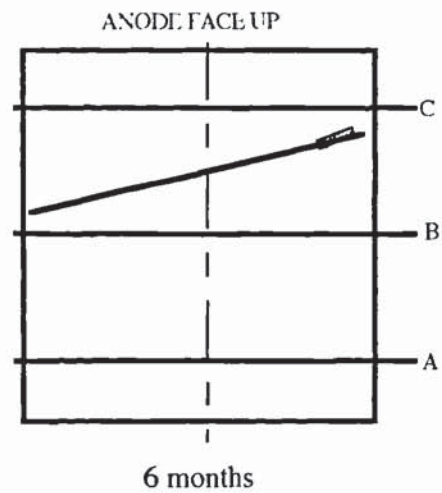
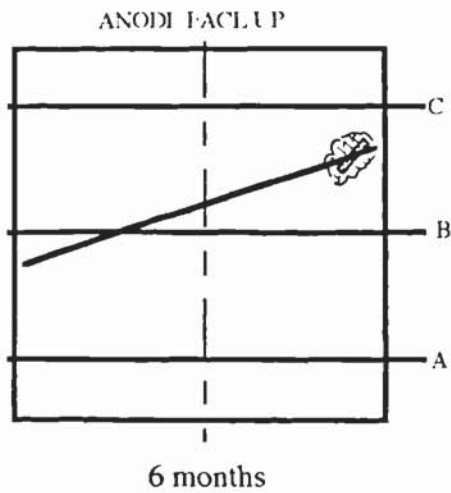


Figure 6.11 Location of on-going cores/ coating pull-offs





**Figure 6.12** Plot of time for ultra-sound pulse to travel through specimen E:2:50:1 against increasing distance from a corner location

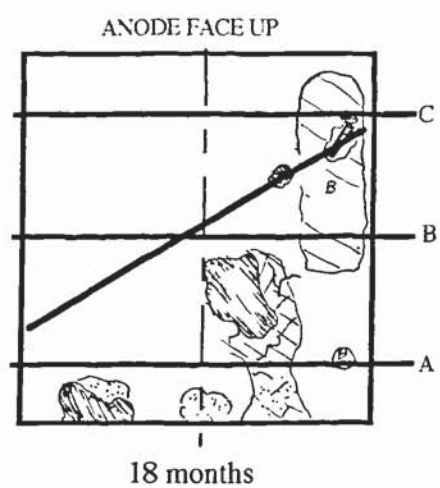
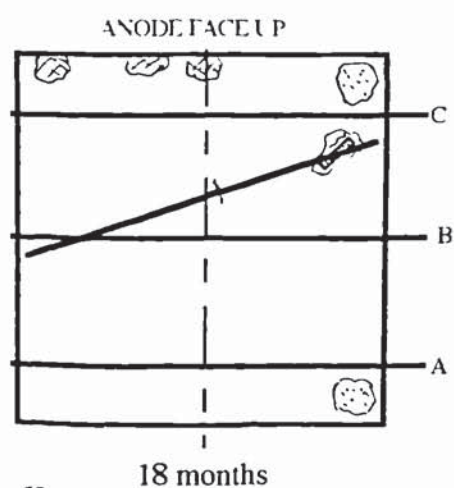
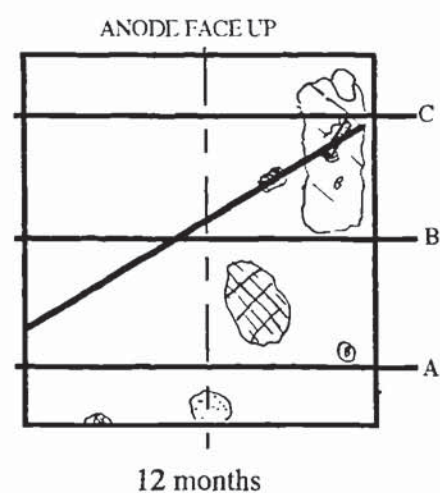
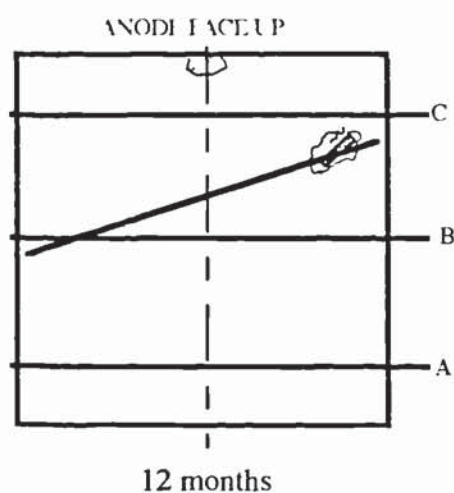
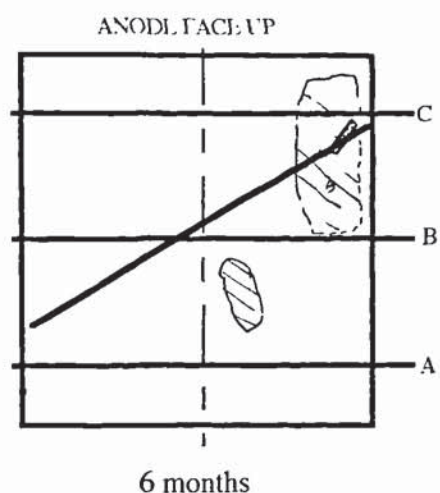
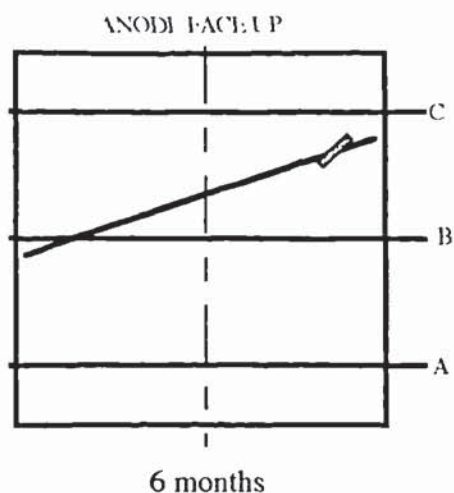


<b>Key</b>			
Bubble		Bleached area	
Crack		Micro-bubbling	
		Blistering/blackening	
		Total paste loss	

**Figure 6.13** Surface visual inspection 6 month summary: Specimen P:2:20:1

**Figure 6.14** Surface visual inspection 6 month summary: Specimen P:0.4:20:1



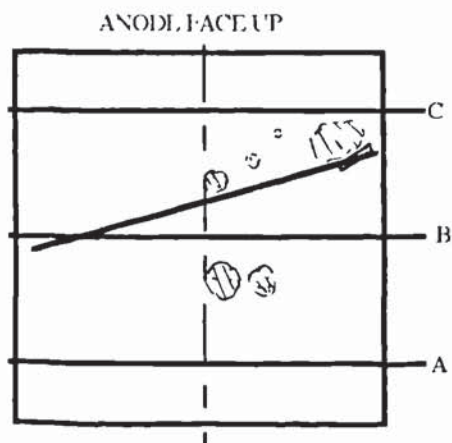


Key

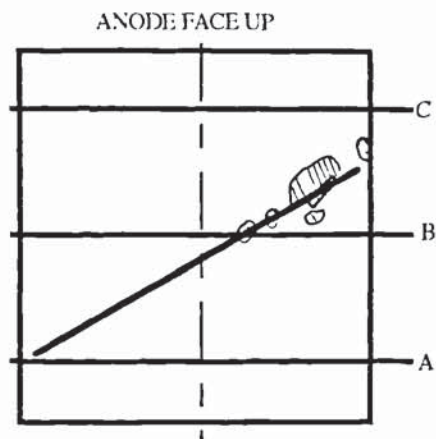
Bubble		Bleached area		Blistering/blackening	
Crack		Micro-bubbling		Total paste loss	

**Figure 6.15** Surface visual inspection 6 month summary: Specimen P:0.4:20:2

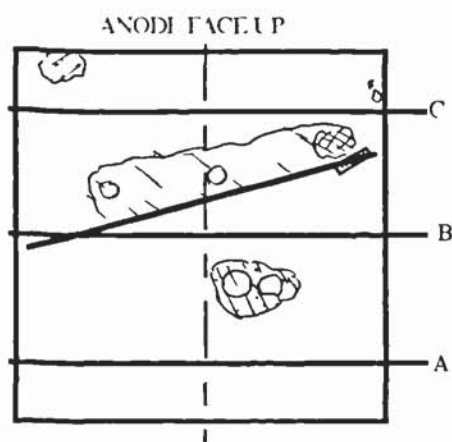
**Figure 6.16** Surface visual inspection 6 month summary: Specimen P:2:50:1



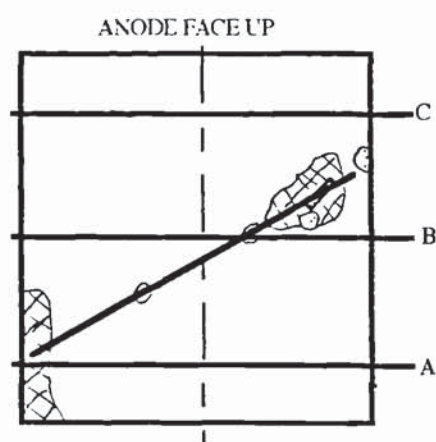
6 months



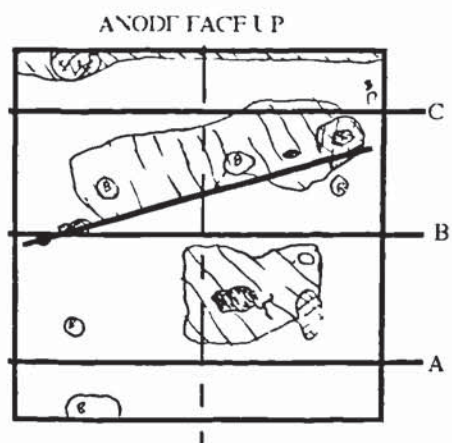
6 months



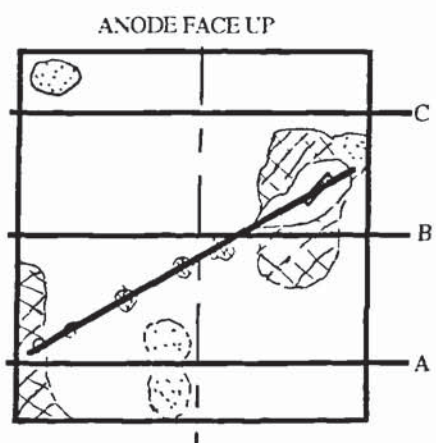
12 months



12 months



18 months



18 months

Key

Bubble		Bleached area		Blistering/blackening	
Crack		Micro-bubbling		Total paste loss	

**Figure 6.17** Surface visual inspection 6 month summary: Specimen P:2:50:2

**Figure 6.16** Surface visual inspection 6 month summary: Specimen P:0.4:50:1



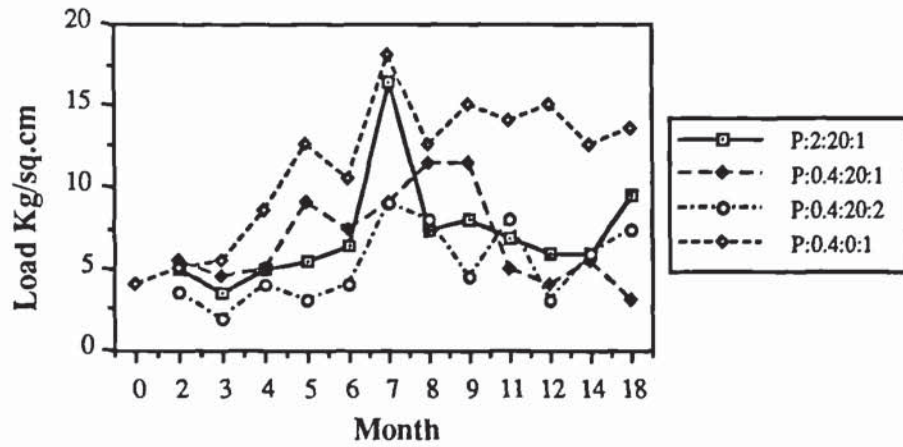


Figure 6.19 Plot of pull-off loads/time for Anode P (20 mA/m<sup>2</sup>) specimens

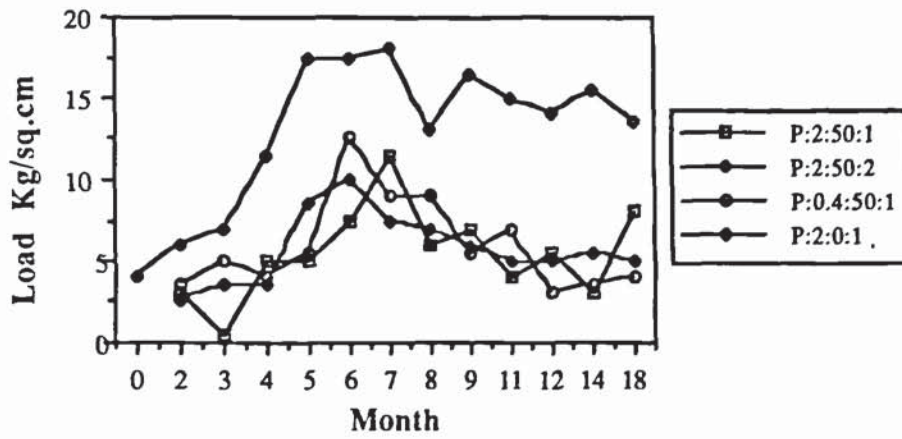
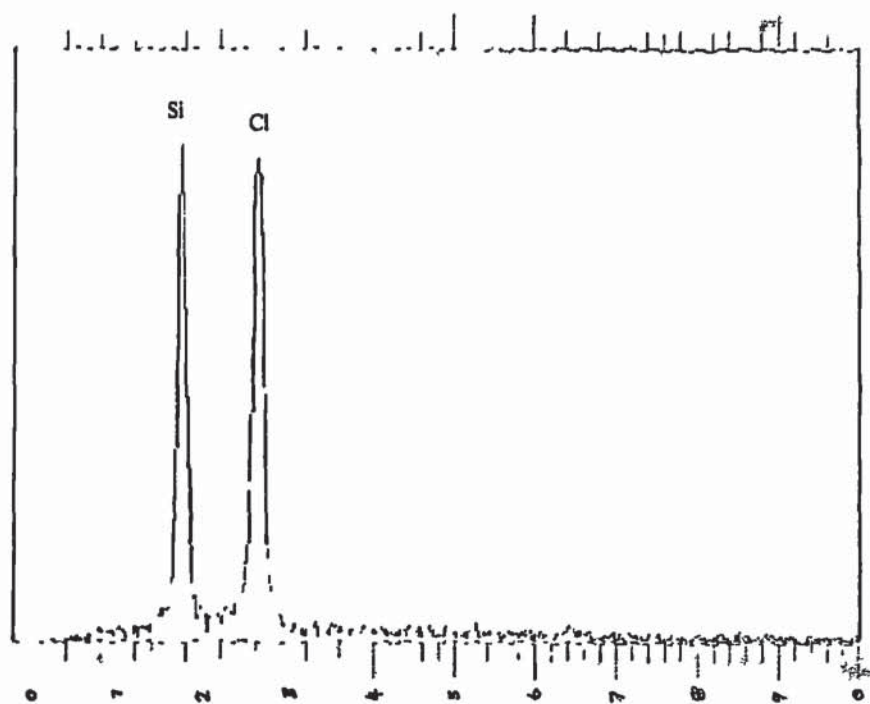
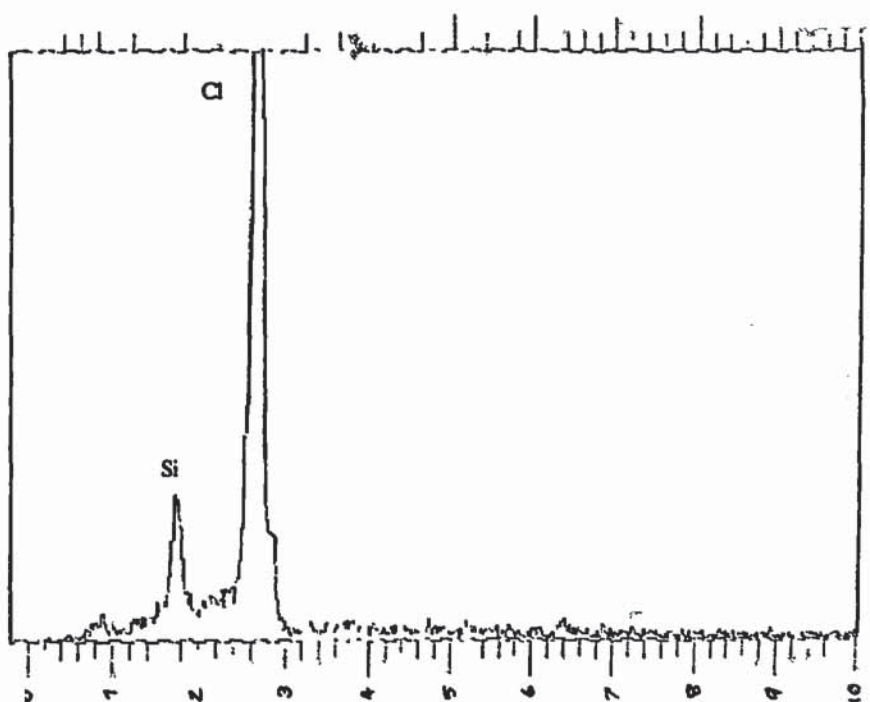


Figure 6.20 Plot of pull-off loads/time for Anode P (50 mA/m<sup>2</sup>) specimens



**Figure 6.21** EDXA elemental plot: Specimen P:2:50:1, 9 months, acidified paste adhering to debonded coating.



**Figure 6.22** EDXA elemental plot: Specimen P:2:50:1, 9 months, acidified paint surface.



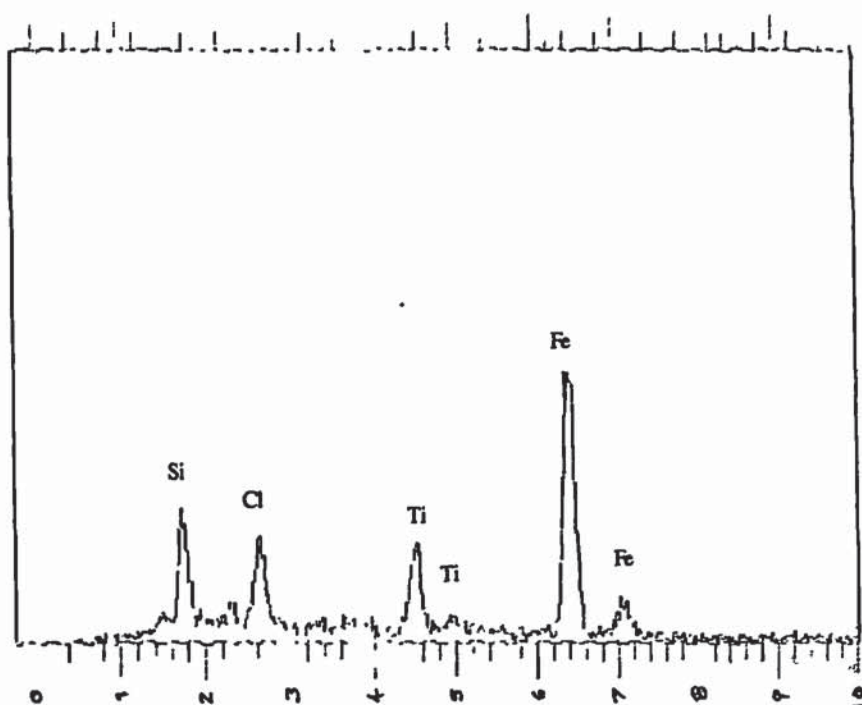


Figure 6.23 EDXA elemental plot: Rust spot on top-coat surface, anode P.

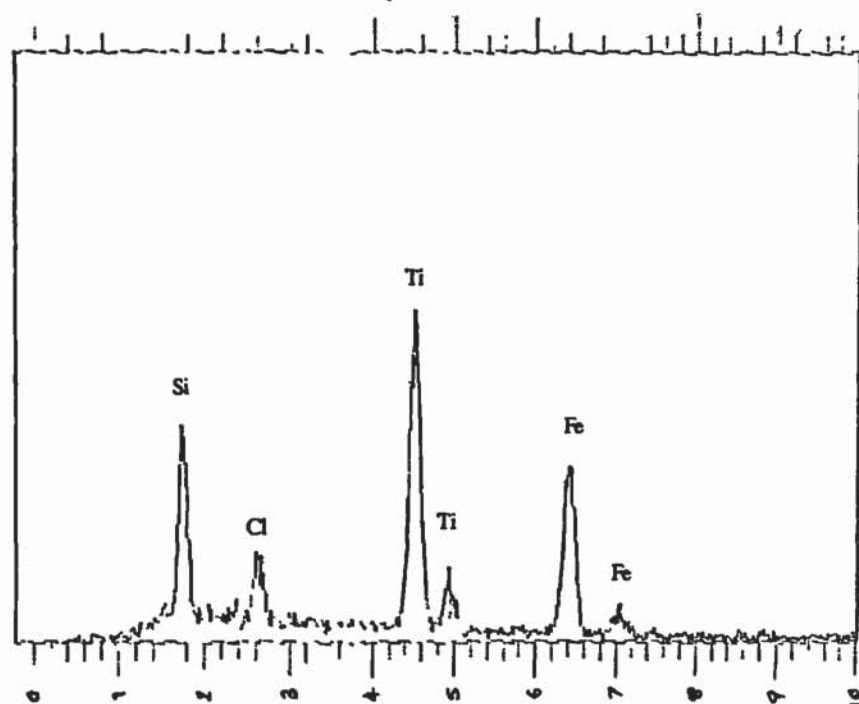


Figure 6.24 EDXA elemental plot: White top-coat surface, anode P.

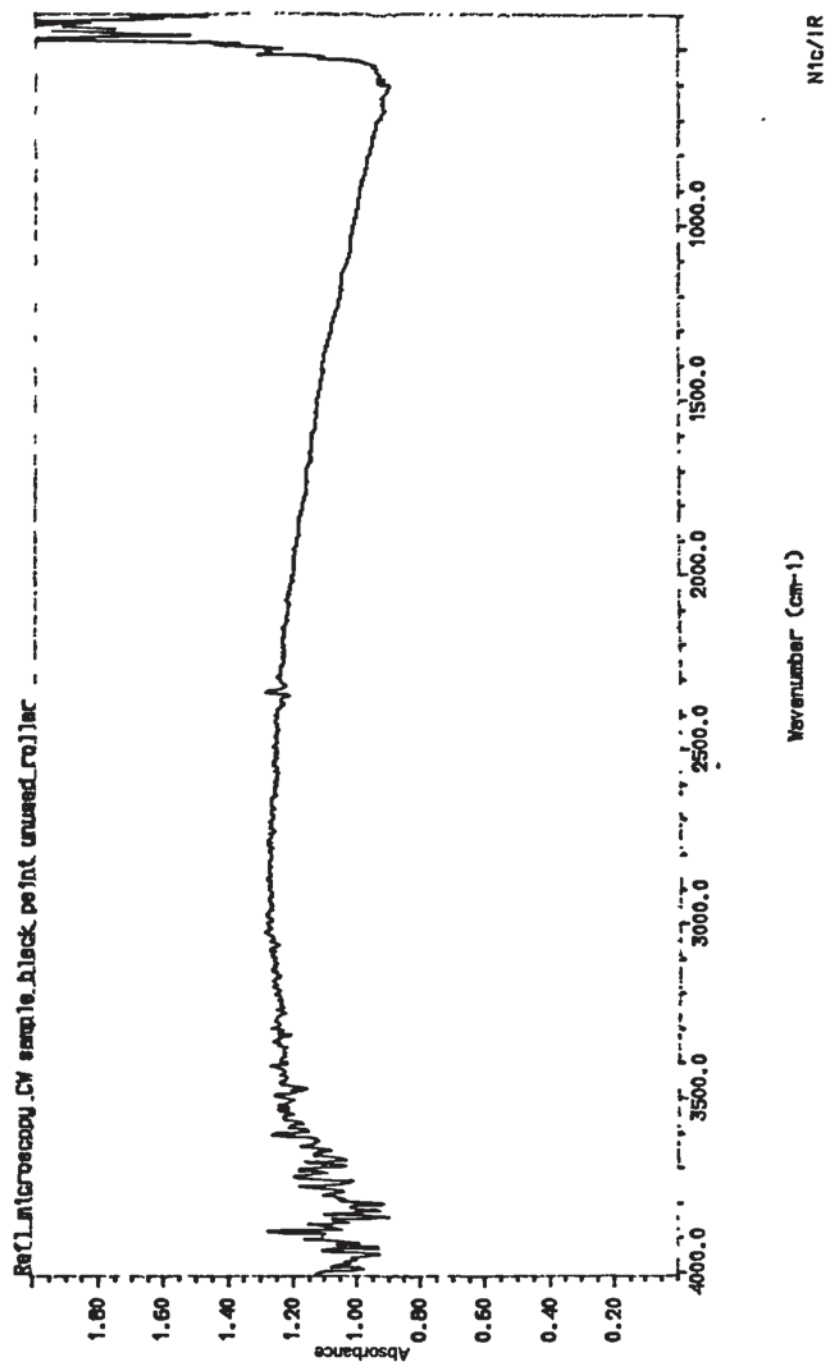
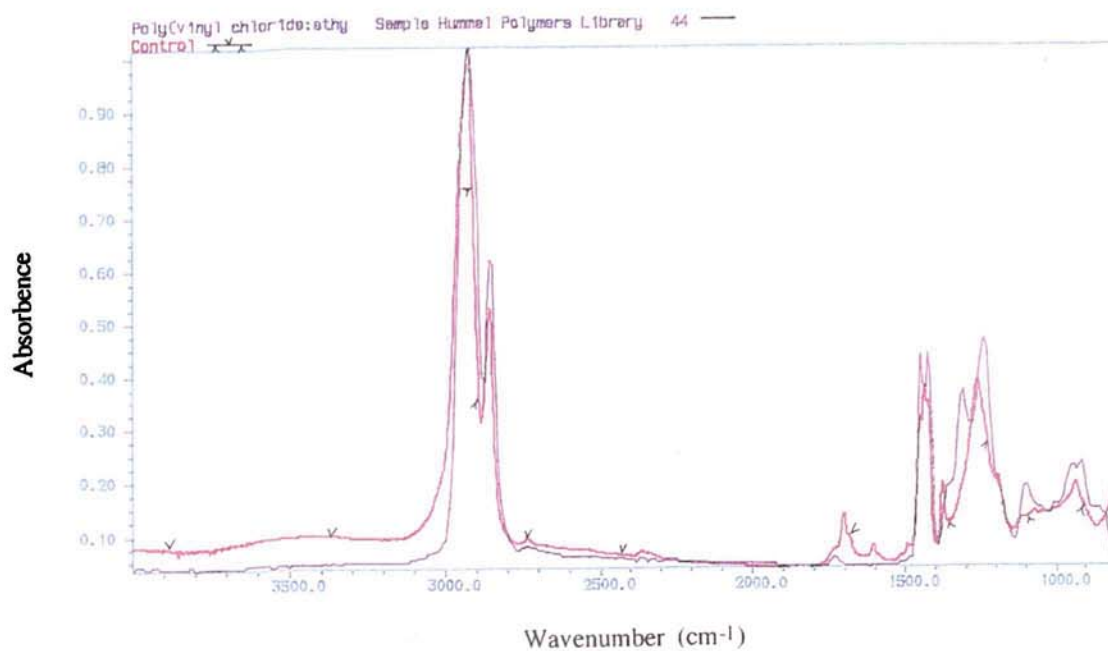


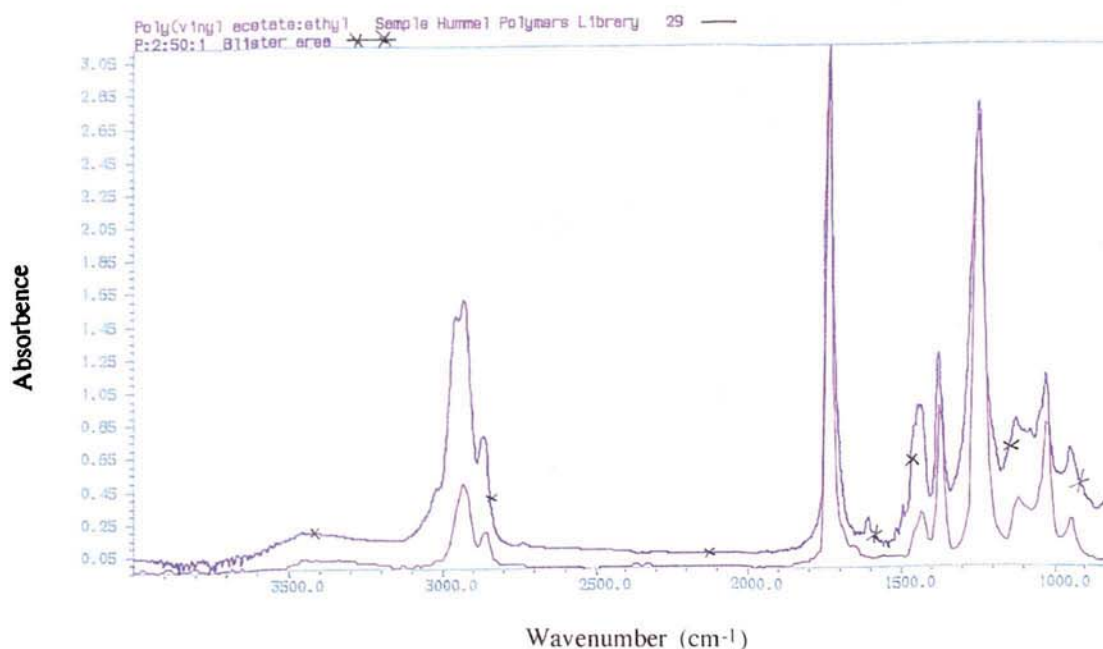
Figure 6.25 FT-IR spectra (reflectance mode): Anode P control sample from microscope slide. Central spike represents carbon dioxide.





N1c/IR

**Figure 6.26** FT-IR spectra (identification): Anode P control sample from painted microscope slide/Poly vinyl chloride:ethylene.



N1c/IR

**Figure 6.27** FT-IR spectra (identification): Specimen P:2:50:1(9 months) highly degraded blister area/Poly vinyl acetate:ethylene.

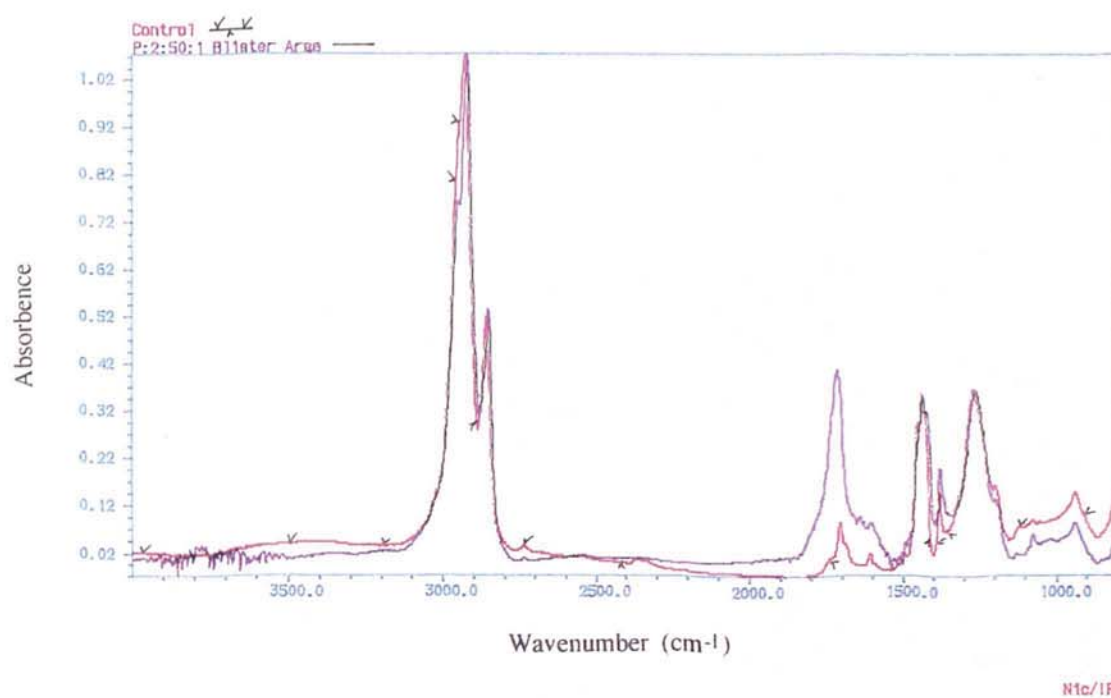


**Figure 6.28** FT-IR spectra: Comparison of Specimen P:2:50:1(9 months) blister area to control sample.

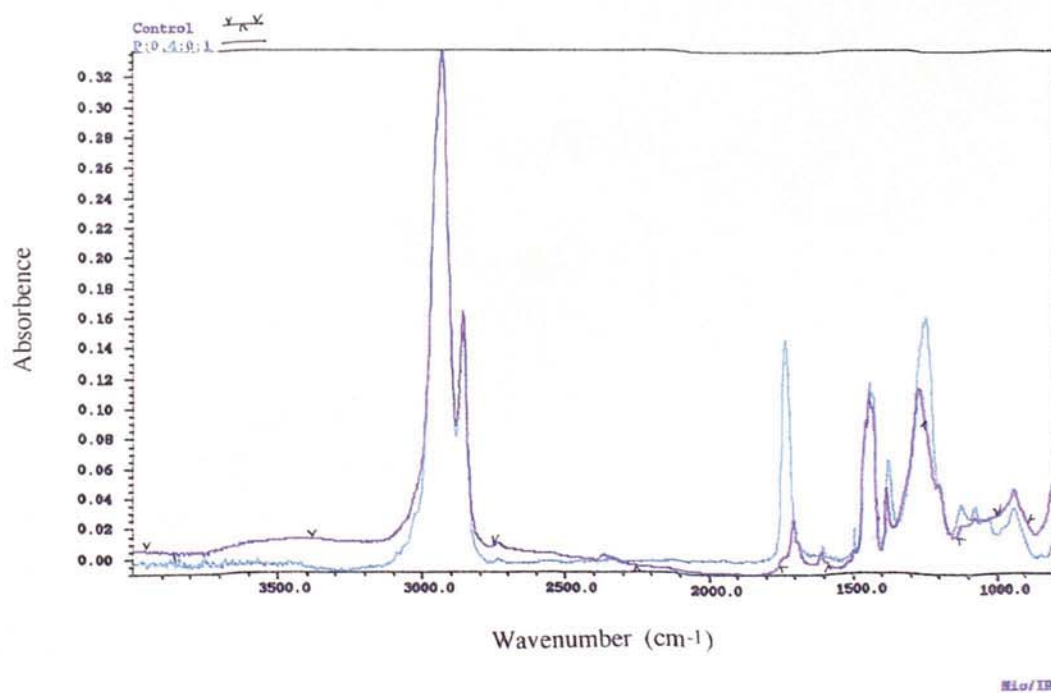


**Figure 6.29** FT-IR spectra: Comparison of specimen P:0.4:0:1(3 months) blister area to control sample.



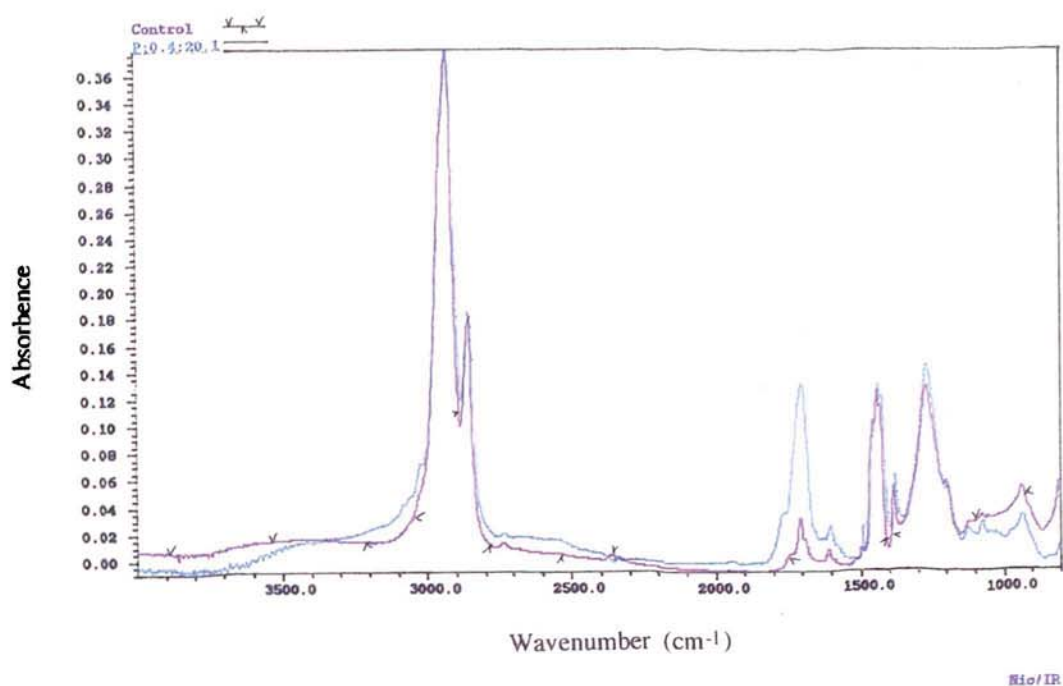


**Figure 6.30** FT-IR spectra: Comparison of specimen P:0.4:20:1(12 months) blister area to control sample.

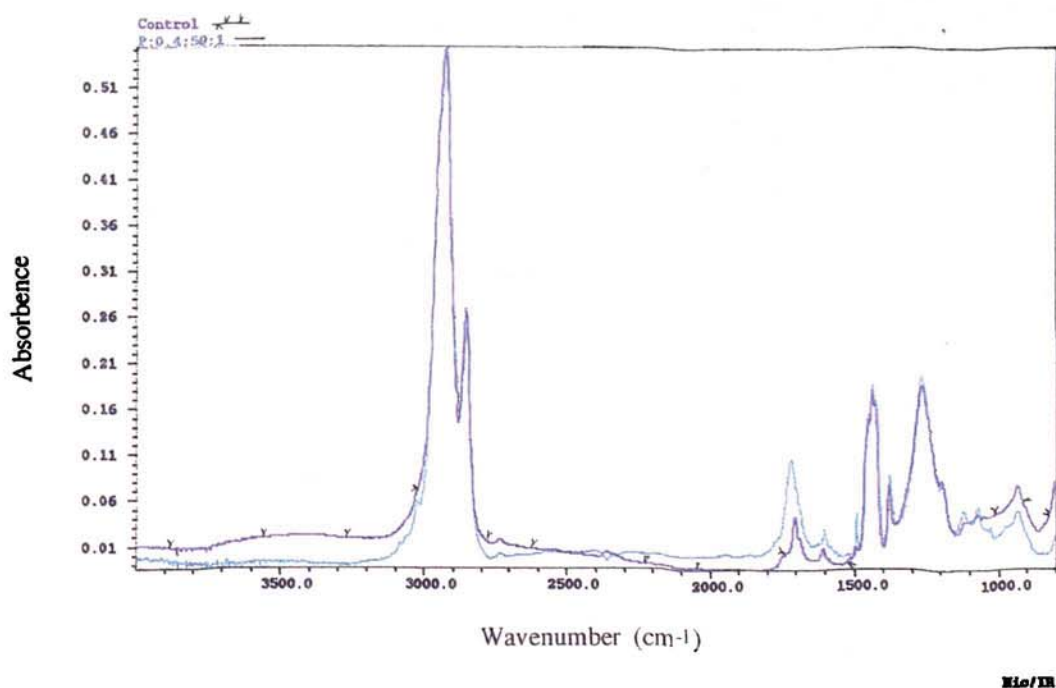


**Figure 6.31** FT-IR spectra: Comparison of specimen P:0.4:50:1(3 months) blister area to control sample.

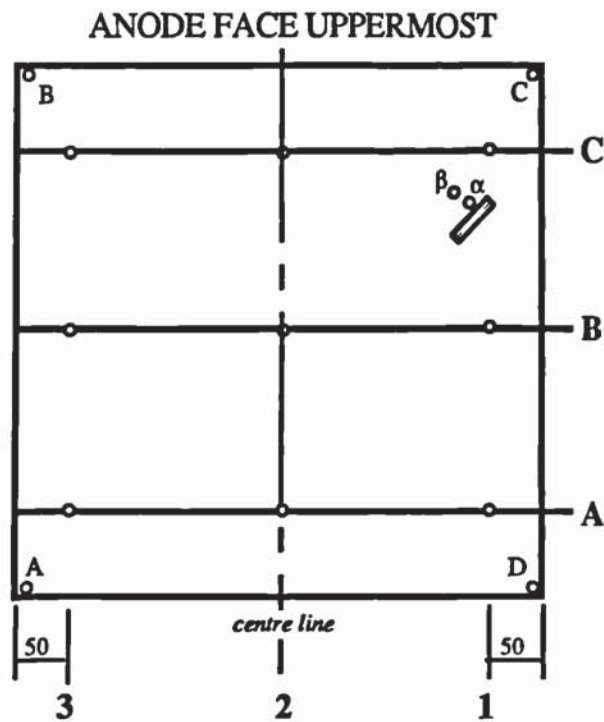


Figure 6.32 Location of drop voltage measurements for anode P specimens

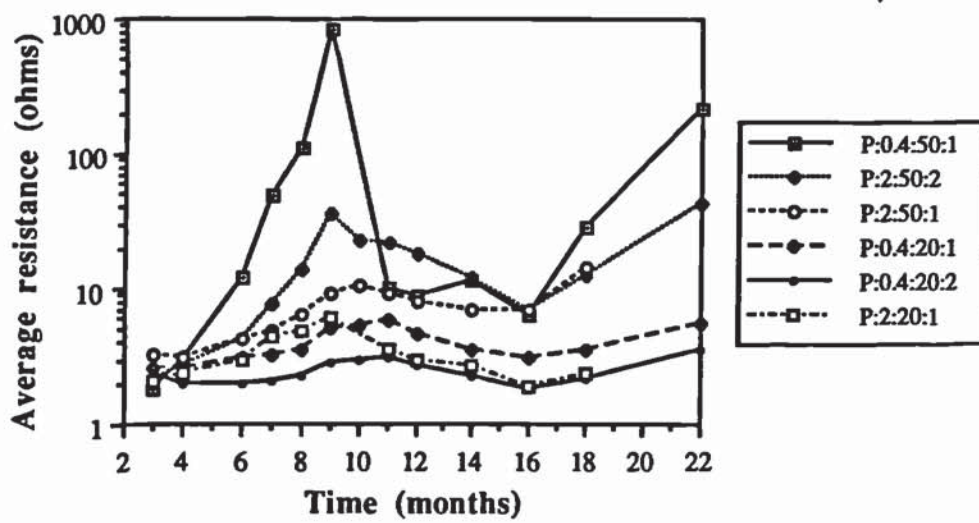
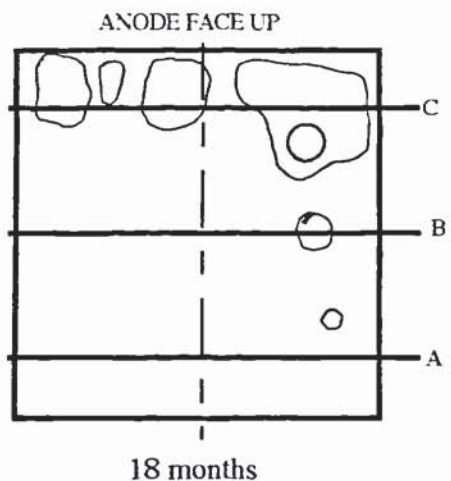
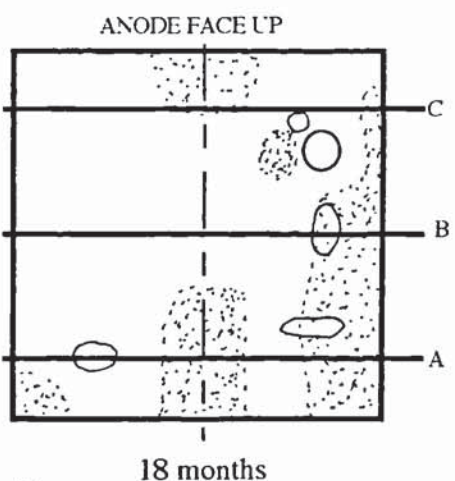
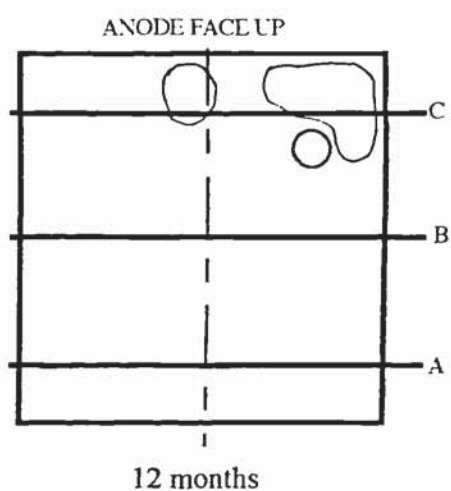
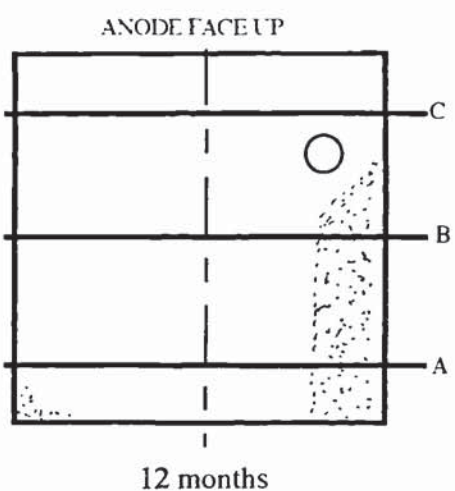
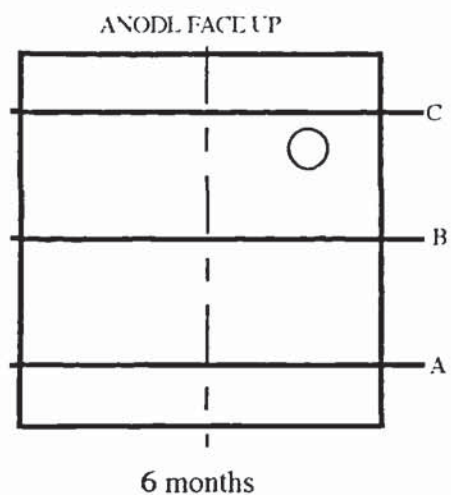
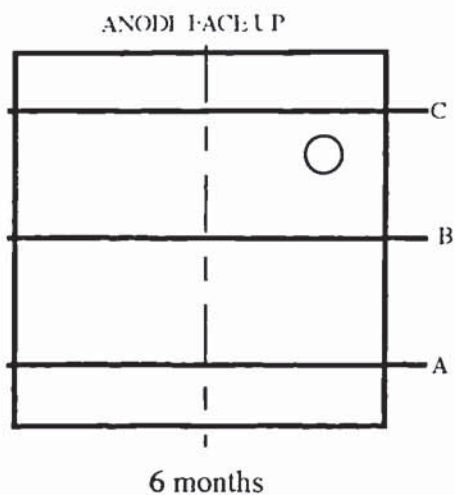




Figure 6.33 Plot of average resistance values vs. time for anode P specimens






Key

Debonded area 

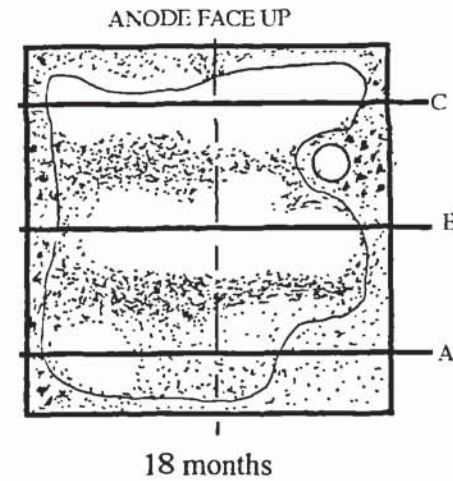
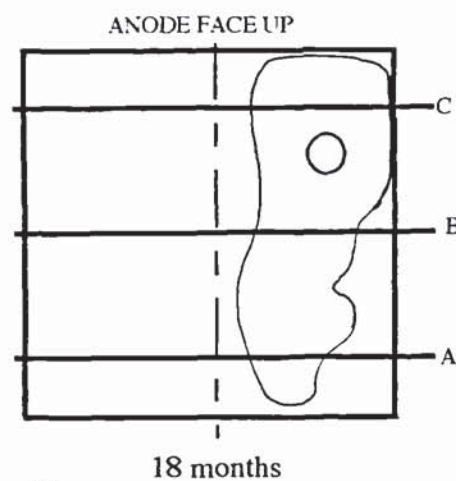
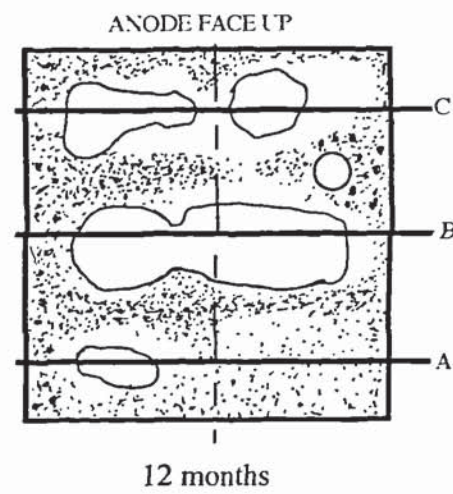
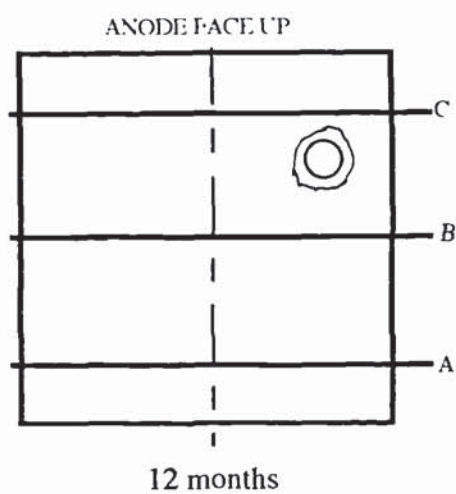
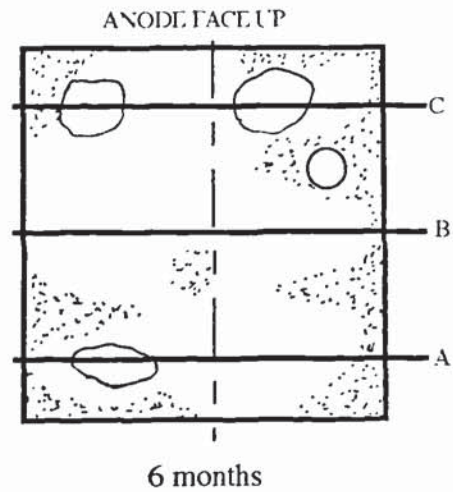
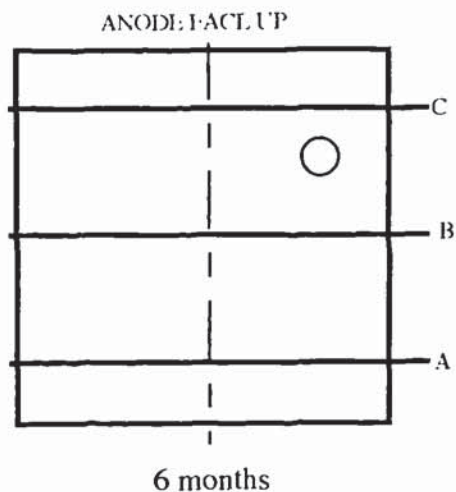
Grey "warts" 

Brass primary anode disc 



Large grey "warts" 


**Figure 6.34** Surface visual inspection 6 month summary: Specimen Z:2:20:1


**Figure 6.35** Surface visual inspection 6 month summary: Specimen Z:0.4:20:1



**Key**

Debonded area   
 Grey "warts" 

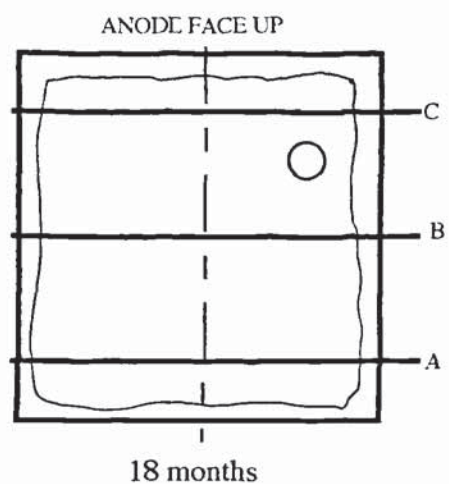
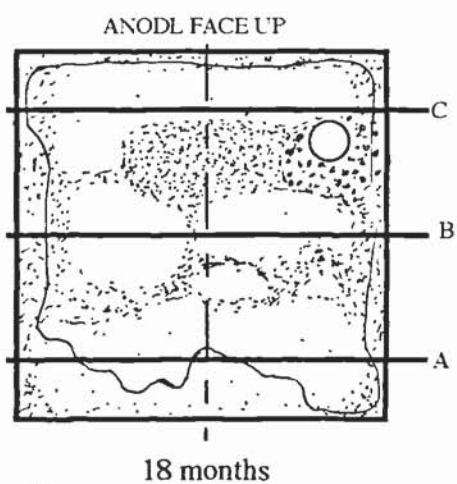
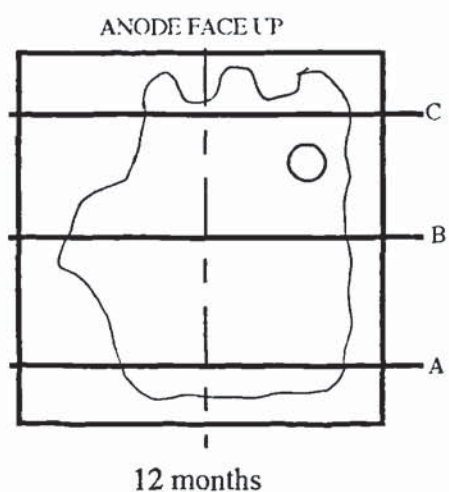
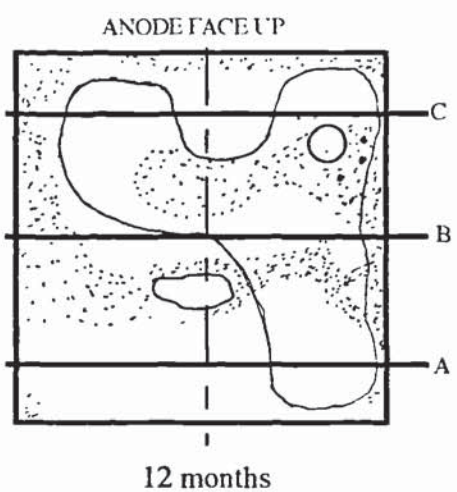
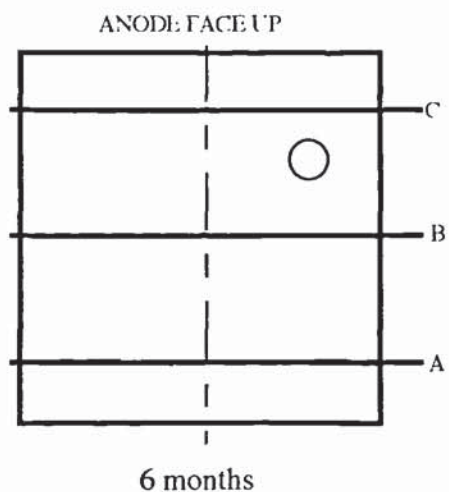
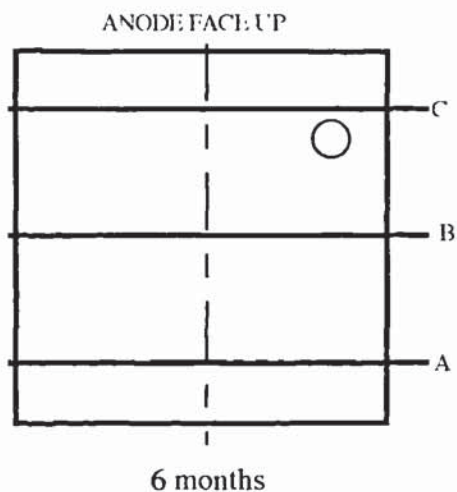
Brass primary anode disc 

Large grey "warts" 



**Figure 6.36** Surface visual inspection 6 month summary: Specimen Z:0.4:20:2


**Figure 6.37** Surface visual inspection 6 month summary: Specimen Z:2:50:1






**Key**

Debonded area   
 Grey "warts" 

Brass primary anode disc 

Large grey "warts" 

**Figure 6.38** Surface visual inspection 6 month summary: Specimen Z:2:50:2

**Figure 6.39** Surface visual inspection 6 month summary: Specimen Z:0.4:50:1

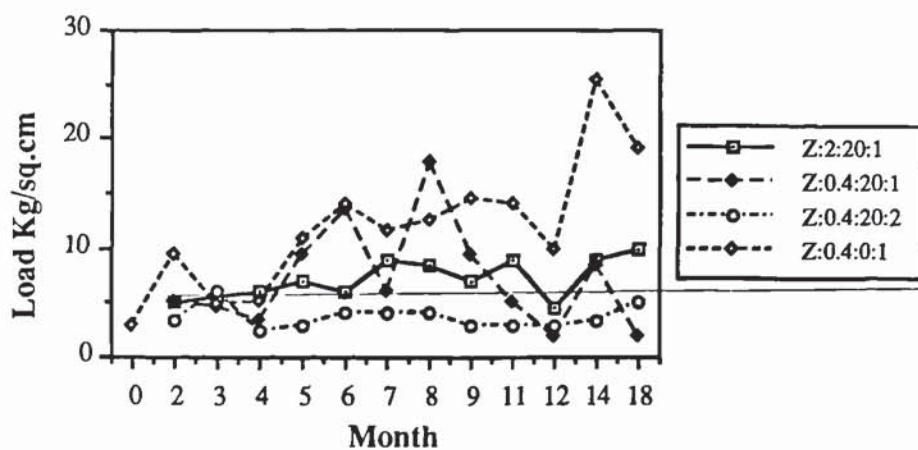


Figure 6.40 Plot of pull-off loads/time for Anode Z ( $20 \text{ mA/m}^2$ ) specimens.

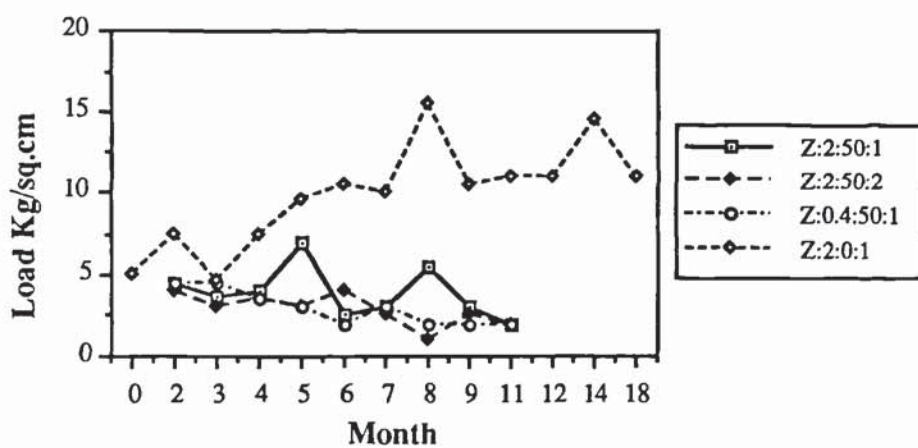


Figure 6.41 Plot of pull-off loads/time for Anode Z ( $50 \text{ mA/m}^2$ ) specimens.



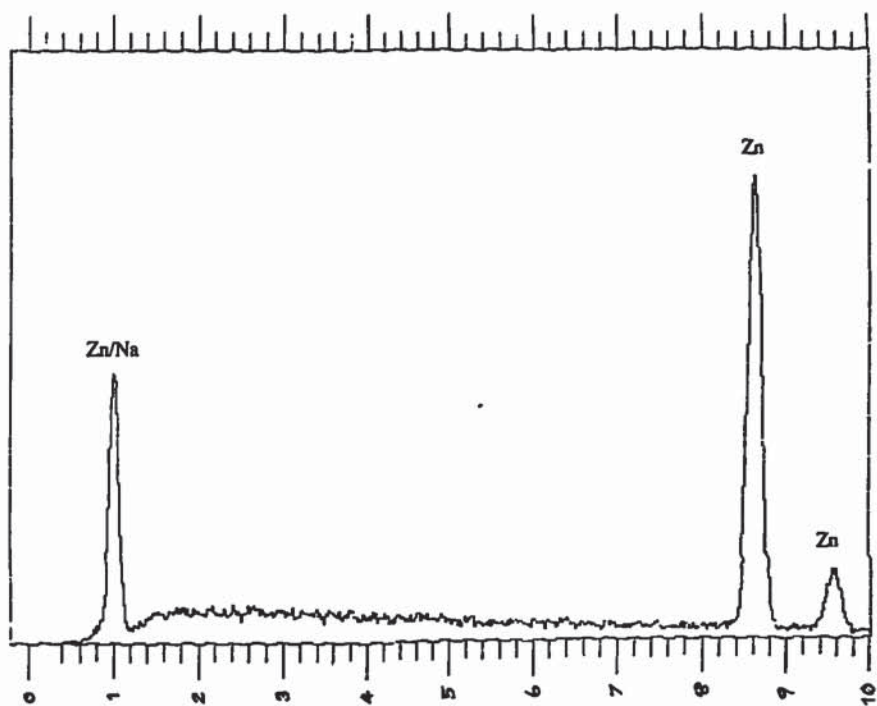


Figure 6.42 EDXA elemental plot: White zinc corrosion product.

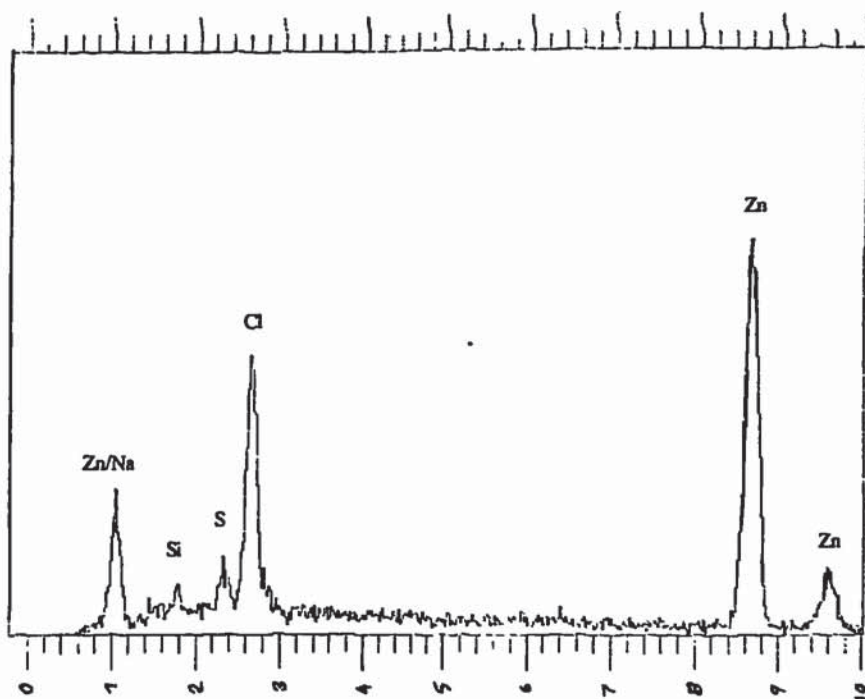


Figure 6.43 EDXA elemental plot: Zinc "wart" corrosion product, inner surface.

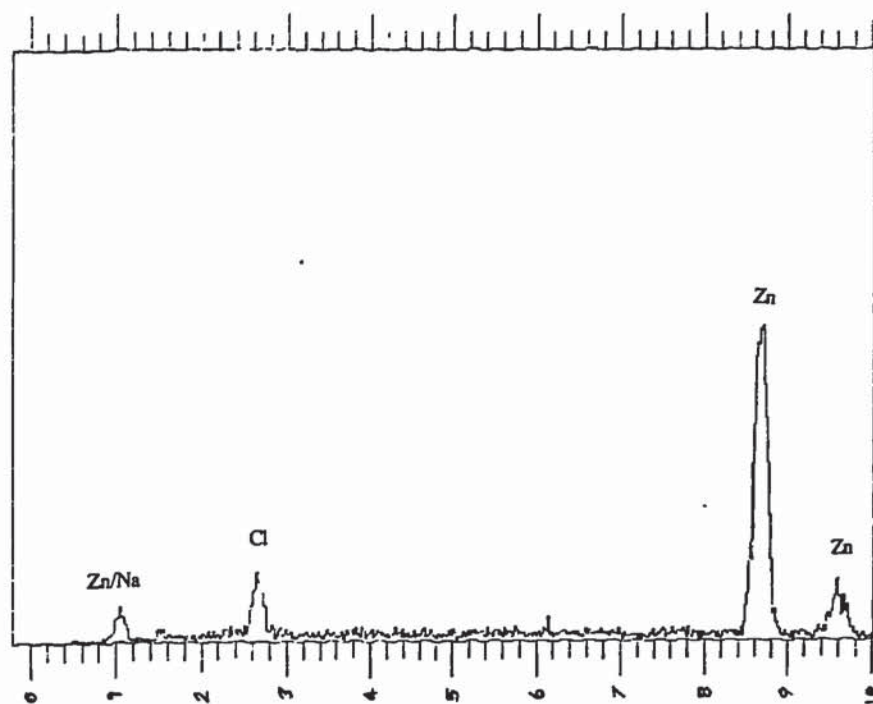


Figure 6.44 EDXA elemental plot: Zinc "wart" corrosion product, outer surface.

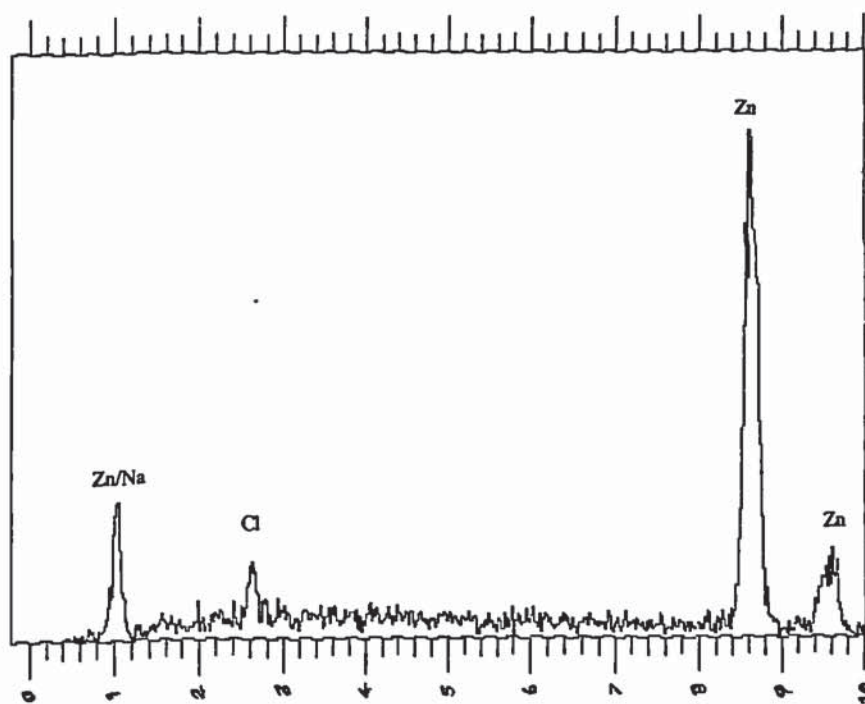
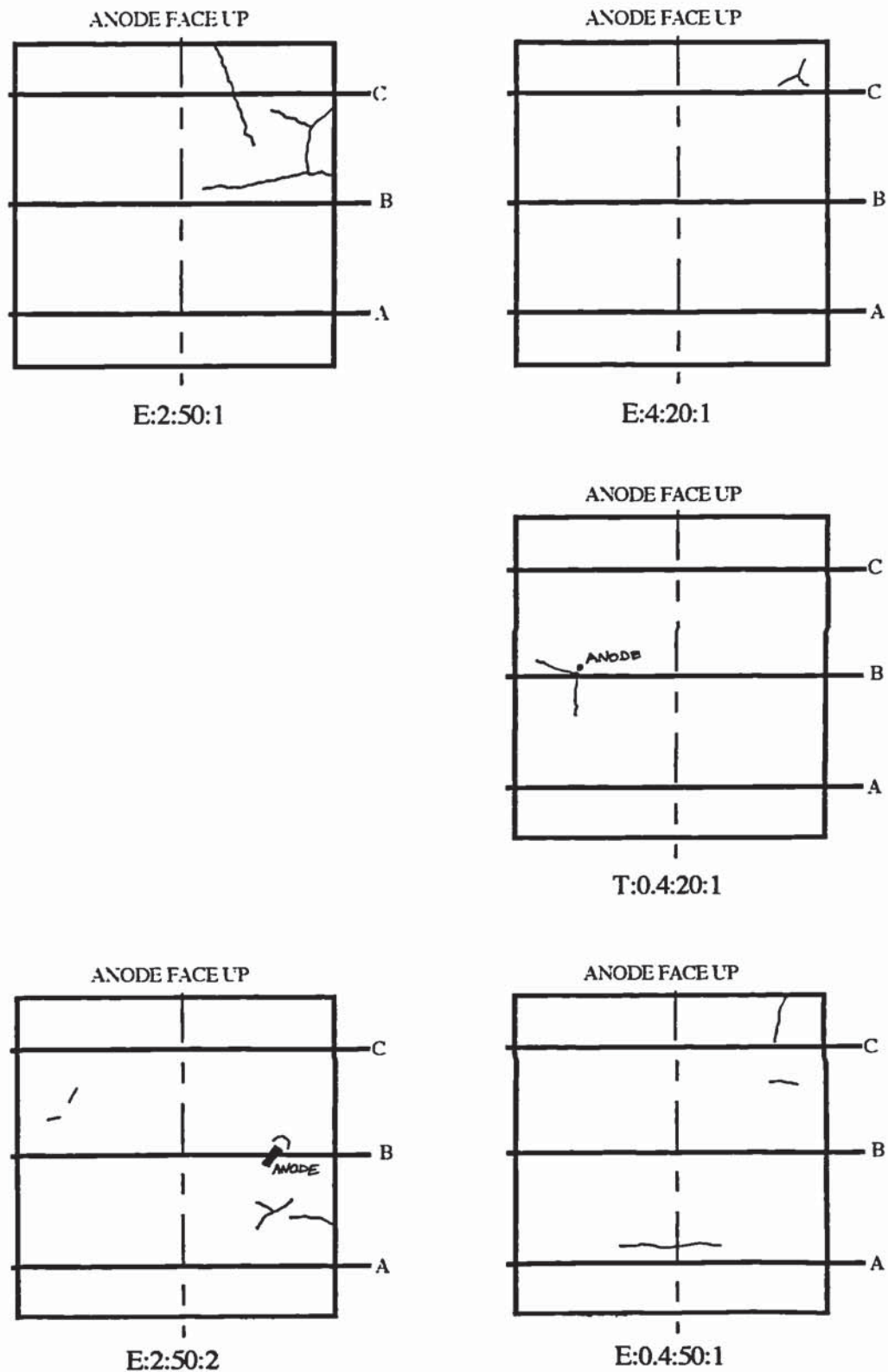
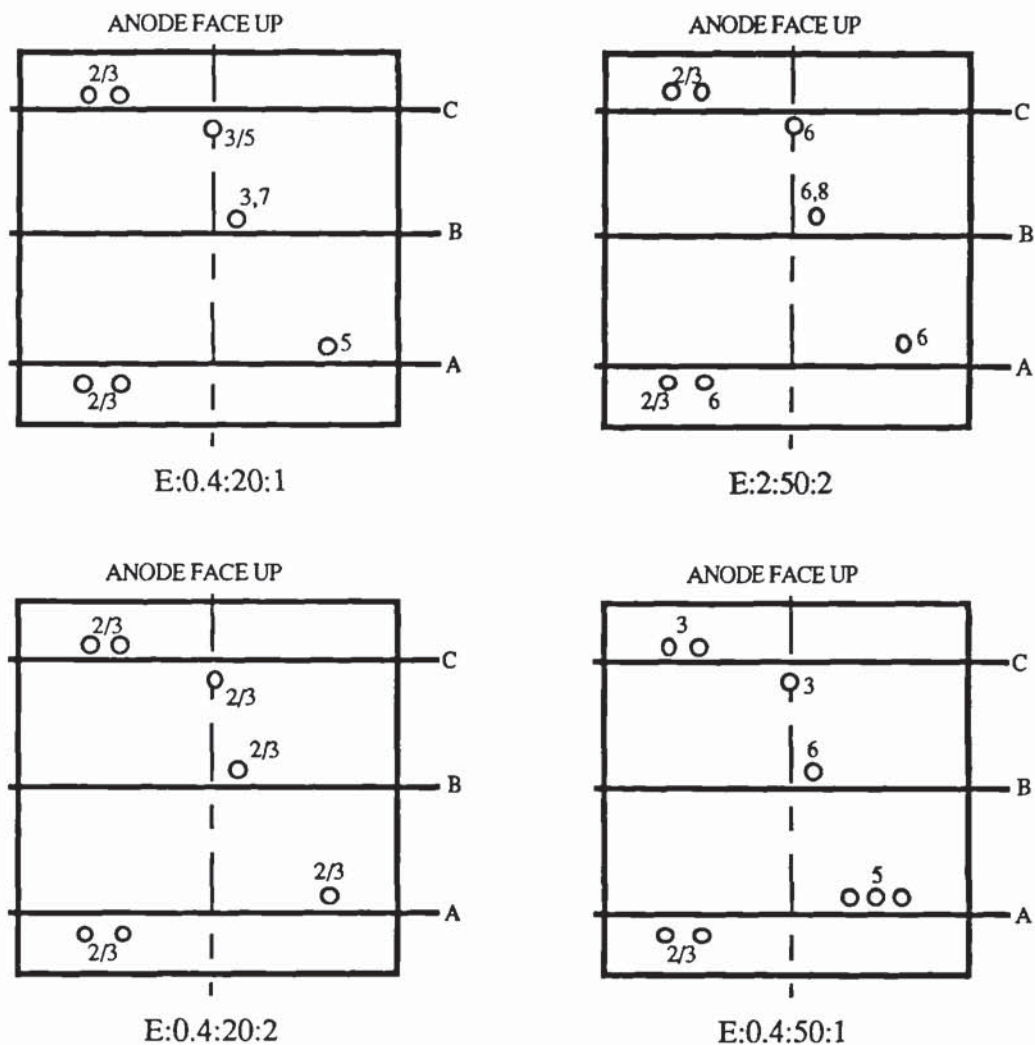


Figure 6.45 EDXA elemental plot: White zinc corrosion product at fracture surface.





**Figure 6.46** Sketches of cementitious overlay surface shrinkage cracking.

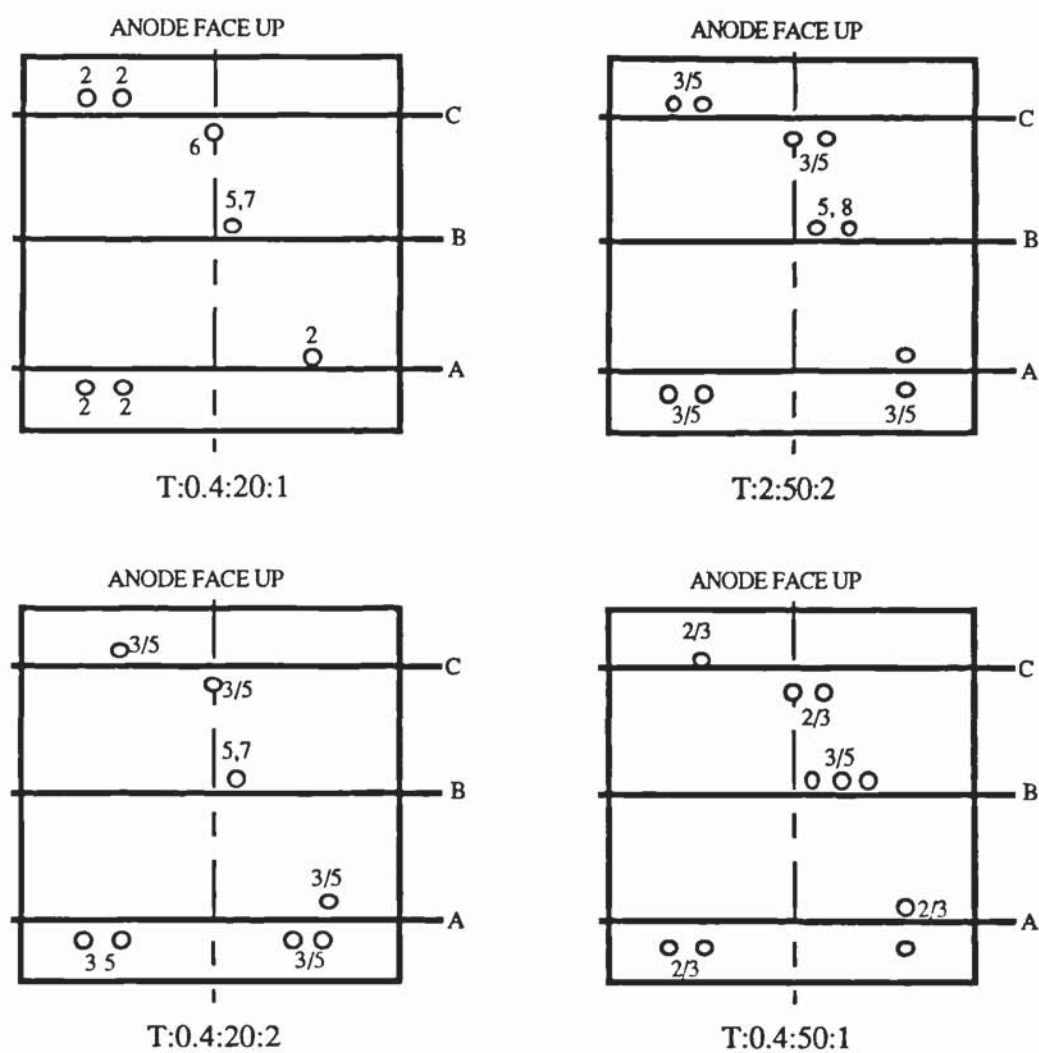


### KEY

- |                  |                        |
|------------------|------------------------|
| 1 No degradation | 5 Beige paste          |
| 2 Darkened ring  | 6 Full paste loss      |
| 3 White ring     | 7 White precipitation  |
| 4 Paste loss     | 8 Orange precipitation |

Figure 6.47 Anode E, 22 months: Summary of anodic degradation within cored holes.





# **KEY**

- |                  |                        |
|------------------|------------------------|
| 1 No degradation | 5 Beige paste          |
| 2 Darkened ring  | 6 Full paste loss      |
| 3 White ring     | 7 White precipitation  |
| 4 Paste loss     | 8 Orange precipitation |

**Figure 6.48** Anode T, 22 months: Summary of anodic degradation within cored holes.

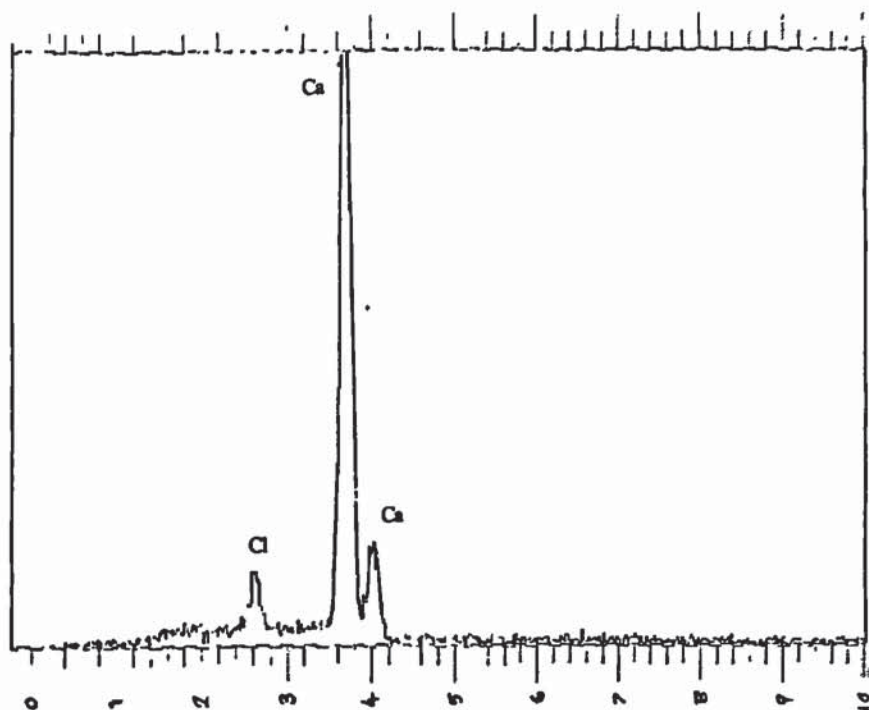


Figure 6.49 EDXA elemental plot: Crystalline white precipitate in cementitious overlay

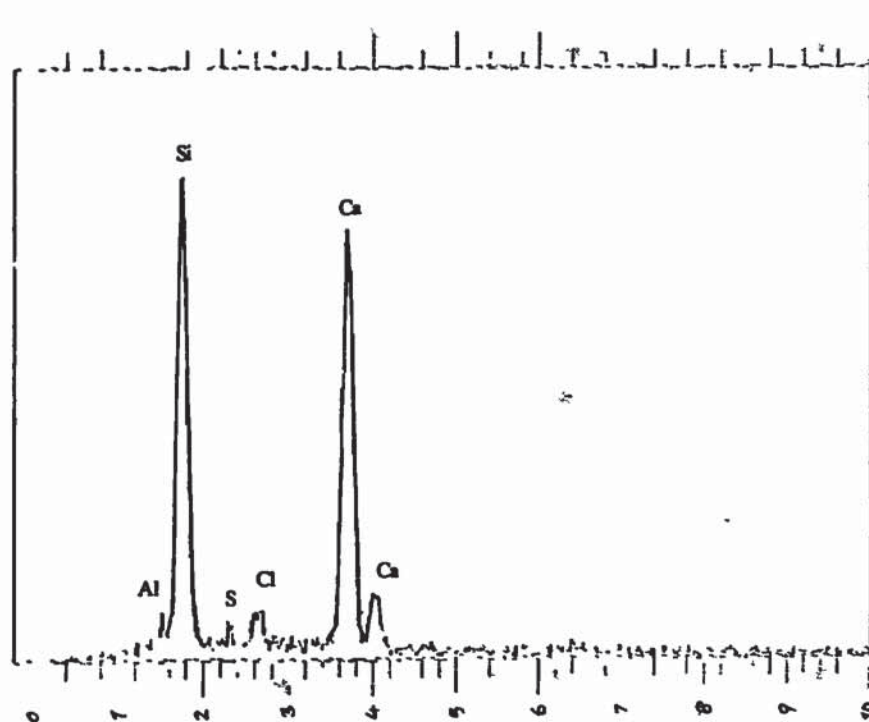
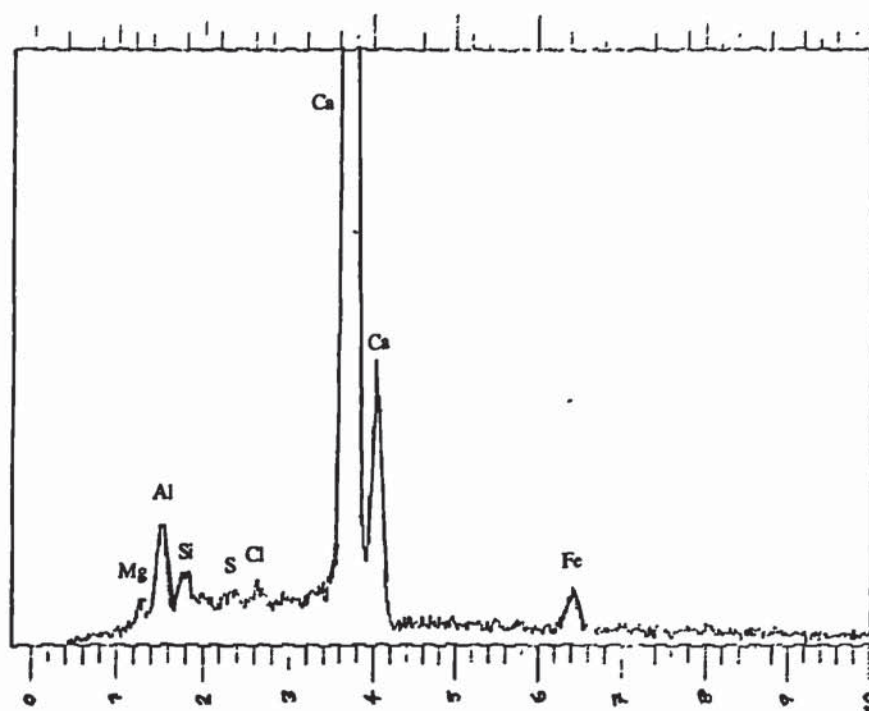


Figure 6.50 EDXA elemental plot: Cementitious overlay





**Figure 6.51** EDXA elemental plot: Coloured precipitate forming within cored hole.

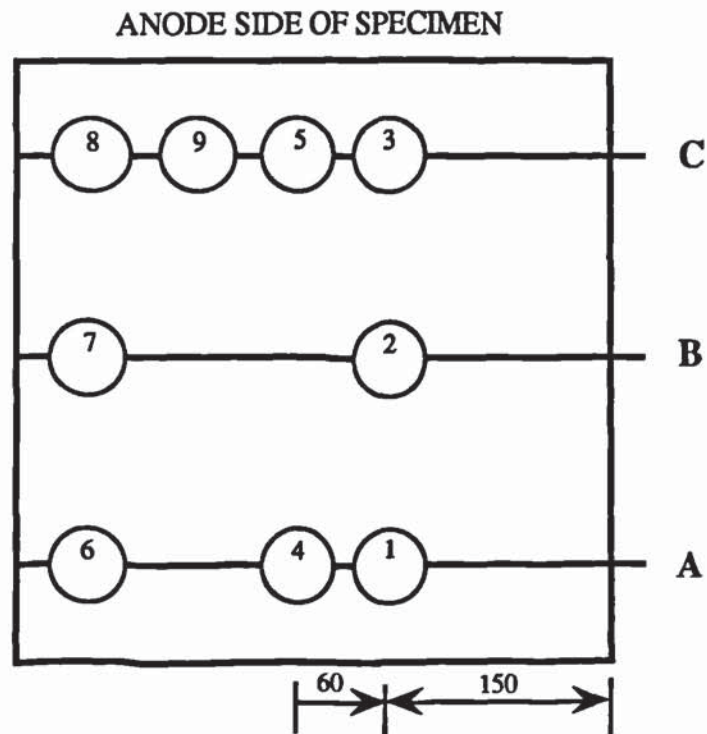
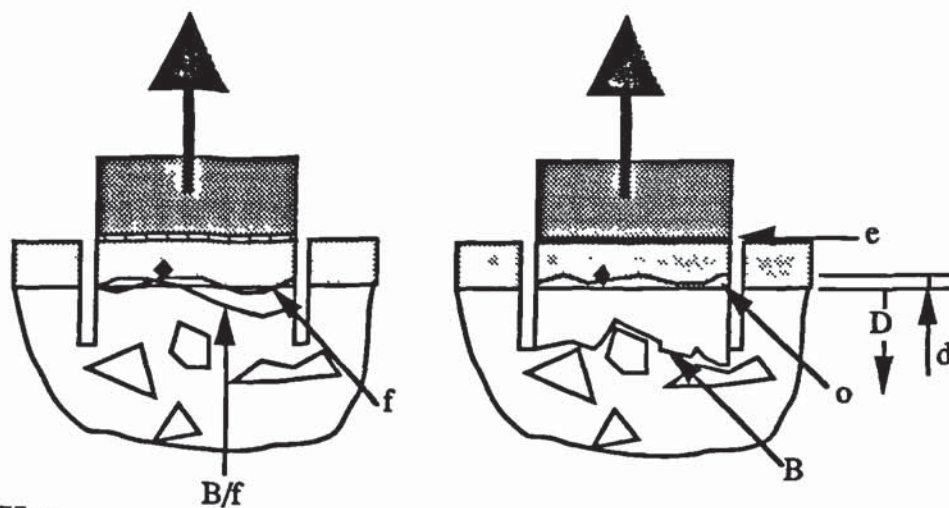


Figure 6.52 Location of 50 mm diameter "Limpit" probes.



**Key**

B = failure in concrete bulk	◆ anode strand
e = failure in epoxy adhesive	▨ steel probe
o = failure in overlay	▬ overlay
f = failure at overlay/substrate interface	▨ epoxy adhesive

D = depth of failure surface from substrate/overlay interface

d = distance of anode strand from substrate surface

Figure 6.53 Failure modes of "Limpit" probes.



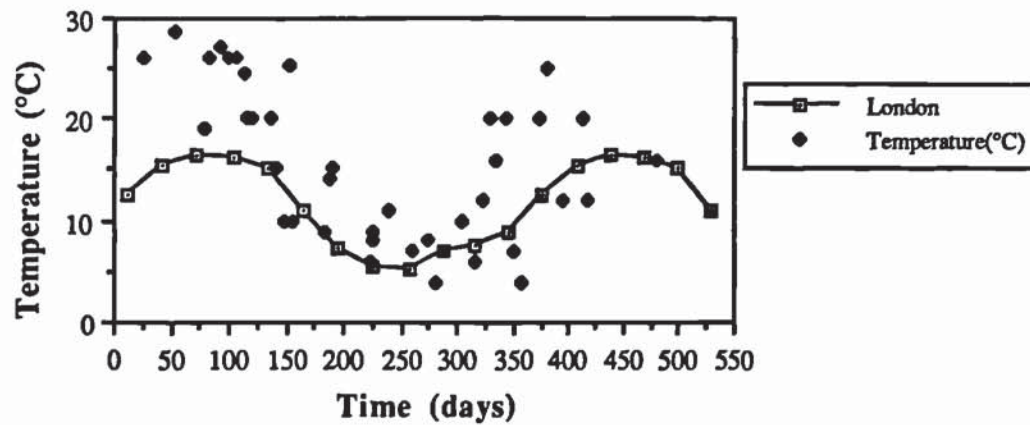


Figure 7.1 Air temperature/time plot at time of potential measurements/ comparative average data for London (adapted from Hankin *et al*, 1985).

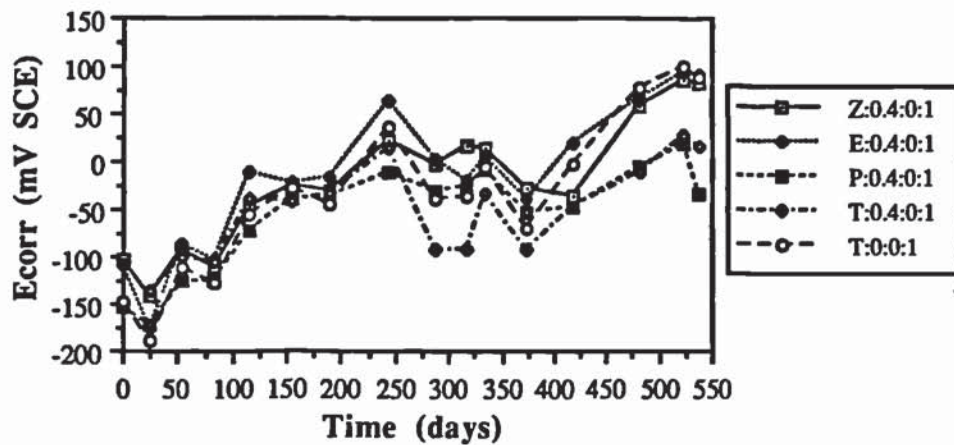


Figure 7.2 Plot of  $E_{corr}$ /time for 0.4% & 0% chloride control specimens.

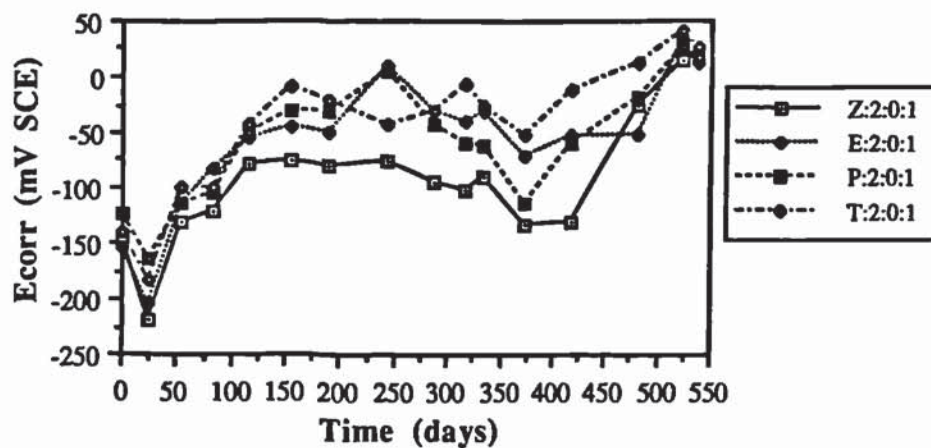


Figure 7.3 Plot of  $E_{corr}$ /time for 2% chloride control specimens.

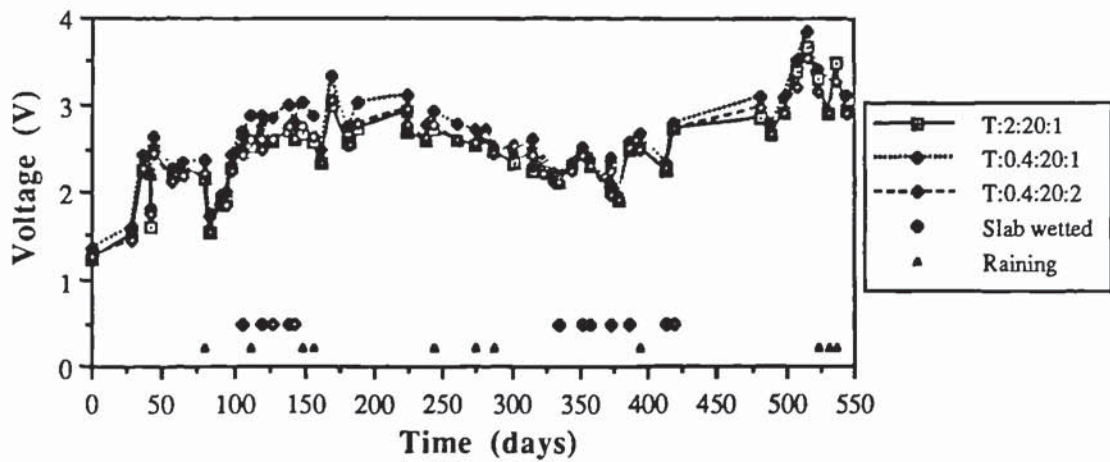


Figure 7.4 Plot of system voltage/time for T:20 specimens.

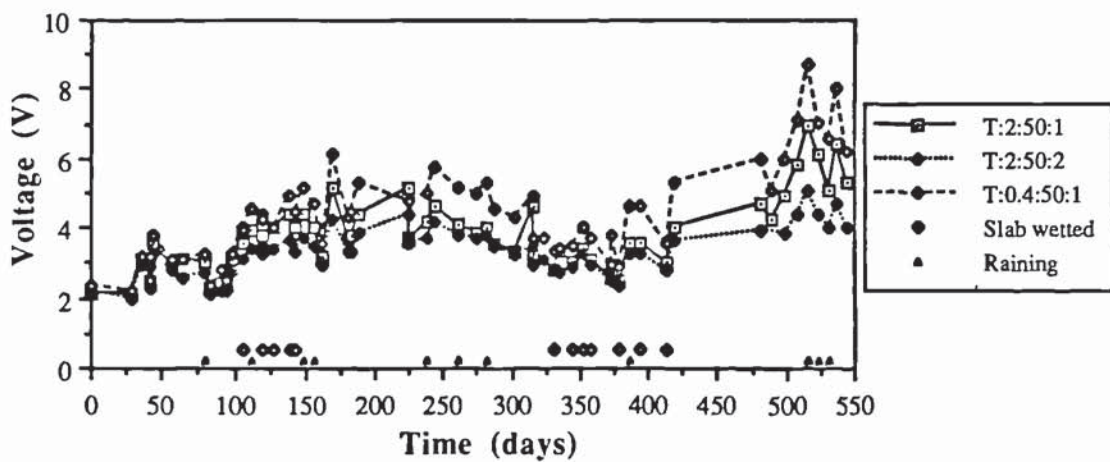


Figure 7.5 Plot of system voltage/time for T:50 specimens.

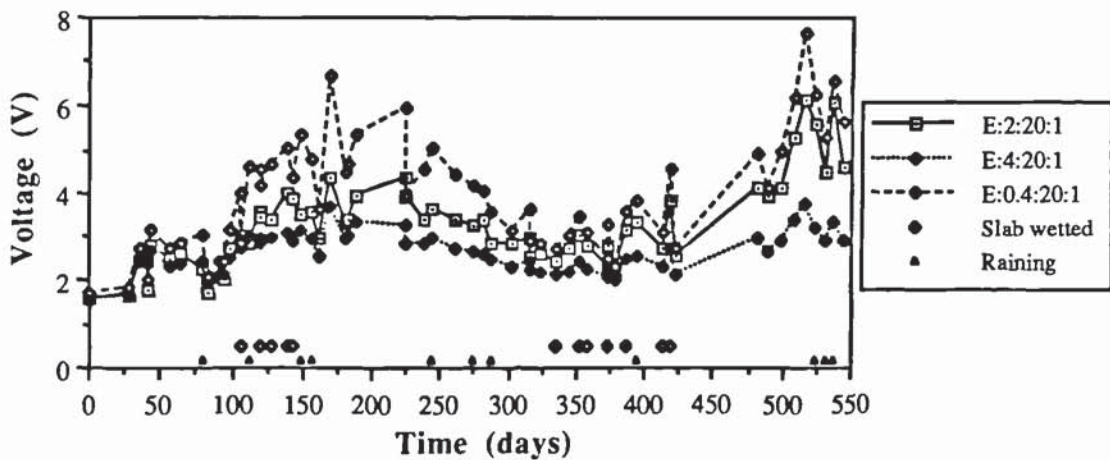


Figure 7.6 Plot of system voltage/time for E:20 specimens.



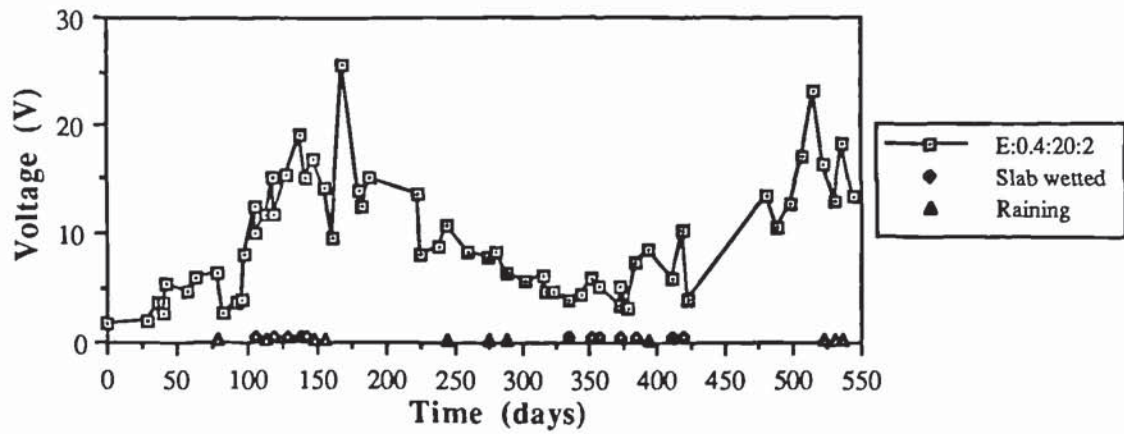


Figure 7.7 Plot of system voltage/time for specimen E:0.4:20:2 .

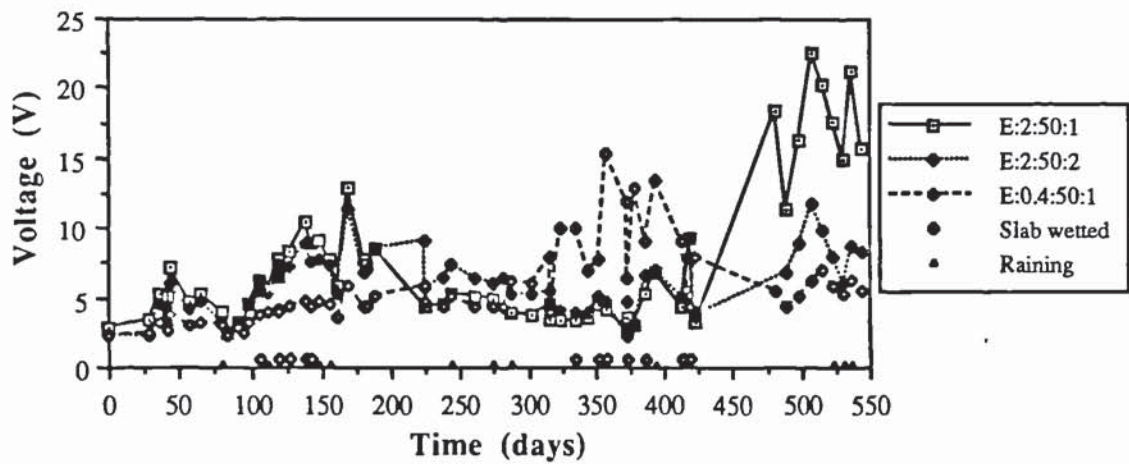


Figure 7.8 Plot of system voltage/time for E:50 specimens.

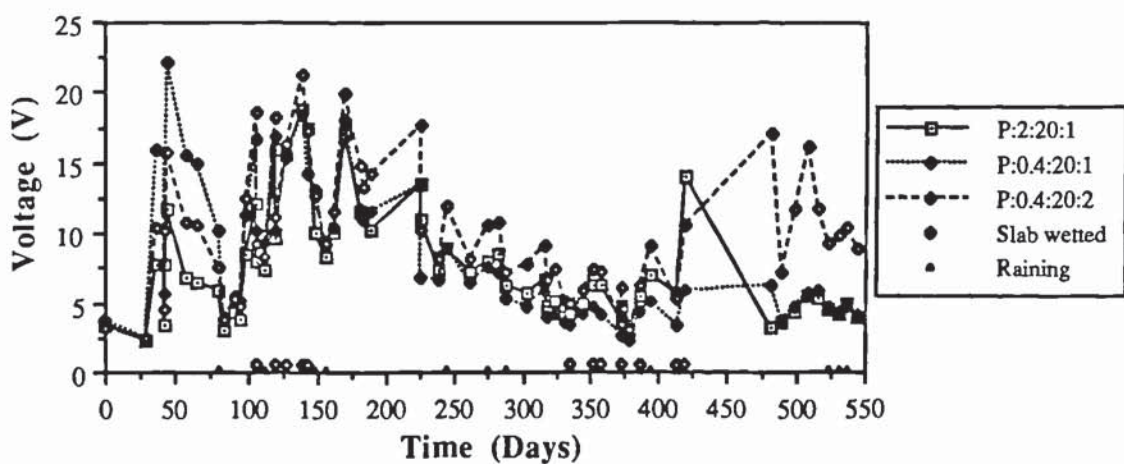


Figure 7.9 Plot of system voltage/time for P:20 specimens.

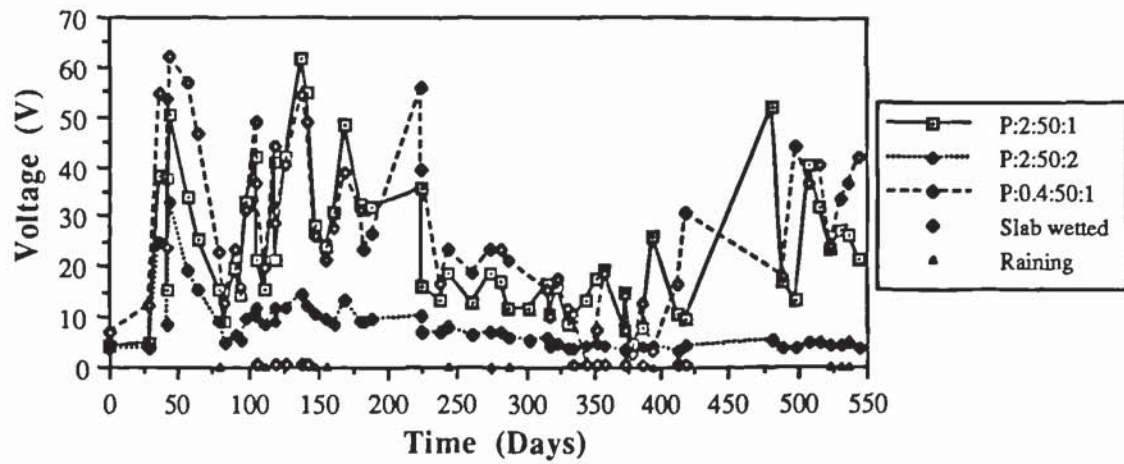


Figure 7.10 Plot of system voltage/time for P:50 specimens.

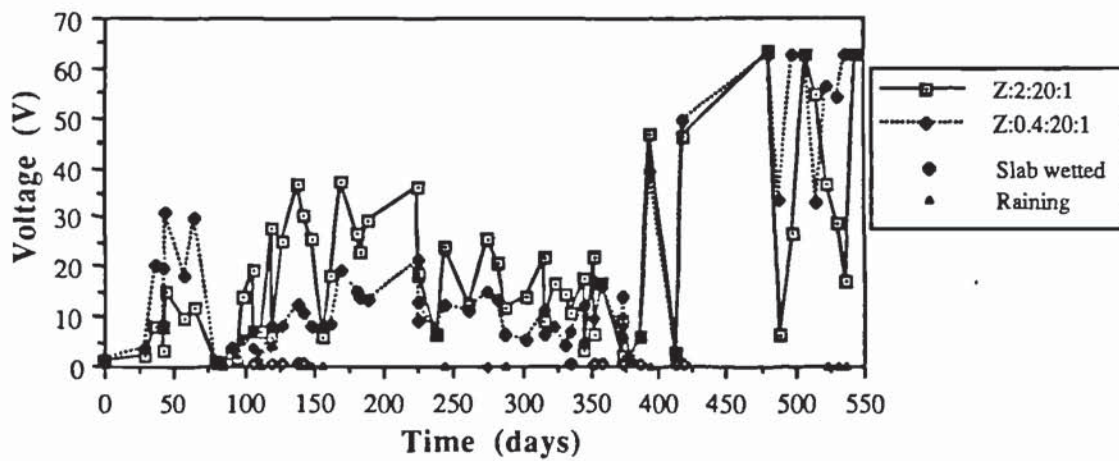


Figure 7.11 Plot of system voltage/time for specimens Z:2:20:1 and Z:0.4:20:1.

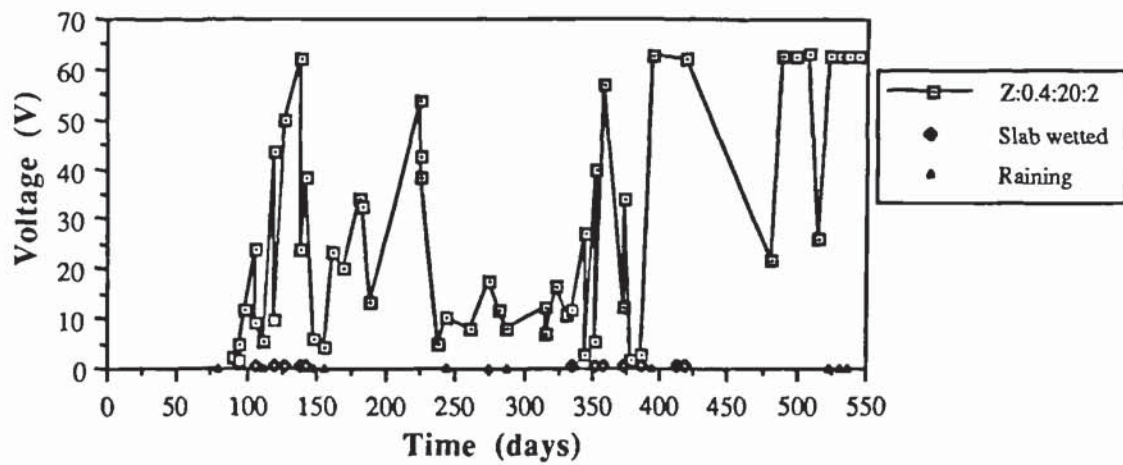


Figure 7.12 Plot of system voltage/time for specimen Z:0.4:20:2.



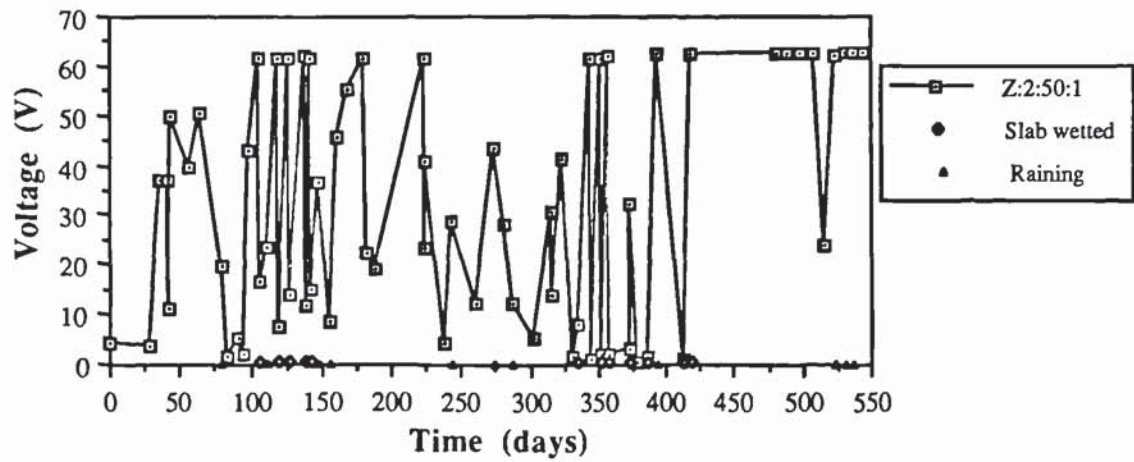


Figure 7.13 Plot of system voltage/time for specimen Z:2:50:1.

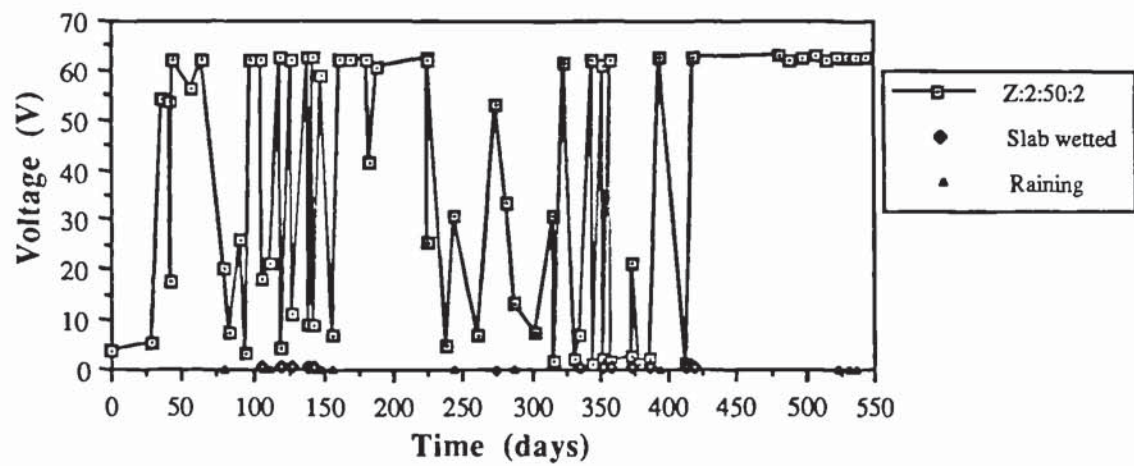


Figure 7.14 Plot of system voltage/time for specimen Z:2:50:2.

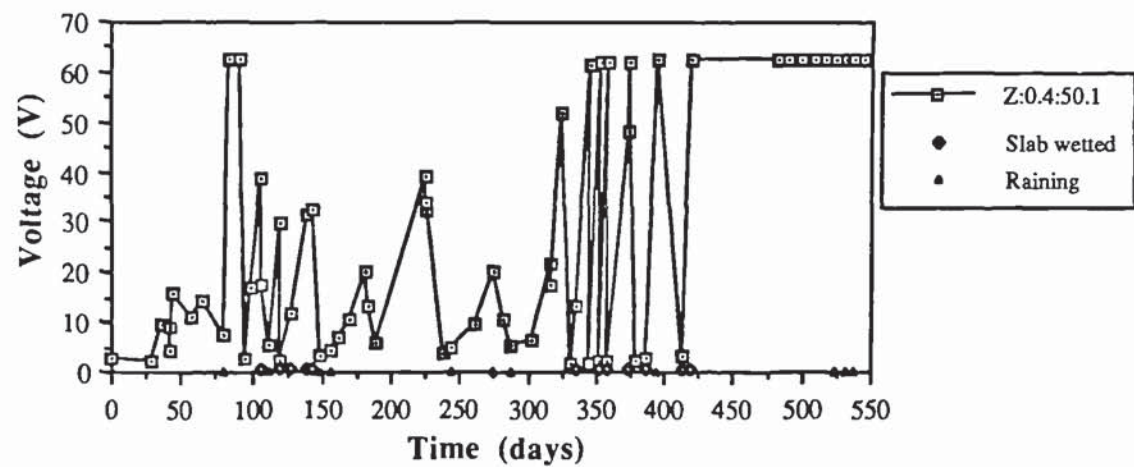


Figure 7.15 Plot of system voltage/time for specimen Z:0.4:50:1.

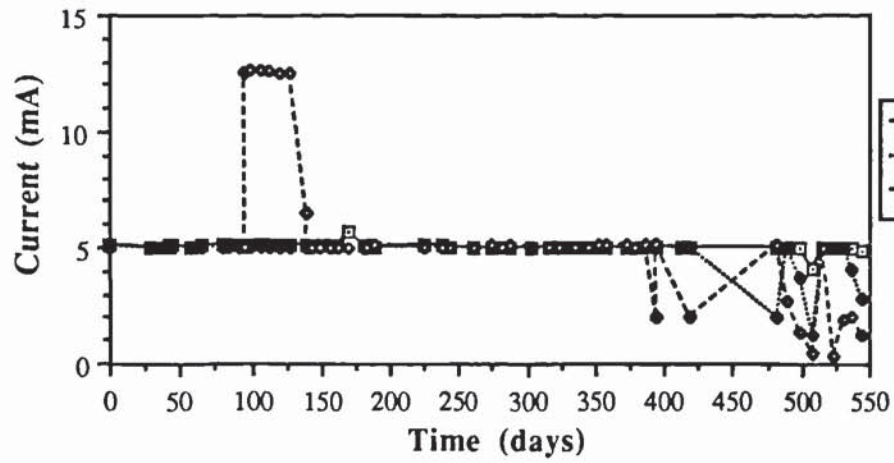


Figure 7.16 Plot of current/time for Z:20 specimens.

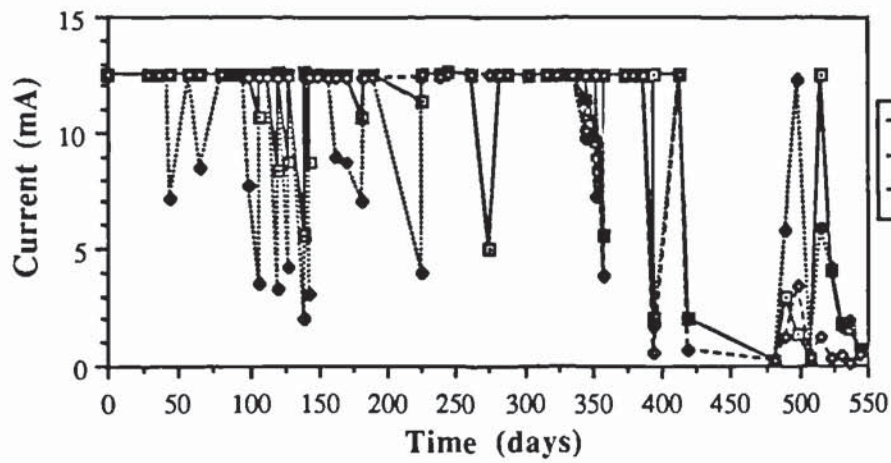


Figure 7.17 Plot of current/time for Z:50 specimens.



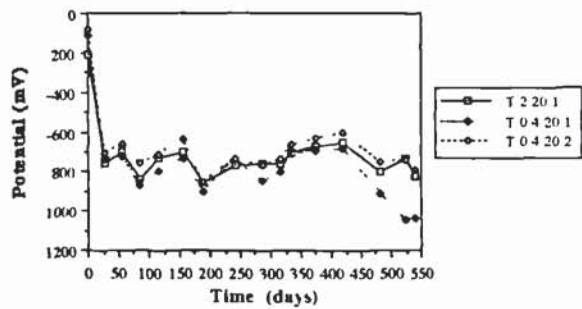


Figure 7.18 Plot of 'on' cathodic potential time T.20 specimens

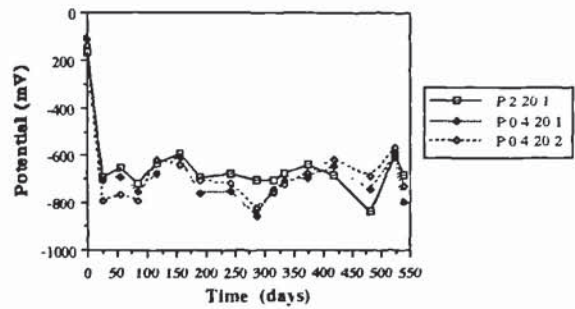


Figure 7.22 Plot of 'on' cathodic potential time P.20 specimens

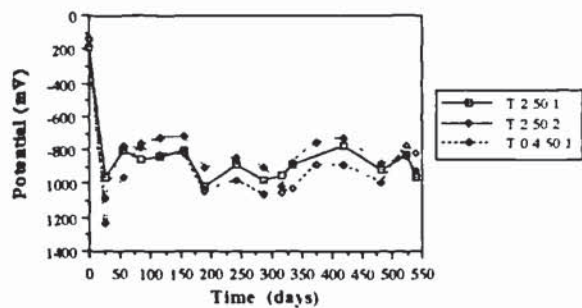


Figure 7.19 Plot of 'on' cathodic potential time T.50 specimens

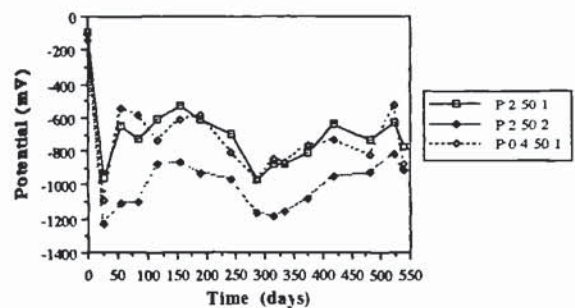


Figure 7.23 Plot of 'on' cathodic potential time P.50 specimens

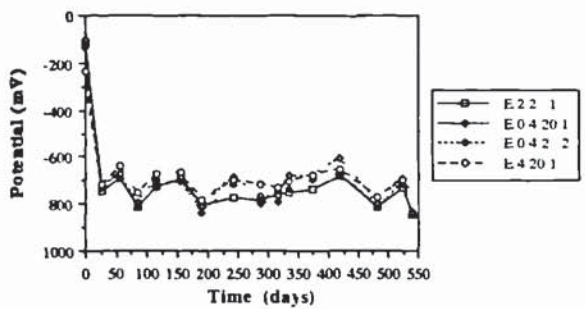


Figure 7.20 Plot of 'on' cathodic potential time E.20 specimens

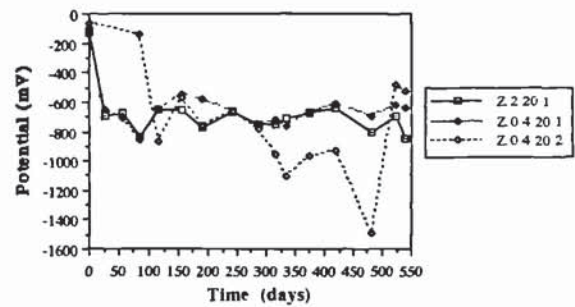


Figure 7.24 Plot of 'on' cathodic potential time Z.20 specimens

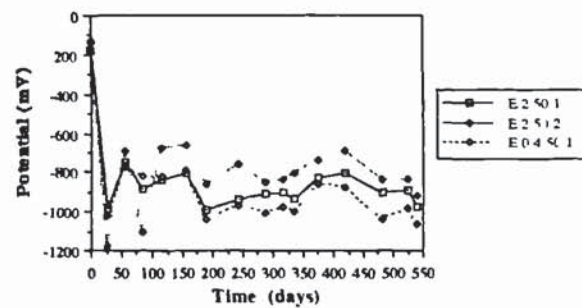


Figure 7.21 Plot of 'on' cathodic potential time E.50 specimens

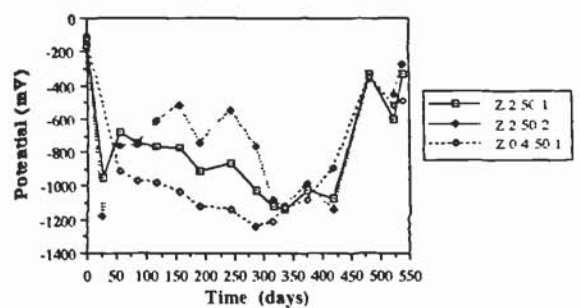


Figure 7.25 Plot of 'on' cathodic potential time Z.50 specimens

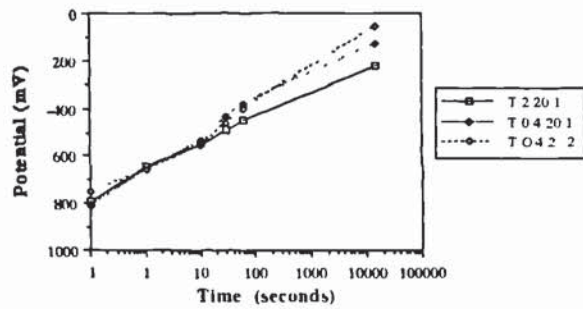


Figure 7.26 Plot of potential decay time T.20 specimens (1 month)

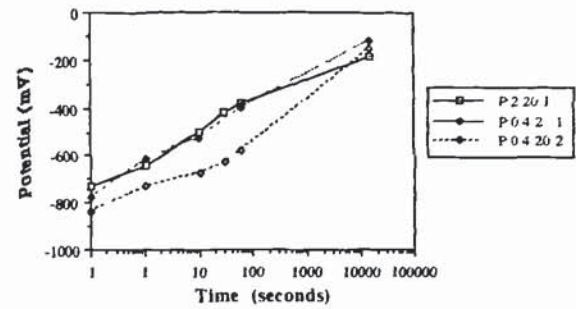


Figure 7.30 Plot of potential decay time P.20 specimens (1 month)

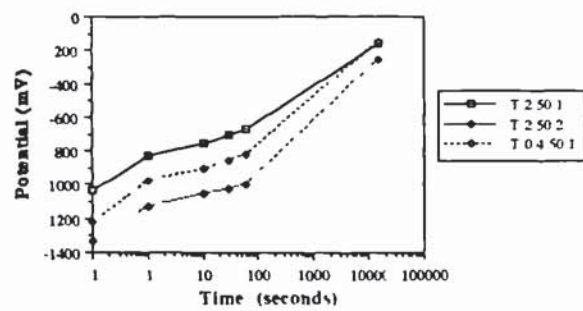


Figure 7.27 Plot of potential decay time T.50 specimens (1 month)

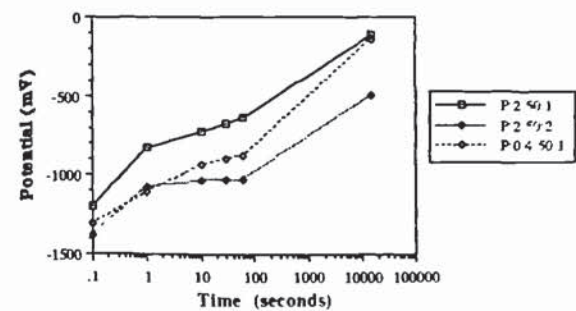


Figure 7.31 Plot of potential decay time P.50 specimens (1 month)

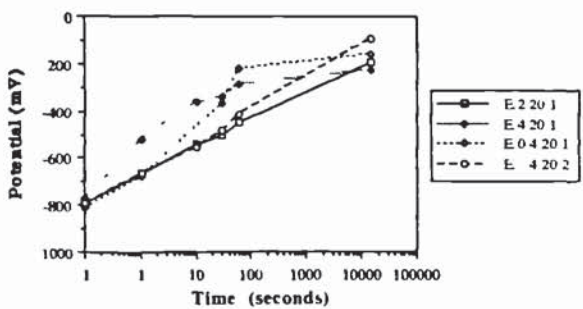


Figure 7.28 Plot of potential decay time E.20 specimens (1 month)

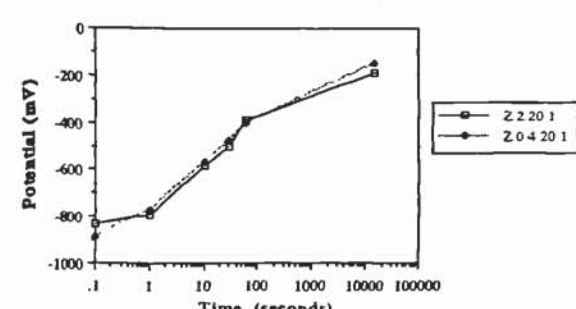


Figure 7.32 Plot of potential decay time Z.20 specimens (1 month)

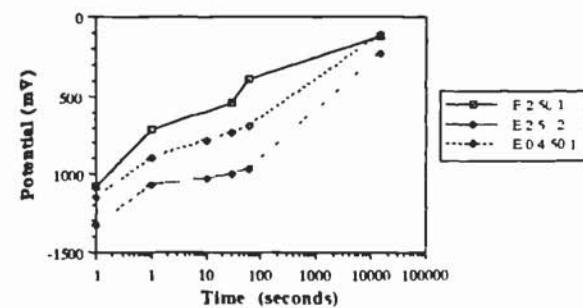


Figure 7.29 Plot of potential decay time E.50 specimens (1 month)

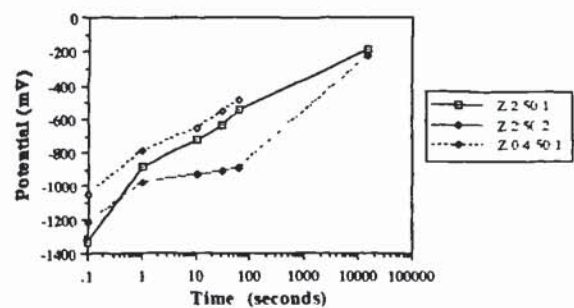


Figure 7.33 Plot of potential decay time Z.50 specimens (1 month)



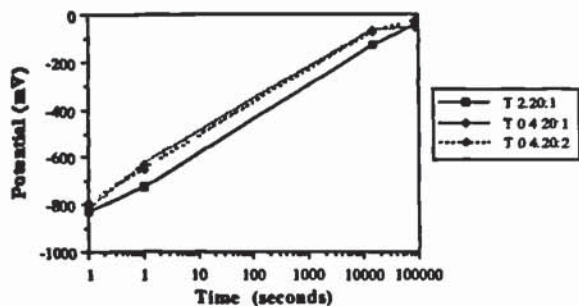


Figure 7.34 Plot of potential decay/time: T-20 specimens (18 month)

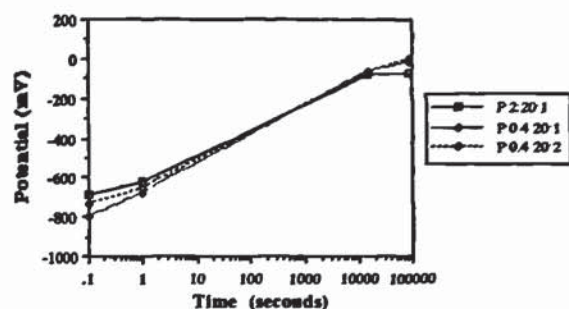


Figure 7.38 Plot of potential decay/time: P-20 specimens (18 month).

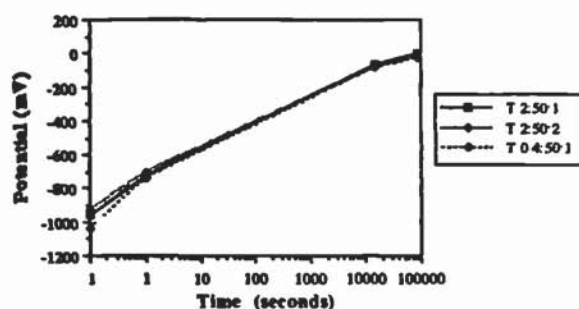


Figure 7.35 Plot of potential decay/time: T-50 specimens (18 month).

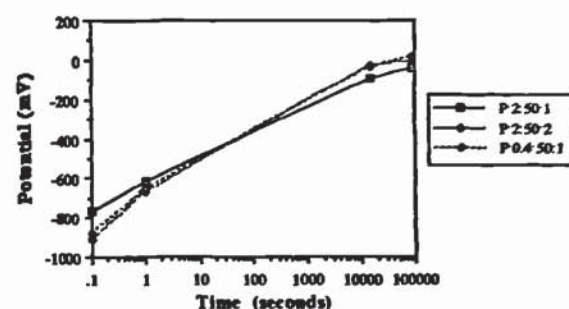


Figure 7.39 Plot of potential decay/time: P-50 specimens (18 month).

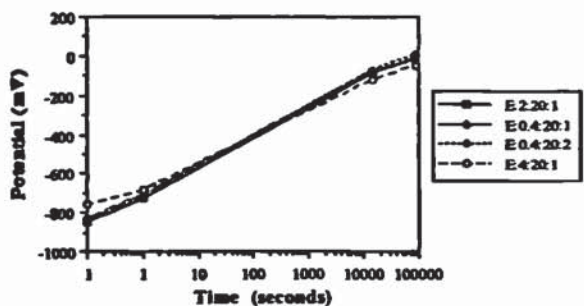


Figure 7.36 Plot of potential decay/time: E-20 specimens (18 months).

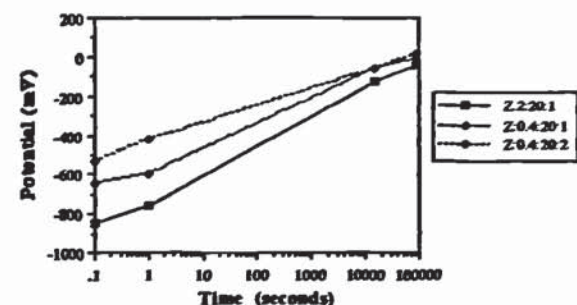


Figure 7.40 Plot of potential decay/time: Z-20 specimens (18 month).

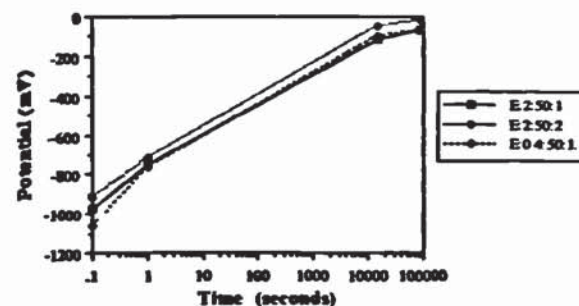


Figure 7.37 Plot of potential decay/time: E-50 specimens (18 month).

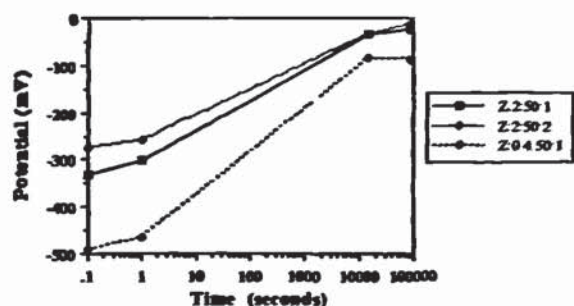


Figure 7.41 Plot of potential decay/time: Z-50 specimens (18 month).

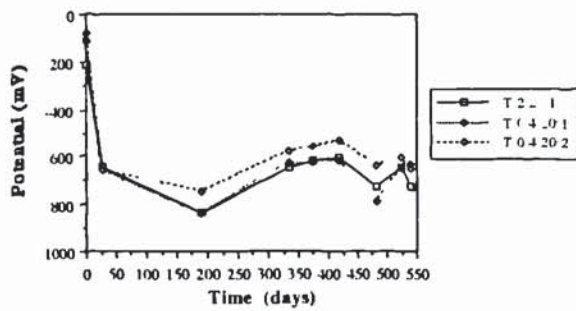


Figure 7.42 Plot of 'off' cathodic potential time T:20 specimens

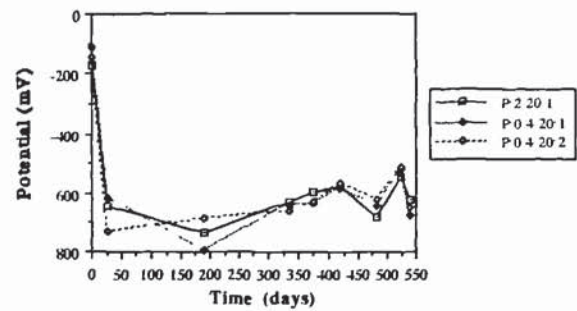


Figure 7.46 Plot of 'off' cathodic potential time P:20 specimens

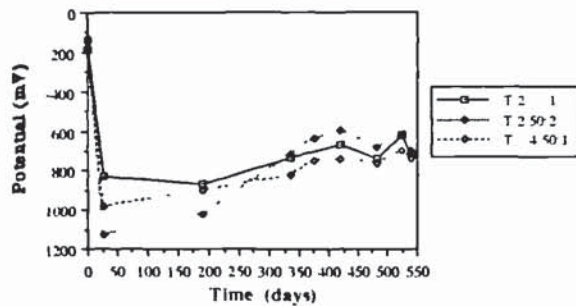


Figure 7.43 Plot of 'off' cathodic potential time T:50 specimens

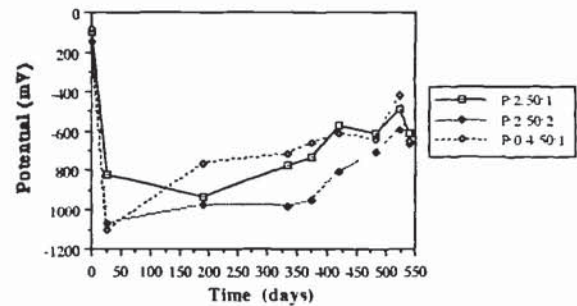


Figure 7.47 Plot of 'off' cathodic potential time P:50 specimens

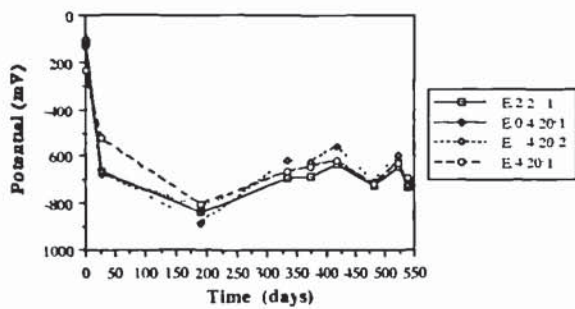


Figure 7.44 Plot of 'off' cathodic potential time E:20 specimens

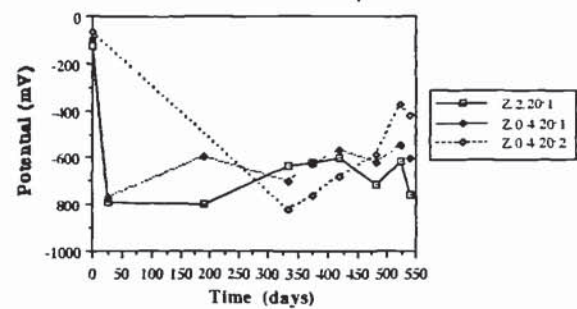


Figure 7.48 Plot of 'off' cathodic potential time Z:20 specimens

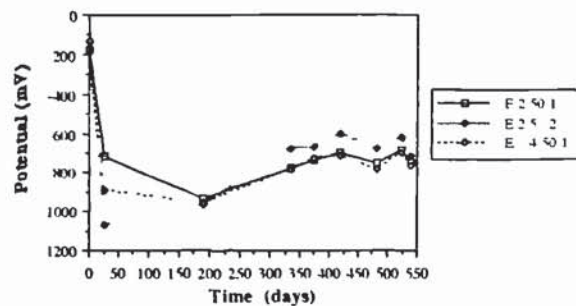


Figure 7.45 Plot of 'off' cathodic potential time E:50 specimens

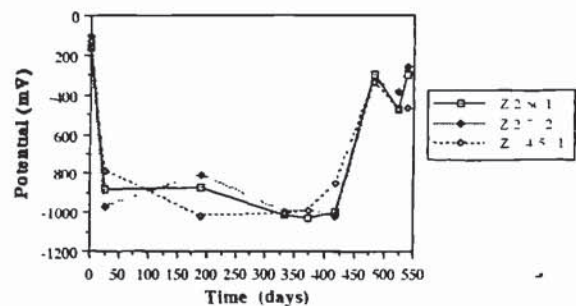


Figure 7.49 Plot of 'off' cathodic potential time Z:50 specimens



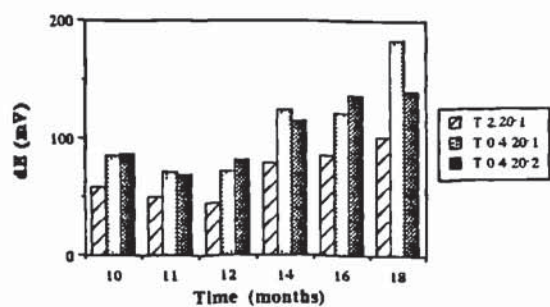


Figure 7.50 Plot of dE/time for T 20 specimens (10-18 months)

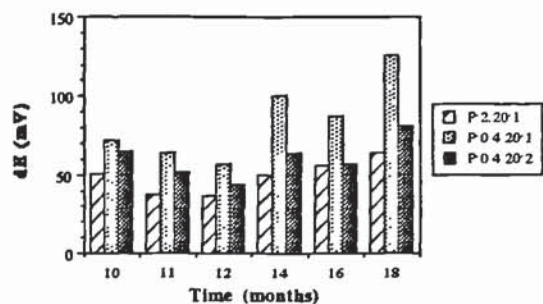


Figure 7.54 Plot of dE/time for P 20 specimens (10-18 months)

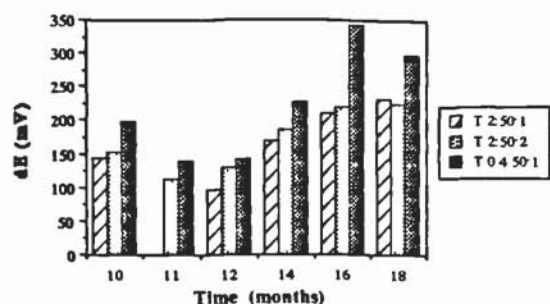


Figure 7.51 Plot of dE/time for T 50 specimens (10-18 months)

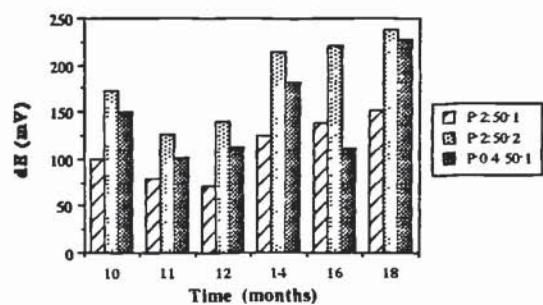


Figure 7.55 Plot of dE/time for P 50 specimens (10-18 months)

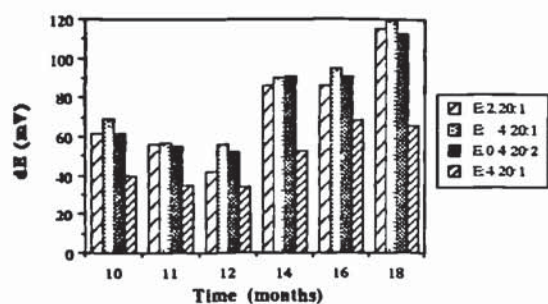


Figure 7.52 Plot of dE/time for E 20 specimens (10-18 months)

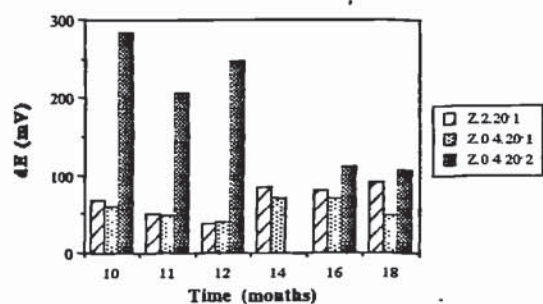


Figure 7.56 Plot of dE/time for Z 20 specimens (10-18 months)

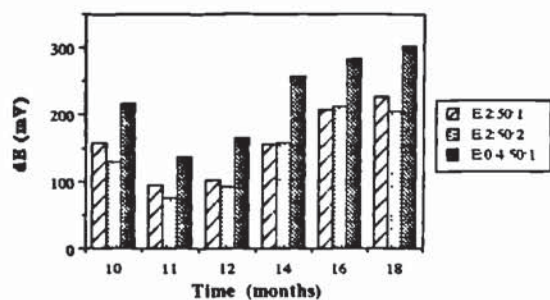


Figure 7.53 Plot of dE/time for E 50 specimens (10-18 months)

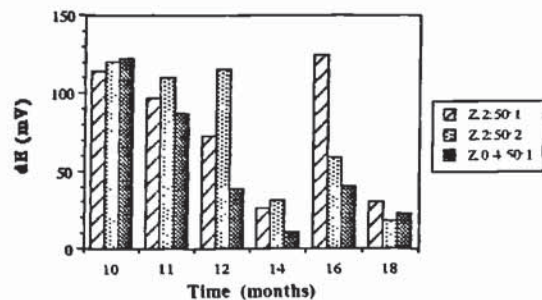


Figure 7.57 Plot of dE/time for Z 50 specimens (10-18 months)

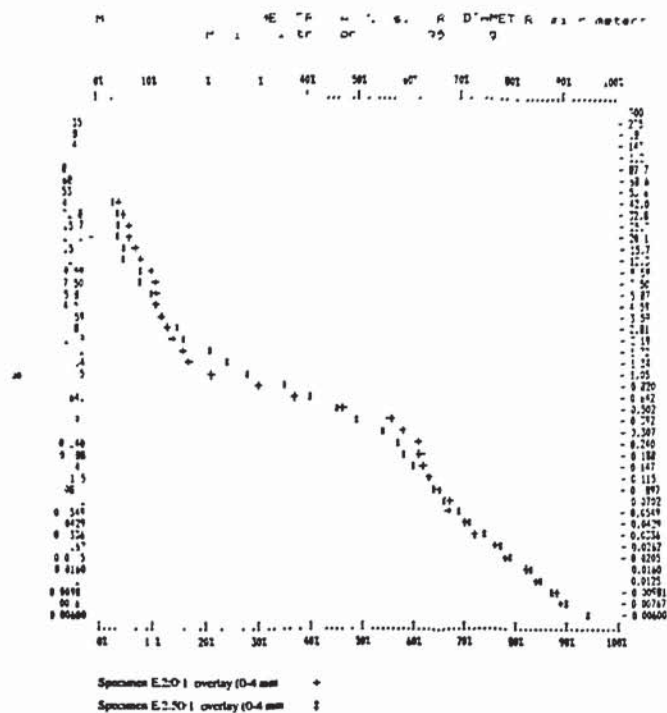


Figure 8.1 Cumulative pore size distribution: Overlay specimens E:2:0:1 & E:2:50:1.

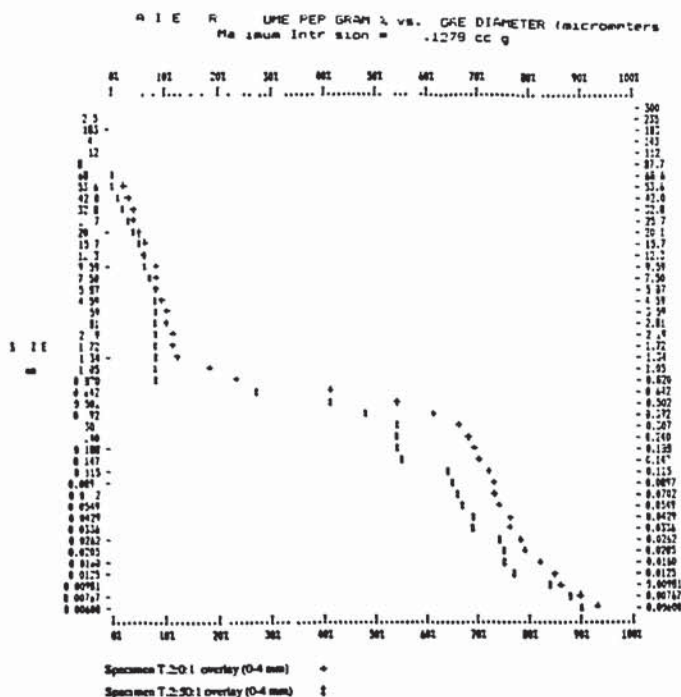


Figure 8.2 Cumulative pore size distribution: Overlay specimens T:2:0:1 & T:2:50:1.



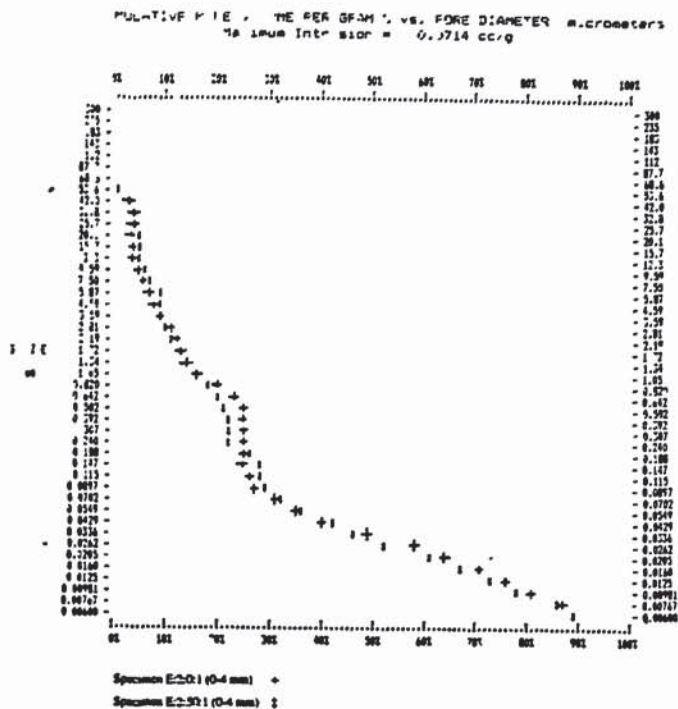


Figure 8.3 Cumulative pore size distribution: Specimens E:2:0:1 & E:2:50:1.

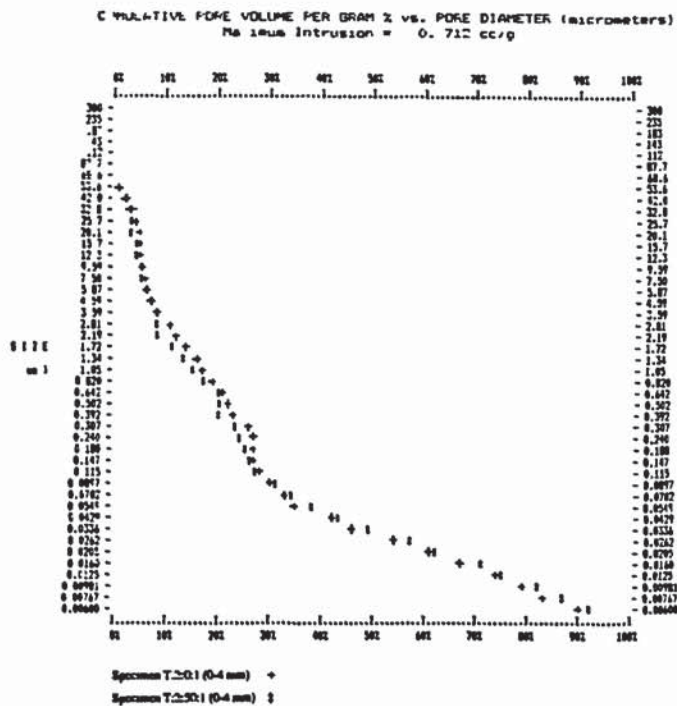


Figure 8.4 Cumulative pore size distribution: Specimens T:2:0:1 & T:2:50:1.

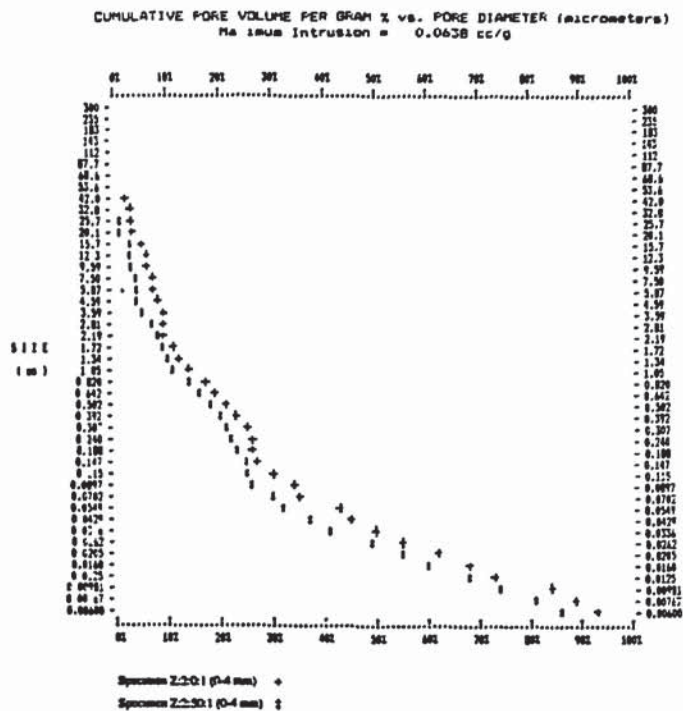


Figure 8.5 Cumulative pore size distribution: Specimens Z:2:0:1 & Z:2:50:1.

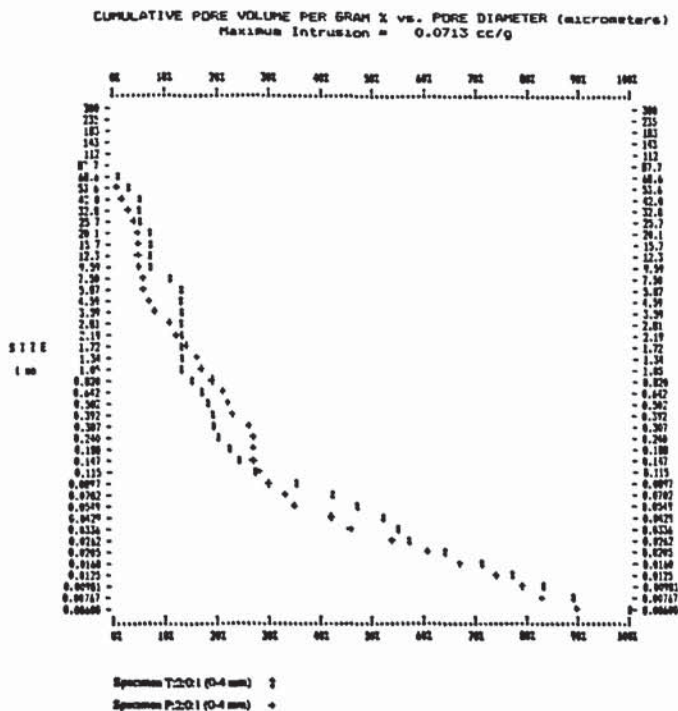


Figure 8.6 Cumulative pore size distribution: Specimens P:2:0:1 & T:2:0:1.



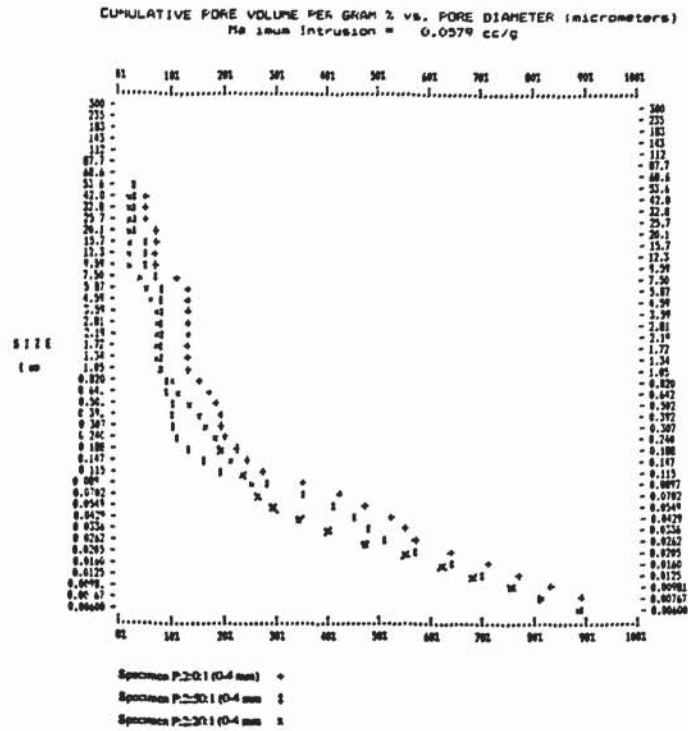


Figure 8.7 Cumulative pore size distribution: Specimens P:2:0:1 & P:2:20:1 & P:2:50:1.

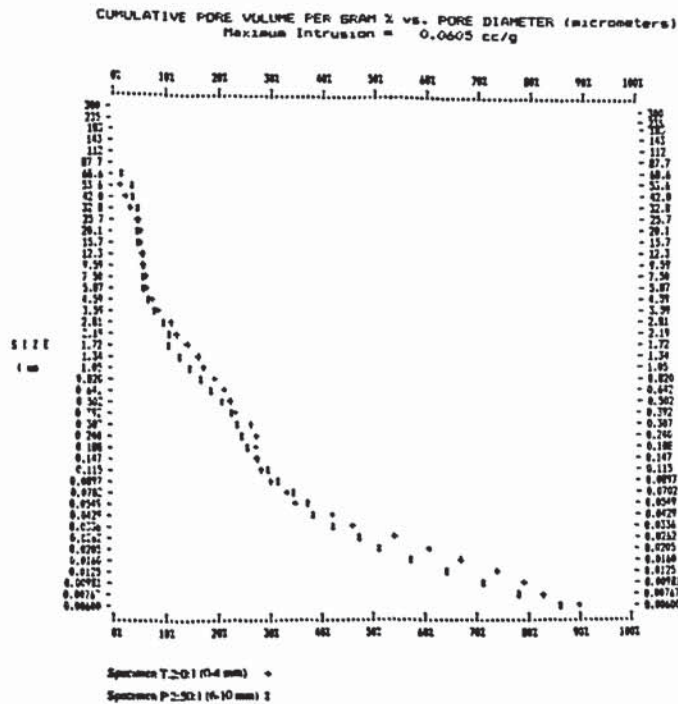


Figure 8.8 Cumulative pore size distribution: Specimens P:2:50:1 & T:2:0:1.

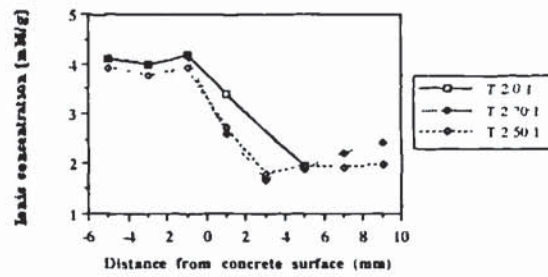


Figure 8.9 Calcium ion concentration profile for anode T

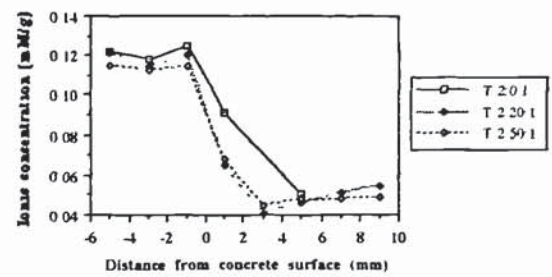


Figure 8.13 Magnesium ion concentration profile for anode T

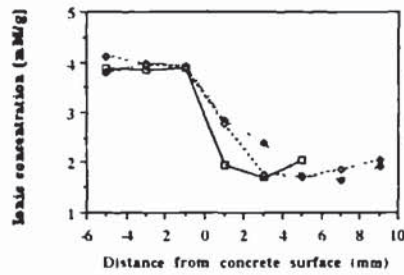


Figure 8.10 Calcium ion concentration profile for anode E

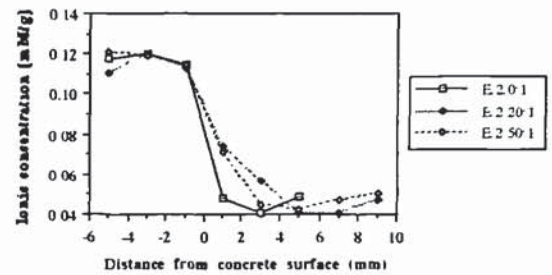


Figure 8.14 Magnesium ion concentration profile for anode E

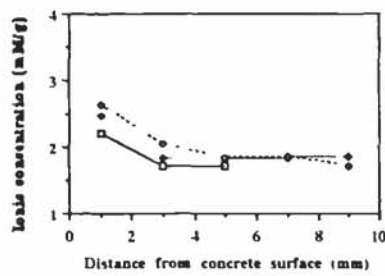


Figure 8.11 Calcium ion concentration profile for anode P

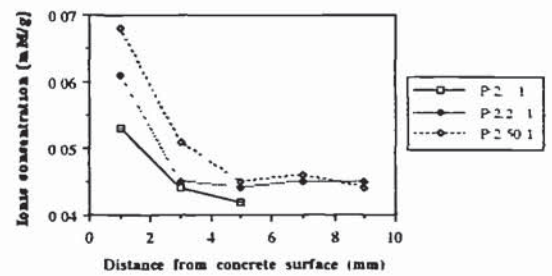


Figure 8.15 Magnesium ion concentration profile for anode P

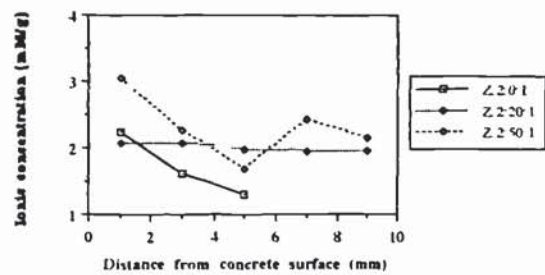


Figure 8.12 Calcium ion concentration profile for anode Z

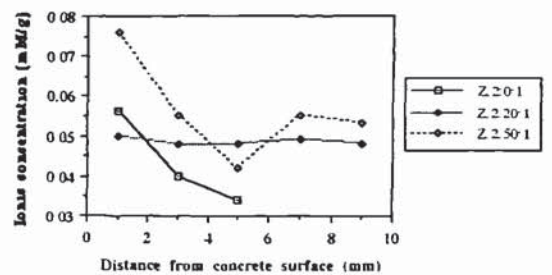


Figure 8.16 Magnesium ion concentration profile for anode Z



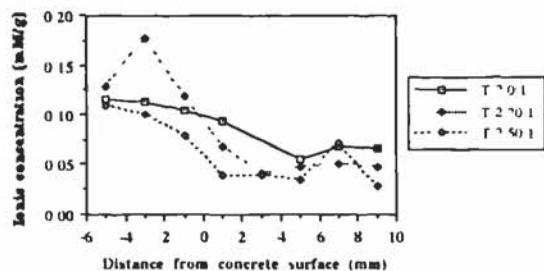


Figure 8.17 Chloride ion concentration profile for anode T

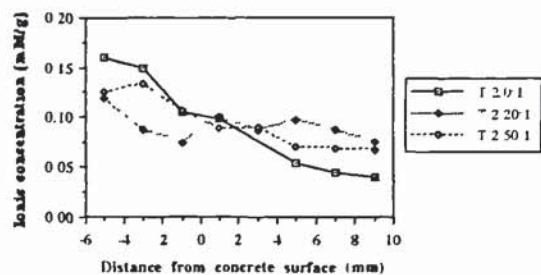


Figure 8.22 Sodium ion concentration profile for anode T

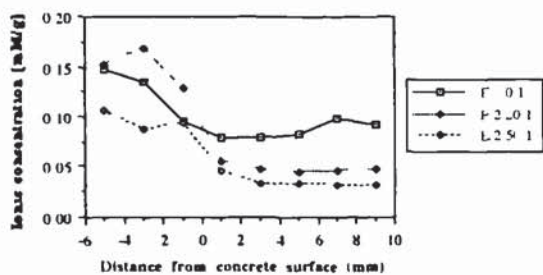


Figure 8.18 Chloride ion concentration profile for anode E

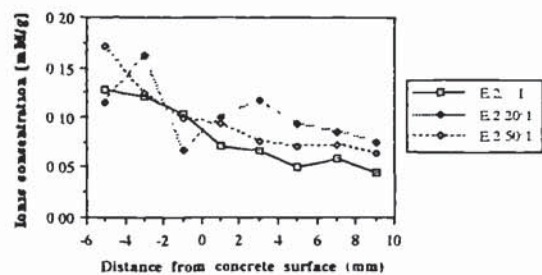


Figure 8.23 Sodium ion concentration profile for anode E

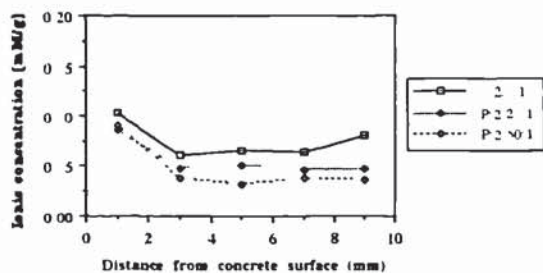


Figure 8.19 Chloride ion concentration profile for anode P

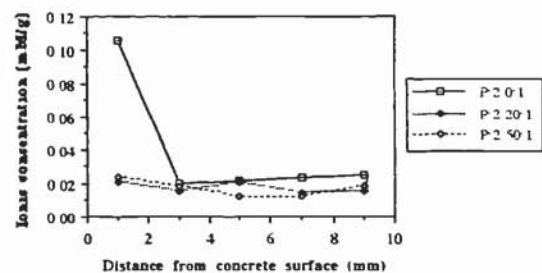


Figure 8.24 Sodium ion concentration profile for anode P

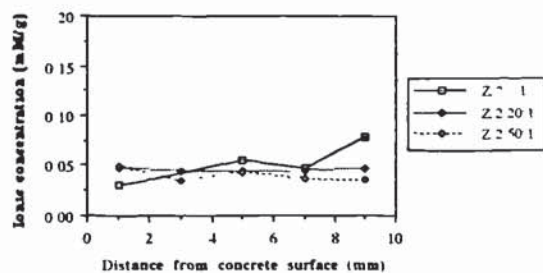


Figure 8.20 Chloride ion concentration profile for anode Z

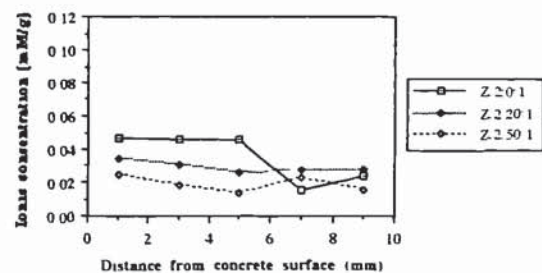


Figure 8.25 Sodium ion concentration profile for anode Z

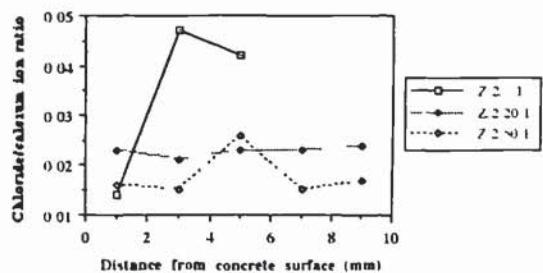


Figure 8.21 Ratio of chloride calcium ion concentrations for anode Z

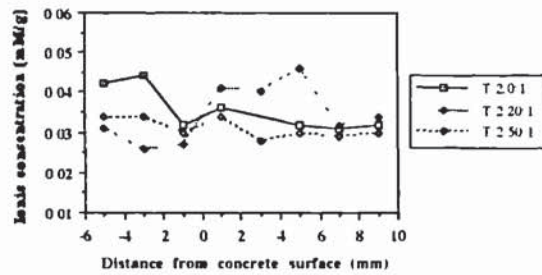


Figure 8.26 Potassium ion concentration profile for anode T

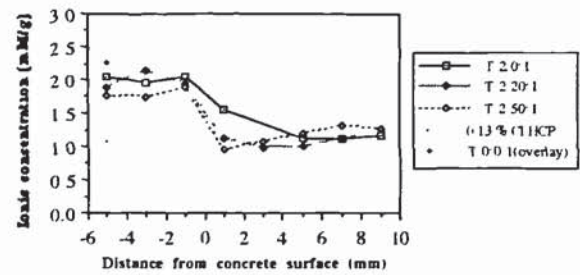


Figure 8.30 Hydroxyl ion concentration profile for anode T

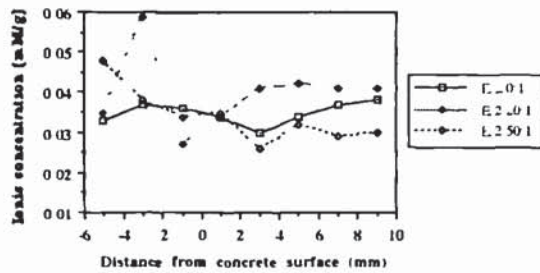


Figure 8.27 Potassium ion concentration profile for anode E

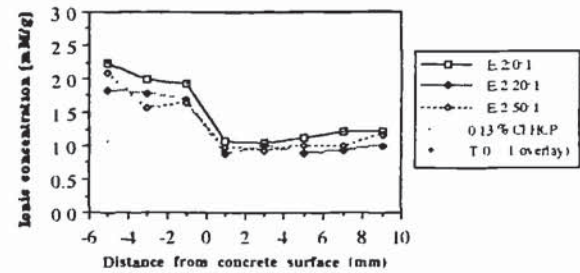


Figure 8.31 Hydroxyl ion concentration profile for anode E

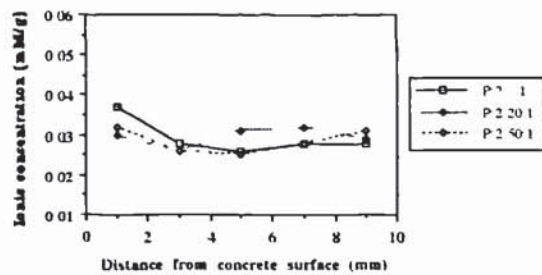


Figure 8.28 Potassium ion concentration profile for anode P

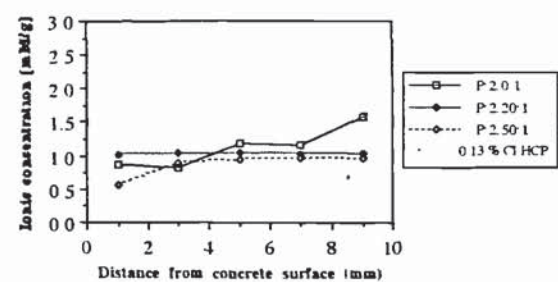


Figure 8.32 Hydroxyl ion concentration profile for anode P

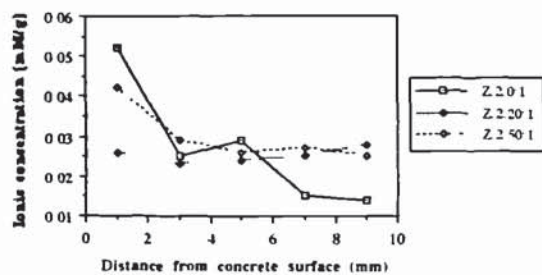


Figure 8.29 Potassium ion concentration profile for anode Z

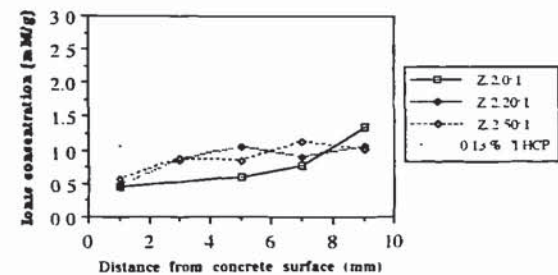


Figure 8.33 Hydroxyl ion concentration profile for anode Z



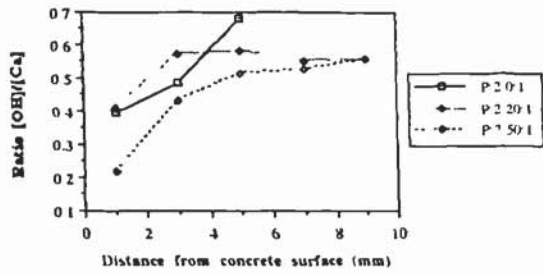


Figure 8.34 Ratio of hydroxyl calcium ion concentrations for anode P

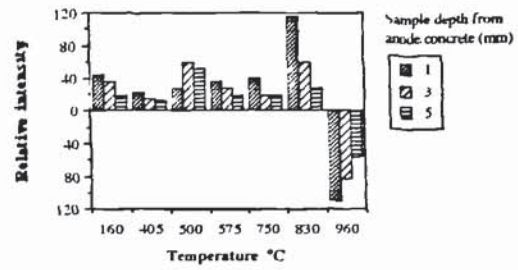


Figure 8.39 Summary of DTA peaks: Specimen Z:2:50:1

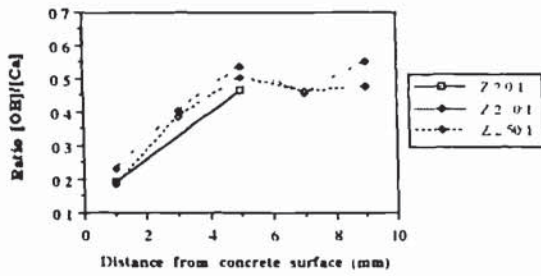


Figure 8.35 Ratio of hydroxyl calcium ion concentrations for anode Z

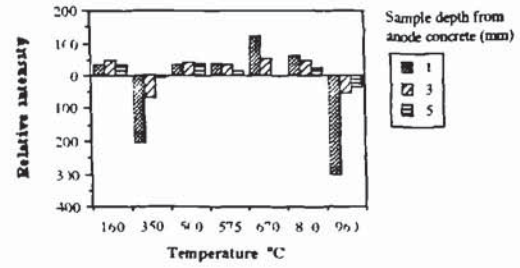


Figure 8.40 Summary of DTA peaks: Specimen P:2:0:1

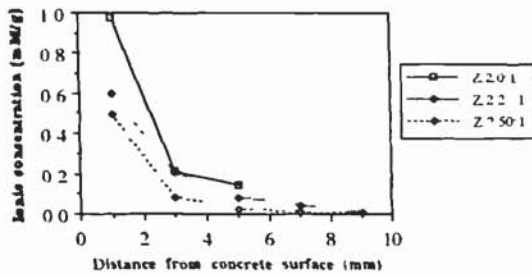


Figure 8.36 Zinc ion concentration profile for anode Z

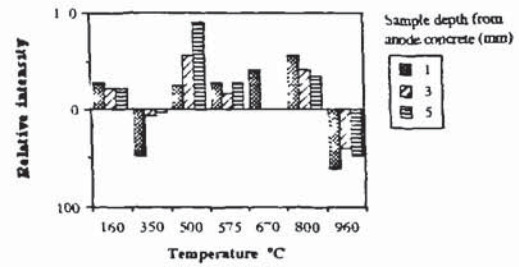


Figure 8.41 Summary of DTA peaks: Specimen P:2:20:1

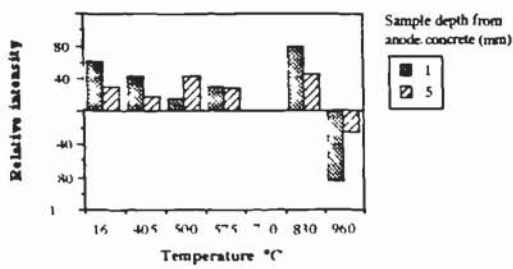


Figure 8.37 Summary of DTA peaks: Specimen Z:2:0:1

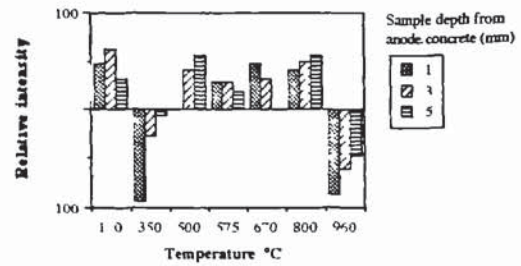


Figure 8.42 Summary of DTA peaks: Specimen P:2:50:1

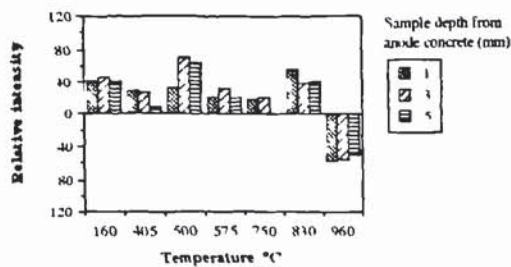


Figure 8.38 Summary of DTA peaks: Specimen Z:2:20:1

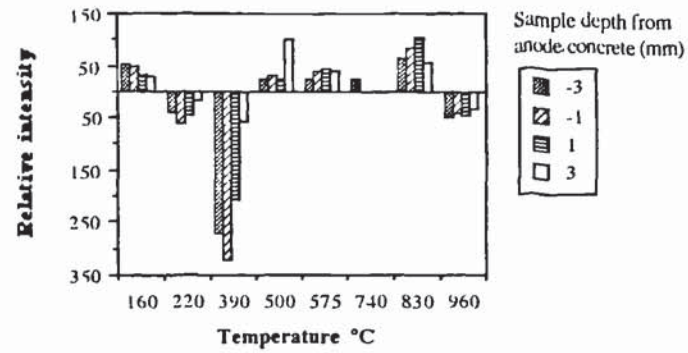


Figure 8.43 Summary of DTA peaks: Specimen T:2:0:1

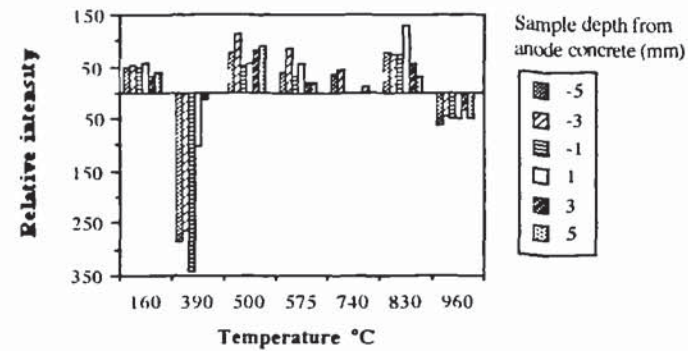


Figure 8.44 Summary of DTA peaks: Specimen T:2:20:1

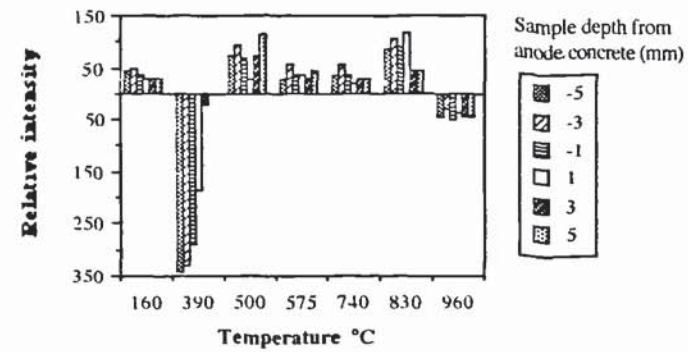


Figure 8.45 Summary of DTA peaks: Specimen T:2:50:1

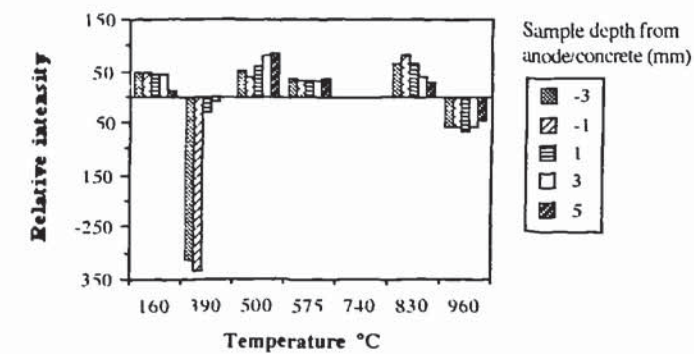


Figure 8.46 Summary of DTA peaks: Specimen E:2:0:1



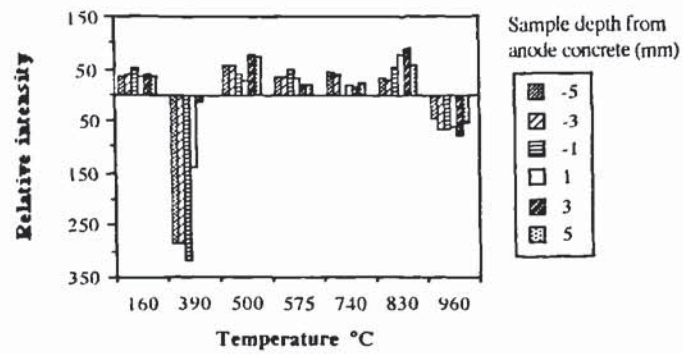


Figure 8.47 Summary of DTA peaks: Specimen E:2:20:1

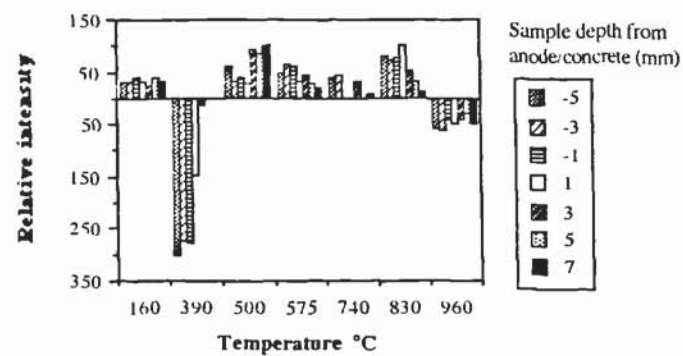


Figure 8.48 Summary of DTA peaks: Specimen E:2:50:1

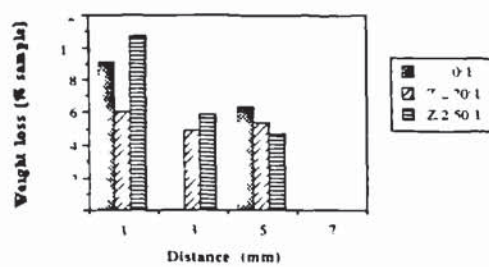


Figure 8.49 Sample weight loss during DTA: Z anode

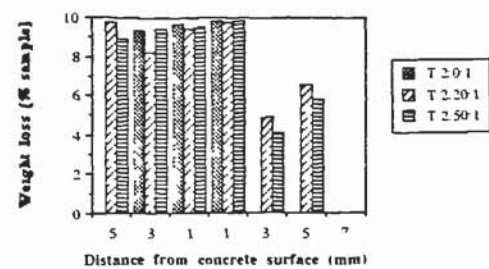


Figure 8.51 Sample weight loss during DTA: T anode

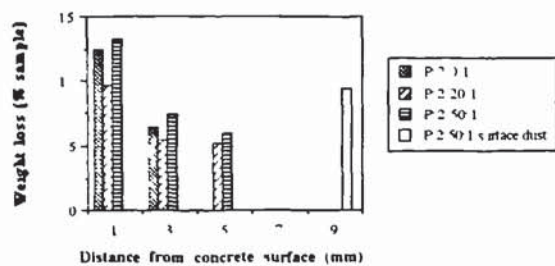


Figure 8.50 Sample weight loss during DTA: P anode

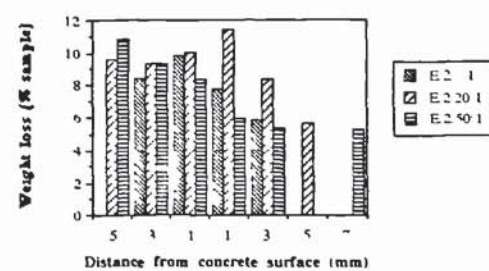


Figure 8.52 Sample weight loss during DTA: E anode

## **Appendix E. List of abbreviations**

The following abbreviations have been used throughout this thesis:

A	amperes
A <sub>sa</sub>	anode surface area
ASR	alkali-silica reaction
ATR	attenuated total reflectance(spectroscopy)
Å	angstroms
β <sub>a</sub>	anodic Tafel constant
β <sub>c</sub>	cathodic Tafel constant
C <sub>sa</sub>	cathode surface area
CD	current density
cm	centimetre
CP	cathodic protection
CS	(from the) Concrete Surface
CSE	copper/saturated copper sulphate reference electrode
d	spacing of crystal planes
dE	potential drop attributable to IR-error on current interruption
DTA	differential thermal analysis
DVM	(high impedance) digital volt meter
E <sub>a</sub>	anode potential
E <sub>c</sub>	cathode potential
E <sub>corr</sub>	corrosion potential
EDXA	energy dispersive X-ray analysis
E <sub>off</sub>	cathode potential with CP current off
E <sub>on</sub>	cathode potential with CP current on
E <sup>θ</sup>	standard reduction potential (for ions at unit activity at 25°C)
FT-IR	fourier transform infrared (spectroscopy)
g	gramme
HCP	hardened cement paste
i <sub>corr</sub>	corrosion current
ICP	inductively coupled plasma spectroscopy
IR	ohmic drop
θ	Bragg angle of reflectance/incidence
K	Water permeability coefficient
Kg	kilogram
M	moles
m	metre



mA	milli-ampere
MIP	mercury intrusion porosimetry
mM	milli-moles
mm	milli-metre
mV	milli-volt
NDT	non-destructive test
OPC	ordinary portland cement
pH	measure of acidity/alkalinity on a scale of 1 to 14, neutral is pH7
PSD	pore size distribution
PTFE	polytetrafluoroethylene (Teflon)
RI	relative intensity (of X-ray diffraction peak)
Rp	polarisation resistance
rpm	revolutions per minute
s	second
SBR	Styrene-butadiene- rubber
SCE	standard calomel reference electrode
SEM	scanning electron microscopy
SHE	standard hydrogen reference electrode
USPV	ultra-sonic pulse velocity
V	volts
$\Omega$	ohm
wt.	by weight
XP	crossed polarised light
XRD	X-ray diffraction
$\mu$ A	micro-amp
$\mu$ m	micro-metre

#### **Additional abbreviations for cement minerals**

C <sub>3</sub> S	tricalcium silicate
C <sub>2</sub> S	dicalcium silicate
C <sub>3</sub> A	tricalcium aluminate
C <sub>4</sub> AF	tetracalcium aluminoferrite
Na <sub>2</sub> O	sodium oxide
K <sub>2</sub> O	potassium oxide
CSH	calcium-silicate-hydrate gel
C <sub>4</sub> AH <sub>13</sub>	calcium aluminate trisulphate (ettringite)
Ca(OH) <sub>2</sub>	calcium hydroxide (portlandite)

#### **Additional abbreviations used in Chapter 4**

$E_m$	maximum potential (during anodic polarisation scan)
$E_n$	potential at which activation polarisation (Tafel behaviour) predominates
$E_t$	potential at which concentration polarisation predominates
$E_{pp}$	passivation potential
$E_{tp}$	trans-passive potential (at which passive film becomes disrupted)
$i_m$	Maximum current density (during anodic polarisation scan)
$i_{crit}$	current density at which passivation potential occurs
$i_l$	passive film leakage current density
$i_t$	current density at which concentration polarisation predominates
$i_n$	current density at which activation polarisation (Tafel behaviour) predominates

#### **Additional abbreviations used in Appendix 3.8**

$dt$	waiting period before “instant-off” potential measurement
$E_{on}^i$	‘on potential’ obtained immediately prior to a 0.1 second instant-off measurement. (test 3)
$E_{on}^f$	‘on potential’ at the end of the multiple measurement sequence (test 3)